San Joaquin Renewables Class VI Permit Application Narrative Permit Application Report

Prepared for

San Joaquin Renewables LLC
McFarland, California

Submitted to

U.S. Environmental Protection Agency Region 9
San Francisco, California

Prepared by

DBS&A
Daniel B. Stephens & Associates, Inc.
a Geo-Logic Company

43 Randolph Road, #129
Silver Spring, Maryland 20904
www.dbstephens.com
Project # DB19.1252.SS

September 8, 2022

CLASS VI PERMIT APPLICATION NARRATIVE
40 CFR 146.82(a)

SAN JOAQUIN RENEWABLES

1. Project Background and Contact Information

San Joaquin Renewables, LLC (SJR) is submitting this application to the U.S. Environmental Protection Agency Region 9 (U.S. EPA) for an Underground Injection Control (UIC) Class VI permit for a planned facility located in McFarland, California. This narrative permit application report is one of several separate documents submitted to the U.S. EPA Geologic Sequestration Data Tool (GSDT), and includes required information regarding the planned facility, geology and hydrogeology of the planned injection Site, planned injection operating conditions, and injection well design. Additional documents submitted in support of this permit application are listed in the subsequent sections. Together, these documents demonstrate that the planned facility will comply with the U.S. EPA UIC Class VI regulations.

This permit application and associated documents were prepared by a team including Daniel B. Stephens & Associates, Inc. (DBS&A), Driltek, Finsterle Geoconsulting, Keystone Diversified Energy, Inc. (KDEI), and Best Core Services.

1.1. Facility Overview

SJR will build, own, and operate a facility in McFarland, California, that will convert agricultural waste biomass into about 80 thousand gasoline gallon-equivalents of natural gas (RNG) per day ("the Facility"). The Facility is planned to be located at the southwest corner of the intersection of Elmo Highway and Melcher Road, at Township 26S Range 25E Section 9, and the latitude-longitude of 35.688330, -119.276642. The Facility will not be located on Indian Lands. The Standard Industrial Classification (SIC) code for the Facility includes 2813 (Industrial Gases).

RNG will be transported by Southern California Gas (SoCalGas) pipelines to be used as vehicle fuel throughout California. The project is expected to be complete 18 months after construction begins.

Figure 1-1 presents the planned facility process to convert orchard wastes to RNG. Feedstock includes waste wood, almond shells, and pistachio shells from agricultural facilities in the San Joaquin Valley. In gasification, the feedstock is conveyed to the gasifier convertor where it is converted at high temperature and pressure into synthesis gas (syngas) in a few seconds. The syngas contains useful components such as hydrogen, carbon monoxide, and methane that are subsequently upgraded into pipeline quality natural gas. In the Gas Cleaning and Upgrading step, a heat exchanger lowers the syngas temperature prior to separating biochar and other constituents from the gas.

Natural gas will be compressed and injected in the natural gas pipeline and used in compressed natural gas (CNG) fueled vehicles. Renewable natural gas used in conjunction with low-nitrogen oxide (NOx) internal combustion engines provide an environmentally superior alternative to diesel engines. The conversion process does not consume water and will actually produce a small quantity of irrigation quality water.

The gasification process will produce several coproducts including biochar, argon, liquid nitrogen, heat, and carbon dioxide. Biochar will be sold as an agricultural lime substitute, fertilizer, or fertilizer ingredient that improves water and nutrient retention for enhanced crop growth. Argon and liquid nitrogen will be sold for industrial use. Waste process heat will be used to generate steam and electricity to reduce the plant's utility usage. Carbon dioxide will be injected underground for geologic sequestration.

The facility will have a positive air-quality impact by significantly reducing emissions of NOx, carbon monoxide and volatile organic compounds (VOCs) as compared to the current practice of pile burning orchard wastes. The RNG produced is considered a renewable cellulosic biofuel because it is produced from woody biomass. Because the gas is renewable and used for transportation, SJR will participate in both the US EPA's Renewable Fuel Standard and California's Low Carbon Fuel Standard.

The plant will normally operate 24 hours per day, 7 days per week, except for planned maintenance, outages, and any unplanned shutdowns. The plant will create 45-50 high paying full time jobs. Many employees will work normal business hours. Some maintenance and operations staff will work shifts to support around-the-clock operations. The renewable natural gas produced in California will displace out-of-state sourced fuels.

Appendix A presents a Site Plan of the planned facility prepared by SJR. The injection well will be located on the northeastern portion of the property. Additional infrastructure will include a natural gas kiosk and pipeline interconnection, renewable natural gas fueling station, electric power generation island, process area, wood yard, bio-char storage, truck dump stations, shell storage area, and stormwater percolation pond. A SoCalGas natural gas transmission line runs north on the west edge of Melcher Road, and the facility will inject the product renewable natural gas into that pipeline.

1.2. Injection Project Overview

The Facility will be located in the San Joaquin Valley of the Central Valley in central California (Figure 1-2). The Central Valley is recognized by the U.S. Department of Energy Carbon Sequestration Atlas (2015) as an assessed Saline Formation for carbon storage, and it comprises the largest assessed Saline formation within U.S. EPA Region 9 (Figure 1-2). The Facility will be located on 80 acres at the southwest corner of intersection of Elmo Highway and Melcher Road, approximately 2 miles west of the City of McFarland proper and immediately north of a parcel also incorporated as part of the City of McFarland (Figure 1-3).

The project Area of Review (AoR) delineation has been determined based on the results of numerical flow modeling and pressure calculations, as described in the Facility AoR and Corrective Action Plan. The AoR delineation is shown on Figure 1-3 and several additional maps in this report. The AoR is 1.5 square miles and encompasses the Facility and surrounding agricultural areas.

The Facility plans on generating and injecting 1,200 tons per day of carbon dioxide per year for a period of 15 years based on SJR's energy and material balance analyses in planned injection well SJR-I1. As discussed in more detail below the planned injection formation is the Vedder

Formation sandstone ("injection zone"), located approximately 7,780 feet below ground at the Facility location. The Freeman-Jewett Formation, comprised of shale and mudstone, overlies the Vedder sandstone and will serve as the primary seal ("confining zone").

Carbon dioxide will be generated on the Facility property and injected at the property, with no carbon dioxide injectate pipelines extending off of the SJR parcel. Appendix B is a carbon dioxide phase study for the planned facility. Carbon dioxide stream at the surface will remain in the liquid phase until it becomes supercritical at approximately 2,400 feet below the surface, after which it remains in the supercritical phase.

1.3. Facility Permitting Information

Table 1-1 presents a list of facility permits and current status. In addition to the Class VI permit, other facility permits include a Conditional Use Permit from the City of McFarland, California Environmental Quality Act (CEQA) determination and review, local building permits, authority to construct and authority to operate from the San Joaquin Valley Air Pollution Control District, a water discharge permit (National Pollution Discharge Elimination System [NPDES]), Water Rights Registration, and stormwater permits from the California Central Valley Regional Water Quality Control Board, a well permit for a water-supply well from the Kern County Public Health Services Department, and registration as a foreign corporation with the California Secretary of State.

1.4. Public Outreach and Environmental Justice

SJR is committed to public outreach to the local community in order to educate stakeholders regarding the planned facility and address any community concerns. To date SJR has held two public meetings at the McFarland Veterans Community Center, in May and July 2021, and intends to have more before the project breaks ground. SJR has also met separately with representatives from the Association of Irritated Residents (a California non-profit corporation based in Kern County formed to advocate for clean air and environmental justice in San Joaquin Valley communities), and the Center for Race, Poverty, and the Environment (CRPE). During these meetings SJR has communicated that the motor fuel produced will be carbon negative, that SJR will prevent pollutants created by open burning of orchard wood and the use of diesel fuel (eliminating over 1,700 tons of particulates, 5,200 tons of nitrous oxides, 25,000 tons of carbon monoxide, and 1.4 million tons of carbon dioxide per year), biochar from the project will improve soil health, and the facility will be water neutral. The facility will also employ 50 full-time employees and create other indirect jobs in the community.

GSDT Submission - Project Background and Contact Information

GSDT Module: Project Information Tracking
Tab(s): General Information tab; Facility Information and Owner/Operator Information tab

Please use the checkbox(es) to verify the following information was submitted to the GSDT:
☒ Required project and facility details ***[40 CFR 146.82(a)(1)]***

2. Site Characterization

Geologic and hydrogeologic data and properties described in this section are used to develop a conceptual model of the proposed carbon dioxide storage Site. The conceptual model is a fundamental part of this Class VI Permit application for the construction and operation of the carbon dioxide injection well. This section provides both regional and local information about the injection zone (the geologic formation that will receive the carbon dioxide) and the confining zones (the geologic formations that will act as a barrier to fluid migration). This information is provided to demonstrate that the proposed Kern County carbon dioxide storage Site is a suitable geologic system for carbon dioxide storage, and the confining zones have sufficient extent and integrity to contain the injected carbon dioxide and displaced formation fluids so as to ensure the protection of nearby underground sources of drinking water (USDWs).

This section provides background information in support of the conceptual model. The information in this section is also critical to the design, construction, and operation of the injection and monitoring wells and in the subsequent well plugging, after the Site has completed carbon dioxide injection.

2.1. Regional Geology, Hydrogeology, and Local Structural Geology

SJR proposes to inject carbon dioxide into the Oligocene Vedder Formation sandstone. The Vedder Formation sandstone is comprised of up to five sand units and is overlain locally by a thin sandstone of the Pyramid Hill Formation. The Pyramid Hill and Vedder are the thickest and most widespread potential carbon dioxide injection Formations in the San Joaquin Valley of California, and at the McFarland Kern County Site (Figure 2-1). The Vedder Formation is an oil productive reservoir in several oil fields to the east and south of the McFarland location. As described below, the Vedder Formation porosity and permeability make it ideal for injection.

The confining zone for the proposed injection zone consists of the Freeman Jewett Formation, a Miocene shale and mudstone. In addition, the Round Mountain silt and overlying Fruitvale Shale (tight Miocene units) overlie the Olcese Formation Sandstone and are located beneath the overlying USDWs.

The combination of the Round Mountain and Fruitvale Formations comprises a significant regional confining zone for sequestration in California. The Walker Formation sandstone and shale unit of Eocene to Oligocene age underlie the Vedder in the vicinity of the McFarland Site. There is a shale in the basal Vedder (termed Vedder 4) that separates the Vedder 4 sand from the Walker. Impermeable Mesozoic-Tertiary-aged basement rocks (granite) underlie the stratigraphic section in the McFarland area and form a no-flow boundary.

2.1.1. Regional Geology

Regional geology of the Central Valley of California is well documented from wells and borings drilled in conjunction with hydrocarbon exploration and oilfield development, aquifer development and use. Related data are largely publicly available through the California State Geological Survey (CGS), the U.S. Geological Survey (USGS) and the California Geologic Energy Management Division (CalGEM). In addition, the U.S. Department of Energy (DOE) has sponsored several studies to evaluate subsurface strata in the San Joaquin and adjacent areas

as possible targets for the containment of anthropogenic carbon dioxide. This section describes the regional geology, including stratigraphy, structure, and seismicity.

USGS previously carried out an in-depth analysis of the petroleum systems of the San Joaquin Basin Province (Gautier, et al., 2007; "Professional Paper 1713"). Professional Paper 1713 addresses key elements of the petroleum systems models of the basin and provides a summary of stratigraphic units, hydrocarbon source units, potential oil reservoirs, and their relationship in time and space in the Basin. Petroleum system analysis from the USGS provides insights into basin geometry and fluid flow within units that occur on the flanks of the basin versus in the center of the Basin. Hydrocarbon analysis provides a well-supported framework for basin development, fill history, hydrocarbon generation, hydrocarbon movement and barriers to fluid flow within key stratigraphic horizons.

While the whole San Joaquin Basin Province is an enclosed system (Figure 2-2), the distribution of the key injection and confinement units within the Basin is of upmost importance. The southern portion of the Basin Province is the target for this permit application (Figure 2-3). Up to 30,000 feet of Cenozoic strata overlies west-sloping Mesozoic granite basement within the San Joaquin Basin Province (Figure 2-4). Basin fill thins eastward onto the granite basement. Figure 2-5 is a west-to-east cross section through the McFarland Site illustrating the wedging relationship of the stratigraphic units overlying west-dipping granite basement. As illustrated in Figure 2-5, the western margin of the San Joaquin Basin is characterized as a fold and thrust belt. Franciscan Formation (Cenozoic) subduction complex shales, cherts, and volcanic rocks that underwent compression during subduction and subsequently low-grade metamorphism during trans-pression associated with San Andreas Fault transform motion are the core of the anticlinal trend. For the eastern San Joaquin, the granite basement has not undergone significant compression. The forearc basin that formed on the combined Franciscan and granite basement provided significant accommodation for detritus to be shed from the Sierran uplift to the east and to a lesser extent from emergent uplands to the west.

Figure 2-6 is a west-to-east schematic chronostratigraphic cross section through the southern San Joaquin Basin illustrating the progradational nature of the Oligocene through Miocene strata that onlaps Mesozoic granite basement. This figure includes indications of the chronostratigraphic units that are depicted in Figures 2-7 to 2-9. Figure 2-7 is a paleogeographic map of the southern San Joaquin from the late Oligocene (~28 Ma) from Boote et al. (2001). The Vedder Sand Formation is an east to west prograding shallow marine shelf system filling the basin from the Sierra Nevada highlands in the east. Shelf edge Vedder sands transition to proximal and distal lowstand wedge sands westward, and eventually into lower Santos Shale at the axis of the basin. Figure 2-8 displays a paleogeographic map of the southern San Joaquin from the early Miocene (~18-20 Ma) from Nilsen, Reid, and Boote (2001). The middle Olcese Sand Formation is an east-to-west prograding shallow marine shelf system filling the basin from the Sierra Nevada highlands in the east. Shelf edge Olcese sands transition to slope and basin floor muds of the Santos Shale westward. Figure 2-9 is a paleogeographic map of the southern San Joaquin from the middle Miocene (~16.5 Ma) from Nilsen, Reid, and Boote (2001). The upper Olcese Sand Formation is an east to west prograding shallow marine shelf system filling the basin from the Serra Nevada highlands in the east. Shelf edge upper Olcese sands transition to slope and basin floor muds of the Media to lower Monterey (Gould) Shale westward. The paleogeographic maps illustrate the shore-line parallel nature of these key formations, their westward extent and

transition into confining shales, and their updip termination into fluvial and alluvial units (Walker Formation).

Figure 2-10 is a focused view on the stratigraphic column shown in Figure 2-1 that displays the relative lateral extent of the Vedder and Olcese sands and the Freeman Jewett Silt, Round Mountain Silt, and Fruitvale Shale of the Antelope-Stevens petroleum system (purple outline) in the southern portion of the Basin Province. Appendix C includes a table that displays the petroleum production by reservoir unit for the Antelope-Stevens petroleum system. Within the vicinity of the Site, only three fields are charged within this petroleum system: Poso Creek, Dyer Creek, and Mount Poso. This data supports the eastward migration of hydrocarbons (oil and gas) into key reservoir units (Vedder, Jewett Sand). The Jewett and Vedder Sands are modest producers while the Olcese Sands are minor petroleum producers on the east side of the basin. Figure 2-11 is a map of the distribution of the source terrain and the charged oil fields associated with the Antelope-Stevens petroleum system in the southern San Joaquin Basin Province (Magoon et al., 2009). Within the vicinity of the Site, three fields in the area are part of this system (Poso Creek, Dyer Creek, Mount Poso). To reach these fields, charge migrated nearly 40 miles from the southern oil generation kitchen.

The northern part of the project vicinity contains the Tumey-Temblor petroleum system hydrocarbons (Figure 2-12). Only two fields (Jasmin and Jasmin West) are part of this system (Figure 2-13), which has the bulk of its coverage in the central San Joaquin Basin Province (SJBP; Magoon et al., 2009). The project vicinity covers the northern portion of the Southern SJBP and the southern portion of the Central SJBP. The stratigraphy from the Southern SJBP was used to characterize the project area strata. The units from the Central SJBP are not present in the vicinity. Appendix C includes a table that displays the petroleum production by reservoir unit for the Tumey-Temblor petroleum system.

2.1.2. Major Stratigraphic Units

The following discussion includes the regional characteristics of the Oligocene Vedder Sands and the Miocene Olcese Sands, the confining zone immediately above the main target injection zone (Freeman-Jewett) and the additional fine-grained units (Round Mountain, and Fruitvale) that overlie the Olcese. Depth to the Mesozoic granitic basement that underlies the primary carbon dioxide injection zone is discussed in the local vicinity of the Site in Section 2.2.

Vedder Formation

Figure 2-14 presents a structure contour map of top of the Vedder Formation from Wagoner (2009). The east side of the San Joaquin Basin in the vicinity of the injection Site (red rectangle) dips at a relatively constant four degrees to the west.

Figure 2-15 displays cross section 1 from Wagoner (2009), trending SW-NW (left to right) displaying correlated spontaneous potential (SP) well logs from oil and gas exploration wells. Units mapped by Wagoner are labeled on the cross section. The Pond Fault cuts both the KCL A83-35 and Tenneco-Sun 11X wells. The Vedder overlies the Tumey Shale that in turn overlies the Famosa Sand. Though not labeled, both of these units onlap granite basement eastward. Figure 2-16 is a focused view of Wagoner (2009) Cross Section 1 displaying correlated SP well logs from oil and gas exploration wells. Units mapped by Wagoner are labeled on the cross

section. Key sand units of the Vedder are correlated from the SP logs. The Pond Fault offsets the Vedder formation (contoured on Figure 2-14) with nearly 200 meters of throw between the KCL A83-35 and Tenneco-Sun 11X wells.

Figure 2-17 displays well and seismic data exercise locations for the area. Figure 2-18 displays a stratigraphic type log from the Southern San Joaquin Basin, California, highlighting the Santa Margarita through Vedder Formations. Location of the Santa Margarita well (Well #1) is shown as a red square on Figure 2-17 (Hewlett and Tye, 2015). Appendix C includes a table of hydrogeologic properties for major stratigraphic units in the area (from Birkholzer, et al., 2011), including those for the Vedder and Olcese Sands.

Miocene Freeman-Jewett Silt, Round Mountain Silt, and Fruitvale Shale Formations

Figure 2-19 presents an interpreted south-to-north oriented wireline-log cross section from Hewlett and Tye (2015). Wells 2 to 6 were correlated to the seismic data with synthetic seismograms (not shown). Note cycles Z, A, B, and C, and the variable wireline-log character of the parasequences. Facies-association interpretations are based on core data. The Vedder and overlying Freeman-Jewett are depicted in salmon and green. The sealing nature of the Freeman-Jewett over the Vedder is illustrated in this section.

Figure 2-20 (top image) depicts five Tertiary-age stratigraphic sequences and their interpreted systems tracts in the eastern San Joaquin Basin (Hewlett et al., 2014). The relationship between Vedder Sand and Freeman Silt is highlighted with a red arrow across the stratigraphic interval. This transition is overlain by a similar interval represented by the Olcese Sand and the overlying Round Mountain Silt. Figure 2-20 (bottom image) displays the lithologic interpretation of the five Tertiary-age stratigraphic sequences (Hewlett et al., 2014). The red arrow denotes the Vedder Sand to Freeman Silt stratigraphic interval. Reservoirs formed in sandstones deposited under conditions of shoreline progradation and retrogradation and transgressive-shelf deposits are capped by highstand-systems tract deposits (i.e., Freeman Silt) that form the overlying seals (Hewlett and Tye, 2015).

Figure 2-21 presents a west-to-east oriented wireline-log cross section intersecting the ARCO Round Mountain No. 1 well (third well from the right). Ten parasequences in the transgressive-systems tract are noted by the upward-coarsening SP log character. Parasequences are overlain by flooding surfaces and marine mudstones. The transgressive-systems tract in each well displays a retrogradational stacking pattern: parasequences thin, and mudstone content increases upward. This transition ensures sands are covered by confining silts and shales.

Appendix C includes a table that contains rock property data from Birkholzer, et al., 2011, including those for the Temblor Freeman (Freeman Silt) and Fruitvale-Round Mountain shale.

2.1.3. Seismic Profile Interpretation

Analysis of reflection seismic data and historical oil and gas wells from the vicinity of the injection Site was undertaken to map each stratigraphic unit in the area (reservoir and containment) and to map the faults that transect the main injection interval (Vedder Sand Formation). Seismic interpretation was performed by Keystone Diversified Energy Inc. (KDEI),

overseen by a California Professional Geophysicist. KDEI's full seismic interpretation report is included in Appendix D, and is briefly summarized here.

Seismic interpretation included obtaining and reviewing existing seismic data; integrating seismic data and well data on formation elevations; mapping faults to determine fault type, throw, and formation offset; producing maps at key formation tops/bottoms; producing a digital grid file; and producing point file location data for pertinent faults and fault intersections with various formations.

Final products from the analysis included interpreted seismic panels, fault delineation, depth horizon maps, isochore maps for relevant horizons, and digital files for all of the above.

The entire area examined by the full scale geologic model is 3,200 square miles (Appendix D Figure 2), overlain by a 200 x 200 meter grid. For purposes of the seismic interpretation a reduced area grid was utilized. This smaller grid aligns with the larger grid with grid nodes being a subset of the full scale model area. Maps of the acquired 2D seismic lines, wells with digital log curves, and velocity survey wells that were used in the analysis are included in Appendix D Figure 3 through Figure 5, and the acquired seismic lines are also displayed on Figure 2-22a.

Eighty-three wells in the area had digital log curves supplied by KDEI. An additional 65 well logs obtained from CalGEM were digitized for a total of 148 wells within the seismic project area. Log curves included (when available) SP, gamma ray, deep resistivity, sonic, density, and neutron. Most wells have only an SP and deep resistivity curve. The SP curves have been normalized across the project area.

Velocity survey data (checkshots) were available for ten wells in the seismic project area. All original checkshot data were reduced to ground level and used to make preliminary ties between wells and seismic data. Further refinements to the well ties were made using the Dynamic Depth Conversion (DDC) method. Propagation of velocity data to all wells was performed using DDC.

Five seismic lines were acquired from a seismic data broker. Three lines were used to define the faulting near the project location acreage. Two lines were acquired for the eastern area and correlation with the eastern well data. Two of the lines are actually portions of the same regional line. The lines are all west-east lines and are roughly perpendicular to regional dip (approximately 15 degrees off of true dip). The data were provided as digital SEGY files for both Stack and Migrated data and were loaded to a project utilizing the Kingdom Suite software. Further post-stack processing (seismic attributes for fault definition) was performed within the project.

The seismic line names are:

<u>West Area</u>

- EC-ENR-NMF-116-1
- W-SJ-023
- W-SJ-082-West

<u>East Area</u>

- GSI-CA-406
- W-SJ-082-East

Data quality ranges from good to excellent. In addition to the actual 2D seismic data a "fake" 3D survey was created with grid nodes that match the 200 x 200 meter area of interest grid. This fake survey allows 3D visualization of all surfaces and continuous fault planes.

Appendix D presents time and depth displays of seismic line W-SJ-082-East (Appendix D Figures 7 and 8), a cross-section displaying breakout of the individual Vedder sands (Appendix D Figure 9), maps of the areal extent of the Vedder units and Pyramid Hill sand (Appendix D Figure 10 through Figure 15), maps of fault locations at the elevation of the Vedder formation (Appendix D Figures 21 through 23), and cross-sections along the Pond Fault zone (Appendix D Figures 24 and 25).

The seismic interpretation described in Appendix D was used to develop a digital grid model of the area that provides the top elevation of the following formations on the 200 meter grid:

- Ground surface
- Etchegoin
- Miocene
- Santa-Margarita
- Round-Mountain
- Olcese
- Freeman-Jewett
- Pyramid Hills
- Vedder 1
- Vedder 1A
- Vedder 2
- Vedder 3
- Vedder 4
- Cantleberry Sand
- Walker
- Basement

The digital grid elevation file was used to plots additional maps and cross-sections of unit elevations, as described in Section 2.2.

2.2. Maps and Cross Sections of the AoR

Figure 2-22 displays surface geology of the eastern San Joaquin Valley in the vicinity of the Site illustrating granite basement to the east (pink) overlain by Miocene (upper and lower) sediments, Quaternary alluvial fans, and Quaternary fluvial deposits. The Site is indicated in the red box. The primary structural feature in the vicinity of the Site is a homocline underlain by granite. Cenozoic strata onlap the granite basement and wedge to the east.

Cross sections A-A' through E-E' (Figures 2-23 through 2-27) were constructed from a digital elevation grid from the well and seismic analysis described in Section 2.1.3, and are used to identify main flow units and probable barriers to flow. Figure 2-28 shows the location of the wells projected onto each of the cross sections. Figures 2-29 through 2-36 display the interpreted top elevation of the Pyramid Hill, Vedder Units, Walker, and Basement overlain with the cross-section locations and the fault locations at the elevation of the Vedder. Table 2-1 presents formation thickness and elevation at the SJR property.

The Fruitvale Shale (basal Santa Margarita) and Round Mountain Silt are approximately 900 feet thick at the Site and comprise low-permeability sealing units that overlie the Olcese Sand. The Olcese Sand is a coarsening upward sandstone with sharp top and base contacts. The Olcese overlies the Freeman-Jewett Silt and is overlain by the Round Mountain Silt and Fruitvale Shale. The Freeman Jewett Silt is approximately 700 feet thick at the injection Site (Figure 2-23).

The Pyramid Hill Formation is a fluvial depositional system that prograded on top of the deltaic and shallow marine Vedder Formation. The Pyramid Hill thins to the west, so not all wells drilled through the Vedder have Pyramid Hill present. Where Pyramid Hill and Vedder 1 are present, there is no clay separation between the two formations. SJR injection will target the Temblor 1, but it is likely that without a clay barrier between the Vedder and the Pyramid Hill, injectant and increased pressure will move into the Pyramid Hill. Vedder 1 and Pyramid Hills properties are similar. As both the units are overlain by Freeman-Jewett shale and claystone, the sealing formation is not impacted by the presence or absence of the Pyramid Hill, as the shale represents a transgressive flooding event that over-tops the sands below.

The Vedder has several sub-units composed of up to five sands separated by shales of various thickness (see Appendix D Figure 9). In the Site area, the Vedder contains the Vedder 1, Vedder 1A, Vedder 2, Vedder 3, and Vedder 4. The Cantleberry does not occur at the Site. The Pyramid Hill Sand overlies the Vedder 1 at the Site with no separating shale. The Vedder 1, 1A and Vedder 2 are not separated appreciably by shales. There is a shale between the Vedder 2 and the Vedder 3, and another shale between the Vedder 3 and the Vedder 4. The Vedder 4 is relatively thin and pinches out to the south.

2.3. Faults and Fractures

The eastern homocline of the San Joaquin Basin Province overlies the granite basement. The nature of the prograding, agrading, and retrograding stratigraphy indicates that the basin formed at a variable but increasing subsidence rate (Figure 2-21). The lateral extent of the stratigraphic units indicates a broad shelf for deposition. To assess the structure at the Site, the potential for faulting near the Site, and the potential presence of faults that could compartmentalize the injection intervals, a detailed seismic evaluation and extensive well data evaluation was undertaken (Section 2.1.3).

2.3.1. Fault Sealing Potential

Estimates can be made using Allan diagrams as to the probability that a fault will seal within a reservoir (Allan, 1989). Fault seal can result for example from the juxtaposition of reservoir with nonreservoir rock. However, experience from many petroleum provinces has shown that faults can seal even where reservoir quality sand bodies are juxtaposed across a fault. The most

common mechanism for sealing results from the incorporation of fine grained or dense material into the fault plane. Five different processes may cause this (Fisher and Knipe, 1998; Mitra and Marshak, 1988):

- Clay smear: Faults in clay-rich sediments are believed to form clay smears by the shearing of mudstone beds into the fault zone (Weber et al., 1978; Lehner and Pilaar, 1997).
- Cataclasis (shale gouge): Fault movement affecting clean sandstones will cause grain crushing and the breakage of rock in the fault plane, which will form a fault gouge (Lindsay et al., 1993).
- Diagenesis or cementation: Fine grained fault rock and associated open fractures in fault zones can be prone to cementation. Fluids migrating up the fault zone can cause the mineralization of the host rock. It is a common observation to find carbonate-cemented intervals in wells drilled close to faults, whereas wells drilled farther away from the faults do not contain carbonate cements (e.g., Reynolds et al., 1998). This is an indication that the fault zones have acted as the locus for the fluids causing carbonate cementation.
- Pore volume collapse: Ductile deformation during fault movement can cause poorly sorted sediments to mix and homogenize with a resultant decrease in porosity.
- Grain contact dissolution: Fault zones can act as planes for intergranular grain contact dissolution and subsequent recementation of the dissolved material. This can be an important mechanism for fault sealing in carbonate rocks (Peacock et al., 1998).

Algorithms are available for predicting the clay smear and shale gouge sealing potential of a fault. The basis for these algorithms is that the chances for clay smear to cause fault seal is controlled by the number and thickness of the shale beds displaced past a particular point on the fault. The thickness of the clay smear within the fault plane will decrease with distance from the source beds and with increasing throw of the fault (Yielding et al., 1997). The method involves taking the sand and shale distribution from a well close to the fault as a template for making the fault seal analysis.

Clay smear potential is calculated for a particular point on the fault plane as a function of the distance of that point from a shale bed acting as the source for the clay smear and the shale bed thickness (Bouvier et al., 1989; Fulljames et al., 1997). Figure 2-37 presents an example fault seal analysis. The shale smear factor (SSF) is dependent on the shale bed thickness and the fault throw but not on the smear distance (Lindsay et al., 1993). Smaller values of the SSF correspond to a more continuous development of smear on the fault plane. A large fault is likely to seal where the SSF is equal to or less than 4 (Faerseth, 2006).

Shale gouge ratio works on the assumption that the sealing capacity is related directly to the percentage of shale beds or clay material within the slipped interval (Yielding et al., 1997). Shale gouge ratio is the proportion of the sealing lithology in the rock interval that has slipped past a given point on the fault (Figure 2-37). To calculate the shale gouge ratio, the proportion of shale and clay in a window equivalent to the throw is measured.

Fault seal prediction assumes that if there is enough shale in the section undergoing faulting, then sealing is likely. There is often a continuous shale gouge or shale smear along fault planes where there is sufficient mudstone material available to be incorporated (Lindsay et al., 1993; Foxford

et al, 1998). Nevertheless, a number of field studies show that fault zones can have a significant degree of complexity and variation in deformation style along their lengths (e.g., Childs et al., 1997; James et al, 1997; Foxford et al., 1998; Doughty, 2003). Yielding et al. (1999) made a fault seal analysis for the Gullfaks field in the Norwegian North Sea. Areas of higher shale gouge ratios (>20%) were more likely to seal on the basis of pressure history and chemical tracer movement between wells.

2.3.2. Pond-Poso Creek Fault Complex

The Pond-Poso Creek Fault system extends from basement to the surface. It is a west dipping high angle normal fault (down to the west) with up to 395 meters of throw at its center point near the injection Site. While the fault is nearer to the surface location of the injection well, it is several kilometers from the injection well at the injection depth in the Pyramid Hill-Temblor I-Temblor II.

Allan Diagrams

An analysis of the fault and horizon geometry was made along the extent of the fault from northwest to southeast. Figure 2-38 displays a map of the vicinity of the injection Site (black rectangle) illustrating the locations of 23 cross sections (yellow) that were created and evaluated to create Allan Diagrams of the Pond-Poso Creek Fault to assess offset and seal. Cross sections are approximately one mile apart. Cross sections were created from the static reservoir model of the area. Stratigraphic interval tops are based on the structure contour maps created for the AoR. Three seismic lines used in our study cross the Pond-Poso Creek Fault. They were used to guide horizon extrapolation to the fault. Individual cross sections are included in Appendix E. Cross Section 1 (Appendix E) illustrates how the analysis was performed, displaying the Hanging and Foot Wall sides of the fault and the stratigraphic units offset across the fault. There is less than 10 meters of normal offset at the Pyramid Hill-Vedder 1-Vedder 2 level. The dipping horizon planes were projected to the fault so true fault throw could be measured. As the cross sections progress southward, the offset on the fault varies.

Figure 2-39 is a compilation of all 23 cross sections created to measure fault throw across the Pond-Poso Creek fault system. The throw at the northernmost and southernmost cross sections is less than 10 meters. The maximum throw of ~395 meters occurs at cross section 13. Fault splays in the system can be seen in cross sections 9 to 11. The maximum throw of ~395 meters bring Pyramid Hill+Vedder 1+Vedder 2 in juxtaposition with the Olcese Sand. The Vedder 3 sand is in juxtaposition with the Freeman Jewett. This juxtaposition brings the upper injection zone on the footwall into contact with a sand on the hanging wall, while also bringing the lower injection zone (Vedder 3) into contact with shale on the hanging wall.

Individual fault offset analyses were combined in Figure 2-40. The combination diagram of the fault throw juxtaposition on each side of the Pond-Poso Creek fault system was created from the 23 cross sections drawn normal to the trend of the fault. Formation tops on the footwall and hanging wall side of the fault are plotted as an overlay on the fault plane. Distance across the section is 23 miles. Units were then color filled (sand vs shale) to create an Allan Diagram (Figure 2-41). Figure 2-41 displays shading of the units based on footwall and hanging wall intersection. Formation tops on the footwall and hanging wall side of the fault are plotted as an overlay on the fault plane and shaded by lithology (gray or blue are shale, light yellow and cream

are sand). An alternative display of the Allan Diagram is displayed in Figure 2-42, showing shading of the units based on footwall and hanging wall intersection. Formation tops on the footwall and hanging wall side of the fault are plotted as an overlay on the fault plane and shaded by lithology (gray is shale, yellow is sand). Hanging wall units are indicated by darker stratigraphic top and base picks. Allan diagrams were used to infer footwall to hanging wall lithologic unit offsets and to measure throw at each shale and sand layer. These data are then used to estimate Shale Gouge Ratio as shown in Figure 2-43.

Table 2-2 displays the determination of Shale Gouge Ratio (SGR) based on the formula SGR = (sum of shale thickness / fault throw) * 100%. The calculation is made for each shale layer at each cross section along the Pond-Poso Creek fault plane. The shading of the units on the table is based on Shale Gouge Ratio. Darker colors indicate SGR > 50%. For the bulk of the fault, SGR exceeds 15%. Shading is also plotted on the Allan Diagram shown in Figure 2-43 on the basis of Shale Gouge Ratio. The bulk of the SGR exceeds 15% and, in most cases, exceeds 50%. These results indicate that the Pond-Poso fault is not transmissive at the depths of the Vedder formation in the vicinity of the project.

Porosity trends

No core data is available that was gathered from both sides of the fault that would further confirm sealing. Porosity trends have been used as surrogates for pore pressure (Ramm, 1992; Nelson and Bird, 2005). In over-pressure regimes, reservoir porosity can be retained at depth because pore pressure enables preservation of porosity. In normally pressured regimes, porosity degrades due to overburden stress. In the Monterey Formation to the west of the Pond Poso Creek Fault porosity is higher in the center of the basin as seen in numerous exploration wells, and in Rose and North Shafter oil fields than in the fields that occupy the western fold belt (Lost Hills, Belridge, Elk Hills) on the western side of the San Joaquin.

To evaluate whether there are normal pressures east of the fault, on the eastern homocline, porosity data was plotted against depth for samples gathered during the current analysis. Figure 2-44 depicts porosity-depth trends from the San Joaquin Basin for the Monterey Formation. The pentagonal data points represent east-side samples from our current analysis. They fit the normal pressure curve drawn for the west-side fold belt at Belridge Field. Overpressure samples are taken from the center of the basin. This data would indicate that east of the Pond-Poso Creek Fault, the Monterey is normally pressured. West of the fault it is overpressured. Porosity at Rose is 30% at 7,500 feet, which falls off the normal porosity-depth curve and is in the area of the overpressure data. This would support the concept that the Pond-Poso Creek fault is sealing.

Tectonic Stress

Orientation and relative magnitudes of in-situ tectonic stress can be inferred from various indicators: earthquake focal mechanisms; stress-induced elliptical borehole enlargement; hydraulic fracturing stress measurements; and young fault slip alignment (Zobach and Zobach, 1989). Stress orientation in the vicinity of the injection Site was interpreted from well bore breakouts compiled by Mount and Suppe (1995) and supplemented by Castillo and Younker (1997) (Figure 2-45). This enabled an assessment of whether the northwest-to-southeast oriented Pond-Poso Creek Fault could be at a high state of stress parallel to the fault plane and therefore

could dislocate by injection induced pore pressure increase in the fault plane. The stress data indicate that, in the immediate vicinity of the injection Site, the maximum horizontal earth stress (SHmax) is oriented at a high angle to the Pond-Poso Creek Fault (Figure 2-45). There is a regionally consistent stress pattern with SHmax oriented northeast-southwest nearly perpendicular to the strike of the fault. This implies that the fault is in low shear closure mode and is not likely to be penetrated by injectant.

Pressure Data

Based on the methodology of Castillo and Younker (1997), mud weight data from three wells drilled in the vicinity of the injection Site (see Figure 2-45: Kimberlina 1, Parsons 1, EOG 1) were overlain on their Figure 6c, which depicts pressure versus depth results for wells in the San Joaquin Valley greater than 20 kilometers from the San Andreas Fault (SAF), and wells drilled at Elk Hills (Figure 2-46). This base figure excludes data from less than 20 km from the SAF that do not show an increase in SHmax direction that is more indicative of stresses in closer proximity to the SAF.

The results from the three wells indicates that there is normal pressure response (no significant over pressure and a significant buffer between effective stress and overburden stress) where: at 4 km depth, the difference between effective stress and overburden stress (e.g. pore pressure) is 35 MPa (ES - OS is 85 MPa – 50 MPa = 35 MPa). At 3 km depth, the difference is 30 MPa (ES - OS is 65 MPa – 35 MPa = 30 MPa), while at 1 km, the difference is 20 MPa (ES - OS is 45 MPa – 25MPa = 20 MPa). For our injection interval at approximately 2.4 km (7,780 feet), this would mean there is a 25 MPa buffer before injection could cause rock fracture (55 MPa – 30 MPa = 25 MPa).

For the Kimberlina Site Birkholzer et al. (2011) predicted that injection would cause a 30 Bar increase in pressure in a faulted model and 23 Bar increase in a non-faulted model. Converting Bar to MPa would mean that pressure increases of 3.0 and 2.3 MPa would be expected respectively. Based on TOUGH modeling (see AoR and Corrective Action Plan) the pressure increase nearest to the injection well is expected to be as large as approximately 5.0 Bar (0.50 MPa) which is significantly lower than the expected overburden stress at 2.4 Km (55 MPa or 550 Bar). Of note from the data, the Kimberlina and EOG wells are west of the Pond-Poso Creek Fault while Parsons is east of the fault. Kimberlina and EOG pressure vs depth curves on Figure 2-46 are more closely aligned with hydrostatic pressure than Parsons, which is closer to the lithostatic gradient. This supports the observation that west of the fault is over pressured while east of the fault it is more normally pressured.

Further support for the sealing capacity of the Pond-Poso Creek Fault comes from reservoir pressure gradient data from producing fields east and west of the fault show. Fields east of McFarland (Jasmin, West Jasmin, Dyer Creek) have gradients ranging from 0.23 - 0.32 psi/ft while the gradient at Rose Field west of McFarland and the Pond Poso Creek fault is 0.84 psi/ft. Eastern fields are normally pressured while Rose and North Shafter are over pressured.

2.4. Injection and Confining Zone Details

Geologic properties of the key formations were obtained from laboratory analyses of archived well core samples from oil and gas wells previously drilled in the vicinity. Specifically, information on permeability, porosity, geochemistry (x-ray diffraction, scanning electron microscopy) and geomechanics (triaxial compressive strength, micro-computed tomography) were collected. Porosity and permeability data were collected from existing well-log reports obtained from CalGEM and from new laboratory analyses of archived geologic core samples Driltek obtained from the California Well Sample Repository at California State University, Bakersfield. New core analyses were conducted or subcontracted by Best Core Services in Bakersfield, California and all laboratory reports are presented in Appendix F. Figure 2-47 displays wells with geologic core data that were analyzed, and Table 2-3 lists the wells and analyses that were conducted on each core sample. Porosity and permeability data are discussed in Section 2.4.1 below, and geomechanics is discussed in Section 2.5 below. Geochemical data is discussed in Section 2.7 below.

2.4.1. Geologic Core Data

Table 2-4 lists porosity and permeability values obtained from core laboratory analyses. For each core interval, the associated geologic formation was identified based on comparison of the depth interval to the occurrence of geologic formations within our three-dimensional geologic model grid (Section 2.1.3) and review of the well data for each individual well. Porosity and permeability data are available for the overlying alluvium and the Etchegoin, Round Mountain, Olcese, Freeman Jewett, Vedder, and Walker Formations. For the Vedder, specific formations were identified relating to the Upper Vedder sand units (comprising the Pyramid Hills, Vedder 1 and Vedder 2), the Vedder 2 shale, Vedder 3 sand, Vedder 3 shale, Vedder 4 sand and Vedder 4 shale. For the Olcese, cores from shale and sand sequences were identified based on review of the accompanying well logs.

Table 2-5 summarizes porosity and permeability values for each formation. Horizontal permeability was calculated based on the geometric mean or all sample results, and vertical permeability was calculated based on the harmonic mean of all sample results (Fetter, 2001). Horizontal permeability for Vedder sand units ranges from 192 to 613 millidarcies (mD) and vertical permeability ranges from 62 to 154 mD. Vedder shale units range in horizontal permeability from 0.11 to 0.91 mD, and vertical permeability 0.0052 to 0.025 mD. The Freeman Jewett formation horizontal permeability is calculated to be 0.26 mD, and vertical permeability is 0.0036 mD. The Olcese permeability values were calculated from weighted geometric and harmonic averages assuming 90 percent sands and 10 percent shales, and horizontal and vertical permeability are 77 and 4.3 mD respectively. Round Mountain horizontal and vertical permeability values are 0.037 and 0.00073 mD.

Representative porosity values were obtained from the median of all values for each formation, and ranged from 15 percent (Vedder 3 shale) to 34 percent (Upper Vedder sands).

Permeability and porosity values obtained from the laboratory core analyses generally compare well to a previous compilation given by Birkholzer et al. (2011) and reproduced in Appendix C. Birkholzer et al. (2011) present a Vedder sand horizontal permeability of 303 mD and vertical permeability of 61 mD; Vedder shale values are horizontal permeability of 0.1 mD and vertical

permeability of 0.05 mD. Freeman-Jewett (referred to as Temblor-Freeman in Birkholzer et al., 2011) horizontal permeability is given as 0.002 mD and vertical as 0.001 mD. Porosity values are also generally similar, with a value of 0.26 given for the Vedder sand units (compared to a range of 0.26 to 0.34 given in Table 2-5).

In summary, permeability and porosity values obtained from laboratory results compare well to previously reported values and confirm that the Vedder sand units exhibit high permeability and porosity values conducive to carbon dioxide injection and storage, and the Freeman-Jewett Formation has a low permeability conducive to serving as the primary confining zone.

2.4.2. Facies Succession

Vedder facies succession is related to progradation from the source terrain in the Sierra Nevada Mountains into the marine San Joaquin Basin. Succession from Castleberry to Pyramid Hill is one of repeated progradational and retrogradational sequences. Castleberry is mainly a fluvial and delta plain succession that is only found in the east, near the Sierra. Vedder 4 consists of a basal shale overlain by siltstone and mudstone, grading into a sandstone at the top. This lithofacies transition has been related to a toe-set shale and mudstone deposit overlain by a fore set mudstone and siltstone deposit that is in turn overlain by a fine-to-medium grained sand in top-set strata. The vertical depositional succession changes from outer marine shelf to shallow marine to delta plain to fluvial. Vedder 3, 2, and 1 have similar lithofacies and depositional settings. The volume of fluvial facies at the tops of each sand is related to accommodation within the basin. Variations in sedimentation rate, progradation distance, shale compaction, and sea level fluctuations causes variable thickness and extent in each sand unit. All are topped by a transgressive shale associated with either auto cyclic events (shale overtopping sand due to delta shifting) or eustatic coastal onlap that results in widely distributed shale deposition over deltaic and fluvial facies. Base level fluctuations appear to dominate the San Joaquin during Vedder deposition. There is little evidence for delta shifting.

Within this type of setting, where shallow marine and deltaic deposits intermingle, it is possible to have channels cutting normal to inter-channel delta plain and shoreline deposits. As the system of the Vedder is quite sandy, channel cuts in shoreline deposits result in sand-on-sand relationships without significant erosion of channels into underlying shallow marine units. This reduces the risk of flow pathways. The basal shale for each unit is deposited during a transgression so it tends to deposit mud and clay over the shallow marine – delta plain – fluvial plain deposits.

Occurrence of fluid flow pathways within the Freeman Jewett has not been reported. This siltstone and shale unit represents a maximum flooding event in the basin where deeper marine sediments were deposited on top of the deltaic Vedder 1 and in some areas on top of the fluvial Pyramid Hill sandstone (fluvial deposits).

Fluid flow pathways in the Vedder in the region of McFarland have not been observed in well logs or in 2-D seismic. While there are Vedder productive fields to the east, they appear to contain a predominance of strandline - deltaic - fluvial deposits than at the proposed injection Site. The western ends of the Vedder prograding units appear to be more silt and clay rich associated with outer shelf deposits. Fluid flow pathways in producing fields have been identified, where fluvial channels cut into underlying delta plain and shoreline deposits. The

degree of channel erosion diminishes westward, so flow pathways are less likely to occur on the eastern extremes of the Vedder units.

2.5. Geomechanical and Petrophysical Information

Geomechanical properties are derived from laboratory analyses of core plugs drilled from archived whole core from four wells in the McFarland region. Data from Birkholzer et al., 2011 is displayed in Appendix C and is a compilation of analyses from various sources for the range of stratigraphic units encountered in the area. Data from Birkholzer et al. (2011) includes pore compressibility, which is a key geomechanics parameter used in the TOUGH model described in the AoR and Corrective Action Plan. This data was augmented with newly measured data from sand samples from two wells, Shell KCL-A 83-85 (Vedder; API 402930606, location shown on Figure 2-47) (sample 3) and General Petroleum KCL 25#1 (Olcese; API 402930604, location shown on Figure 2-47) (sample 5). Samples from shale zones in two other wells failed during initial loading into the test apparatus, so there are no static or dynamic properties listed for sample 1 and 6. Appendix F (Geomechanical Report) contain the measured data from the Vedder and Olcese.

Appendix F contains triaxial compressive strength results for the two core plugs. Of interest are Bulk Density, Peak Strength, Static Poissons' Ratio, and Static and Dynamic Young's Modulus. For the Vedder sample from 8,499 feet bgs, the results are expected to be quite like that which will be encountered in the planned facility injection well. Injection depth is expected to be at approximately 8,000 feet bgs. The Olcese samples from 6,194 feet are considered representative of that sand.

Appendix F also contains dynamic properties measured from triaxial compressive strength testing for the Olcese and Vedder samples. Compressive Wave (Vp) and Shear Wave (Vs) data are reasonable for sandstone samples from the respective sample depths. Vp:Vs Ratio is consistent (2.31 vs 2.32) for the samples. Dynamic Young's Modulus of 1.78 million psi for the Vedder and 2.72 million psi for the Olcese sands are also consistent with sandstones from other areas in this depth range. Appendix F also contains figures that display the measured geomechanical results from the analytical program and a summary of the analytical technique and procedure.

Properties of the Olcese and Vedder are similar in terms of depositional setting (prograding sands of shallow marine to fluvial origin, sourced from the east, depositing toward the west). Porosity appears to be better aligned for the Olcese and Vedder (10 porosity unit range), but permeability is quite scattered, with an order of magnitude or more range at various depths. Data collected from core obtained from the California Well Sample Repository was used as the basis for analyzing similarity for the Olcese and Vedder Sands. Based on data from mercury injection capillary pressure analysis-derived values for porosity and permeability, the sands from various wells across a wide range of depths has an adequate correlation coefficient ($R2 = 0.654$) for porosity but a widely scattered result for permeability ($R2= 0.015$) (Figure 2-48). For samples from 7,780' (2,371 m) to 8500' (2,590 m) the data appears to be well behaved for porosity, but permeability has an order of magnitude range for the same samples.

Appendix G contains calculations of the fracture gradient from the observed geomechanical results. Based on the equations in Appendix G and utilizing the data from our samples, we calculate a fracture gradient of 0.5 psi/ft. We have assumed a factor for tectonic stress of 0.15. The tectonic stress factor (0.15) was provided by production engineers familiar with hydraulic fracturing calculations in the San Joaquin Basin. Their recommendation was to add that factor based on their experience in the basin. Anisotropy between maximum and minimum horizontal earth stress derived from the analysis of borehole anisotropy measurement as discussed by Zobach and Zoback (1985), Mount and Suppe (1992), and Castillo and Younker (1997) is in the same order of magnitude. This would indicate a total fracture gradient of 0.66 psi/ft. Section 7, below, discusses the planned injection pressure and demonstrates that the injection pressures will be much less than the fracture pressure of the Vedder formation.

2.6. Seismic History

Fault and earthquake databases from the USGS and the CGS have been evaluated in the vicinity of the McFarland Site. CGS maps show the approximate locations of faults near the Site:

- Recent Pond Fault
- Pond-Poso Creek Fault (Quaternary)
- Un-named faults near Rag Gulch in the Sierra Nevada foothills (Quaternary).

CGS maintains a database of earthquakes with magnitudes in excess of 5.0M. There are two periods of earthquake activity, none in the McFarland vicinity:

- 1905 (two earthquakes) south and east of Bakersfield
- 1952 (three earthquakes) south and east of Bakersfield

USGS also maintains a database of earthquakes (USGS, 2021a). This includes events in the vicinity of McFarland. Within a 65 km x 75 km box centered on nearby Shafter, CA there were 152 seismic events between 1970 and May, 2021. Within a 25 km x 18 km box centered on McFarland, there were 9 seismic events (plus one sonic boom) between 1970 and May, 2021. Seismic epicenters for the 9 seismic events occurred between 4.76 km and 28.58 km below sea level. Seismic magnitudes ranged from 2.5 to 3.09 M. None of the earthquakes occurred within the stratigraphic deposits above granite basement, and none of the earthquakes are associated with mapped recent or Quaternary faults.

Figure 2-49 displays the locations of earthquakes and their depths from the USGS earthquake database. The plotted points represent earthquakes between 1970 and 2021. To put these events into context, a CGS faults map is presented in Figure 2-50. The distribution of historic (Figure 2-51) and Quaternary (Figure 2-52) faults provides spatial context with respect to the injection Site near the historic Pond Fault that has shown some creep, previously associated with groundwater withdrawal (Smith, 1983). Figure 2-53 is a map of historic earthquakes in relation to mapped faults. Of note is that there have been no significant earthquakes associated with the faults in the McFarland area. Seismic epicenters for the 9 seismic events occurred between 4.76 km and 28.58 km below sea level. Seismic magnitudes ranged from 2.5 to 3.09 M. None of the earthquakes occurred within the sedimentary deposits above granite basement. None of the

earthquakes are associated with mapped recent or Quaternary faults. Table 2-6 summarizes information on known earthquakes in the USGS catalog.

2.7. Hydrologic and Hydrogeologic Information

The SJR property is located within the San Joaquin Valley groundwater basin and Kern County subbasin. Figure 2-54 displays the project location and AoR relative to the jurisdiction of various Groundwater Sustainability Agencies (GSAs). The AoR includes the McFarland GSA, and Kern Groundwater Authority GSA and the vicinity of the project includes the Cawelo GSA, and Semitropic Water Storage District GSA. Static water depth ranges from about 70 to 400 feet below ground surface (Table 2-7), and therefore first groundwater occurrence is within the Alluvium. The Kern Groundwater Authority Groundwater Sustainability Plan (GEI, 2020) and Southern San Joaquin Municipal Utility District Management Area Plan (GEI, 2019) provide a detailed description of shallow groundwater occurrence, groundwater conditions, and current and planned groundwater monitoring programs.

2.7.1. Water Supply Wells within AoR

Groundwater dependent communities within the vicinity of the project include the City of McFarland, City of Delano, Agbayani Village Water System and Pond Mutual Water Company (Figure 2-55). Water supply wells located within the vicinity of the project are shown on Figure 2-56 and wells within the storage complex are listed with available data in Table 2-7. Information on water supply wells was obtained from the California Department of Water Resources, the SGMA Data Viewer, and GeoTracker (CDWR, 2021; SGMA, 2022; SWRCB, 2022). Well completion depth in the vicinity ranges from 85 to 1,240 feet below ground surface and maximum known completion depth for wells within the Storage Complex is 1,005 ft bgs (Table 2-7). Well uses are listed as domestic, agricultural, unknown, industrial, monitoring, and cathodic protection. The CDWR website does not have exact locations for most wells in the vicinity, and instead places them at the centroid of the section. Well completion reports were reviewed and if location information was provided (by hand -drawn map, parcel APN, or by location within the Section), the well location was added as an estimated location.

2.7.2. Depth to USDWs and Base of Fresh Water

Elevation of the base of freshwater (3,000 micromhos, approximately 2,100 mg/L total dissolved solids [TDS]) is given by Page (1973) for the San Joaquin Valley. Base-of-freshwater elevation ranges from -1,200 to -2,000 feet above mean sea level (ft msl) within the vicinity (ground surface elevation ranges from approximately 300 to 500 ft msl).

Maximum depth of underground sources of drinking water (USDW), defined as 10,000 mg/L TDS, is given at select oil and gas fields in the project vicinity in Gillespie et al. (2017), Kong (2016) and Metzger and Landon (2018). Both reports used TDS data from the California Division of Oil, Gas, and Geothermal Resources (DOGGR). Samples in the DOGGR archives range from 1910-2015. Information from each of these reports was combined in order to extrapolate depth-to-base of freshwater (Figure 2-57) and depth-to-base of USDW throughout the project area and vicinity. Figure 2-58 displays reported depth-to-base of USDW values and the extrapolated base of USDW depth throughout the area. USDW depth was extrapolated using standard geostatistical techniques (kriging). USDWs extend to basement at the Jasmin oil field due to freshwater recharge along the Kern Sierran foothills, and range as deep as 2,800 ft bgs at

the Poso Creek oil field. Depth-to-base of USDW is approximately 2,400 ft bgs at the Facility location and ranges from 2,100 ft bgs to 2,900 ft bgs within the vicinity. Depth to the base of freshwater and the USDW depth are also plotted on each cross section, as displayed in Figures 2-23 through 2-27.

Metzger and Landon (2018) also present generalized distributions of TDS versus depth for areas of the San Joaquin Valley, and values are reproduced for Middle Kern Valley Floor in Figure 2-59. As mapped by the USGS in this report, the deeper formations, greater than about 3,000 ft bgs, are essentially filled with high salinity water (approximately 25,000 to 29,000 mg/L TDS). Incursion of lower salinity is occurring from the east via outcrops in the Sierran Foothills. Because there is no widely circulated dispersion zone between the aquifer and the incursion of fresh water, the mixing zone is minimal. There is little mixing between 500 and 10,000 mg/L TDS (as mapped by the USGS and others), and there is less mixing between 10,000 and 25,000 mg/L TDS.

Data from Metzger and Landon (2018) was used in conjunction with depth-to-USDW data presented in Figure 2-58 to develop a map of the estimated salinity of the Vedder formation (Figure 2-60). This map was created based on the relationship of depth-to-salinity and the Vedder formation minimal depth at each location. Towards the east, the 10,000 mg/L isohaline was mapped based on the intersection of USDW depth and Vedder formation depth and was also used in interpolating Vedder salinity (Figure 2-60). Based on this analysis, Vedder formation salinity is estimated to be 25,000 mg/L throughout the AoR.

2.7.3. Baseline Geochemistry

Two groundwater samples from the Vedder formation are available from the Rio Bravo oil field (Table 2-8; location shown on Figure 2-60). TDS is 21,982 and 24,757 mg/L for the two samples, with the larger value associated with a sample that had the full suite of cations and anions analyzed. Chloride is the major anion and sodium is the major cation in both samples. Listed pH values were 7.25 and 7.6.

For overlying freshwater aquifers water quality data is available from the Southern San Joaquin Municipal Utility District Management Area Plan (GEI, 2019). For groundwater dependent public water systems within the vicinity of the project (Figure 2-55), sodium levels are listed as elevated greater than 70 mg/L in 9 of 18 wells. Several wells used by the City of Delano and Pond Mutual Water Company report arsenic concentrations greater than the drinking water maximum contaminant level of 11 micrograms per liter (µg/L); nitrate concentrations above the MCL are limited within these systems to one well used by the City of Delano. Trichloropropane (TCP), associated with legacy pesticide application, is also of concern at several groundwater supply wells.

2.7.4. Oil and Gas Fields

Oil and gas fields in the vicinity of the project are shown on Figures 2-61a and 2-61b. No oil and gas fields are present within the AoR. Several oil and gas fields have obtained aquifer exemptions, as shown on Figure 2-61a and listed in Table 2-9. Aquifer exemptions include the Cantleberry Sand of the Vedder Formation in the Jasmin and the Vedder Formation in the Mount Poso Oil Field. According to U.S. EPA (2017) there are Class II injection wells for water disposal and steam-flood enhanced oil recovery (EOR) in the Jasmin Oil Field.

From a geochemical perspective, the hydrocarbons east of the McFarland Site were sourced from the Eocene to middle Miocene hydrocarbon systems. The productive fields in the area east of McFarland (updip) include the Jasmin Field, the West Jasmin Field, and the Dyer Creek Field. These produced from the Pyramid Hill (Miocene) and Vedder (Oligocene), and the deeper Famoso Sand (Eocene), and the Vedder respectively. There are no significant differences in oil properties in these producing (or now abandoned) fields. The oil gravity of these fields ranges from 14 to 22 degrees API, reflecting the degree of bio-degradation in a freshwater environment. Shallower reservoirs tend to be more bio-degraded (Pyramid Hill; 14 degrees API), while deeper reservoirs (Famoso; 22-degree API) are less bio-degraded. Reservoirs are 1,700 to 4,000 feet deep. The Kreyenhagen-Temblor system source rocks tend to have high conversion rates (95%).

To the west of McFarland there are two productive fields (Rose and North Shafter) that are also west of the Pond-Poso Creek fault. Both of these fields produce from quartz phase Monterey Formation (Mid-Late Miocene) siliceous shales, that were charged from Monterey Formation source rocks that reached maturity in the center of the San Joaquin Basin. The oil properties of these fields is different from the fields to the east. The Monterey Formation hydrocarbons of the McLure-Tulare petroleum system are different from the older Tumey-Temblor system. Table 8.2 in Appendix C shows the main differences in oil properties for McLure-Tulare oils vs Tumey-Temblor oils. Oil gravity at Rose and North Shafter is above 25 degrees API and the oil has not been biodegraded. Monterey source rocks have good conversion rates (83-87%), reflecting less burial than the deeper Tumey-Temblor beds. North Shafter oil gravity is 27.5 degrees API and the Monterey reservoir is 7,575 feet of depth. Rose Oil Field is a Monterey producer with a thin reservoir at 7500 feet. The initial reservoir pressure was 6300 psi (Appendix C). The pressure gradient is 0.84 psi/ft. Monterey formation oil fields west of McFarland (and the Pond Poso Creek fault) are over pressured. See Appendix C for productive pool and fluid information from CalGEM.

2.8. Geochemistry

Geochemical modeling was conducted to evaluate the compatibility of the injectate with groundwater and rocks or sediments composing the aquifer system. The intent of the modeling is to identify the major potential reactions that may affect injection or containment (US EPA, 2013).

Geochemical modeling using the PHREEQC (pH-REdox-Equilibrium) software was used to calculate the behavior of minerals and changes in aqueous chemistry based on chemical equilibrium conditions (Parkhurst and Appelo, 2013). Two geologic formations were considered during this evaluation:

- Vedder Formation: injection formation
- Freeman-Jewett Formation: sealing formation

The geology of the formations is typical of clastic marine sediments. The Vedder Formation consists of arkosic arenites and graywacke sandstones (Nguyen et al., 2013) and is predominantly composed of quartz and feldspar minerals. The Freeman-Jewett Formation consists of siltstones and shales (Nguyen et al., 2013) and has a high clay content. While rocks are buried in the earth's crust, chemical reactions between the rocks and groundwater are termed

diagenesis, which involves the dissolution of minerals into groundwater and precipitation of minerals onto the formation. Reactions are driven by fluid movement, temperature, and pressure changes due to burial depth and compaction. Over time, minerals and cements may dissolve and form new minerals. Important reactions that have occurred in the Vedder Formation include (Nguyen et al., 2013):

- Precipitation and dissolution of cements consisting of various minerals including quartz, clays, potassium feldspar (K-feldspar), dolomite, and pyrite
- Dissolution of feldspars, quartz, lithic fragments
- Albitization of plagioclase and K-feldspars
- Formation of feldspar and quartz overgrowths
- Precipitation of kaolinite and other clays

2.8.1. Vedder Formation Fluid Geochemistry

Data for two water samples from the Vedder Formation are available from the USGS Produced Waters database (USGS, 2021b). Samples were collected on 4/6/1960 and 4/2/1968 (Table 2-8) (Section 2.7.3). The sample from 1960 has a complete suite of major ions and pH, so it was used for the geochemical modeling. With a calculated total dissolved solids (TDS) greater than 24,000 parts per million (ppm), the Vedder groundwater is considered brackish.

The net charge of a water sample may be calculated using the results for the cation and anion data. Based on the fact that water has a net neutral charge, the sum of the cation and anion charges should be zero. Variations due to sampling and analyses often cause the calculated value to vary and a value within 5% of neutral is considered a "good" balance. The charge balance for the sample from 1960 was calculated in PHREEQC at -0.10%.

2.8.2. Vedder and Freeman-Jewett Mineralogy

Mineralogy for the Vedder and the Freeman-Jewett Formations was evaluated using x-ray diffraction (XRD) to determine the bulk and clay mineralogy of core samples.

The Vedder Formation consists of arkosic sandstones (Nguyen et al., 2013) and is composed predominantly of quartz and feldspar minerals. The amount of clay minerals varies from 5 to 30% and is mostly smectite minerals. Based on the XRD analyses, about 4.5% to 30% of the formation consists of clay minerals.

The Freeman-Jewett Formation consists of shale and siltstone (Nguyen et al., 2013), and the mineralogy identified by XRD is typically dominated by smectite clay minerals, quartz, and plagioclase feldspar minerals (Table 2-10). Based on the XRD analyses, about half of the formation consists of clay minerals (Table 2-10). Appendix F contains Best Core Services Laboratory Reports with XRD data.

2.8.3. Injectate Chemistry

Chemical data was provided for the composition of the carbon dioxide injectate that was modeled in ASPEN process simulation software (Table 2-11; AspenPlus model distributed by Aspen Technology Inc. located in Bedford, Massachusetts). The modeled composition accounts of 99.9% of the mass.

2.8.4. Equilibrium Geochemical Modeling

When modeling groundwater geochemistry, the water chemistry, gas chemistry, and mineralogy are used to constrain the model because mineral solubility controls the concentrations of its components in groundwater (Appelo and Postma, 2005). Mineral dissolution-precipitation reactions directly impact the aqueous chemistry. In general, as minerals dissolve the concentrations in groundwater increase and when minerals precipitate the concentrations in groundwater decrease. Chemical equilibrium indicates that congruent reactions will appear balanced between reactants and products with no apparent change in the chemical system.

The PHREEQC model was used to evaluate potential changes to mineralogy and aqueous composition in the subsurface due to carbon dioxide injection. The mineral, gas and aqueous phases were assumed to be in chemical equilibrium.

Geochemical Database

For reactions involving water and minerals, the equilibrium relationship between products and reactant activities (concentrations) can be calculated using known values for parameters like Gibb's energy found in thermodynamic databases (Zhu and Anderson, 2002). Thermodynamic values for these calculations are compiled in databases from several entities including the US Geological Survey (USGS) and Lawrence Livermore National Laboratory. A database developed at the Lawrence Livermore National Laboratory (LLNL.dat) was used for this evaluation. The LLNL.dat database includes a temperature range for the thermodynamic data provided from 0-300 C. This database is appropriate for the groundwater concentrations, pressure, and temperature used in the modeled scenarios.

When modeling saline waters, the Pitzer database (Parkhurst and Appelo, 2013) is often used but it has thermodynamic data for a limited number of minerals including calcite, dolomite, gypsum, and quartz. The Vedder and Freeman-Jewett Formations are predominantly composed of minerals that are not included in the Pitzer database, so the LLNL.dat database was used because it also includes smectite, illite, pyrite and the minerals listed in Table 2-10.

Saturation Indices

Saturation indices (SIs) were calculated that represent whether a particular mineral (e.g., calcite) is in chemical equilibrium with the groundwater. SI calculations are used to predict if a mineral is likely to precipitate or dissolve in the groundwater and if these reactions changed the concentrations of dissolved elements.

Equilibrium modeling sets the saturation indices to a zero (0) value for a given mineral using the mineral abundance determined by XRD. The assumption of chemical equilibrium allows dissolution and precipitation reactions to be quantified in the model.

The formula for calculating saturation indices (SI) is as follows:

$$SI = \frac{IAP}{K_{sp}} \quad (1)$$

where SI = saturation index

IAP = ion activity product
K_{sp} = solubility product

Using gypsum as an example (Clark, 2015), the ion activity product of gypsum (IAP_{gypsum}) is the product of the activity (a, activity is approximately equal to concentration in dilute solutions) of calcium (Ca) and sulfate (SO_4):

$$IAP = a_{Ca^{2+}} \times a_{SO_4{}^{2-}} \quad (2)$$

The solubility product, K_{sp}, is an indication of the relative solubility of a mineral in water. A large value indicates that the mineral will dissolve and contribute ions to solution, resulting in a relatively high activity or concentration. A small value indicates that the mineral has a low solubility and will not contribute many ions to the solution. For the mineral gypsum, the K_{sp} based on the dissociation reaction of gypsum in water is:

$$CaSO_4 \cdot 2H_2O \leftrightarrow Ca^{2+} + SO_4^{2-} + 2H_2O$$

$$K_{sp} = \frac{a_{Ca^{2+}} + a_{SO_4{}^{2-}} + a_{H_2O}}{a_{gypsum}} = 10^{-4.60} \quad (3)$$

Interpreting the results of the SI calculation is straightforward:

- SI > 0 indicates that mineral is supersaturated in solution and may precipitate onto aquifer matrix
- SI = 0 indicates that mineral is at chemical equilibrium with the water
- SI < 0 indicates that mineral is undersaturated in solution and may dissolve from aquifer matrix

Due to potential systematic errors introduced during sampling and analysis, results within the range of ±0.5 of zero are typically considered in or near chemical equilibrium.

Geochemical Model Input

Site specific data was used as input to construct the equilibrium models. Water chemistry for the Vedder Formation (Table 2-8) and mineralogy as determined by x-ray diffraction (XRD) of the Vedder and Freeman-Jewett Formations (Table 2-10) are the date used for geochemical modeling in PHREEQC. The water chemistry (Table 2-8) was entered as received in parts per million (ppm). The mineralogy data from XRD (Table 2-10) included primary and clay minerals normalized to 100%. For input into PHREEQC, the mineralogy in Table 2-10 was converted to moles per liter (mol/L) using assumed values for the porosity and rock density for each formation (Table 2-12). The converted values for mineralogy that were input into PHREEQC are in shown Table 2-13.

Temperature and pressure data were provided at 78 C and 4.3 atmospheres (atm). The amount of carbon dioxide in 1 liter of gas at 4.3 atm and 78 C based on ideal gas law (PV=nRT) is 0.149 moles.

In order to model the geochemistry of the quartz and clay minerals identified by XRD, silica (SiO_2) and aluminum (Al) concentrations not in the original water chemistry sample were modeled in PHREEQC. The water chemistry sample collected from the Vedder Formation in 1960 was equilibrated with quartz and montmorillonite minerals as equilibrium phases at 78 C and 4.2 atmospheres (atm). The modelled aqueous concentrations were used in subsequent modeling: SiO_2= 16.22 parts per million (ppm) and Al = 0.005 ppm. These concentrations are reasonable for a sandstone aquifer at the neutral pH values in the Vedder Formation. Al concentrations are typically low in the neutral pH range of groundwater.

Geochemical Modeling Results and Discussion

Model results are presented in Table 2-14 for the changes in mineralogy of equilibrium phases and presented in Table 2-15 for the water chemistry based on the equilibrium phases. The modeling steps were:

- Vedder Formation: use the Vedder groundwater sample and equilibrate with each mineralogy data set for the Vedder Formation and carbon dioxide
- Freeman-Jewett Formation: Use the model results for Vedder 4,308-4,333 depth and equilibrate with both Freeman-Jewett mineralogy and carbon dioxide

The results of the equilibrium geochemical modeling the injection of carbon dioxide indicate that changes in mineralogy and aqueous chemistry are likely to occur, but overall, the mineralogy of the Vedder and Freeman-Jewett Formations consists of stable minerals like quartz, feldspar and kaolinite. These silicate minerals are fairly stable and have a low reactivity. Minerals with a low relative abundance like calcite and dolomite are more reactive than the silicates when the carbon dioxide injection is modeled.

Both geologic formations are composed dominantly of silicate minerals like quartz, feldspar, and clays that are not expected to be highly reactive during carbon dioxide sequestration. More reactive minerals like calcite and dolomite are present in relatively smaller amounts compared to the silicate minerals. Although the model indicates minerals will dissolve and precipitate, the net volume change is a small increase of about 1 percent. The porosity of the Vedder and Freeman-Jewett Formations is not expected to be sustainably impacted by mineral dissolution and precipitation reactions during carbon dioxide sequestration.

Based on the modeling the following reactions are expected to occur:

- Dissolution of calcite when present and the precipitation of dolomite
- Illite dissolution that may contribute magnesium (Mg) for the precipitation of dolomite as well as silica and aluminum that may be at least partially precipitated as other aluminosilicate minerals like k-feldspar.
- Dolomite, kaolinite, quartz and k-feldspar are stable and tend to precipitate in all models removing calcium, magnesium, bicarbonate, silica, aluminum, oxygen, and potassium from solution.
- Gypsum when initially present is not stable and dissolves releasing calcium and sulfate to solution

- Pyrite dissolution releases ferrous iron, sulfate to solution, and lowers pH due to release of hydrogen ions

The formation of carbonates like dolomite were predicted to occur in each model scenario. The formation of carbonate minerals can be an important mechanism to remove and immobilize carbon dioxide from solution through incorporation in the mineral phase. Another carbonate mineral, Dawsonite [$NaAl(CO_3)(OH)_2$], is expected to become saturated in groundwater and precipitate from solution in both the Vedder and Freeman-Jewett Formations.

Based on the equilibrium modeling, the aqueous chemistry results are in Table 2-15. Results indicate that:

- Carbon dioxide will dissolve into solution and is included in the total inorganic carbon (TIC), which also includes bicarbonate and carbonate species. Results indicate that when carbon dioxide is dissolved in solution, the following species will occur bicarbonate ion, iron carbonate ion, carbon dioxide, and sodium bicarbonate.
- Ferrous iron (Fe2+) is in solution in samples with reducing (pE is negative) conditions. The dominant dissolved species related to ferrous ion include iron carbonate ion, ferrous ion, and ferrous sulfate complex.
- The pH values ranged from 6.5 to 7.5
- Calcium concentrations are relatively small due to precipitation of minerals like dolomite. The calcium remaining in solution includes calcium and calcium bicarbonate ions, and calcium sulfate complex.

Based on the geochemical equilibrium modeling, the injection of carbon dioxide into the Vedder Formation does not cause significant reactions that will affect the injection or containment of the gas.

2.9. Site Suitability

As demonstrated in the preceding sections, the proposed Site is suitable for injection of carbon dioxide and containment. Answers to recommended U.S. EPA considerations are listed below.

- *What is the subsurface distribution of lithological facies? What are the implications for carbon dioxide plume migration?*

Major stratigraphic units underlying the Site are discussed in Section 2.1.2, and facies succession is discussed in Section 2.4.2. As the system of the Vedder is quite sandy, channel cuts in shoreline deposits result in sand-on-sand relationships without significant erosion of channels into underlying shallow marine units. This reduces the risk of preferential flow pathways. Basal shale for each Vedder unit is deposited during a transgression so it tends to deposit mud and clay over the shallow marine – delta plain – fluvial plain deposits.

Occurrence of fluid flow pathways within the Freeman Jewett has not been reported. This siltstone and shale unit represents a maximum flooding event in the basin where deeper marine sediments were deposited on top of the deltaic Vedder 1 and in some areas on top of the fluvial Pyramid Hill sandstone (fluvial deposits).

- *How will carbon dioxide be confined to the injection zone? How do the site characterization data demonstrate the lack of potential leakage pathways?*

The confining zone for the proposed injection zone consists of the Freeman Jewett, a Miocene shale and mudstone. In addition, the Round Mountain silt and overlying Fruitvale Shale (tight Miocene units) overlie the Olcese Formation Sandstone and are located beneath the overlying USDWs (Section 2.1). Thickness of these units are listed in Table 2-1 and they are displayed in cross-sections as discussed in Section 2.2. Geologic core data laboratory analysis (Section 2.4.1) demonstrates that the Freeman Jewett has sufficiently low permeability to contain carbon dioxide. Section 7.1, below, also discusses that the Freeman Jewett has a sufficiently high entry pressure to preclude carbon dioxide intrusion. Fluid flow modeling in the AoR and Corrective Action Plan also demonstrates that carbon dioxide will be contained below the Freeman Jewett.

Fault sealing potential is discussed in Section 2.3 and demonstrates that fluid leakage will not occur through the Pond-Poso Creek fault complex. Based on the buoyant properties of carbon dioxide, the plume is not expected to migrate down-dip towards the fault complex.

- *How will the carbon dioxide stream interact with well materials and subsurface formations (injection and confining zones)?*

Geochemical modeling presented in Section 2.8 demonstrates that the injection of carbon dioxide into the Vedder Formation does not cause significant reactions that will affect injection or containment. Modeling presented in the AoR and Corrective Action Plan indicates that the carbon dioxide plume will not come into contact with abandoned wells. Carbon dioxide reaction with cement in any well materials is not expected to cause degradation leading to leakage (e.g., Newell and Carey, 2012; Bachu and Bennion, 2009).

- *What is the total storage capacity of the injection zone? How was this determined? How is this sufficient to receive the proposed amount of carbon dioxide?*

TOUGH2 modeling presented in the AoR and Corrective Action Plan demonstrates that injected carbon dioxide will be contained with the AoR. Due to the nature of the depositional environment and lack of structural traps, the full capacity of the injection zone likely exceeds the total volume of carbon dioxide to be injected.

- *Are there any potential concerns regarding confining zone integrity? What site characterization data support this determination? Is secondary confinement necessary to ensure USDW protection?*

As discussed above, available site characterization data demonstrate that the primary confining system is thick and extensive and there are no transmissive faults or fractures that would result in fluid leakage. As discussed in the AoR and Corrective Action Plan there are no wells that penetrate the Freeman Jewett within the AoR. Secondary confinement is not necessary; however, as an additional safety factor the Round Mountain silt and overlying Fruitvale Shale (tight Miocene units) overlie the Olcese Formation Sandstone and are located beneath the overlying USDWs.

3. AoR and Corrective Action

SJR's AoR and Corrective Action Plan describes the process, software, and results to establish the AoR.

AoR and Corrective Action GSDT Submissions
GSDT Module: AoR and Corrective Action ***Tab(s):*** All applicable tabs Please use the checkbox(es) to verify the following information was submitted to the GSDT: ☒ Tabulation of all wells within AoR that penetrate confining zone ***[40 CFR 146.82(a)(4)]*** ☒ AoR and Corrective Action Plan ***[40 CFR 146.82(a)(13) and 146.84(b)]*** ☒ Computational modeling details ***[40 CFR 146.84(c)]***

4. Financial Responsibility

SJR's Financial Responsibility information has been uploaded to the GSDT.

Financial Responsibility GSDT Submissions
GSDT Module: Financial Responsibility Demonstration ***Tab(s):*** Cost Estimate tab and all applicable financial instrument tabs Please use the checkbox(es) to verify the following information was submitted to the GSDT: ☒ Demonstration of financial responsibility ***[40 CFR 146.82(a)(14) and 146.85]***

5. Injection Well Construction

This section describes specifics of how the injection well will be constructed and operated, including injection volumes, injectate properties, injection pressure, and well design.

5.1. Proposed Stimulation Program

SJR has provided a well stimulation plan prepared by Driltek dated January 6, 2022 to the GSDT.

5.2. Construction Procedures

Surface and intermediate casings for the injection well (SJR-I1) will be installed using standard J55 and N80 steels. Surface casing will be placed across fresh water and USDW zones, with a shoe at 2,600 ft bgs (Figure 5-1). The injection casing may be able to be installed using standard L80 or lower spec, assuming the estimated purity of the carbon dioxide injection stream. Another option will be to place 13Cr casing across the injection sands below the intermediate pipe, and non-chrome inside the intermediate section.

Casing centralizers will be used on the surface, intermediate and injection casings. All casing strings shall be cemented to surface. A dual completion will enable two injection zones, the first (and primary) target in the upper Vedder formation (i.e., Pyramid Hill, Vedder1, and Vedder2 sands) and the lower completion in the Vedder 3 sand that can be utilized for injection if needed. The dual injection string design (Figure 5-1) using 2 3/8" tubing may restrict certain logging options to special smaller diameter logging tools. Conventional Class G cement will be adequate for the surface and intermediate casings. A latex additive in the tail cement for the injection casing will help eliminate potential gas migration. Packer fluid will consist of water with corrosion inhibiting additives. The surface casing will extend through the lowermost USDW estimated at 2495 ft bgs.

Table 5-1 provides additional construction information.

Table 5-1. Construction Details.

CASING SIZE	WEIGHT	TOP-BOTTOM	TYPE	ID	DRIFT	HOLE	TOC	TENSILE	BURST	COLLAPSE
13.375"	61#	0-2600'	J55	12.515"	12.359"	17.5"	Surface	962,000	3,090	1,540
9.625"	53.5#	0-7700'	N80	8.535"	8.379"	12.25"	Surface	1,062,000	7,930	6,620
7"	29#	0-8700'	L80 13Cr	6.184"	6.059"	8.5"	Surface	676,000	8,160	7,020
2.375"	4.7#	0-7750'	J55	1.995"	1.901"			72,000	7,700	8,100
2.375"	4.7#	0-8150'	J55	1.995"	1.901"			72,000	7,700	8,100

6. Pre-Operational Logging and Testing

SJR's Pre-Injection Logging and Testing plan has been submitted to the GSDT.

Pre-Operational Logging and Testing GSDT Submissions

GSDT Module: Pre-Operational Testing
Tab(s): Welcome tab

Please use the checkbox(es) to verify the following information was submitted to the GSDT:
☒ Proposed pre-operational testing program ***[40 CFR 146.82(a)(8) and 146.87]***

7. Well Operation

7.1. Operational Procedures

The Facility plans on generating and injecting up to an average of 1,200 tons per day of carbon dioxide every year for a period of 15 years based on SJR's energy and material balance analyses. This is equal to an injection of 438,000 tons per year, and a total injection of 6,570,000 tons over the lifetime of the project.

Injection will include a maximum daily injection volume of 1,500 tons per day to allow for some operational fluctuation and a quarterly (three-month) average maximum of 1,200 tons per day and annual maximum of 438,000 tons per year. Injection rate and volume will be continuously monitored as discussed in the Monitoring and Testing Plan to ensure the maximum injection rates will not be exceeded. During injection well workovers or operational interruptions injection will be temporarily ceased.

Class VI requirements are that injection pressure shall not exceed 90% of the fracture pressure of the injection zone. Section 2.5 and Appendix G provide a calculation of the fracture gradient at the Vedder formation, which is 0.66 psi/ft, or 5,132 psi (35,384,000 Pa; 354 bar) at the planned injection depth of approximately 7,775 ft bgs. Maximum pressure predicted from TOUGH modeling during the injection phase is 265 bar, and over-pressure is on the order of 5.5 bar (550,000 Pa; see AoR and Corrective Action Plan). The maximum overpressure at the well is somewhat higher and will be derived from the experimentally determined injectivity index during well testing. It is apparent, however, that the injection pressure will be safely below the fracture initiation pressure.

Appendix B includes a study of anticipated injection-well conditions and a carbon-dioxide phase study that indicates injection pressure of 2,150 psia (148 bar) at the surface is adequate in addition the static head to meet anticipated pressure at the injection point. Annulus pressure will be set at 50 psi for monitoring. The annulus/tubing differential will equal the injection pressure on the tubing less the annulus pressure (50 psig).

Several options will be conducted to confirm the fracture pressure in the wellbore during and after completion of the injection well, and to calibrate calculated results achieved prior to drilling:

- Triaxial stress test for rock mechanics for a static measurement from the rock core to be taken
- Dipole full wave sonic log, a dynamic result that can be calibrated back to the static triaxial test
- Leak-off test to determine the fracture pressure after the well has been perforated

If the injection zone height is 50 foot the maximum carbon dioxide/brine capillary pressure (Pc) would be 17 psi which is well below the entry pressure of 557 psi measured for Freeman-Jewett. According to the KCLA Freeman-Jewett sample at 8,161 feet bgs, the seal can handle a carbon dioxide/brine reservoir over 1,600 feet thick before reaching the entry pressure of the seal. The TOUGH2 modeling analysis (see AoR and Corrective Action Plan) showed a pressure of 69.6

psi, still well below the entry pressure of the Freeman-Jewett. Figure 7-1 contains a graph of capillary pressure versus wetting phase saturation for MICP core data.

7.2. Proposed Carbon Dioxide Stream

Table 7-1 lists the detailed anticipated injectate composition based on facility ASPEN process simulation modeling (AspenPlus model distributed by Aspen Technology Inc. located in Bedford, Massachusetts), and Table 2-10 lists a simplified composition that was used in geochemical modeling. The injectate is predicted to be 98.7 percent carbon dioxide by mass, with less than one percent of methane, benzene, ethane, and nitrogen making up the composition to 99.9 percent by mass. Remaining components, present in very minor concentrations, are listed in Table 7-1.

8. Testing and Monitoring

SJR's Testing and Monitoring plan describes the strategies for testing and monitoring to ensure USDW protection, mechanical integrity testing and plume and pressure monitoring.

Testing and Monitoring GSDT Submissions
GSDT Module: Project Plan Submissions ***Tab(s):*** Testing and Monitoring tab Please use the checkbox(es) to verify the following information was submitted to the GSDT: ☒ Testing and Monitoring Plan ***[40 CFR 146.82(a)(15) and 146.90]***

9. Injection Well Plugging

SJR's Injection Well Plugging Plan has been submitted to the GSDT.

Injection Well Plugging GSDT Submissions
GSDT Module: Project Plan Submissions ***Tab(s):*** Injection Well Plugging tab Please use the checkbox(es) to verify the following information was submitted to the GSDT: ☒ Injection Well Plugging Plan ***[40 CFR 146.82(a)(16) and 146.92(b)]***

10. Post-Injection Site Care (PISC) and Site Closure

SJR's PISC plan is submitted to the GSDT and includes post-injection monitoring activities, and a proposed alternative PISC timeframe.

PISC and Site Closure GSDT Submissions
GSDT Module: Project Plan Submissions ***Tab(s):*** PISC and Site Closure tab Please use the checkbox(es) to verify the following information was submitted to the GSDT: ☒ PISC and Site Closure Plan ***[40 CFR 146.82(a)(17) and 146.93(a)]***
GSDT Module: Alternative PISC Timeframe Demonstration ***Tab(s):*** All tabs (only if an alternative PISC timeframe is requested) Please use the checkbox(es) to verify the following information was submitted to the GSDT: ☒ Alternative PISC timeframe demonstration ***[40 CFR 146.82(a)(18) and 146.93(c)]***

11. Emergency and Remedial Response

SJR's Emergency and Remedial Response plan has been submitted to the GSDT.

Emergency and Remedial Response GSDT Submissions
GSDT Module: Project Plan Submissions ***Tab(s):*** Emergency and Remedial Response tab Please use the checkbox(es) to verify the following information was submitted to the GSDT: ☒ Emergency and Remedial Response Plan ***[40 CFR 146.82(a)(19) and 146.94(a)]***

References

Allegra Hosford Scheirer, 2003. The Three-Dimensional Geologic Model Used for the 2003 National Oil and Gas Assessment of the San Joaquin Basin Province, California. in Scheirer A.H., ed., Petroleum Systems and Geologic Assessment of Oil and Gas in the San Joaquin Basin Province, California: United States Geological Survey Professional Paper 1713, Chapter 7, p. 1-81

Allan, U. S. (1989). Model for hydrocarbon migration and entrapment within faulted structures. AAPG bulletin, 73(7), 803-811.

Appelo, C. A. J., & Postma, D. (2005). Geochemistry, groundwater and pollution. 2nd. Ed. Balkema, Rotterdam.

Bachu. S. and D.B. Bennion (2009). Experimental assessment of bring and/or carbon dioxide leakage through well cements at reservoir conditions. International Journal of Greenhouse Gas Control, v.3 p.494-501.

Birkholzer, J. T., Nicot, J. P., Oldenburg, C. M., Zhou, Q., Kraemer, S., & Bandilla, K. (2011). Brine flow up a well caused by pressure perturbation from geologic carbon sequestration: Static and dynamic evaluations. International journal of greenhouse gas control, 5(4), 850-861.

Bouvier, J. D., Kaars-Sijpesteijn, C. H., Kluesner, D. F., Onyejekwe, C. C., & Van der Pal, R. C. (1989). Three-dimensional seismic interpretation and fault sealing investigations, Nun River Field, Nigeria. AAPG bulletin, 73(11), 1397-1414.

California Department of Water Resources (CDWR). 2021. Well Completion Report Map Application. Accessed June 2021. <https://dwr.maps.arcgis.com/apps/webappviewer/index.html?id=181078580a214c0986e2da28f8623b37>.

Castillo, D. A., & Younker, L. W. (1997). A High shear stress segment along the San Andreas Fault: Inferences based on near-field stress direction and stress magnitude observations in the Carrizo Plain Area. United States. https://doi.org/10.2172/490160

Childs, C. J. J. P., Walsh, J. J., & Watterson, J. (1997). Complexity in fault zone structure and implications for fault seal prediction. In Norwegian Petroleum Society Special Publications (Vol. 7, pp. 61-72). Elsevier.

Clark, I. (2015). Groundwater Geochemistry and Isotopes (1st ed.). CRC Press. https://doi.org/10.1201/b18347

Doughty, P. T. (2003). Clay smear seals and fault sealing potential of an exhumed growth fault, Rio Grande rift, New Mexico. AAPG bulletin, 87(3), 427-444.

Færseth, R. B. (2006). Shale smear along large faults: continuity of smear and the fault seal capacity. Journal of the Geological Society, 163(5), 741-751.

Fetter, C. W. (2001). Applied Hydrogeology, Prentice-Hall. Inc., New Jersey.

Fisher, Q. J., & Knipe, R. (1998). Fault sealing processes in siliciclastic sediments. Geological Society, London, Special Publications, 147(1), 117-134.

Foxford, K. A., Walsh, J. J., Watterson, J., Garden, I. R., Guscott, S. C., & Burley, S. D. (1998). Structure and content of the Moab Fault Zone, Utah, USA, and its implications for fault seal prediction. Geological Society, London, Special Publications, 147(1), 87-103.

Fulljames, J. R., Zijerveld, L. J. J., & Franssen, R. C. M. W. (1997). Fault seal processes: systematic analysis of fault seals over geological and production time scales. In Norwegian Petroleum Society Special Publications (Vol. 7, pp. 51-59). Elsevier.

Gautier, D.L. and A.H. Scheirer, M.E. Tennyson, K.E. Peters, L.B. Magoon, P.G. Lillis, R.R. Charpentier, T.A. Cook, C.D. French, T.R. Klett, R.M. Pollastro, and C.J. Shenk, (2003). Executive Summary – Assessment of Undiscovered Oil and Gas Resources of the San Joaquin Province of California. In Scheirer, A.H., ed., Petroleum Systems and Geologic Assessment of Oil and Gas in the San Joaquin Basin Province, California: United States Geological Survey Professional Paper 1713, Chapter 1, p. 1-3.

Gautier, D. L., & Scheirer, A. H. (2007). Miocene total petroleum system: Southeast stable shelf assessment unit of the San Joaquin Basin province. Petroleum systems and geologic assessment

of oil and gas in the San Joaquin Basin province, California: US Geological Survey Professional Paper 1713.

GEI Consultants (GEI), 2019. Southern San Joaquin Municipal Utility District Management Area Plan. Submitted to Southern San Joaquin Municipal. December 2019.

GEI Consultants (GEI), 2020. Kern Groundwater Authority Groundwater Sustainability Plan. January 2020.

Gillespie, J., Kong, D., & Anderson, S. D. (2017). Groundwater salinity in the southern San Joaquin Valley. AAPG Bulletin, 101(8), 1239-1261.

Historic Earthquake Online Database, 2017. [online] Available at: <https://maps.conservation.ca.gov/cgs/historicearthquakes/> [Accessed 1 August 2021].

Hewlett, J. S., Phillips, S., and Bazeley, W. J. M., (2014), Middle Tertiary sequence stratigraphy, Southern San Joaquin Basin, California in MP51, in Pacific Section, AAPG, Book MP51, 73 p.

Hewlett, James S. and Robert S. Tye, (2015). SEPM Strata, Exercise 2: Ramp-Margin Setting– Oligocene Vedder/Jewett Sands. www.sepmstrata.org/page.aspx?&pageid=760&3

James, D. M. D. (1997). Discussion on a model for the structure and development of fault zones. Journal of the Geological Society-London, 154(2), 366.

Kong, D. Y. (2016). Establishing the base of underground sources of drinking water (USDW) using geophysical and chemical reports in the southern San Joaquin Basin, CA (Doctoral dissertation, California State University, Bakersfield). https://scholarworks.calstate.edu/downloads/q237hv60b

Leslie B. Magoon, Paul G. Lillis, and Kenneth E. Peters, (2009). Petroleum Systems Used to Determine the Assessment Units in the San Joaquin Basin Province, California. in Scheirer A.H., ed., Petroleum Systems and Geologic Assessment of Oil and Gas in the San Joaquin Basin Province, California: United States Geological Survey Professional Paper 1713, Chapter 8, p. 1-67.

Lehner, F. K., & Pilaar, W. F. (1997). The emplacement of clay smears in synsedimentary normal faults: inferences from field observations near Frechen, Germany. In Norwegian Petroleum Society Special Publications (Vol. 7, pp. 39-50). Elsevier.

Lillis, P. G., Warden, A., Claypool, G. E., & Magoon, L. B. (2008). Petroleum systems of the San Joaquin Basin Province--geochemical characteristics of gas types: Chapter 10 in Petroleum systems and geologic assessment of oil and gas in the San Joaquin Basin Province, California (No. 1713-10). US Geological Survey.

Lindsay, N. G., Murphy, F. C., Walsh, J. J., Watterson, J., Flint, S., & Bryant, I. D. (1993). Outcrop studies of shale smears on fault surfaces. The geological modelling of hydrocarbon reservoirs and outcrop analogues, 15, 113-123.

Metzger, L. F., & Landon, M. K. (2018). Preliminary groundwater salinity mapping near selected oil fields using historical water-sample data, central and southern California (No. 2018-5082). US Geological Survey.

Mitra, G., and S. Marshak. Basic methods of structural geology. Prentice Hall, 1988.

Mount, V. S., & Suppe, J. (1992). Present-day stress orientations adjacent to active strike-slip faults: California and Sumatra. Journal of Geophysical Research: Solid Earth, 97(B8), 11995-12013.

Needham, D. T., G. Yielding, and B. Freeman, 1996. Analysis of fault geometry and displacement patterns, in P. G. Buchanan and D. A. Nieuwland, eds., 1996, Modern developments in structural interpretation, validation and modelling: Geological Society Special Publication 99, p. 189–199g.

Nelson, P. H., & Bird, K. J. (2005). Porosity-depth trends and regional uplift calculated from sonic logs, National Petroleum Reserve in Alaska (pp. 1-28). US Department of the Interior, US Geological Survey. https://pubs.usgs.gov/sir/2005/5051/

Newell, D.L. and J.W. Carey (2013). Experimental Evaluation of Wellbore Integrity Along the Cement-rock Boundary. Environmental Science and Technology, v.47 p.276-282.

Nguyen, D., Horton, R. A., & Kaess, A. B. (2013, October). Diagenesis Of The Oligocene Vedder Formation, Greeley Oil Field, Southern San Joaquin Basin, California. In Pacific Section AAPG, SPE and SEPM Joint Technical Conference.

Nilsen, T. H., Reid, S.A., Boote, D.R.D., 2001. Tectonic, Paleogeographic, and Relative Sea Level Controls on Deep-Water Depositional Systems of the Southern San Joaquin Basin, California. AAPG Annual Meeting, Denver, CO, June 3-6, 2001.

Page, R. W., (1973). Base of Fresh Ground Water (approximately 3,000 micromhos) in the San Joaquin Valley, California. USGS Hydrologic Investigations Atlas HA-489.

Parkhurst, D. L., & Appelo, C. A. J. (2013). Description of input and examples for PHREEQC version 3: a computer program for speciation, batch-reaction, one-dimensional transport, and inverse geochemical calculations (No. 6-A43). US Geological Survey.

Peacock, D. C. P., Fisher, Q. J., Willemse, E. J. M., & Aydin, A. (1998). The relationship between faults and pressure solution seams in carbonate rocks and the implications for fluid flow. Geological Society, London, Special Publications, 147(1), 105-115.

Ramm, M. (1992). Porosity-depth trends in reservoir sandstones: theoretical models related to Jurassic sandstones offshore Norway. Marine and Petroleum Geology, 9(5), 553-567. https://doi.org/10.1016/0264-8172(92)90066-N

Reynolds, A. D., Simmons, M. D., Bowman, M. B., Henton, J., Brayshaw, A. C., Ali-Zade, I. S. Guliyev, S. F. Suleymanova, E. Z. Ateava, D. N. Mamedova, and Koshkarly, R. O. (1998).

Implications of outcrop geology for reservoirs in the Neogene Productive Series: Apsheron Peninsula, Azerbaijan. AAPG bulletin, 82(1), 25-49.

Scheirer, A.H. and L.B. Magoon, 2007. Age, Distribution, and Stratigraphic Relationship of Rock Units in the San Joaquin Basin Province, California, in Scheirer, A.H., ed., Petroleum Systems and Geologic Assessment of Oil and Gas in the San Joaquin Basin Province, California: United States Geological Survey Professional Paper 1713, Chapter 5, p. 1-107.

Schwartz, Daniel E., 2016. Recent Characterization of the Monterey Formation in the San Joaquin Basin. Pacific Section AAPG Annual Meeting, Oxnard, CA, May 3-5, 2015.

SGMA Data Viewer. Available online: https://sgma.water.ca.gov/webgis/?appid=SGMADataViewer#currentconditions (accessed on 5 August 2022).

California State Water Resources Control Board (SWRCB) GeoTracker Data Management System. https://geotracker.waterboards.ca.gov/

Smith, Z. A. (1983). Rewriting California Groundwater Law: Past Attempts and Prerequisites to Reform. Cal. WL Rev., 20, 223.

U.S. EPA, 2017. Aquifer Exemption Request for the Jasmin Oil Field, Kern County, California. September 28, 2017.

U.S. EPA, 2013. Geologic Sequestration of Carbon Dioxide Underground Injection Control (UIC) Program Class VI Well Site Characterization Guidance. EPA 816-R-13-004. URL: https://www.epa.gov/uic/final-class-vi-guidance-documents.

U.S. Geologic Survey (USGS), 2021a. Earthquake Catalog. URL: https://earthquake.usgs.gov/earthquakes/search/

U.S. Geological Survey (USGS), 2021b. Produced Waters Database. URL: https://eerscmap.usgs.gov/pwapp/

Wagoner, J.L., 2009. 3D Geologic Modeling of the Southern San Joaquin Basin for the Westcarb Kimberlina Demonstration Project-A Status report. AGU Annual meeting December 14-18, 2009.

Weber, K.L., Mandi, G., Pilaar, W. F., Lehner, F. & Precious, R G. 1978. The role of faults in hydrocarbon migration and trapping in nigerian growth fault structures. Offshore Conference, Houston, Texas, Paper OTC 3356, 2643-2647.

Yielding, G., Freeman, B., & Needham, D. T. (1997). Quantitative fault seal prediction. AAPG bulletin, 81(6), 897-917. June 1, 1997.

Yielding, G., Øverland, J. A., & Byberg, G. (1999). Characterization of fault zones for reservoir modeling: An example from the Gullfaks field, northern North Sea. AAPG bulletin, 83(6), 925-951. https://doi.org/10.1306/E4FD2E29-1732-11D7-8645000102C1865D

Zhu, C. and Anderson, G. 2002. Environmental Applications of Geochemical Modelling. xiv+284 pp. Cambridge, New York, Melbourne. September 2002. Geological Magazine 139(05)

Zoback, M. L., & Zoback, M. D. (1989). Tectonic stress field of the continental United States, Mem. Geol. Soc. Am., 172, 52-539, 1989

Figures

List of Figures

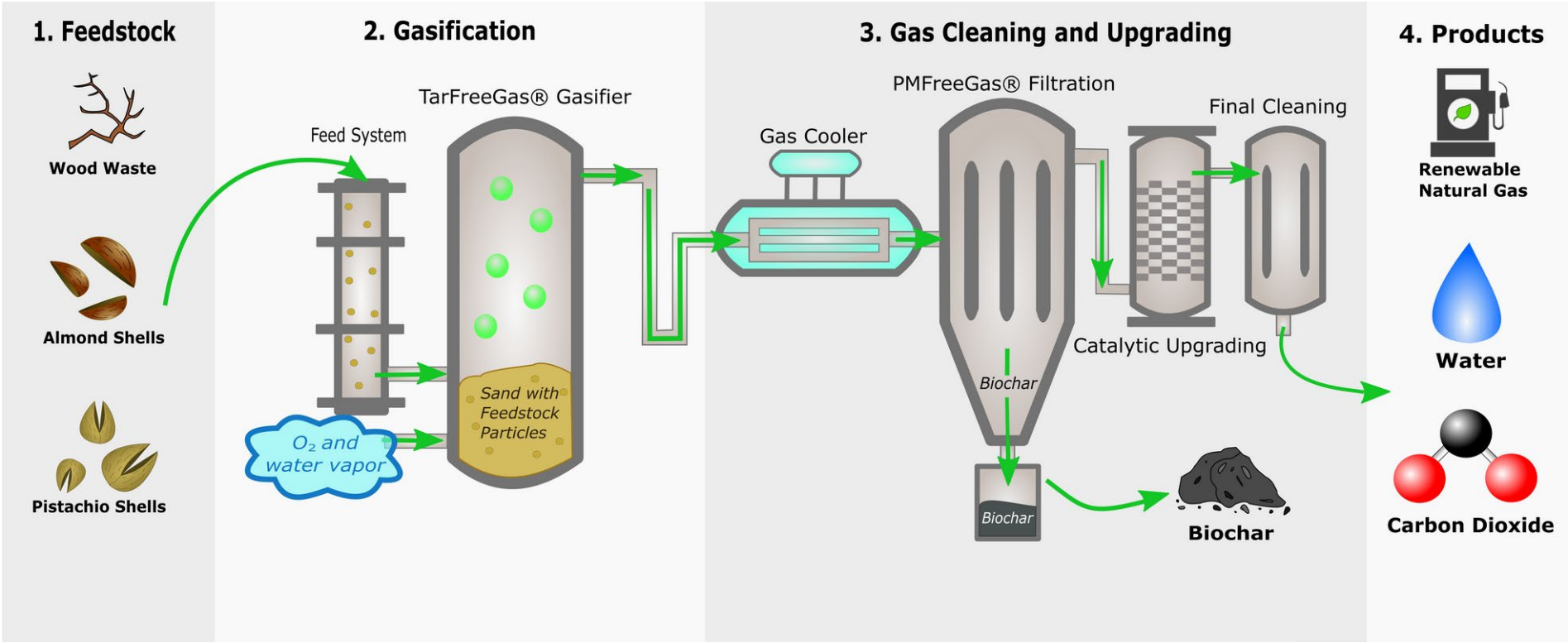

SAN JOAQUIN RENEWABLES

Planned Biomass Gasification Process

SAN JOAQUIN RENEWABLES

Project Location and Saline Formations for Geologic Sequestration

9/13/2021 DB19.1252

Figure 1-2

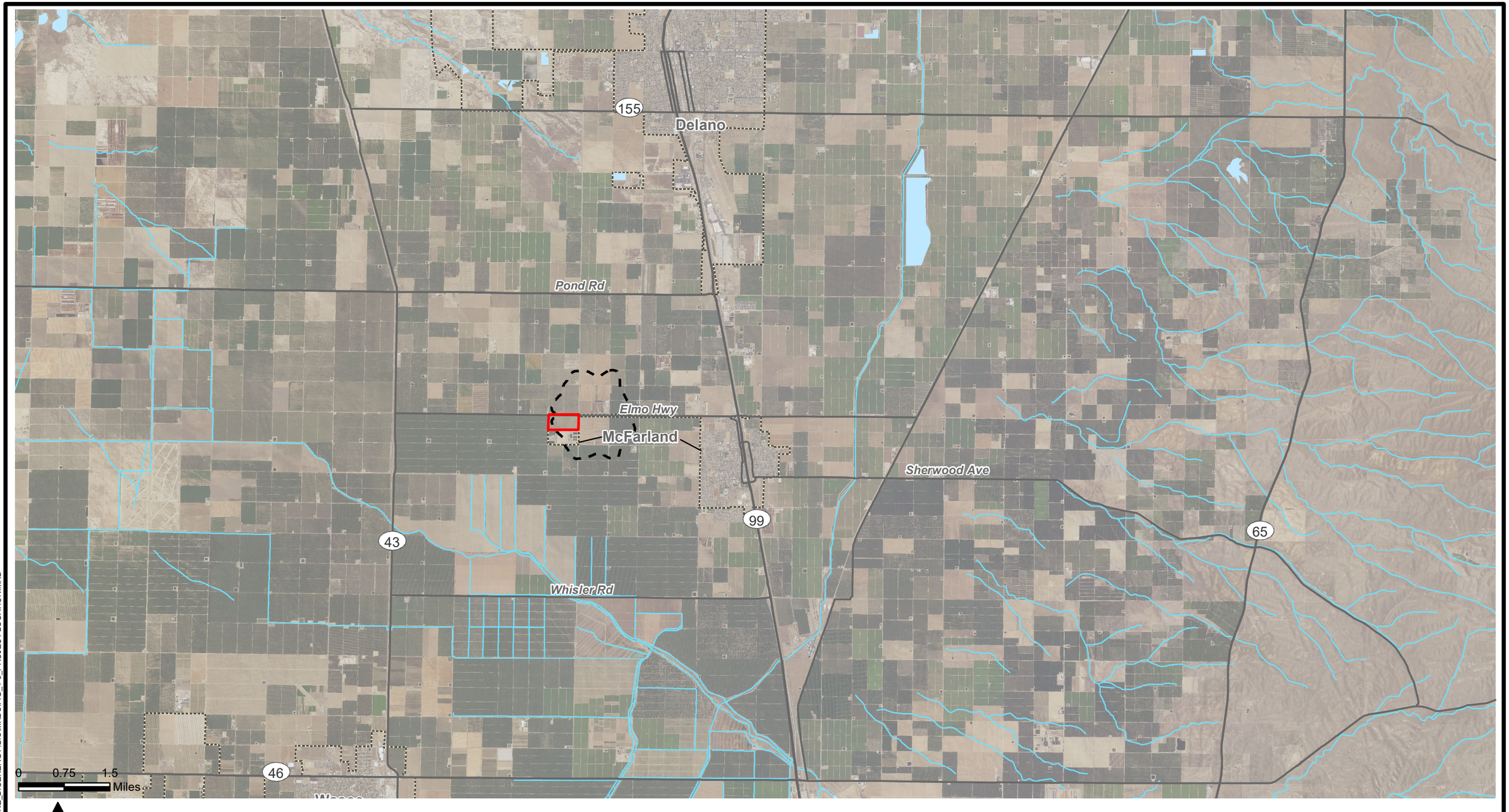

N

Explanation

- Area of review
- Property boundary
- Lake/Pond/Reservoir
- City boundary
- Major highway or road
- Rivers

S:\PROJECTS\DB19.1252_FRONTLINE_BIOENERGY\GIS\MXDS\FIG_1-3_PROJECT LOCATION.MXD

DBS&A
Daniel B. Stephens & Associates, Inc.
6/9/2022 JN DB20.1205

SAN JOAQUIN RENEWABLES

Project Location

Figure 1-3

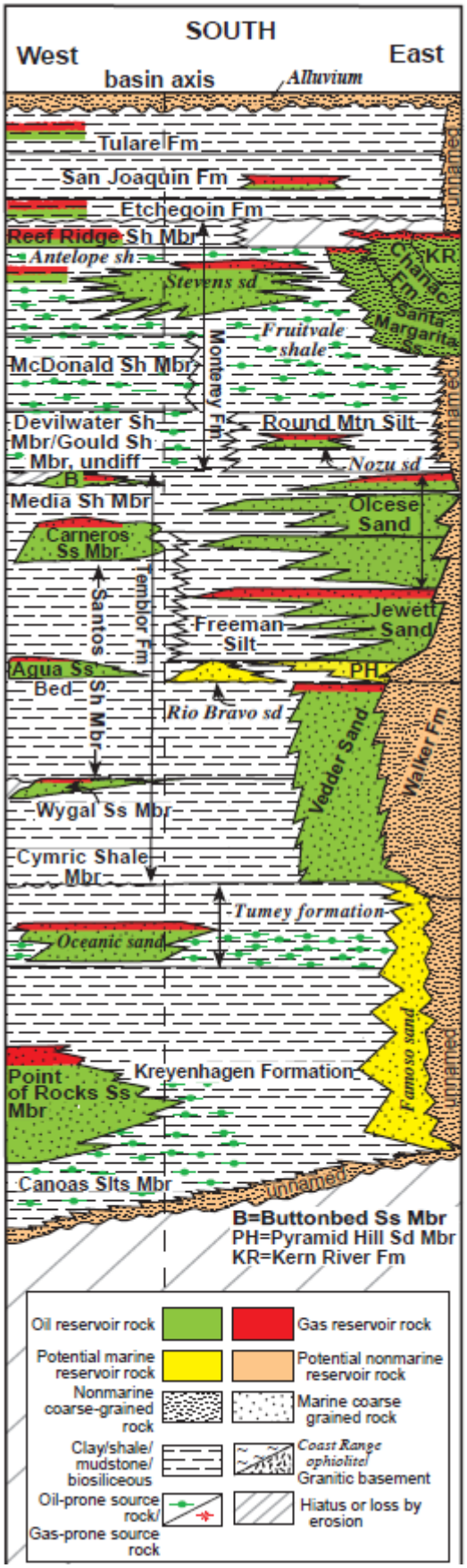

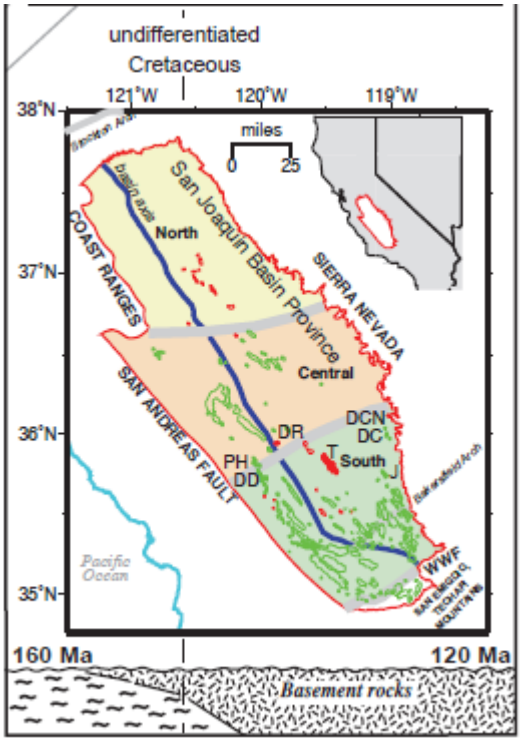

Source: Magoon et al. 2009.

SAN JOAQUIN RENEWABLES

Stratigraphic Column, Southern San Joaquin Basin Province

6/20/2022 DB19.1252 Figure 2-1

S:\Projects\DB19.1252_Frontline_Bioenergy\Final Documents\EPA Class VI permit application\1_Permit Application\Figures\docx\2-1_Stratigraphic Column S SJB.docx

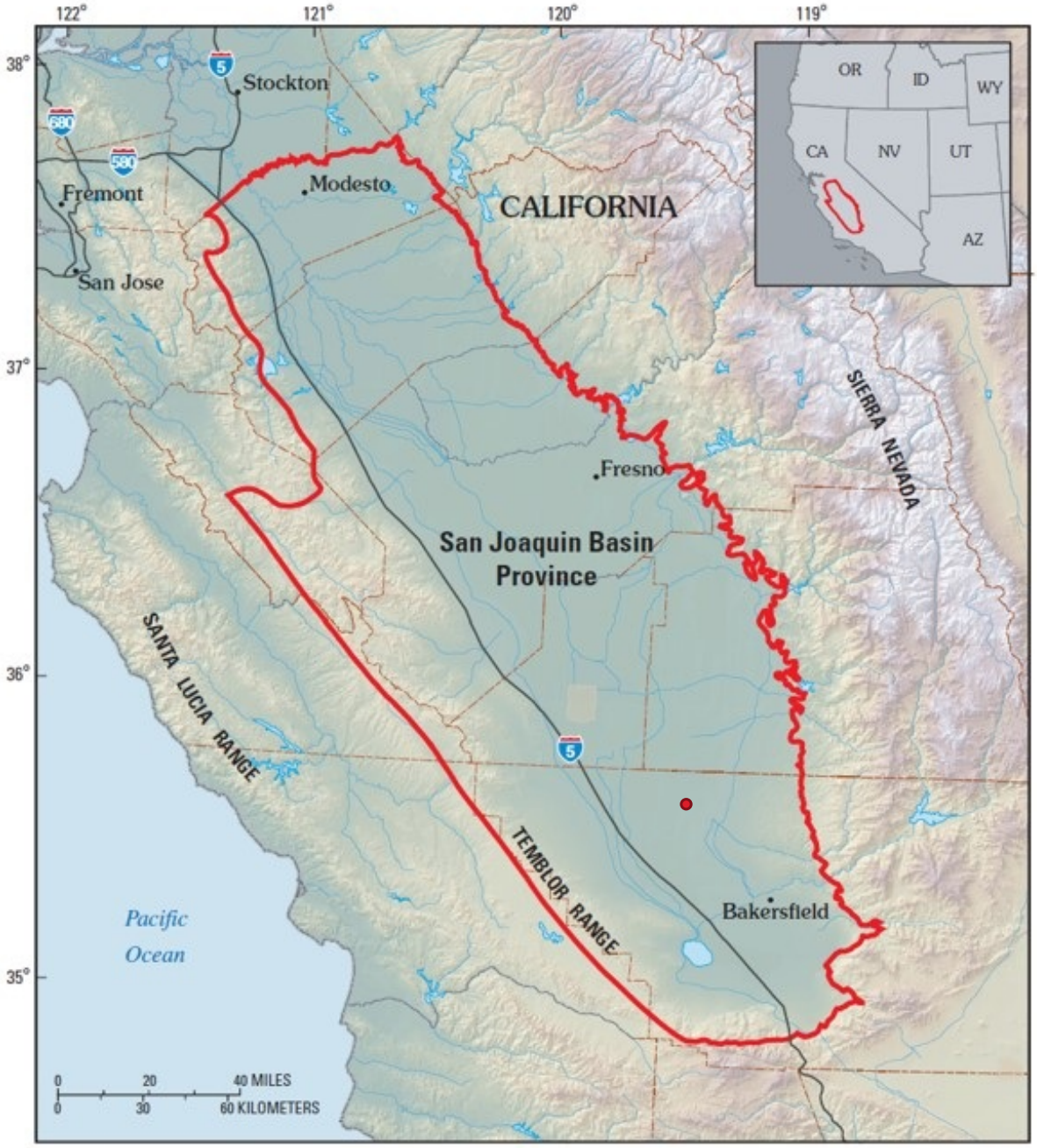

Notes: Location map of the San Joaquin Basin Province illustrating the confinement of the basin to the east by the Sierra Nevada batholith, on the west by the Temblor Range, to the south by the San Emigdio Range, and to the north by the Stockton Arch. The southern portion of the basin, in Kern County, north of Bakersfield is of specific interest in this application. SJR site indicated with red dot.

Source: Gautier et al. 2003.

SAN JOAQUIN RENEWABLES

Location map for San Joaquin Basin Province

06/09/2022 JN DB19.1252

Figure 2-2

S:\Projects\DB19.1252_Frontline_Bioenergy\GIS\QGIS\2-2 Location map for San Joaquin Basin Province.qgz

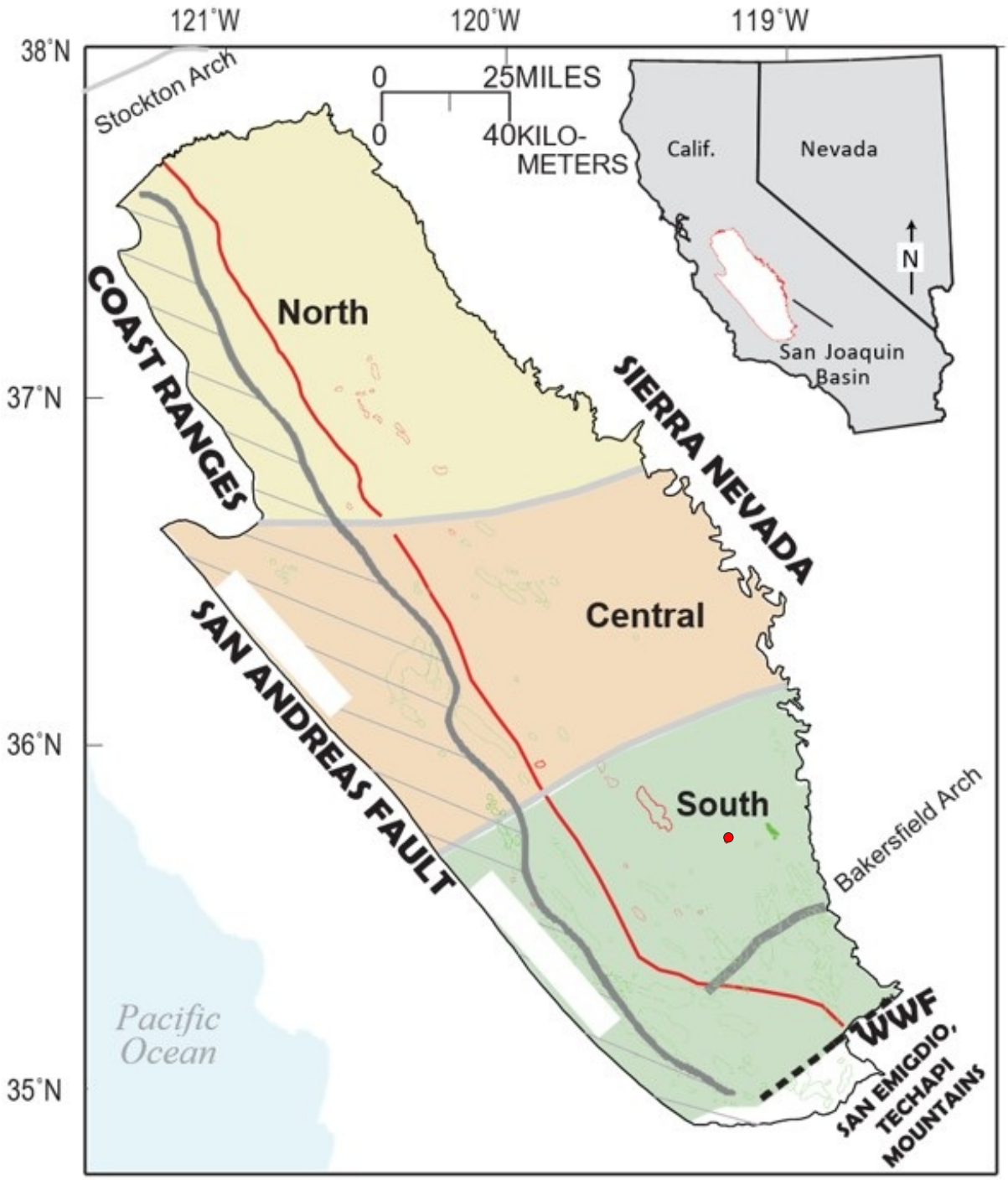

Notes:Location map of the San Joaquin Basin Province illustrating the confinement of the basin to the east by the Sierra Nevada batholith, on the west by the Coast Range (Diablo and Temblor Ranges), to the south by the San Emigdio Range, and to the north by the Stockton Arch. The southern portion of the basin, in Kern County, north of Bakersfield is of specific interest in this application. The SJR site is indicated with a red dot.

Source: Scheirer, 2003.

SAN JOAQUIN RENEWABLES

Location map for San Joaquin Basin Province with Regions

06/14/2022 JN DB19.1252

Figure 2-3

S:\Projects\DB19.1252_Frontline_Bioenergy\GIS\QGIS\2-3 SJ basin provinces.qgz

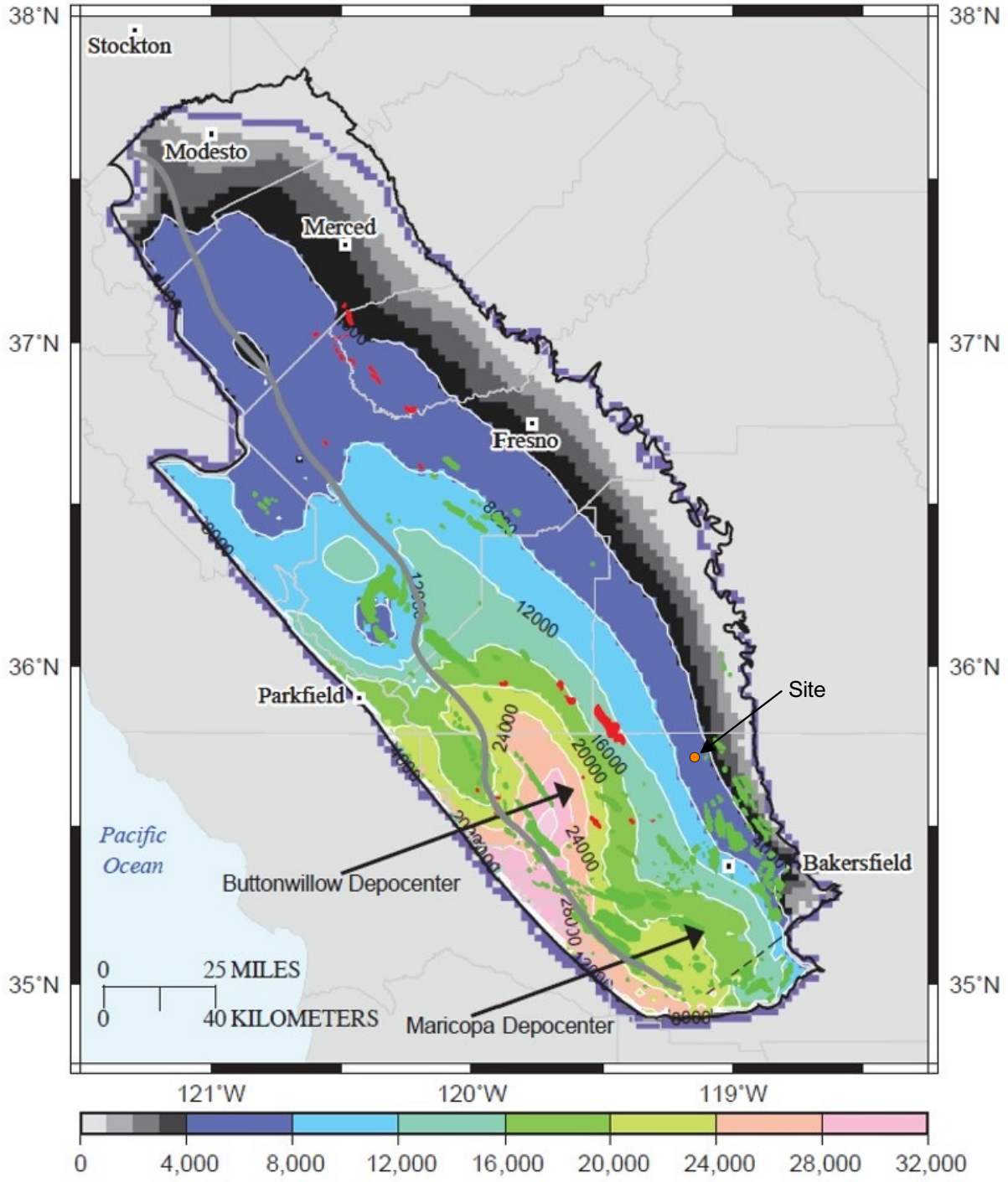

Notes: Thickness of Cenozoic deposits in the San Joaquin Basin Province illustrating the maximum thickness in excess of 28,000' west of the injection site and the thinning of the fill to the north, east, and south. The southern portion of the basin, in Kern County, north of Bakersfield is of specific interest in this application. The SJR site is indicated with a orange dot.

Source: Scheirer, 2003.

SAN JOAQUIN RENEWABLES

Thickness of Cenozoic Deposits in the San Joaquin Basin

06/20/2022 JN DB19.1252

Figure 2-4

S:\Projects\DB19.1252_Frontline_Bioenergy\GIS\QGIS\2-4 Thickness Cenozoic.qgz

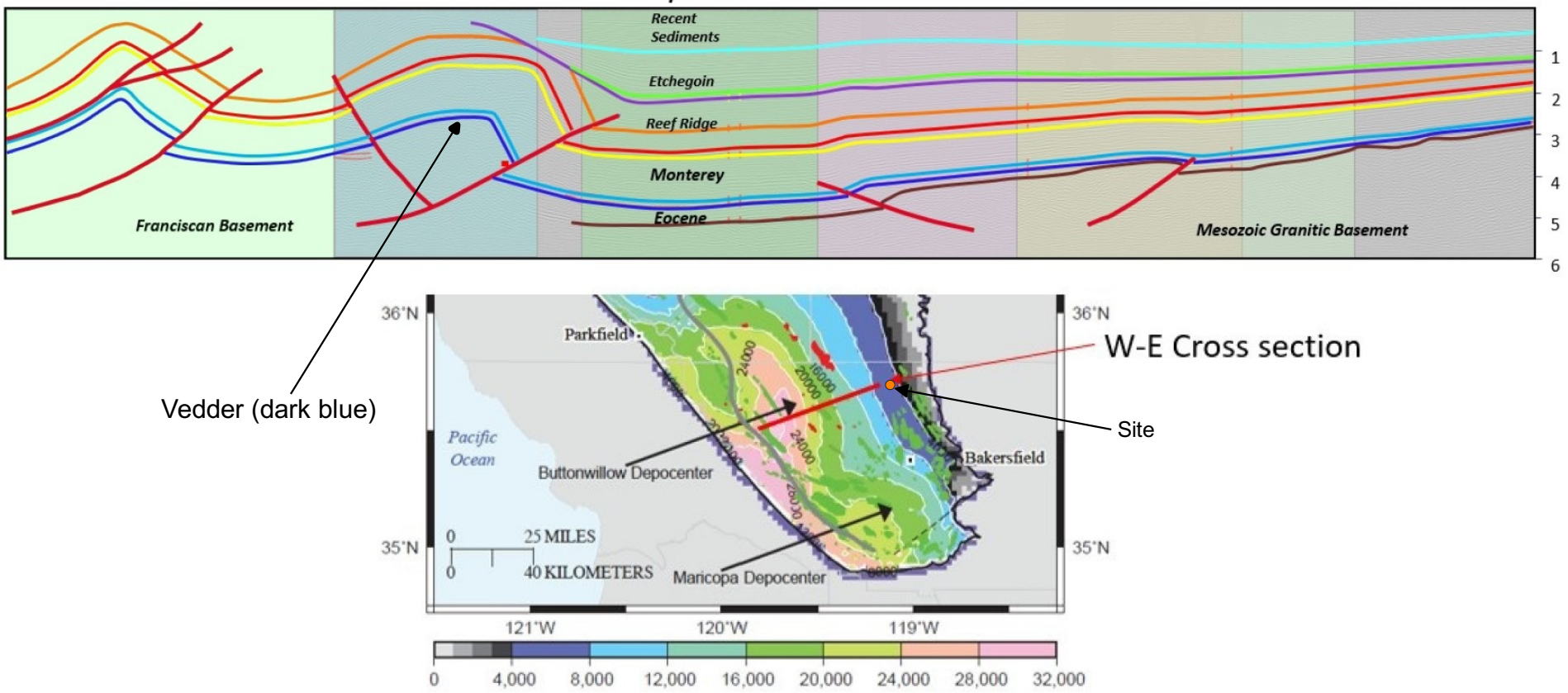

Notes: West-East cross section across the southern San Joaquin Basin Province illustrating the maximum thickness of Cenozoic strata in the Buttonwillow Depocenter. To the west a fold and thrust belt with Franciscan ductile basement is juxtaposed to an eastern Sierran homocline that overlies Mesozoic granitic basement.

Source: Schwartz, 2016

SAN JOAQUIN RENEWABLES

Generalized West – East Cross-Section Across Central/South San Joaquin Valley

06/14/2022 JN DB19.1252

Figure 2-5

S:\Projects\DB19.1252_Frontline_Bioenergy\GIS\QGIS\2-5 Generalized West – East Cross Section.qgz

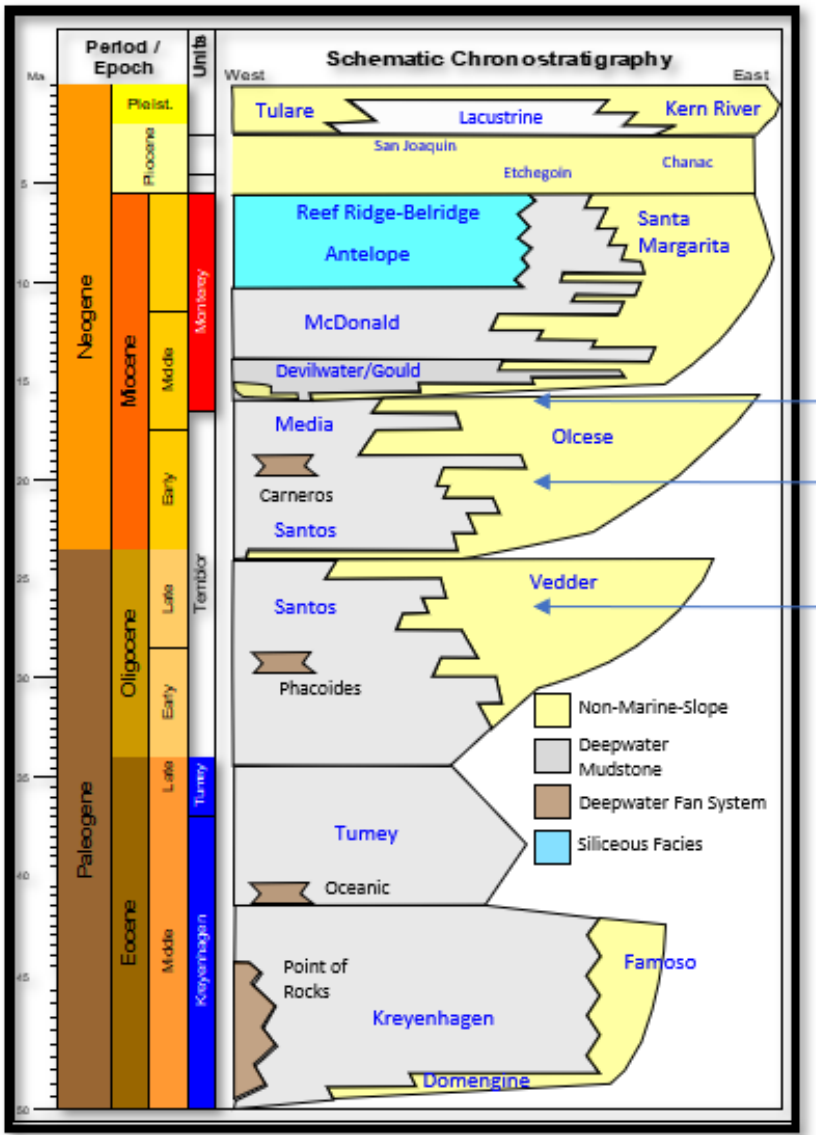

Paleogeographic Maps

Middle Miocene: Figure 2-9

Early Miocene: Figure 2-8

Late Oligocene: Figure 2-7

Notes: West to east schematic chronostratigraphic cross section through the southern San Joaquin Basin illustrating the progradational nature of the Oligocene through Miocene strata that onlaps Mesozoic Granite basement.Time periods for three key paleogeographic maps (Late Oligocene, Early Miocene, and Middle Miocene) are highlighted.

Source: Nilsen, Reid, & Boote, 2001.

SAN JOAQUIN RENEWABLES

Schematic Chronostratigraphy of the southern San Joaquin Basin

9/13/2021 DB19.1252

Figure 2-6

K:\Projects\Environmental Services\Private\Frontline Bioenergy\Final Documents\Permit Application\Figures\docx\Fig_2-1_Stratigraphic Column S SJB.docx

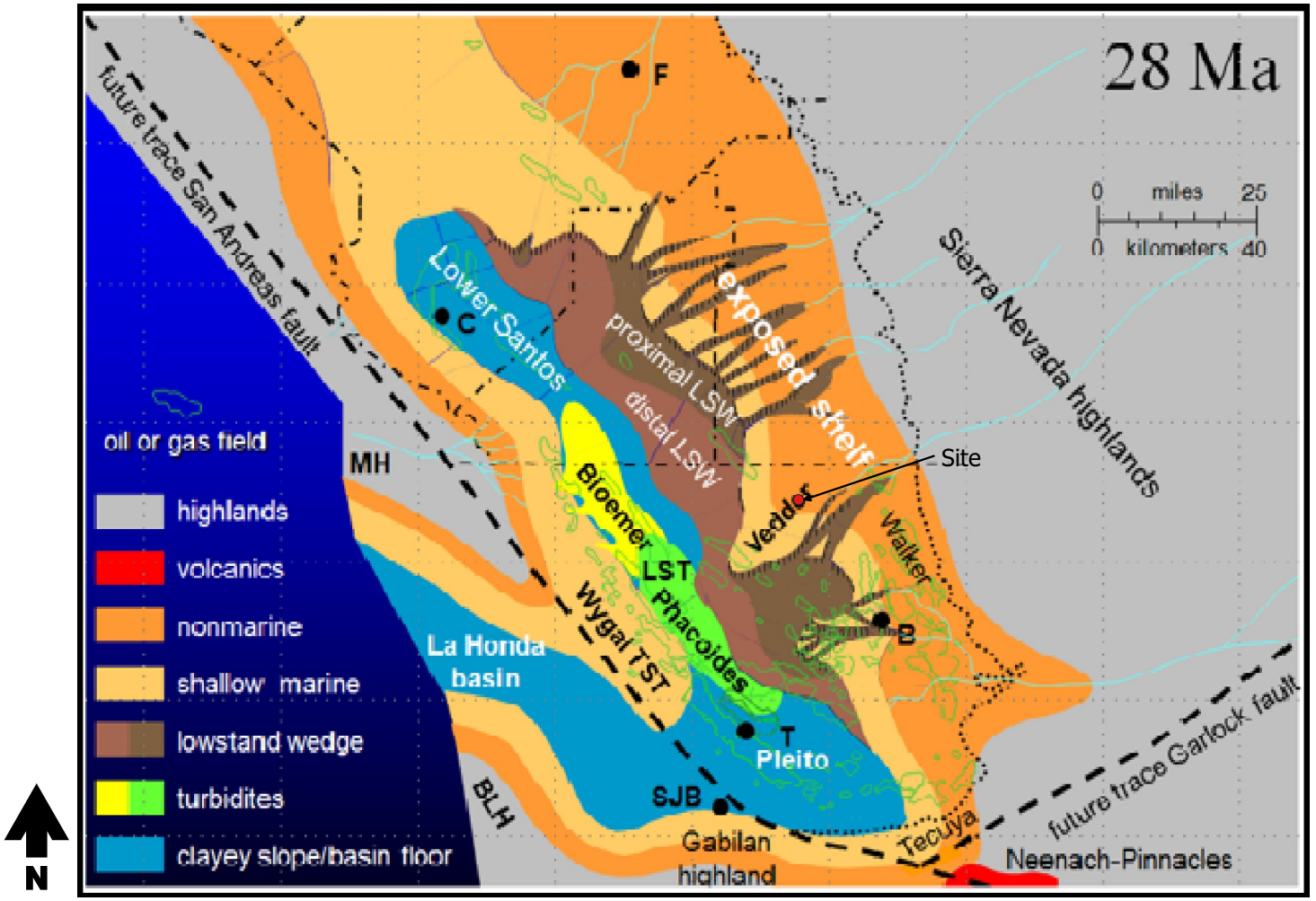

Paleogeographic map of the southern San Joaquin from the late Oligocene (~28 Ma) from Boote et al, 2001. The Vedder Sand Formation is an east to west prograding shallow marine shelf system filling the basin from the Sierra Nevada highlands in the east. Shelf edge Vedder sands transition to proximal and distal lowstand wedge sands westward, and eventually into lower Santos Shale at the axis of the basin. Locations: B = Bakersfield, T = Taft, C = Coalinga, F = Fresno, SJB = San Juan Bautista. The SJR site is indicated with a red dot.

Source: Nilsen, Reid, & Boote, 2001.

SAN JOAQUIN RENEWABLES

Late Oligocene Paleogeography of the San Joaquin Basin

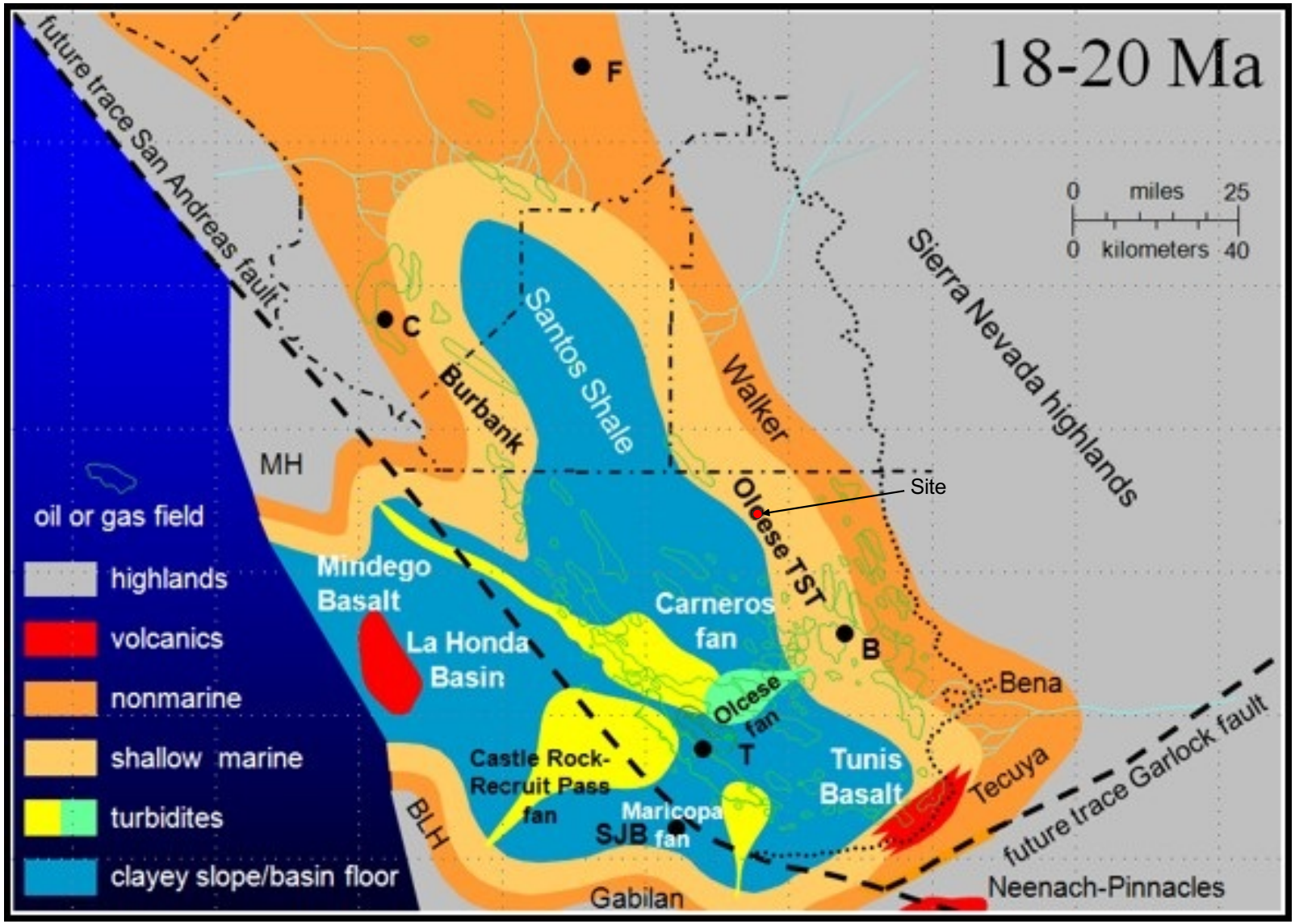

Paleogeographic map of the southern San Joaquin from the early Miocene (~18-20 Ma) from Boote et al, 2001.
The Olcese Sand Formation is an east to west prograding shallow marine shelf system filling the basin from the Serra Nevada highlands in the east. Shelf edge Olcese sands transition to slope and basin floor muds of the Santos Shale westward. Locations: B = Bakersfield, T = Taft, C = Coalinga, F = Fresno, SJB = San Juan Bautista
The SJR site is indicated with a red dot.

Source: Boote et al., 2001.

SAN JOAQUIN RENEWABLES

Early Miocene Paleogeography of the San Joaquin Basin

06/09/2022 JN DB19.1252

Figure 2-8

S:\Projects\DB19.1252_Frontline_Bioenergy\GIS\QGIS\2-8_early miocene paleogeography.qgz

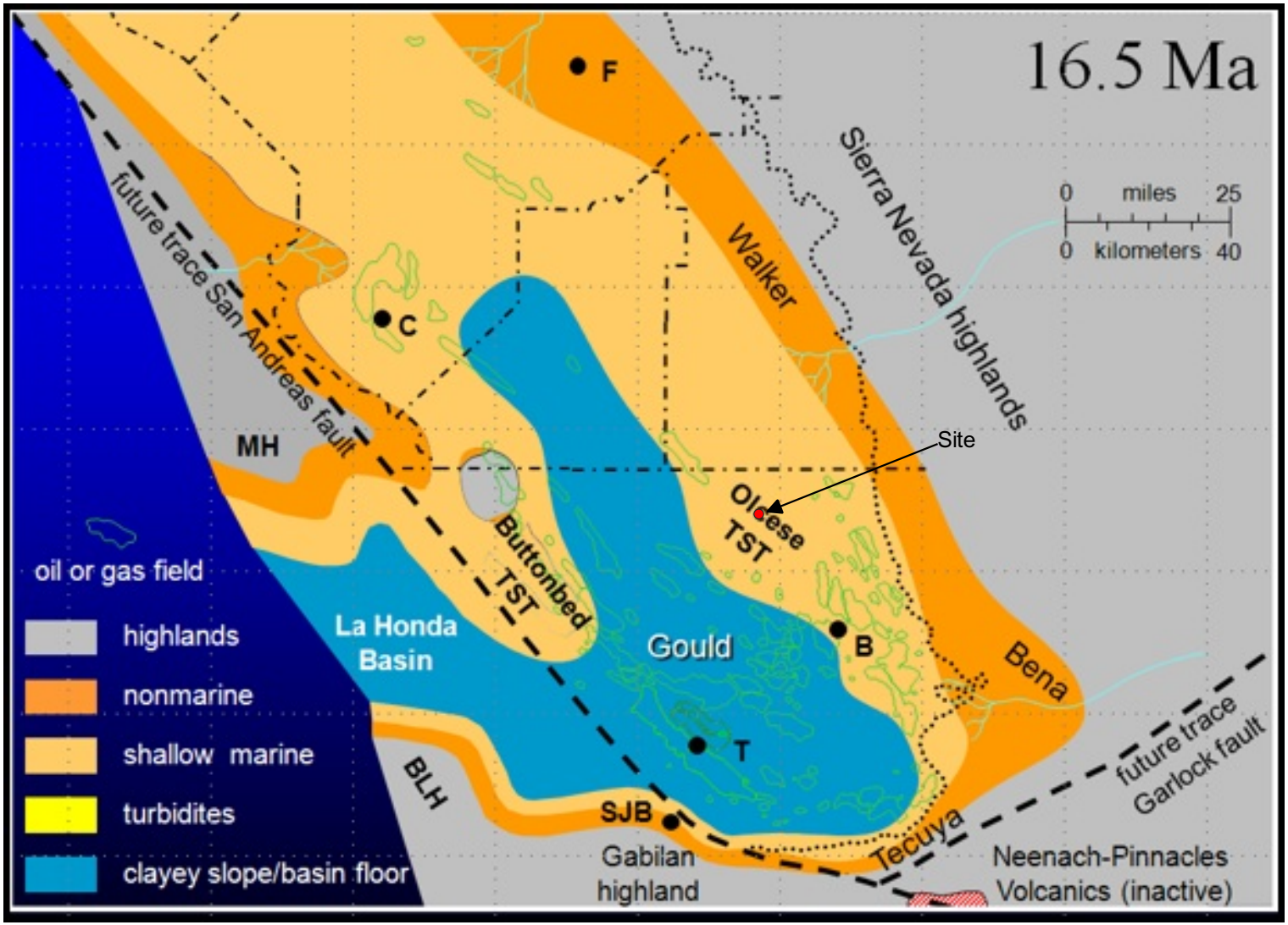

Paleogeographic map of the southern San Joaquin from the middle Miocene (~16.5 Ma) from Boote et al, 2001.
The Olcese Sand Formation is an east to west prograding shallow marine shelf system filling the basin from the Serra Nevada highlands in the east. Shelf edge Olcese sands transition to slope and basin floor muds of the Media to lower Monterey (Gould) Shale westward. Locations: B = Bakersfield, T = Taft, C = Coalinga, F = Fresno, SJB = San Juan Bautista
The SJR site is indicated with a red dot.

Source: Boote et al, 2001.

SAN JOAQUIN RENEWABLES

Middle Miocene Paleogeography of the San Joaquin Basin

06/09/2022 JN DB19.1252

Figure 2-9

S:\Projects\DB19.1252_Frontline_Bioenergy\GIS\QGIS\2-9_middle miocene paleogeography.qgz

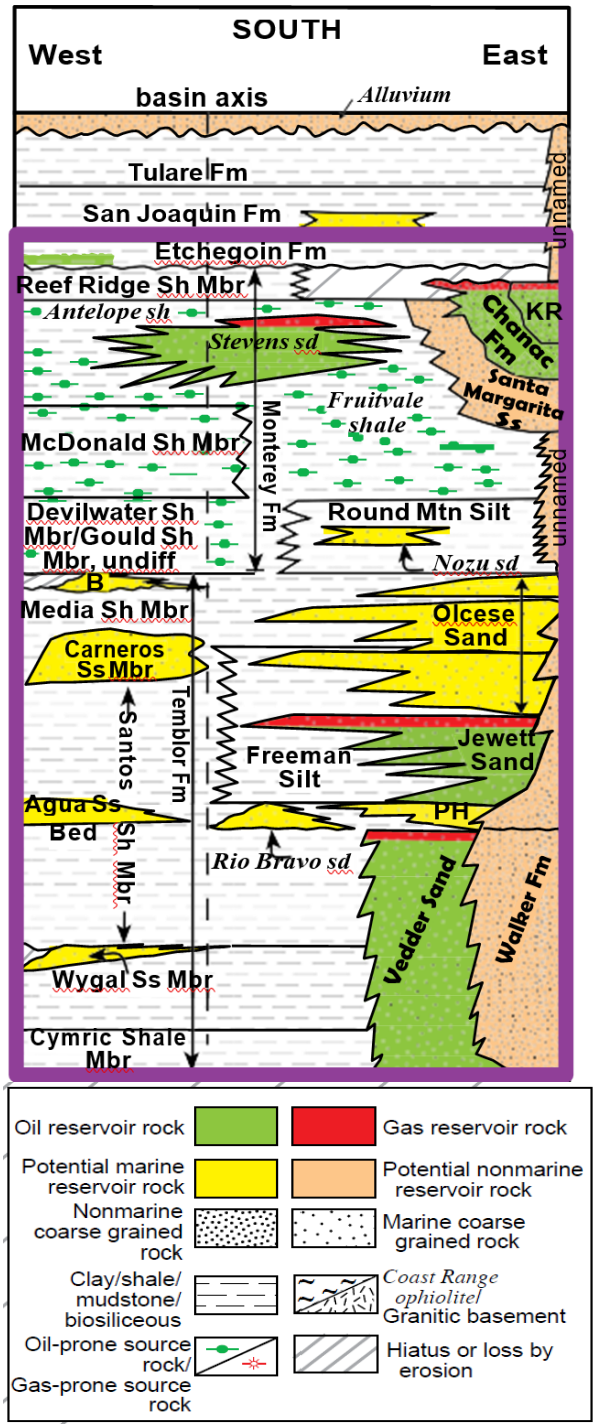

Notes: Detailed portion of the Stratigraphic column shown in Figure 2-1 that displays the lateral extent of the Vedder and Olcese Sands and the Freeman Jewett Silt, Round Mountain Silt, and Fruitvale Shale confining layers of the Antelope-Stevens petroleum system (purple outline) in the southern portion of the Basin Province. It also annotates the depositional origins of the sedimentary units (e.g. marine vs non-marine).

Source: Magoon et al. 2009.

SAN JOAQUIN RENEWABLES

Stratigraphy of Southern San Joaquin Basin Province Antelope-Stevens Petroleum System

6/20/2022 DB19.1252

Figure 2-10

K:\Projects\Environmental Services\Private\Frontline Bioenergy\Final Documents\Permit Application\Figures\docx\ Fig_2-10_Stratigraphy of Antelope-Stevens

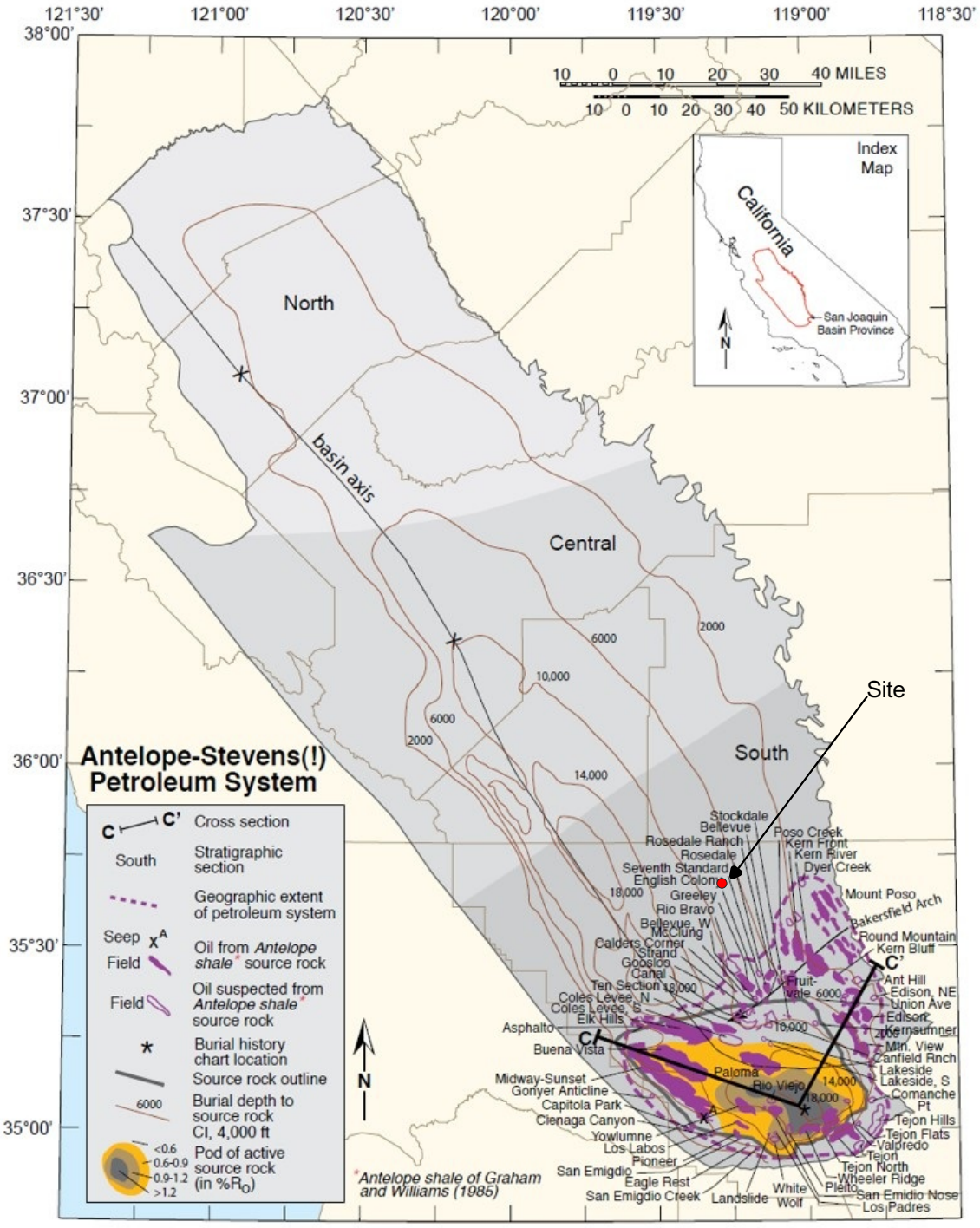

Figure 8.14. The Antelope-Stevens(!) petroleum system map shows the present-day burial depth of the known source rock—the Antelope shale (brown contours)—as well as the extent of the source rock thought to have good source rock qualities (such as facies, hydrogen index, and total organic carbon; gray line), location of cross section C-C', location(*) of burial history chart, and a purple dashed line indicating the geographic extent of the system. Petroleum accumulations in this system are shown in purple; solid polygons indicate accumulations based on geochemical analysis, whereas outlines indicate suspected accumulations based on stratigraphic proximity. Seep location is from Cole and others (1999). CI, contour interval; $\%R_o$, percent vitrinite reflectance.

Source: Magoon et al. 2009.

Notes: SJR site indicated with a red dot.

SAN JOAQUIN RENEWABLES

Antelope-Stevens Petroleum System

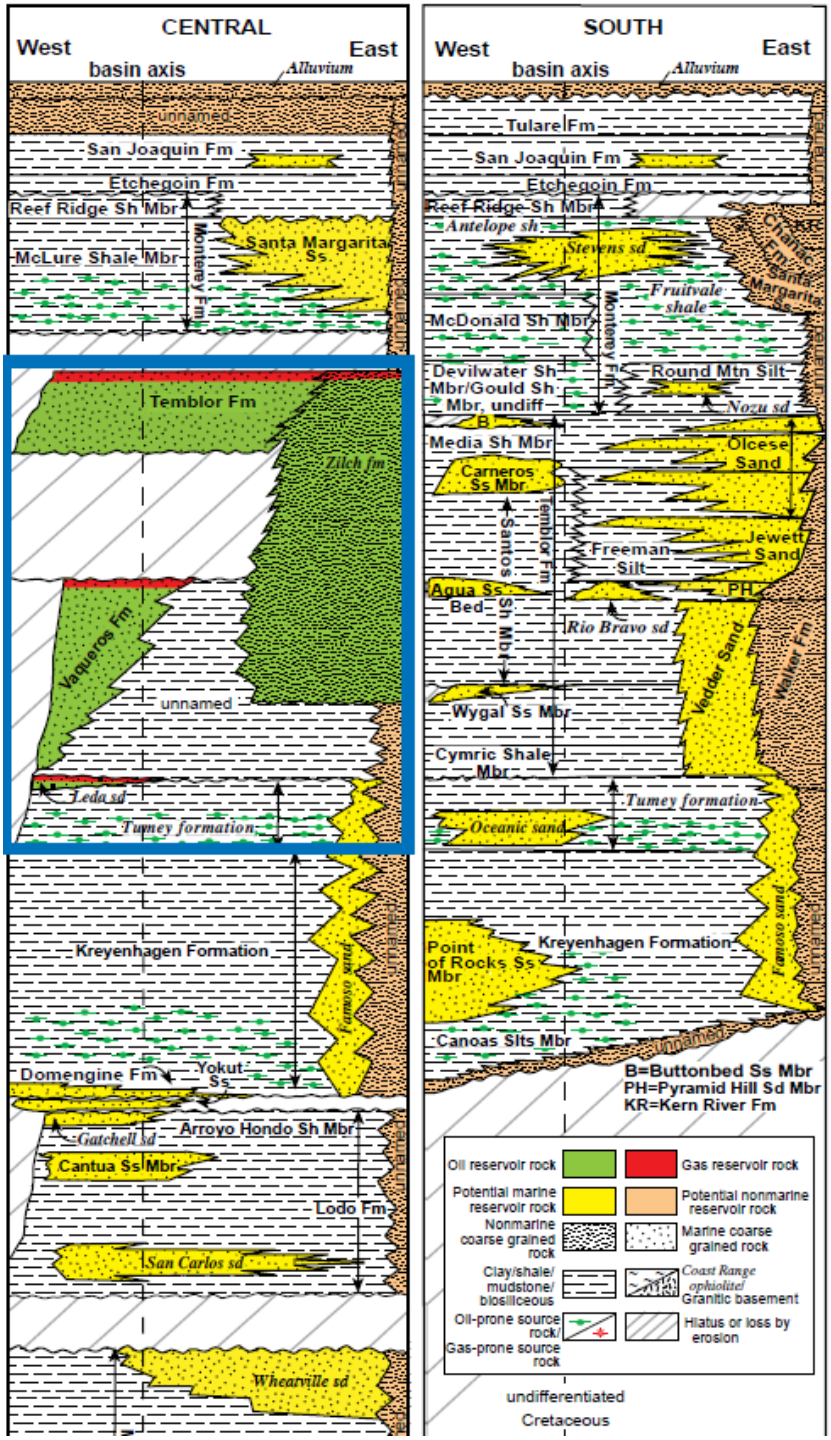

Notes: Detailed portion of the Stratigraphic column shown in Figure 2-1 that displays the lateral extent of the Vedder and Olcese Sands and the Freeman Jewett Silt "Freeman Silt", Round Mountain Silt, and Fruitvale Shale confining layers of the Tumey-Temblor petroleum system (blue outline) in the central portion of the Basin Province. It also annotates the origins of the sedimentary units (e.g. marine vs non-marine).The northern part of the AoR goes into the central SJBP but the stratigraphy of the area is aligned with the southern SJBP.

Source: Magoon et al. 2009.

SAN JOAQUIN RENEWABLES

Stratigraphy of Southern San Joaquin Basin Province Tumey-Temblor Petroleum System

6/20/2022 DB19.1252 Figure 2-12

S:\Projects\DB19.1252_Frontline_Bioenergy\Final Documents\EPA Class VI permit application\1_Permit Application\Figures\docx\Fig_2-12_Stratigraphy of Tumney-Temblor system.docx

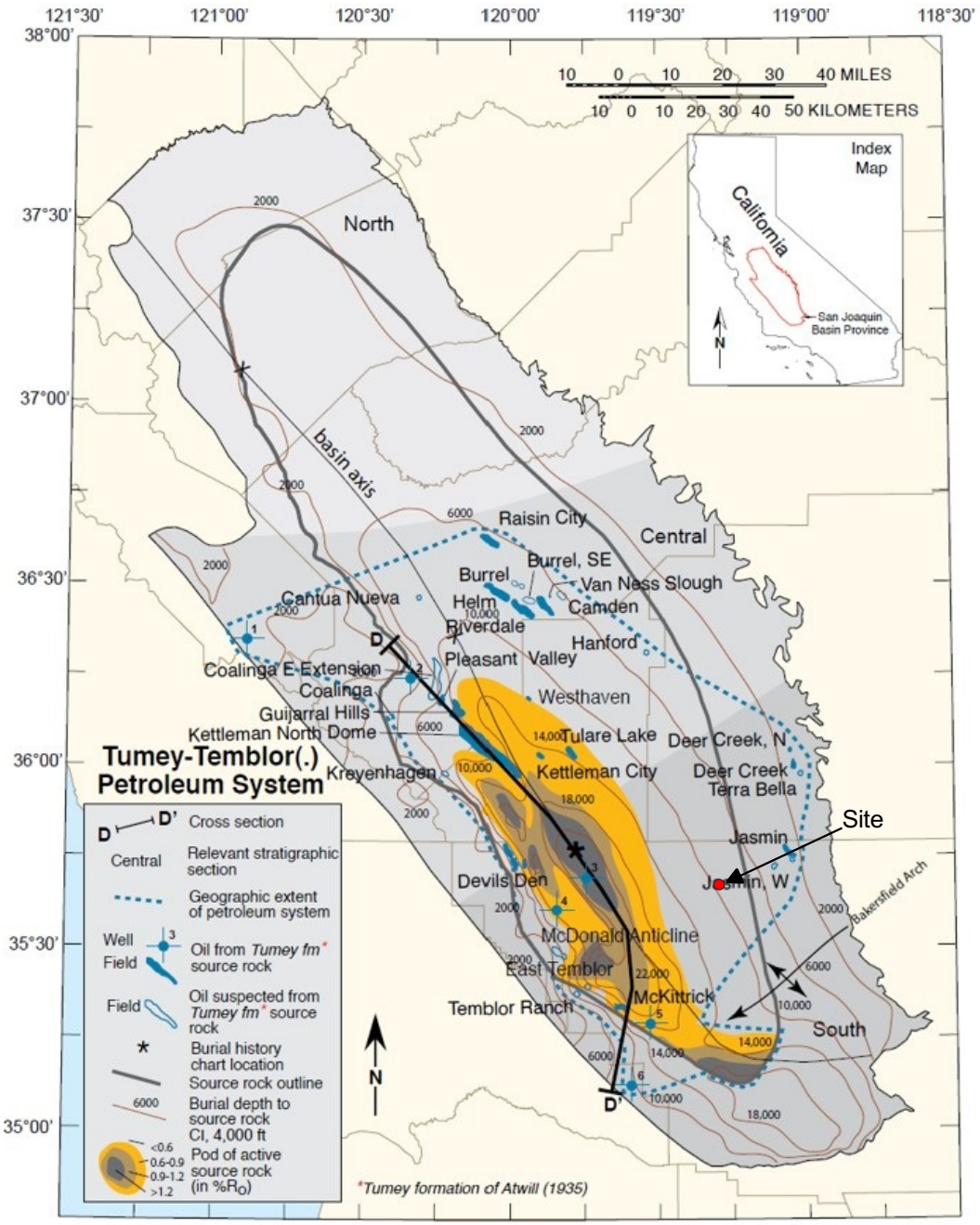

Map of the distribution of the source terrain and the charged oil fields associated with the Tumey-Temblor petroleum system in the southern San Joaquin Basin Province. Within the AoR, two fields in the area are part of this system (Jasmin and Jasmin west). Charge migrated nearly 30 miles from the center of the basin to the west.
SJR property indicated with a red dot.

Source: Magoon et al. 2009.

SAN JOAQUIN RENEWABLES

Aerial Distribution of the Tumney-Temblor Petroleum System Source Terrain and Charged Fields

06/20/2022 JN DB19.1252 Figure 2-13

S:\Projects\DB19.1252_Frontline_Bioenergy\GIS\QGIS\2-13 Tumney-Temblor.qgz

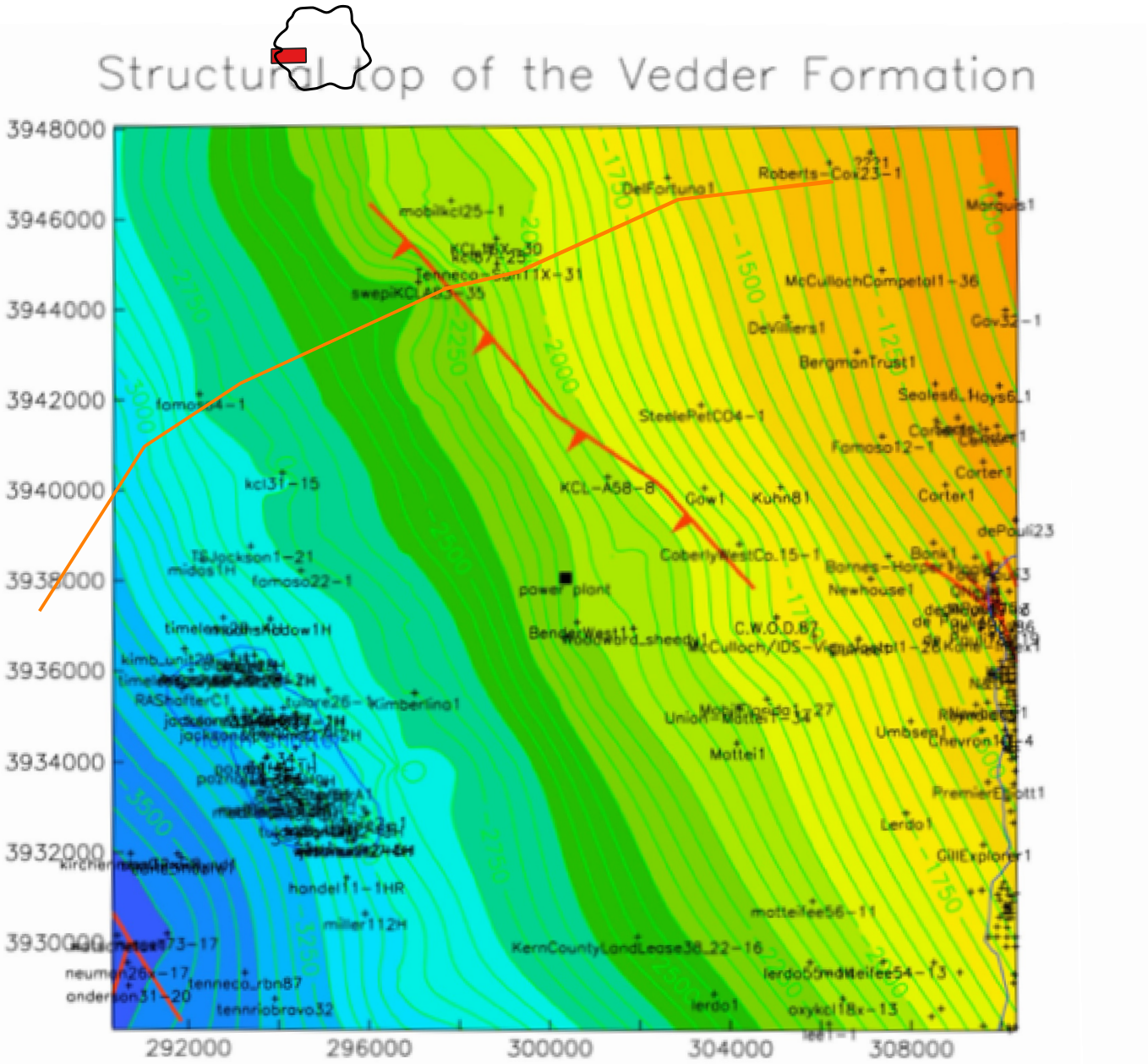

Structure contour map of top of the Vedder Formation from Wagoner (2009). The east side of the San Joaquin Basin in the vicinity of the injection site (red rectangle) dips at a relatively constant four degrees to the west. Cross section 1 from Wagoner displayed in Figures 2-15 and 2-16 is indicated in orange. Contours are based on well log analysis and seismic interpretation. Mapped fault is the Pond fault (shown in red). Contour interval is 100 meters.

Source: : J.L. Wagoner, 2009

Explanation

- SJR Property
- Wagoner 1
- Area of Review

SAN JOAQUIN RENEWABLES

Structure Contour Map of top of the Vedder Formation

S:\Projects\DB19.1252_Frontline_Bioenergy\GIS\QGIS\EPA comments\2-14 Structural top of vedder formation.qgz

06/09/2022 JN DB19.1252

Figure 2-14

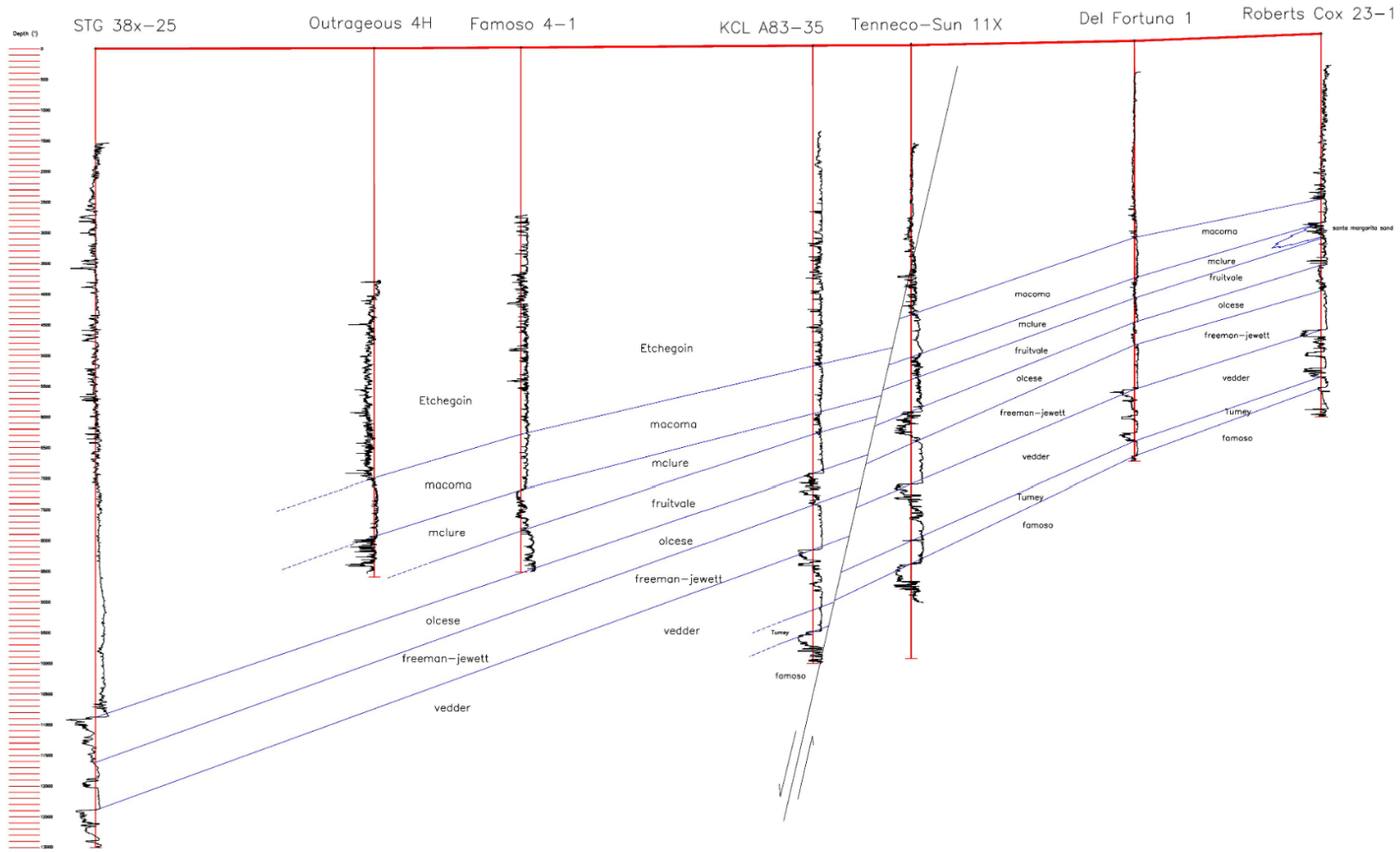

Notes: Cross section 1 from Wagoner (2009) trends SW-NW displaying correlated Spontaneous Potential well logs from oil and gas exploration wells. Units mapped by Wagoner are labeled on the cross section. The Pond Fault cuts both the KCL A83-35 and Tenneco-Sun 11X wells. The Vedder overlies the Tumey Shale that in turn overlies the Famosa Sand. Though not labeled, both of these units onlap granite basement eastward.

SAN JOAQUIN RENEWABLES

Cross Section 1 from Wagoner (2009)

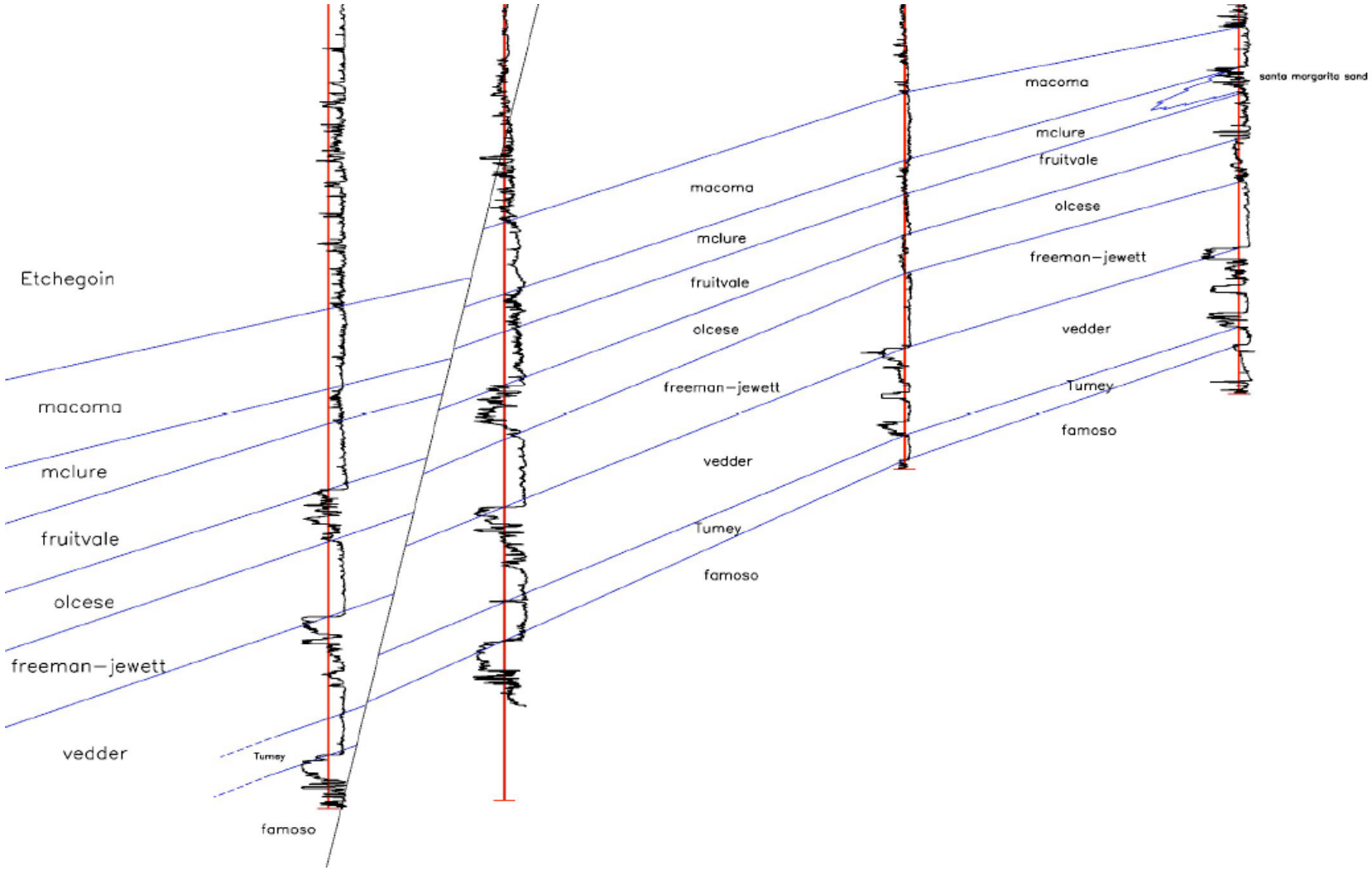

Notes: Close-up of Wagoner (2009) cross section 1 displaying correlated Spontaneous Potential well logs from oil and gas exploration wells. Units mapped by Wagoner are labeled on the cross section. The key sand units of the Vedder are correlated from the SP logs and colored on the cross section. The Pond Fault offsets First Vedder (contoured on Figure 2-14) nearly 200 meters between the KCL A83-35 and Tenneco-Sun 11X wells.

SAN JOAQUIN RENEWABLES

Focused View of Cross Section from Wagoner (2009)

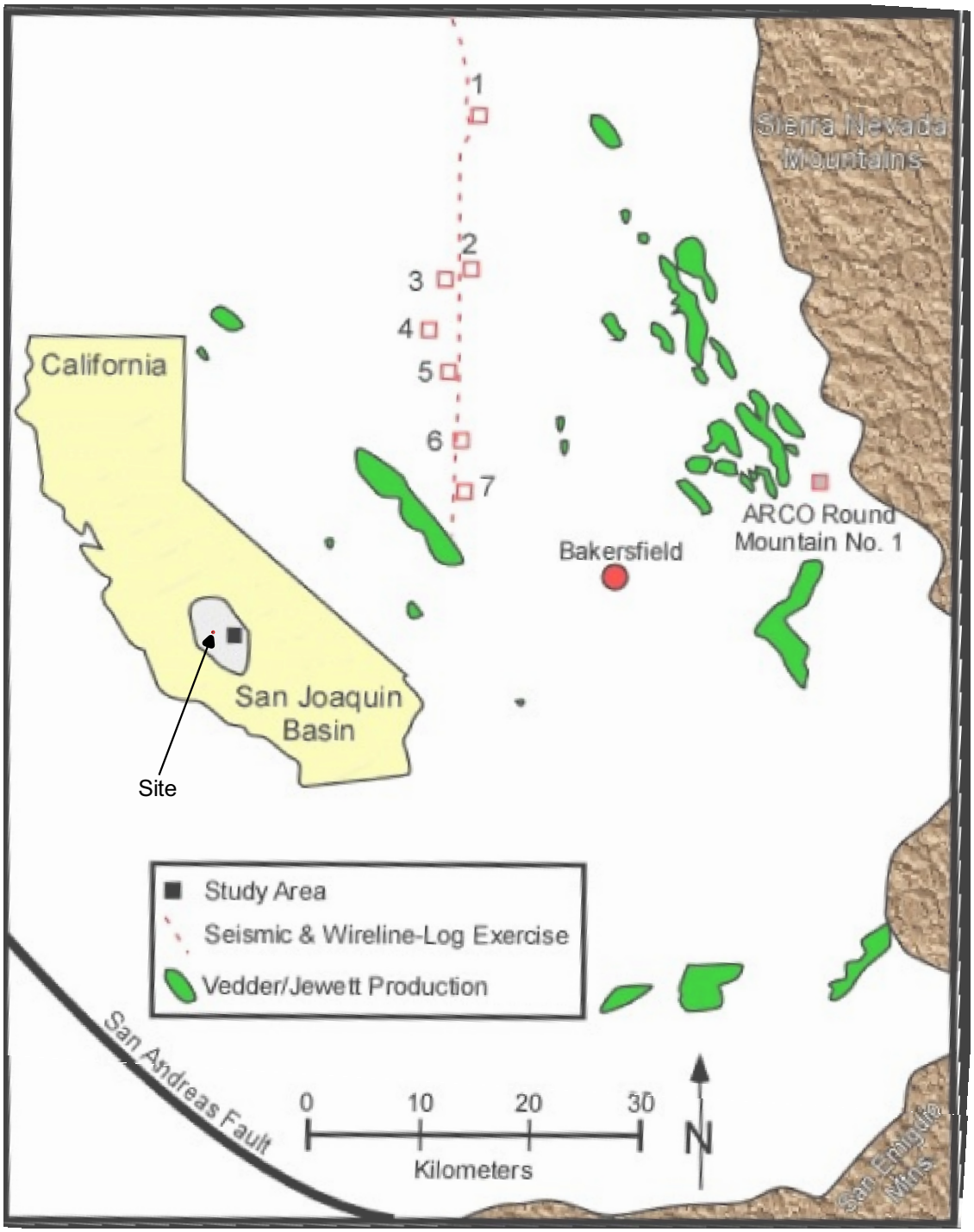

Notes: Southern San Joaquin Basin, California, showing well and seismic data exercise locations. Vedder/ Jewett Formation oil fields are shown with green shading. The Vedder and the overlying Freeman-Jewett ("Freeman Silt") are depicted in green.

Explanation

Area of Review

Source: Hewlett & Tye, 2015.

SAN JOAQUIN RENEWABLES

Wells and Seismic Data Exercise Locations for Southern San Joaquin Basin

06/09/2022 JN DB19.1252

Figure 2-17

S:\Projects\DB19.1252_Frontline_Bioenergy\GIS\QGIS\EPA comments\2-17 Wells and Seismic Data Exercise.qgz

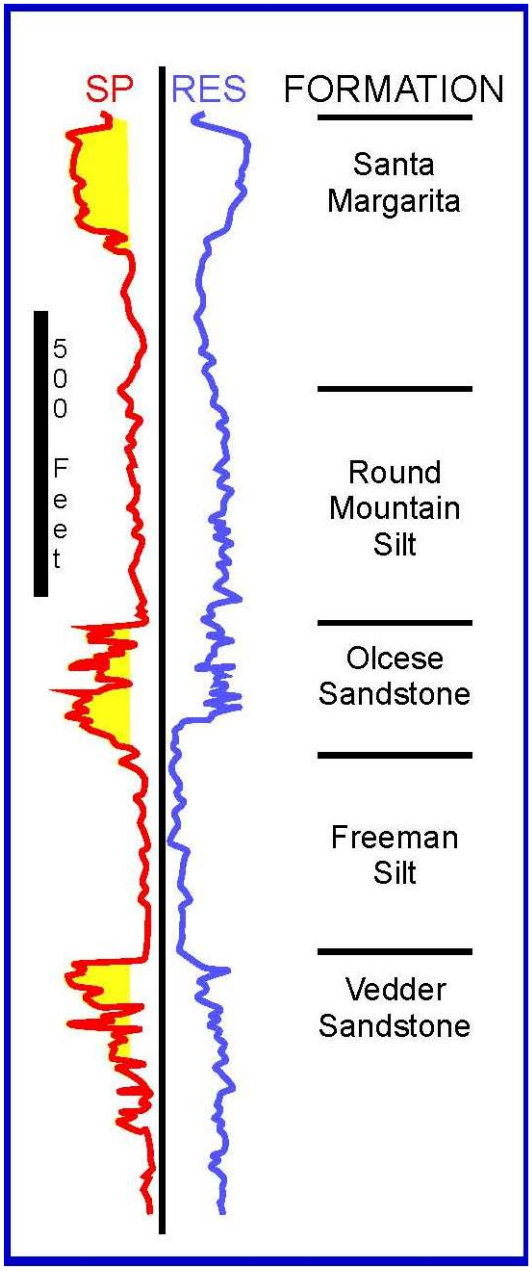

Notes: Southern San Joaquin Basin, California, stratigraphic type log of the Santa Margarita through Vedder Formations. Location of the Santa Margarita well (Well #1) is shown on Figure 2-17.

Source: Hewlett and Tye, 2015

SAN JOAQUIN RENEWABLES

Stratigraphic Type Log of the Santa Margarita Through Vedder Formations

6/16/2022 DB19.1252

Figure 2-18

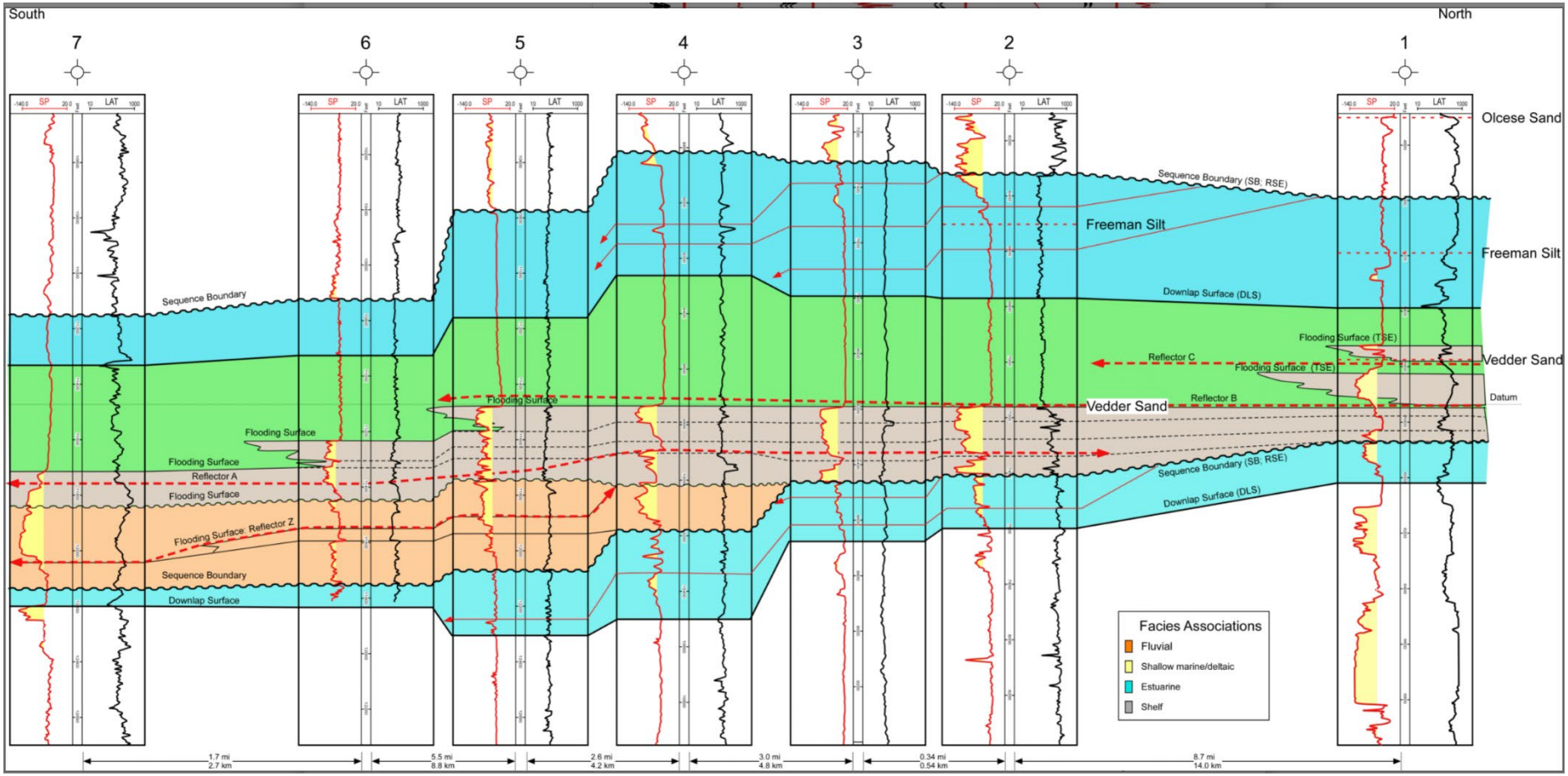

Notes: Interpreted south-to-north oriented wireline-log cross section (Figure 2-17) paralleling the seismic line. Wells 2-6 were correlated to the seismic data with synthetic seismograms. Note cycles Z, A, B, and C, and the variable wireline-log character of the parasequences. Facies-association interpretations are based on core data. The Vedder and overlying Freeman-Jewett ("Freeman Silt") are depicted in salmon and green.

Source: Hewlett & Tye, 2015.

SAN JOAQUIN RENEWABLES

Interpreted South-to-North Oriented Wireline-Log Cross-Section

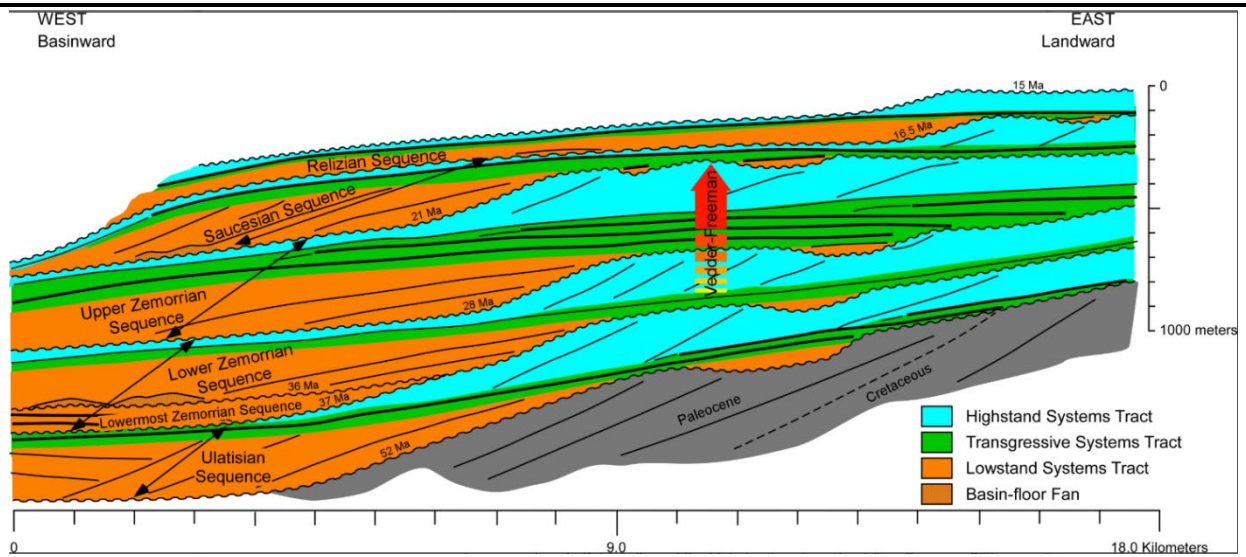

Notes: Five Tertiary-age stratigraphic sequences and their interpreted systems tracts in the eastern San Joaquin Basin, California (Hewlett et al., 2014). The red arrow denotes the Vedder Sand to Freeman Silt stratigraphic interval.

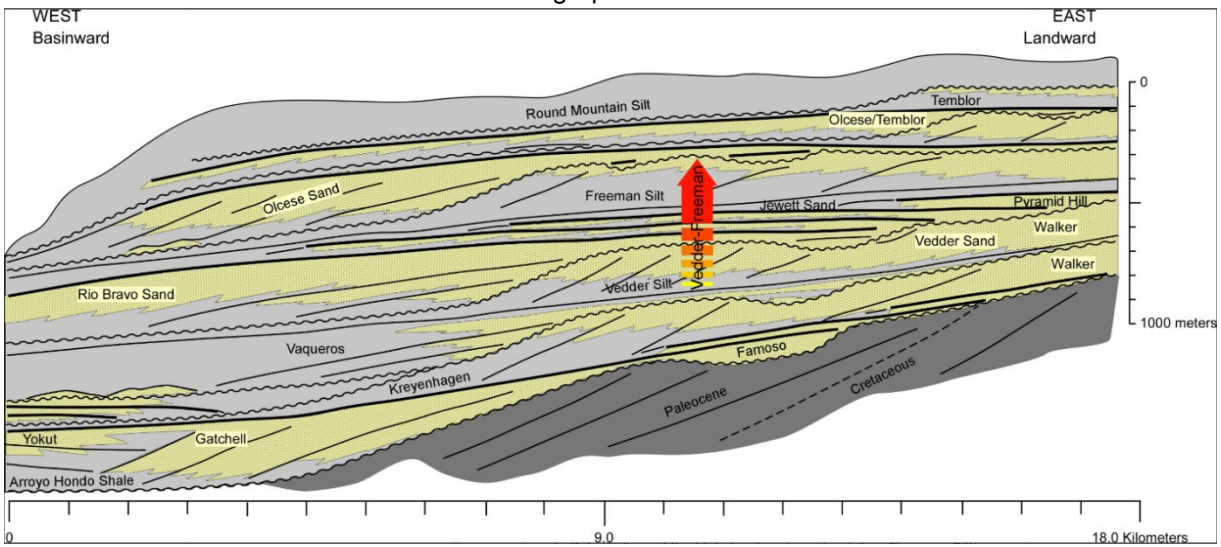

Notes: Lithologic interpretation of the five Tertiary-age stratigraphic sequences in the eastern San Joaquin Basin, California (Hewlett et al., 2014). The red arrow denotes the Vedder Sand to Freeman Silt stratigraphic interval. Reservoirs formed in sandstones deposited under conditions of shoreline progradation and retrogradation. Transgressive-shelf deposits are capped by highstand-systems tract strata (i.e., Freeman Silt) that form overlying seals.

Source: Hewlett & Tye, 2015.

SAN JOAQUIN RENEWABLES

Lithologic Interpretation, Eastern San Joaquin Basin

10/4/2021 DB19.1252

Figure 2-20

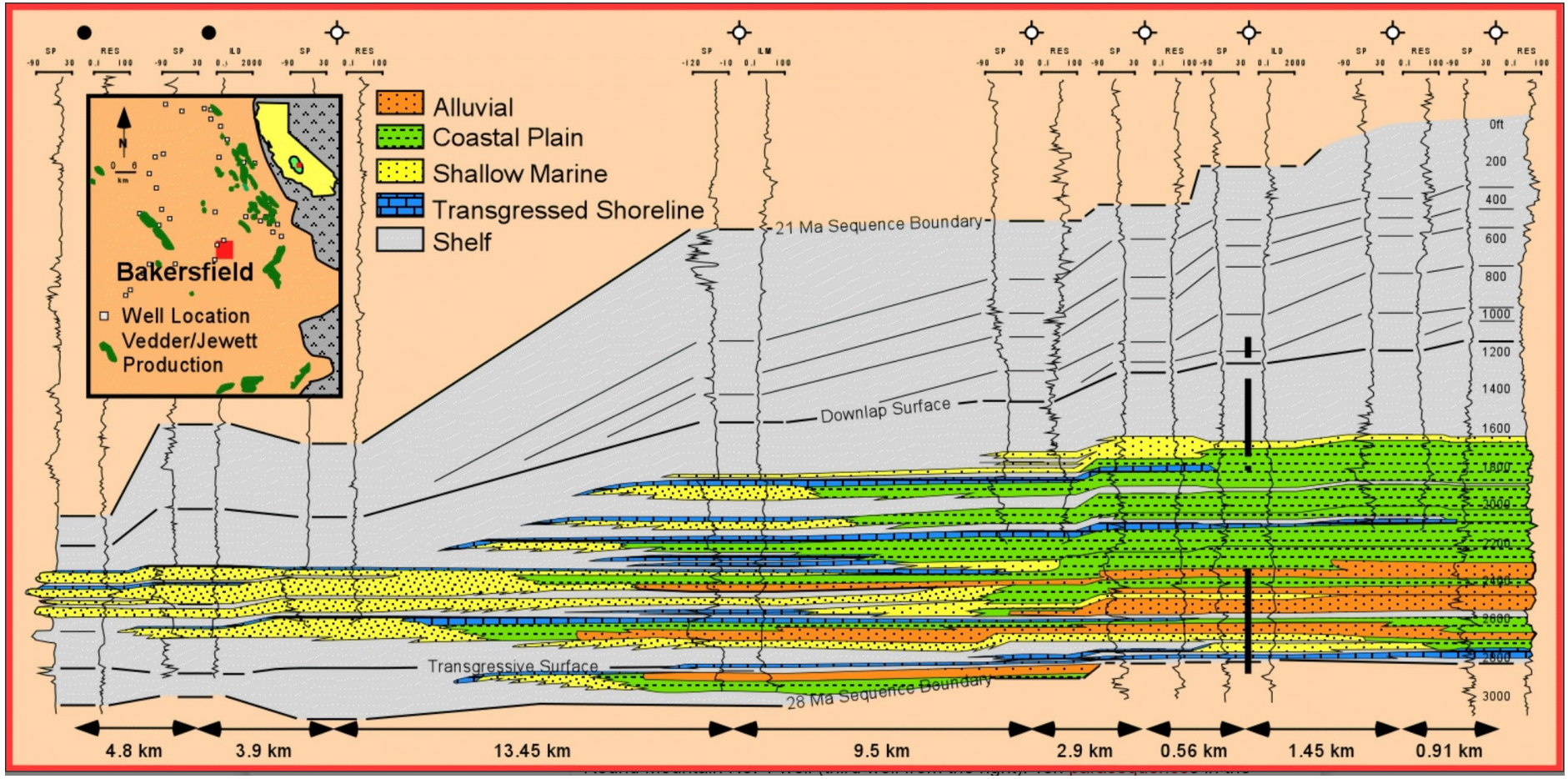

Notes: West-to-east oriented wireline-log cross section intersecting the ARCO Round Mountain No. 1 well (third well from the right).
Ten parasequences in the transgressive-systems tract are noted by the upward-coarsening SP log character. Parasequences are overlain by flooding surfaces and marine mudstones. The transgressive-systems tract in each well displays a retrogradational stacking pattern, parasequences thin, and mudstone content increases upward.

Source: Hewlett & Tye, 2015.

SAN JOAQUIN RENEWABLES

Interpreted West-to-East Oriented Wireline Log Cross Section

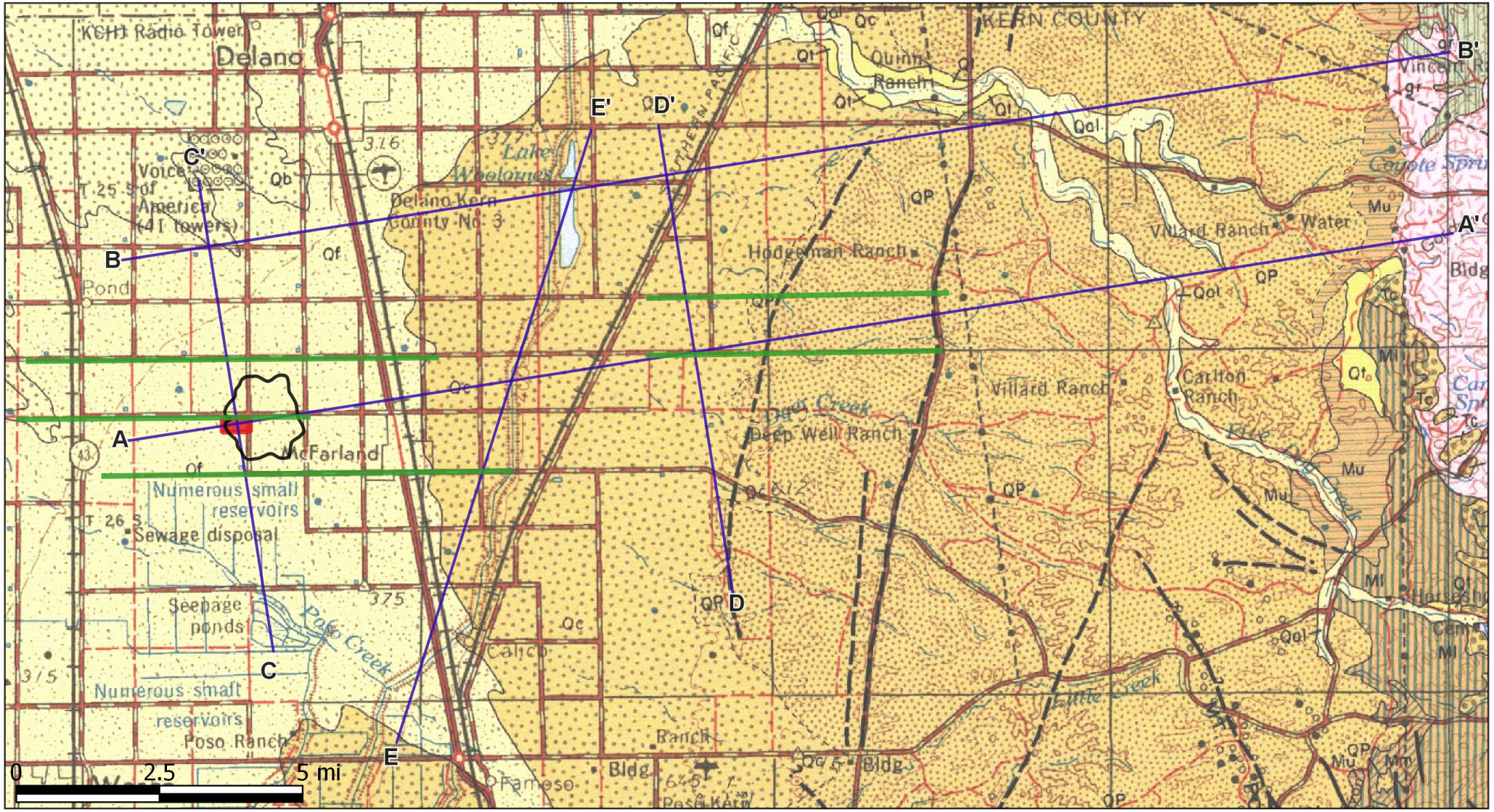

Notes: Map display of surface geology of the eastern San Joaquin Valley in the vicinity of McFarland illustrating granite basement to the east (pink) overlain by Miocene (upper and lower) sediments, Quaternary alluvial fans, and Quaternary fluvial deposits. The injection site is indicated in the red box. Cross sections A-A' through E-E' were constructed from well and seismic analysis, and are used to identify main flow units and probable barriers to flow. See figure 2-22b for the USGS legend.

Explanation

- Cross Section
- Area of Review
- SJR Property
- Seismic lines (see Appendix D)

N

SAN JOAQUIN RENEWABLES

Project Site and USGS Geologic Map of California (Bakersfield Sheet)

S:\Projects\DB19.1252_Frontline_Bioenergy\GIS\QGIS\Fig_2-22a Project site and geologic map.qgz

06/14/2022 JN DB19.1252

Figure 2-22a

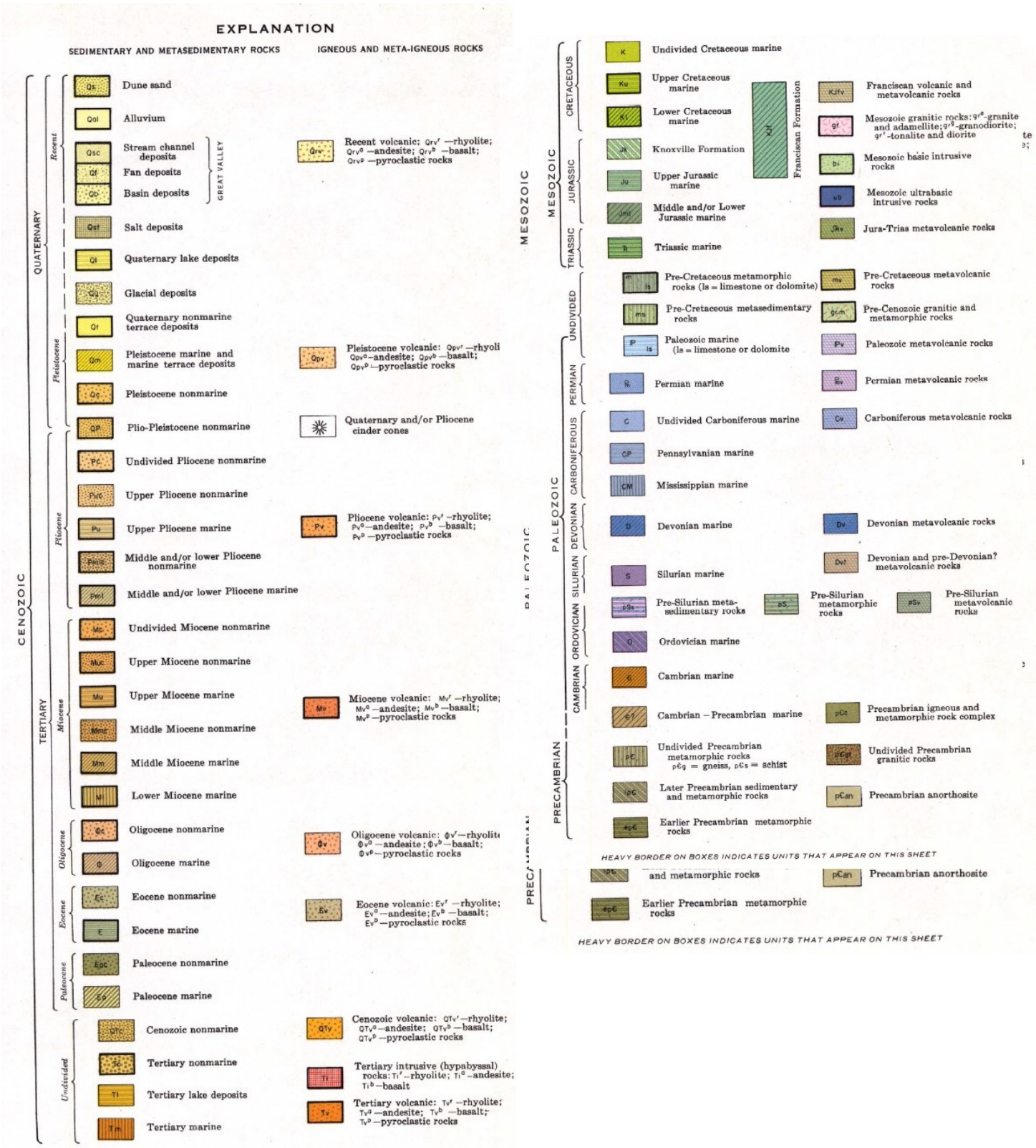

SAN JOAQUIN RENEWABLES

Legend for Site Map and Geologic Map of California

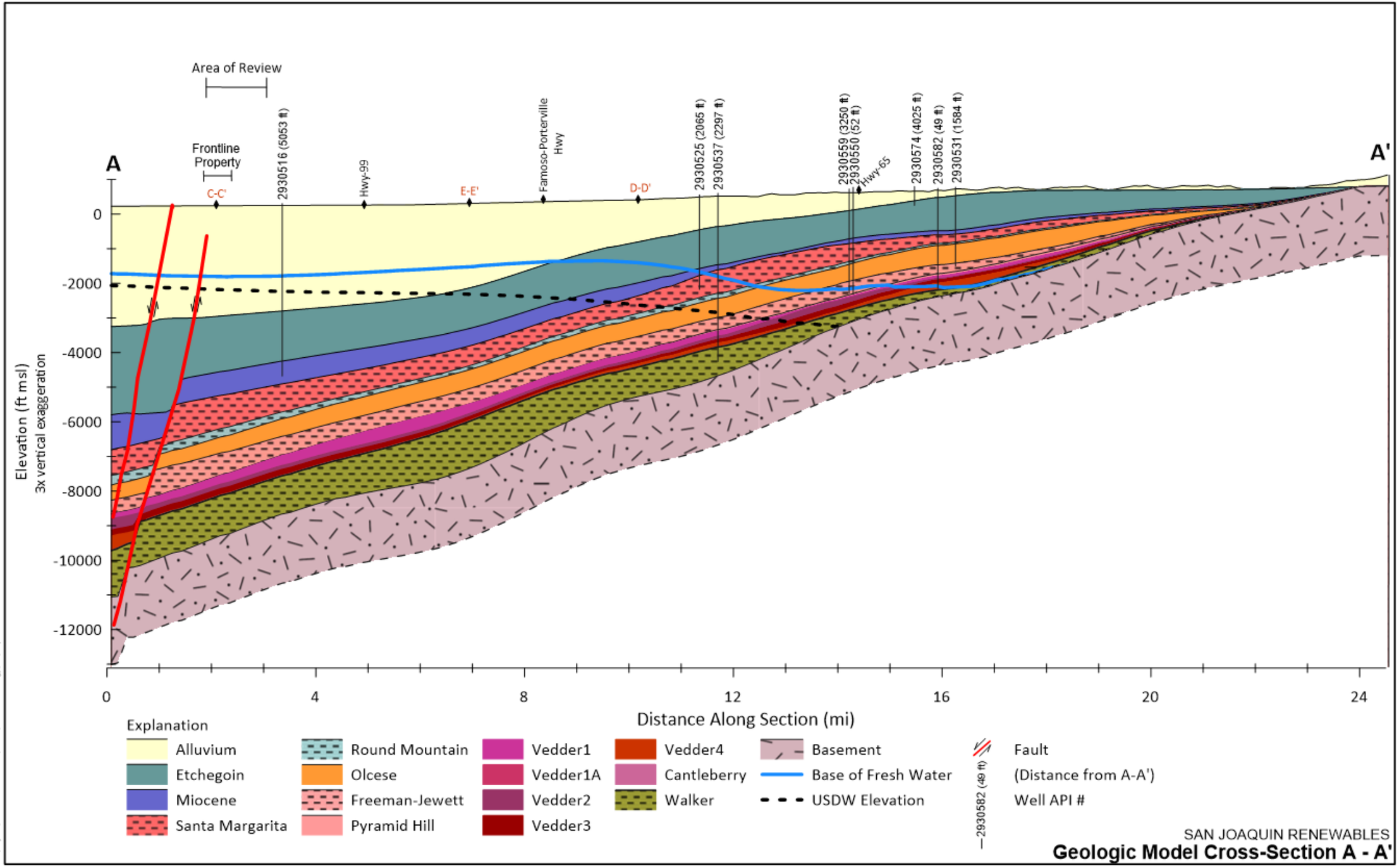

8/12/2021 DB19.1252

Figure 2-23

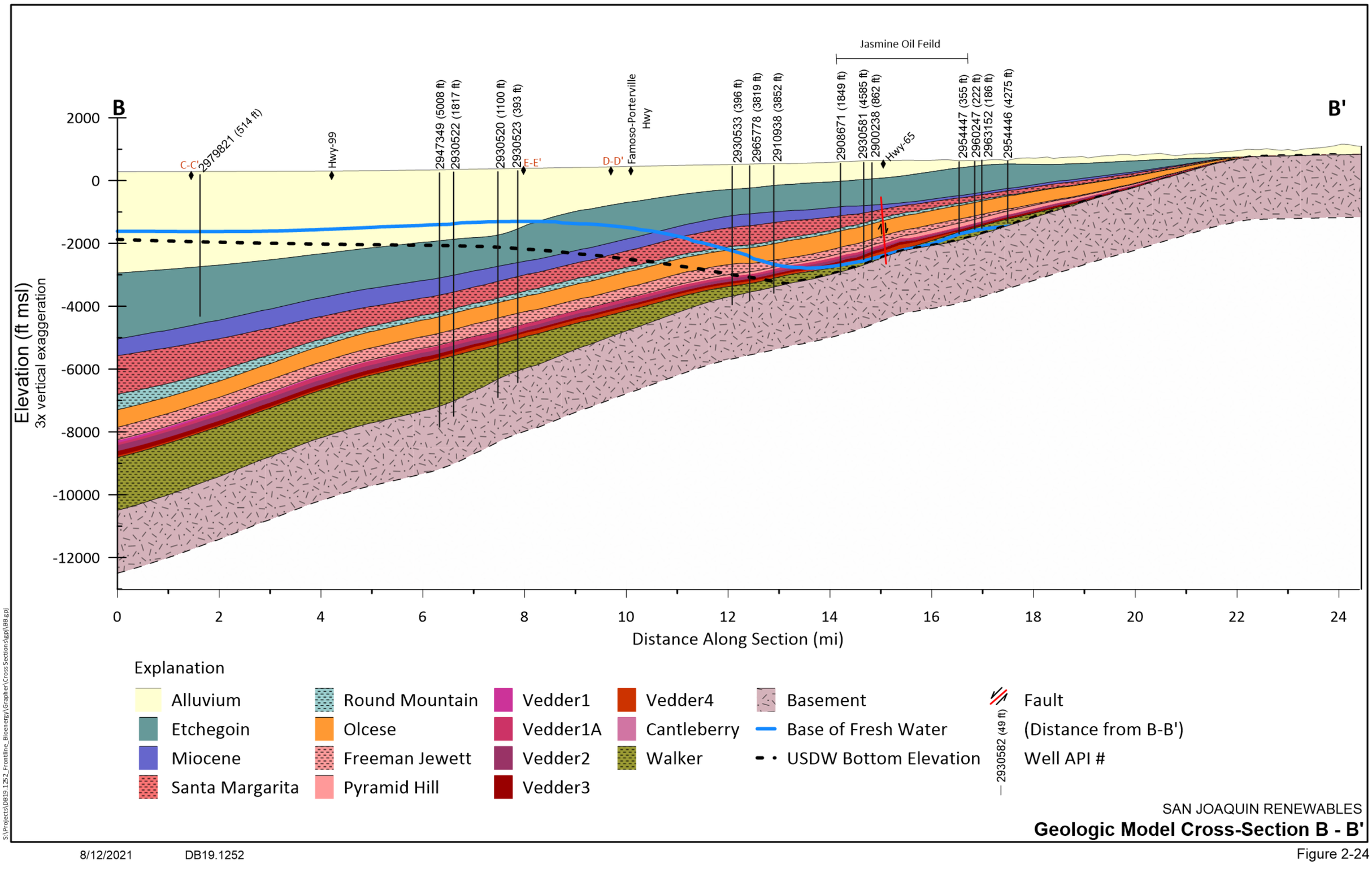

S:\Projects\DB19.1252_Frontline_Bioenergy\Grapher\Cross Section 3\gpj\BB.gpj

SAN JOAQUIN RENEWABLES

Geologic Model Cross-Section B - B'

8/12/2021 DB19.1252

Figure 2-24

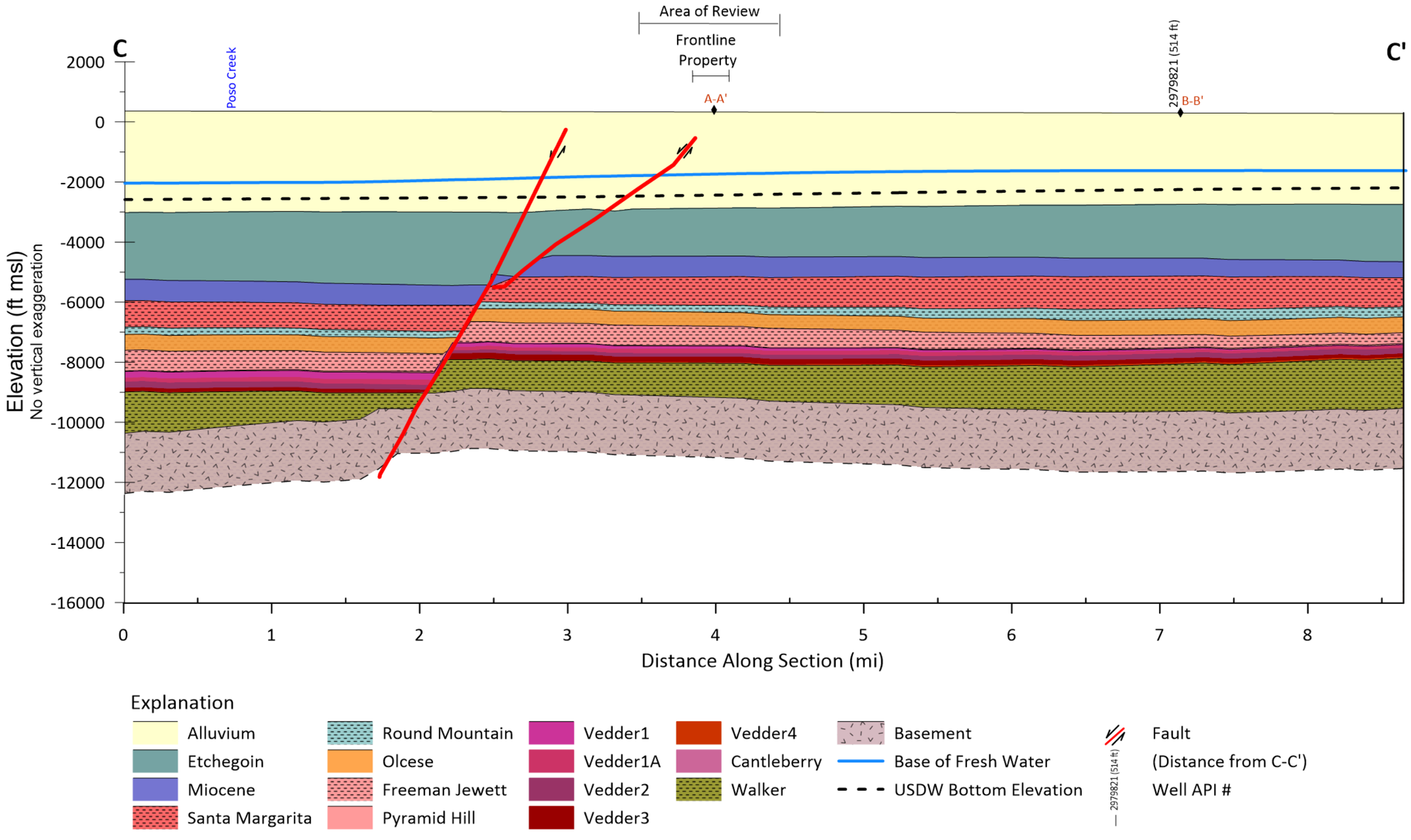

K:\Projects\Environmental Services\Private\Frontline Bioenergy\Grapher\Cross Section\gpj

SAN JOAQUIN RENEWABLES

Geologic Model Cross-Section C - C'

8/12/2021 DB19.1252

Figure 2-25

D

D'

2942325 (6260 ft)

2948221 (861 ft)

2930613 (1725 ft)

2930610 (665 ft)

A-A'

2930524 (768 ft)

2930521 (675 ft)

Famoso-Porterville Hwy

B-B'

Elevation (ft msl)
2x vertical exaggeration

1000
0
-1000
-2000
-3000
-4000
-5000
-6000
-7000
-8000

0 1 2 3 4 5 6 7 8

Distance Along Section (mi)

Explanation

- Alluvium
- Etchegoin
- Miocene
- Santa Margarita
- Round Mountain
- Olcese
- Freeman Jewett
- Pyramid Hill
- Vedder1
- Vedder1A
- Vedder2
- Vedder3
- Vedder4
- Cantleberry
- Walker
- Basement
- Base of Fresh Water
- USDW Bottom Elevation (Distance from D-D')
- 2930582 (49 ft) Well API #

K:\Projects\Environmental Services\Private\Frontline Bioenergy\GIS\Grapher

SAN JOAQUIN RENEWABLES

Geologic Model Cross-Section D - D'

8/12/2021 DB19.1252

Figure 2-26

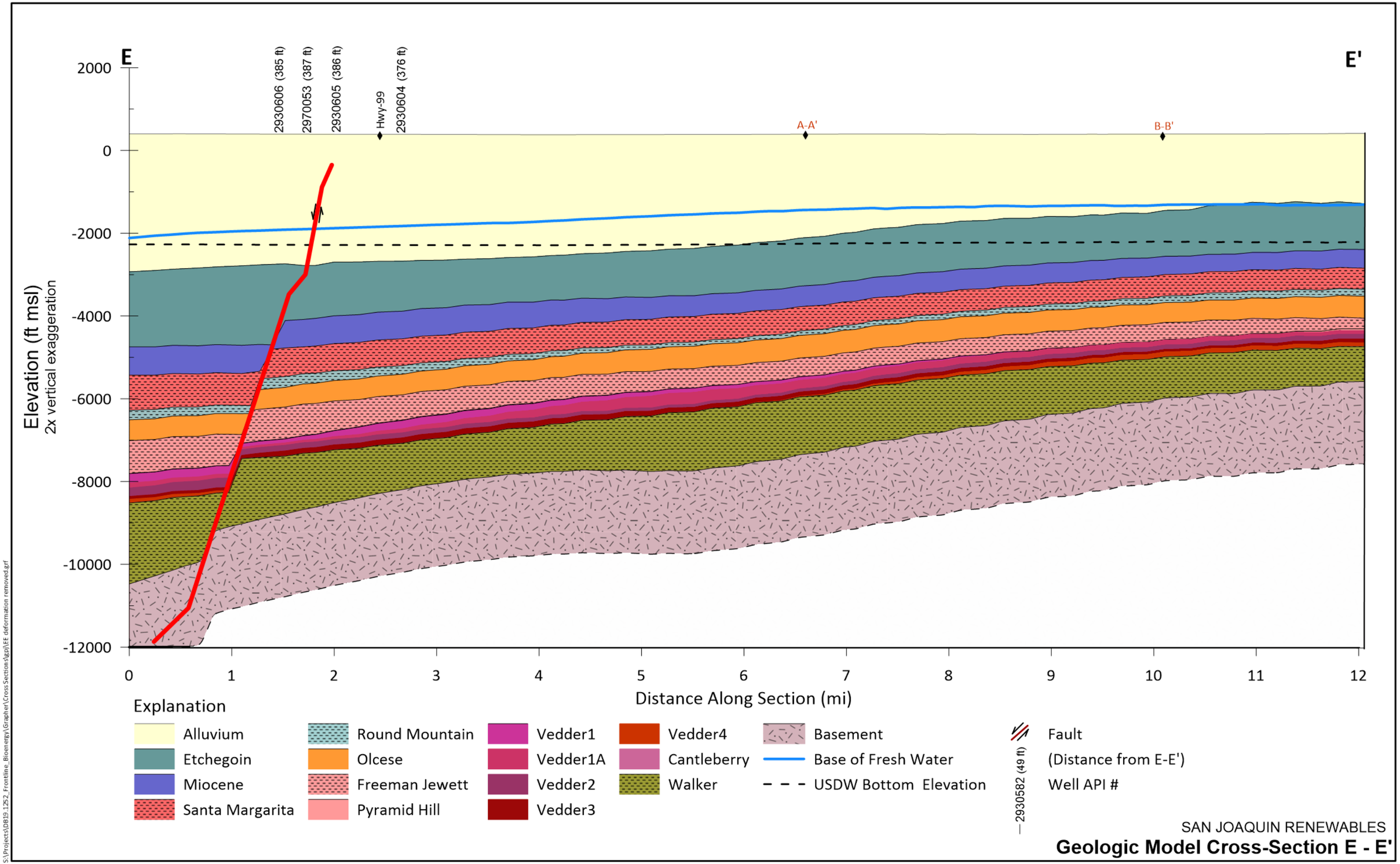

SAN JOAQUIN RENEWABLES

Geologic Model Cross-Section E - E'

8/12/2021 DB19.1252

Figure 2-27

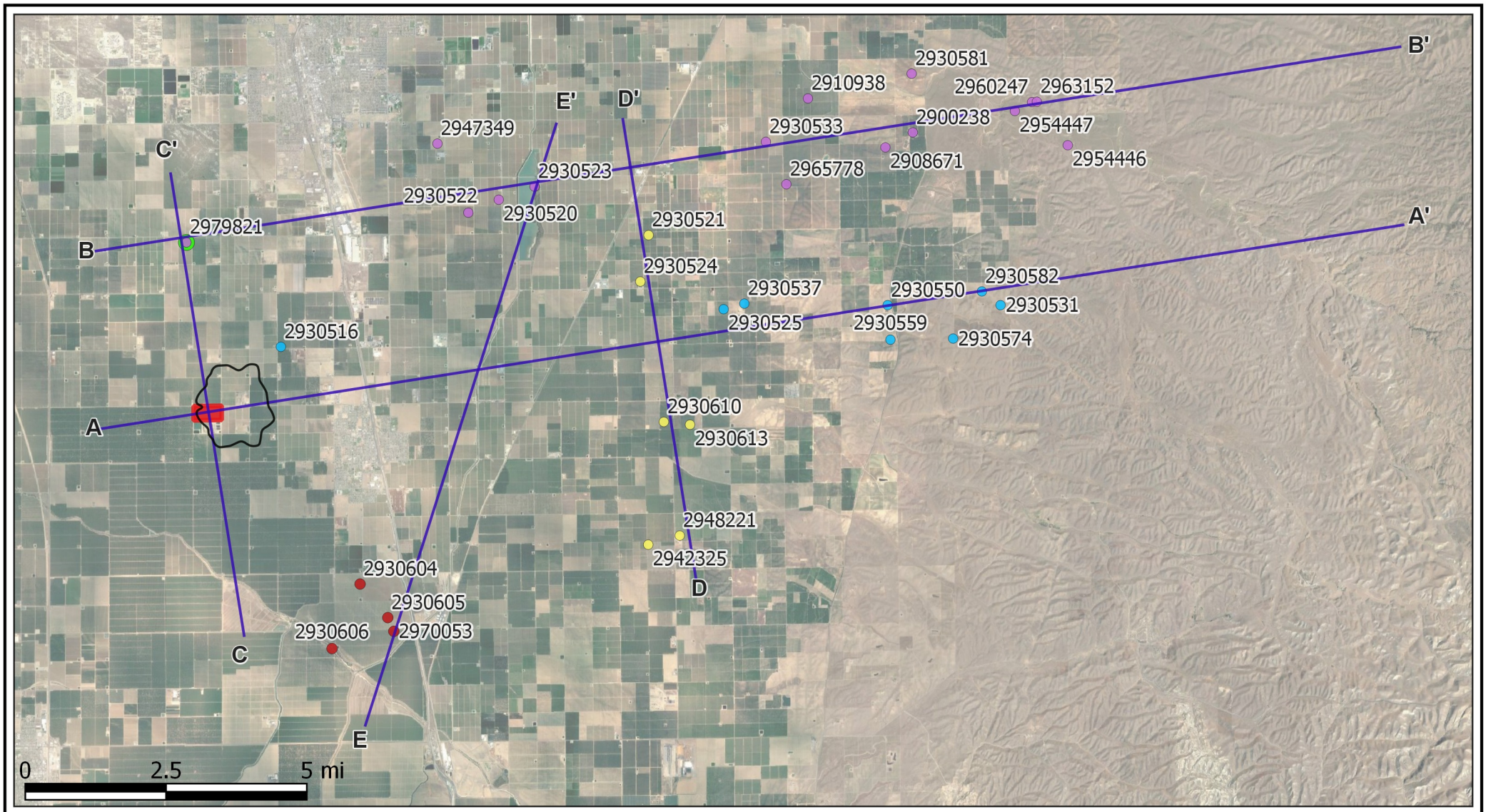

S:\Projects\DB19.1252_Frontline_Bioenergy\GIS\QGIS\EPA comments\Cross sections and wells.qgz

SAN JOAQUIN RENEWABLES

Wells Projected onto Cross Sections

06/13/2022 JN DB19.1252

Figure 2-28

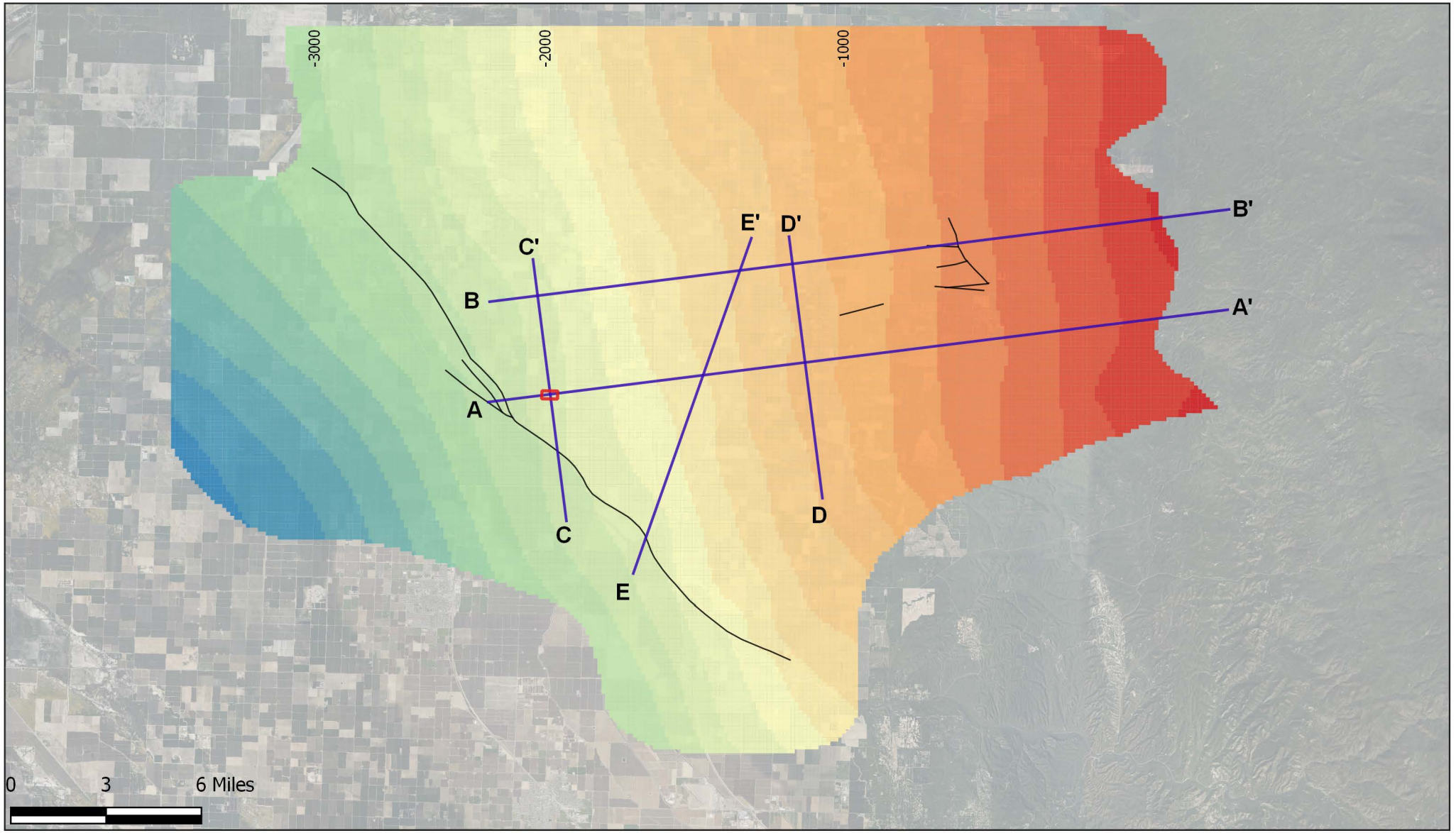

SAN JOAQUIN RENEWABLES

Elevation, Pyramid Hills

S:\Projects\DB19.1252_Frontline_Bioenergy\GIS\QGIS\pyramid-hills-elev.qgz

06/13/2022 JN DB19.1252

Figure 2-29

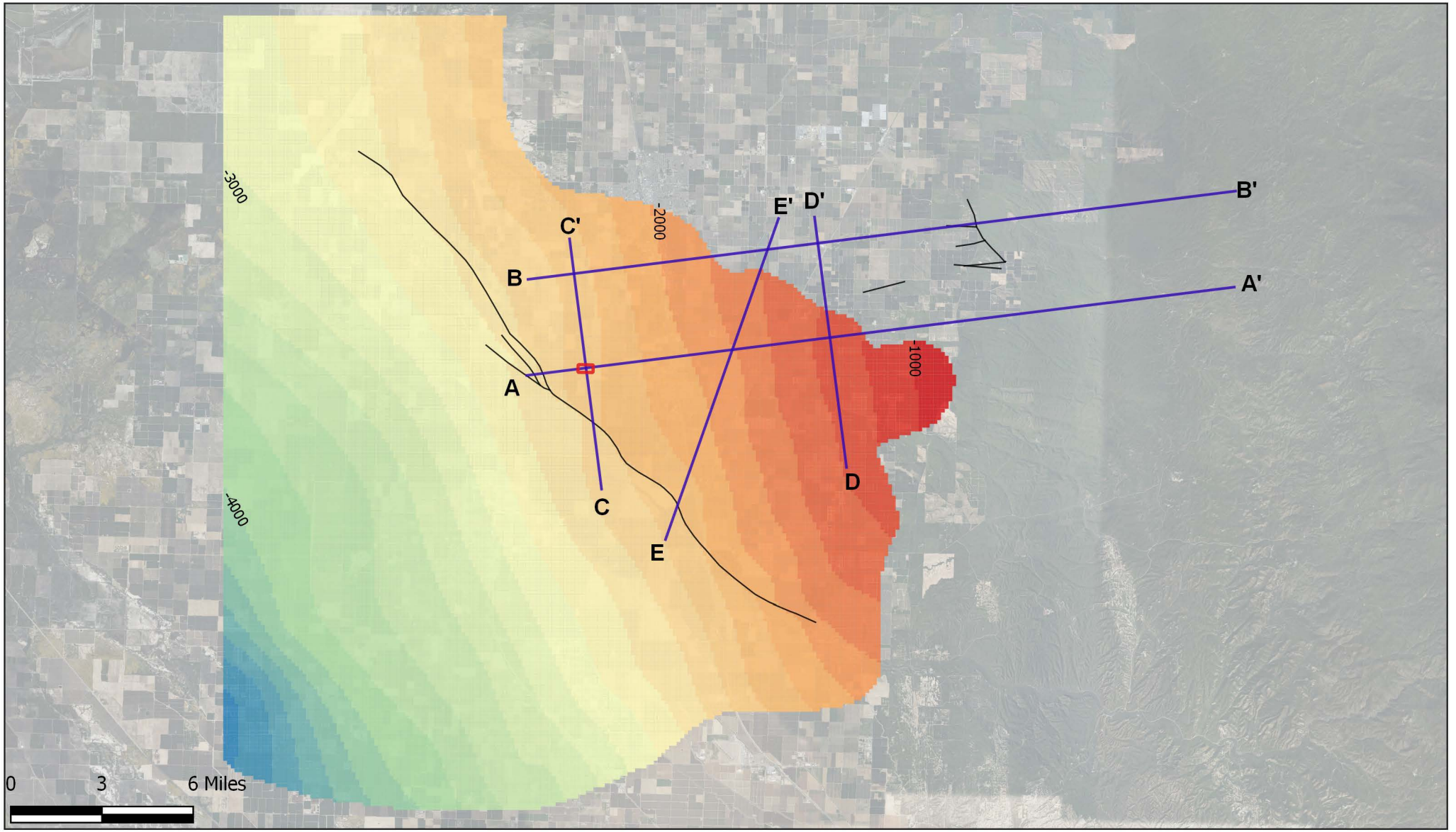

S:\Projects\DB19.1252_Frontline_Bioenergy\GIS\QGIS\ved1_elev.qgz

SAN JOAQUIN RENEWABLES

Elevation, Vedder 1

06/13/2022 JN DB19.1252

Figure 2-30

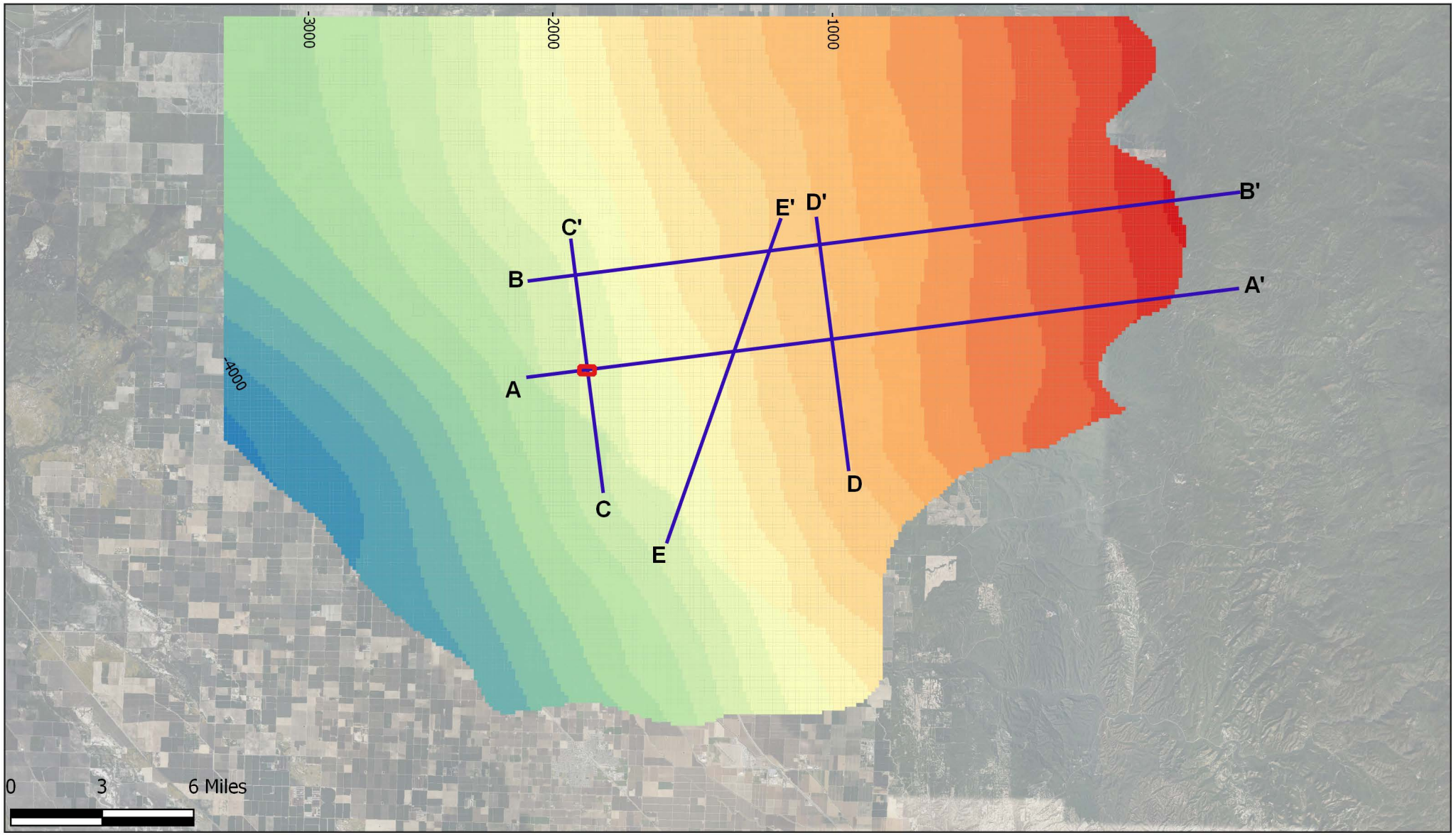

S:\Projects\DB19.1252_Frontline_Bioenergy\GIS\QGIS\ved2_elev.qgz

SAN JOAQUIN RENEWABLES

Elevation, Vedder 2

06/13/2022 JN DB19.1252

Figure 2-31

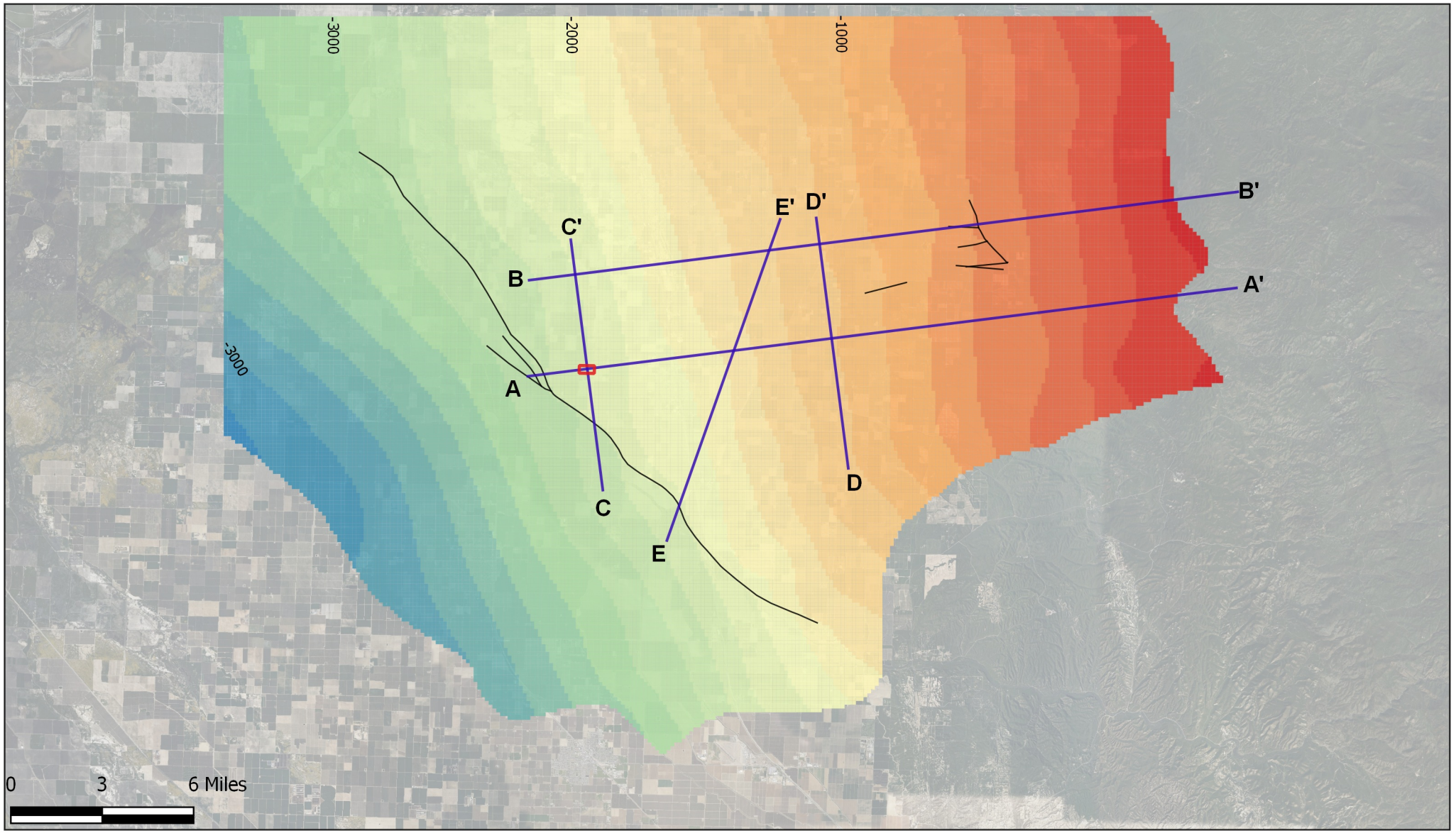

Explanation

- Property
- Cross section
- Faults at Vedder

Elevation (m msl)

- -4268 - -4200
- -4200 - -4000
- -4000 - -3800
- -3800 - -3600
- -3600 - -3400
- -3400 - -3200
- -3200 - -3000
- -3000 - -2800
- -2800 - -2600
- -2600 - -2400
- -2400 - -2200
- -2200 - -2000
- -2000 - -1800
- -1800 - -1600
- -1600 - -1400
- -1400 - -1200
- -1200 - -1000
- -1000 - -800
- -800 - -600
- -600 - -400
- -400 - -200
- -200 - 0
- 0 - 200
- 200 - 288

N

SAN JOAQUIN RENEWABLES

Elevation, Vedder 3

S:\Projects\DB19.1252_Frontline_Bioenergy\GIS\QGIS\ved3_elev.qgz

06/13/2022 JN DB19.1252

Figure 2-32

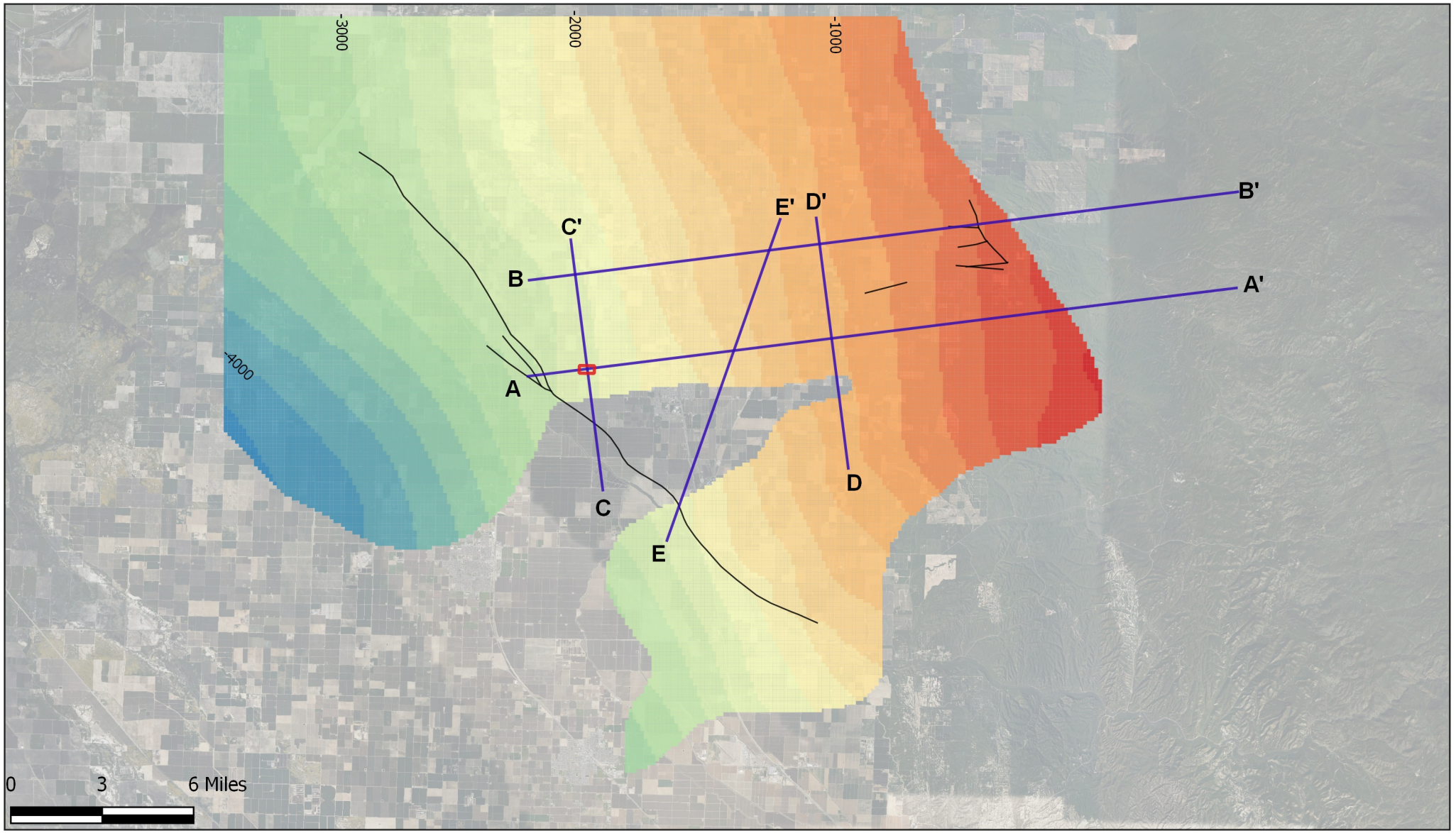

Explanation

- Property
- Cross section
- Faults at Vedder

Elevation (m msl)

- -4261 - -4200
- -4200 - -4000
- -4000 - -3800
- -3800 - -3600
- -3600 - -3400
- -3400 - -3200
- -3200 - -3000
- -3000 - -2800
- -2800 - -2600
- -2600 - -2400
- -2400 - -2200
- -2200 - -2000
- -2000 - -1800
- -1800 - -1600
- -1600 - -1400
- -1400 - -1200
- -1200 - -1000
- -1000 - -800
- -800 - -600
- -600 - -400
- -400 - -200
- -200 - -106

N

SAN JOAQUIN RENEWABLES

Elevation, Vedder 4

S:\Projects\DB19.1252_Frontline_Bioenergy\GIS\QGIS\ved4_elev.qgz

06/13/2022 JN DB19.1252

Figure 2-33

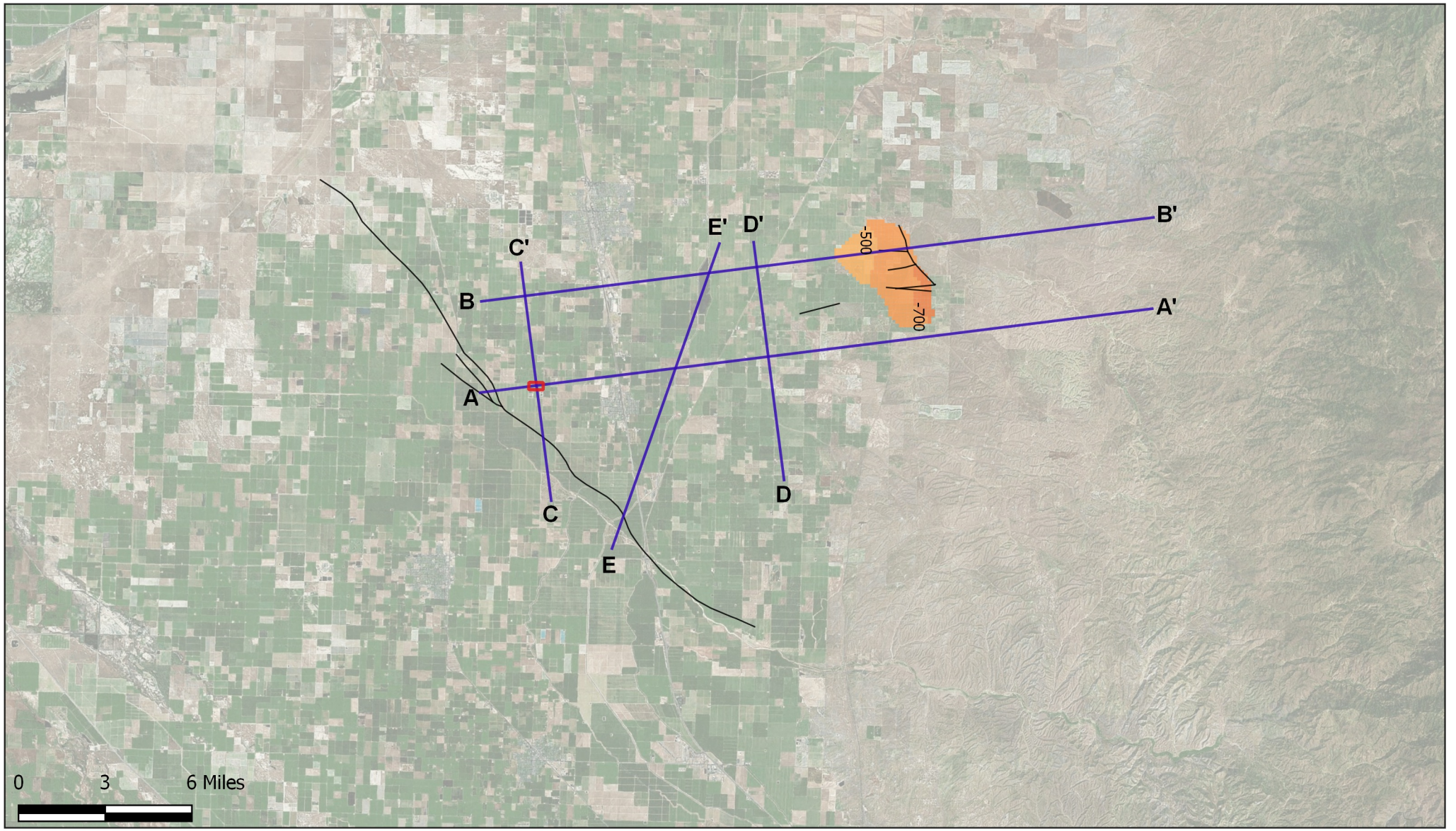

Explanation

- Property
- Cross section
- Faults at Vedder

reduced_blnk_050321

- -4087 - -4000
- -4000 - -3800
- -3800 - -3600
- -3600 - -3400
- -3400 - -3200
- -3200 - -3000
- -3000 - -2800
- -2800 - -2600
- -2600 - -2400
- -2400 - -2200
- -2200 - -2000
- -2000 - -1800
- -1800 - -1600
- -1600 - -1400
- -1400 - -1200
- -1200 - -1000
- -1000 - -800
- -800 - -600
- -600 - -400
- -400 - -200
- -200 - 0
- 0 - 200
- 200 - 289

N

SAN JOAQUIN RENEWABLES

Elevation, Cantleberry Sand

06/13/2022 JN DB19.1252

Figure 2-34

S:\Projects\DB19.1252_Frontline_Bioenergy\GIS\QGIS\cantleberry_elev.qgz

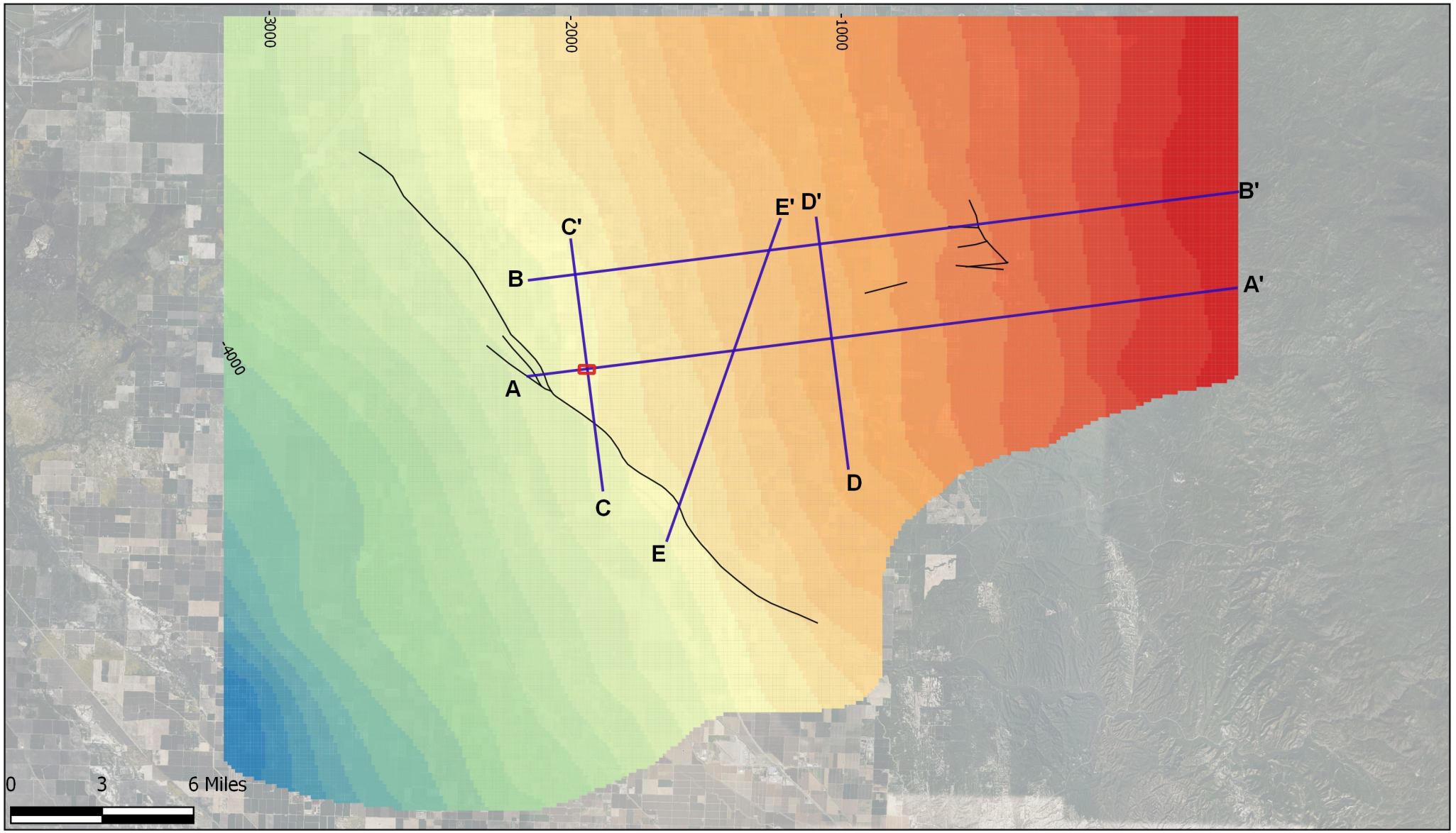

S:\Projects\DB19.1252_Frontline_Bioenergy\GIS\QGIS\walker_elev.qgz

SAN JOAQUIN RENEWABLES

Elevation, Walker

06/13/2022 JN DB19.1252

Figure 2-35

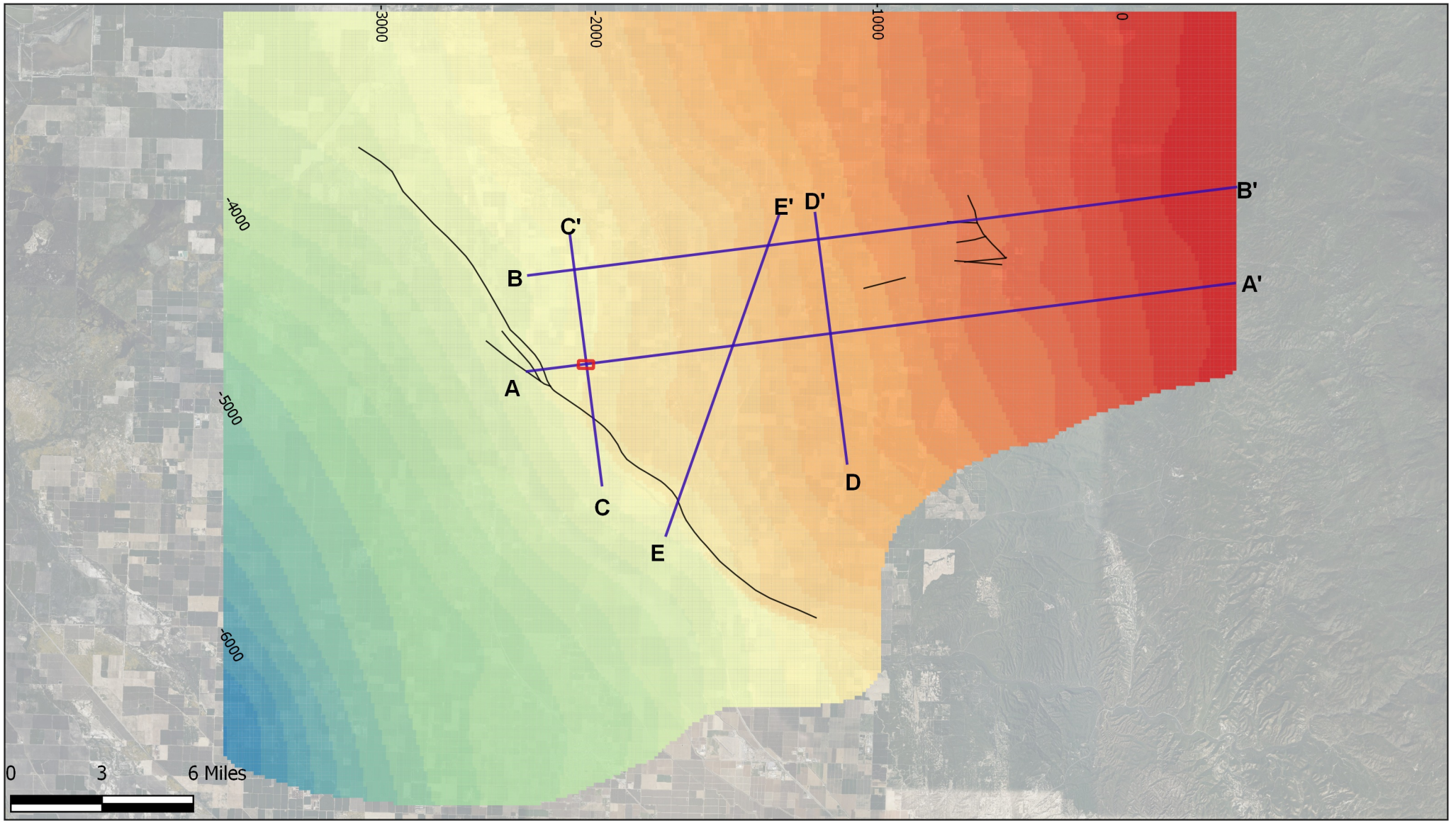

S:\Projects\DB19.1252_Frontline_Bioenergy\GIS\QGIS\basement_elev.qgz

SAN JOAQUIN RENEWABLES

Elevation, Basement

06/13/2022 JN DB19.1252

Figure 2-36

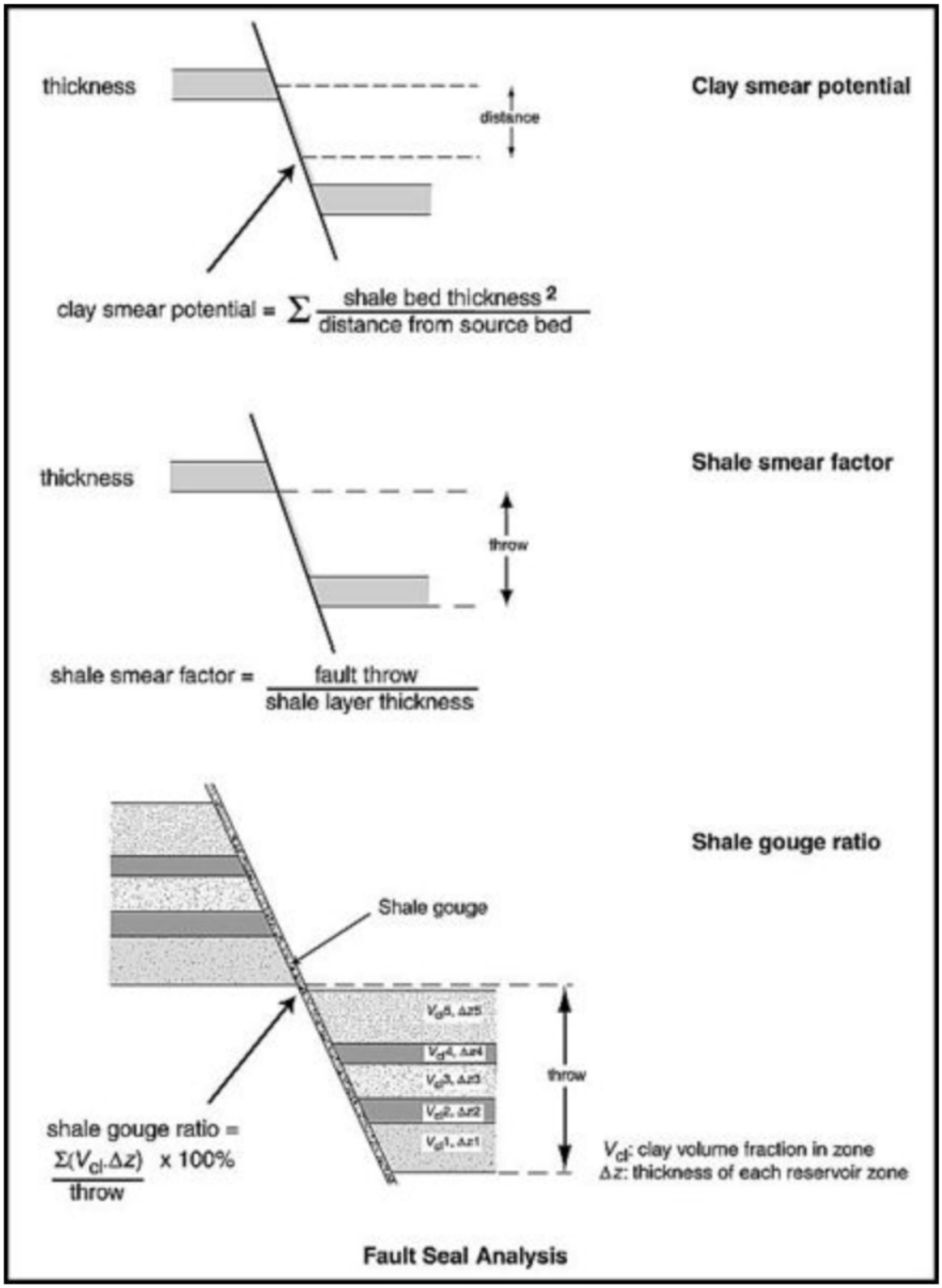

Notes: Fault seal analysis involves numerical methods of predicting the likelihood of fault seal (from Yielding et al., 1997).

Source: Yielding, Freeman, and Needham, 1997.

SAN JOAQUIN RENEWABLES

Example Fault Seal Analysis

6/14/2022 DB19.1252

Figure 2-37

K:\Projects\Environmental Services\Private\Frontline Bioenergy\Final Documents\Permit Application\Figures\docx\Fig_2-36_Example Fault Seal Analysis.docx

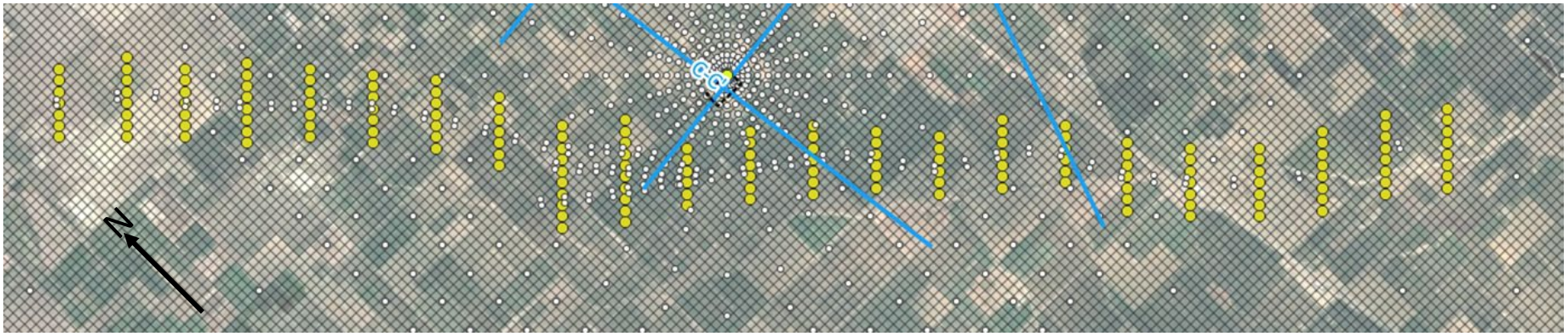

Notes: Map of the vicinity of the injection site (black rectangle) illustrating the locations of 23 cross sections (yellow) that were created and evaluated as input to creating Allan Diagrams of the Pond-Poso Creek Fault to assess offset and seal. Cross sections are approximately one mile apart.

Explanation:
Blue lines represent regional cross sections, and the yellow dots represent cross sections along Pond-Poso Creek Fault Complex.

SAN JOAQUIN RENEWABLES

Cross Section Location Along Pond-Poso Creek Fault Complex

9/13/2021 DB19.1252

Figure 2-38

K:\Projects\Environmental Services\Private\Frontline Bioenergy\Final Documents\Permit Application\Figures\docxK:\Fig_2-38_docx

Cross Section 1:
northern Pond-Poso Creek Fault trend

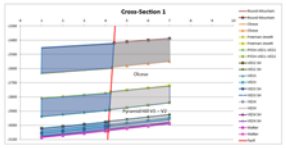

Cross Section 2:
northern Pond-Poso Creek Fault trend

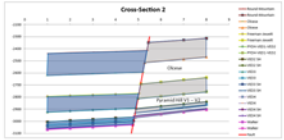

Cross Section 3:
northern Pond-Poso Creek Fault trend

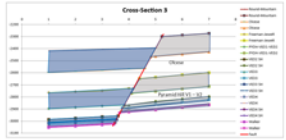

Cross Section 4:
northern Pond-Poso Creek Fault trend

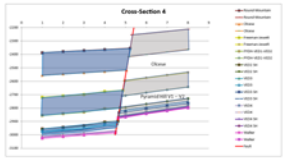

Cross Section 5:
northern Pond-Poso Creek Fault trend

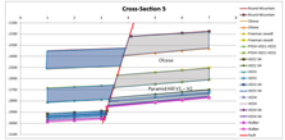

Cross Section 21:
south Pond-Poso Creek Fault trend

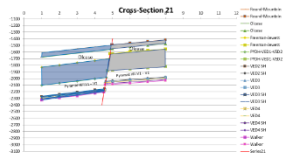

Cross Section 6:
northern Pond-Poso Creek Fault trend

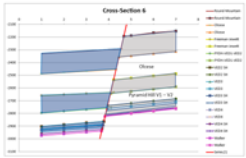

Cross Section 7:
northern Pond-Poso Creek Fault trend

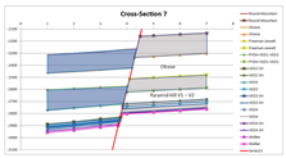

Cross Section 8:
north-central Pond-Poso Creek Fault trend

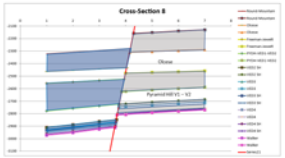

Cross Section 9:
north-central Pond-Poso Creek Fault trend

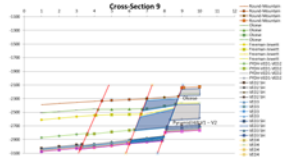

Cross Section 10:
north-central Pond-Poso Creek Fault trend

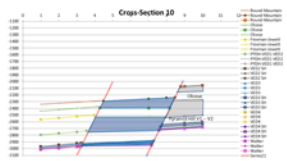

Cross Section 22:
south Pond-Poso Creek Fault trend

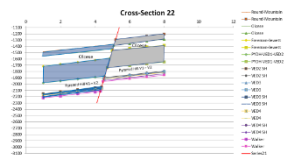

Cross Section 11:
central Pond-Poso Creek Fault trend

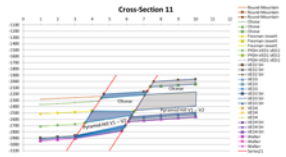

Cross Section 12:
central Pond-Poso Creek Fault trend

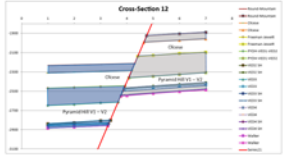

Cross Section 13:
central Pond-Poso Creek Fault trend

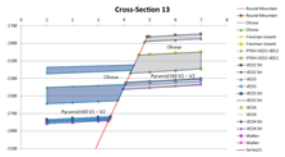

Cross Section 14:
central Pond-Poso Creek Fault trend

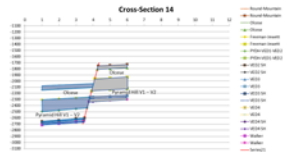

Cross Section 15:
central Pond-Poso Creek Fault trend

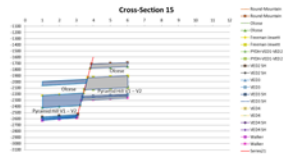

Cross Section 23:
south Pond-Poso Creek Fault trend

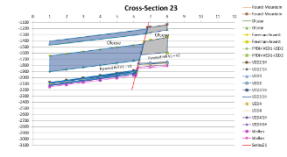

Cross Section 16:
south-central Pond-Poso Creek Fault trend

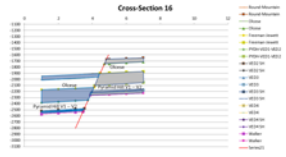

Cross Section 17:
south-central Pond-Poso Creek Fault trend

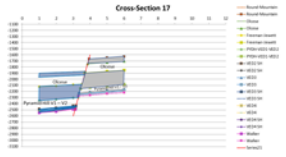

Cross Section 18:
south-central Pond-Poso Creek Fault trend

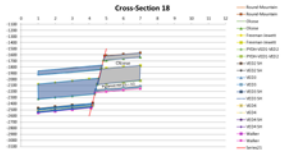

Cross Section 19:
south Pond-Poso Creek Fault trend

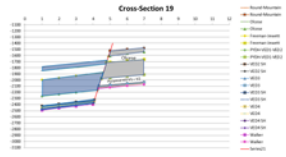

Cross Section 20:
south Pond-Poso Creek Fault trend

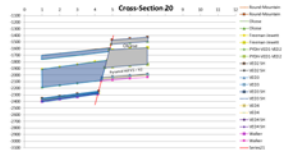

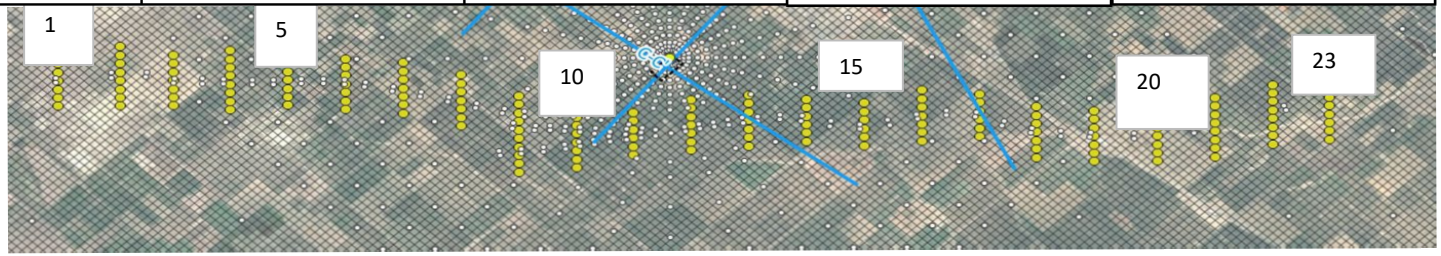

Notes: Compilation of all 23 cross sections created to measure fault throw across the Pond-Poso Creek fault system. The throw at the ends is less than 10 meters. The maximum throw of ~395 meters occurs at cross section 13, approximately one mile apart. See Appendix C for full-scale copies.

SAN JOAQUIN RENEWABLES

Pond-Poso Fault Cross Section Compilation

9/13/2021 DB19.1252

Figure 2-39

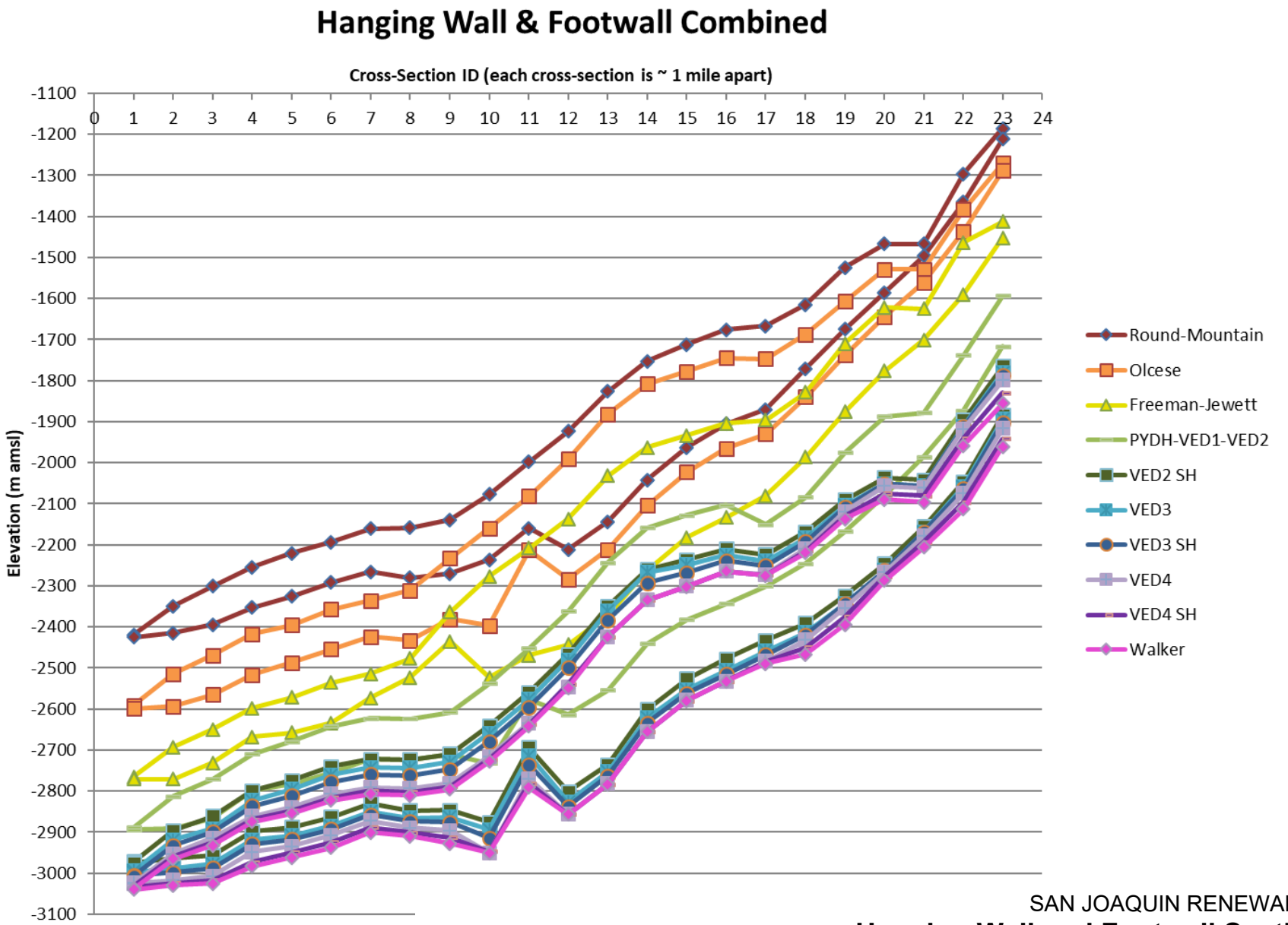

SAN JOAQUIN RENEWABLES

Hanging Wall and Footwall Sections Projected onto the Pond-Poso Creek Fault

9/13/2021 JB DB19.1252

Figure 2-40

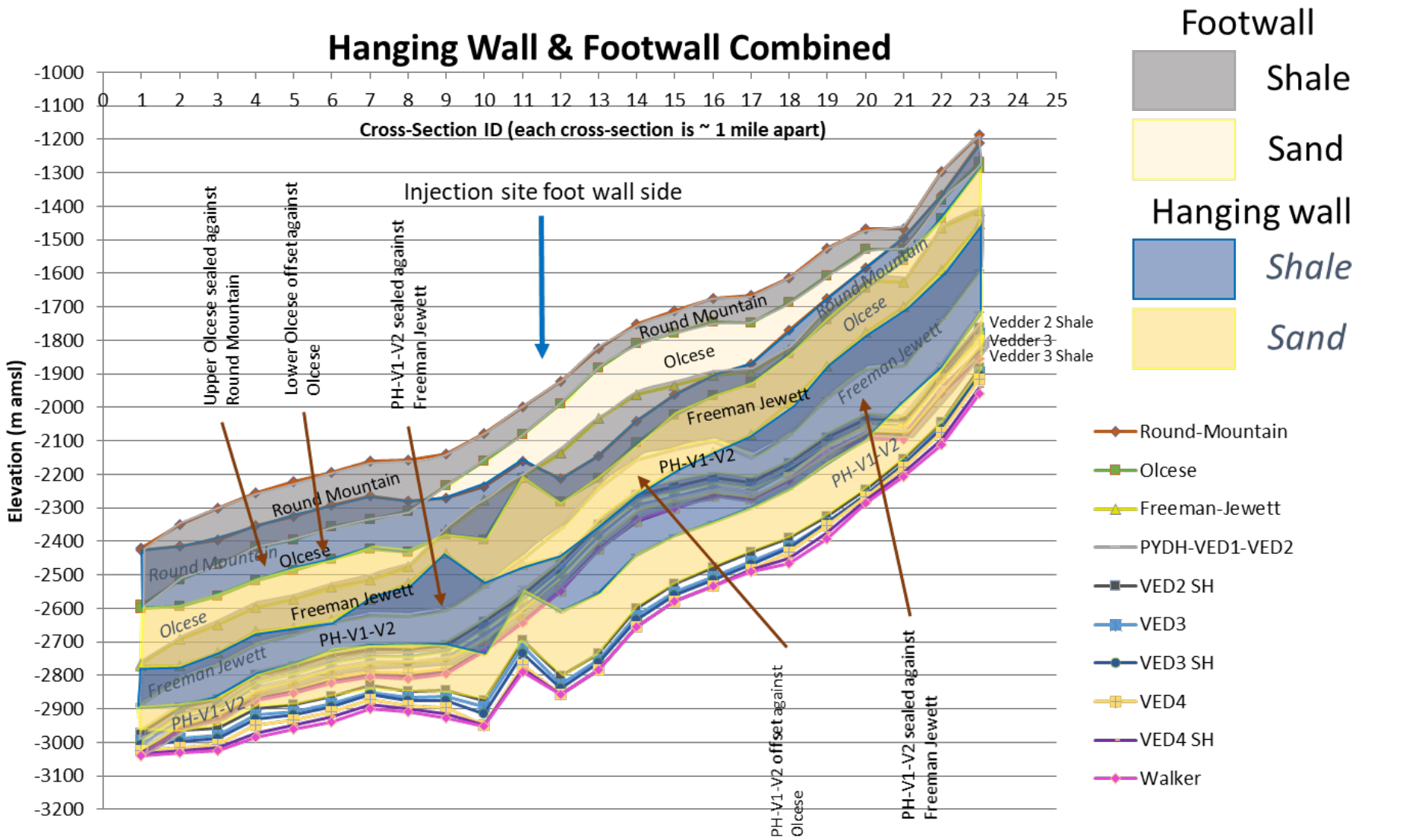

SAN JOAQUIN RENEWABLES

Allan Diagram, Pond-Poso Fault Complex

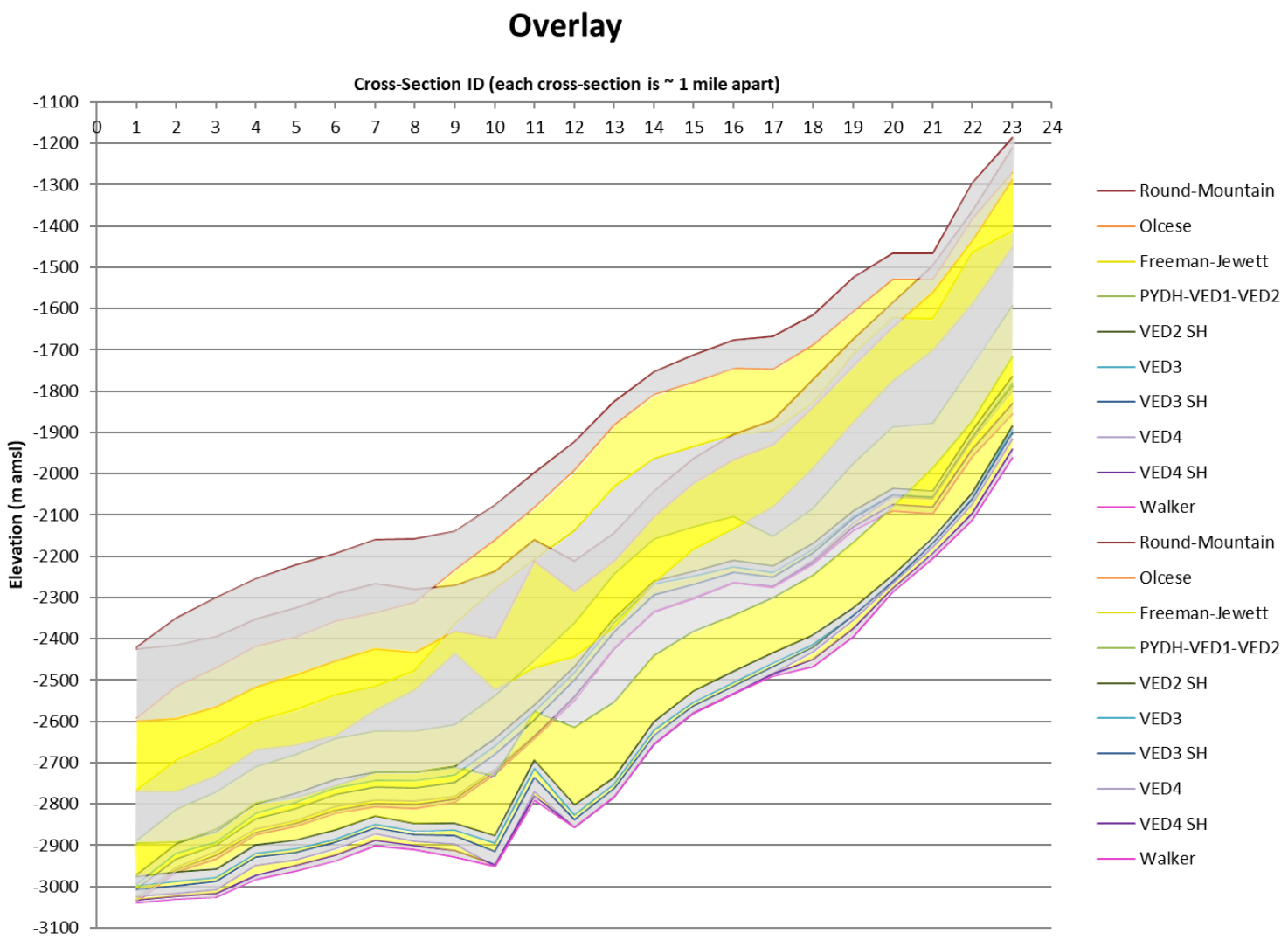

Notes: Allan Diagram of the combination of stratigraphic units projected onto the Pond-Poso Creek fault plane. Shading of the units based on footwall and hanging wall intersection. Formation tops on the footwall and hanging wall side of the fault are plotted as an overlay on the fault plane and shaded by lithology (gray is shale, yellow is sand). Hanging wall units are indicated by darker stratigraphic top and base picks.

SAN JOAQUIN RENEWABLES

Allan Diagram, Pond-Poso Fault Complex (Footwall and Hanging wall Intersection)

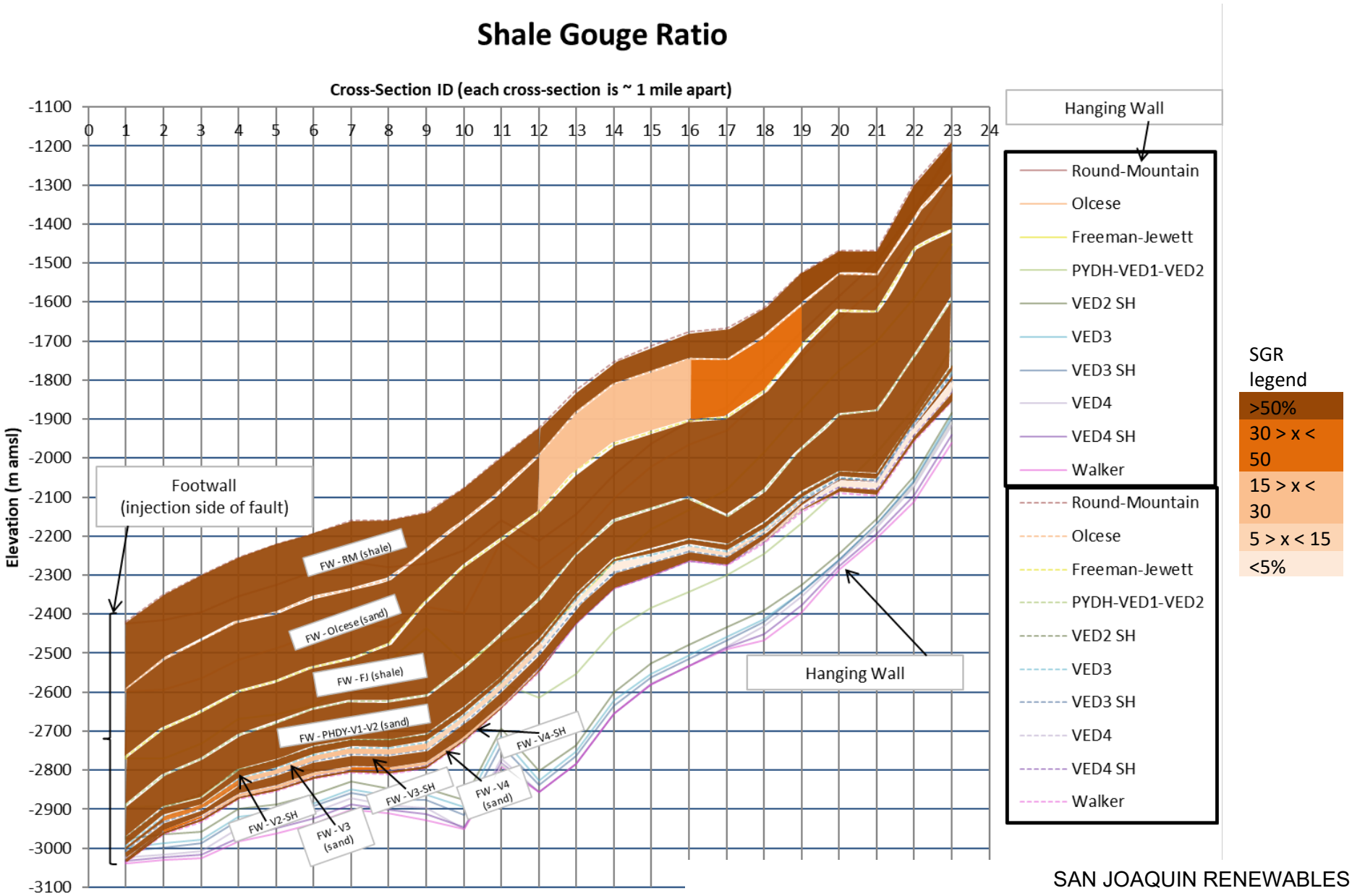

SAN JOAQUIN RENEWABLES

Shale Gouge Ratio

Pond-Poso Fault Complex

9/13/2021 JB DB19.1252

Figure 2-43

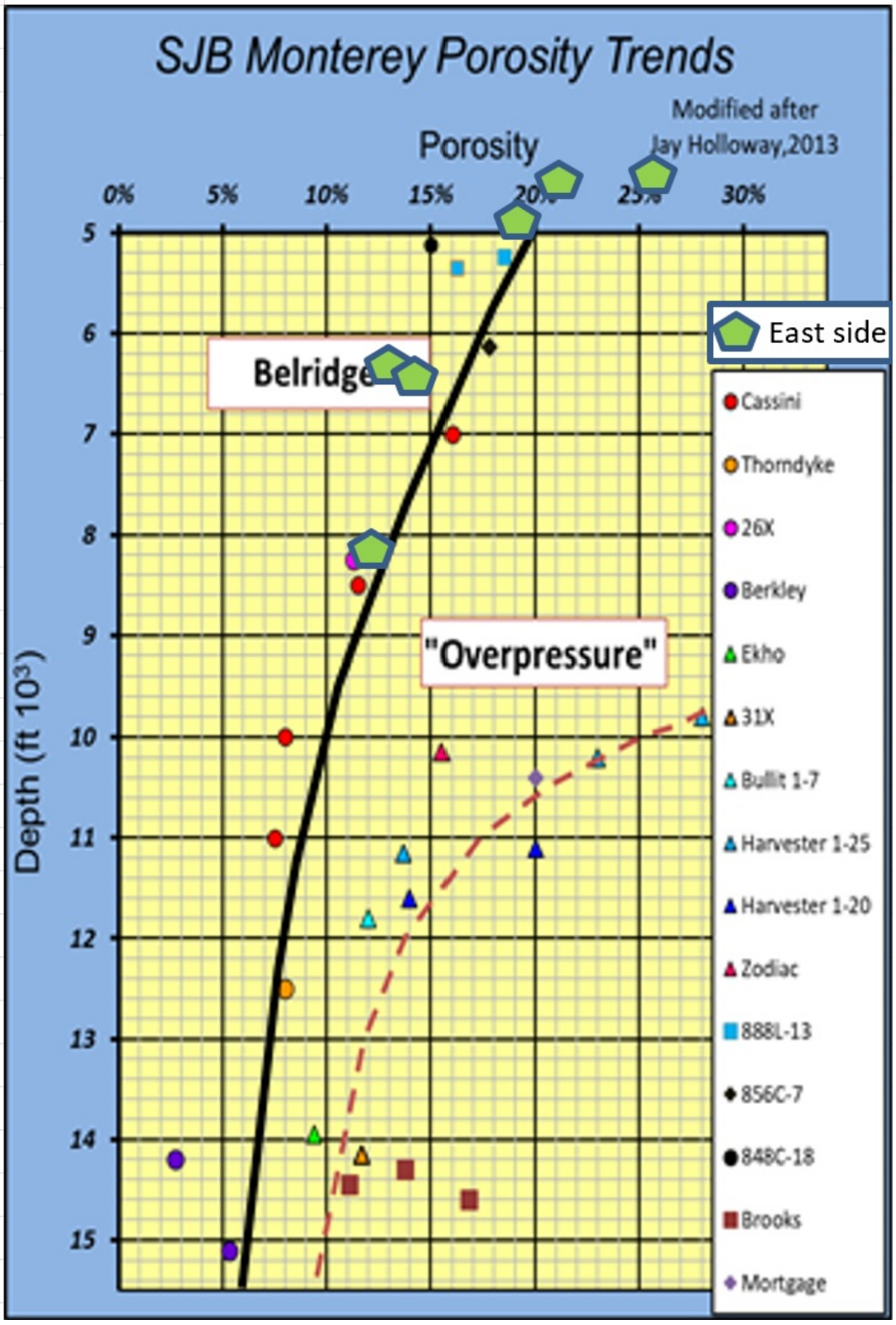

Notes: Porosity versus depth plot for the Monterey Formation in the San Joaquin Basin. Overpressure caused retention of porosity in the Monterey in the center of the basin. Normal pressure impacted porosity versus depth on both the east and west side of the basin. Samples were analyzed using mercury injection capillary pressure. Samples are from Monterey Formation samples from the McFarland data set.

Source: Schwartz, 2016.

SAN JOAQUIN RENEWABLES

San Joaquin Basin Monterey Porosity Trends

06/16/2022 JN DB19.1252

Figure 2-44

S:\Projects\DB19.1252_Frontline_Bioenergy\GIS\QGIS\EPA comments\SJB Monterey Porosity trends.qgz

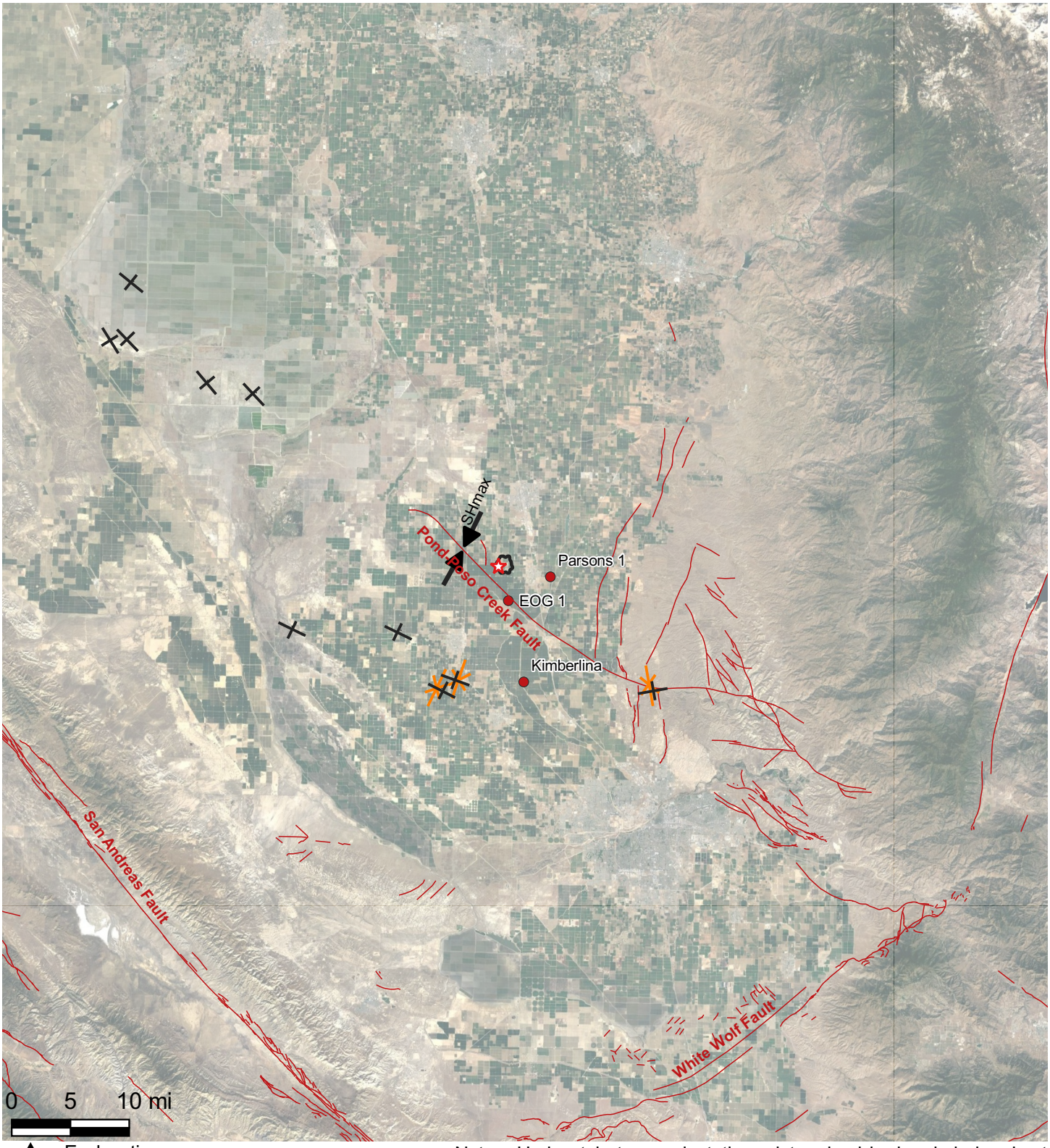

Notes: Horizontal stress orientations determined by borehole breakout analysis reported by Mount and Suppe, (1992) and Castillo and Younker, (1997). The black symbols are aligned with the minimum earth stress. Maximum earth stress is normal to those values. The orange symbols are Castillo and Younker interpretations of maximum horizontal earth stress. Wells used to determine vertical stress are shown with red circles. Faults recorded by the USGS and CGS are displayed.
SHmax = Principle horizontal earth stress

SAN JOAQUIN RENEWABLES

Stress Data

06/13/2022 JN DB19.1252

Figure 2-45

S:\Projects\DB19.1252_Frontline_Bioenergy\GIS\QGIS\EPA comments\Stress Data.qgz

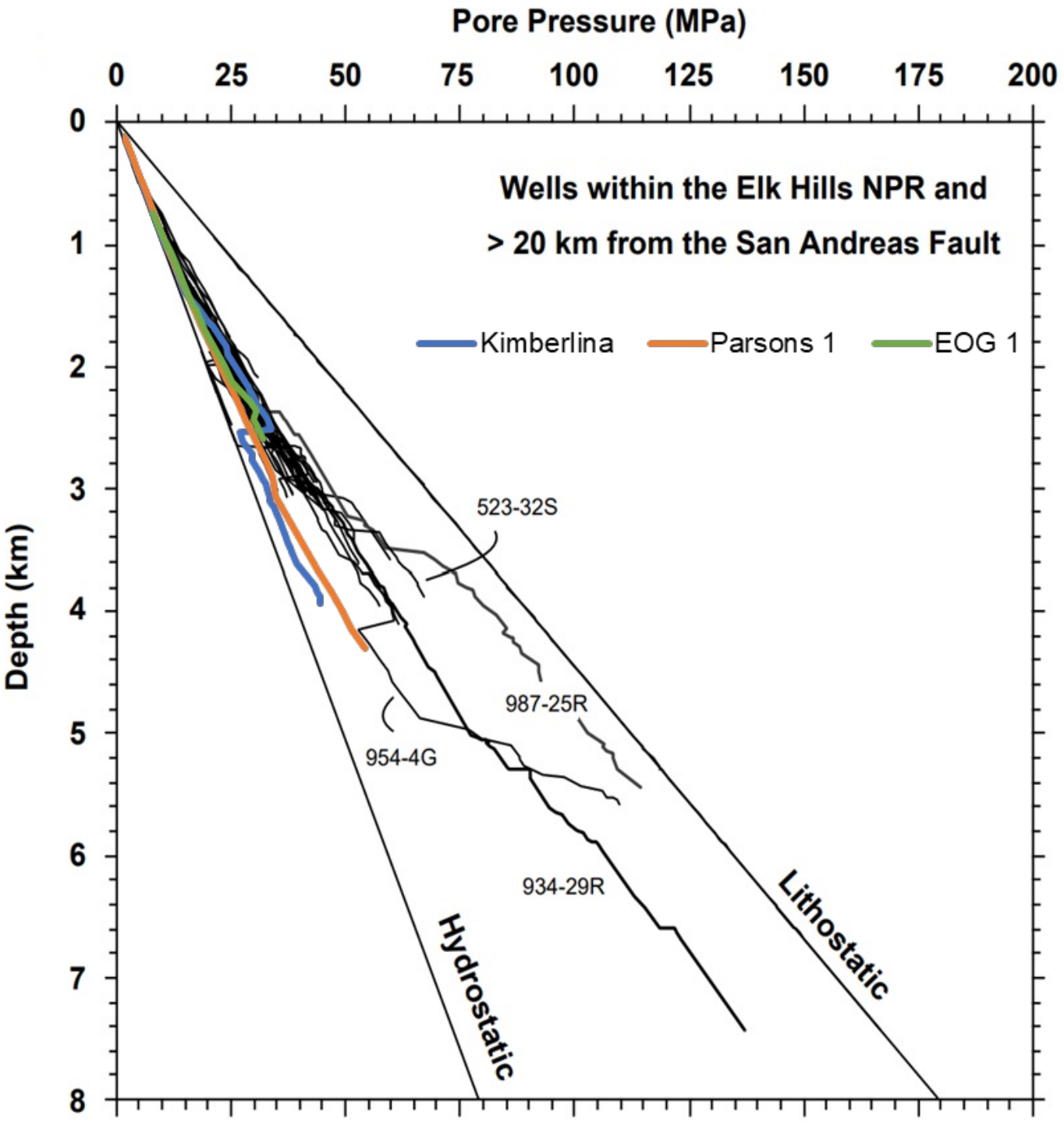

Notes: Pressure Depth plot for the San Joaquin from Castillo and Younker (1997) depicting effective stress determined from mud weight data for wells drilled more than 20 km from the San Andreas Fault and Elk Hills. Three wells (Kimberlina 1, Parsons 1, EOG 1) from the vicinity of the injection site have been added to the diagram with blue, orange, and green curves. The low effective stress associated with the three wells is indicative of a significant buffer between effective and overburden stress in the vicinity of the injection site.

SAN JOAQUIN RENEWABLES

Pore Pressure versus Depth

06/14/2022 JN DB19.1252

Figure 2-46

S:\Projects\DB19.1252_Frontline_Bioenergy\GIS\QGIS\CARB\PorePressure_v_depth.qgz

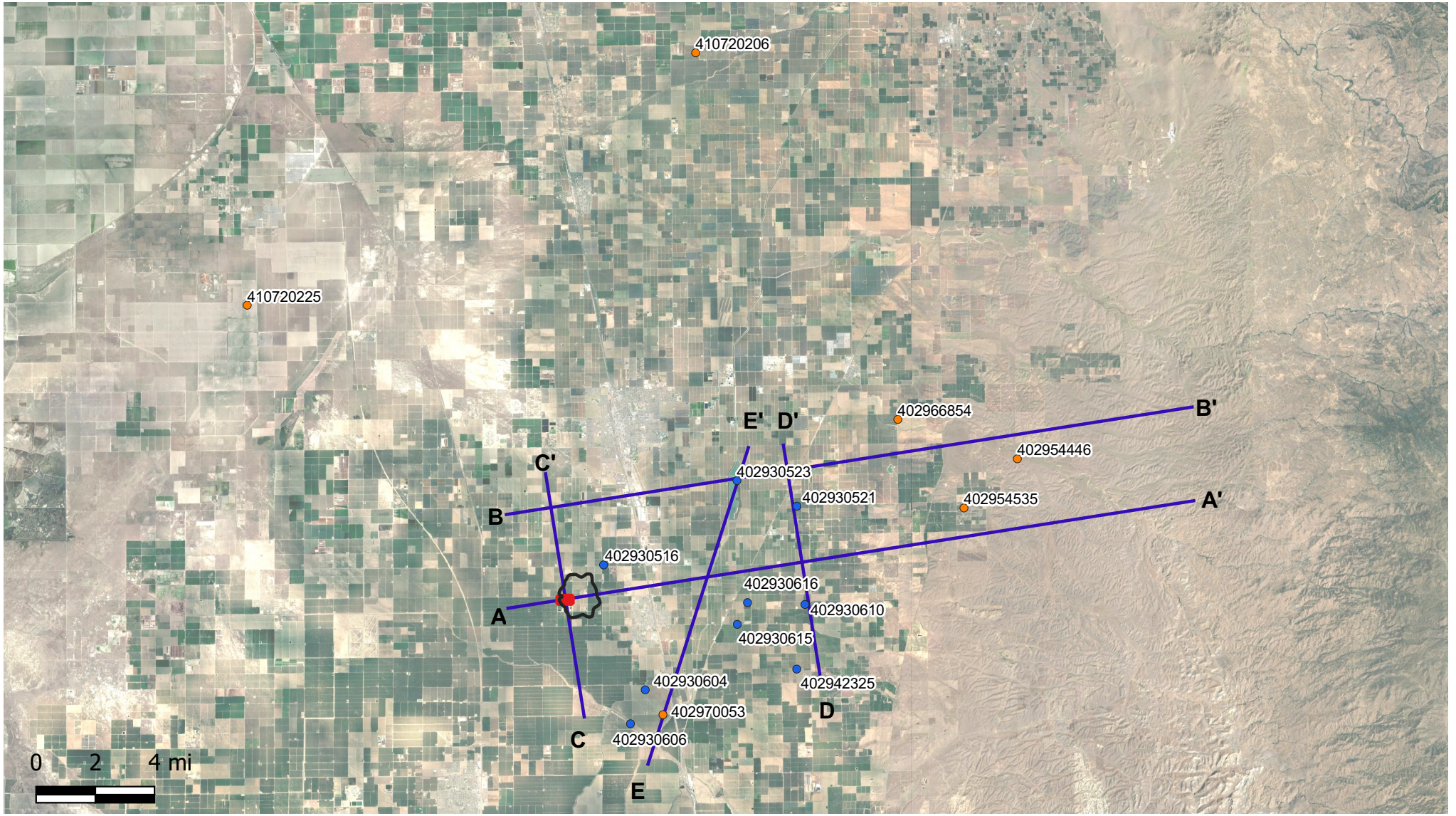

Explanation

- Cross Section
- SJR Property
- Area of Review

Wells with core analyses data

- Best Core Services
- Existing

SAN JOAQUIN RENEWABLES

Well Locations, Wells with Core Analysis Data

06/13/2022 JN DB19.1252

Figure 2-47

S:\Projects\DB19.1252_Frontline_Bioenergy\GIS\QGIS\2-43 wells with core analysis data.qgz

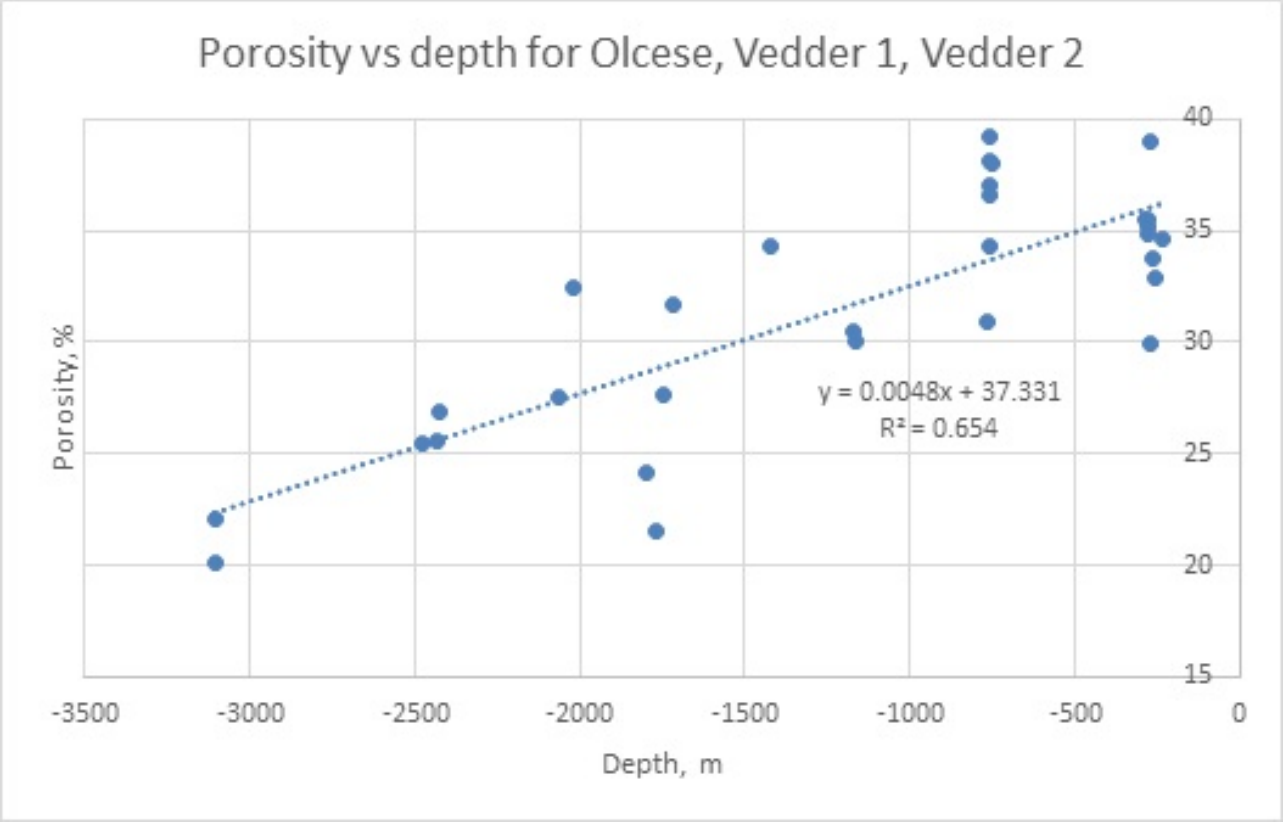

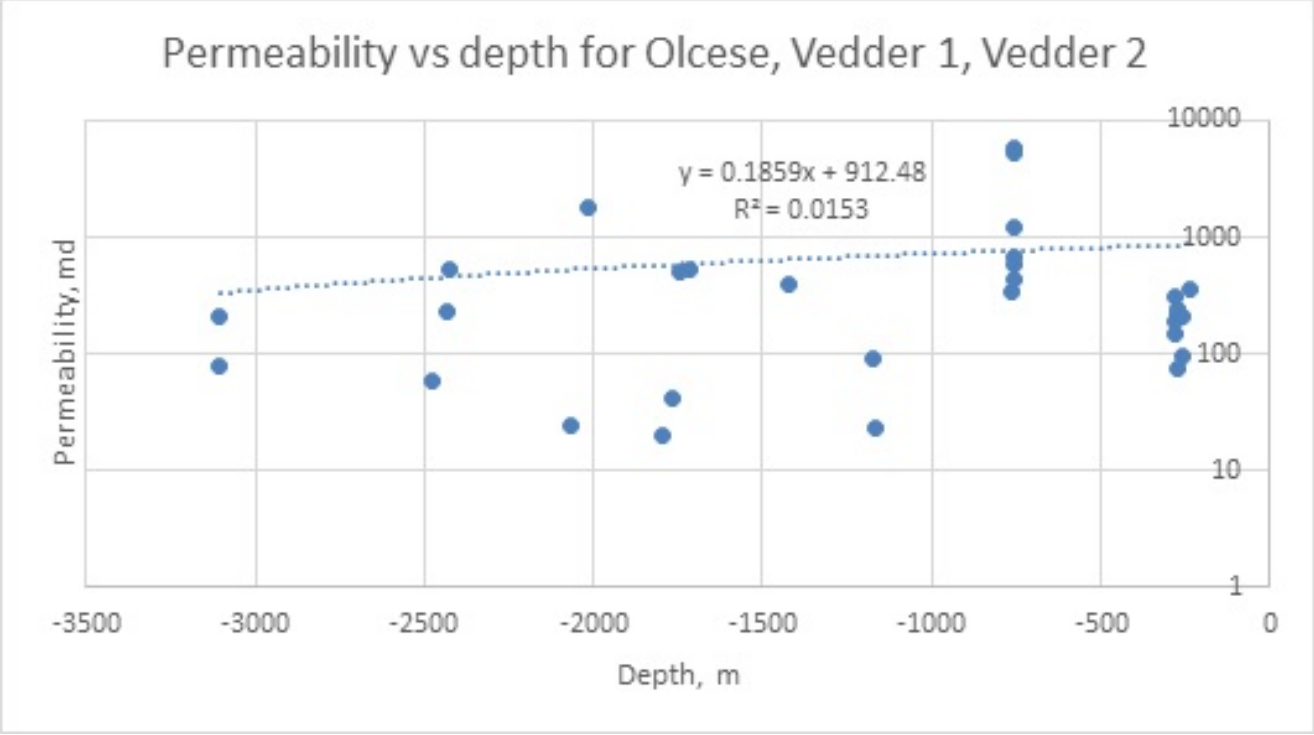

S:\Projects\DB19.1252_Frontline_Bioenergy\GIS\QGIS\EPA comments\Porosity and Permeability vs depth for Olcese, Vedder 1 and Vedder 2.qgz

SAN JOAQUIN RENEWABLES

Porosity and Permeability vs depth for Olcese, Vedder 1 and Vedder 2

06/13/2022 JN DB19.1252

Figure 2-48

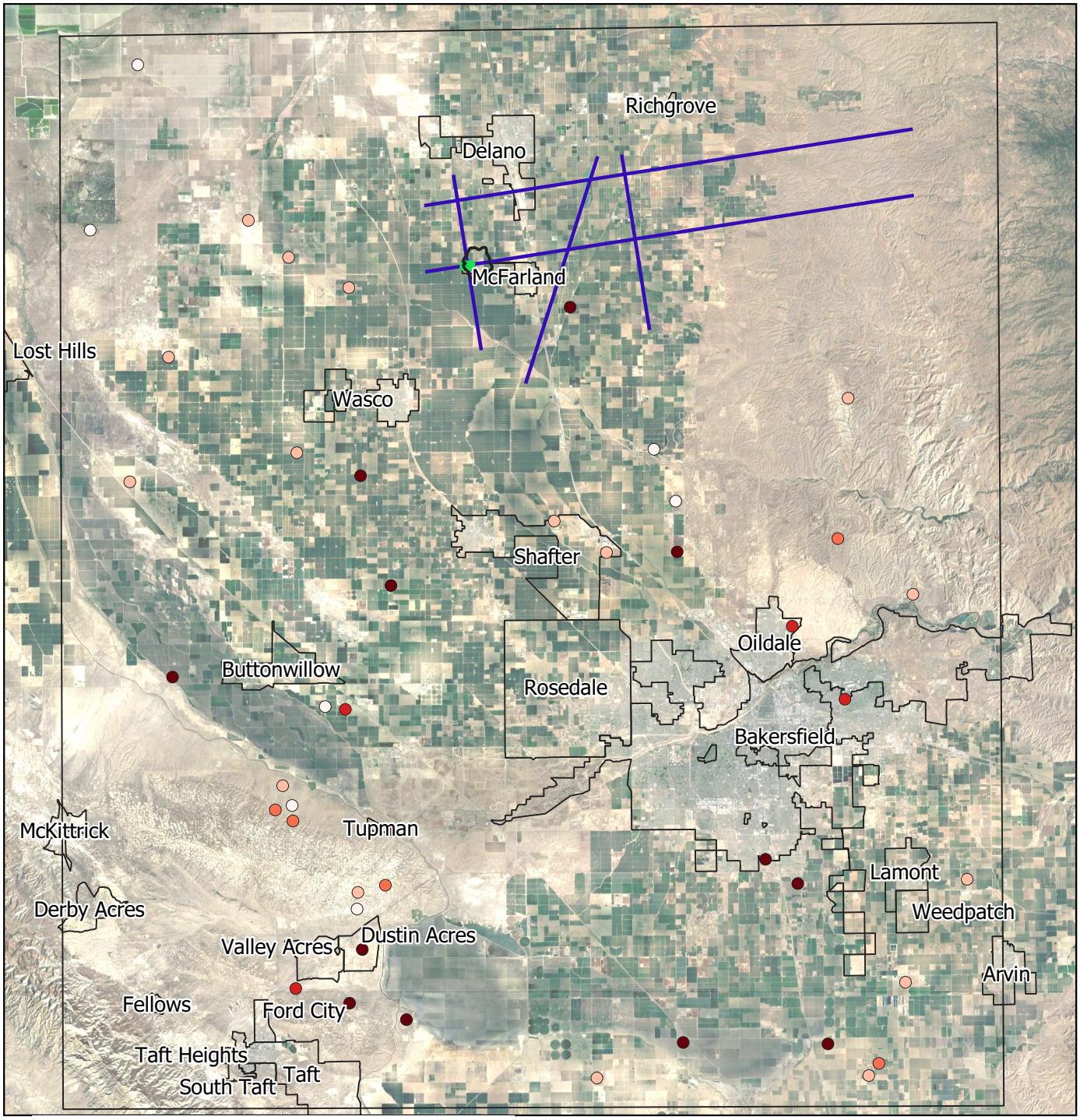

Explanation

- USGS Search Box
- Property
- Cross Section
- Area of Review/ Storage Complex
- City outlines

Earthquake Depth (km)

- 0.61 - 5
- 5 - 10
- 10 - 15
- 15 - 20
- 20 - 28.9

Notes: All earthquakes with magnitude > 3.0

SAN JOAQUIN RENEWABLES

Project Site and Earthquakes from 1970 – 2021 from the USGS Catalog

S:\Projects\DB19.1252_Frontline_Bioenergy\GIS\QGIS\Earthquakes from 1970-2021.qgz

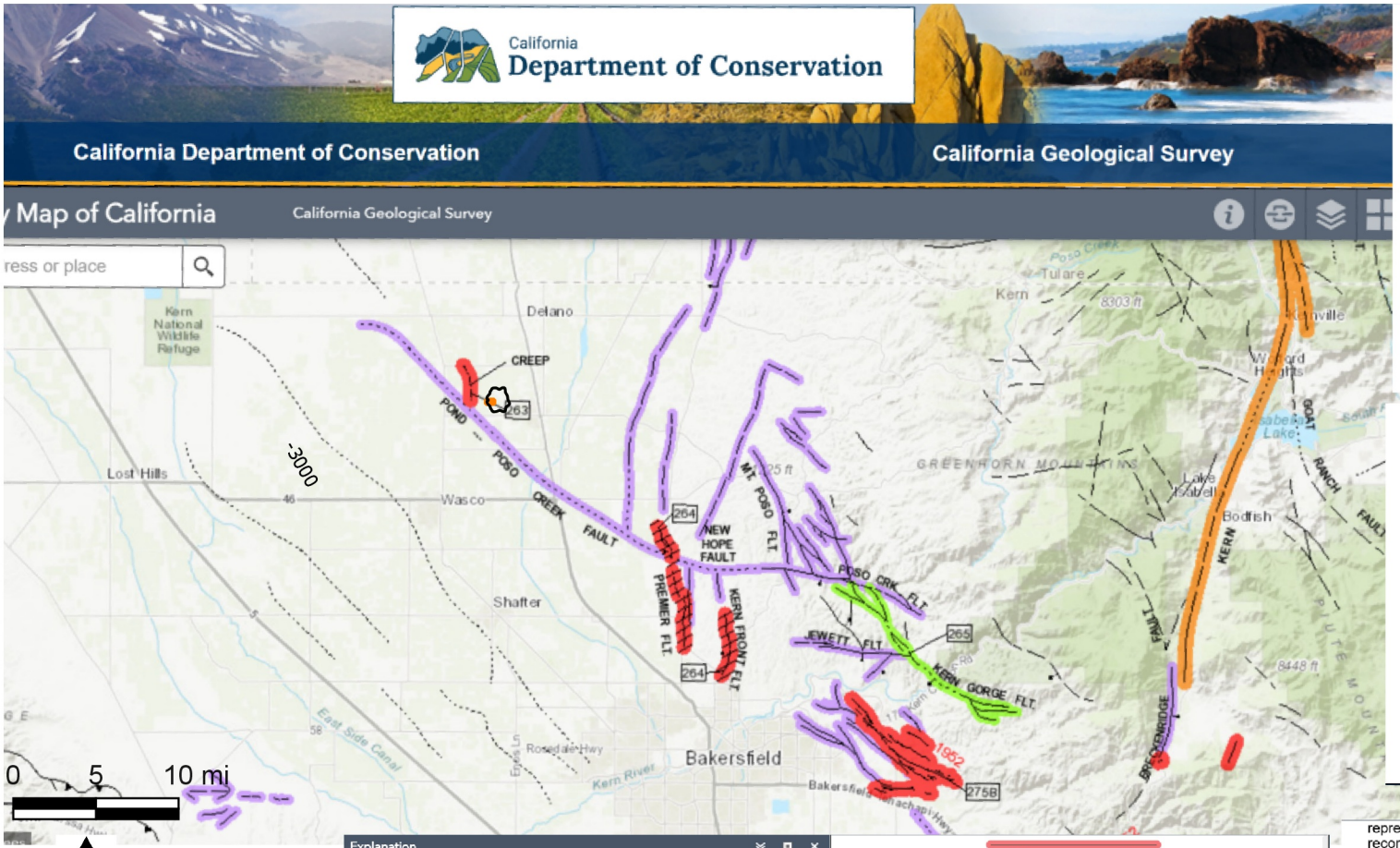

Explanation

- Area of Review
- SJR Property

Explanation

California Geological Survey, Geologic Data Map No. 6

Compilation and Interpretation by: Charles W. Jennings and William A. Bryant

Graphics by: Milind Patel, Ellen Sander, Jim Thompson, Barbara Wanish and Milton Fonseca

SYMBOL EXPLANATION

Fault traces on land are indicated by solid lines where well located, by dashed lines where approximately located or inferred, and by dotted lines where concealed by younger rocks or by lakes or bays. Fault traces are queried where continuation or existence is uncertain. All offshore faults based on seismic reflection profile records are shown as solid lines where well defined, dashed where inferred, queried where uncertain.

FAULT CLASSIFICATION COLOR CODE
(Indicating Recency of Movement)

Fault along which historic (last 200 years) displacement has occurred.

1906 1906

1838 1838

A triangle to the right or left of the date indicates termination point of observed surface displacement. Solid red triangle indicates known location of rupture termination point. Open black triangle indicates uncertain or estimated location of rupture termination point.

1951

Date bracketed by triangles indicates local fault break.

1992

No triangle by date indicates an intermediate point along faultbreak.

CREEP

Fault that exhibits fault creep slippage. Hachures indicate linear extent of fault creep. Annotation (creep with leader) indicates representative locations where fault creep has been observed and recorded.

representative locations where fault creep has been observed and recorded.

1969
1968 1968

Square on fault indicates where fault creep slippage has occured that has been triggered by an earthquake on some other fault. Date of causative earthquake indicated. Squares to right and left of date indicate terminal points between which triggered creep slippage has occurred (creep either continuous or intermittent between these end points).

Holocene fault displacement (during past 11,700 years) without historic record.

Late Quaternary fault displacement (during past 700,000 years).

Quaternary fault (age undifferentiated).

Pre-Quaternary fault (older that 1.6 million years) or fault without recognized Quaternary displacement.

ADDITIONAL FAULT SYMBOLS

Bar and ball on downthrown side (relative or apparent).

Arrows along fault indicate relative or apparent direction of lateral movement.

Arrow on fault indicates direction of dip.

Low angle fault (barbs on upper plate).

Low angle fault (barbs on upper plate).

OTHER SYMBOLS

491

Numbers refer to annotations listed in the appendices of the accompanying report.

Structural discontinuity (offshore) separating differing Neogene structural domains. May indicate discontinuities between basement rocks.

Brawley Seismic Zone, a linear zone of seismicity locally up to 10 km wide associated with the releasing step between the Imperial and San Andreas faults.

SAN JOAQUIN RENEWABLES

CGS Fault Activity map of Kern County

S:\Projects\DB19.1252_Frontline_Bioenergy\GIS\QGIS\EPA comments\CGS Fault activity map of Kern County.qgz

06/13/2022 JN DB19.1252

Figure 2-50

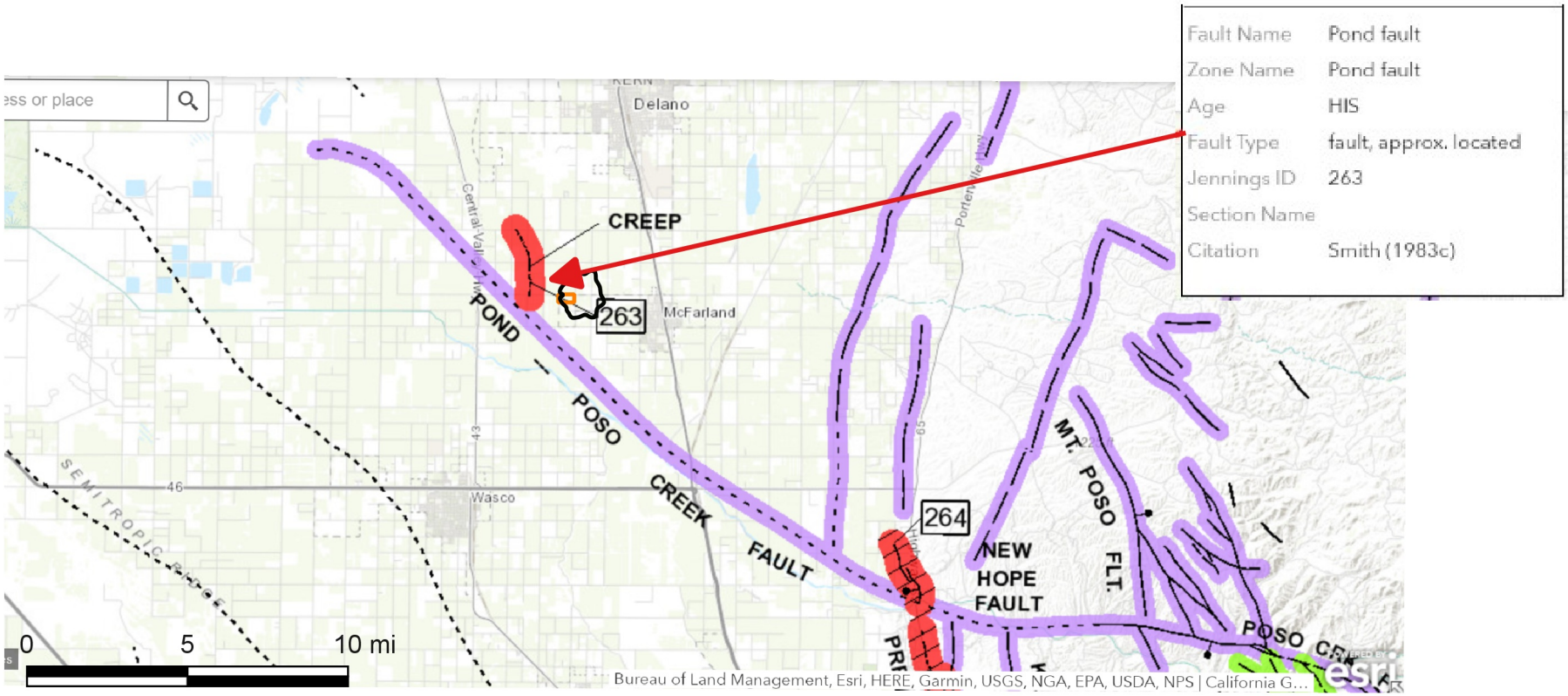

N

Explanation

- Area of Review
- SJR Property

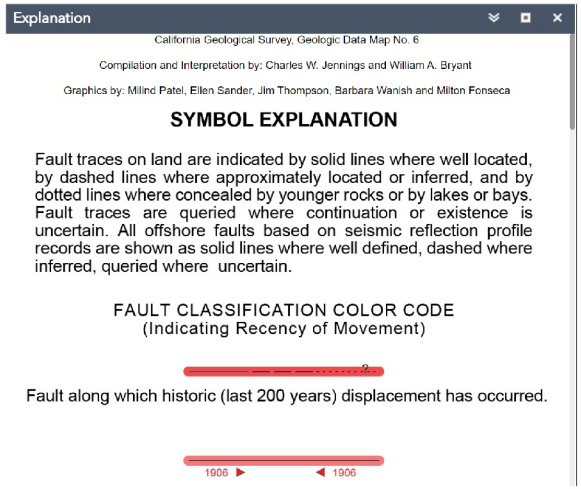

Notes: Pond fault has shown creep due to groundwater withdrawal. There have been no earthquakes associated with this feature

Source: https://maps.conservation.ca.gov/cgs/fam/

SAN JOAQUIN RENEWABLES

McFarland Area Historic Faults

06/13/2022 JN DB19.1252 Figure 2-51

S:\Projects\DB19.1252_Frontline_Bioenergy\GIS\QGIS\EPA comments\Mcfarland area historic faults.qgz

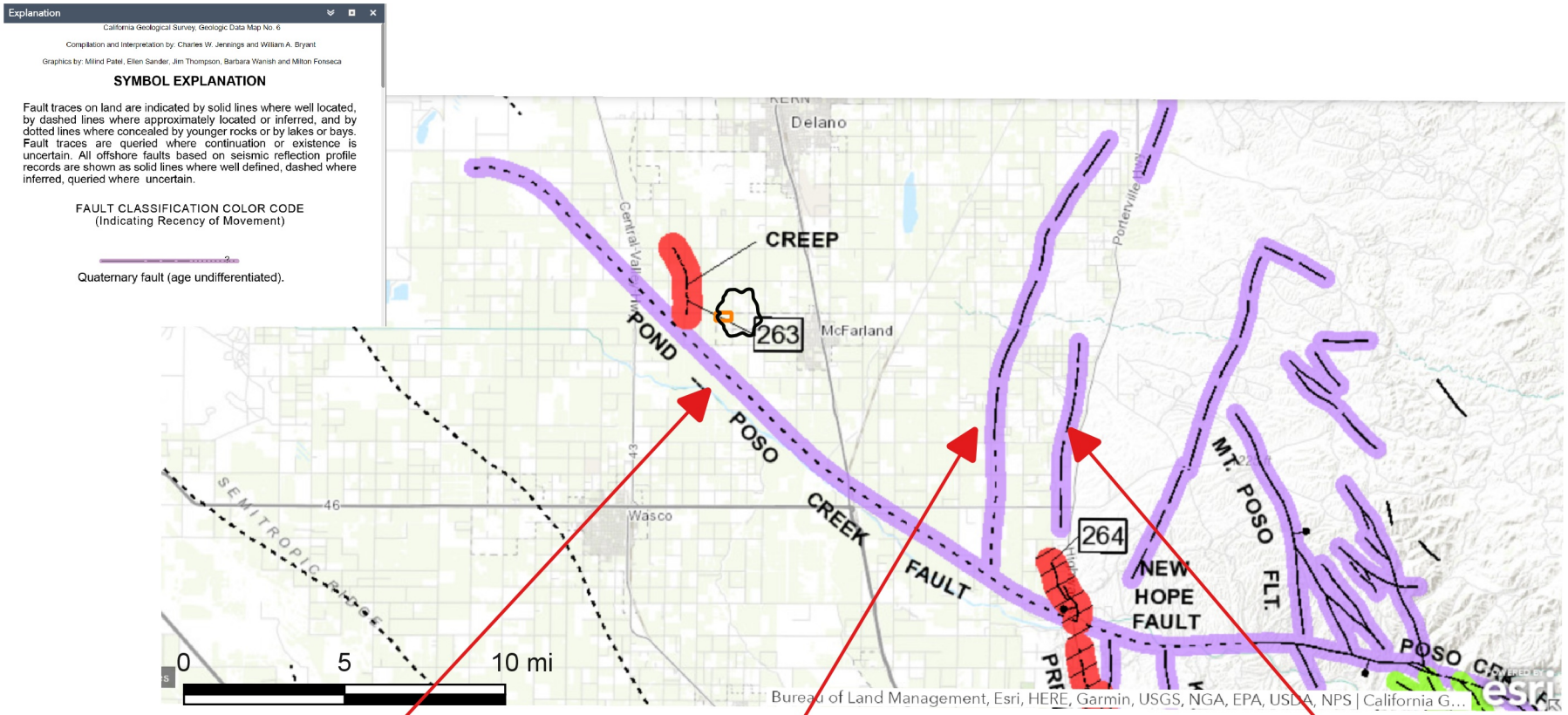

Quaternary Faults:

Fault Name	Poso Creek fault
Zone Name	Poso Creek fault
Age	QT
Fault Type	fault, concealed
Jennings ID	na
Section Name	
Citation	Bartow (1984)

Quaternary Faults:

Fault Name	unnamed
Zone Name	Unnamed faults near Rag Gulch
Age	QT
Fault Type	fault, approx. located
Jennings ID	na
Section Name	
Citation	Bartow (1984)

Quaternary Faults:

Fault Name	unnamed
Zone Name	Unnamed faults near Rag Gulch
Age	QT
Fault Type	fault, approx. located (ball and bar)
Jennings ID	na
Section Name	
Citation	Bartow (1984)

N

Explanation

- Area of Review
- SJR Property

Notes: Quaternary: in the past 1.6 million years

Source: https://maps.conservation.ca.gov/cgs/fam/

SAN JOAQUIN RENEWABLES

McFarland Area Quaternary Faults

06/13/2022 JN DB19.1252

Figure 2-52

S:\Projects\DB19.1252_Frontline_Bioenergy\GIS\QGIS\EPA comments\Mcfarland area Quaternary faults.qgz

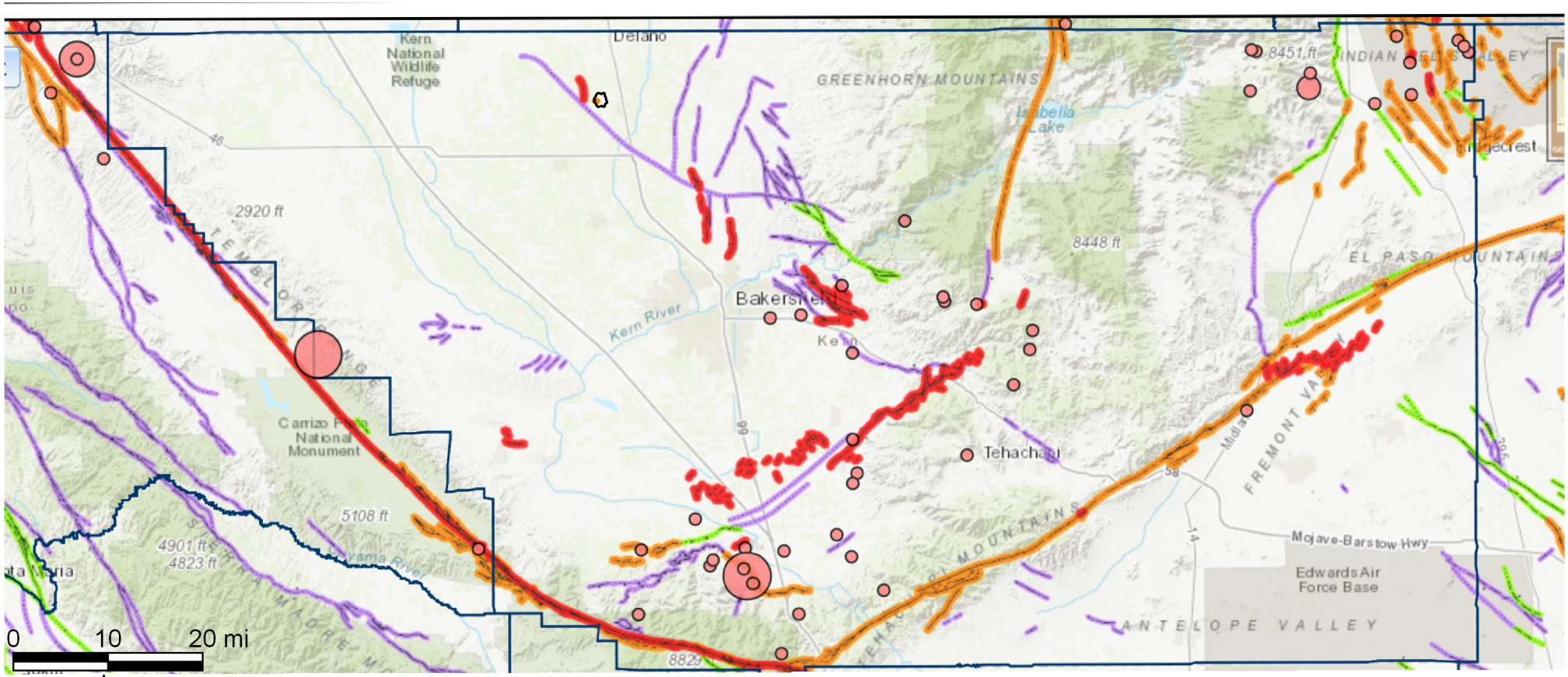

Explanation

- Area of Review
- SJR Property

Epicenters

- < 6.0
- 6.0 - 6.4
- 6.4 - 7.0
- 7.0 +

Background Data (Quaternary Fault Map):
The background of this map includes quaternary faults from the *2010 Fault Activity Map*. Faults with activity in the past approximately 200 years are highlighted in red. Orange indicates faults with activity in the Holocene period (the last ~11,700 years). Green highlighted faults show evidence of displacement during the late Quaternary time (<700,000 years before present); and purple highlighted faults show evidence of displacement during the Quaternary (the last 1.6 million years). For more information about these data, please visit the *Fault Activity Map* web page.

Source: https://maps.conservation.ca.gov/cgs/historicearthquakes/

SAN JOAQUIN RENEWABLES

Historic Earthquakes Kern County, California

06/14/2022 JN DB19.1252

Figure 2-53

S:\Projects\DB19.1252_Frontline_Bioenergy\GIS\QGIS\EPA comments\Historic Earthquakes.qgz

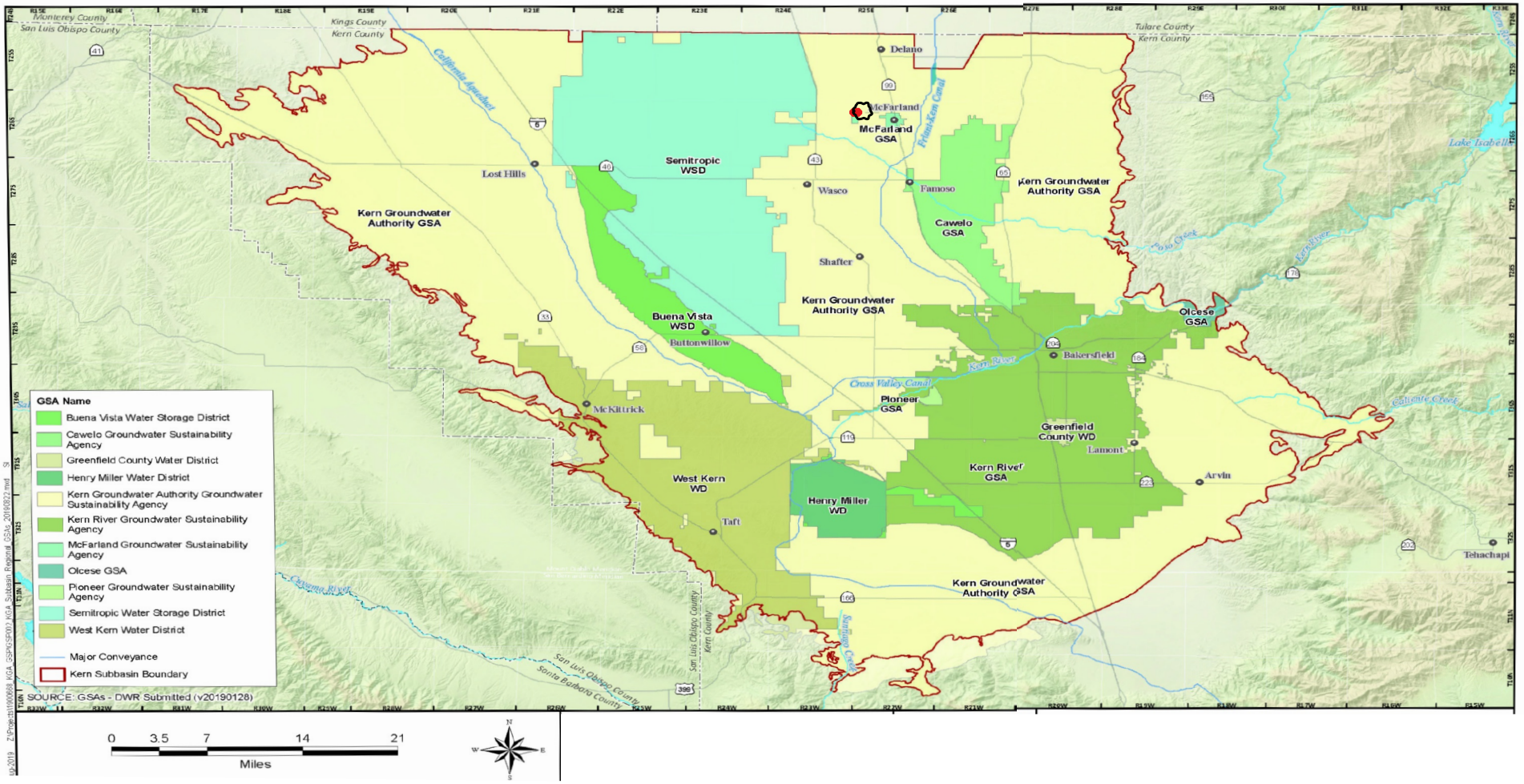

Source: GEI Consultants INC for Kern Water Authority, 2020.

Explanation

- Area of Review
- SJR Property

SAN JOAQUIN RENEWABLES

Groundwater Sustainability Agencies within Kern County Subbasin

06/13/2022 JN DB19.1252

Figure 2-54

S:\Projects\DB19.1252_Frontline_Bioenergy\GIS\QGIS\2-50 GW sustainability agencies.qgz

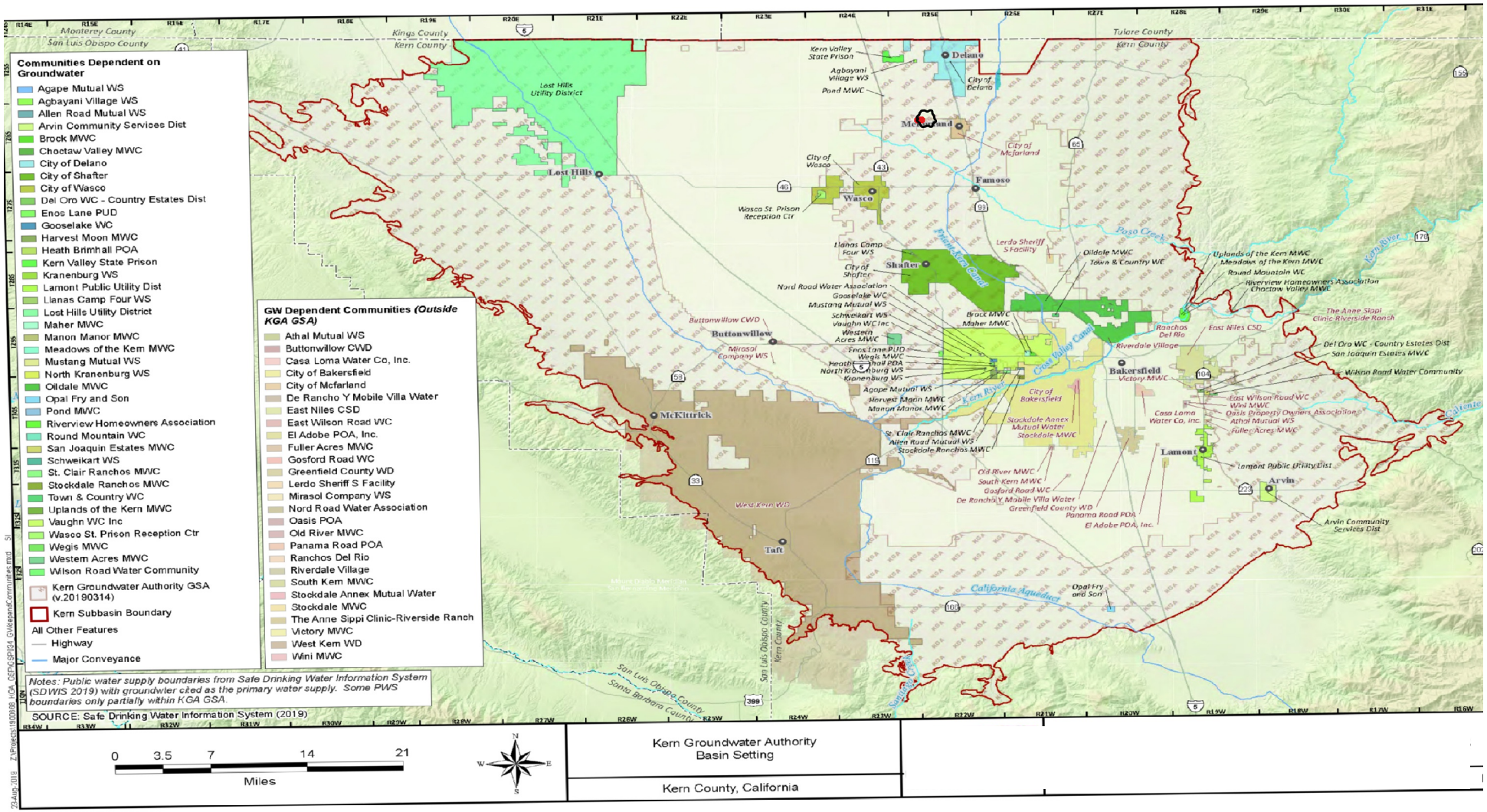

Explanation

Area of Review

SJR

KGA - Kern Groundwater Authority

Source: GEI Consultants INC for Kern Water Authority, 2020.

SAN JOAQUIN RENEWABLES

Groundwater Dependent Communities

S:\Projects\DB19.1252_Frontline_Bioenergy\GIS\QGIS\2-51 GW dependent comm.qgz

06/09/2022 JN DB19.1252

Figure 2-55

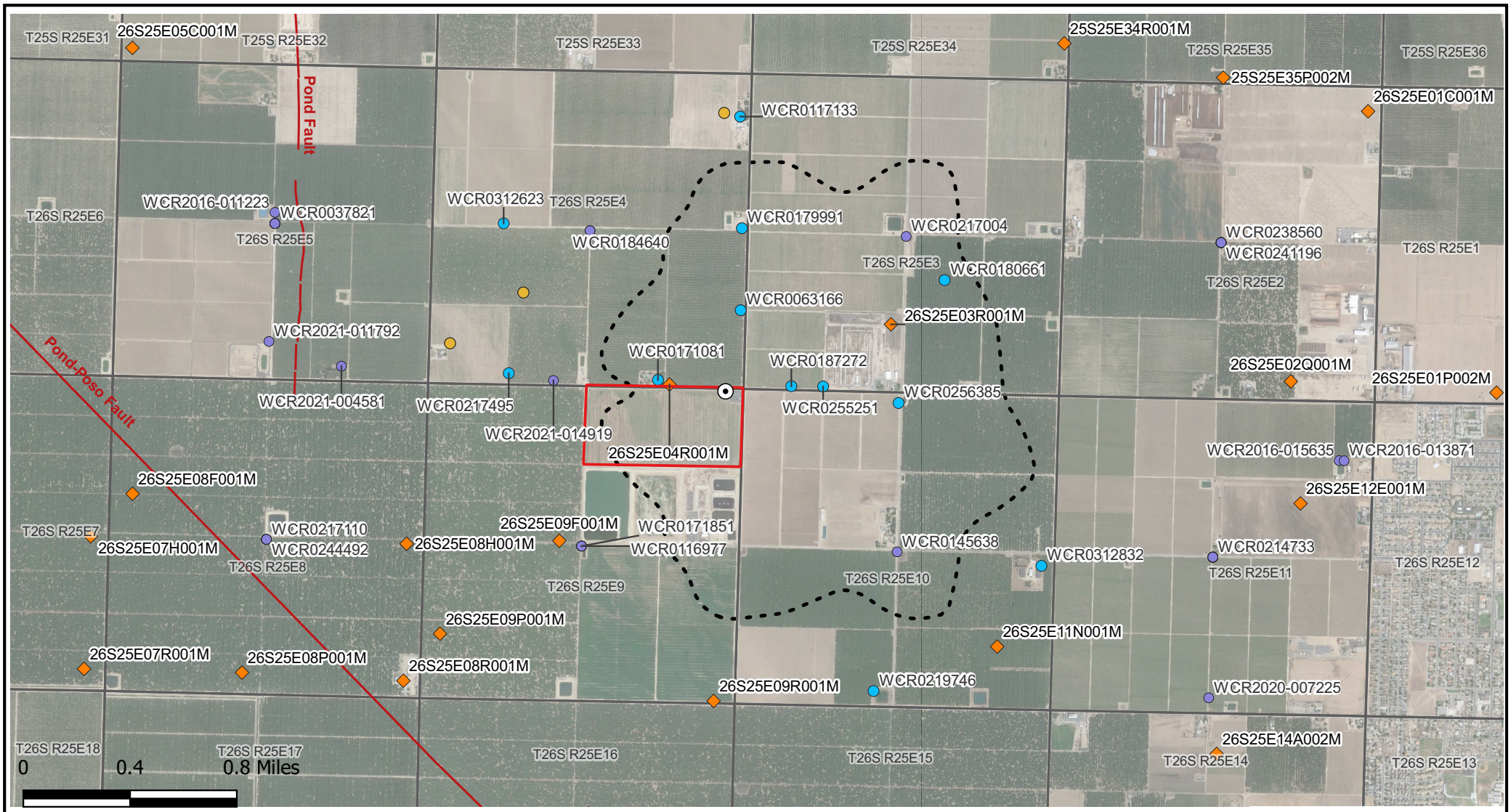

S:\Projects\DB19.1252_Frontline_Bioenergy\GIS\QGIS\Fig_2-56_Water Supply Wells Within The AoR (CHRISTINE QA).qgz

SAN JOAQUIN RENEWABLES

Water Supply Wells within the Project Vicinity

09/02/2022 JN DB19.1252 Figure 2-56

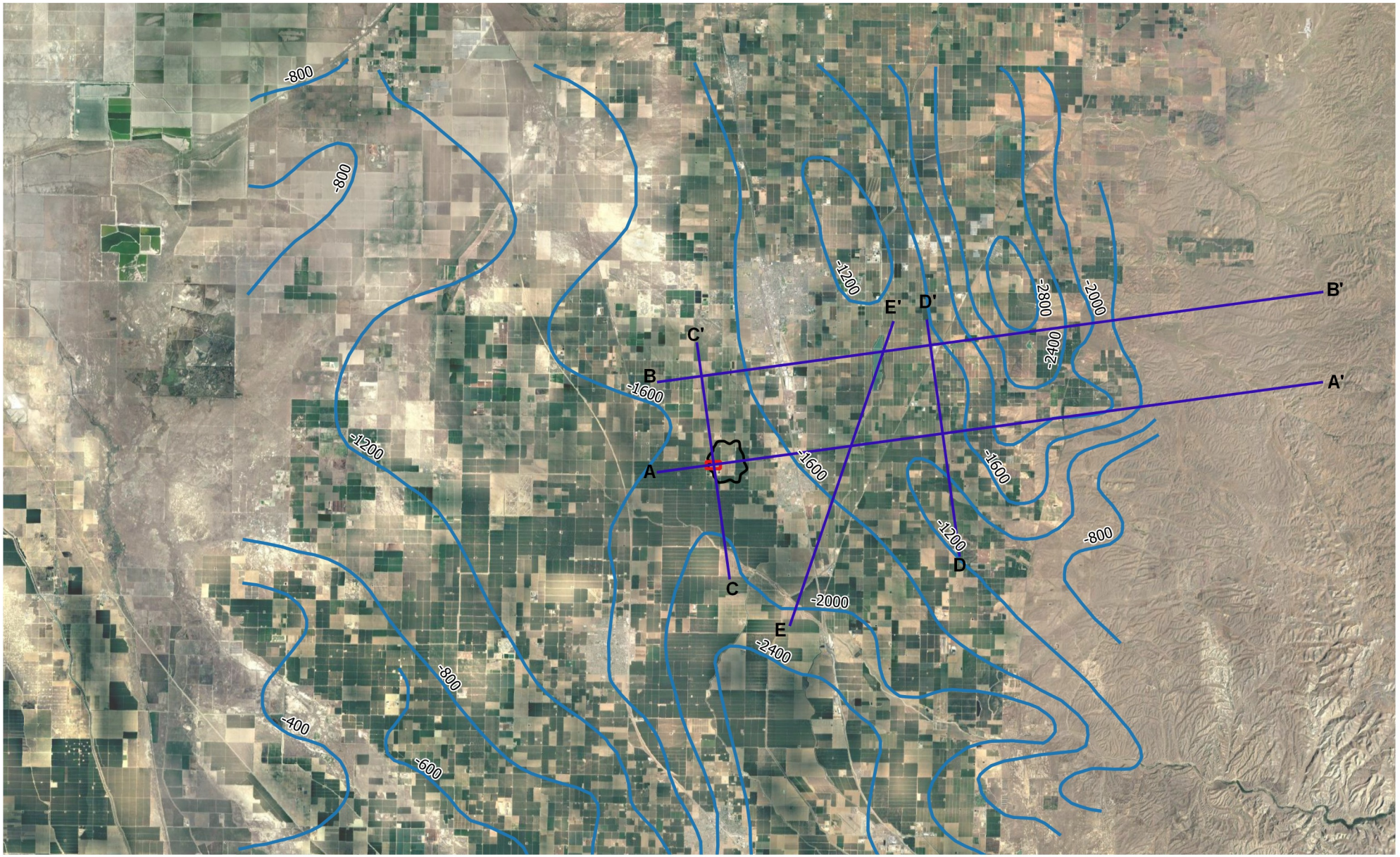

Explanation

- Cross Section
- Fresh Water Elevation Contours, feet (Page, 1973)
- Area of Review
- Property

SAN JOAQUIN RENEWABLES

Elevation, Base of Freshwater

06/13/2022 JN DB19.1252

Figure 2-57

S:\Projects\DB19.1252_Frontline_Bioenergy\GIS\QGIS\Fig_2-53_Depth to Fresh Water.qgz

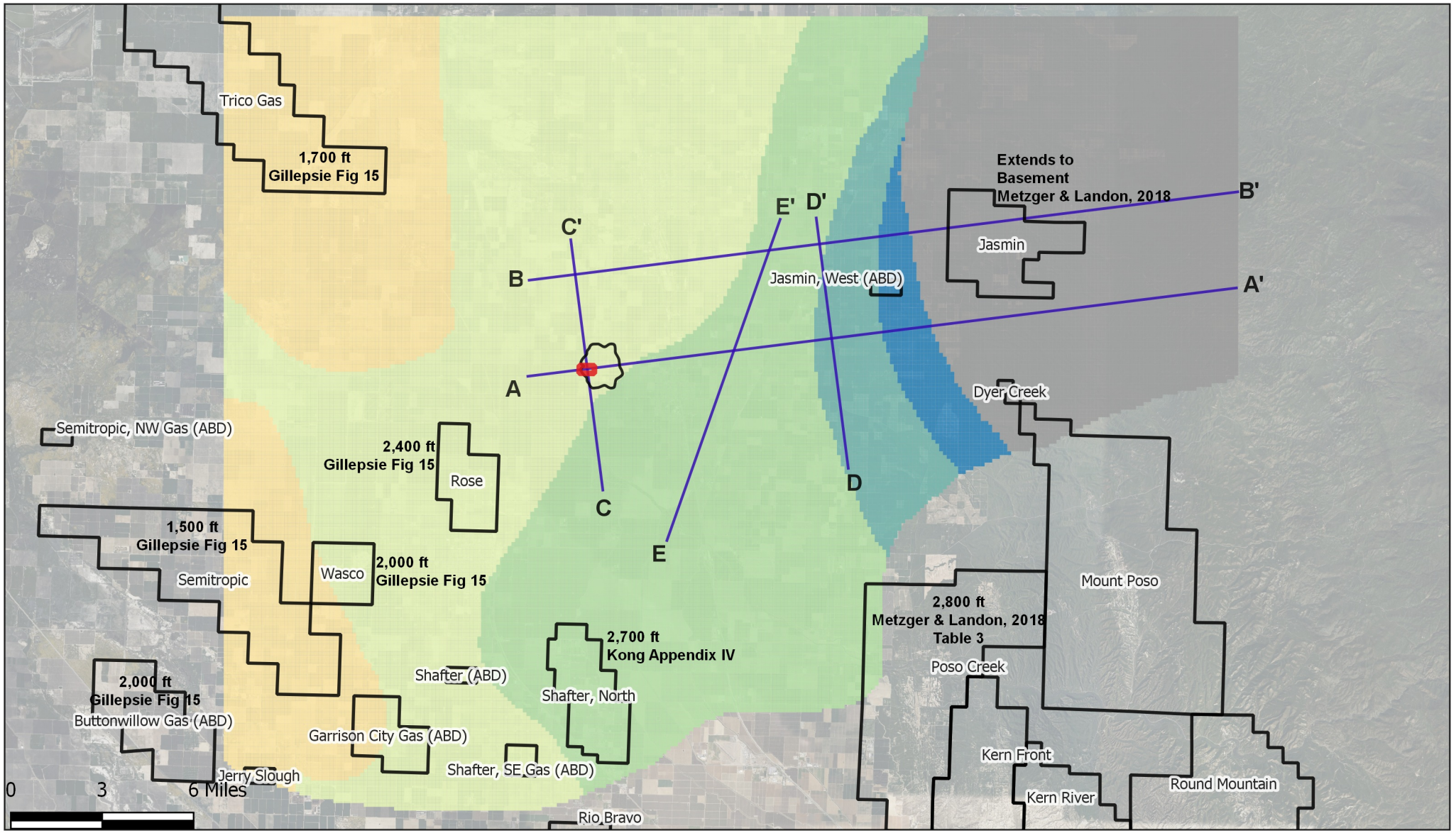

SAN JOAQUIN RENEWABLES

Depth to Base of USDWs

S:\Projects\DB19.1252_Frontline_Bioenergy\GIS\QGIS\gs\qgz\usdw-depth.qgz

06/13/2022 JN DB19.1252

Figure 2-58

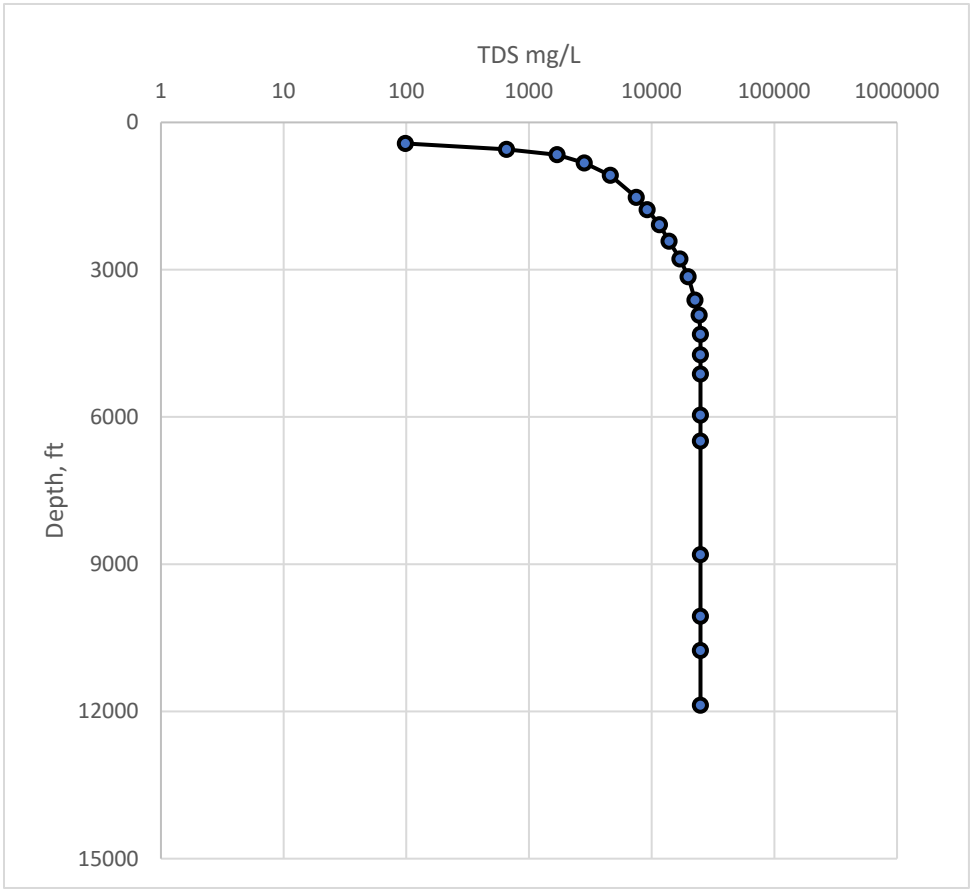

Middle Kern Valley Floor TDS v Depth, semi-log scale

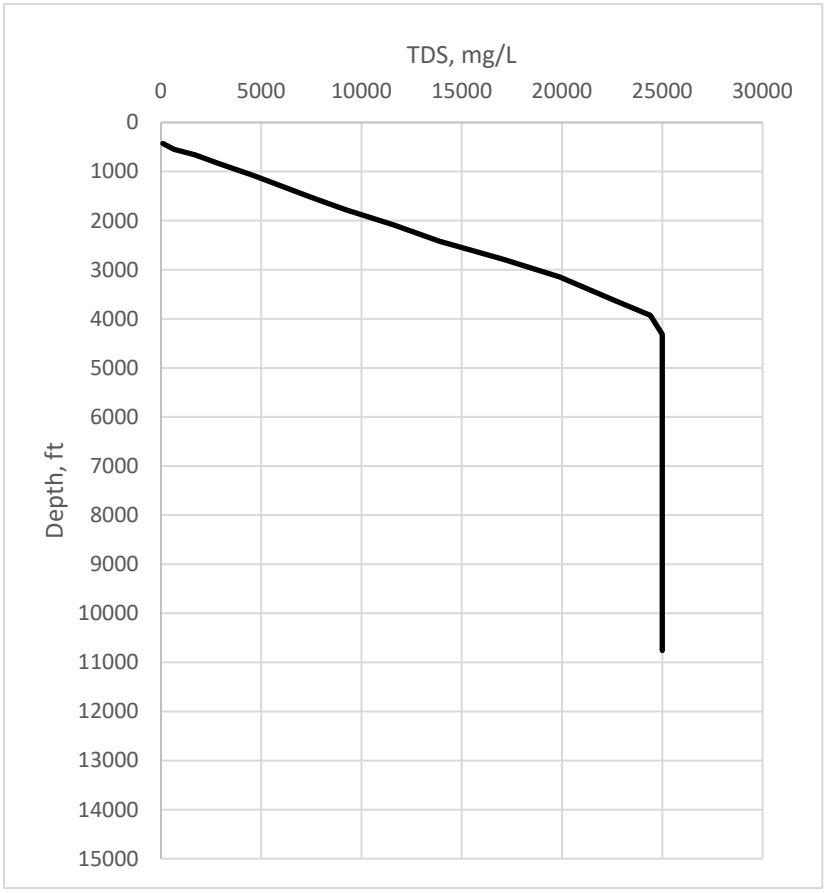

Linear Scale

Source: Metzger & Landon, 2018. (https://doi.org/10.3133/sir20185082)

Note: TDS maximum is approximately 29,000 mg/L in USGS (2018) Figure 19; however, maximum was adjusted to 25,000 mg/L to be more consistent with various brine data from Vedder in oil and gas fields (e.g., see Table 2-7).

SAN JOAQUIN RENEWABLES

Middle Kern Valley TDS vs. Depth

9/13/2021 DB19.1252

Figure 2-59

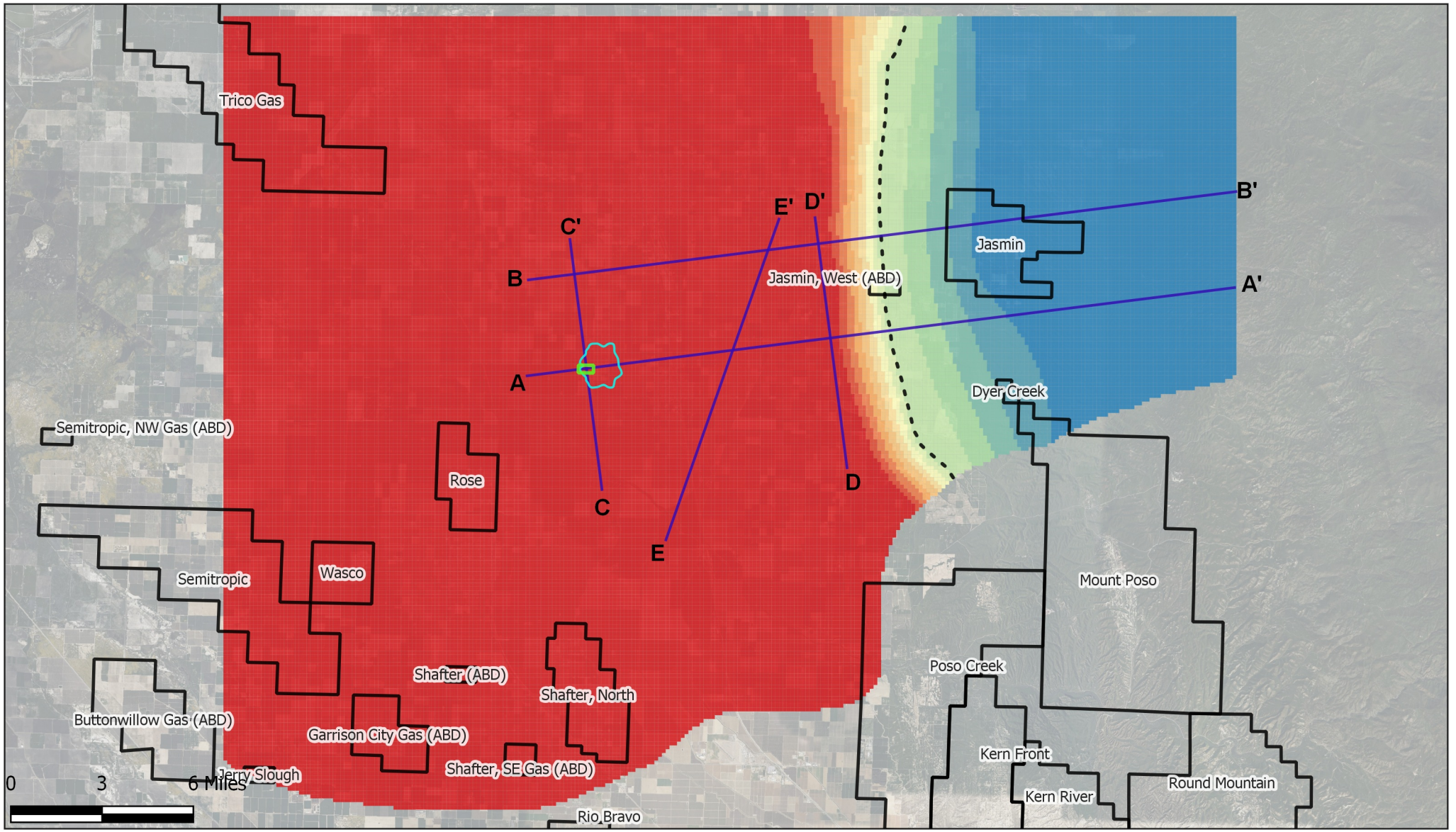

SAN JOAQUIN RENEWABLES

Salinity Isohaline Map, Vedder Formation

S:\Projects\DB19.1252_Frontline_Bioenergy\GIS\QGIS\Salinity Isohaline Map.qgz

06/14/2022 JN DB19.1252

Figure 2-60

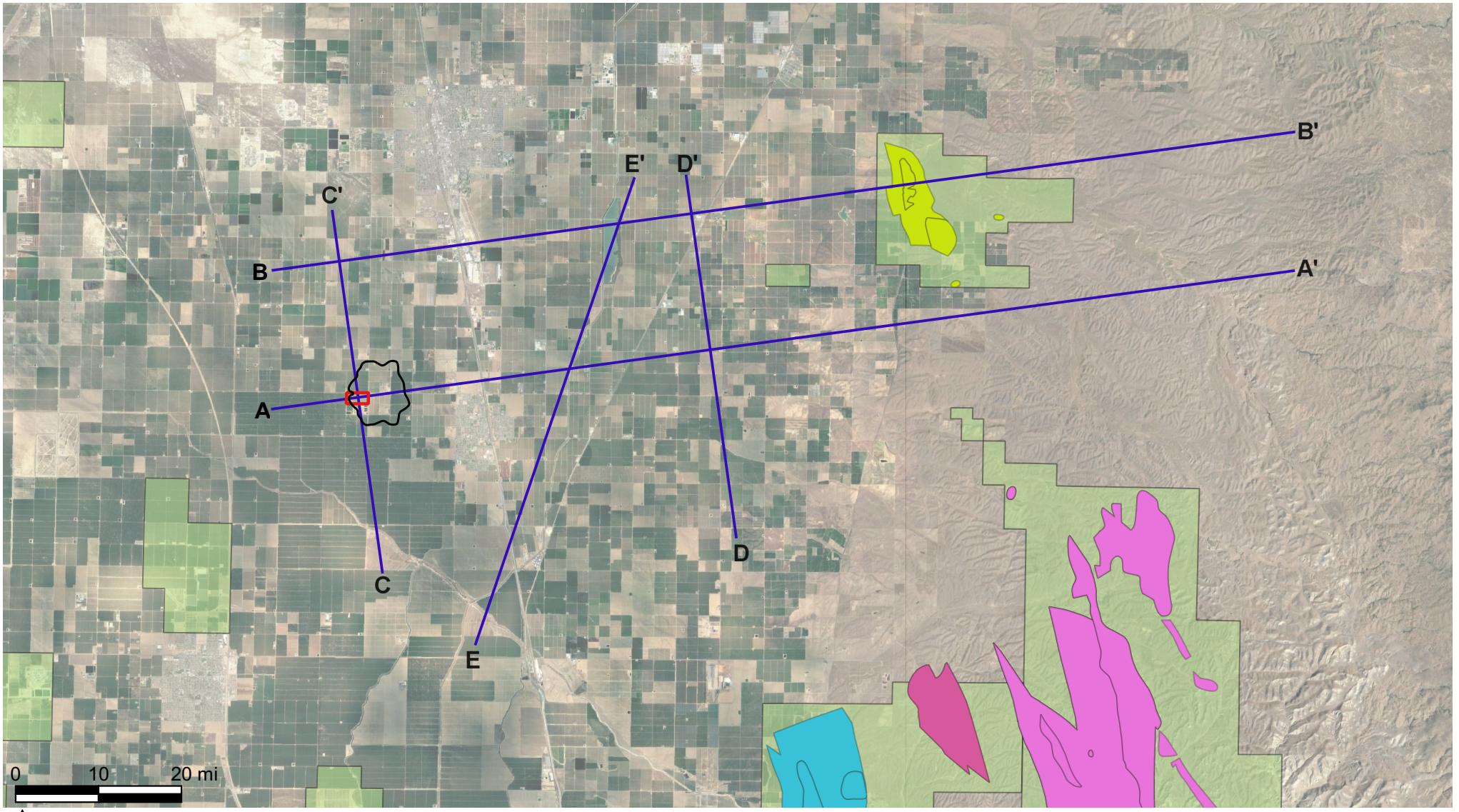

Explanation

- Area of Review
- Property
- Cross Section
- Oil and Gas Fields

Kern County Aquifer Exemptions

- Jasmin Oil Field
- Mount Poso Oil Field
- Poso Creek Oil Field - McVan Area
- Poso Creek Oil Field - Premier & Enas Area

SAN JOAQUIN RENEWABLES

Oil and Gas Fields

S:\Projects\DB19.1252_Frontline_Bioenergy\GIS\QGIS\Fig_2-57_Oil and Gas Fields.qgz

06/13/2022 JN DB19.1252

Figure 2-61a

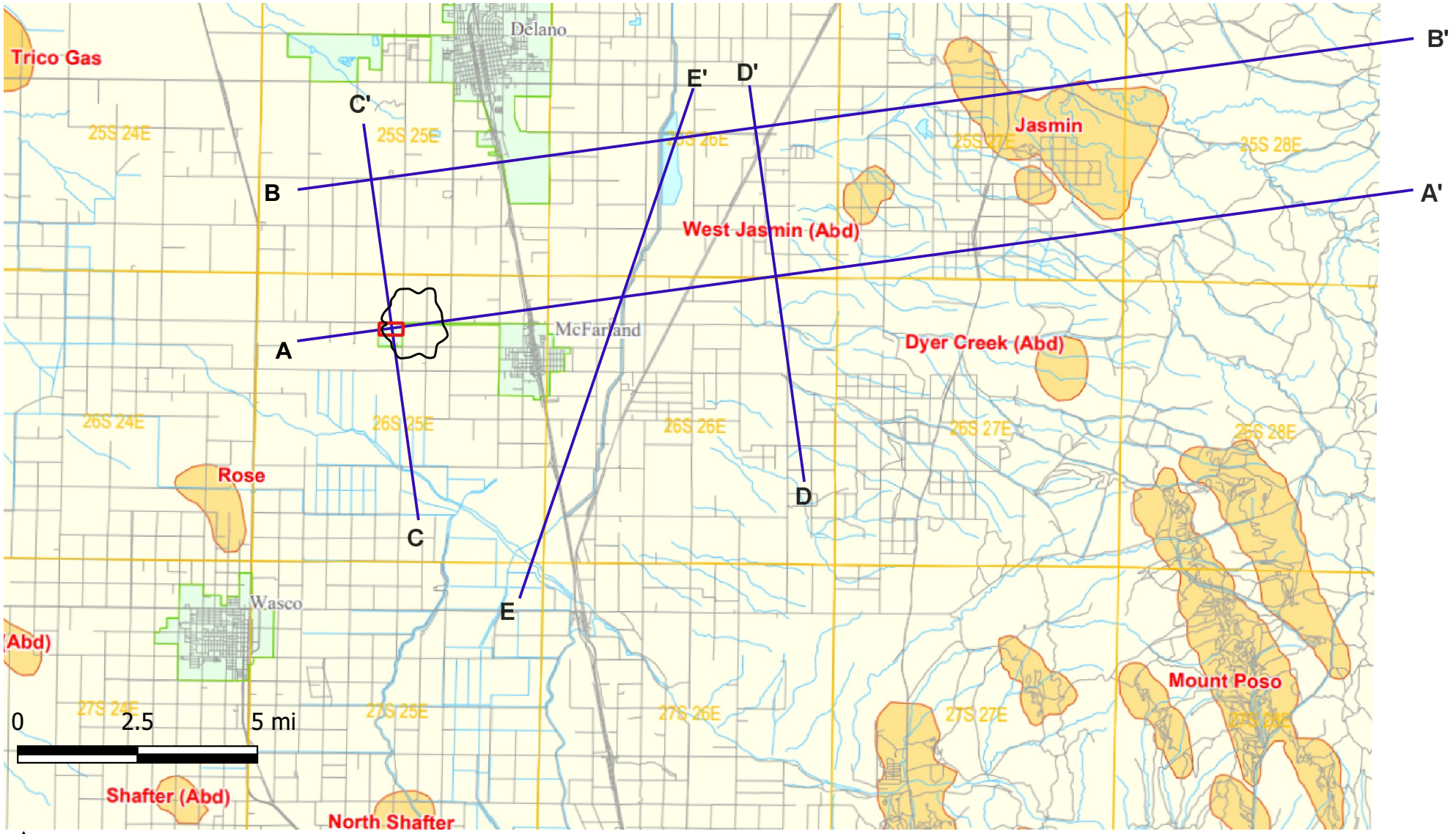

Explanation

- Area of Review
- Property
- Cross Section

Notes: Map from CalGEM displaying the oil fields in the vicinity of Mc Farland. Rose and North Shafter are Monterey formation producers while Jasmin, West Jasmin, and Dyer Creek are (or were) Pyramid Hill, Vedder, or Famoso producers. Details for productive pool information are provided below.

SAN JOAQUIN RENEWABLES

Kern County Oil Fields in the vicinity of McFarland

06/13/2022 JN DB19.1252 Figure 2-61b

S:\Projects\DB19.1252_Frontline_Bioenergy\GIS\QGIS\EPA comments\oil and gas fields DS.qgz

Proposed Wellbore Schematic

CO2 Injection Well
Two Injection Zones, Two Strings
Short String: Pyramid Hill + Vedder 1 + Vedder 2
Long String: Vedder 3

San Joaquin Renewables

Geo Marker	INCL/TVD	Hole		Casing & Perf	Details
				Depths are MD	
		26"	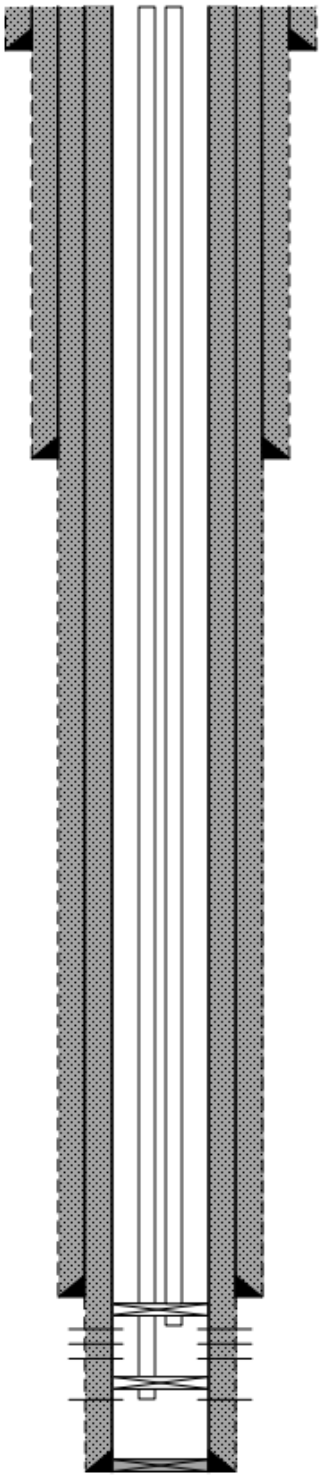	20" 94# J-55 BTC Csg @ 250'	20" Csg cmt'd @ 250'-Surf w/ 489 CF cmt
		17-1/2"			
BFW @ ~1750'					
USDW @ ~2495'				13-3/8" 61# J-55 BTC Csg @ 2600'	13-3/" Csg cmt'd @ 2600'-Surf w/ 2377 CF cmt
		12-1/4"			
Pyramid Hills @ 7775' Vedder 1 @ 7789' Vedder 2 @ 8040'				9-5/8" 53.5# N-80 LTC Csg @ 7700' Perforated @ 7775'-7789' (PH), 7789'-7900' (V1), 8040'-8132' (V2)	9-5/8" Csg cmt'd @ 7700'-Surf w/ 3207 CF cmt Hydraulic set packer @ 7725' 2-3/8" IC Cr13 tbg @ 7750'
Vedder 3 @ 8167' Vedder 4 @ 8344'		8-1/2"		Perforated @ 8167'-8255' (V3)	2-3/8" IC Cr13 tbg @ 7725' Wireline set packer @ 8120' 2-3/8" IC/EC Cr13 tbg @ 8150'
		TD @ 8700'		7" 29# L-80 Cr13 LTC Csg @ 8700'	7" Csg cmt'd @ 8700'-Surf w/ 1166 CF cmt w/ latex additive in tail

Creator & Date: JM 5/26/2021

SAN JOAQUIN RENEWABLES
Injection Well Design

K:\Projects\Environmental Services\Private\Frontline Bioenergy\Final Documents\Permit Application\Figures\docx\ Fig_3-1_Injection Well Design.docx

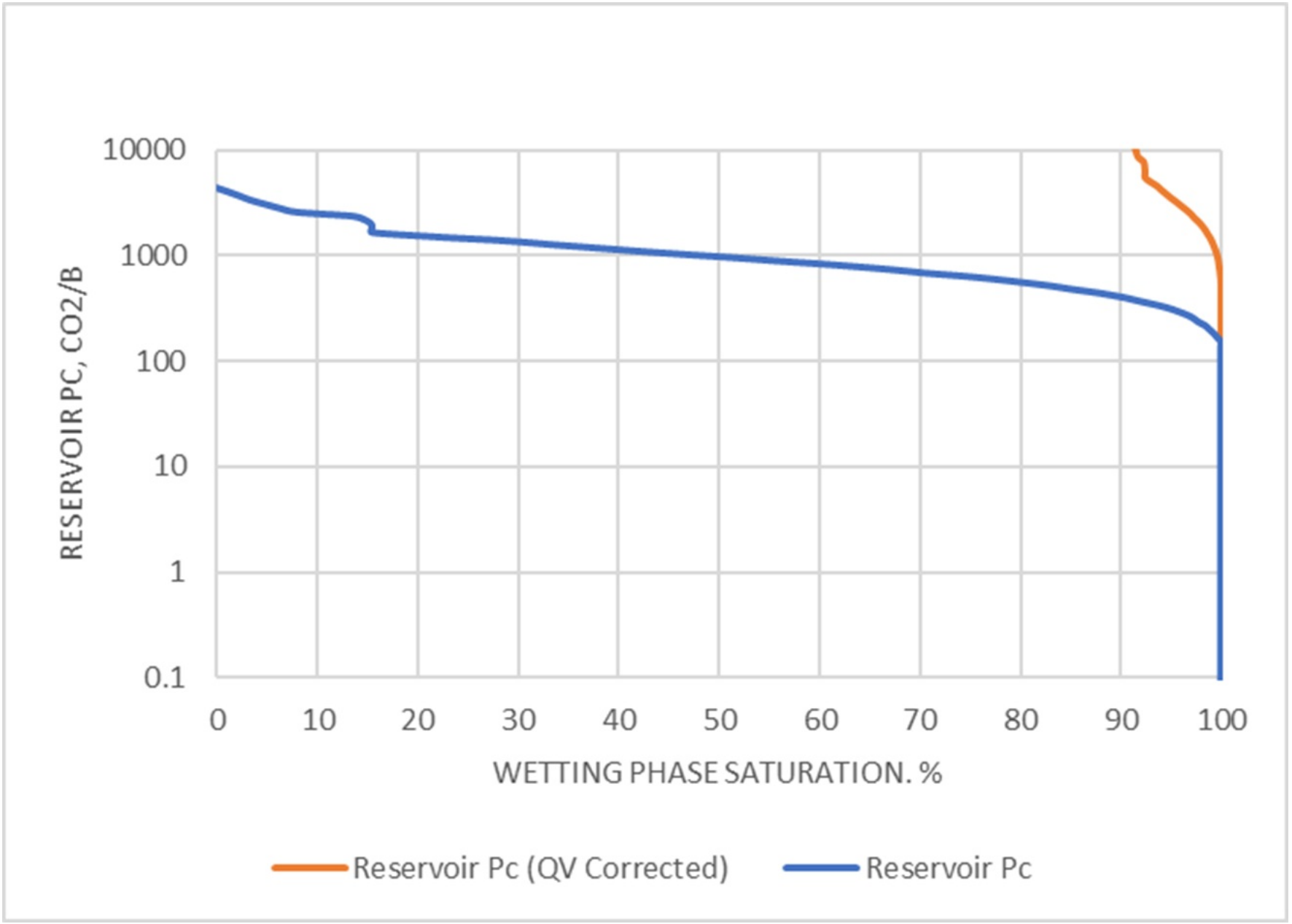

SAN JOAQUIN RENEWABLES

Capillary Pressure versus Wetting Phase Saturation for MICP Core Data, KCLA Depth 8161 – 8170

06/14/2022 JN DB19.1252

Figure 7-1

S:\Projects\DB19.1252_Frontline_Bioenergy\GIS\QGIS\EPA comments\capillary pressure versus wetting phase saturation for MICP core data.qgz

Tables

List of Tables

Table 1-1. Permits Application Information
Page 1 of 2

Permit or Registration Name	Description	Granting Authority	Administrative or Subjective	Cost	Prerequisites	Application Date	Renewal Frequency/ Date	Receipt Date (actual or projected)	Comments
Conditional Use Permit	Required by city to operate plant	City of McFarland	Administrative	Estimated $5K	Site ownership or owner authorization		None required		Will follow after CEQA
California Environmental Quality Act (CEQA) determination and review	Determination of environmental impact of project by project permitting agency	Determination by City of McFarland and San Joaquin Valley Air Pollution Control District, review and approval by "State Clearinghouse"	Administrative and Subjective	CEQA Environmental document filing fee for mitigated negative declaration estimated at $5K. Cost of preparing declaration statement with "initial studies" estimated at $60K.	None remaining	Estimated completion August, 2021, up to 3 months to approve if mitigated neg. dec. is accepted.	None required		We intend to adopt a mitigated negative declaration based on the fact the site has been in continuous agricultural use, the proposed plant has extremely low emissions, and will improve the air quality in the surrounding area. Basis of estimates are proposals from TSS Consultants (Fred Tornatore) and Douglas Brown of Douglas Environmental.
Local building permits	Foundation, structural, mechanical (HVAC and plumbing), electrical, telecommunications, signage	City of McFarland	Administrative	Estimated $10K	Site ownership or owner authorization		None required		
Authority to construct	Air permit	San Joaquin Valley Air Pollution Control District	Administrative	Estimated $50K	Done	Estimated completion August, 2021, up to 6 to 9 months to approve.			Applying as synthetic minor, will be under threshold limits for Title V.
Authority to operate	Air permit	San Joaquin Valley Air Pollution Control District	Administrative	Estimated $10K	Completion of construction				
Water discharge permit (NPDES permit)	Allows discharge of waste water	Central Region Water Board		$2268 application and annual fee (https://www.waterboards.ca.gov/resources/fees/water_quality/docs/fy1819_fee_schedule.pdf)	Not needed with current process design				Jim Marshall, Senior WRCE James.Marshall@waterboards.ca.gov (916) 464-4772

Table 1-1. Permits Application Information
Page 2 of 2

Permit or Registration Name	Description	Granting Authority	Administrative or Subjective	Cost	Prerequisites	Application Date	Renewal Frequency/ Date	Receipt Date (actual or projected)	Comments
Water Rights Registration		Central Region Water Board		~$100 (https://www.waterboards.ca.gov/waterrights/water_issues/programs/applications/)			Annual		https://www.waterboards.ca.gov/waterrights/water_issues/programs/applications/
Well permit	Permission to build water well on the site	Kern County Public Health Services Dept.	Administrative		May not be needed				http://kernpublichealth.com/wp-content/uploads/2016/03/APPLICATION-WATER-WELL-6-7-17.pdf
Industrial Activities Storm Water General Permit	Storm water pollution prevention plan or similar	Central Region Water Board -R5	Administrative						https://www.waterboards.ca.gov/board_decisions/adopted_orders/water_quality/2014/wqo2014_0057_dwq_revised.pdf
General Permit for Storm Water Discharges Associated with Construction Activity	Storm water pollution prevention plan or similar	Central Region Water Board -R5	Administrative						https://www.waterboards.ca.gov/board_decisions/adopted_orders/water_quality/2014/wqo2014_0057_dwq_revised.pdf
Business License		City of McFarland	Administrative	<$200					http://www.kernsheriff.org/documents/sheriff_documents/BusinessLicenseFees.pdf
Carbon Capture and Storage (Class VI) Well permit	Authority to inject CO_2 for permanent carbon capture	U.S. EPA	Administrative	$400k	Extensive geological studies	Estimated submission June 2021	None required		
Registration as foreign corporation		California Secretary of State	Administrative	$800 per year franchise tax		Completed	Completed		

Table 2-1. Formation Thickness and Elevation Under SJR Property

Formation	Thickness (feet)	Top Elevation (ft-msl)
Surface/Alluvium	3223	333
Etchegoin	1583	-2890
Miocene	699	-4473
Santa-Margarita	923	-5172
Round-Mountain	222	-6095
Olcese	464	-6317
Freeman-Jewett	662	-6781
Pyramid-Hills	12	-7443
Vedder1	122	-7455
Vedder1A	134	-7577
Vedder2	121	-7711
Vedder3	180	-7832
Vedder4	19	-8011
Walker	1088	-8031
Basement	--	-9119

Table 2-2. Shale Gouge Ratio Determination

Shale Gouge Ratio (%)				
Round-Mountain	Freeman-Jewett	VED2 SH	VED3 SH	VED4 SH
251.82	153.83	32.21	31.72	8.51
178.98	149.87	22.88	16.79	9.24
164.77	158.53	23.01	27.10	6.04
166.11	125.46	19.27	26.50	6.70
165.75	107.98	17.02	25.92	6.57
167.06	185.30	18.90	31.64	8.02
125.27	313.45	16.11	28.25	7.84
71.98	342.11	14.02	26.24	5.66
51.69	105.74	7.67	15.41	2.56
51.58	93.47	11.95	26.92	3.62
23.53	73.32	4.04	13.97	2.82
17.46	62.00	3.10	10.71	0.00
19.35	65.27	1.81	14.39	–2.34
26.19	78.21	4.47	11.45	0.00
30.11	86.43	5.45	9.52	0.00
39.42	138.47	7.47	9.91	0.74
46.45	161.83	6.59	7.42	2.12
55.11	160.32	5.81	4.26	3.34
52.30	172.07	6.83	2.83	7.23
215.30	333.93	13.39	3.52	13.78
125.04	217.21	10.15	4.18	11.70
327.51	452.21	12.01	10.83	22.87

x >50%
30%> x <50%
15%> x <30%
5%> x <15%
x <5%

Note: Determination of shale gouge ratio is based on the formula (sum of shale thickness/fault throw) x 100%. The calculation is made for each shale layer at each cross section along the Pond-Poso Creek fault plane.

VED2 SH = Vedder 2 Shale
VED3 SH = Vedder 3 Shale
VED4 SH = Vedder 4 Shale

Table 2-3. Wells with Geologic Core Data

API	Lease Name	Alternative Name	Section	Township	Range	Latitude	Longitude	Existing Data	Best Core Services Analysis				
								MICP	MICP	XRD	SEM	TXC	Micro-CT
402954535	Betts	Sec 26-25S-27E	26	25S	27E	35.73006058	–119.04081726	X					
402966854	Quinn	SEC.9-25S-27E	9	25S	27E	35.77361298	–119.08001709	X					
402954446	Quinn	SEC 18-25S-28E	18	25S	28E	35.7537727	–119.0084076	X					
402970053	Tenneco-Sun	T26S R26E S31	31	26S	26E	35.6304092	–119.2226715	X					
410720225	Neufeld	22-24S-23E	22	24S	23E	35.8318253	–119.4707336	X					
410720206	Lessley	SEC. 6-T23S/R26E	6	23S	26E	35.9535751	–119.1997147	X					
402930606	KCL-A	KCL A 83-35	35	26S	25E	35.6261101	–119.2422104		X	X	X	X	X
402930516	Stiles	Gen Pet Stiles 1	35	25S	25E	35.7037964	–119.2575989		X	X			
402930615	Alta	Bailey Alta 1	16	26S	26E	35.6742401	–119.1776047		X	X			
402930604	K.C.L. 25	KCL 25 1	25	26S	25E	35.6426392	–119.2331924		X	X	X	X	X
402930523	Bell	Shell Bell 52-21	21	25S	26E	35.7444572	–119.1770554		X	X	X	X	X
402930610	Wright-Bloomer	Wright Bloemer 74-11	11	26S	26E	35.6836586	–119.1368713		X	X		X	X
402930521	Abrams	Rocket Abrams 1	26	25S	26E	35.7317047	–119.1411514		X	X	X		
402930616	White-Harp	Armstrong 1	9	26S	26E	35.6848221	–119.1713409		X	X			
402942325	Roberts-Cox	Roberts Cox 23-1	23	26S	26E	35.6521263	–119.1421433			X			

MICP = Mercury intrusion capillary pressure
XRD = X-ray diffraction
SEM = Scanning electron microscopy
TXC = Triaxial compressive strength
Micro-CT = Micro computed tomography

Table 2-4. Porosity and Permeability from Core Data
Page 1 of 9

API #	Location	Depth (feet)	Formation	MICP Permeability	MICP Porosity	ROUTINE Permeability	ROUTINE Porosity	Source	Date
402930516	Gen Pet Stiles 1	2,803–2,806	Alluvium	0.039	26.5			Best	2/23/2021
402930516	Gen Pet Stiles 1	4,809–4,812	Alluvium	0.0023	18.1			Best	2/23/2021
402930521	Rocket Abrams 1	4,233–4,258	Freeman-Jewett	0.97	26.9	1.5	24.2	Best	2/23/2021
402930521	Rocket Abrams 1	4,308–4,333	PYDH-VED1-VED2	90.5	30.5	56.6	24.6	Best	2/23/2021
402930523	Shell Bell 52-21	4,801–4,805	Freeman-Jewett	2.33	18.9	2.0	24.1	Best	2/23/2021
402930523	Shell Bell 52-21	5,057–5,068	PYDH-VED1-VED2	395.8	34.3	121.8	27.7	Best	2/23/2021
402930604	KCL 25 1	6,131	Olcese (shale)	0.0003	9.6			Best	2/23/2021
402930604	KCL 25 1	6,194	Olcese (shale)	0.46	6.2	1.2	4.1	Best	2/23/2021
402930606	KCL A 83-85	6,400–6,410	Round Mountain	0.0006	12.9			Best	2/23/2021
402930606	KCL A 83-85	6,410–6,420	Round Mountain	0.0010	14.3			Best	2/23/2021
402930606	KCL A 83-85	6,440–6,450	Round Mountain	0.0011	13.3			Best	2/23/2021
402930606	KCL A 83-85	6,720–6,728	Round Mountain	0.0001	8.4			Best	2/23/2021
402930606	KCL A 83-85	6,971–6,980	Round Mountain	0.0093	1.9			Best	2/23/2021
402930606	KCL A 83-85	7,000–7,010	Olcese (sand)	1800.8	32.5	1709.1	20.0	Best	2/23/2021
402930606	KCL A 83-85	7,155–7,177	Olcese (sand)	24.3	27.5			Best	2/23/2021
402930606	KCL A 83-85	8,161–8,170	Freeman-Jewett	0.0009	12.3	0.01	3.42	Best	2/23/2021
402930606	KCL A 83-85	8,350–8,360	PYDH-VED1-VED2	529.7	26.9			Best	2/23/2021
402930606	KCL A 83-85	8,360–8,367	PYDH-VED1-VED2	227.1	25.6			Best	2/23/2021
402930606	KCL A 83-85	8,380–8,390	VED1 SH	1.18	17.7			Best	2/23/2021
402930606	KCL A 83-85	8,499–8,510	PYDH-VED1-VED2	5.25	18.4	0.1	5.4	Best	2/23/2021

Best = Best Core Services
Core = Core Laboratories
Good = Good Core Analysis
PTS = Petroleum Testing Services, Inc.

PYDH-VED1-VED2 = Pyramid Hills/Vedder 1/Vedder 2 Sand
VED1 SH = Vedder 1 Shale
VED2 SH = Vedder 2 Shale
VED4 SH = Vedder 4 Shale

VED4 = Vedder 4 Sand
VED3 = Vedder 3 Sand

Table 2-4. Porosity and Permeability from Core Data
Page 2 of 9

API #	Location	Depth (feet)	Formation	MICP Permeability	MICP Porosity	ROUTINE Permeability	ROUTINE Porosity	Source	Date
402930606	KCL A 83-85	8,520–8,530	PYDH-VED1-VED2	58.0	25.5			Best	2/23/2021
402930606	KCL A 83-85	8,633–8,643	VED2 SH	0.0026	9.8	0.2	10.3	Best	2/23/2021
402930606	KCL A 83-85	8,833–8,843	VED4 SH	0.105	14.8			Best	2/23/2021
402930606	KCL A 83-85	8,985–8,991	VED4 SH	0.0033	11.9			Best	2/23/2021
402930610	Wright Bloemer 74-11	4,369–4,379	Freeman-Jewett	2.12	21.9	3.4	26.2	Best	2/23/2021
402930610	Wright Bloemer 74-11	4,389–4,399	PYDH-VED1-VED2	23.3	30.0	12.2	18.8	Best	2/23/2021
402930615	Bailey Alta 1	1,470	Alluvium	0.13	35.4			Best	2/23/2021
402930615	Bailey Alta 1	2,028	Alluvium	1.49	33.3			Best	2/23/2021
402930616	Armstrong 1	2,105–2,125	Alluvium	0.17	46.5	0.8	45.8	Best	2/23/2021
402954446	SEC 18-25S-28E	1,481	PYDH-VED1-VED2	360	34.6	—	—	Core	12/20/1976
402954446	SEC 18-25S-28E	1,546	PYDH-VED1-VED2	210	32.9	—	—	Core	12/20/1976
402954446	SEC 18-25S-28E	1,560	PYDH-VED1-VED2	96	33.8	—	—	Core	12/20/1976
402954446	SEC 18-25S-28E	1,584	PYDH-VED1-VED2	440	38.7	—	—	Core	12/20/1976
402954446	SEC 18-25S-28E	1,591	PYDH-VED1-VED2	290	37	—	—	Core	12/20/1976
402954446	SEC 18-25S-28E	1,597	PYDH-VED1-VED2	215	39	—	—	Core	12/20/1976
402954446	SEC 18-25S-28E	1,602	PYDH-VED1-VED2	74	29.9	—	—	Core	12/20/1976
402954446	SEC 18-25S-28E	1,610	PYDH-VED1-VED2	240	35.5	—	—	Core	12/20/1976
402954446	SEC 18-25S-28E	1,614	PYDH-VED1-VED2	150	34.9	—	—	Core	12/20/1976
402954446	SEC 18-25S-28E	1,624	PYDH-VED1-VED2	190	35.2	—	—	Core	12/20/1976
402954446	SEC 18-25S-28E	1,634	PYDH-VED1-VED2	310	35.5	—	—	Core	12/20/1976

Best = Best Core Services
Core = Core Laboratories
Good = Good Core Analysis
PTS = Petroleum Testing Services, Inc.

PYDH-VED1-VED2 = Pyramid Hills/Vedder 1/Vedder 2 Sand
VED1 SH = Vedder 1 Shale
VED2 SH = Vedder 2 Shale
VED4 SH = Vedder 4 Shale

VED4 = Vedder 4 Sand
VED3 = Vedder 3 Sand

Table 2-4. Porosity and Permeability from Core Data
Page 3 of 9

API #	Location	Depth (feet)	Formation	MICP Permeability	MICP Porosity	ROUTINE Permeability	ROUTINE Porosity	Source	Date
402954535	Sec 26-25S-27E	2,608	VED4	86	18.4	—	—	Core	1/9/1977
402954535	Sec 26-25S-27E	2,626	VED4	49	20.5	—	—	Core	1/9/1977
402954535	Sec 26-25S-27E	2,632	Walker	75	19.9	—	—	Core	1/9/1977
402954535	Sec 26-25S-27E	2,634	Walker	240	30.6	—	—	Core	1/9/1977
402954535	Sec 26-25S-27E	2,650	Walker	91	21.1	—	—	Core	1/9/1977
402954535	Sec 26-25S-27E	2,652	Walker	75	20.6	—	—	Core	1/9/1977
402954535	Sec 26-25S-27E	2,654	Walker	88	22.5	—	—	Core	1/9/1977
402954535	Sec 26-25S-27E	2,667	Walker	110	18.8	—	—	Core	1/9/1977
402954535	Sec 26-25S-27E	2,670	Walker	74	19.6	—	—	Core	1/9/1977
402954535	Sec 26-25S-27E	2,676	Walker	69	18.3	—	—	Core	1/9/1977
402954535	Sec 26-25S-27E	2,678	Walker	52	17.3	—	—	Core	1/9/1977
402966854	SEC.9- 25S- 27E	3,028–3,030	PYDH-VED1-VED2	8294	34.7	—	—	Good	4/22/1982
402966854	SEC.9- 25S- 27E	3,030–3,033	PYDH-VED1-VED2	7641	32.5	—	—	Good	4/22/1982
402966854	SEC.9- 25S- 27E	3,033–3,036	PYDH-VED1-VED2	5829	38.0	—	—	Good	4/22/1982
402966854	SEC.9- 25S- 27E	3,036–3,040	PYDH-VED1-VED2	581	39.2	—	—	Good	4/22/1982
402966854	SEC.9- 25S- 27E	3,040–3,042	PYDH-VED1-VED2	683	38.1	—	—	Good	4/22/1982
402966854	SEC.9- 25S- 27E	3,042–3,045	PYDH-VED1-VED2	441	37.0	—	—	Good	4/22/1982
402966854	SEC.9- 25S- 27E	3,045–3,049	PYDH-VED1-VED2	1207	36.6	—	—	Good	4/22/1982
402966854	SEC.9- 25S- 27E	3,049–3,052	PYDH-VED1-VED2	5186	34.3	—	—	Good	4/22/1982
402966854	SEC.9- 25S- 27E	3,072	VED3	350	30.9	—	—	Good	4/22/1982

Best = Best Core Services
Core = Core Laboratories
Good = Good Core Analysis
PTS = Petroleum Testing Services, Inc.

PYDH-VED1-VED2 = Pyramid Hills/Vedder 1/Vedder 2 Sand
VED1 SH = Vedder 1 Shale
VED2 SH = Vedder 2 Shale
VED4 SH = Vedder 4 Shale

VED4 = Vedder 4 Sand
VED3 = Vedder 3 Sand

Table 2-4. Porosity and Permeability from Core Data
Page 4 of 9

API #	Location	Depth (feet)	Formation	MICP Permeability	MICP Porosity	ROUTINE Permeability	ROUTINE Porosity	Source	Date
402966854	SEC.9- 25S- 27E	3,086	VED3	520	30.7	—	—	Good	4/22/1982
402966854	SEC.9- 25S- 27E	3,114	VED3	88	33.9	—	—	Good	4/22/1982
402966854	SEC.9- 25S- 27E	3,120	VED3	190	34.6	—	—	Good	4/22/1982
402966854	SEC.9- 25S- 27E	3,146	VED4	510	32.8	—	—	Good	4/22/1982
402966854	SEC.9- 25S- 27E	3,154	VED4	110	26	—	—	Good	4/22/1982
402966854	SEC.9- 25S- 27E	3,160	VED4	72	33.7	—	—	Good	4/22/1982
402966854	SEC.9- 25S- 27E	3,184	Walker	1090	29.6	—	—	Good	4/22/1982
402966854	SEC.9- 25S- 27E	3,190	Walker	810	23.6	—	—	Good	4/22/1982
402966854	SEC.9- 25S- 27E	3,200	Walker	970	32.8	—	—	Good	4/22/1982
402966854	SEC.9- 25S- 27E	3,208	Walker	270	33.8	—	—	Good	4/22/1982
402966854	SEC.9- 25S- 27E	3,214	Walker	95	34.3	—	—	Good	4/22/1982
402966854	SEC.9- 25S- 27E	3,224	Walker	620	25	—	—	Good	4/22/1982
402966854	SEC.9- 25S- 27E	3,236	Walker	210	33.9	—	—	Good	4/22/1982
402966854	SEC.9- 25S- 27E	3,244	Walker	140	32.2	—	—	Good	4/22/1982
402970053	T26S R26E S31	2,129	Etchegoin	0.9	44.2	—	—	Core	12/30/1983
402970053	T26S R26E S31	2,156	Etchegoin	0.2	40.2	—	—	Core	12/30/1983
402970053	T26S R26E S31	2,185	Etchegoin	7	37.2	—	—	Core	12/30/1983
402970053	T26S R26E S31	2,190	Etchegoin	5	37.1	—	—	Core	12/30/1983
402970053	T26S R26E S31	2,263	Etchegoin	620	37.8	—	—	Core	12/30/1983
402970053	T26S R26E S31	2,343	Etchegoin	740	34.6	—	—	Core	12/30/1983

Best = Best Core Services
Core = Core Laboratories
Good = Good Core Analysis
PTS = Petroleum Testing Services, Inc.

PYDH-VED1-VED2 = Pyramid Hills/Vedder 1/Vedder 2 Sand
VED1 SH = Vedder 1 Shale
VED2 SH = Vedder 2 Shale
VED4 SH = Vedder 4 Shale

VED4 = Vedder 4 Sand
VED3 = Vedder 3 Sand

Table 2-4. Porosity and Permeability from Core Data
Page 5 of 9

API #	Location	Depth (feet)	Formation	MICP Permeability	MICP Porosity	ROUTINE Permeability	ROUTINE Porosity	Source	Date
402970053	T26S R26E S31	2,348	Etchegoin	0.4	46.6	—	—	Core	12/30/1983
402970053	T26S R26E S31	2,363	Etchegoin	18	39.5	—	—	Core	12/30/1983
402970053	T26S R26E S31	2,544	Etchegoin	410	35.6	—	—	Core	12/30/1983
402970053	T26S R26E S31	2,556	Etchegoin	4170	28.7	—	—	Core	12/30/1983
402970053	T26S R26E S31	2,562	Etchegoin	1630	27.5	—	—	Core	12/30/1983
402970053	T26S R26E S31	2,574	Etchegoin	10	36.5	—	—	Core	12/30/1983
402970053	T26S R26E S31	2,588	Etchegoin	2.8	36.6	—	—	Core	12/30/1983
402970053	T26S R26E S31	5,239	Round Mountain	2.1	43.9	—	—	Core	12/30/1983
402970053	T26S R26E S31	5,253	Round Mountain	1.1	37.5	—	—	Core	12/30/1983
402970053	T26S R26E S31	5,255	Round Mountain	1	35.8	—	—	Core	12/30/1983
402970053	T26S R26E S31	5,261	Round Mountain	2	37.6	—	—	Core	12/30/1983
402970053	T26S R26E S31	5,265	Round Mountain	1.5	43.9	—	—	Core	12/30/1983
402970053	T26S R26E S31	5,994	Olcese (sand)	85	29.1	—	—	Core	12/30/1983
402970053	T26S R26E S31	6,013	Olcese (sand)	530	31.7	—	—	Core	12/30/1983
402970053	T26S R26E S31	6,115	Olcese (sand)	500	27.7	—	—	Core	12/30/1983
402970053	T26S R26E S31	6,193	Olcese (sand)	42	21.5	—	—	Core	12/30/1983
402970053	T26S R26E S31	6,288	Olcese (sand)	20	24.2	—	—	Core	12/30/1983
402970053	T26S R26E S31	7,170	PYDH-VED1-VED2	39	28.7	—	—	Core	12/30/1983
402970053	T26S R26E S31	7,187	PYDH-VED1-VED2	18	26	—	—	Core	12/30/1983
402970053	T26S R26E S31	7,220	PYDH-VED1-VED2	21	24.7	—	—	Core	12/30/1983

Best = Best Core Services
Core = Core Laboratories
Good = Good Core Analysis
PTS = Petroleum Testing Services, Inc.

PYDH-VED1-VED2 = Pyramid Hills/Vedder 1/Vedder 2 Sand
VED1 SH = Vedder 1 Shale
VED2 SH = Vedder 2 Shale
VED4 SH = Vedder 4 Shale

VED4 = Vedder 4 Sand
VED3 = Vedder 3 Sand

Table 2-4. Porosity and Permeability from Core Data
Page 6 of 9

API #	Location	Depth (feet)	Formation	MICP Permeability	MICP Porosity	ROUTINE Permeability	ROUTINE Porosity	Source	Date
402970053	T26S R26E S31	7,414	VED1 SH	9	26.4	—	—	Core	12/30/1983
402970053	T26S R26E S31	7,680	VED4 SH	3	26.8	—	—	Core	12/30/1983
402970053	T26S R26E S31	7,716	VED4 SH	8	29.8	—	—	Core	12/30/1983
402970053	T26S R26E S31	8,063	VED4 SH	5	29.1	—	—	Core	12/30/1983
402970053	T26S R26E S31	8,445	VED4 SH	0.9	27	—	—	Core	12/30/1983
402970053	T26S R26E S31	8,456	VED4 SH	1.8	24.9	—	—	Core	12/30/1983
402970053	T26S R26E S31	8,464	VED4 SH	7	27.2	—	—	Core	12/30/1983
402970053	T26S R26E S31	8,470	Walker	25	27.9	—	—	Core	12/30/1983
402970053	T26S R26E S31	8,482	Walker	52	26.4	—	—	Core	12/30/1983
402970053	T26S R26E S31	8,498	Walker	31	29.4	—	—	Core	12/30/1983
402970053	T26S R26E S31	8,502	Walker	50	27.7	—	—	Core	12/30/1983
402970053	T26S R26E S31	8,657	Walker	120	26.5	—	—	Core	12/30/1983
402970053	T26S R26E S31	8,750	Walker	43	23.5	—	—	Core	12/30/1983
402970053	T26S R26E S31	8,830	Walker	7	26.4	—	—	Core	12/30/1983
402970053	T26S R26E S31	8,840	Walker	2	25.7	—	—	Core	12/30/1983
402970053	T26S R26E S31	8,843	Walker	0.6	30.9	—	—	Core	12/30/1983
402970053	T26S R26E S31	8,858	Walker	0.2	32	—	—	Core	12/30/1983
402970053	T26S R26E S31	8,920	Walker	0.1	20.5	—	—	Core	12/30/1983
402970053	T26S R26E S31	8,962	Walker	0.6	21.3	—	—	Core	12/30/1983
402970053	T26S R26E S31	9,000	Walker	0.5	26.2	—	—	Core	12/30/1983

Best = Best Core Services
Core = Core Laboratories
Good = Good Core Analysis
PTS = Petroleum Testing Services, Inc.

PYDH-VED1-VED2 = Pyramid Hills/Vedder 1/Vedder 2 Sand
VED1 SH = Vedder 1 Shale
VED2 SH = Vedder 2 Shale
VED4 SH = Vedder 4 Shale

VED4 = Vedder 4 Sand
VED3 = Vedder 3 Sand

Table 2-4. Porosity and Permeability from Core Data
Page 7 of 9

API #	Location	Depth (feet)	Formation	MICP Permeability	MICP Porosity	ROUTINE Permeability	ROUTINE Porosity	Source	Date
410720225	22-24S-23E	10,398.7	VED2 SH	4.3	19.2	—	—	PTS	1/19/1988
410720225	22-24S-23E	10,399.5	VED3	78	20.1	—	—	PTS	1/19/1988
410720225	22-24S-23E	10,400.5	VED3	213	22.1	—	—	PTS	1/19/1988
410720225	22-24S-23E	10,657.5	VED4	1610	24.6	—	—	PTS	1/19/1988
410720225	22-24S-23E	10,658.5	VED4	1550	25.6	—	—	PTS	1/19/1988
410720225	22-24S-23E	10,659.5	VED4	1250	27.8	—	—	PTS	1/19/1988
410720225	22-24S-23E	10,660.5	VED4	1720	26.8	—	—	PTS	1/19/1988
410720225	22-24S-23E	10,661.3	VED4	1530	23.6	—	—	PTS	1/19/1988
410720225	22-24S-23E	10,662.5	VED4	1280	21.8	—	—	PTS	1/19/1988
410720225	22-24S-23E	10,663.4	VED4	994	23.8	—	—	PTS	1/19/1988
410720225	22-24S-23E	10,664.5	VED4	2860	26.2	—	—	PTS	1/19/1988
410720225	22-24S-23E	10,665.7	VED4	1850	22	—	—	PTS	1/19/1988
410720225	22-24S-23E	10,666.5	VED4	1540	27.3	—	—	PTS	1/19/1988
410720225	22-24S-23E	10,667.5	VED4	1440	19.2	—	—	PTS	1/19/1988
410720225	22-24S-23E	10,668.5	VED4	1140	25.2	—	—	PTS	1/19/1988
410720225	22-24S-23E	10,669.3	VED4	1350	25.3	—	—	PTS	1/19/1988
410720225	22-24S-23E	10,670.5	VED4	1850	23.8	—	—	PTS	1/19/1988
410720225	22-24S-23E	10,671.5	VED4	1220	25.2	—	—	PTS	1/19/1988
410720225	22-24S-23E	10,672.5	VED4	555	26.3	—	—	PTS	1/19/1988
410720225	22-24S-23E	10,673.5	VED4	951	24.6	—	—	PTS	1/19/1988

Best = Best Core Services
Core = Core Laboratories
Good = Good Core Analysis
PTS = Petroleum Testing Services, Inc.

PYDH-VED1-VED2 = Pyramid Hills/Vedder 1/Vedder 2 Sand
VED1 SH = Vedder 1 Shale
VED2 SH = Vedder 2 Shale
VED4 SH = Vedder 4 Shale

VED4 = Vedder 4 Sand
VED3 = Vedder 3 Sand

Table 2-4. Porosity and Permeability from Core Data
Page 8 of 9

API #	Location	Depth (feet)	Formation	MICP Permeability	MICP Porosity	ROUTINE Permeability	ROUTINE Porosity	Source	Date
410720225	22-24S-23E	10,674.5	VED4	630	25.7	—	—	PTS	1/19/1988
410720225	22-24S-23E	10,675.5	VED4	813	25.7	—	—	PTS	1/19/1988
410720225	22-24S-23E	10,676.6	VED4	577	26.2	—	—	PTS	1/19/1988
410720225	22-24S-23E	10,677.5	VED4	600	20.4	—	—	PTS	1/19/1988
410720225	22-24S-23E	10,678.5	VED4	834	26.3	—	—	PTS	1/19/1988
410720225	22-24S-23E	10,679.5	VED4	584	25.8	—	—	PTS	1/19/1988
410720225	22-24S-23E	10,680.5	VED4	1370	25.1	—	—	PTS	1/19/1988
410720225	22-24S-23E	10,681.4	VED4	858	23.5	—	—	PTS	1/19/1988
410720225	22-24S-23E	10,682.55	VED4	642	24.1	—	—	PTS	1/19/1988
410720225	22-24S-23E	10,683.5	VED4	313	15.3	—	—	PTS	1/19/1988
410720225	22-24S-23E	10,684.4	VED4	6570	25.4	—	—	PTS	1/19/1988
410720225	22-24S-23E	10,698.5	VED4	3.4	18.1	—	—	PTS	1/19/1988
410720225	22-24S-23E	10,699.5	VED4	181	27.5	—	—	PTS	1/19/1988
410720225	22-24S-23E	10,700.5	VED4	284	22.9	—	—	PTS	1/19/1988
410720225	22-24S-23E	10,701.5	VED4	451	28.6	—	—	PTS	1/19/1988
410720225	22-24S-23E	10,702.5	VED4	532	29	—	—	PTS	1/19/1988
410720225	22-24S-23E	10,703.5	VED4	365	31.7	—	—	PTS	1/19/1988
410720225	22-24S-23E	10,704.5	VED4	386	26.7	—	—	PTS	1/19/1988
410720225	22-24S-23E	10,705.6	VED4	801	29.4	—	—	PTS	1/19/1988
410720225	22-24S-23E	10,706.5	VED4	1370	28	—	—	PTS	1/19/1988

Best = Best Core Services
Core = Core Laboratories
Good = Good Core Analysis
PTS = Petroleum Testing Services, Inc.
PYDH-VED1-VED2 = Pyramid Hills/Vedder 1/Vedder 2 Sand
VED1 SH = Vedder 1 Shale
VED2 SH = Vedder 2 Shale
VED4 SH = Vedder 4 Shale
VED4 = Vedder 4 Sand
VED3 = Vedder 3 Sand

Table 2-4. Porosity and Permeability from Core Data
Page 9 of 9

API #	Location	Depth (feet)	Formation	MICP Permeability	MICP Porosity	ROUTINE Permeability	ROUTINE Porosity	Source	Date
410720225	22-24S-23E	10,707.5	VED4	316	19.5	—	—	PTS	1/19/1988
410720225	22-24S-23E	10,708.55	VED4	1050	27.2	—	—	PTS	1/19/1988
410720225	22-24S-23E	10,709.85	VED4	713	28.6	—	—	PTS	1/19/1988
410720225	22-24S-23E	10,710.7	VED4	757	26.9	—	—	PTS	1/19/1988
410720225	22-24S-23E	10,711.6	VED4	322	28.4	—	—	PTS	1/19/1988
410720225	22-24S-23E	10,712.3	VED4	316	27.2	—	—	PTS	1/19/1988

Best = Best Core Services
Core = Core Laboratories
Good = Good Core Analysis
PTS = Petroleum Testing Services, Inc.

PYDH-VED1-VED2 = Pyramid Hills/Vedder 1/Vedder 2 Sand
VED1 SH = Vedder 1 Shale
VED2 SH = Vedder 2 Shale
VED4 SH = Vedder 4 Shale

VED4 = Vedder 4 Sand
VED3 = Vedder 3 Sand

Table 2-5. Summary of Porosity and Permeability from Core Data

Formation	Permeability					Porosity	
	Horizontal mD	Horizontal Basis	Vertical mD	Basis	Anisotropy Ratio	Value (%)	Basis
Round-Mountain	0.037	GM of all values	0.00073	HM of all values	50.0	20	Assumed same as Freeman-Jewett
Olcese [a]	76.6	Weighted GM assuming 90% sands, 10% shales	4.3	Weighted HM assuming 90% sands, 10% shales	17.9	28	Median all values
Freeman-Jewett	0.26	GM of all values	0.0036	HM of all values	71.3	20	Median all values
PYDH-VED1-VED2	254.31	GM of all values	62.0	HM of all values	4.1	34	Median all values
VED2 SH	0.11	GM of all values	0.0052	HM of all values	20.3	15	Median all values
VED3	192.29	GM of all values	154.15	HM of all values	1.2	31	Median all values
VED3 SH	0.11	No samples, assumed same as VED 2 SH	0.0052	No samples, assumed same as VED 2 SH	20.3	15	No values, assumed same as VED 2 SH
VED4	613	GM of all values	116	HM of all values	5.3	26	Median all values
VED4 SH	0.91	GM of all values	0.025	HM of all values	35.8	27	Median all values
Walker	36.37	GM of all values	1.41	HM of all values	25.8	26	Median all values

[a] Excludes KCL-25-1 sample at 6,131 feet bgs (very low-k shale) for permeability values.

GM = Geometric mean
HM = Harmonic mean
PYDH-VED1-VED2 = Pyramid Hills/Vedder 1/Vedder 2 Sand
VED2 SH = Vedder 2 Shale
VED3 = Vedder 3 Sand
VED3 SH = Vedder 3 Shale
VED4 = Vedder 4 Sand
VED4 SH = Vedder 4 Shale

Table 2-6. Earthquakes from USGS Catalog
Page 1 of 7

Time	Latitude	Longitude	Depth	Magnitude	Magnitude Type	Place
2020-06-24T20:49:41.770Z	35.27033	–119.179	19.67	2.97	ml	13 km SSW of Rosedale, CA
2020-05-27T04:52:31.080Z	35.385	–118.965	15.96	3.66	mw	6 km SE of Oildale, CA
2020-01-29T12:56:21.840Z	35.43583	–119.008	17.99	3.19	ml	2 km NNE of Oildale, CA
2020-01-13T01:01:01.180Z	35.46967	–119.333	25.76	2.66	ml	6 km WSW of Shafter, CA
2020-01-06T22:17:40.850Z	35.471	–119.331	26.74	2.54	ml	6 km WSW of Shafter, CA
2019-12-07T17:17:41.410Z	35.46867	–119.328	25.85	2.63	ml	6 km SW of Shafter, CA
2019-08-15T18:26:11.620Z	35.1995	–118.934	13.33	2.62	ml	7 km SSW of Lamont, CA
2018-11-09T04:12:24.100Z	35.22667	–118.876	14.06	2.98	ml	5 km WNW of Arvin, CA
2018-07-21T03:25:34.330Z	35.19967	–118.917	17.16	2.84	ml	7 km S of Lamont, CA
2018-02-06T03:22:15.050Z	35.71	–119.294	17.82	2.76	ml	7 km WNW of McFarland, CA
2016-07-12T22:32:07.560Z	35.16633	–119.337	22.09	3.02	ml	11 km ENE of Taft, CA
2016-04-01T00:47:29.350Z	35.54283	–119.371	22.59	2.98	ml	6 km SSW of Wasco, CA
2016-03-26T01:48:31.460Z	35.27983	–119.217	19.92	2.55	ml	13 km SSW of Rosedale, CA
2016-02-24T00:34:48.860Z	35.5365	–119.365	22.04	2.5	ml	7 km SSW of Wasco, CA
2016-02-24T00:11:53.980Z	35.53567	–119.364	23	2.62	ml	7 km SSW of Wasco, CA
2016-02-24T00:02:23.630Z	35.54233	–119.373	22.14	4.87	mw	6 km SSW of Wasco, CA
2015-11-17T19:00:26.680Z	35.82483	–119.519	25.82	2.55	ml	8 km SSW of Alpaugh, CA
2015-09-07T03:29:34.840Z	35.17433	–119.048	13.65	2.62	ml	15 km SW of Lamont, CA
2015-08-28T22:29:17.370Z	35.44817	–119.07	18.92	2.53	ml	6 km NW of Oildale, CA
2015-04-20T00:51:59.280Z	35.25783	–119.48	13.75	2.55	ml	13 km N of Taft, CA
2013-11-21T08:23:23.220Z	35.46867	–119.31	20.059	2.71	ml	5 km SW of Shafter, CA
2012-12-05T12:52:25.510Z	35.19417	–119.259	23.138	2.79	ml	19 km ENE of Taft, CA

Table 2-6. Earthquakes from USGS Catalog
Page 2 of 7

Time	Latitude	Longitude	Depth	Magnitude	Magnitude Type	Place
2012-10-11T04:03:26.650Z	35.21383	–119.53	13.16	2.86	ml	10 km NW of Taft, CA
2012-10-11T00:00:40.950Z	35.2065	–119.521	14.455	2.51	ml	9 km NW of Taft, CA
2012-09-05T12:31:06.740Z	35.3225	–119.487	-0.835	2.77	ml	9 km S of Buttonwillow, CA
2012-04-27T14:47:12.350Z	35.25883	–119.306	19.541	2.56	ml	19 km NE of Taft, CA
2012-04-17T00:12:03.710Z	35.46633	–119.348	24.389	3.43	ml	8 km WSW of Shafter, CA
2012-02-04T00:39:39.400Z	35.77817	–119.097	18.5	2.53	ml	14 km E of Delano, CA
2011-11-18T04:33:20.750Z	35.17467	–119.391	-0.914	2.98	ml	7 km ENE of Taft, CA
2010-03-11T21:15:25.340Z	35.3255	–119.363	26.872	2.52	ml	13 km SE of Buttonwillow, CA
2010-02-22T21:55:30.570Z	35.75283	–119	20.803	2.5	ml	22 km ENE of McFarland, CA
2009-12-13T10:26:09.280Z	35.75533	–119.007	18.282	2.97	ml	22 km E of Delano, CA
2009-05-01T23:31:25.620Z	35.31867	–119.605	2.921	2.58	ml	15 km SW of Buttonwillow, CA
2009-02-16T01:03:38.980Z	35.30417	–119.432	14.045	3.89	ml	11 km SSE of Buttonwillow, CA
2008-09-23T15:57:09.910Z	35.41533	–118.921	17.517	2.72	ml	9 km E of Oildale, CA
2008-09-18T17:32:09.200Z	35.18833	–119.43	18.712	3.33	ml	6 km NNE of Taft, CA
2008-07-15T10:35:44.020Z	35.488	–119.105	23.776	3.15	ml	11 km NW of Oildale, CA
2008-04-04T16:16:58.460Z	35.3385	–119.14	16.748	2.57	ml	5 km S of Rosedale, CA
2008-04-01T21:27:56.770Z	35.47267	–119.346	23.051	2.95	ml	7 km WSW of Shafter, CA
2006-01-22T10:28:07.150Z	35.65767	–119.194	24.17	3.02	ml	4 km SE of McFarland, CA
2005-07-15T15:35:31.250Z	35.5345	–119.443	27.778	2.84	ml	11 km SW of Wasco, CA
2004-12-22T06:12:24.530Z	35.40283	–119.302	25.206	2.72	ml	11 km SSW of Shafter, CA
2004-07-15T01:43:22.650Z	35.31483	–119.433	0.608	3.5	ml	10 km SSE of Buttonwillow, CA
2003-11-01T14:52:35.880Z	35.13317	–118.939	14.213	3.28	ml	13 km SW of Arvin, CA

Table 2-6. Earthquakes from USGS Catalog
Page 3 of 7

Time	Latitude	Longitude	Depth	Magnitude	Magnitude Type	Place
2003-07-22T18:20:18.310Z	35.171	–119.012	20.882	2.66	ml	13 km SW of Lamont, CA
2003-05-25T21:01:12.410Z	35.335	–119.221	24.019	2.56	ml	9 km SW of Rosedale, CA
2003-04-08T05:28:20.470Z	35.1975	–119.384	7.455	2.57	ml	9 km NE of Taft, CA
2002-08-13T18:03:25.610Z	35.31183	–119.447	13.567	3.15	ml	10 km SSE of Buttonwillow, CA
2002-02-16T20:10:34.430Z	35.16983	–119.398	20.177	2.87	ml	6 km ENE of Taft, CA
2001-05-02T14:26:01.870Z	35.383	–119.41	6.319	2.8	mc	6 km ESE of Buttonwillow, California
2001-02-27T23:04:13.340Z	35.2465	–119.325	16.471	2.55	ml	17 km NE of Taft, CA
2001-01-02T05:22:44.990Z	35.3	–119.443	5.252	2.69	ml	11 km SSE of Buttonwillow, California
2000-12-18T18:43:45.520Z	35.327	–119.433	5.189	2.61	ml	9 km SSE of Buttonwillow, CA
2000-12-18T18:42:17.380Z	35.312	–119.44	5.282	2.78	ml	10 km SSE of Buttonwillow, CA
2000-10-11T19:30:48.410Z	35.6135	–119.5	5.415	2.93	ml	15 km W of Wasco, CA
2000-10-08T00:17:50.880Z	35.275	–119.033	20.157	3.11	ml	9 km S of Bakersfield, CA
1999-08-07T12:57:54.550Z	35.68333	–119.299	28.575	2.78	mc	6 km W of McFarland, California
1999-05-31T01:52:20.870Z	35.248	–119.259	5.225	2.72	ml	18 km SW of Rosedale, California
1999-05-19T07:13:55.700Z	35.311	–118.949	14.078	2.98	ml	6 km NNW of Lamont, California
1999-04-16T08:40:01.800Z	35.501	–119.524	5.165	2.83	mc	12 km NNW of Buttonwillow, California
1999-03-29T01:50:56.250Z	35.28	–118.894	12.388	2.56	ml	3 km NE of Lamont, California
1998-10-30T09:54:29.260Z	35.559	–119.124	4.831	3.31	ml	15 km ENE of Shafter, California
1998-04-22T17:40:18.740Z	35.295	–119.301	5.225	2.6	mc	17 km SW of Rosedale, California
1996-11-01T22:20:41.430Z	35.622	–119.303	0	2.62	md	5 km NE of Wasco, California
1996-07-27T13:35:35.400Z	35.6935	–119.433	5.01	3.19	ml	14 km NW of Wasco, CA
1995-07-08T00:26:29.530Z	35.404	–119.533	20.459	3.13	ml	6 km W of Buttonwillow, California

Table 2-6. Earthquakes from USGS Catalog
Page 4 of 7

Time	Latitude	Longitude	Depth	Magnitude	Magnitude Type	Place
1995-03-28T05:36:41.850Z	35.331	–119.4	5.095	2.92	ml	10 km SE of Buttonwillow, California
1994-11-24T06:43:32.130Z	35.381	–119.387	19.095	3.62	ml	8 km ESE of Buttonwillow, California
1994-07-11T00:40:28.130Z	35.454	–118.912	13.085	2.65	ml	10 km ENE of Oildale, California
1994-05-09T17:15:28.860Z	35.201	–119.314	20.681	2.58	ml	14 km ENE of Taft, California
1993-10-20T13:48:40.080Z	35.656	–119.318	4.76	2.77	ml	7 km NNE of Wasco, California
1993-06-01T09:52:31.550Z	35.143	–119.096	22.052	2.74	mc	21 km SW of Lamont, California
1993-05-28T23:18:40.060Z	35.145	–119.1	21.922	2.86	ml	21 km SW of Lamont, California
1993-05-28T04:47:40.600Z	35.149	–119.104	20.612	5.19	ml	21 km SW of Lamont, California
1992-07-17T23:37:57.110Z	35.72	–119.585	4.986	2.63	mc	21 km SSW of Alpaugh, California
1992-03-05T18:24:22.840Z	35.215	–119.374	22.683	3.84	ml	11 km NE of Taft, California
1991-12-17T02:18:50.750Z	35.625	–119.288	4.762	2.5	mc	6 km NE of Wasco, CA
1991-06-21T17:41:43.080Z	35.258	–119.006	27.899	3.28	ml	8 km W of Lamont, CA
1991-05-03T12:32:47.640Z	35.367	–119.089	19.265	2.56	ml	5 km WNW of Bakersfield, CA
1991-04-15T17:10:29.390Z	35.263	–119.396	5.027	2.61	mc	14 km NNE of Taft, CA
1991-03-22T00:22:56.340Z	35.488	–119.165	5.279	3.09	mc	10 km E of Shafter, CA
1990-12-22T16:26:44.370Z	35.727	–119.107	4.963	2.61	mc	12 km ENE of McFarland, CA
1990-11-01T00:06:35.070Z	35.214	–119.271	23.523	2.78	mc	19 km ENE of Taft, CA
1989-12-26T19:58:35.870Z	35.346	–119.456	28.911	3.2	ml	6 km SSE of Buttonwillow, CA
1989-06-28T06:04:58.850Z	35.149	–118.984	28.573	2.73	mc	14 km SSW of Lamont, CA
1989-06-27T20:27:46.450Z	35.147	–118.982	26.123	3.23	ml	14 km SSW of Lamont, CA
1989-03-10T16:14:54.160Z	35.469	–118.906	14.095	2.76	ml	12 km ENE of Oildale, CA
1988-09-17T15:50:20.680Z	35.625	–119.535	5.155	3.18	ml	18 km W of Wasco, CA

Table 2-6. Earthquakes from USGS Catalog
Page 5 of 7

Time	Latitude	Longitude	Depth	Magnitude	Magnitude Type	Place
1988-04-13T14:28:13.730Z	35.178	–119.385	21.327	3.45	ml	8 km ENE of Taft, CA
1987-09-25T15:01:26.470Z	35.496	–118.969	14.065	3.02	ml	10 km NNE of Oildale, CA
1986-12-01T19:32:07.030Z	35.19	–119.016	13.592	2.7	ml	12 km SW of Lamont, CA
1986-06-17T05:04:41.140Z	35.438	–119.289	5.307	2.5	mc	7 km SSW of Shafter, CA
1985-10-19T13:17:52.960Z	35.299	–119.312	4.784	2.63	ml	18 km WSW of Rosedale, CA
1985-06-18T03:15:23.530Z	35.316	–119.496	5.097	2.57	mc	10 km SSW of Buttonwillow, CA
1985-05-06T23:14:33.020Z	35.297	–119.346	23.617	4.41	ml	16 km SE of Buttonwillow, CA
1985-02-16T20:28:32.920Z	35.718	–119.374	4.762	2.95	ml	13 km WSW of Delano, CA
1985-02-08T06:58:16.860Z	35.457	–118.906	5.041	4.61	ml	11 km ENE of Oildale, CA
1983-11-24T09:20:05.020Z	35.485	–119.348	5.228	2.5	mc	7 km WSW of Shafter, CA
1983-11-11T10:28:46.260Z	35.16217	–119.086	17.449	2.53	mc	19 km SW of Lamont, CA
1983-10-27T16:26:39.630Z	35.561	–119.01	13.241	2.72	mc	16 km N of Oildale, CA
1983-07-22T00:07:03.110Z	35.212	–119.31	13.515	2.65	mh	15 km ENE of Taft, CA
1983-02-19T17:54:42.030Z	35.32783	–119.224	4.848	2.9	mc	9 km SW of Rosedale, CA
1983-01-28T09:11:07.230Z	35.69567	–119.582	5.054	2.54	mc	23 km SSW of Alpaugh, CA
1982-12-06T17:54:19.270Z	35.288	–119.269	4.738	2.59	mc	16 km SW of Rosedale, CA
1982-11-11T23:19:09.690Z	35.713	–119.601	4.833	3.09	ml	22 km SSW of Alpaugh, CA
1982-10-19T00:49:42.280Z	35.523	–119.106	4.738	3.54	ml	14 km NW of Oildale, CA
1982-09-20T17:33:35.280Z	35.827	–119.56	4.993	3.11	mc	9 km SW of Alpaugh, CA
1982-08-17T17:16:01.190Z	35.805	–119.491	4.993	2.9	mc	9 km S of Alpaugh, CA
1982-07-21T09:28:18.610Z	35.383	–119.404	4.772	3.18	ml	6 km ESE of Buttonwillow, CA
1982-07-15T06:30:03.250Z	35.714	–119.615	4.954	2.7	mc	22 km SSW of Alpaugh, CA

Table 2-6. Earthquakes from USGS Catalog
Page 6 of 7

Time	Latitude	Longitude	Depth	Magnitude	Magnitude Type	Place
1982-05-16T02:18:12.860Z	35.326	–118.957	4.759	2.5	mc	8 km ESE of Bakersfield, CA
1982-05-07T17:04:19.150Z	35.13	–118.859	-0.901	2.66	mc	9 km SSW of Arvin, CA
1982-04-01T13:14:16.710Z	35.137	–118.991	4.57	2.67	mc	15 km SSW of Lamont, CA
1980-12-12T21:02:05.360Z	35.2475	–119.391	6	2.63	ml	13 km NNE of Taft, CA
1980-11-21T11:11:35.380Z	35.273	–119.415	6	2.96	ml	15 km NNE of Taft, CA
1980-11-21T11:11:12.290Z	35.243	–119.378	2.96	3.03	ml	13 km NNE of Taft, CA
1980-09-30T21:12:15.380Z	35.26767	–119.375	2.03	2.52	mh	16 km NNE of Taft, CA
1980-09-26T13:18:41.460Z	35.2545	–119.377	9.9	4.29	ml	14 km NNE of Taft, CA
1980-09-17T04:35:43.820Z	35.67233	–119.382	6	3.09	ml	9 km NNW of Wasco, CA
1980-08-17T06:32:41.430Z	35.43467	–118.898	6	2.81	ml	11 km E of Oildale, CA
1979-11-23T06:38:28.060Z	35.30933	–118.924	6	2.99	ml	6 km N of Lamont, CA
1979-09-23T05:13:24.560Z	35.29383	–119.27	2.79	2.52	mh	15 km SW of Rosedale, CA
1979-06-15T11:11:59.480Z	35.26	–119.236	2.26	2.98	ml	16 km SSW of Rosedale, CA
1979-01-21T01:16:22.880Z	35.78267	–119.339	6	2.54	mh	8 km W of Delano, CA
1978-12-31T21:04:03.410Z	35.33483	–118.953	6	2.9	ml	8 km ESE of Bakersfield, CA
1978-07-10T09:05:30.920Z	35.32783	–118.95	0.36	2.85	ml	8 km ESE of Bakersfield, CA
1978-06-02T14:39:18.000Z	35.22817	–119.297	7.5	2.85	ml	17 km ENE of Taft, CA
1978-05-01T11:53:56.270Z	35.77183	–119.366	6	2.74	ml	11 km W of Delano, CA
1978-03-23T06:29:19.440Z	35.24133	–118.941	6.56	2.72	ml	3 km SW of Lamont, CA
1978-03-10T19:47:21.980Z	35.51367	–119.209	6	2.52	mh	6 km ENE of Shafter, CA
1977-10-01T10:07:40.600Z	35.25933	–119.354	10.64	3.36	ml	16 km NE of Taft, CA
1977-09-03T21:46:56.110Z	35.4255	–119.373	2.84	2.92	ml	9 km ENE of Buttonwillow, CA

Table 2-6. Earthquakes from USGS Catalog
Page 7 of 7

Time	Latitude	Longitude	Depth	Magnitude	Magnitude Type	Place
1977-08-17T03:21:41.880Z	35.12483	–118.948	9.16	3.53	ml	14 km SW of Arvin, CA
1977-08-15T16:41:03.940Z	35.28117	–119.45	23.5	2.5	mh	13 km S of Buttonwillow, CA
1977-02-18T20:19:25.260Z	35.42233	–118.928	5.25	2.53	ml	8 km E of Oildale, CA
1977-02-15T23:44:48.920Z	35.33833	–118.901	5.67	2.91	ml	9 km N of Lamont, CA
1977-01-13T14:53:47.710Z	35.3285	–119.44	6	3.03	ml	8 km SSE of Buttonwillow, CA
1976-11-27T06:56:32.330Z	35.307	–118.941	5.5	2.84	mh	6 km NNW of Lamont, CA
1976-07-22T06:45:44.070Z	35.207	–118.892	6	2.66	ml	6 km W of Arvin, CA
1976-07-19T05:47:29.890Z	35.51	–119.209	6	3.29	ml	6 km E of Shafter, CA
1976-06-19T11:42:04.370Z	35.147	–118.899	6	2.94	ml	9 km SW of Arvin, CA
1976-03-04T17:42:54.400Z	35.189	–118.916	6	3.44	ml	8 km S of Lamont, CA
1975-08-14T04:29:58.210Z	35.125	–119.177	6	3.78	ml	22 km ENE of Maricopa, CA
1975-04-26T17:16:21.700Z	35.593	–118.959	6	3.43	ml	20 km NNE of Oildale, CA
1974-05-27T09:21:25.400Z	35.80333	–119.317	8	2.8	mh	7 km WNW of Delano, CA
1973-07-30T04:13:03.710Z	35.28567	–119.166	6	2.97	ml	11 km S of Rosedale, CA
1972-11-15T16:44:10.340Z	35.25967	–118.863	6	3.05	ml	5 km E of Lamont, CA
1972-05-27T00:07:23.910Z	35.5585	–119.427	6	3.05	ml	9 km WSW of Wasco, CA
1971-11-07T14:03:29.180Z	35.539	–119.568	6	3.31	ml	18 km NNW of Buttonwillow, CA
1971-08-17T06:26:47.760Z	35.71917	–119.467	6	3.32	ml	18 km NW of Wasco, CA
1970-09-10T11:14:29.490Z	35.217	–119.285	6	2.53	mh	18 km ENE of Taft, CA
1970-05-13T06:20:16.110Z	35.34383	–118.922	6	2.78	ml	9 km N of Lamont, CA

Note: For definition of Magnitude Type see https://www.usgs.gov/natural-hazards/earthquake-hazards/science/magnitude-types?qt-science_center_objects=0#qt-science_center_objects

Table 2-7. Water Supply Wells within the Area of Review/Storage Complex
Page 1 of 1

WCR Number	Location Accuracy	Permit Number	Planned Use	Decimal Latitude	Decimal Longitude	Total Completion Depth (feet)	Perforated Interval (feet)		Static Water Depth (feet)	Source
							Top	Bottom		
WCR0058089	Estimated	WP1894	Water Supply Domestic	35.689510	-119.263130	585			222	DWR
WCR0256385	Estimated	NA	Cathodic Protection	35.688294	-119.267670	325				DWR
WCR0171081	Estimated	WP13711	Water Supply Domestic	35.689100	-119.281260	589			290	DWR
WCR0063166	Estimated	NA	Water Supply Irrigation - Agricultural	35.692390	-119.276690	1004	288	1004		DWR
WCR0179991	Estimated	NA	Water Supply Irrigation - Agricultural	35.696161	-119.276730	1005	362	1005		DWR
WCR0187272	Estimated	NA	Other Unknown	35.688953	-119.273740					DWR
WCR0255251	Estimated	NA	Water Supply Domestic	35.688972	-119.271940	602	401	602		DWR
WCR0180661	Estimated	NA	Other Unknown	35.693992	-119.265240					DWR
WCR0017619	Centroid	NA	Other Unknown	35.68138	-119.28534					DWR
WCR0217004	Centroid	NA	Water Supply Irrigation	35.69596	-119.26746	810	480	810		DWR
WCR0093095	Centroid	NA	Water Supply Domestic	35.69589	-119.28528	525	360	525		DWR
WCR0145638	Centroid	NA	Other Unknown	35.68145	-119.26756					DWR
26S25E03R001M	Provided	NA	Unknown	35.6919	-119.2682					SGMA
26S25E04R001M	Provided	NA	Unknown	35.6889	-119.2806					SMGA

Source:
DWR: https://data.ca.gov/dataset/well-completion-reports/resource/da700efb-beca-45b0-bb85-8b096cb792c7
SGMA: https://sgma.water.ca.gov/webgis/?appid=SGMADataViewer#gwlevels

Table 2-8. Baseline Geochemistry, Vedder Formation

Analyte	Concentration (ppm [a]) at Rio Bravo Field	
	4/6/1960	4/2/1968
Bicarbonate	961	671
Calcium	433	283
Chloride	13,788	12,340
Magnesium	68	42
pH (s.u.)	7.25	7.6
Potassium	187	—
Sodium	8,799	8,211
Sulfate	354	—
Total dissolved solids	24,757	21,982
Data Source	USGS 4001271	USGS 4000447

[a] Unless otherwise noted
ppm = Parts per million
— = Not reported
s.u. = Standard units

Table 2-9. Aquifer Exemptions

Injection Field	Well Class	Injection Type	Aquifer Exemption Area (acres)	Depth (feet)	Injection Formation
Jasmin Oil Field	II	Oil and gas extraction	909	2,650	Cantleberry Sand (Vedder)
Jasmin Oil Field	II	Oil and gas extraction	454	2,650	Cantleberry Sand (Vedder)
Mount Poso Oil Field	II	Oil and gas extraction	6,434	160	Pyramid Hill Sand
Mount Poso Oil Field	II	Oil and gas extraction	4,965	160	Pyramid Hill Sand
Mount Poso Oil Field	II	Water disposal and EOR	6,434	810	Remaining Vedder
Mount Poso Oil Field	II	Water disposal and EOR	3,998	810	Remaining Vedder
Mount Poso Oil Field	II	Oil and gas extraction	6,104	590	Upper Vedder Formation
Mount Poso Oil Field	II	Oil and gas extraction	4,965	590	Upper Vedder Formation
Poso Creek Oil Field - McVan Area	II	EOR	1,243	830	Basal Etchegoin Member
Poso Creek Oil Field - McVan Area	II	EOR	288	830	Basal Etchegoin Member
Poso Creek Oil Field - McVan Area	II	EOR	1,532	915	Chanac Formation
Poso Creek Oil Field - Premier & Enas Area	II	EOR	3,576	1,800	Basal Etchegoin Member
Poso Creek Oil Field - Premier & Enas Area	II	EOR	4,293	1,800	Basal Etchegoin Member

Table 2-10. Mineralogy of the Vedder and Freeman-Jewett Formations

Mineral Constituent	Chemical Formula	Relative Abundance (%)			
	Well	*Rocket Abrams 1*	*KCA A 83-35*	*Wright Bloemer 74-11*	*Shell Bell 52-21*
	Depth (feet)	*4308-4333*	*8350-8360*	*4369-4379*	*4801-4805*
	Formation	*Vedder*		*Freeman-Jewett*	
Bulk Minerals					
Quartz	SiO_2	29	41	14	14
Opal A	$SiO_2 \cdot nH_2O$	5			5
Opal C/T	$SiO_2 \cdot nH_2O$				1
Plagioclase feldspar	$(Na,Ca)AlSi_3O_8$	29	31	23	21
K-feldspar	$KAlSi_3O_8$	6	18.5	5	2
Calcite	$CaCO_3$		0.5	6	
Dolomite	$(Ca,Mg)(CO_3)_2$		3	5	
Pyrite	FeS_2		0.5	2	1
Gypsum	$CaSO_4 \cdot 2H_2O$				0.5
Fluorapatite	$Ca_5F(PO_4)_3$			7	
Magnetite	alpha-Fe_3O_4	1	1		
	Bulk Subtotal	*70*	*95.5*	*62*	*44.5*
Clay Minerals					
Kaolinite	$Al_2Si_2O_5(OH)_4$	1	2		0.5
Illite/mica	$KAl_2(Si_3AlO_{10})(OH)_2$	2	0.5	6	4
Smectite	$Na_{0.3}(Al,Mg)_2Si_4O_{10}(OH)_2 \cdot xH_2O$	27	2	32	51
	Clay Subtotal	*30*	*4.5*	*38*	*55.5*
	Sample Total	100	100	100	100

Table 2-11. Modeled Composition of CO_2 Injectate

Gas	Mass Fraction	Mass %
Carbon dioxide	0.9866	98.7%
Methane	0.0047	0.5%
Benzene	0.0036	0.4%
Ethane	0.0024	0.2%
Nitrogen	0.0014	0.1%
Total		99.9%

Table 2-12. Physical Properties of Geologic Formations

Formation	Rock Density (kg/L)	Modeled Porosity (%)	Modeled Porosity	Bulk Density (kg/L)
Freeman-Jewett	2.2	20	0.2	1.76
Vedder	2.65	34	0.34	1.749

kg/L = Kilograms per liter

Table 2-13. Mineralogy Input for PHREEQC

Mineral	Chemical Formula	Molar Mass (g/mol)	Freeman-Jewett 4,801-4,805 ft		Freeman-Jewett 4,369-4,379 ft		Vedder 4,308-4,333 ft		Vedder 8,350-8,360 ft	
			Relative Abundance (%)	moles/L	Relative Abundance (%)	moles/L	Relative Abundance (%)	moles/L	Relative Abundance (%)	moles/L
Albite (for plagioclase)	NaAlSi3O8	262.223	21	7.05	23	7.72	31	6.08	29	5.69
Smectite-low-Fe-Mg	Ca.02Na.15K.2Fe++.29Fe+++.16Mg.9Al1.25Si3.75H2O1	549.07	51	8.17	32	5.13	2	0.19	27	2.53
K-Feldspar (orthoclase)	KAlSi3O8	278.33	2	0.63	5	1.58	18.5	3.42	6	1.11
Calcite	Ca(CO3)	100.09	0	0	6	5.28	0.5	0.26	0	0
Dolomite	CaMg(CO3)2	184.4	0	0	5	2.39	3	0.84	0	0
Illite	K0.6Mg0.25Al1.8Al0.5Si3.5O10(OH)2	389.34	4	0.90	6	1.36	0.5	0.07	2	0.26
Kaolinite	Al2Si2O5(OH)4	258.16	0.5	0.17	0	0.00	2	0.40	1	0.20
Gypsum	CaSO4:2H2O	172.17	0.5	0.26	0	0.00	0	0.00	0	0
Pyrite	FeS2	119.98	1	0.73	2	1.47	0.5	0.21	0	0
Fluorapatite	Ca5(PO4)3F	486.82	0	0	7	1.27	0	0	0	0
Quartz (+opal)	SiO2	60.08	20	29.29	14	20.51	41	35.10	34	29.11

Table 2-14. Mineralogical Changes based on Equilibrium Geochemical Modeling

Mineral	Initial	Final	Delta	Initial	Final	Delta	Initial	Final	Delta	Initial	Final	Delta
Formation	*Vedder*			*Vedder*			*Freeman-Jewett*			*Freeman-Jewett*		
Depth (feet)	*4,308-4,333*			*8,350-8,360*			*4,369-4,379*			*4,801-4,805*		
Albite	6.08	5.93	–0.15	5.69	5.46	–0.23	7.05	6.65	–0.40	7.72	8.97	1.25
CO2(g)	10.00	9.44	–0.56	10.00	9.72	–0.28	10.00	9.56	–0.44	10.00	1.26	–8.74
Calcite	0.26	0.09	–0.17	—	0.00	0.00	—	0.00	0.00	5.28	0.42	–4.85
Dolomite	0.84	1.02	0.19	—	0.01	0.01	—	0.26	0.26	2.39	7.34	4.96
Gypsum	—	0.00	0.00	—	0.00	0.00	0.26	0.00	–0.26	—	0.00	0.00
Illite	0.07	0.00	–0.07	0.26	0.19	–0.07	0.90	0.00	–0.90	1.36	0.00	–1.36
K-Feldspar	3.42	3.50	0.08	1.11	1.15	0.05	0.63	1.18	0.55	1.58	3.42	1.84
Kaolinite	0.40	0.63	0.23	0.20	0.37	0.17	0.17	1.16	0.99	—	3.22	3.22
Pyrite	0.21	0.21	0.00	—	0.00	0.00	0.73	0.73	0.00	1.47	1.41	–0.06
Quartz	35.10	35.79	0.69	29.11	29.56	0.45	29.29	30.17	0.88	20.51	28.77	8.26
Smectite-low-Fe-Mg	0.18	0.00	–0.18	2.53	2.53	0.00	8.17	8.14	–0.04	5.13	0.00	–5.13

Table 2-15. Modeled Equilibrium Aqueous Concentrations

Constituent	Concentration (mg/L [a])			
Formation	*Vedder*		*Freeman-Jewett*	
Depth (feet)	*4,308-4,333*	*8,350-8,360*	*4,369-4,379*	*4,801-4,805*
Al^{3+}	0.006	0.006	0.004	0.044
TIC	16,535	12,327	13,454	184,974
Ca^{2+}	5.96	0.004	0.28	0.68
Cl^{-}	14,226	14,233	14,354	14,662
Fe^{2+}	4,791	0.012	5,808	142,027
K^{+}	110	118.9	211.1	15.2
Mg^{2+}	0.144	242.52	76.02	0.01
Na^{+}	13,254	14,316	22,751	2,158
SO_4^{2-}	774	366	25,802	12,478
SiO_2	15.7	15.6	15.6	16.0
pH (s.u.)	6.7	6.7	6.53	7.6
pe (s.u.)	–2.8	5.9	–2.41	–3.7

[a] Unless otherwise noted
mg/L = Milligrams per liter
s.u. = Standard units

Table 7-1. Injectate Composition
Page 1 of 2

Component	Mass Fraction
N_2	0.001372
O_2	0
CO	0.000193
H_2	2.11×10^{-10}
H_2O	0.00058
CO_2	0.986649
CH_4	0.004707
C_2H_2	0
C_2H_4	5.05×10^{-10}
C_2H_6	0.002387
C_3H_8	2.25×10^{-9}
MEOH	4.62×10^{-8}
DME	2.56×10^{-13}
Acetone	1.05×10^{-10}
ETOH	1.65×10^{-11}
CH_2O (formaldehyde)	4.11×10^{-6}
NH_3	8.5×10^{-11}
Benzene	0.003609
Toluene	0.000188
Xylenes	2.83×10^{-6}
Styrene	8.72×10^{-6}
Phenol	5.1×10^{-11}
Indene	1.79×10^{-8}
O-Cresol	0
M-Cresol	8.58×10^{-12}
Naphthalene	7.88×10^{-8}
2-methylnaphthalene	1.45×10^{-11}
1-methylnaphthalene	1.26×10^{-8}
Biphenyl	3.15×10^{-12}
Acenaphthene	4.25×10^{-13}
H_2S	1.46×10^{-5}
COS	4.28×10^{-5}

Table 7-1. Injectate Composition
Page 2 of 2

Component	Mass Fraction
CS_2	0
Thiols	1.6×10^{-10}
Thiophen	0
HCl	1.97×10^{-14}
HCN	5.3×10^{-14}
Cyclohexane	0.000186
Methylcyclohexane	1.95×10^{-5}
Tetralin	2.89×10^{-10}
Decalin	4.51×10^{-6}

List of Appendices

Appendix A: Site Plan

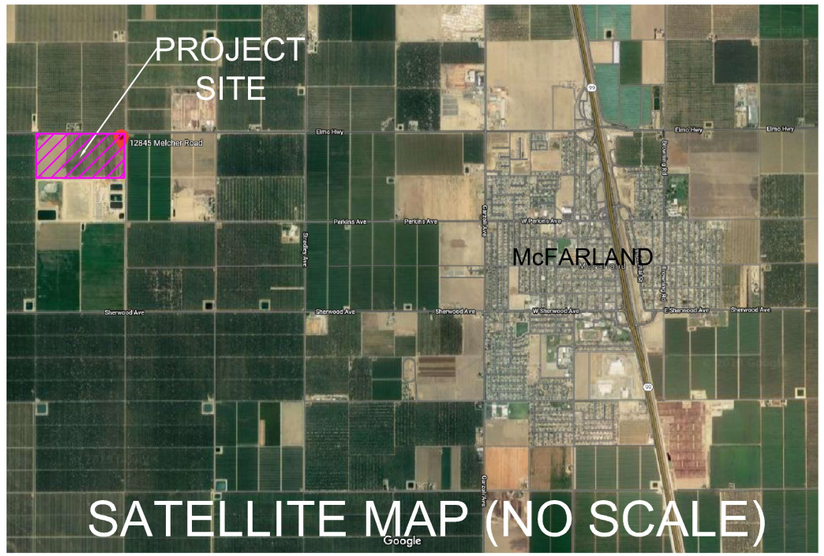

GENERAL NOTES:

SITE ADDRESS: 12845 MELCHER RD, MCFARLAND, CA, 93250
ASSESSORS PARCEL NUMBER: 060-050-24-00
TOTAL SITE SIZE: 80 ACRES
EXISTING USE: AGRICULTURAL
PROPOSED USE: BIOMASS INTO RENEWABLE NATURAL GAS FACILITY
EXISTING ZONING: HEAVY INDUSTRIAL (M3)
SEWAGE DISPOSAL: CITY OF McFARLAND WASTEWATER TREATMENT
WATER SUPPLY: ONSITE WELL (EXISTING)
DRAINAGE: GROUNDWATER RECHARGE POND ONSITE

0 250'
Scale: 1" = 250'

N

Legend

- Project Equipment Boundary
- Fence
- Natural Gas Pipeline
- Pavement
- Proposed Groundwater Pond
- Admin./Storage Building
- Required Construction Area
- Property Line
- Proposed Landscaping

DEVELOPER:

FRONTLINE BIOENERGY, LLC
1521 WEST F AVENUE
NEVADA, IA 50201
(515) 292-1200

Owner:

SAN JOAQUIN RENEWABLES, LLC
1521 WEST F AVENUE
NEVADA, IA 50201
(515) 292-1200

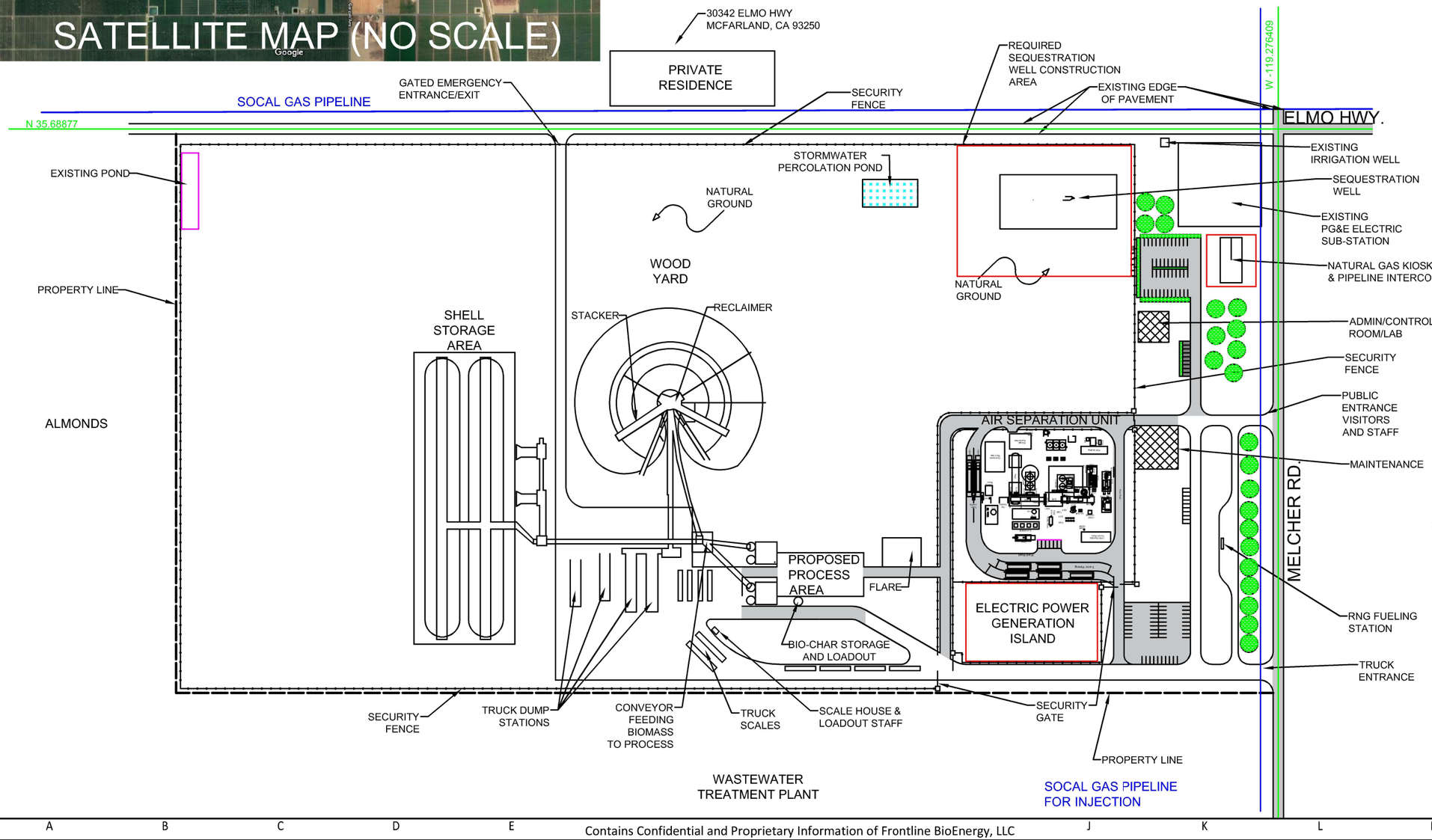

NOTES:

REV	DESCRIPTION	BY	CHK	APR	PM	DATE
G	GENERAL UPDATES	MPZ				6/10/21

FRONTLINE BIOENERGY, LLC
Renewable Energy & Products

TITLE:
SJR Site Plan

PROJECT
129 - San Joaquin Renewables

DOCUMENT No.

REV.
G

Appendix B: Carbon Dioxide Phase Study

FRONTLINE BIOENERGY, LLC

Capture the energy ⚡ Release the potential

Carbon Dioxide Phase Study

San Joaquin Renewables Class VI Carbon Dioxide Sequestration Well

T. J. Paskach and Michael Zembrzuski

REVISION: **A**
03 January 2022

1521 West F Avenue · Nevada, IA 50201 · 515-292-1200 · www.frontlinebioenergy.com

Background

In an effort to characterize and understand the chemical and physical properties of the stream that San Joaquin Renewables (SJR) is proposing to inject into the Class VI well, Frontline has utilized rigorous thermodynamic calculations making use of the UNIQUAC equation of state[1], using binary interaction parameters calculated using the UNIFAC method[2] within ASPEN Plus process modelling software. The main constituents of the stream analyzed are summarized below in Table 1 and expanded in the narrative submitted by DBS&A in Table 3-1 of that document.

Table 1. Composition of Carbon Dioxide Stream for Sequestration

Component	Mass Fraction
CO_2	0.98665
Methane	0.00471
Benzene	0.00361
Ethane	0.00239
N_2	0.00137
H_2O	0.00058
CO	0.00019
Toluene	0.00019

In its response to the EPA Class VI sequestration well permit application submitted in early November 2021, the reviewer has asked what the phase (liquid, vapor, or supercritical) the CO_2 stream is in at the surface.

Methodology

To determine the surface phase, the pressure at the surface must be known in addition to the composition. However, the pressure at the surface depends on many factors, including the pressure and temperature at the CO_2 storage complex (downhole conditions), the density of the head of CO_2 in the well bore (which varies with depth and therefore pressure, as it a compressible fluid), the heat generated by adiabatic compression of the fluid downhole, the heat ingress from the earth surrounding the wellbore, and the conditions (temperature and composition) at the surface. To determine all of these variables with internal consistency, the following methodology was employed.

The raw carbon dioxide (CO_2) stream from the SJR process is produced at approximately 150 psig and is compressed to 800 psig before it is cooled past its liquefaction point (~80°F) at that pressure, where the CO_2 condenses into a liquid. The liquid carbon dioxide having the composition shown in Table 1 is then pumped to a higher pressure before it is injected into the Class VI sequestration well pipe at the surface. At the surface, the temperature is assumed to be 80°F, which is below the estimated critical temperature for the mixture. Whether it remains in the liquid phase or is supercritical is the question to be answered by the study herein.

The sequestration well pipe was modelled in ASPEN Plus. The ASPEN Plus pipe model allows a user to rigorously calculate pressure drop and heat transfer in a single segmented pipe by numerically

[1] Maurer, G.; Prausnitz, J.M. (1978). "On the derivation and extension of the uniquac equation". Fluid Phase Equilibria. 2 (2): 91–99. doi:10.1016/0378-3812(78)85002-X. ISSN 0378-3812.

[2] Fredenslund, Aage; Jones, Russell L.; Prausnitz, John M. (1975). "Group-contribution estimation of activity coefficients in nonideal liquid mixtures". AIChE Journal. 21 (6): 1086–1099. doi:10.1002/aic.690210607. ISSN 0001-1541

integrating in sufficiently small steps to account for property changes along its length. The following assumptions are required as inputs to the model:

1) Surrounding temperature (at grade and downhole): The temperature gradient in the Earth's crust within was assumed to be linear at 0.0165°F/ft (30°C/km) based on Steven Earle's work.[3] For our well, therefore, assuming a surrounding crust temperature at the inlet of 45°F, the crust temperature at the downhole depth of injection would be 173°F.
2) Inlet Temperature: The carbon dioxide stream at the inlet of the pipe was assumed to be 86.2°F at the outlet of the liquid carbon dioxide pump. This value was calculated in the larger Aspen Plus simulation of the renewable natural gas project.
3) Heat Transfer Coefficient: The earth's thermal conductivity was assumed to be 1.4 btu/hr-ft-°F after H. J. Ramsey[4]. This was translated to an equivalent heat transfer coefficient for ASPEN Plus using the shape factor for a cylinder conducting into an infinite solid, considering both conduction through the pipe and conduction heat transfer away from the pipe surface. Using this method, the resulting heat transfer coefficient used for the Aspen Plus pipe model was 2.8 btu/hr-ft^2-°F.
4) Downhole Pressure and Depth: From the results of the plume modeling study performed by Stefan Fensterle, the carbon dioxide will be injected at a depth of 7,775 ft bgs and will reach a peak pressure of 266 bara or 3,865 psia.
5) Frictional Correlation: The Beggs-Brill[5] frictional correlation was selected, which is a comprehensive method appropriate for multi-phase flow in pipes with elevation changes.
6) Integration step size: Determination of the results down pipe can only be calculated rigorously by integration using a sufficiently small step size. The pipe was divided into 500 segments for this work, (fractional step of 0.002), which allowed the model to converge and give very reasonable results we believe to be accurate.

Naturally, the pressure rise in the wellbore depends on the head of material above it, which depends on its density. The density, in turn, depends on pressure. The surface pressure was determined *via* an iterative process in which the injection pressure was varied until the boundary condition, namely the outlet pressure of the pipe model in Aspen Plus at injection depth (7,775 ft bgs.) was the same as the maximum predicted downhole pressure estimated by DBS&A (265 barg or 3,850 psig).

3 Steven Earle, Physical Geology, 2nd Edition, 2018, Chapter 9, Section 2: The Temperature of the Earth's Interior: available at: https://opentextbc.ca/physicalgeology2ed/chapter/9-2-the-temperature-of-earths-interior/

4 H. J. Ramey, JR. Wellbore Heat Transmission

5 D.H. Beggs and J. P. Brill, A Study of Two-Phase Flow in Inclined Pipes, J Pet Technol 25 (05): 607–617 (1973)

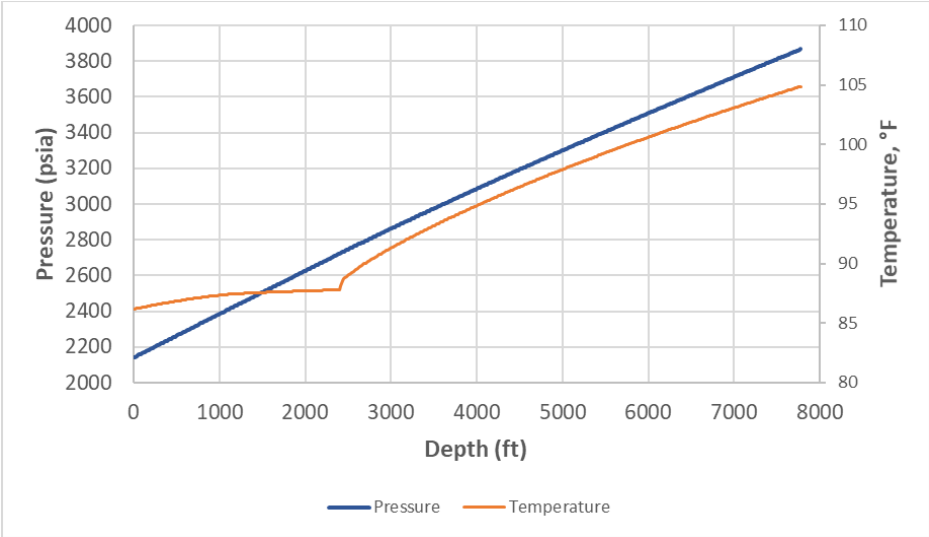

Figure 1. Estimated pressure and temperature in the injection wellbore

As expected, the pressure increases with depth below grade due to the static head of material in the pipe. The results summarized in the graph above predict that an injection pressure of 2,150 psia at the surface is adequate in addition to the static head to meet the anticipated pressure at the injection point.

Also, we see that the temperature increases The model results also included the physical properties and phase at each point along the pipe. The model predicted that the surface phase will be liquid, and it is clear from the discontinuity in density that the critical point is reached at approximately 2400 feet below the surface.

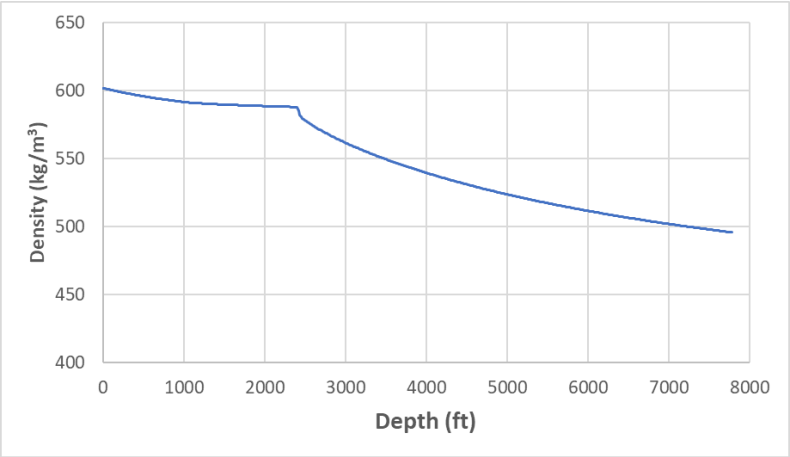

Figure 2. Density of the carbon dioxide in the wellbore.

Finally, it is helpful to look at the well on a CO_2 phase diagram[6].

[6] https://ocolabs.com/co2-phase-diagram/

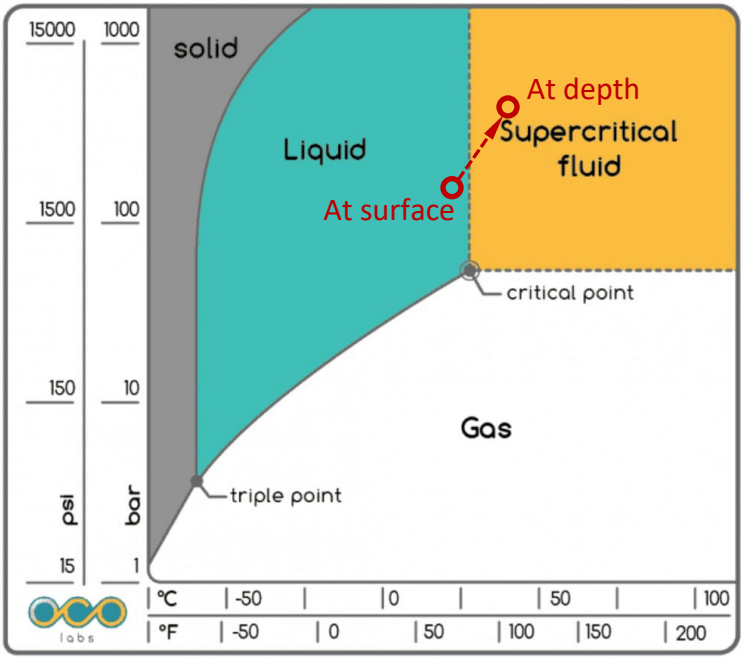

Figure 3. Well conditions on CO_2 phase diagram

We conclude that the carbon dioxide stream at the surface remains in the liquid phase until it becomes supercritical at approximately 2400 feet below the surface, whereafter it remains in the supercritical phase.

Appendix C: Tables from Previous Reports

Antelope-Stevens petroleum system petroleum volumes by reservoir rock

Antelope-Stevens petroleum system petroleum volumes by reservoir rock. The Vedder and Olcese Sands are modest producers on the east side of the basin.

Table 8.7. Antelope-Stevens(!) petroleum system petroleum volumes by reservoir rock.

[Data from appendix 8.1 and appendix 8.2. Res No., Reservoir Number corresponding to column 8 in appendix 8.1; Ma, million years ago; EUR Oil, Estimated ultimate recovery of oil; Mbo, thousands of barrels of oil; EUR Gas, Estimated ultimate recovery of gas; MMcfg, millions of cubic feet of gas; GOR, gas-to-oil ratio; cfg/bo, cubic feet of gas per barrel of oil; Boe, Barrel of oil equivalent; Fm, Formation; NA, Not Applicable; zz-undesignated, unknown reservoir rock; ?, unknown age. ** and yellow shading highlight the major reservoir rock for the petroleum system; * and green shading highlight source rock interval for the petroleum system]

Res No.	Reservoir Rock Unit	Age Range (Ma)	Number of Pools	EUR Oil (Mbo)	EUR Gas (MMcfg)	GOR (cfg/bo)	Oil (%)	Gas (%)	EUR Boe (Mbo)	Boe (%)
1	Tulare Formation	2.5-0.6	2	20	1	50	0.0	0.0	20	0.0
2	Kern River Formation	8-0.7	4	2,076,205	19,308	9	21.6	0.2	2,079,423	18.1
3	San Joaquin Formation	4.5-2.5	11	2,313	44,191	19,105	0.0	0.4	9,678	0.1
4	Etchegoin Formation	5.5-4.5	34	734,882	459,986	626	7.7	4.1	811,546	7.1
6	Antelope shale of Graham and Williams (1985)*	16.5-5.5	4	9,646	49,800	5,163	0.1	0.4	17,946	0.2
7	Reef Ridge Shale Member of Monterey Fm	6.5-5.5	9	12,928	6,859	531	0.1	0.1	14,071	0.1
8	Chanac Formation	11-6	29	457,593	164,567	360	4.8	1.5	485,021	4.2
9	Santa Margarita Sandstone	11-6.5	25	52,002	15,453	297	0.5	0.1	54,578	0.5
10	**Stevens sand of Eckis (1940)****	**9.5-7**	**92**	**1,849,775**	**9,080,344**	**4,909**	**19.3**	**80.5**	**3,363,166**	**29.3**
11	Round Mountain Silt	16-13.5	12	8,556	5,219	610	0.1	0.0	9,426	0.1
12	Temblor Formation	33-14	10	5,558	165,509	29,779	0.1	1.5	33,143	0.3
14	Olcese Sand	21-16.5	14	25,160	20,948	833	0.3	0.2	28,651	0.2
15	Jewett Sand	25-21	19	442,058	56,505	128	4.6	0.5	451,476	3.9
16	Basalt formation(?)	?	1	1,384	18,742	13,542	0.0	0.2	4,508	0.0
17	Vedder Sand	33.5-25	28	282,779	459,535	1,625	2.9	4.1	359,368	3.1
18	Walker Formation	34-25	2	0	0	0	0.0	0.0	0	0.0
19	Vaqueros Formation	33-24	1	0	0	0	0.0	0.0	0	0.0
28	San Emigdio Formation	?	5	24,347	58,663	2,409	0.3	0.5	34,124	0.3
29	Tejon Formation	?	5	204	2,488	12,196	0.0	0.0	619	0.0
33	schist	NA	4	18	0	0	0.0	0.0	18	0.0
34	zz-undesignated	NA	6	3,611,230	657,980	182	37.6	5.8	3,720,893	32.4
		Total	317	9,596,658	11,286,098	1,176	100.0	100.0	11,477,674	100.0

Table B-1. From: Leslie B. Magoon, Paul G. Lillis, and Kenneth E. Peters, 2007. **Petroleum Systems Used to Determine the Assessment Units in the San Joaquin Basin Province, California.** in Scheirer A.H., ed., Petroleum Systems and Geologic Assessment of Oil and Gas in the San Joaquin Basin Province, California: United States Geological Survey Professional Paper 1713, Chapter 8, p. 1-67.

Tumey-Temblor petroleum system petroleum volumes by reservoir rock

Tumey-Temblor petroleum system petroleum volumes by reservoir rock. The Vedder Sands are modest producers on the east side of the basin. There is no Olcese production from this petroleum system.

Table 8.8. Tumey-Temblor(.) petroleum system petroleum volumes by reservoir rock.

[Data from appendix 8.1 and appendix 8.2. Res No., Reservoir Number corresponding to column 8 in appendix 8.1; Ma, million years ago; EUR Oil, Estimated ultimate recovery of oil; Mbo, thousands of barrels of oil; EUR Gas, Estimated ultimate recovery of gas; MMcfg, millions of cubic feet of gas; GOR, gas-to-oil ratio; cfg/bo, cubic feet of gas per barrel of oil; Boe, Barrel of oil equivalent; NA, Not Applicable; zz-undesignated, unknown reservoir rock. ** and yellow shading highlight the major reservoir rock for the petroleum system; * and green shading highlight source rock interval for the petroleum system]

Res No.	Reservoir Rock Unit	Age Range (Ma)	Number of Pools	EUR Oil (Mbo)	EUR Gas (MMcfg)	GOR (cfg/bo)	Oil (%)	Gas (%)	EUR Boe (Mbo)	Boe (%)
9	Santa Margarita Sandstone	11-6.5	3	3,352	7	2	0.5	0.0	3,353	0.3
10	Stevens sand of Eckis (1940)	9.5-7	1	0	0	0	0.0	0.0	0	0.0
12	**Temblor Formation****	**33-14**	**32**	**485,214**	**1,976,597**	**4,074**	**79.2**	**93.3**	**814,647**	**84.3**
13	Zilch formation of Loken (1959)	30-14	9	78,989	62,500	791	12.9	3.0	89,406	9.3
15	Jewett Sand	25-21	1	2	0	0	0.0	0.0	2	0.0
17	Vedder Sand	33.5-25	1	4,005	5	1	0.7	0.0	4,006	0.4
18	Walker Formation	25-34	1	71	0	0	0.0	0.0	71	0.0
19	Vaqueros Formation	33-24	3	27,339	49,114	1,796	4.5	2.3	35,525	3.7
20	Leda sand of Sullivan (1962)	34-33	2	10,240	22,758	2,222	1.7	1.1	14,033	1.5
21	Tumey formation of Atwill (1935)*	37-33.5	4	173	889	5,139	0.0	0.0	321	0.0
34	zz-undesignated	NA	1	3,617	5,998	1,658	0.6	0.3	4,617	0.5
		Total	58	613,002	2,117,868	3,455	100.0	100.0	965,980	100.0

Table B-2. From: Leslie B. Magoon, Paul G. Lillis, and Kenneth E. Peters, 2007. **Petroleum Systems Used to Determine the Assessment Units in the San Joaquin Basin Province, California.** in Scheirer A.H., ed., Petroleum Systems and Geologic Assessment of Oil and Gas in the San Joaquin Basin Province, California: United States Geological Survey Professional Paper 1713, Chapter 8, p. 1-67.

Table 1. Hydrogeologic properties assigned to each formation: k_h is horizontal permeability, k_v is vertical permeability, Φ is porosity, β_p is pore compressibility, α is the van Genuchten parameter for entry capillary pressure, and m is the van Genuchten parameter for pore-size distribution.

Formations	k_h [mDarcy]	k_v [mDarcy]	Φ [-]	β_p [10^{-10} Pa^{-1}]	α [10^{-5} Pa^{-1}]	m [-]
Non-Fault Zones						
Pre-Etchegoin	3000	3000	0.35	15.5	5.0	0.457
Etchegoin	1200	1200	0.32	15.5	5.0	0.457
Macoma-Chanac	1900	1900	0.31	10.5	5.0	0.457
Santa Margarita-McLure	2000	2000	0.275	10.5	5.0	0.457
Stevens Sand	240	48	0.22	10.5	5.0	0.457
Fruitvale-Round Mountain	0.002	0.001	0.338	14.5	0.42	0.457
Olcese Sand	170	34	0.336	4.9	5.0	0.457
Temblor-Freeman	0.002	0.001	0.338	14.5	0.42	0.457
Vedder Sand (sand layers)	303	60.6	0.264	4.9	13.0	0.457
Vedder Sand (shale layers)	0.1	0.05	0.32	14.5	0.42	0.457
Tumey-Eocence	0.07	0.07	0.07	14.5	0.42	0.457
Baserock	0.0001	0.0001	0.01	22.7	0.5	0.457

Table B-3. Hydrogeologic properties from Birkholzer et al., (2011), providing an initial compilation of rock properties used for the various formations in the McFarland injection area, including granitic basement on the east side of the San Joaquin Basin.

Jasmin productive pool and fluid information from CalGEM:

ITEM	POOL DATA			
	PYRAMID HILL	CANTLEBERRY SANDS		
Discovery date	January 1964	July 1946		
Initial production rates				
Oil (bbl/day)	3	65		
Gas (Mcf/day)				
Flow pressure (psi)	on pump	on pump		
Bean size (in.)				
Initial reservoir pressure (psi)	530**	850**		
Reservoir temperature (°F)	98	112**		
Initial oil content (STB/ac.-ft.)	1,200**	1,700**		
Initial gas content (MSCF/ac.-ft.)				
Formation	Jewett	Vedder		
Geologic age	Miocene	Oligocene		
Average depth (ft.)	1,705	2,750		
Average net thickness (ft.)	130	30-80		
Maximum productive area (acres)				
RESERVOIR ROCK PROPERTIES				
Porosity (%)	37**	40		
S_{oi} (%)	47**	70**		
S_{wi} (%)	53**	30**		
S_{gi} (%)				
Permeability to air (md)	1,300**	2,400**		
RESERVOIR FLUID PROPERTIES				
Oil:				
Oil gravity (°API)	14	14		
Sulfur content (% by wt.)				
Initial solution GOR (SCF/STB)	10**	18**		
Initial oil FVF (RB/STB)	1.02**	1.08**		
Bubble point press. (psia)				
Viscosity (cp) @ °F				
Gas:				
Specific gravity (air = 1.0)	0.53**	0.53**		
Heating value (Btu/cu. ft.)				
Water:				
Salinity, NaCl (ppm)	-	150		
T.D.S. (ppm)	-	730		
R_w (ohm/m) (77°F)				

West Jasmin productive pool and fluid information from CalGEM:

ITEM	POOL DATA			
	FAMOSO			
Discovery date	April 1959			
Initial production rates				
Oil (bbl/day)	15			
Gas (Mcf/day)				
Flow pressure (psi)	on pump			
Bean size (in.)				
Initial reservoir pressure (psi)	1,080			
Reservoir temperature (°F)	122			
Initial oil content (STB/ac.-ft.)	1,000**			
Initial gas content (MSCF/ac.-ft.)	-			
Formation	Walker			
Geologic age	Eocene			
Average depth (ft.)	4,200			
Average net thickness (ft.)	30			
Maximum productive area (acres)	40			
RESERVOIR ROCK PROPERTIES				
Porosity (%)	25**			
S_{oi} (%)	47**			
S_{wi} (%)	43**			
S_{gi} (%)				
Permeability to air (md)	200-500			
RESERVOIR FLUID PROPERTIES				
Oil:				
Oil gravity (°API)	22			
Sulfur content (% by wt.)				
Initial solution GOR (SCF/STB)				
Initial oil FVF (RB/STB)	1.03			
Bubble point press. (psia)				
Viscosity (cp) @ °F				
Gas:				
Specific gravity (air = 1.0)				
Heating value (Btu/cu. ft.)				
Water:				
Salinity, NaCl (ppm)				
T.D.S. (ppm)				
R_w (ohm/m) (77°F)				

S:\Projects\DB19.1252_Frontline_Bioenergy\GIS\QGIS\EPA comments\Jasmine and west jasmine Productive pool and fluid information.qgz

SAN JOAQUIN RENEWABLES

Jasmine and West Jasmine Productive Pool and Fluid Information

06/07/2022 JN DB19.1252

Figure 2-59

West Dyer productive pool and fluid information from CalGEM:

ITEM	POOL DATA: VEDDER
Discovery date	September 1941
Initial production rates	
Oil (bbl/day)	185
Gas (Mcf/day)	
Flow pressure (psi)	
Bean size (in.)	
Initial reservoir pressure (psi)	750**
Reservoir temperature (°F)	103
Initial oil content (STB/ac.-ft.)	900**
Initial gas content (MSCF/ac.-ft.)	
Formation	Vedder
Geologic age	Oligocene
Average depth (ft.)	2,340
Average net thickness (ft.)	75
Maximum productive area (acres)	40
RESERVOIR ROCK PROPERTIES	
Porosity (%)	31**
So_i (%)	42**
Sw_i (%)	58**
Sg_i (%)	
Permeability to air (md)	1,800**
RESERVOIR FLUID PROPERTIES	
Oil:	
Oil gravity (°API)	15
Sulfur content (% by wt.)	
Initial solution GOR (SCF/STB)	
Initial oil FVF (RB/STB)	
Bubble point press. (psia)	1,02**
Viscosity (cp) @ °F	
Gas:	
Specific gravity (air = 1.0)	
Heating value (Btu/cu. ft.)	
Water:	
Salinity, NaCl (ppm)	
T.D.S. (ppm)	
R_w (ohm/m) (77°F)	

ShaftervWest productive pool and fluid information from CalGEM:

ITEM	POOL DATA: MCLURE
Discovery date	October 1983
Initial production rates	
Oil (bbl/day)	30
Gas (Mcf/day)	16
Flow pressure (psi)	1,003
Bean size (in.)	
Initial reservoir pressure (psi)	
Reservoir temperature (^{0}F)	170
Initial oil content (STB/ac.-ft.)	
Initial gas content (MSCF/ac.-ft.)	
Formation	Monterey
Geologic age	Miocene
Average depth (ft.)	7,575
Average net thickness (ft.)	800
Maximum productive area (acres)	5
RESERVOIR ROCK PROPERTIES	
Porosity (%)	
So_i (%)	21
Sw_i (%)	79
Sg_i (%)	
Permeability to air (md)	
RESERVOIR FLUID PROPERTIES	
Oil:	
Oil gravity (^{0}API)	27.5
Sulfur content (% by wt.)	
Initial solution GOR (SCF/STB)	
Initial oil FVF (RB/STB)	
Bubble point press. (psia)	
Viscosity (cp) @ ^{0}F	
Gas:	
Specific gravity (air = 1.0)	
Heating value (Btu/cu. ft.)	
Water:	
Salinity, NaCl (ppm)	27,000
T.D.S. (ppm)	
R_w (ohm/m) (77^{0}F)	1.7

S:\Projects\DB19.1252_Frontline_Bioenergy\GIS\QGIS\EPA comments\West Dyer and Shafter Productive pool and fluid information.qgz

SAN JOAQUIN RENEWABLES

West Dyer and Shafter North Productive Pool and Fluid Information

Reservoir Properties (ca. 2002)

RES. PRESSURE	6200-6300 PSI
RES. TEMP	190-195 F
RES. THICKNESS	20-40 FT
PERM	0.04-0.06 mD
POROSITY	0.3
SP. GRAV., OIL	0.8996
INITIAL WATER SAT.	0.45
OIL COMPRESSIBILITY	7.8 E-06 PSI^{-1}
OIL VISCOSISTY	2.8 cP
BHP LIMIT	3360-3800 PSI

Source: *Ganong, et al, 2003 (SPE paper 83501)*

Notes: Reservoir properties for the Rose Oil Field. Reservoir depth is 7500' below ground surface. Pressure gradient (psi/ft) is 0.84.

SAN JOAQUIN RENEWABLES

Reservoir Properties

Table 8.2. Summary of oil and gas volume by petroleum system.

[Data from appendix 8.1 and appendix 8.2. EUR, estimated ultimate recovery; Mbo, thousands of barrels; MMcfg, millions of cubic feet of gas; GOR, gas-to-oil ratio; cfg/bo, cubic feet of gas per barrel of oil; Boe, Barrel of oil equivalent; NA, Not Applicable. World Scale Size, from Klemme (1994), is defined as: "Super Giant" Petroleum System (PS)>$100x10^9$ Boe; "Giant" PS=$20x10^9$ to $100x10^9$ Boe; "Large" PS=$5x10^9$ to $20x10^9$ Boe; "Significant" PS=$0.2x10^9$ Boe; and "Small" PS<$0.2x10^9$ Boe]

Petroleum System	EUR Oil (Mbo)	Oil (%)	EUR Gas (MMcfg)	Gas (%)	GOR (cfg/bo)	EUR Boe (Mbo)	Boe (%)	World Scale Size
San Joaquin(?)	0	0.0	367,897	2.0	NA	61,316	0.3	Small
McLure-Tulare(!)	2,606,588	17.9	1,804,291	9.6	692	2,907,303	16.4	Significant
Antelope-Stevens(!)	9,596,658	65.8	11,286,098	60.1	1,176	11,477,674	64.8	Large
Tumey-Temblor(.)	613,002	4.2	2,117,868	11.3	3,455	965,980	5.5	Significant
Kreyenhagen-Temblor(!)	1,776,710	12.2	3,020,627	16.1	1,700	2,280,148	12.9	Significant
Moreno-Nortonville(.)	158	0.0	182,774	1.0	1,156,797	30,620	0.2	Small
Total	14,593,116	100.0	18,779,555	100.0	1,287	17,723,042	100.0	

Notes: This Table highlights the main differences in oil properties for McLure-Tulare oils vs Tumey-Temblor oils. GOR is 692 cfg/bo for the McLure-Tulare, and 3,455 cfg/bo for the Tumey Temblor

Source: USGS PP 1713

S:\Projects\DB19.1252_Frontline_Bioenergy\GIS\QGIS\Summary of oil and gas volume by petroleum system.qgz

SAN JOAQUIN RENEWABLES

Summary of Oil and Gas Volume by Petroleum System

06/10/2022 JN DB19.1252

Figure xxx

Appendix D: Keystone Diversified Energy Seismic Interpretation Report

FRONTLINE PROJECT SEISMIC INTERPRETATION
KERN COUNTY, CALIFORNIA

May 27, 2022

Prepared by

Keystone Diversified Energy Inc

Bakersfield, California

Project Scope

The project scope for the geophysical interpretation was to:

- Acquire seismic data in order to determine fault locations relative to the Frontline Project area with respect to various formation horizons (See **Figure 1** Simplified Stratigraphic Column).
- Integrate seismic data and well data.
- Map faults to determine fault type, fault throw, and formation offset across the faults.
- Produce maps at key formation tops/bases.
- Produce grid files for mapped formations.
- Produce point file location data for pertinent faults and fault intersections with various formations.

Final products to be delivered:

- Interpreted seismic panels.
- Faults delineated and characterized as to:
    - Fault type,
    - Fault throw,
    - Formation offsets across faults (Allen Diagrams). NOTE: Allen Diagrams were created by other team members using the final model grids.
    - Fault locations detailed by XY points such that vertical fault surfaces could be used for modeling purposes.
- Depth horizon maps at relevant formation tops and bottoms.
- Isochore maps for relevant horizons.
- All products to be supplied in digital format as X, Y, Z points.

All required products have been produced.

Project Work (Figure 2)

The Frontline Project will be attempting to integrate previous work and modeling to determine relevance and usefulness for the Frontline Project. The project area is defined by cartographic reference system UTM 11N NAD 27 with X-Y-Z values in meters. The entire area examined by the full scale model is encompassed by a rectangle with the following corner points which use a 200 x 200 meter grid.

- NW 264000.0000 3997000.0000
- NE 341000.0000 3997000.0000
- SE 341000.0000 3889000.0000
- SW 264000.0000 3889000.0000

For purposes of the seismic interpretation a reduced area grid was utilized. This grid aligns with the larger grid with grid nodes being a subset of the full scale model area. The corner points of the seismically defined project area are a 200 x 200 meter grid with corner points at:

- NW 274200.0000 3970400.0000
- NE 323400.0000 3970400.0000
- SE 323400.0000 3919600.0000
- SW 274200.0000 3919600.0000

The focus of the seismic inspection area is shown on **Figures 3 & 4**.

Well and Velocity Data

Well Data (Figures 3 & 4)

83 wells in the area had digital log curves supplied by KDEI. An additional 65 well logs were digitized for a total of 148 wells within the seismic project area. Log curves included (when available) the spontaneous potential (SP), gamma ray, deep resistivity, sonic, density, and neutron. Most wells have only an SP and deep resistivity curve. The SP curves have been normalized across the project area.

Velocity Data (Figure 4)

Velocity survey data (checkshots) were available for ten wells in the seismic project area. All original checkshot data were reduced to ground level and used to make preliminary ties between wells and seismic data. Further refinements to the well ties were made using the Dynamic Depth Conversion (DDC) method described below. Propagation of velocity data to all wells was performed using DDC.

Seismic Data (Figures 4 & 5)

Five seismic lines were acquired from a seismic data broker. Three lines were used to define the faulting near the project location acreage. Two lines were acquired for the eastern area and correlation with the eastern well data. Two of the lines are actually portions of the same regional line. The lines are all west-east lines and are roughly perpendicular to regional dip (approximately 15 degrees off of true dip). The data were provided as digital SEGY files for both Stack and Migrated data and were loaded to a project utilizing the Kingdom Suite software. Further post-stack processing (seismic attributes for fault definition) was performed within the project.

The seismic line names are:

- West Area
    - EC-ENR-NMF-116-1
    - W-SJ-023
    - W-SJ-082-West
- East Area
    - GSI-CA-406
    - W-SJ-082-East

The data quality ranges from good to excellent.

In addition to the actual 2D seismic data a “fake” 3D survey was created with grid nodes that match the 200 x 200 meter area of interest grid. This fake survey allows 3D visualization of all surfaces and continuous fault planes.

Seismic Data Zero Time Registration

The seismic data came from three different seismic projects acquired over various years by different contractors and processed by different contractors. Differing assumptions were made by the various contractors which lead to differences in data presentation. Four lines were registered as “Sea Level Datum” while one line had a “300 Foot Datum”. Regardless of what datum is described or posted for a given seismic set the variations in Zero Time often do not match between various datasets. This was true of the project seismic data. Normally, this problem is addressed by having seismic tie lines which connect the various seismic lines. That was not possible for the acquired data.

The zero time problem was handled by interpreting the seismic data and then comparing contour maps using both seismic/well integration data and well data only maps. The true strike of the subsurface formations could be determined from the well only mapping. Zero time differences were compensated for by vertically adjusting the seismic data until strike data perturbations were removed due to the zero time mismatches. The Western seismic lines were taken as the base dataset and the other lines were adjusted to match Western zero time.

Another potential problem occurs when 2D seismic data are not exactly perpendicular to true dip. There can be discrepancies with the migrated data being properly positioned in depth and space. Since the west-east lines were only deviated by 15 degrees from true dip the problem is minimal and this was not a factor with this seismic dataset.

Seismic Interpretation and Well Data Integration (Figures 6, 7, 8)

Preliminary integration of seismic data with well data was performed by using wells closest to the seismic lines. These wells were tied to the seismic data using velocity data from the nearest checkshot wells and creating synthetic seismograms. Checkshot data from any particular well was reduced to ground level and then copied to other wells adjusting the time-depth pairs for any differences in ground level at the various well locations.

The synthetics were all created using wavelets extracted from the seismic which was used to tie the well. The synthetic traces were compared to the actual seismic data using a combination of nearest trace, traces within a radius around the borehole, and inserting the synthetic into an extracted portion of a seismic line. The wells listed below were directly tied to the indicated seismic lines. The quality of the synthetic-seismic tie is also indicated. The synthetic traces in all cases were created using the deep resistivity curve because no sonic curves were available.

Seismic-well ties were enhanced by having several “anchor points” based on stratigraphy and formation picks. The seismic expression of the Santa Margarita interval is well known as a spectacular prograding sigmoid-oblique complex (**Figures 7 & 8**) and provides an extremely accurate zone to which the well logs can be tied to the seismic data. Similarly, the Vedder sands also exhibit a progradational sequence which can be used as a marker event. Finally, wells that drilled into basement have a final concrete tie point.

- Line W-SJ-023
  - 04029306030000 Tidewater KCL 1
    - Fair.
  - 04030032220000 Dowser Exploration Ventures Parsons 1
    - Good to excellent.
- Line W-SJ-082-West
  - 04029305160000 General Petroleum Stiles 1
    - Fair. This well is shallow.
- Line W-SJ-082-East
  - 04029602780000 McCulloch O & G Corp Beck 1-6
    - Excellent.
  - 04029305420000 British American Oil Production Davis 36-32
    - Excellent.
- Line GSI-CA-406
  - 04029305240000 Tiger Oil Company Sunland Olive 1
    - Fair

Once definitive seismic-well ties had been established the seismic data were interpreted. In the absence of tie lines between the west-east seismic sections "jump ties" were effected. This involves taking a portion of one seismic line and comparing it to the next closest seismic line. Due to the excellent data quality, the fact that the lines are relatively close to one another, and the unique seismic stratigraphic character of some of the formations the jump ties work extremely well.

Seismic interpretation was performed for the following formation tops:

- Unnamed shallow seismic marker used for continuity purposes.
- Top Miocene
- Santa Margarita top
- Round Mountain (Fruitvale Shale). Note: This marker is picked as the Round Mountain top in many wells. However, when extended to the south it is correlative to the top of the Fruitvale Shale. To keep nomenclature the same with a multitude of well picks in the immediate area this horizon was called Round Mountain for this project.
- Round Mountain v2. Note: This marker has been differentiated from the Fruitvale Shale. This is the actual Round Mountain section although it has not been called this in many wells in the area. This pick ties much better with the seismic data and yields very good time to depth conversion results.
- Olcese Sand top
- Freeman-Jewett (Olcese Sand base)
- Vedder Sands (the Vedder zone has been sub-divided into sub-zones which have various areal extents. **Figures 9, 10, 11, 12, 13, 14, 15**)
    - Vedder1 (top)
    - Vedder1A
    - Vedder2
    - Vedder3
    - Vedder4
    - Cantleberry Sand
- Walker top (Vedder Sands base)
- Basement

Breakout of the Vedder interval was performed by interpreting the top and base Vedder. A well-defined Vedder prograding sequence can be observed on seismic line W-SJ-082-East. The prograding sequence was interpreted and then the sands were defined using the well logs with the interpretation being extended outward from the seismic line. This process was a collaborative effort between the geophysicist and geologist.

Seismic Time to Depth Conversion (Dynamic Depth Conversion – DDC)

The interpreted seismic data were converted to depth using the Dynamic Depth Conversion (DDC) module within Kingdom Suite. DDC allows integration of time data and depth data to produce grids for mapped intervals. Additionally, it provides instantaneous conversion of seismic time sections to seismic depth sections. The following grids have been created for all mapped formation tops and intervals:

- Time.
- Depth.
- Isochore.
- Isochron.
- Average Velocity.

The DDC model was created using a 200 x 200 meter grid spacing to match the model defined for the area. Such large grid spacing encompasses a large number of seismic traces which are spaced at approximately 16 meters. Thus, one 200 x 200 meter grid encompasses about 12 traces. While this is acceptable (and produces useful maps) it must be remembered that a seismically delineated fault gap extends for about three traces. The discrimination of the fault gap can be affected by the coarser model grid spacing. The model grid spacing can be changed at any time if so required.

Problems

Problem #1

Oftentimes, the velocity conversion around or beneath faults can be fraught with error. The calculated velocities introduce low or high velocity zones which can cause abnormal push down or pull up of the mapped horizons. These problems are then carried forward to produce non-geologic maps. To alleviate the problem "fake" wells can be introduced. The fake wells use localized regional dip to predict where the horizons should actually be placed. The process is iterated until a best fit is created and the resultant depth converted seismic data and maps look correct. For the current set of seismic lines six fake wells were created. Three wells are along line W-SJ-023 and three wells are along line W-SJ-082-West.

Problem #2 (Figures 16, 17, 18)

If grids are created using only well control there will be wells that do not extend all the way through a given stratigraphic interval and will thus be missing formation tops. Grid surfaces can be created which cross one another creating negative isochore values. This can even occur when using seismic time sections if there is a lack of seismic coverage. To alleviate this problem DDC conversion has a multitude of options available for describing the relationship of one horizon to another. They describe whether a horizon is non-conformable, conformable upward/downward, and whether a horizon pinches out onto another horizon or is terminated by another horizon.

To alleviate this problem estimated formation tops can be added to existing wells using available data from the nearby 3D space such as nearby wells. These estimated tops constrain the DDC algorithm to produce proper grids.

Problem #3 (Figure 19)

The third problem that can arise is when a mapped horizon is of limited extent and terminates against another horizon. Edge effects can produce surfaces that are not geologic.

To mitigate this problem, areally limited formation tops were extended to the grid boundaries by making the depth values equal to the truncating surface. Furthermore, additional wells were added to the project using raster logs so that more formation tops could be used for gridding.

Proper application of these methods requires iteration through added well tops and comparison of the resultant grids. The goal is to add as much data as necessary without adding too much data. The iterative process is time consuming. However, the final product is very good, internally consistent, and geologically correct.

Fault Interpretation (Figures 20, 21, 22, 23)

The original study and many published geologic studies indicate that there are two main bounding faults at the Vedder level. The faults are designated the Pond Fault (in the west) and the Hope Fault (in the

east). The seismic data utilized for this study found that in the vicinity of the project area the Pond Fault system is comprised of three faults.

Western Area

The original fault picture (prior to the seismic interpretation) showed a northwest to southeast trending fault (Pond Fault). While this simplified fault picture is more or less accurate the fault trend is comprised of two or three faults that merge and separate in the area where the western seismic lines are located. The various portions of this fault trend have been named Pond Deep (PD), Pond East (PE), and Pond West (PW). The PW is a minor splay which only cuts the Vedder and Walker formations over a very limited area.

The original extension away from the seismic area has been modified in the northwest to accommodate well control and historical drilling. Historical drilling was designed to test the Vedder Sands (and others) downthrown to the Pond Fault (now called Pond Fault East). The original pre-interpretation fault trend does not match the historical drilling nor does it match the actual well results.

Three wells help define the fault trend to the northwest. They are the Harry Magee Amalgamated Happold 2 (04029229970000), Intex Oil Co Dearinger 46-23 (04029229990000), and the Ebert & Brandt Russell 1 (04029080920000). The PE must run between the Dearinger 46-23 and Russell 1 wells to maintain the proper regional dip. Regional dip at the Vedder level is about 4 degrees to the west-southwest. If the two wells were on the same side of the fault the dip in this area would almost double to more than 7 degrees. Hence, the PE runs between these wells. The fault has been extended along general trend to approximately the Kern County-Tulare County line.

To the southeast the PE terminates at the splay of the PD. The PD runs between the Shell Oil KCL 83-35 (04029306060000) and wells Moriqui Exploration KCL 87-25 (04029306050000) and Tenneco Tenneco-Sun 11X-31 (04029700530000). Inconsistent dip rate changes exist if the fault does not run between these wells.

The PD continues to the southeast where it runs between the Shell Oil KCL A 58-8 (04029307250000) and the Texaco GOW 1 (04029307280000). Again, localized anomalous dip rate changes would exist if the fault did not run between these wells. Hence, the fault runs between these wells. The fault has been terminated to the east-southeast.

These faults with relation to the Vedder Sand horizon can best be seen using 3D visualization.

Eastern Area

The original fault configuration to the east showed at least one fault intersecting the Pond Deep Fault in the south, trending north and turning north-northeast where it ran to the west of the West Jasmin Oil Field.

While such a fault (or faults) may exist at some level it is not observed in either of the two seismic lines that cover that area near the Jasmin and West Jasmin field areas.

Faults at the Vedder level have been incorporated. These faults are found in the Jasmin Field Aquifer Exemption and in the California Oil & Gas Fields Book (commonly known as the Gold Book).

Fault Discussion (Figures 24, 25)
The various faults observed in the Pond Fault trend could be connected as one main fault with a few splay faults if only the deeper formations are examined. However, examining the fault characteristics and trends throughout entire stratigraphic interval yields a picture of a fault group.

Starting in the southeast PD intersects line W-SJ-023 where it traverses the entire vertical section from basement to ground level. There is a splay fault (PE) intersecting PD. Moving north to line EG-ENC-NMF-116-1 the PD starts to fade away while the PE fault now cuts the entire section from basement to ground level. Moving one mile north to line W-SJ-082-West the PE fault continues.

If the PD fault was assumed to be the easternmost fault on each seismic line there would be an abrupt turn in the fault plane between the two northern lines. This would not fit a reasonable geologic picture.

Previous interpretations indicated that the Pond Fault (or fault zone) penetrated the surface. This does not appear to be the case based on the seismic data. The faults appear to terminate below ground surface.

Final Maps, Grids
Final grids were created for the following surfaces:

- Ground Level
- Etchegoin
- Santa Margarita Sand
- Round Mountain (v2). Note this pick is slightly below the formal Round Mountain pick.
- Olcese Sand
- Freeman-Jewett
- Pyramid Hills Sand
- Vedder
    - Vedder 1
    - Vedder 1A
    - Vedder 2
    - Vedder 3
    - Vedder 4
    - Cantleberry Sand
- Walker
- Basement

Note that the grids generally reflect the overall regional picture. Within the oil field boundaries detailed mapping will be necessary to obtain exact contour orientations.

Files Supplied With This Report
The following files have been supplied with this report.

- Fault files.
    - As per request, the fault locations for the pertinent horizons have been provided as a point file so that vertical fault locations can be defined for the modeling portion of the project. Because the fault dips are relatively steep using a point file for locations is a very good approximation.

- Fault line point files at formations Miocene, Santa Margarita, Round Mountain v2, Olcese, Freeman-Jewett, Vedder (used for Pyramid Hills, Vedder1, Vedder1A, Vedder2, Vedder3, Vedder4, and Cantleberry Sand), Walker, and Basement. Files are named using the formation and fault names.
    - Seismic faults
        - 2-Pond East.
        - 2-Pond West.
        - 2-Pond Deep
        - 2-East1
        - 2-East2
    - Faults from CA Gold Book or Aquifer Exemption
        - Jasmin Field
            - Jasmin 1
            - Jasmin 2
            - Jasmin 3
            - Jasmin 4
        - West Jasmin Field
            - Jasmin-West 1
- NOTE: Because the Pyramid Hills and Vedder deposits are directly related the same fault position polylines and polygons have been used for these zones.

- Horizon grids
    - Horizon grid files are based on the model grid nodes as described above and are on a 200 x 200 meter grid spacing. The grid spacing can be modified as required.
    - The format for the horizon derived grids is X, Y, Z.
        - Etchegoin
        - Miocene
        - Santa Margarita
        - Round Mountain v2
        - Olcese
        - Freeman-Jewett
        - Pyramid Hills
        - Vedder tops
            - Vedder 1
            - Vedder 1A
            - Vedder 2
            - Vedder 3
            - Vedder 4
            - Cantleberry Sand
        - Walker
        - Basement
    - Isochore grid files are provided for the following intervals.
        - Surface - Etchegoin
        - Etchegoin - Miocene
        - Miocene - Santa Margarita
        - Santa Margarita - Round Mountain v2
        - Round Mountain v2 - Olcese
        - Olcese - Freeman-Jewett

        - Freeman-Jewett – Pyramid Hills
        - Pyramid Hills – Vedder 1
        - Vedder 1 – Vedder 1A
        - Vedder 1A – Vedder 2
        - Vedder 2 – Vedder 3
        - Vedder 3 – Vedder 4
        - Vedder 4 – Cantleberry Sand
        - Cantleberry Sand – Walker
        - Vedder1 - Walker
        - Walker-Basement
        - Vedder 1 – Walker (composite of all of the Vedder interval)
- Cross Sections Files
    - The XYZ values for each of the individual horizons have been output along cross section lines A, B, C, D, and E.
    - The grids were exported every 100 feet.

Donald S. Greenfield PGp
California Professional Geophysicist #963

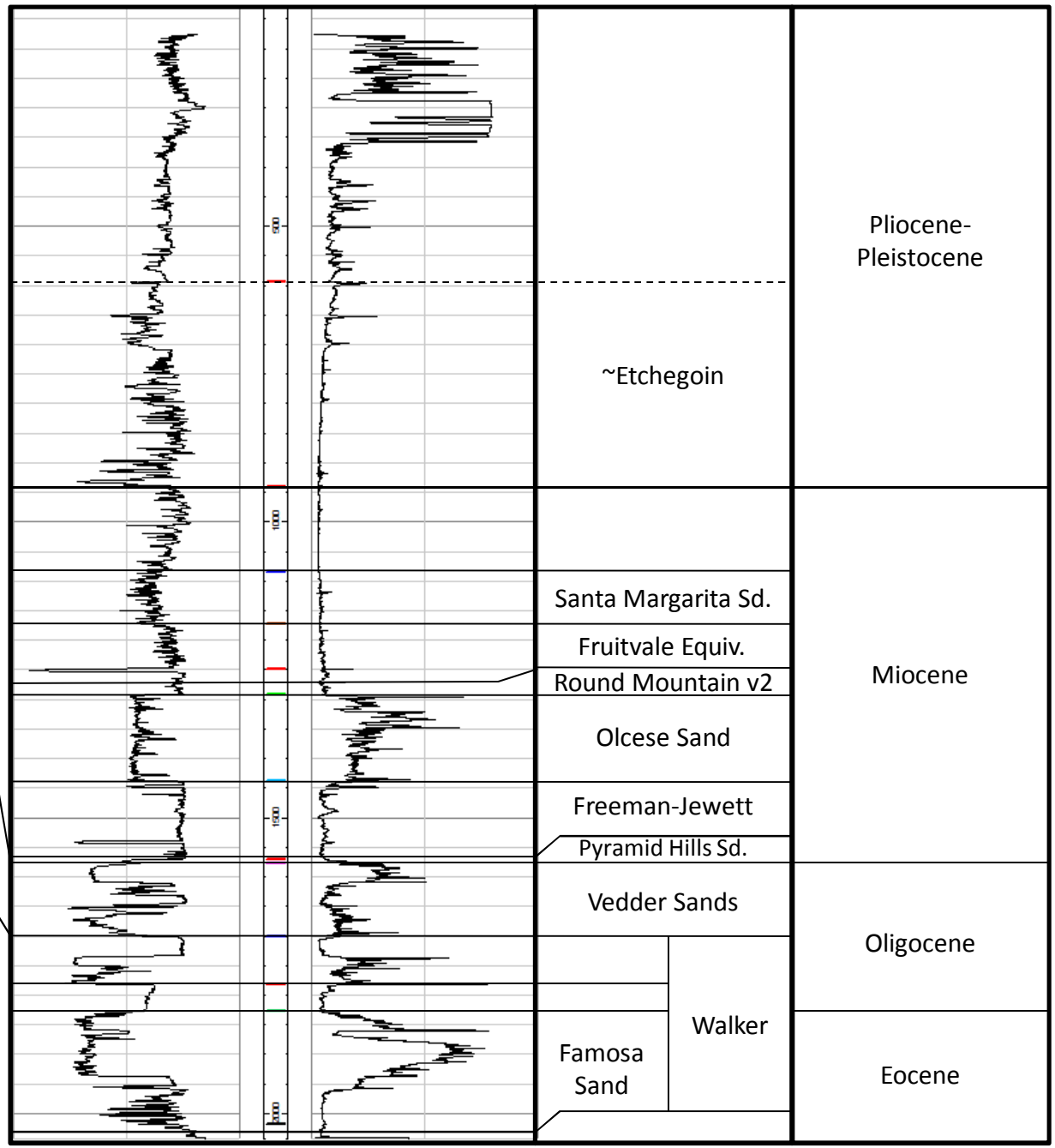

NOTE: The Vedder Sands have been broken out into sub-sands:

- Vedder 1
- Vedder 1A
- Vedder 2
- Vedder 3
- Vedder 4
- Cantleberry Sand

Keystone Diversified Energy Inc

Frontline Project

Figure 1
Simplified Stratigraphic Column
(from CA Gold Book)

DSG

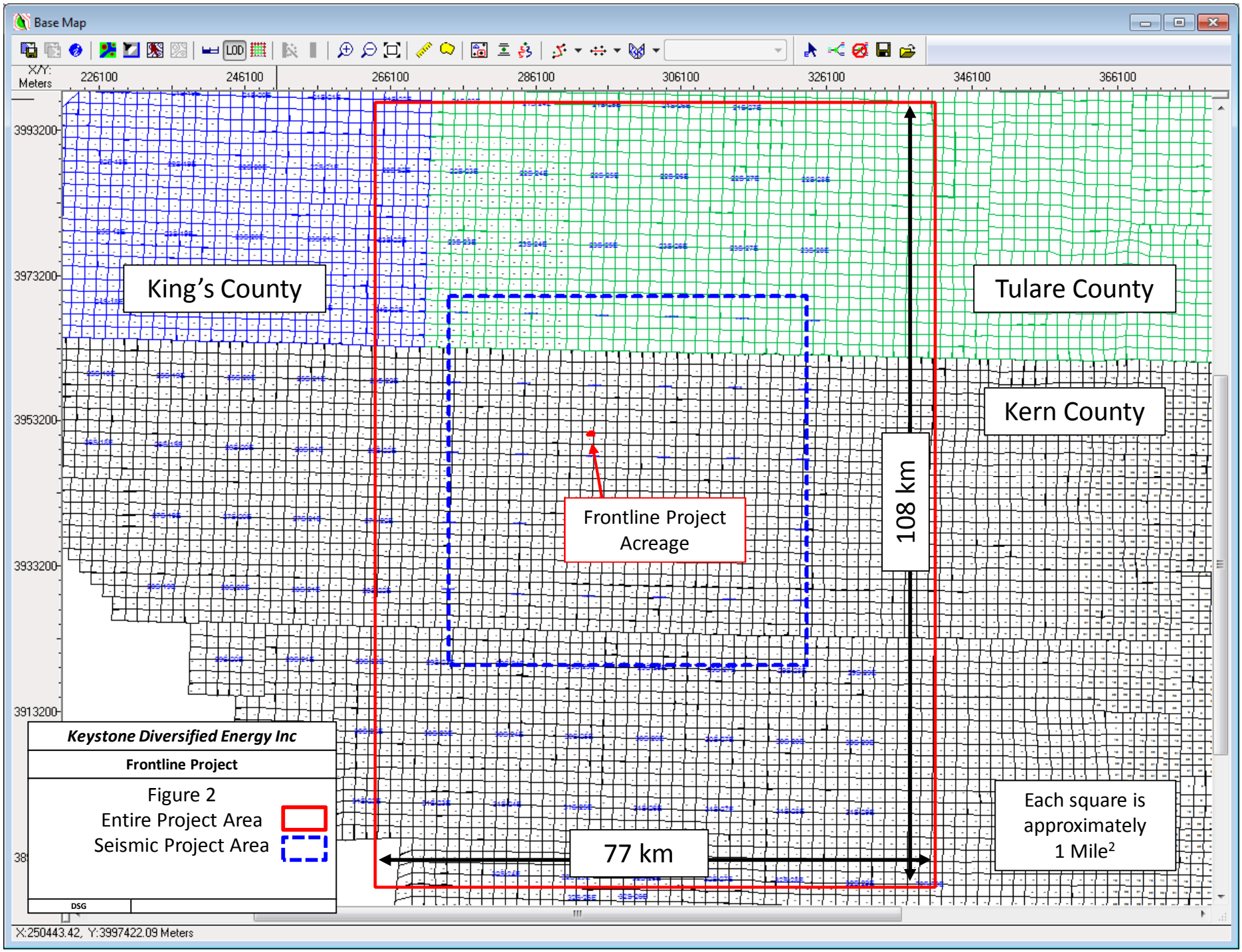
Base Map
X/Y: Meters
226100
246100
266100
286100
306100
326100
346100
366100
3993200
3973200
3953200
3933200
3913200
King's County
Tulare County
Kern County
Frontline Project Acreage
108 km
77 km
Each square is approximately 1 Mile²
Keystone Diversified Energy Inc
Frontline Project
Figure 2
Entire Project Area
Seismic Project Area
DSG
X:250443.42, Y:3997422.09 Meters

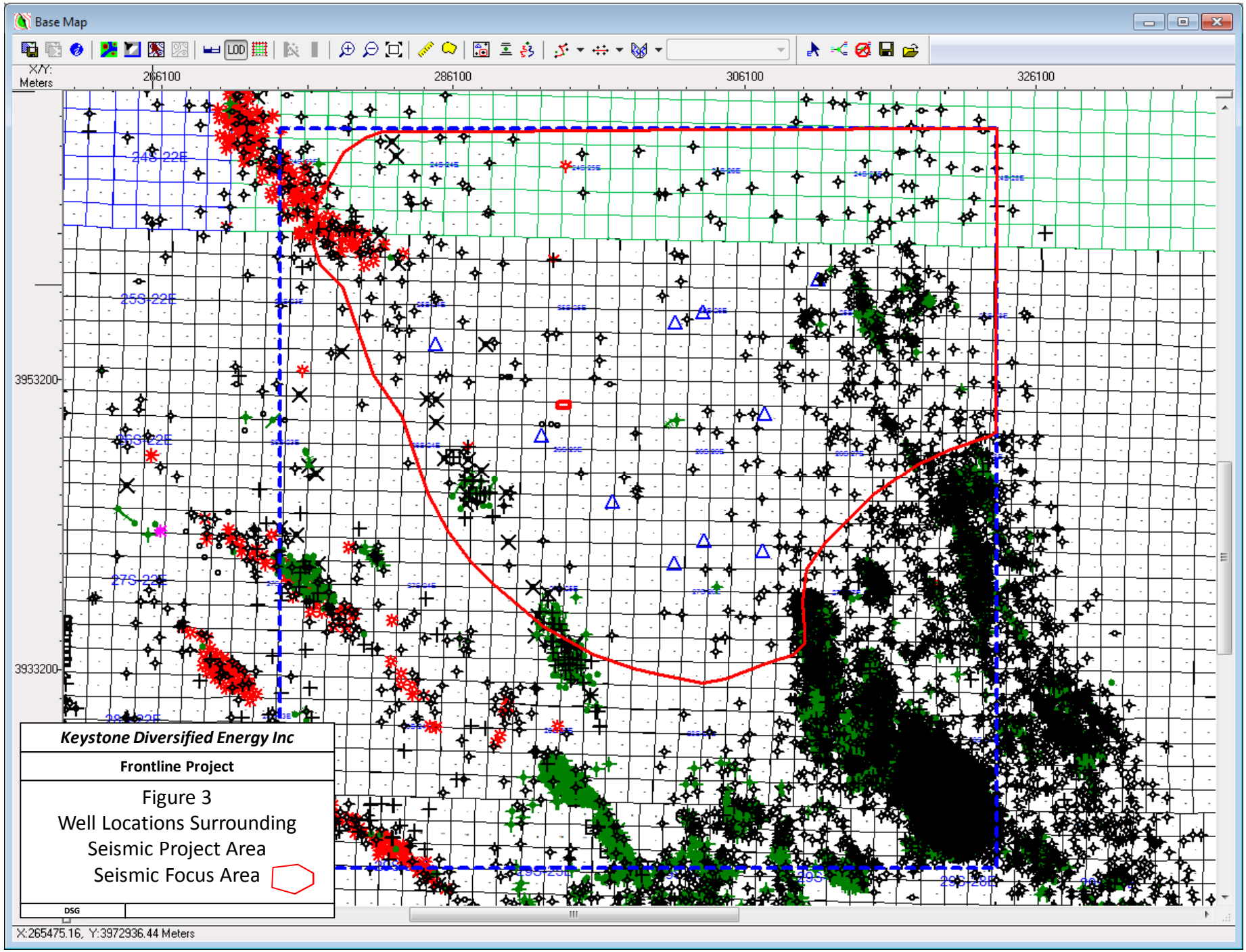
Base Map
X/Y:
Meters
286100
286100
306100
326100
24S-22E
25S-22E
3953200
3933200
27S-22E
Keystone Diversified Energy Inc
Frontline Project
Figure 3
Well Locations Surrounding
Seismic Project Area
Seismic Focus Area
DSG
X:265475.16, Y:3972936.44 Meters

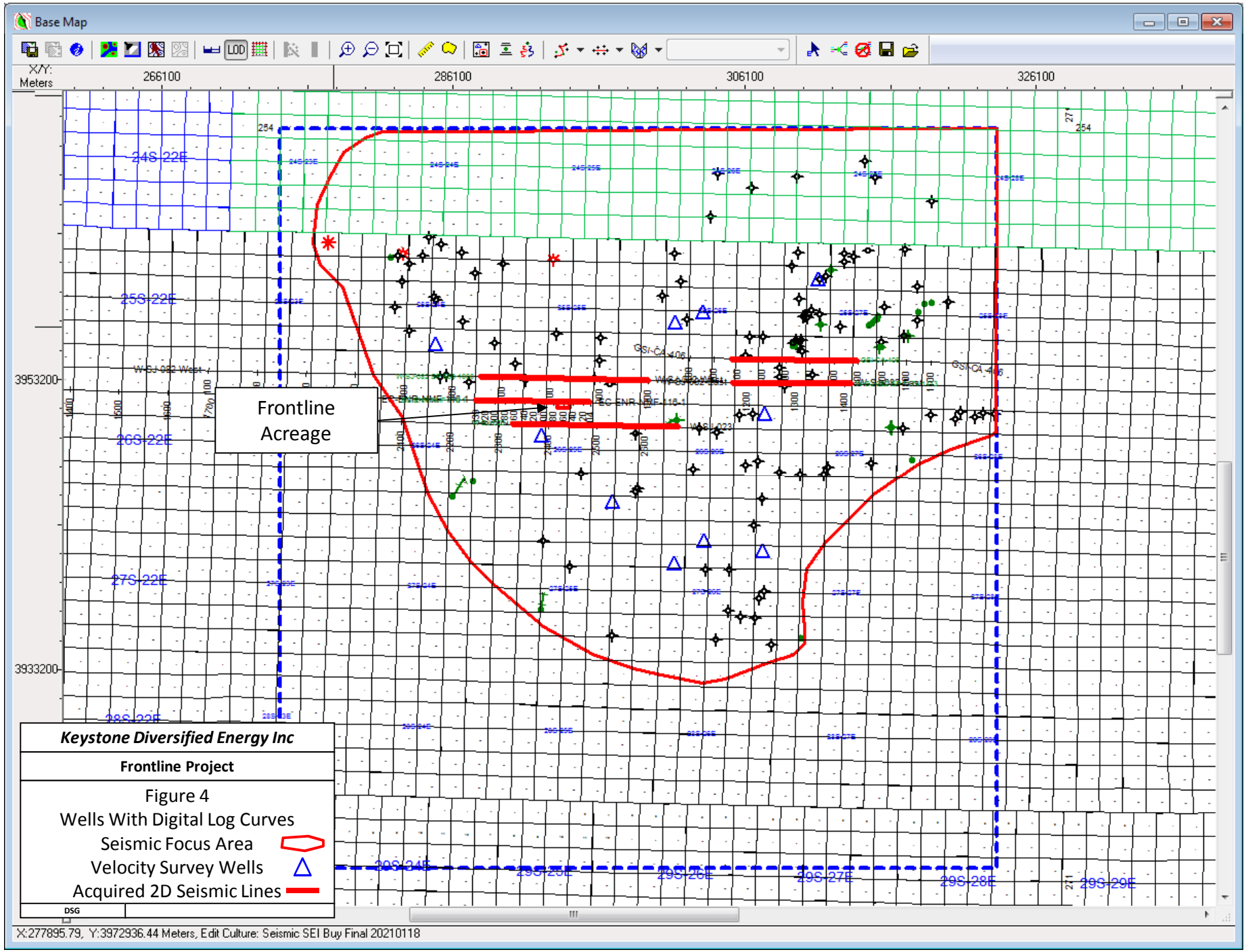
Base Map
X/Y: Meters
266100
286100
306100
326100
3953200
3933200
24S-22E
25S-22E
26S-22E
27S-22E
28S-22E
29S-24E
29S-25E
29S-26E
29S-27E
29S-28E
29S-29E
Frontline Acreage
Keystone Diversified Energy Inc
Frontline Project
Figure 4
Wells With Digital Log Curves
Seismic Focus Area
Velocity Survey Wells
Acquired 2D Seismic Lines
DSG
X:277895.79, Y:3972936.44 Meters, Edit Culture: Seismic SEI Buy Final 20210118

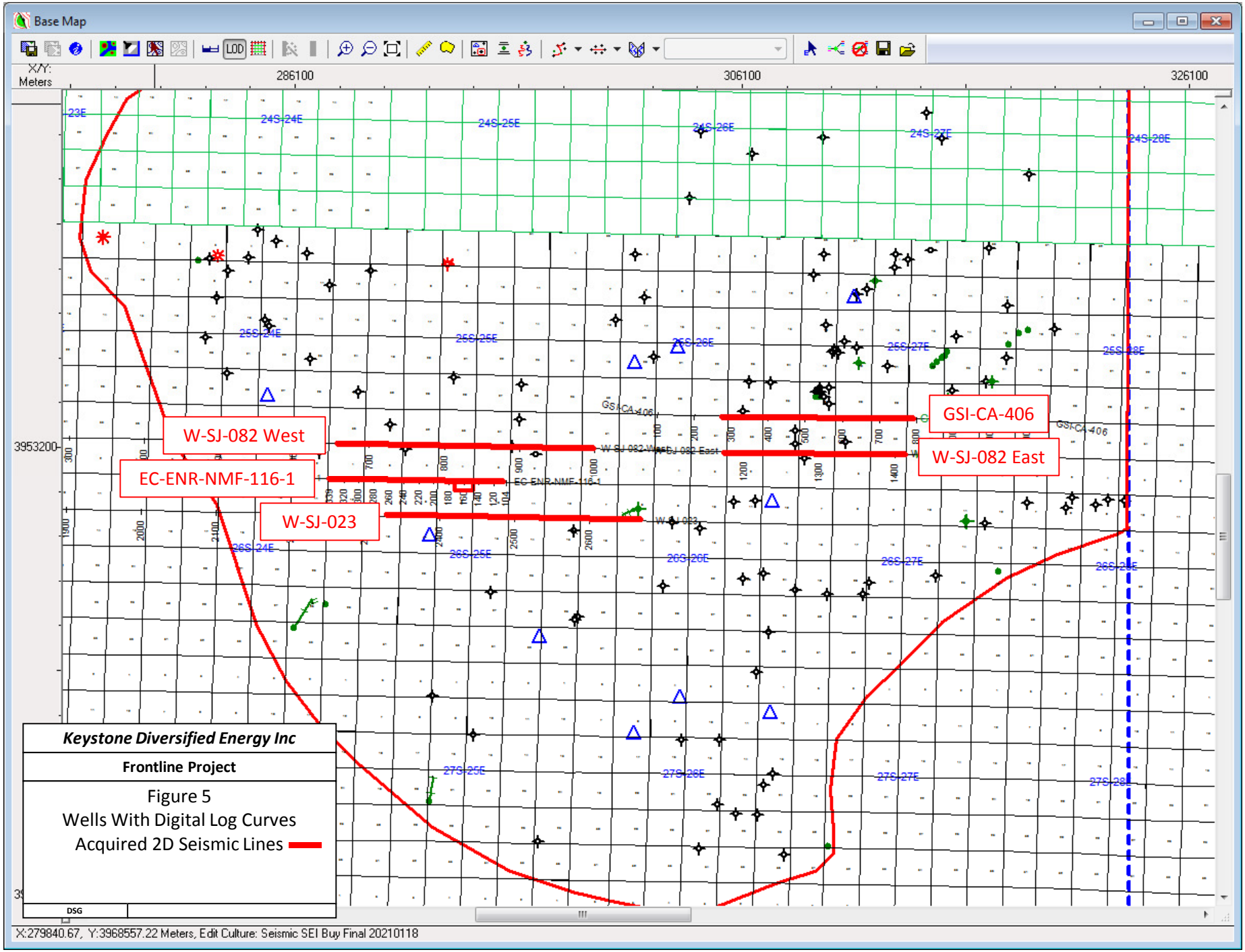
Base Map
X/Y:
Meters
286100
306100
326100
3953200
W-SJ-082 West
EC-ENR-NMF-116-1
W-SJ-023
GSI-CA-406
W-SJ-082 East
Keystone Diversified Energy Inc
Frontline Project
Figure 5
Wells With Digital Log Curves
Acquired 2D Seismic Lines
DSG
X:279840.67, Y:3968557.22 Meters, Edit Culture: Seismic SEI Buy Final 20210118

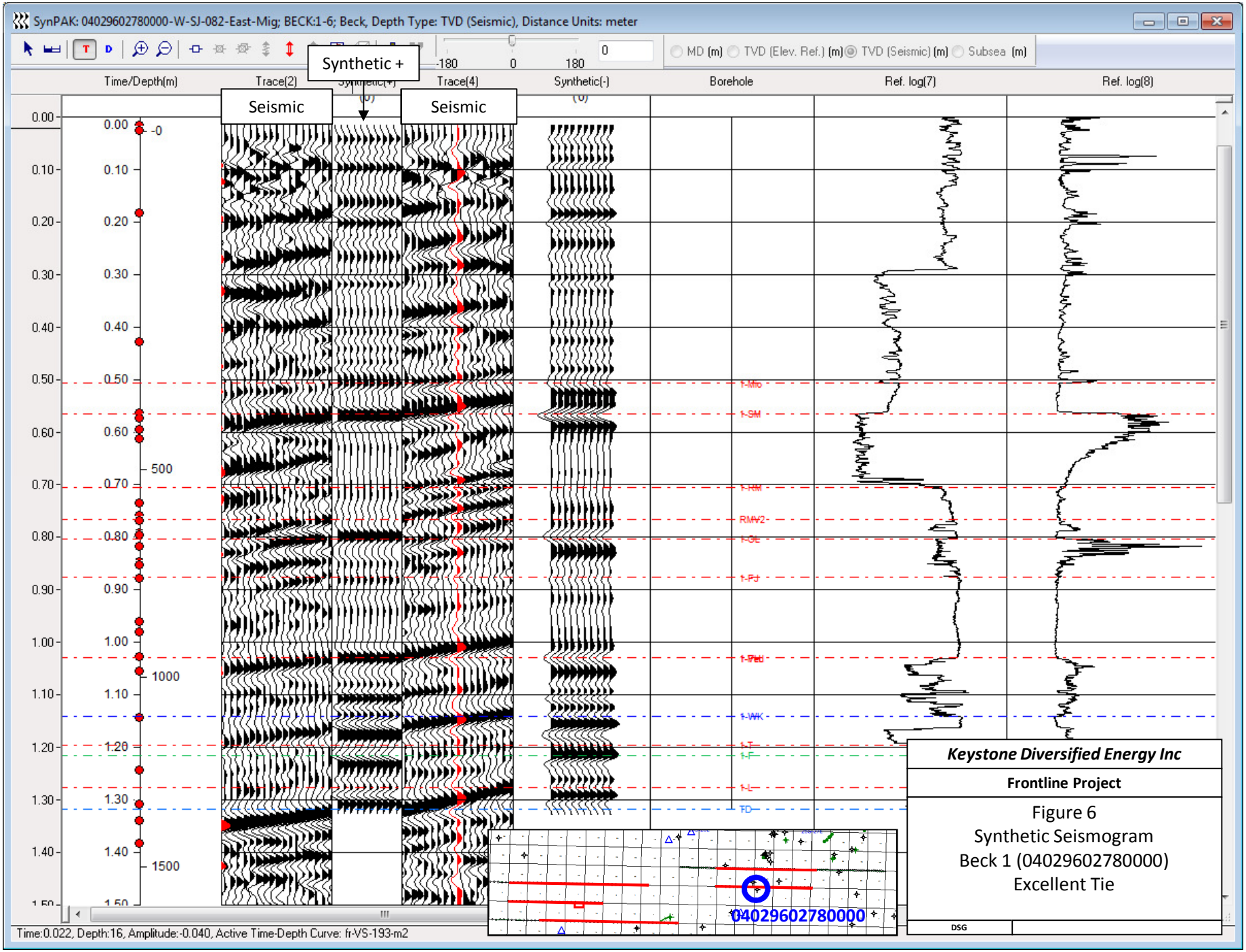
SynPAK: 04029602780000-W-SJ-082-East-Mig; BECK:1-6; Beck, Depth Type: TVD (Seismic), Distance Units: meter
MD (m)
TVD (Elev. Ref.) (m)
TVD (Seismic) (m)
Subsea (m)
Synthetic +
Time/Depth(m)
Trace(2)
Trace(4)
Synthetic(-)
Borehole
Ref. log(7)
Ref. log(8)
Seismic
Seismic
0.00
0.10
0.20
0.30
0.40
0.50
0.60
0.70
0.80
0.90
1.00
1.10
1.20
1.30
1.40
1.50
500
1000
1500
1-Mfo
1-SM
RMV2
1-PJ
1-WK
1-T
1-F
1-L
TD
04029602780000
Time:0.022, Depth:16, Amplitude:-0.040, Active Time-Depth Curve: fr-VS-193-m2
Keystone Diversified Energy Inc
Frontline Project
Figure 6
Synthetic Seismogram
Beck 1 (04029602780000)
Excellent Tie
DSG

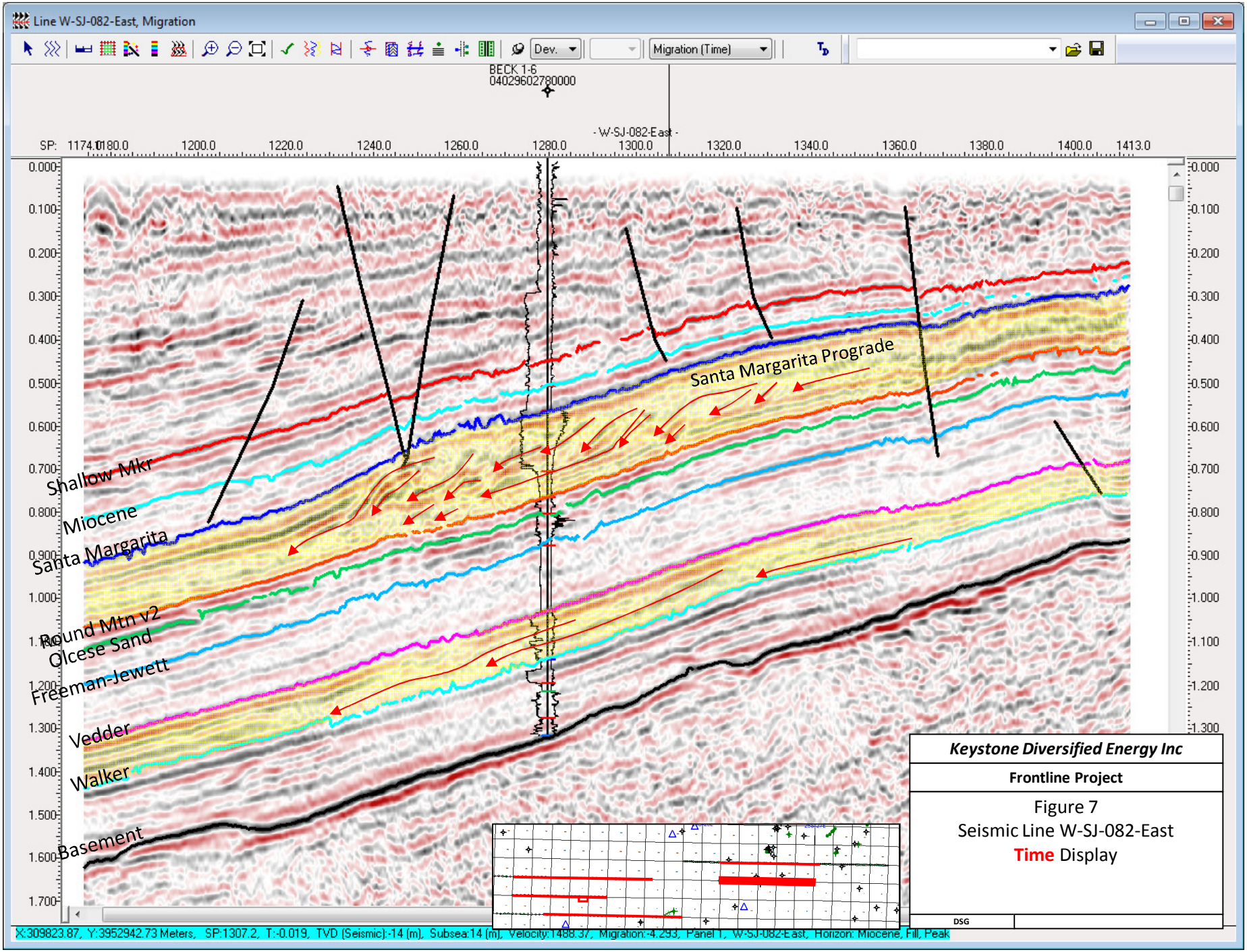
Line W-SJ-082-East, Migration
Dev.
Migration (Time)
BECK 1-6
040296027800000
- W-SJ-082-East -
SP: 1174.0 1180.0 1200.0 1220.0 1240.0 1260.0 1280.0 1300.0 1320.0 1340.0 1360.0 1380.0 1400.0 1413.0
0.000 0.100 0.200 0.300 0.400 0.500 0.600 0.700 0.800 0.900 1.000 1.100 1.200 1.300 1.400 1.500 1.600 1.700
Santa Margarita Prograde
Shallow Mkr
Miocene
Santa Margarita
Round Mtn v2
Olcese Sand
Freeman-Jewett
Vedder
Walker
Basement
Keystone Diversified Energy Inc
Frontline Project
Figure 7
Seismic Line W-SJ-082-East
Time Display
DSG
X:309823.87, Y:3952942.73 Meters, SP:1307.2, T:-0.019, TVD (Seismic):-14 (m), Subsea:14 (m), Velocity:1488.37, Migration:-4.293, Panel 1, W-SJ-082-East, Horizon: Miocene, Fill, Peak

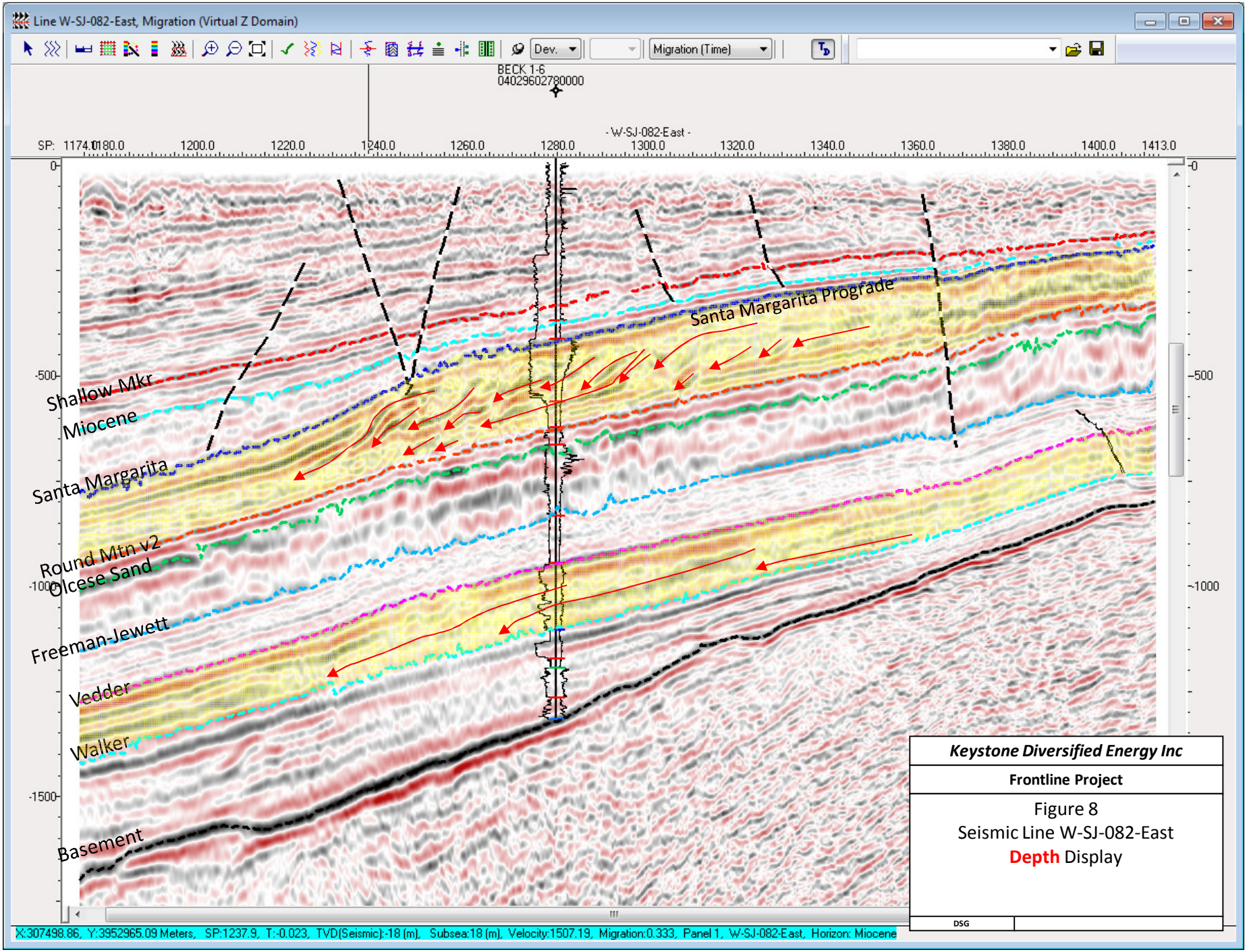
Line W-SJ-082-East, Migration (Virtual Z Domain)
Dev.
Migration (Time)
BECK 1-6
04029602780000
- W-SJ-082-East -
SP: 1174.0
1180.0
1200.0
1220.0
1240.0
1260.0
1280.0
1300.0
1320.0
1340.0
1360.0
1380.0
1400.0
1413.0
0
-500
-1000
-1500
Shallow Mkr
Miocene
Santa Margarita
Round Mtn v2
Olcese Sand
Freeman-Jewett
Vedder
Walker
Basement
Santa Margarita Prograde
X:307498.86, Y:3952965.09 Meters, SP:1237.9, T:-0.023, TVD(Seismic):-18 (m), Subsea:18 (m), Velocity:1507.19, Migration:0.333, Panel 1, W-SJ-082-East, Horizon: Miocene
Keystone Diversified Energy Inc
Frontline Project
Figure 8
Seismic Line W-SJ-082-East
Depth Display
DSG

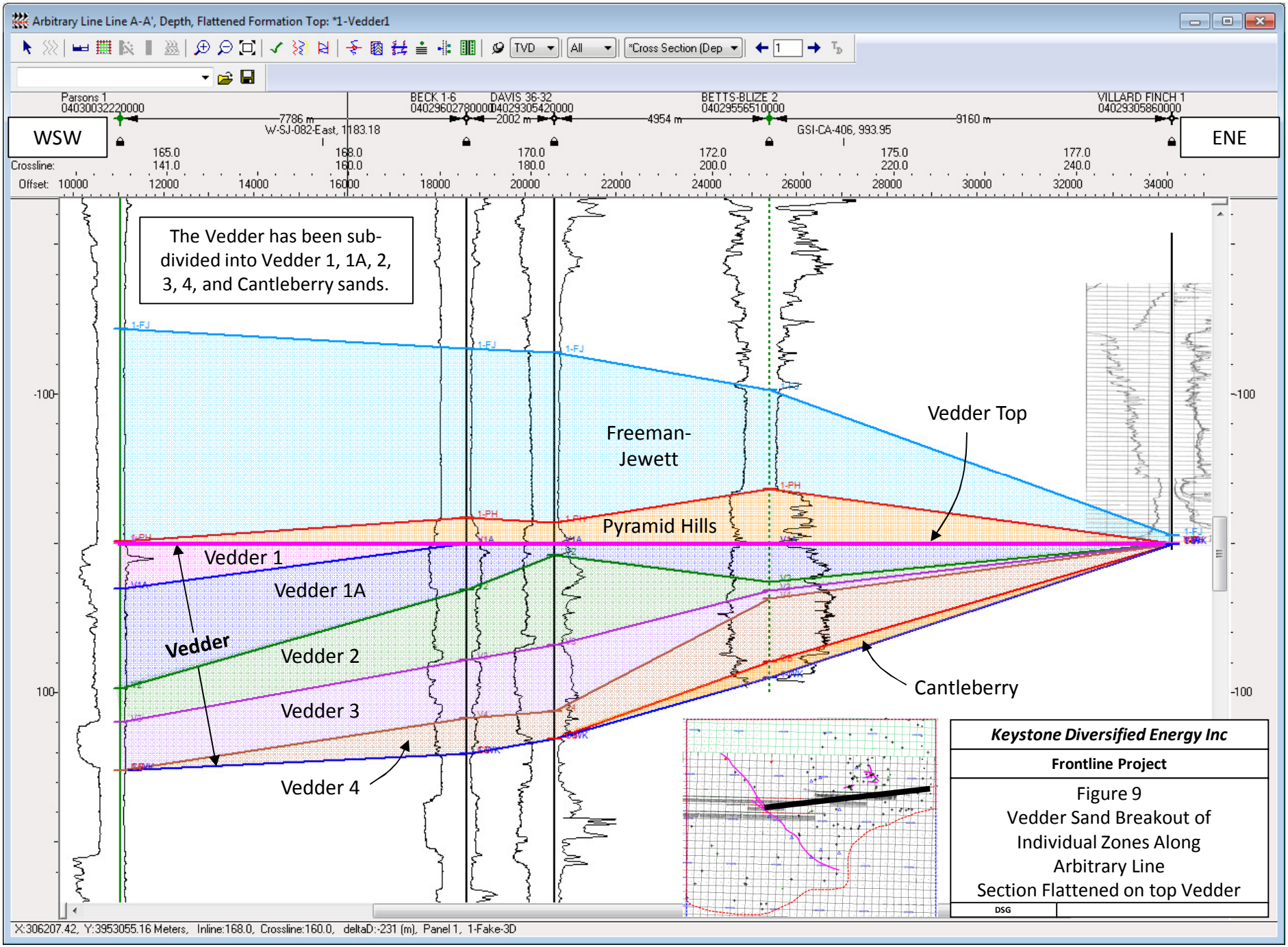
Arbitrary Line Line A-A', Depth, Flattened Formation Top: *1-Vedder1
WSW
ENE
Parsons 1
04030032220000
BECK 1-6
04029602780000
DAVIS 36-32
04029305420000
BETTS-BLIZE 2
04029556510000
VILLARD FINCH 1
04029305860000
7786 m
2002 m
4954 m
9160 m
W-SJ-082-East, 1183.18
GSI-CA-406, 993.95
Crossline:
Offset:
The Vedder has been sub-divided into Vedder 1, 1A, 2, 3, 4, and Cantleberry sands.
Freeman-Jewett
Vedder Top
Pyramid Hills
Vedder 1
Vedder 1A
Vedder
Vedder 2
Vedder 3
Vedder 4
Cantleberry
Keystone Diversified Energy Inc
Frontline Project
Figure 9
Vedder Sand Breakout of Individual Zones Along Arbitrary Line
Section Flattened on top Vedder
DSG
X:306207.42, Y:3953055.16 Meters, Inline:168.0, Crossline:160.0, deltaD:-231 (m), Panel 1, 1-Fake-3D

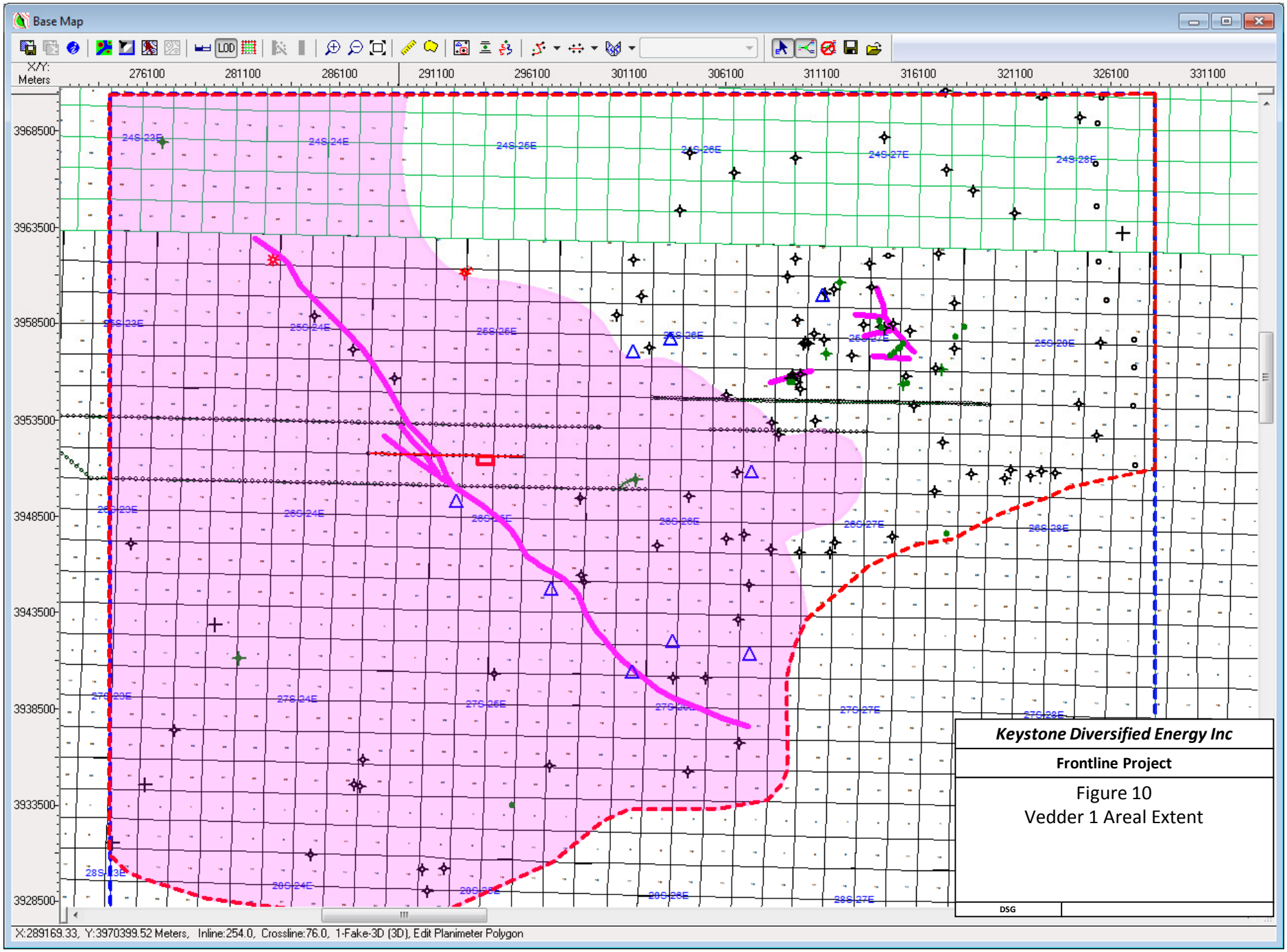
Base Map
X/Y: Meters
276100
281100
286100
291100
296100
301100
306100
311100
316100
321100
326100
331100
3968500
3963500
3958500
3953500
3948500
3943500
3938500
3933500
3928500
24S-23E
24S-24E
24S-25E
24S-26E
24S-27E
24S-28E
25S-23E
25S-24E
25S-25E
25S-26E
25S-27E
25S-28E
26S-23E
26S-24E
26S-25E
26S-26E
26S-27E
26S-28E
27S-23E
27S-24E
27S-25E
27S-26E
27S-27E
27S-28E
28S-23E
28S-24E
28S-25E
28S-26E
28S-27E
Keystone Diversified Energy Inc
Frontline Project
Figure 10
Vedder 1 Areal Extent
DSG
X:289169.33, Y:3970399.52 Meters, Inline:254.0, Crossline:76.0, 1-Fake-3D (3D), Edit Planimeter Polygon

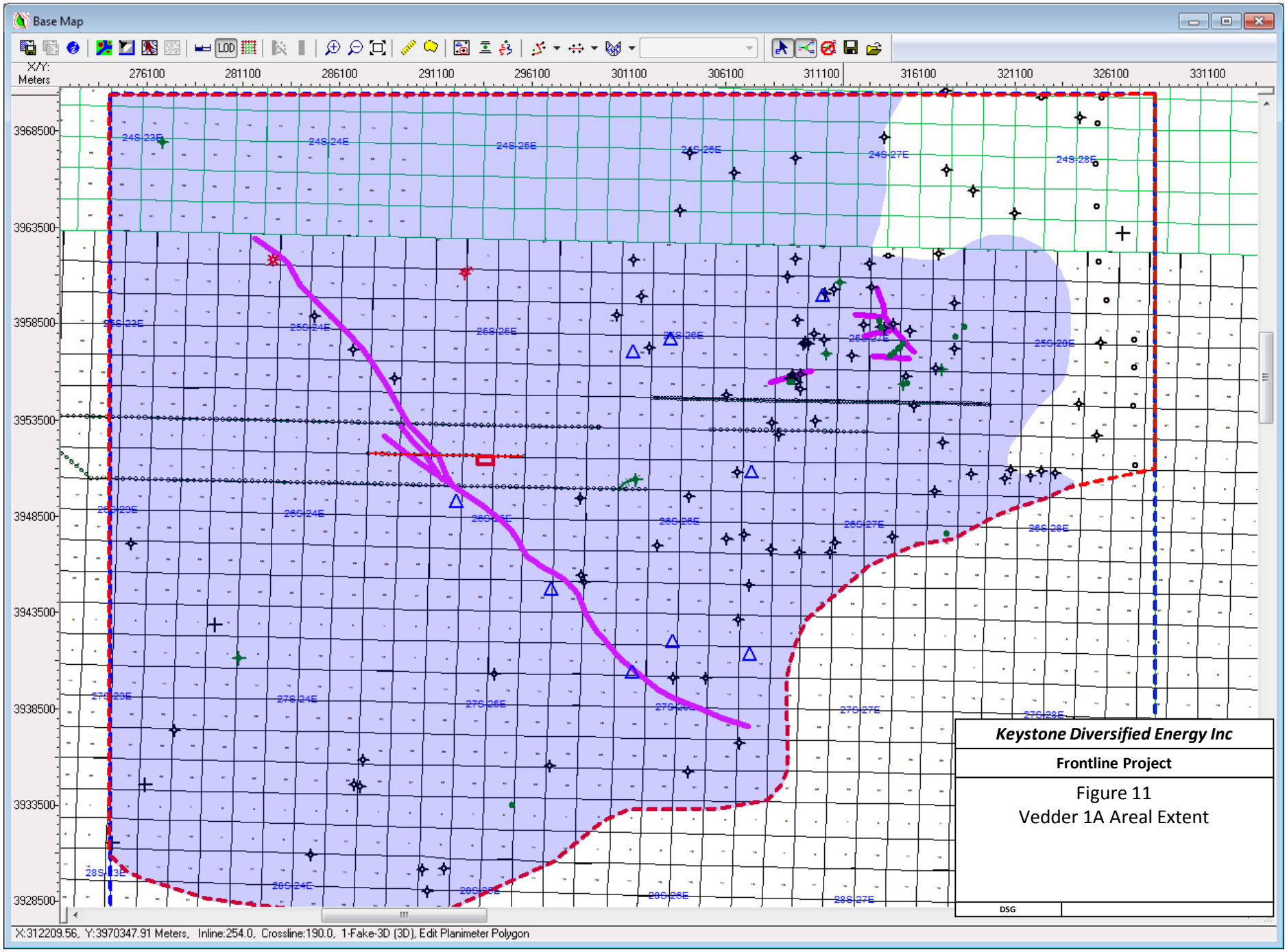
Base Map
X/Y: Meters
276100
281100
286100
291100
296100
301100
306100
311100
316100
321100
326100
331100
3968500
3963500
3958500
3953500
3948500
3943500
3938500
3933500
3928500
24S-23E
24S-24E
24S-25E
24S-26E
24S-27E
24S-28E
25S-23E
25S-24E
25S-25E
25S-26E
25S-27E
25S-28E
26S-23E
26S-24E
26S-25E
26S-26E
26S-27E
26S-28E
27S-23E
27S-24E
27S-25E
27S-26E
27S-27E
27S-28E
28S-23E
28S-24E
28S-25E
28S-26E
28S-27E
Keystone Diversified Energy Inc
Frontline Project
Figure 11
Vedder 1A Areal Extent
DSG
X:312209.56, Y:3970347.91 Meters, Inline:254.0, Crossline:190.0, 1-Fake-3D (3D), Edit Planimeter Polygon

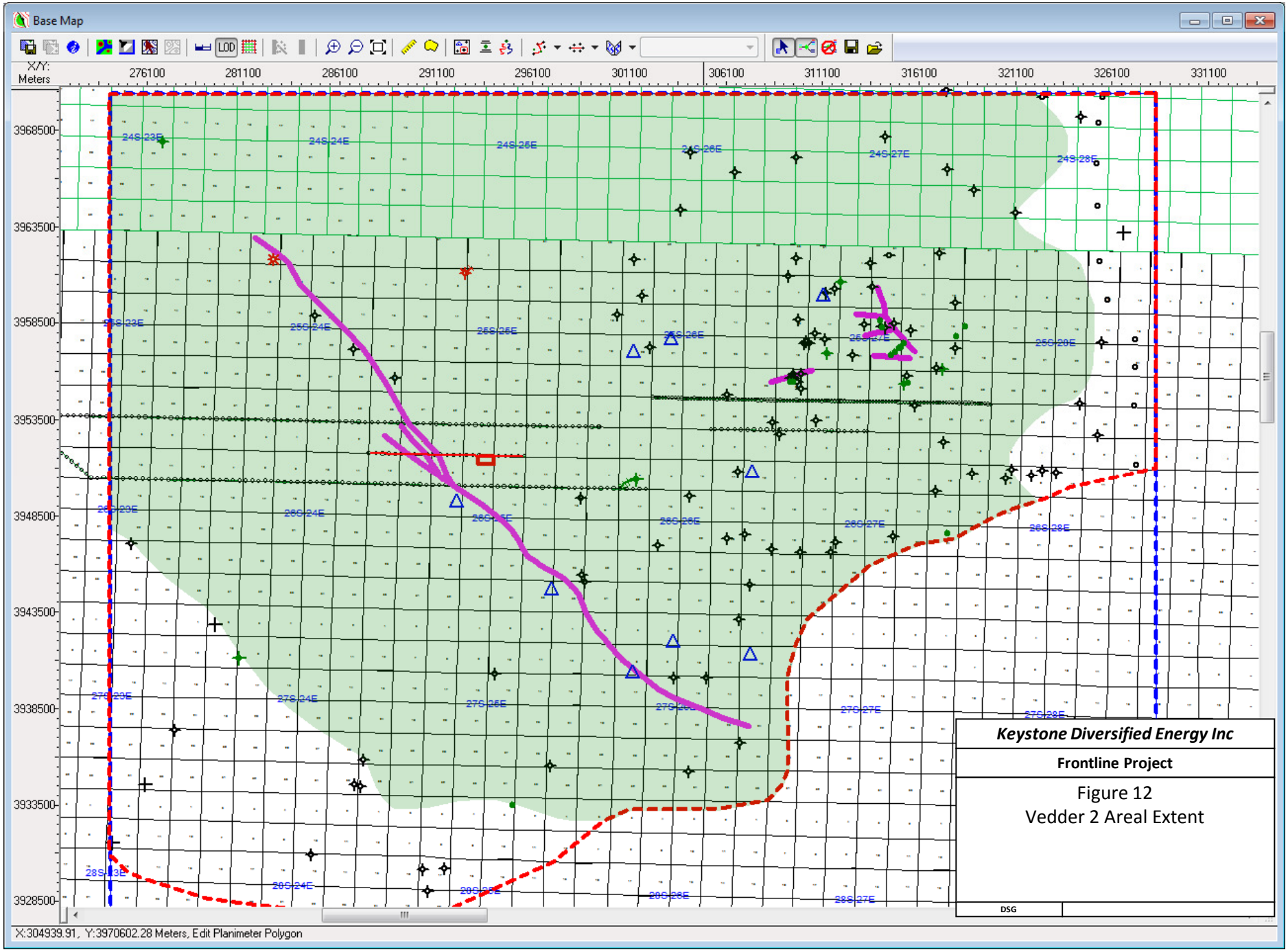
Base Map
X/Y: Meters
276100
281100
286100
291100
296100
301100
306100
311100
316100
321100
326100
331100
3968500
3963500
3958500
3953500
3948500
3943500
3938500
3933500
3928500
24S-23E
24S-24E
24S-25E
24S-26E
24S-27E
24S-28E
25S-23E
25S-24E
25S-25E
25S-26E
25S-27E
25S-28E
26S-23E
26S-24E
26S-25E
26S-26E
26S-27E
26S-28E
27S-23E
27S-24E
27S-25E
27S-26E
27S-27E
27S-28E
28S-23E
28S-24E
28S-25E
28S-26E
28S-27E
Keystone Diversified Energy Inc
Frontline Project
Figure 12
Vedder 2 Areal Extent
DSG
X:304939.91, Y:3970602.28 Meters, Edit Planimeter Polygon

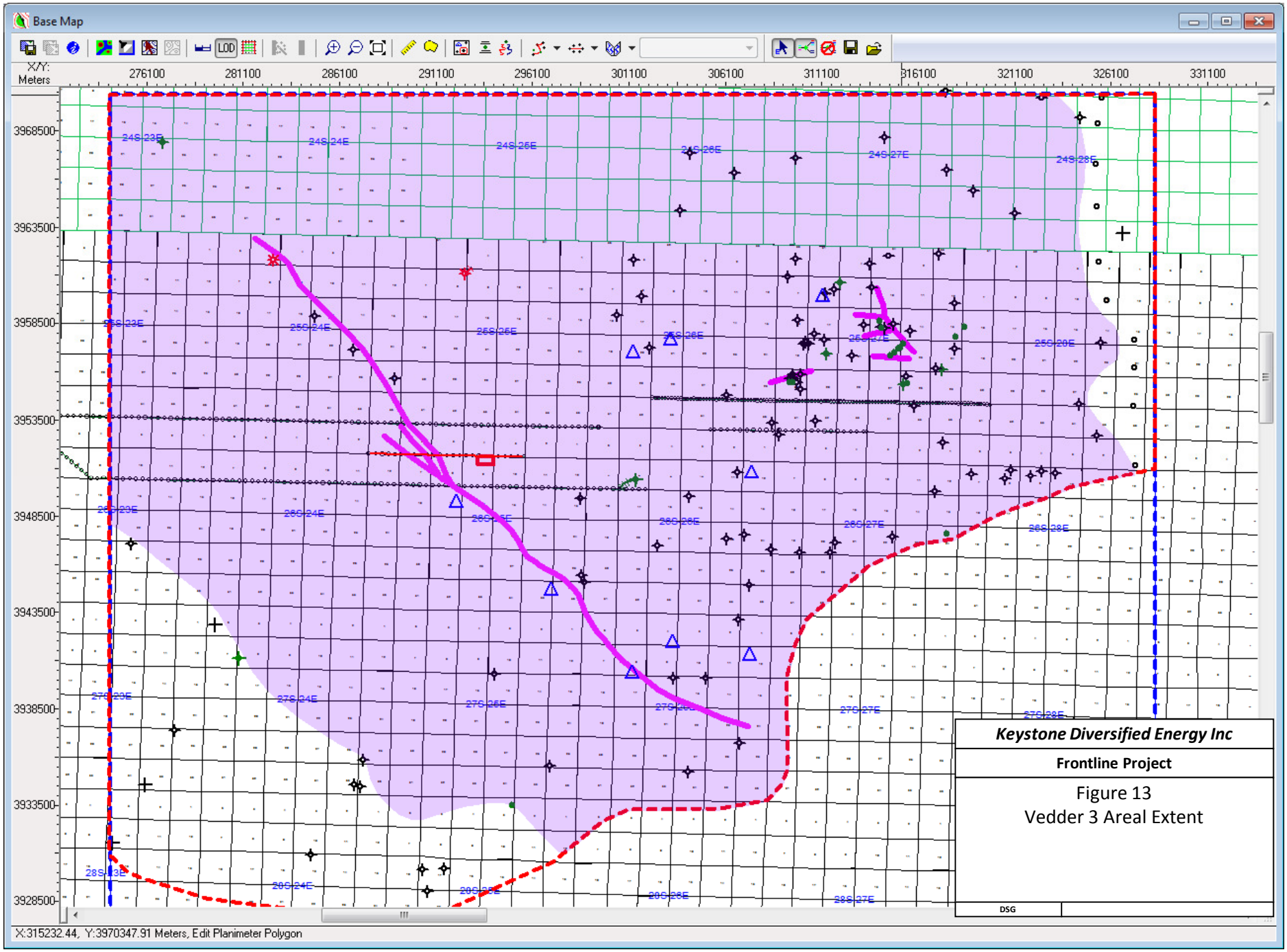
Base Map
X/Y: Meters
276100
281100
286100
291100
296100
301100
306100
311100
316100
321100
326100
331100
3968500
3963500
3958500
3953500
3948500
3943500
3938500
3933500
3928500
24S-23E
24S-24E
24S-25E
24S-26E
24S-27E
24S-28E
25S-23E
25S-24E
25S-25E
25S-26E
25S-27E
25S-28E
26S-23E
26S-24E
26S-25E
26S-26E
26S-27E
26S-28E
27S-23E
27S-24E
27S-25E
27S-26E
27S-27E
27S-28E
28S-23E
28S-24E
28S-25E
28S-26E
28S-27E
Keystone Diversified Energy Inc
Frontline Project
Figure 13
Vedder 3 Areal Extent
DSG
X:315232.44, Y:3970347.91 Meters, Edit Planimeter Polygon

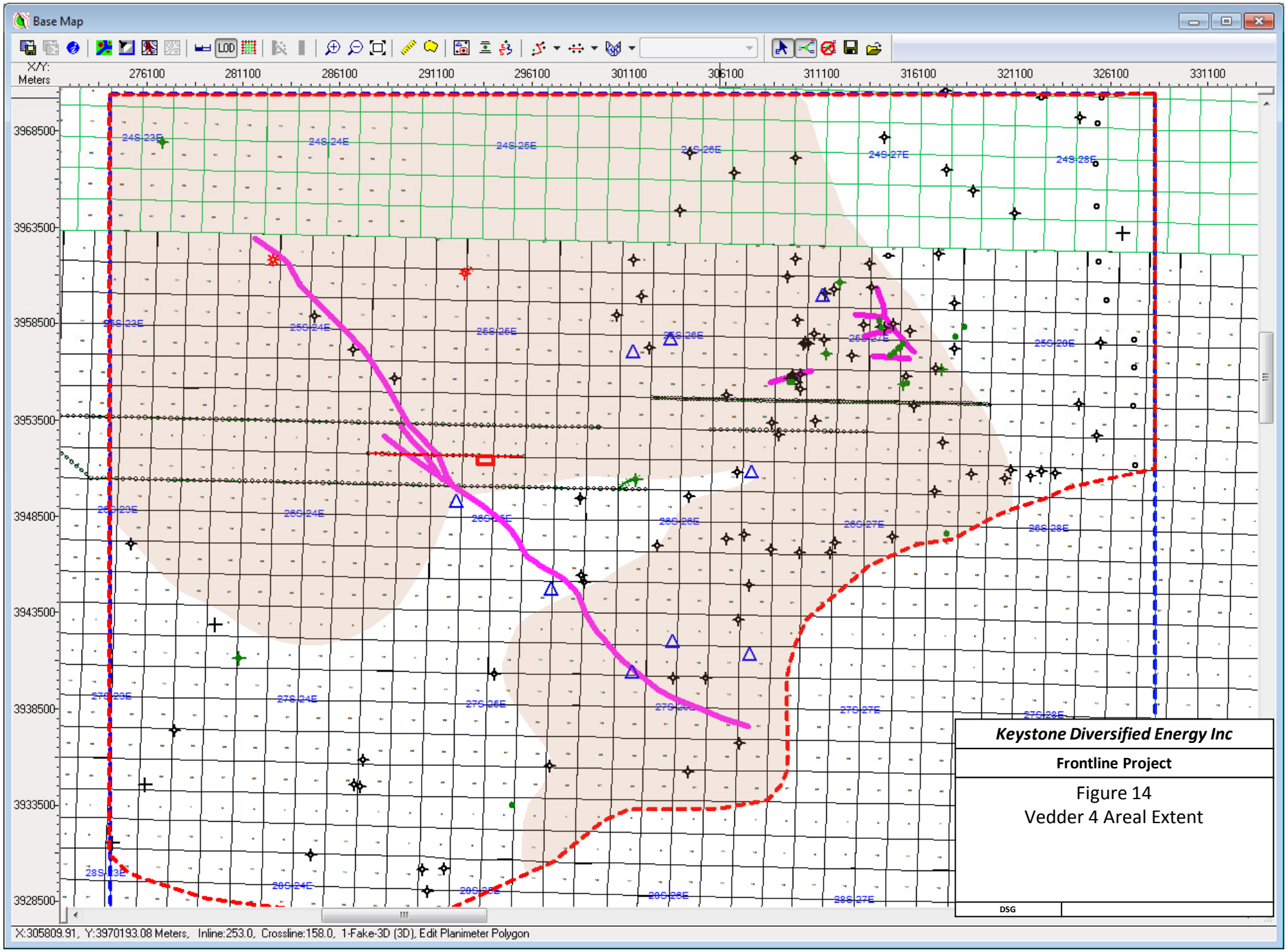
Base Map
X/Y: Meters
276100
281100
286100
291100
296100
301100
306100
311100
316100
321100
326100
331100
3968500
3963500
3958500
3953500
3948500
3943500
3938500
3933500
3928500
24S-23E
24S-24E
24S-25E
24S-26E
24S-27E
24S-28E
25S-23E
25S-24E
25S-25E
25S-26E
25S-27E
25S-28E
26S-23E
26S-24E
26S-25E
26S-26E
26S-27E
26S-28E
27S-23E
27S-24E
27S-25E
27S-26E
27S-27E
27S-28E
28S-23E
28S-24E
28S-25E
28S-26E
28S-27E
Keystone Diversified Energy Inc
Frontline Project
Figure 14
Vedder 4 Areal Extent
DSG
X:305809.91, Y:3970193.08 Meters, Inline:253.0, Crossline:158.0, 1-Fake-3D (3D), Edit Planimeter Polygon

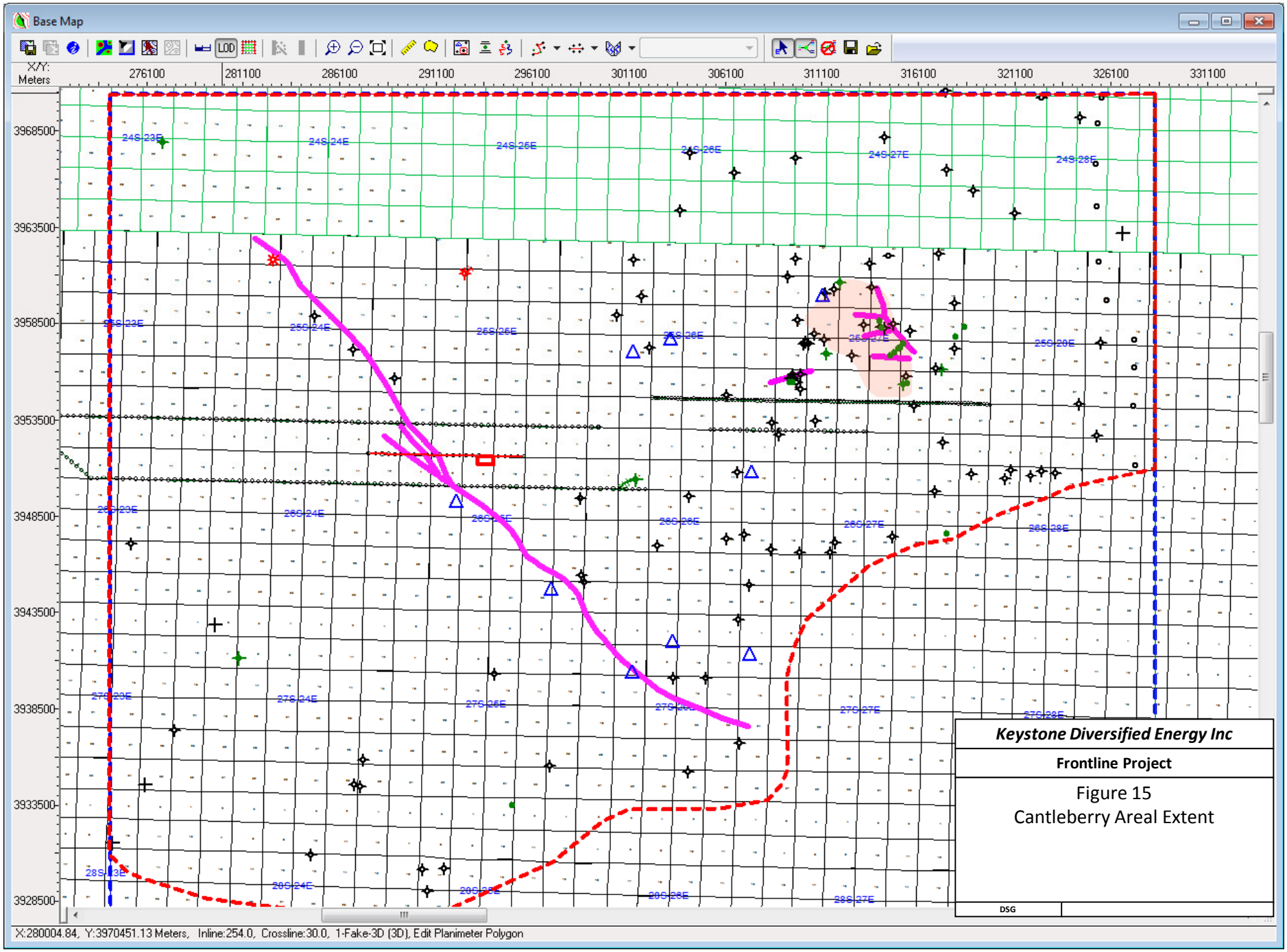
Base Map
X/Y: Meters
276100
281100
286100
291100
296100
301100
306100
311100
316100
321100
326100
331100
3968500
3963500
3958500
3953500
3948500
3943500
3938500
3933500
3928500
24S-23E
24S-24E
24S-25E
24S-26E
24S-27E
24S-28E
25S-23E
25S-24E
25S-25E
25S-26E
25S-27E
25S-28E
26S-23E
26S-24E
26S-25E
26S-26E
26S-27E
26S-28E
27S-23E
27S-24E
27S-25E
27S-26E
27S-27E
27S-28E
28S-23E
28S-24E
28S-25E
28S-26E
28S-27E
Keystone Diversified Energy Inc
Frontline Project
Figure 15
Cantleberry Areal Extent
DSG
X:280004.84, Y:3970451.13 Meters, Inline:254.0, Crossline:30.0, 1-Fake-3D (3D), Edit Planimeter Polygon

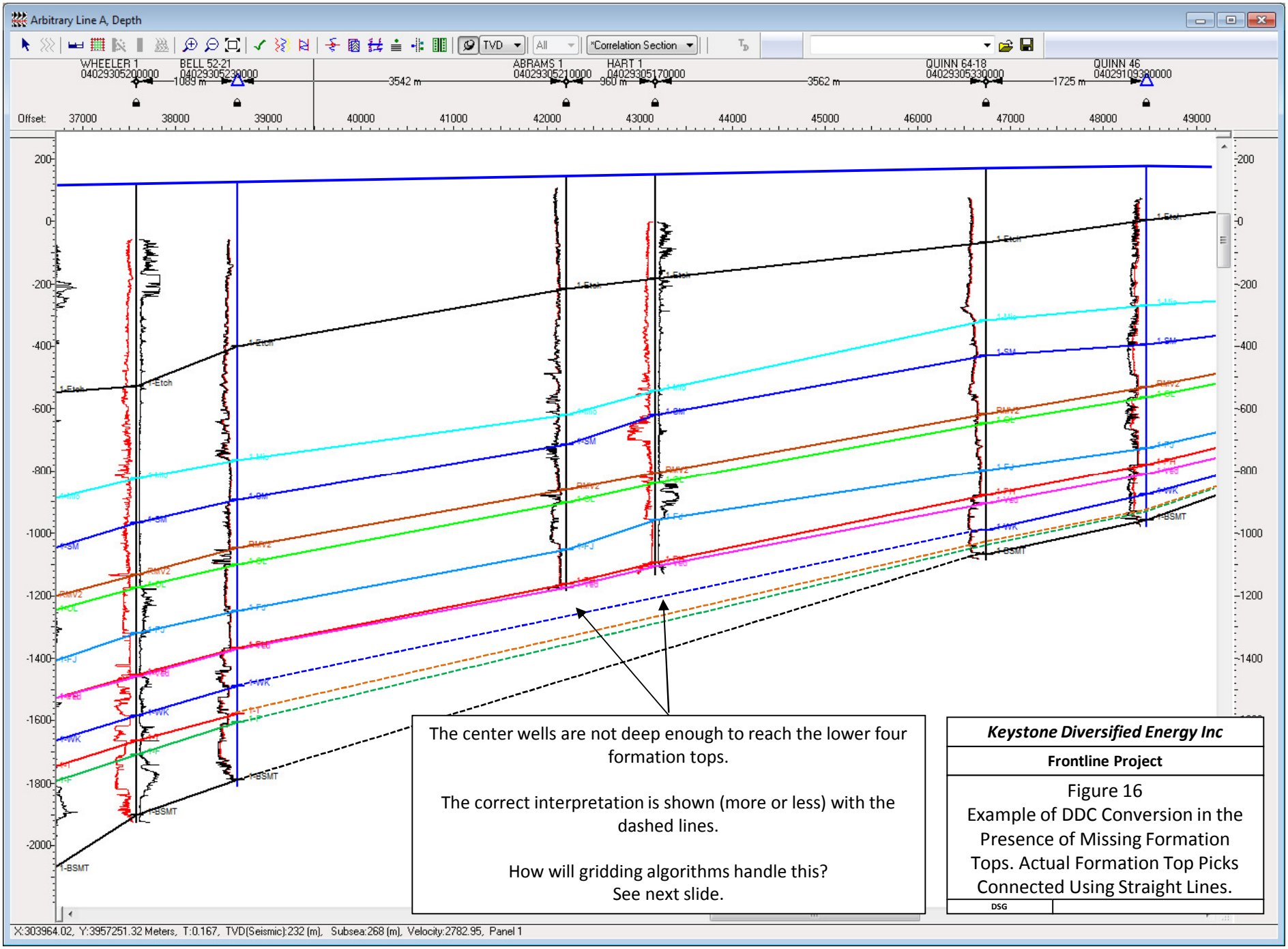

The center wells are not deep enough to reach the lower four formation tops.

The correct interpretation is shown (more or less) with the dashed lines.

How will gridding algorithms handle this?
See next slide.

Keystone Diversified Energy Inc

Frontline Project

Figure 16
Example of DDC Conversion in the Presence of Missing Formation Tops. Actual Formation Top Picks Connected Using Straight Lines.

DSG

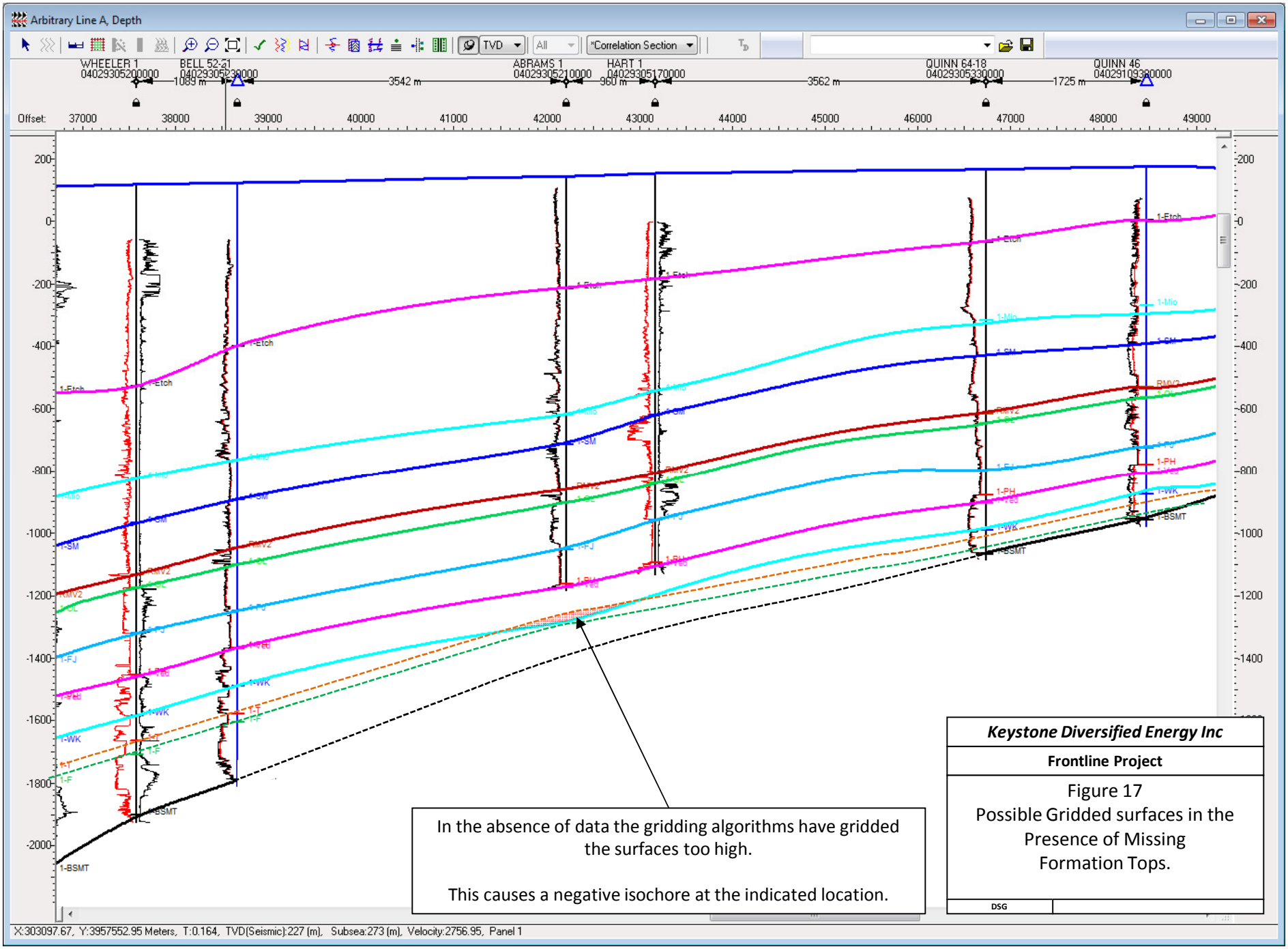
Arbitrary Line A, Depth
WHEELER 1
04029305200000
BELL 52-31
04029305230000
ABRAMS 1
04029305210000
HART 1
04029305170000
QUINN 64-18
04029305330000
QUINN 46
04029109380000
1089 m
3542 m
960 m
3562 m
1725 m
Offset:
37000
38000
39000
40000
41000
42000
43000
44000
45000
46000
47000
48000
49000
200
0
-200
-400
-600
-800
-1000
-1200
-1400
-1600
-1800
-2000
1-Etch
1-Mio
1-SM
1-PH
1-WK
1-BSMT
In the absence of data the gridding algorithms have gridded the surfaces too high.
This causes a negative isochore at the indicated location.
Keystone Diversified Energy Inc
Frontline Project
Figure 17
Possible Gridded surfaces in the Presence of Missing Formation Tops.
DSG
X:303097.67, Y:3957552.95 Meters, T:0.164, TVD(Seismic):227 (m), Subsea:273 (m), Velocity:2756.95, Panel 1

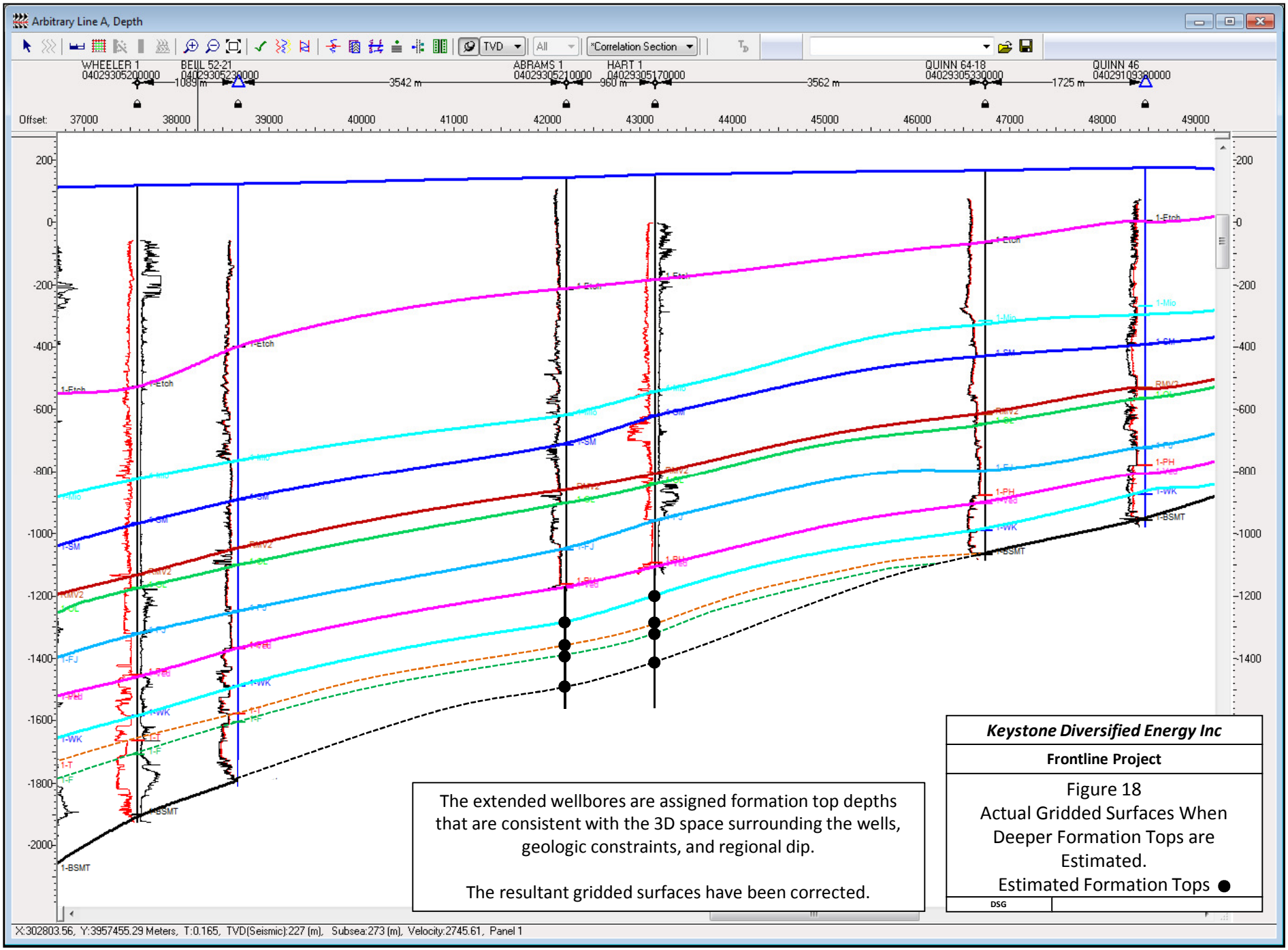

The extended wellbores are assigned formation top depths that are consistent with the 3D space surrounding the wells, geologic constraints, and regional dip.

The resultant gridded surfaces have been corrected.

Keystone Diversified Energy Inc

Frontline Project

Figure 18
Actual Gridded Surfaces When Deeper Formation Tops are Estimated.
Estimated Formation Tops ●

DSG

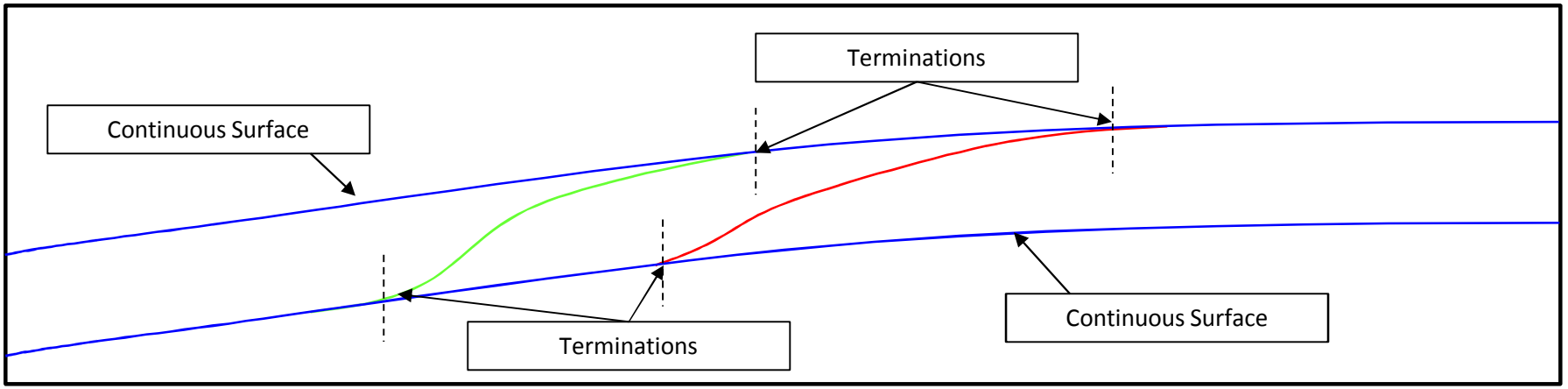

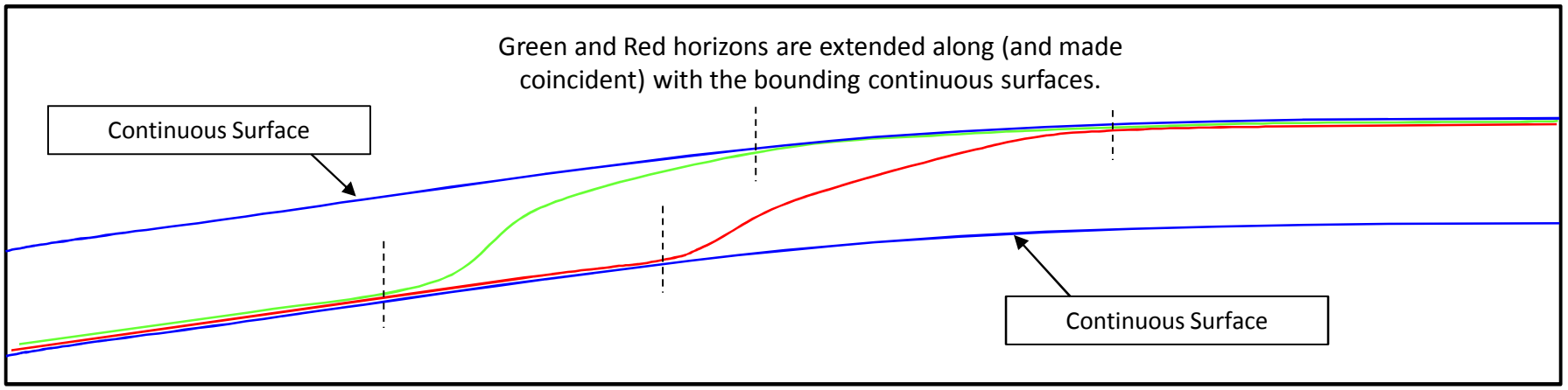

The terminated horizons are extended along the continuous surfaces. This allows the surfaces to be gridded and mapped with little to no edge effects.

Keystone Diversified Energy Inc

Frontline Project

Figure 19
Extension of Areally Limited Formations for Gridding Purposes

DSG

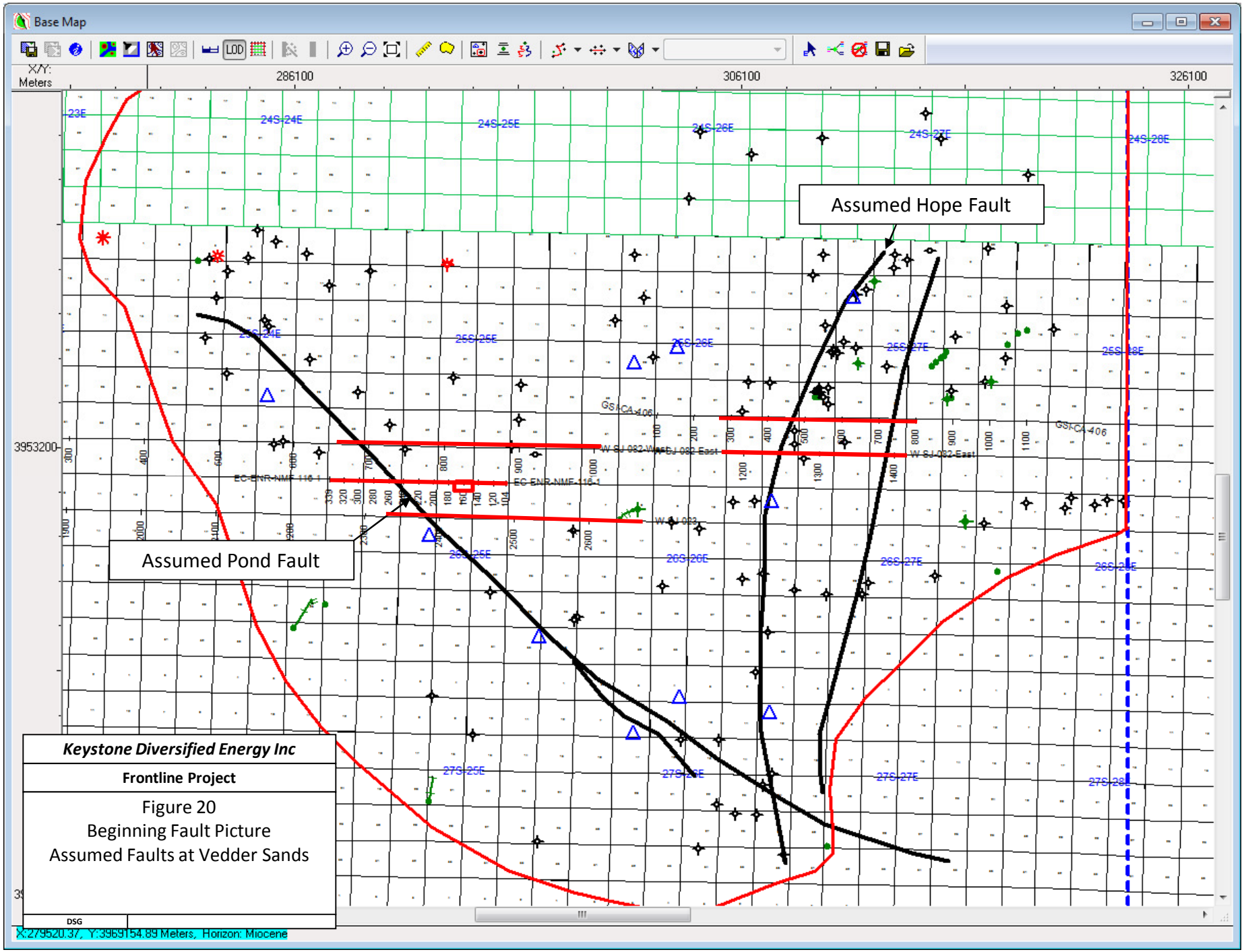

Keystone Diversified Energy Inc

Frontline Project

Figure 20
Beginning Fault Picture
Assumed Faults at Vedder Sands

DSG

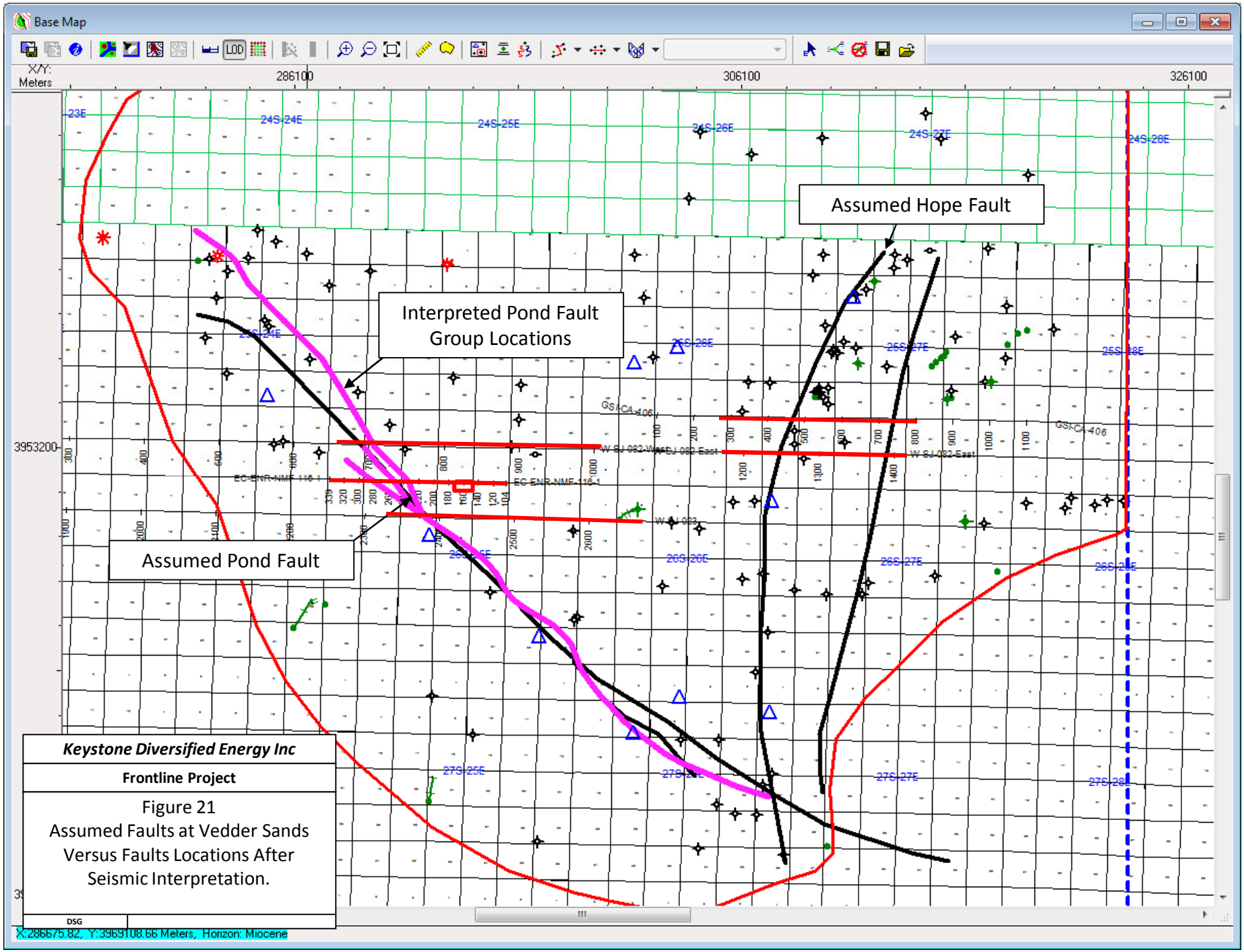
Base Map
X/Y:
Meters
286100
306100
326100
3953200
Assumed Hope Fault
Interpreted Pond Fault
Group Locations
Assumed Pond Fault
23E
24S-24E
24S-25E
24S-26E
24S-27E
24S-28E
25S-26E
25S-27E
26S-26E
26S-27E
27S-25E
27S-27E
GSKCA-406
W SJ 082-West
W SJ 082-East
EC-ENR-NMF-116-1
W SJ 082
Keystone Diversified Energy Inc
Frontline Project
Figure 21
Assumed Faults at Vedder Sands
Versus Faults Locations After
Seismic Interpretation.
DSG
X:286675.82, Y:3969108.66 Meters, Horizon: Miocene

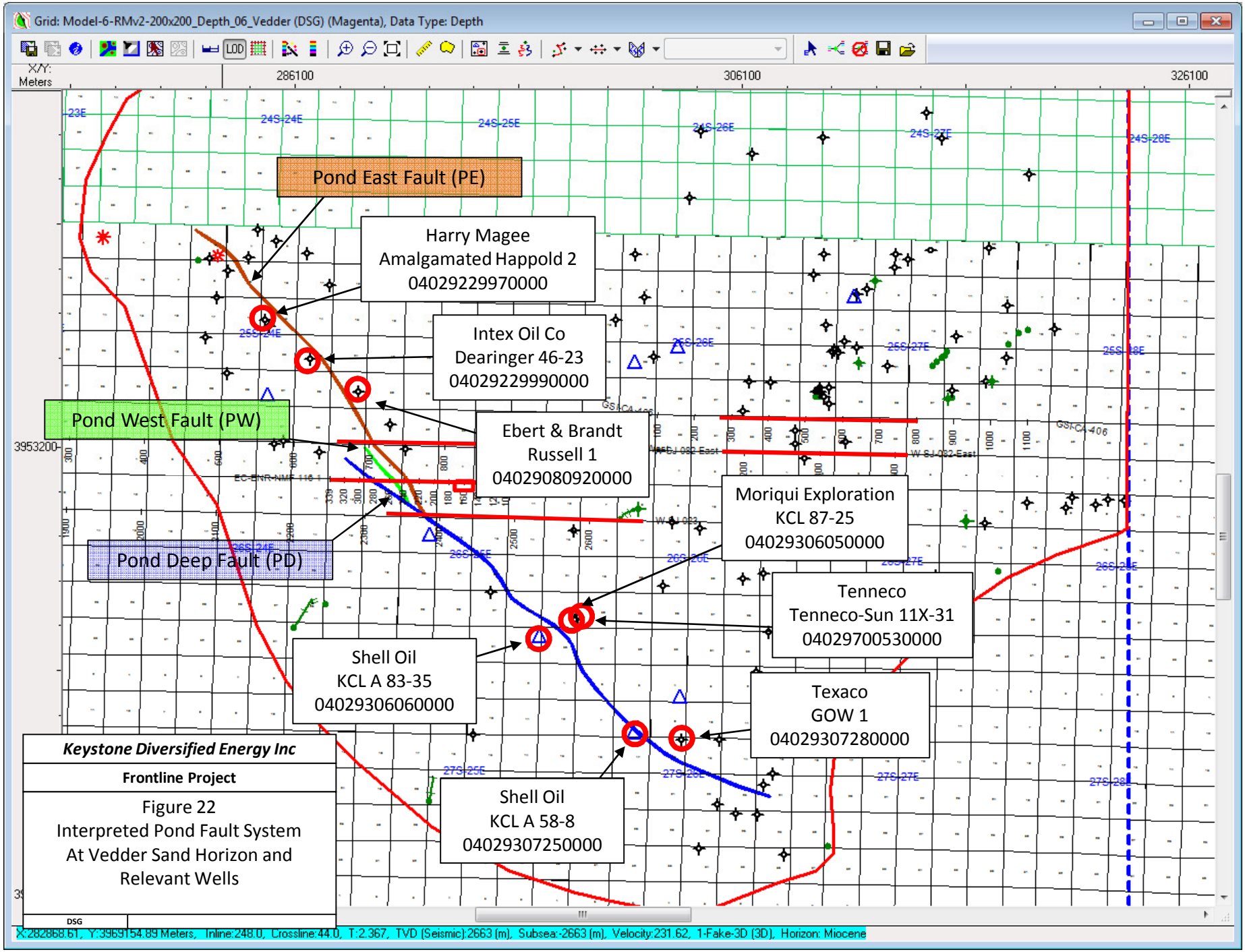
Grid: Model-6-RMv2-200x200_Depth_06_Vedder (DSG) (Magenta), Data Type: Depth
X/Y: Meters
286100
306100
326100
3953200
Pond East Fault (PE)
Harry Magee
Amalgamated Happold 2
04029229970000
Intex Oil Co
Dearinger 46-23
04029229990000
Pond West Fault (PW)
Ebert & Brandt
Russell 1
04029080920000
Moriqui Exploration
KCL 87-25
04029306050000
Pond Deep Fault (PD)
Tenneco
Tenneco-Sun 11X-31
04029700530000
Shell Oil
KCL A 83-35
04029306060000
Texaco
GOW 1
04029307280000
Shell Oil
KCL A 58-8
04029307250000
Keystone Diversified Energy Inc
Frontline Project
Figure 22
Interpreted Pond Fault System
At Vedder Sand Horizon and
Relevant Wells
DSG
X:282868.61, Y:3969154.89 Meters, Inline:248.0, Crossline:44.0, T:2.367, TVD (Seismic):2663 (m), Subsea:-2663 (m), Velocity:231.62, 1-Fake-3D (3D), Horizon: Miocene

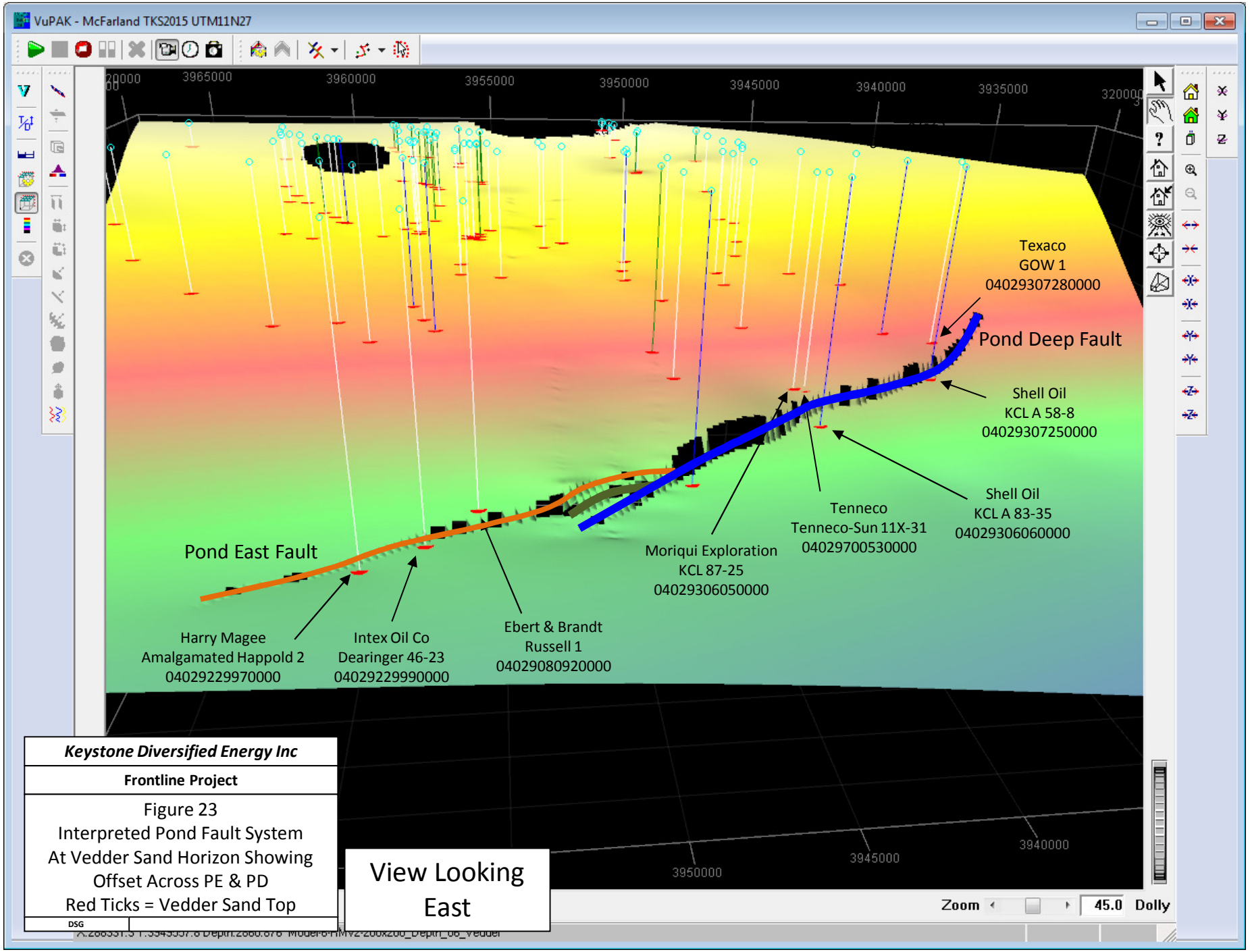

Keystone Diversified Energy Inc
Frontline Project
Figure 23 Interpreted Pond Fault System At Vedder Sand Horizon Showing Offset Across PE & PD Red Ticks = Vedder Sand Top
DSG

View Looking East

Seismic Lines W-SJ-023, EC-ENR-NMF-116-1, W-SJ-082-West

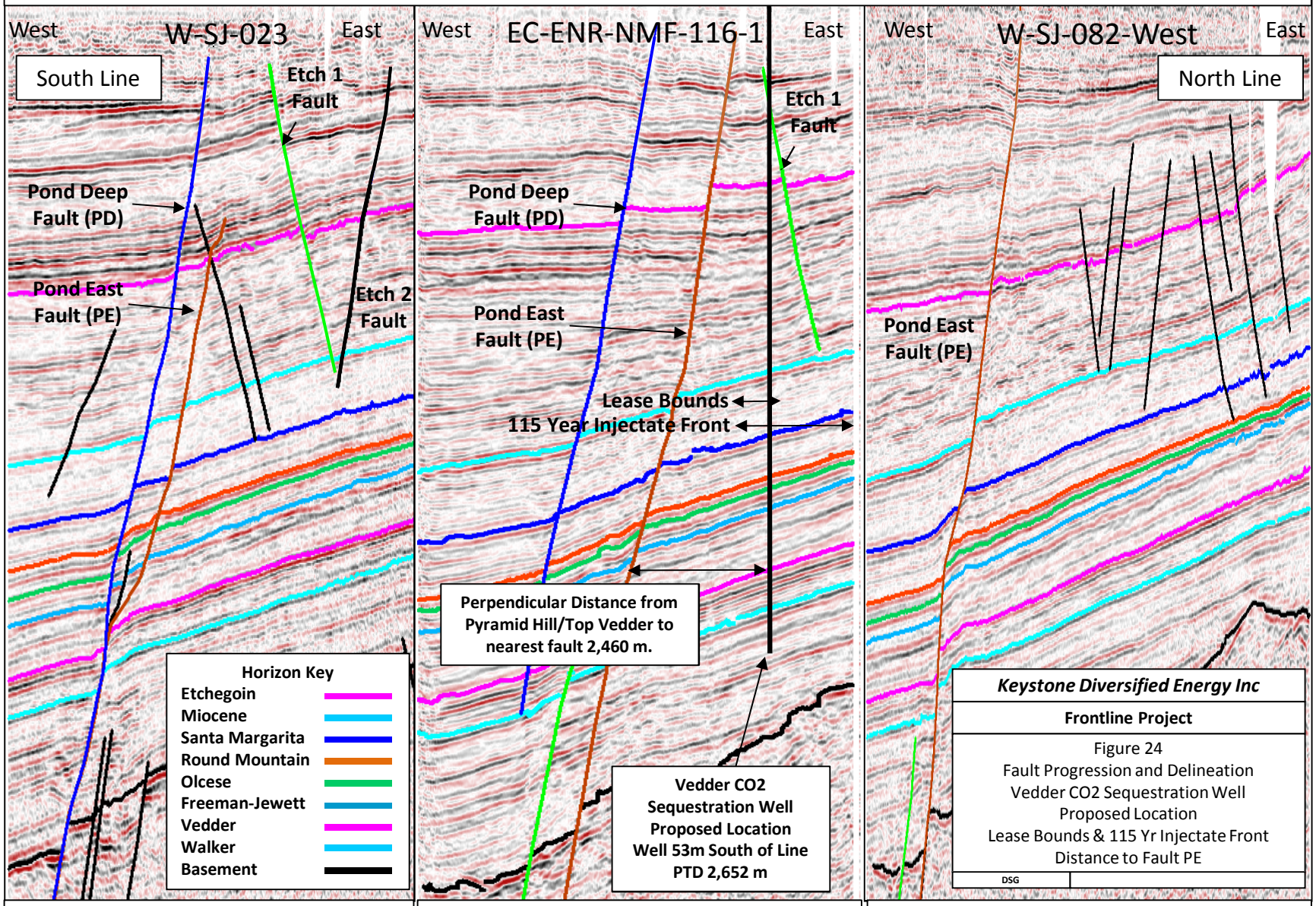

PD Fault extends to surface with a back fault (PE) appearing.

PD starts to disappear above basement. Splay fault (PE) extends to surface and basement.

PD disappears and only PE is remaining.

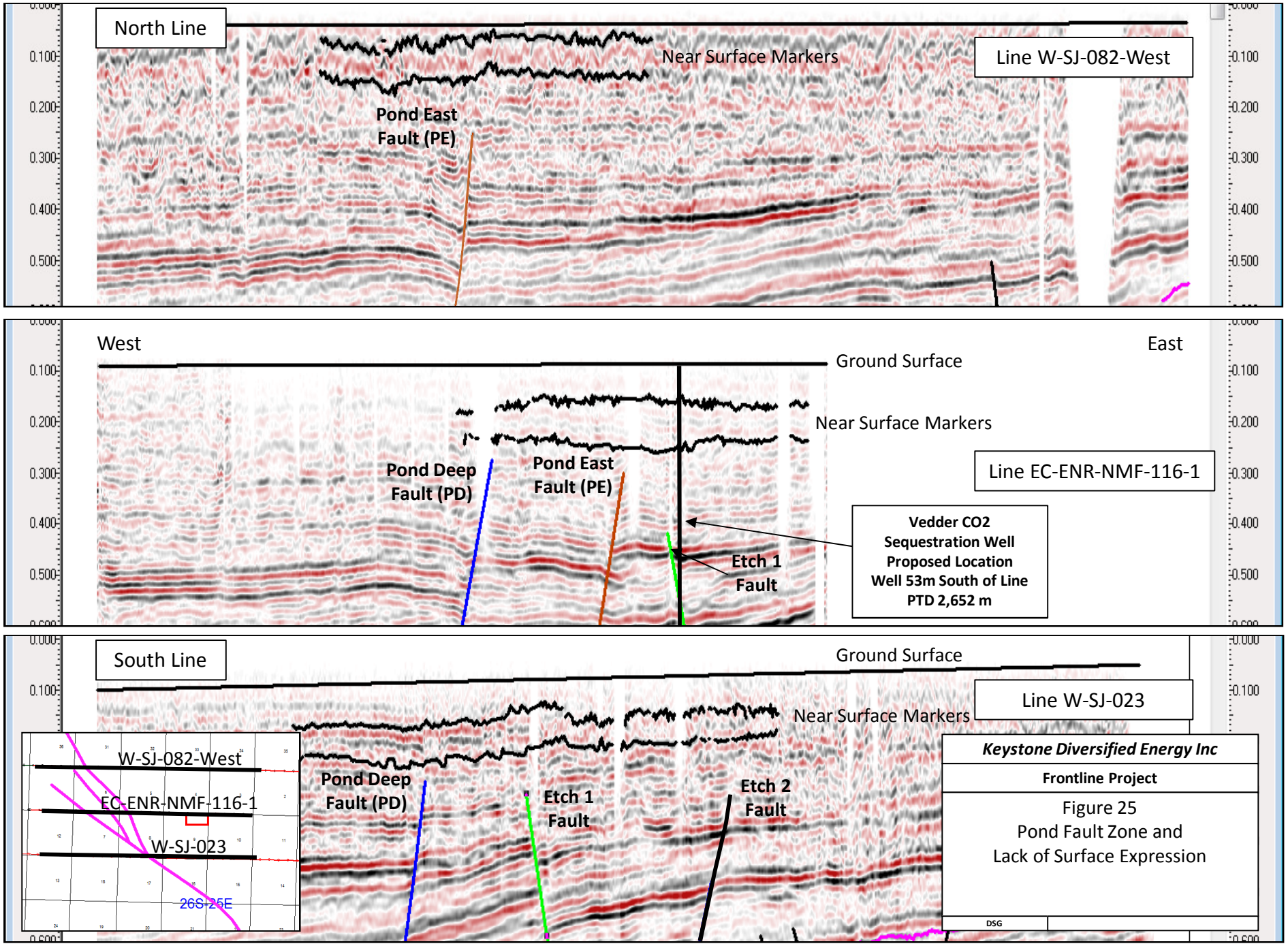
North Line
Near Surface Markers
Line W-SJ-082-West
Pond East
Fault (PE)
West
East
Ground Surface
Near Surface Markers
Pond Deep
Fault (PD)
Pond East
Fault (PE)
Line EC-ENR-NMF-116-1
Vedder CO2
Sequestration Well
Proposed Location
Well 53m South of Line
PTD 2,652 m
Etch 1
Fault
South Line
Ground Surface
Line W-SJ-023
Near Surface Markers
W-SJ-082-West
EC-ENR-NMF-116-1
W-SJ-023
26S-25E
Pond Deep
Fault (PD)
Etch 1
Fault
Etch 2
Fault
Keystone Diversified Energy Inc
Frontline Project
Figure 25
Pond Fault Zone and
Lack of Surface Expression
DSG

Line EC-ENR-NMF-116-1

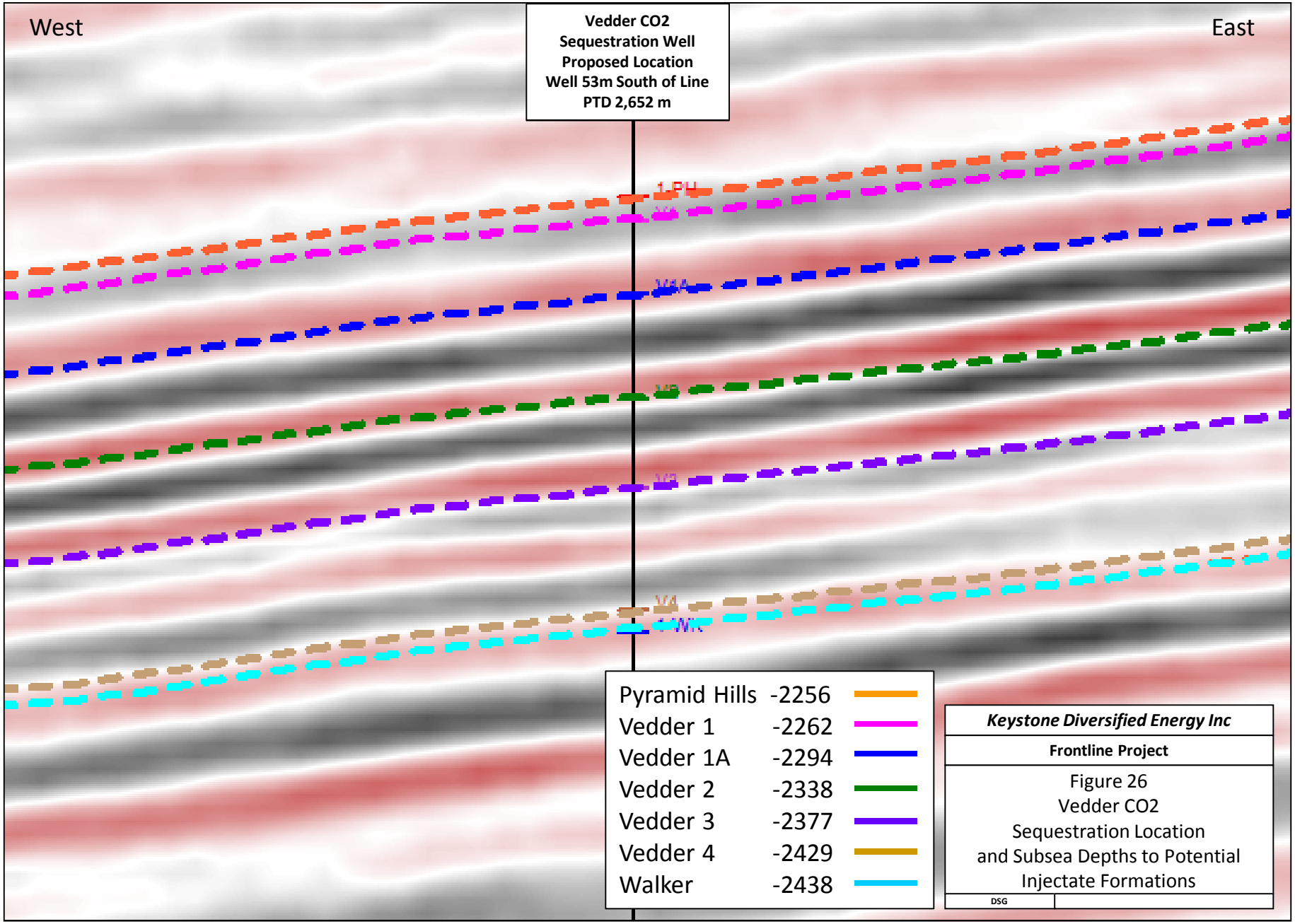

Appendix E: Pond Poso Fault Complex Cross Sections

Cross Section 1:
northern Pond-Poso Creek Fault trend

West East

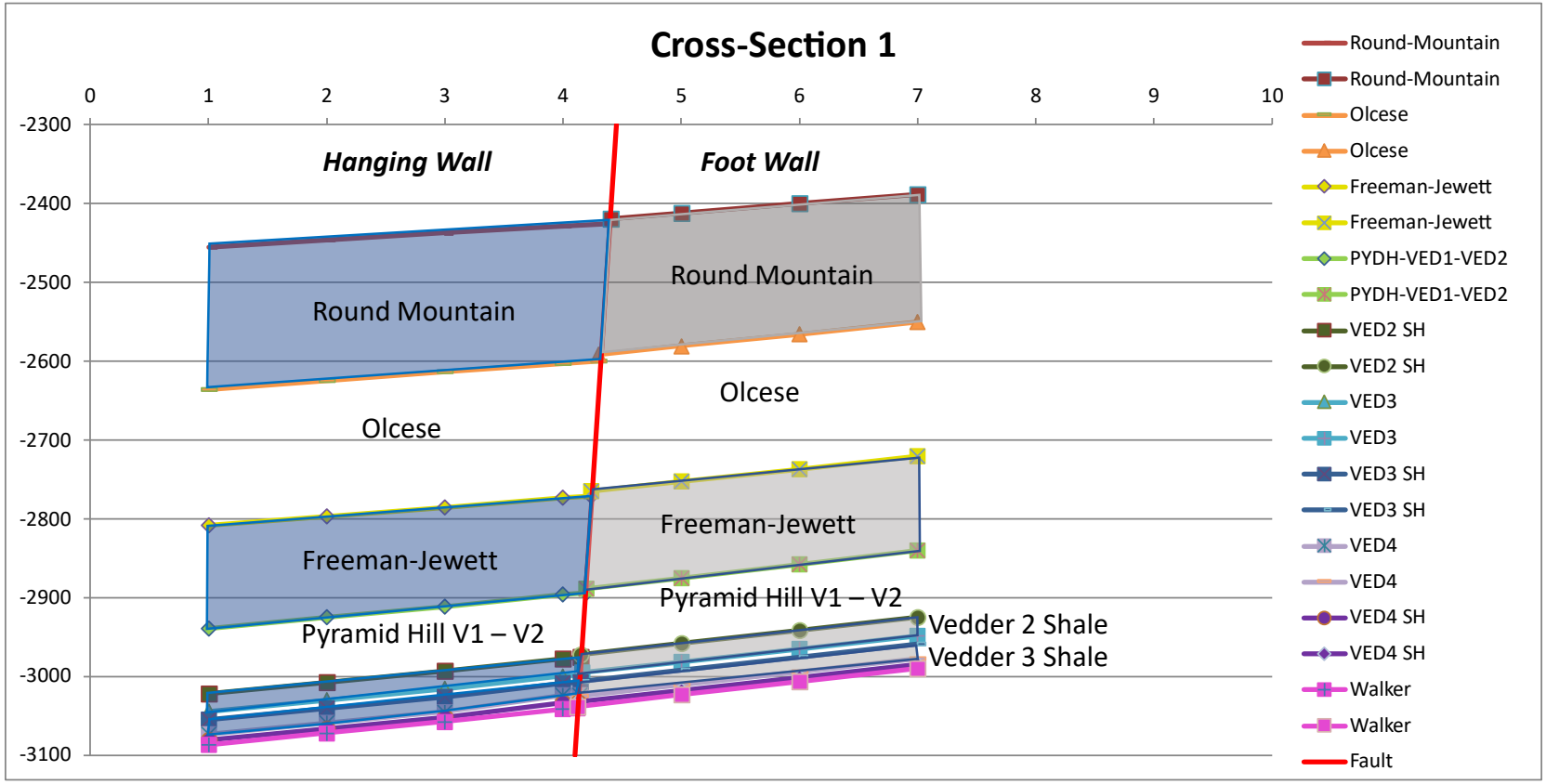

Cross Section 1 at the northern extent of the Pond-Poso Creek System illustrating the Hanging and Foot Wall sides of the fault and the stratigraphic units offset across the fault. There is less than 10 meters of normal offset at the Pyramid Hill-V1-V2 level.

Cross Section 2:
northern Pond-Poso Creek Fault trend

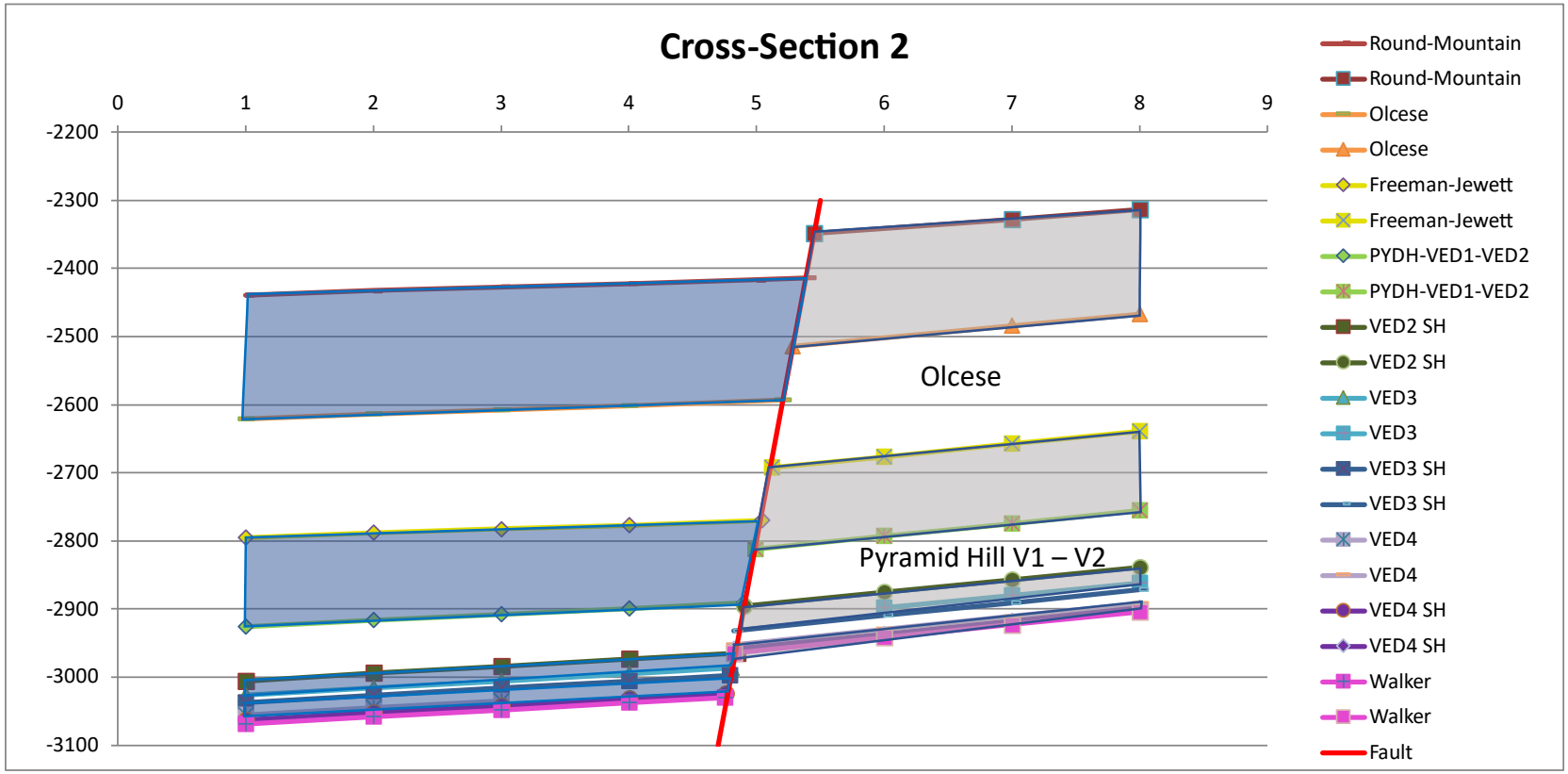

Cross Section 3:
northern Pond-Poso Creek Fault trend

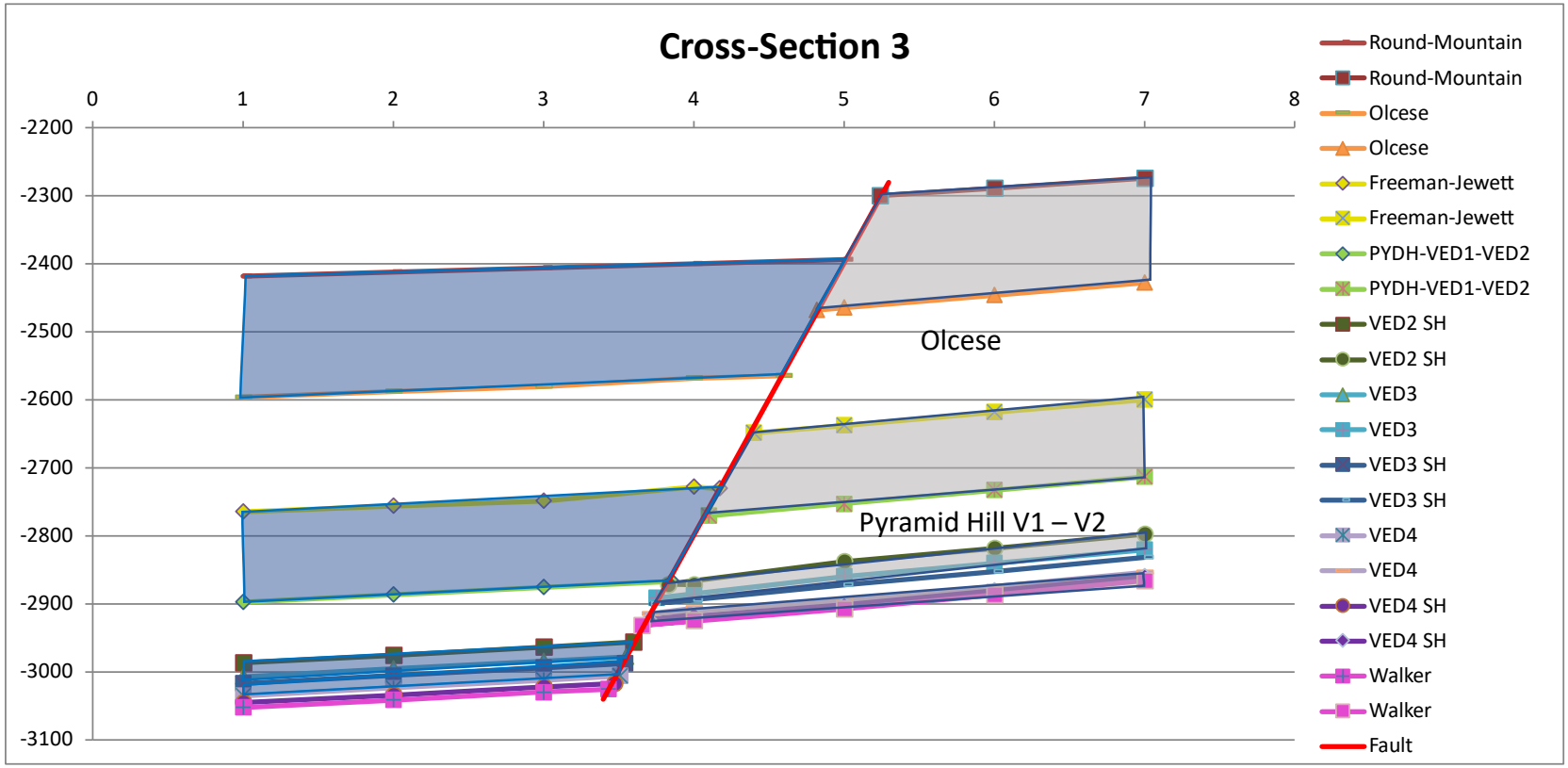

Cross Section 4:
northern Pond-Poso Creek Fault trend

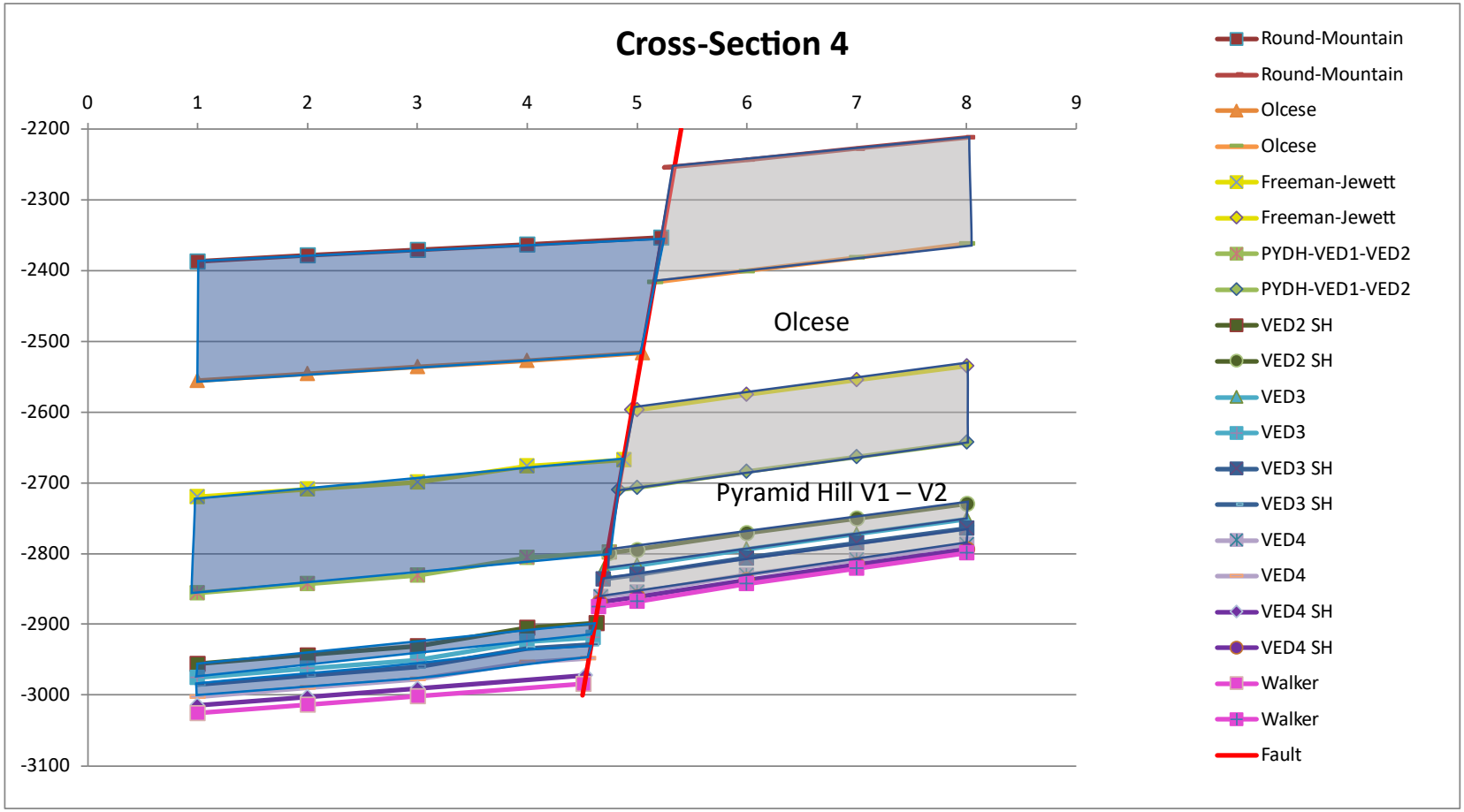

Cross Section 5:
northern Pond-Poso Creek Fault trend

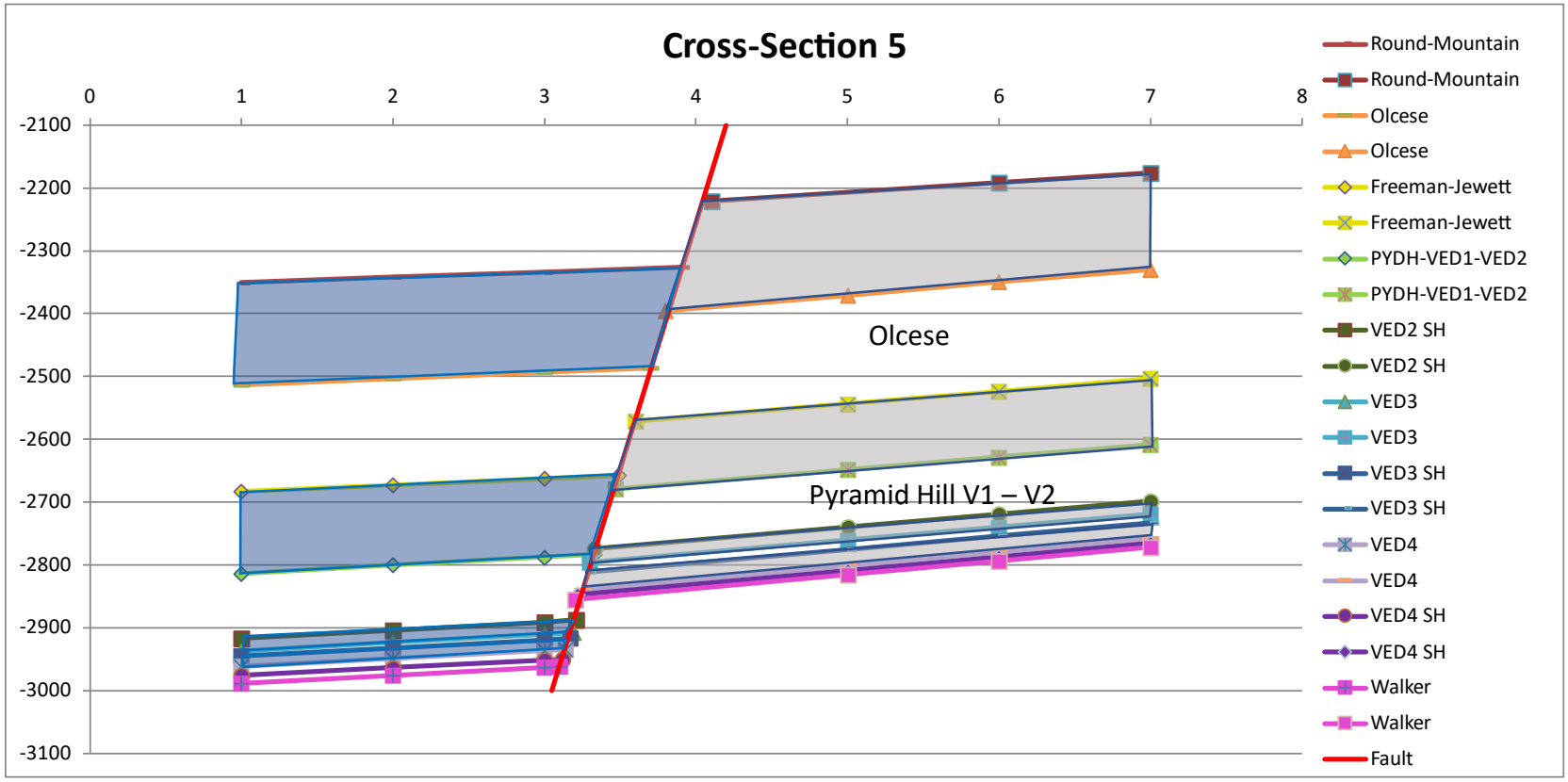

Cross Section 6:
northern Pond-Poso Creek Fault trend

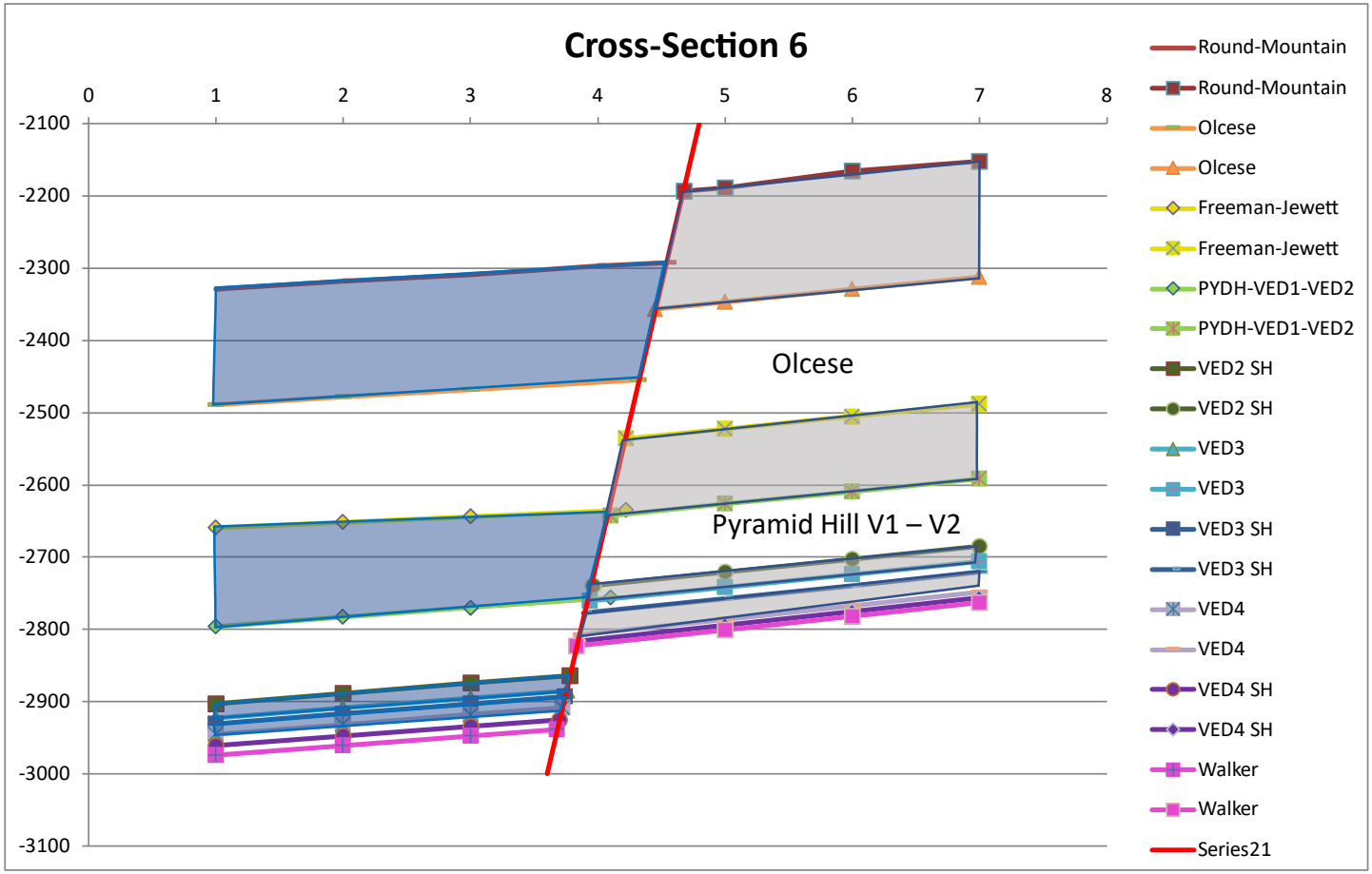

Cross Section 7:
northern Pond-Poso Creek Fault trend

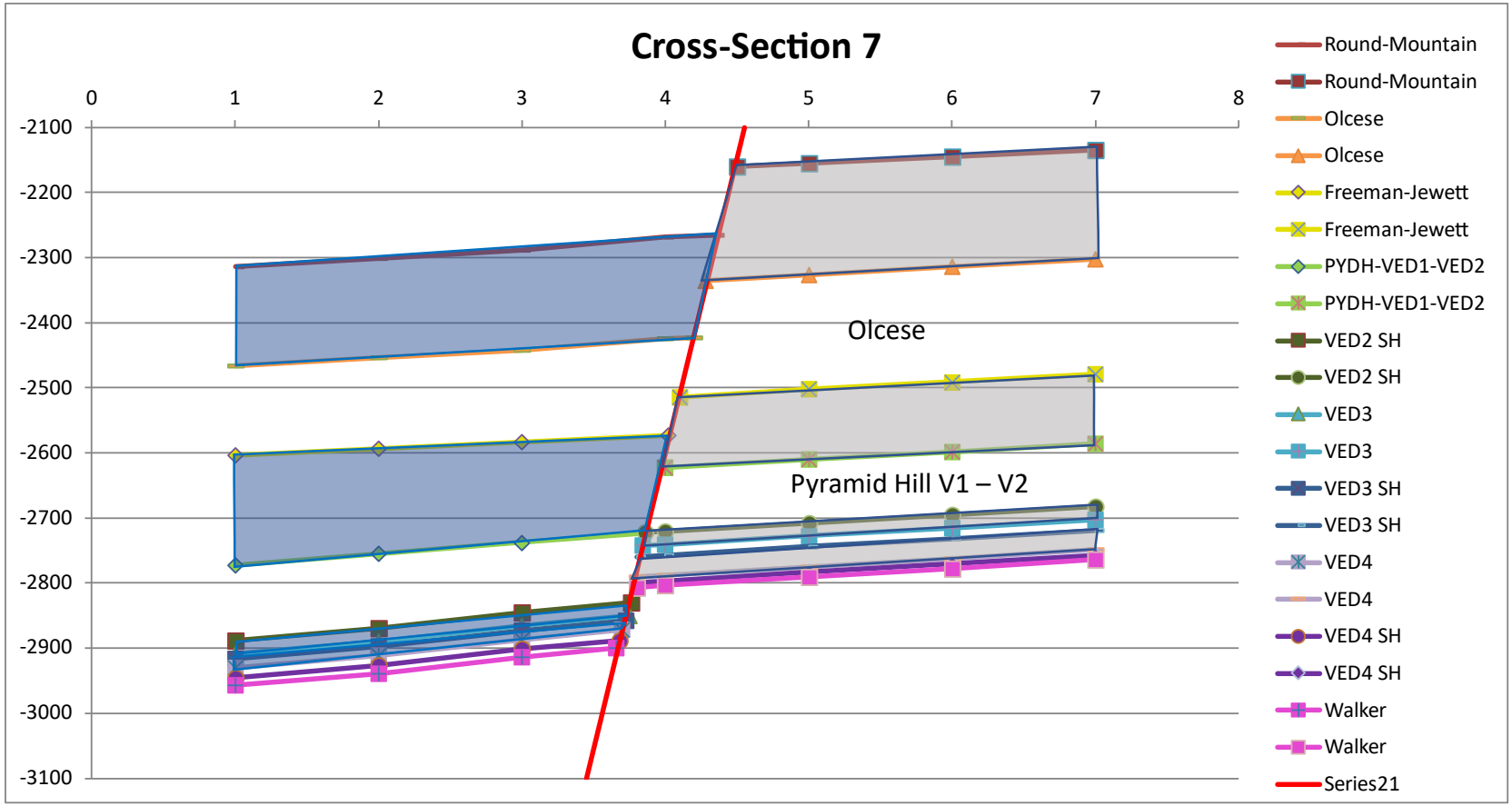

Cross Section 8:
north-central Pond-Poso Creek Fault trend

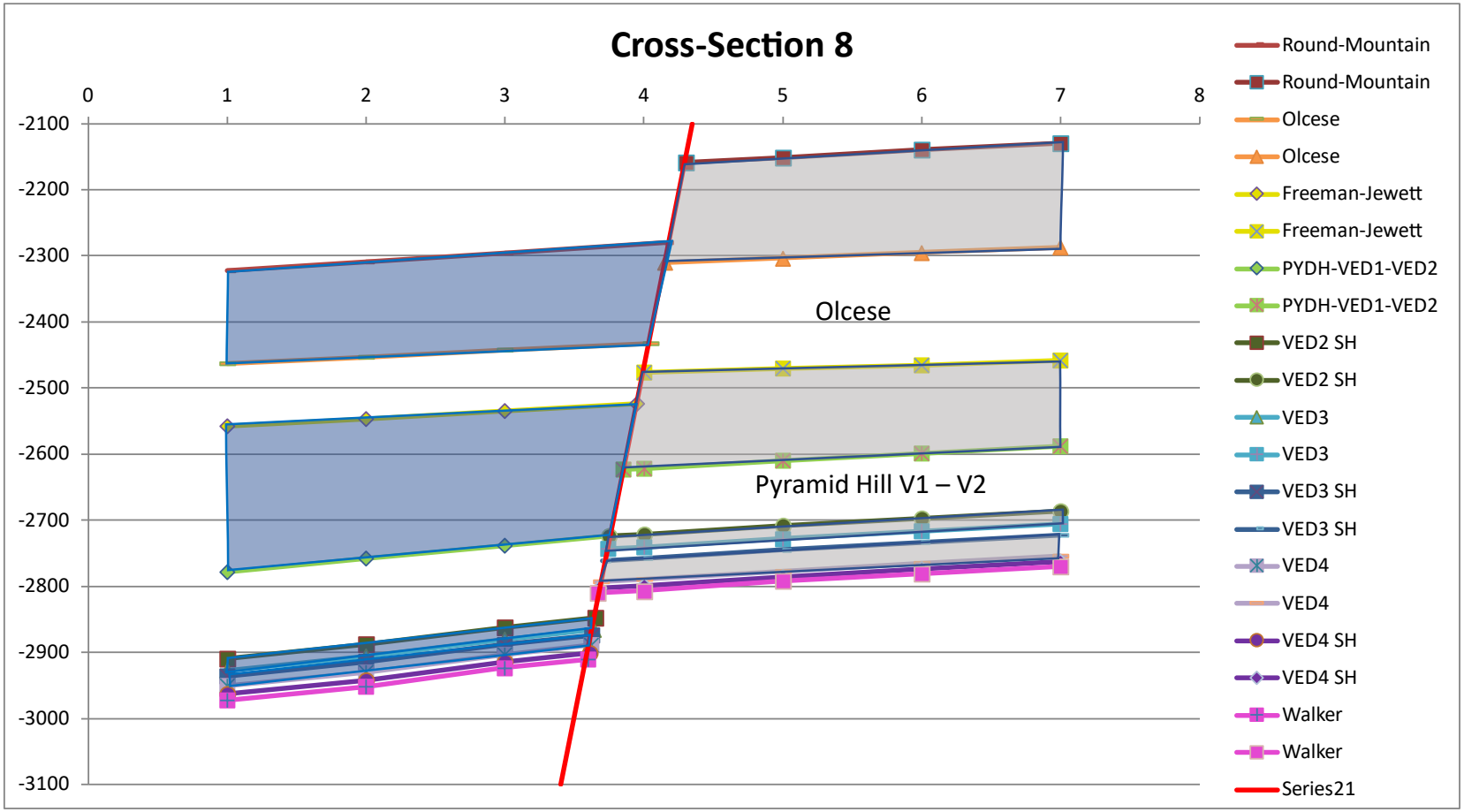

Cross Section 9:
north-central Pond-Poso Creek Fault trend

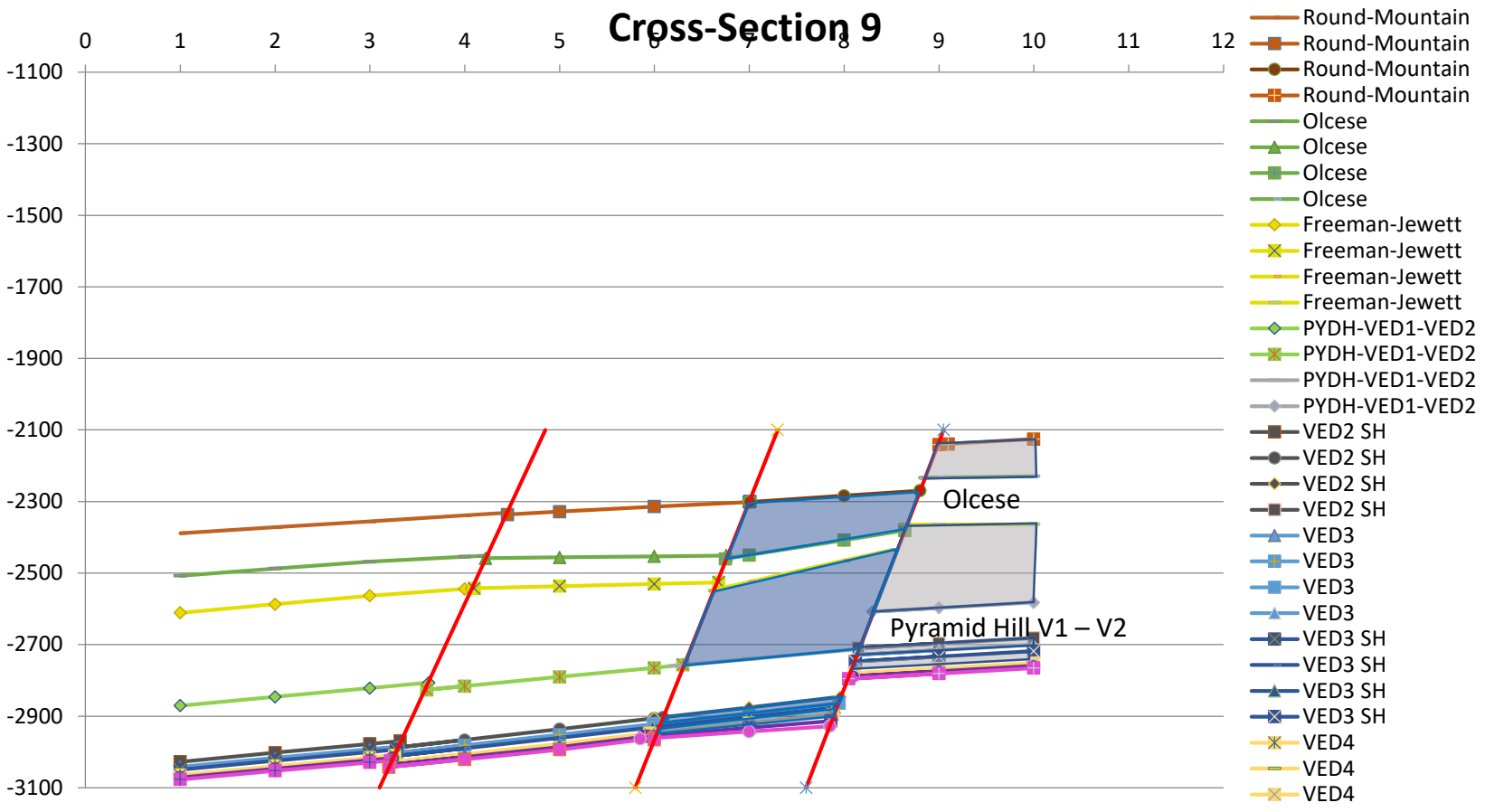

Cross Section 10:
north-central Pond-Poso Creek Fault trend

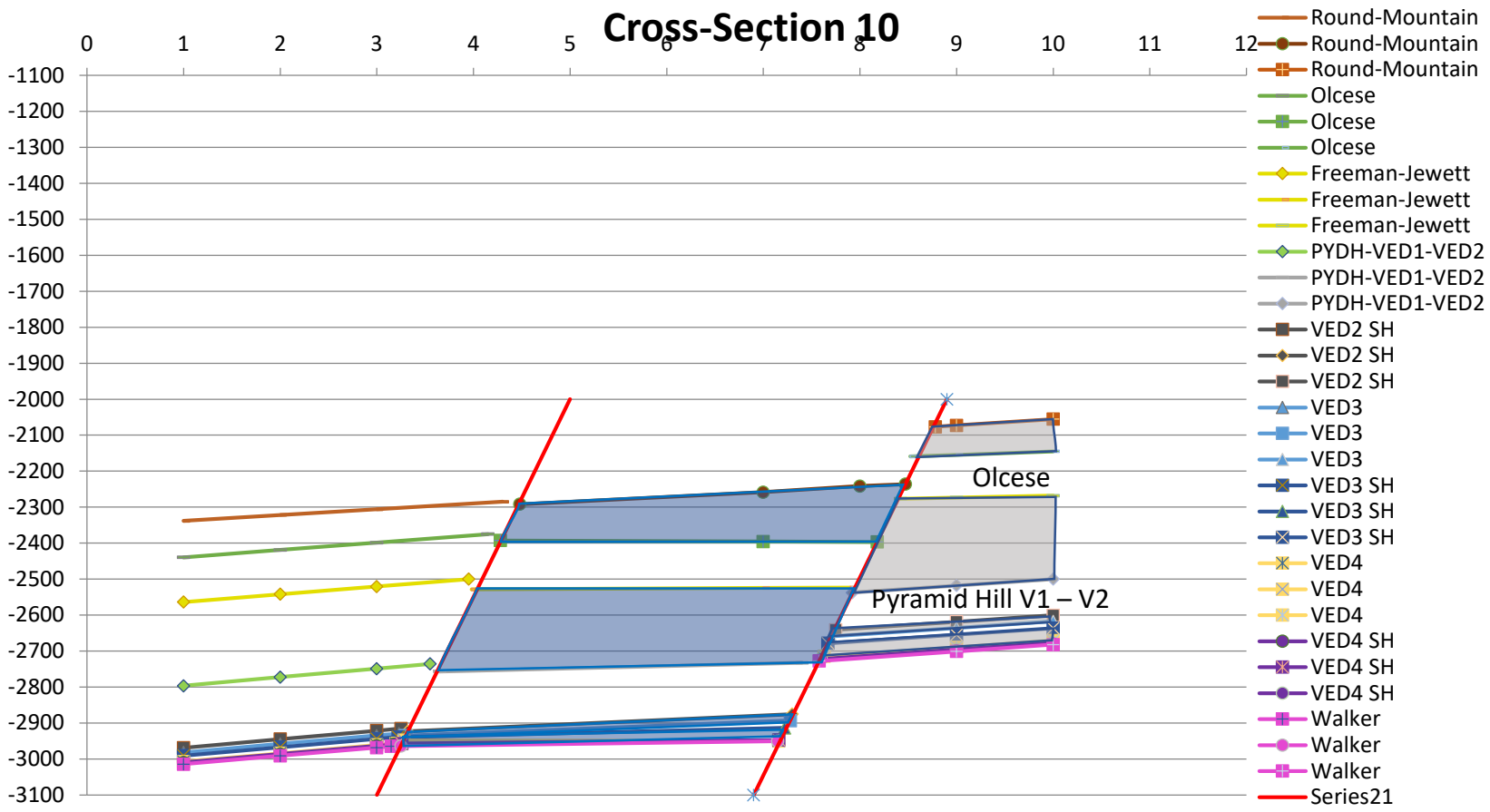

Cross Section 11:
central Pond-Poso Creek Fault trend

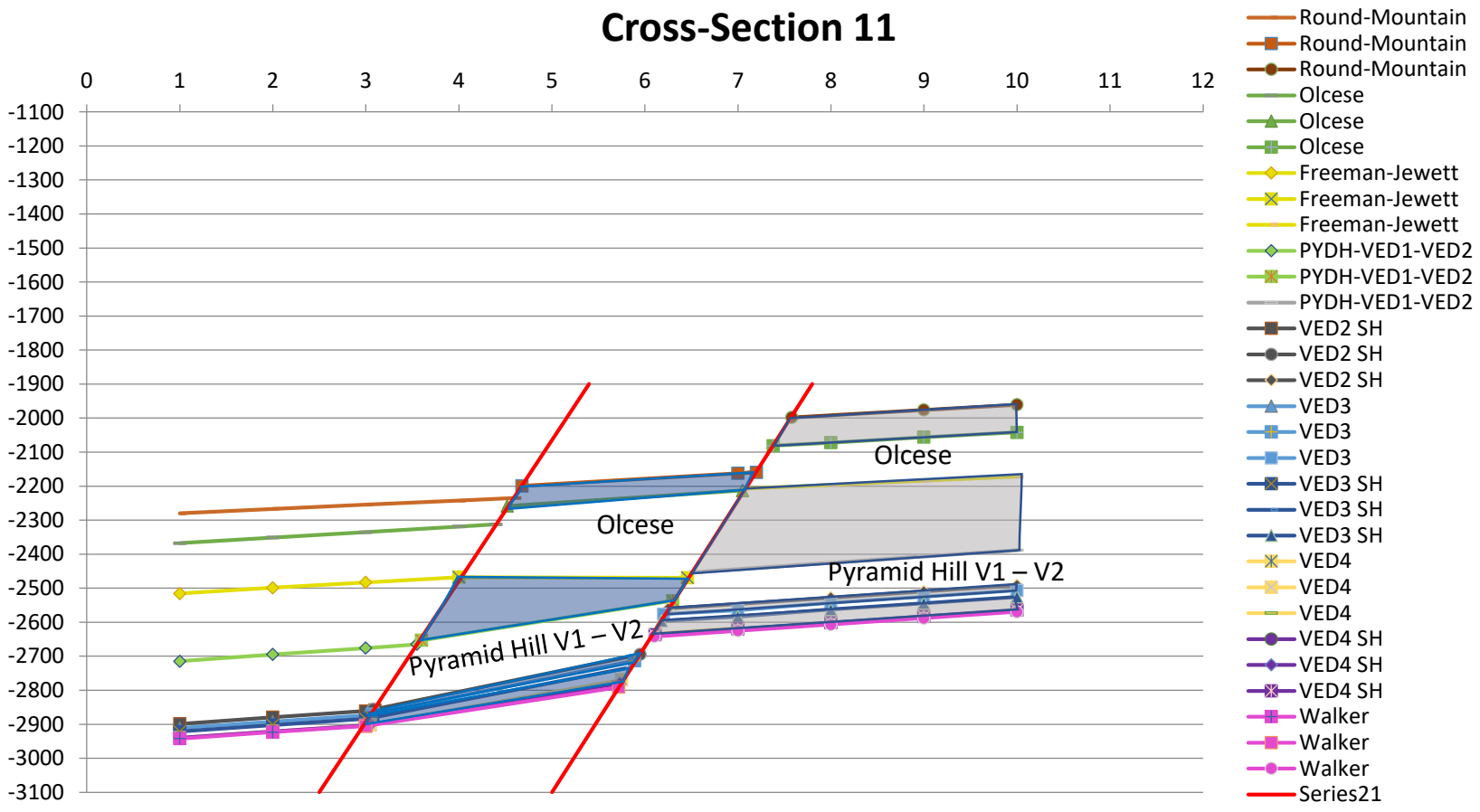

Cross Section 12:
central Pond-Poso Creek Fault trend

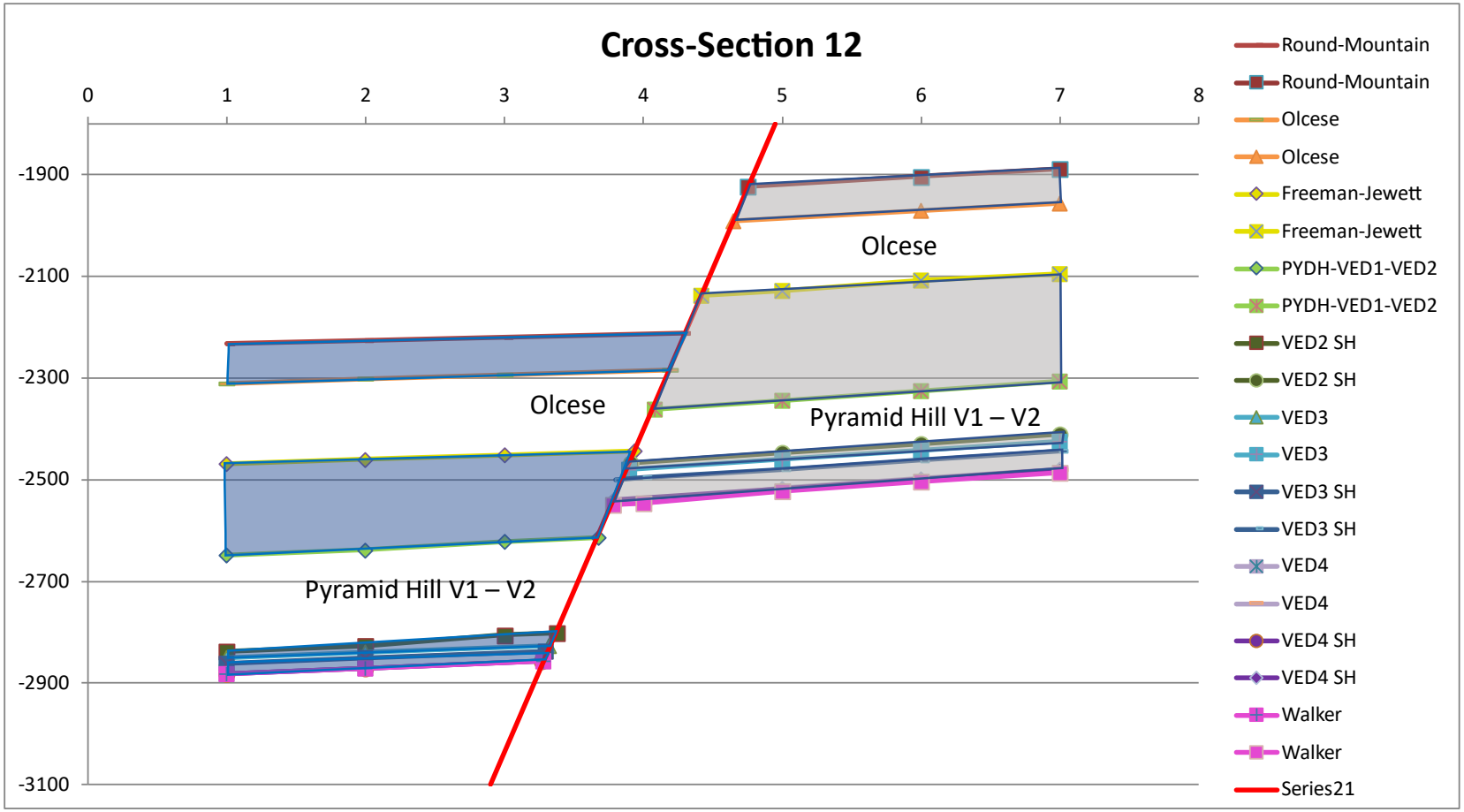

Cross Section 13:
central Pond-Poso Creek Fault trend

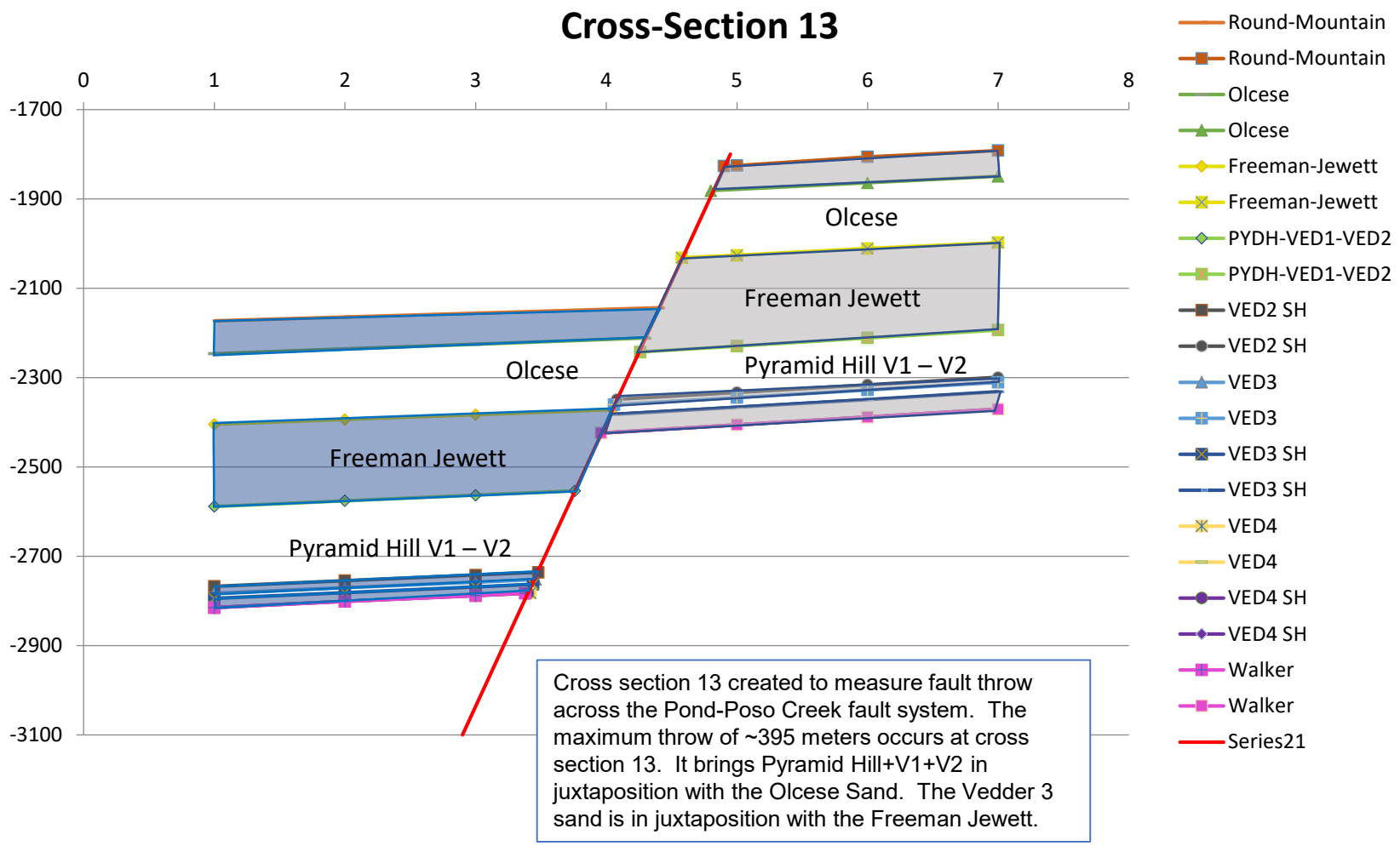

Cross section 13 created to measure fault throw across the Pond-Poso Creek fault system. The maximum throw of ~395 meters occurs at cross section 13. It brings Pyramid Hill+V1+V2 in juxtaposition with the Olcese Sand. The Vedder 3 sand is in juxtaposition with the Freeman Jewett.

Cross Section 14:
central Pond-Poso Creek Fault trend

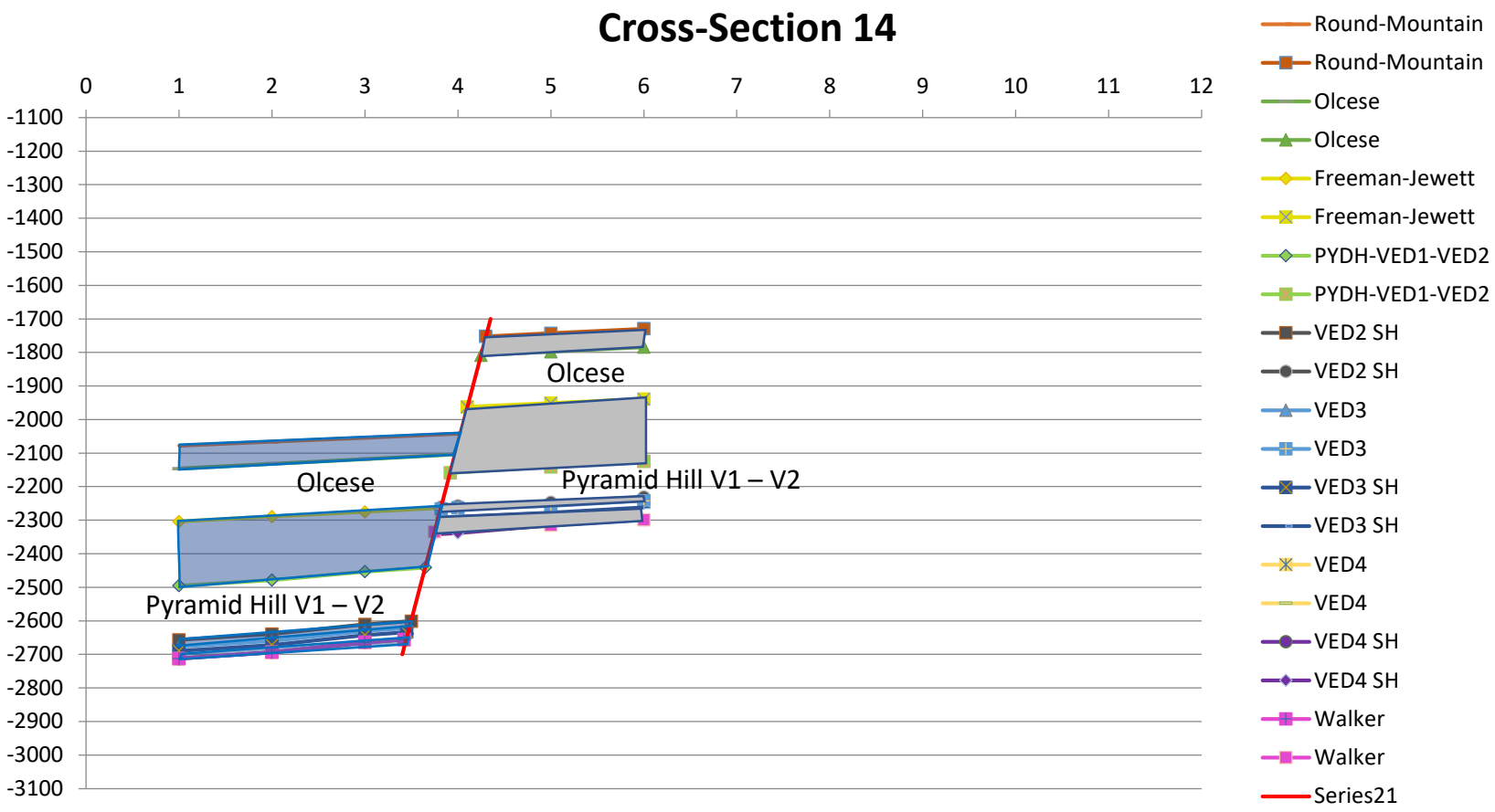

Cross Section 15:
central Pond-Poso Creek Fault trend

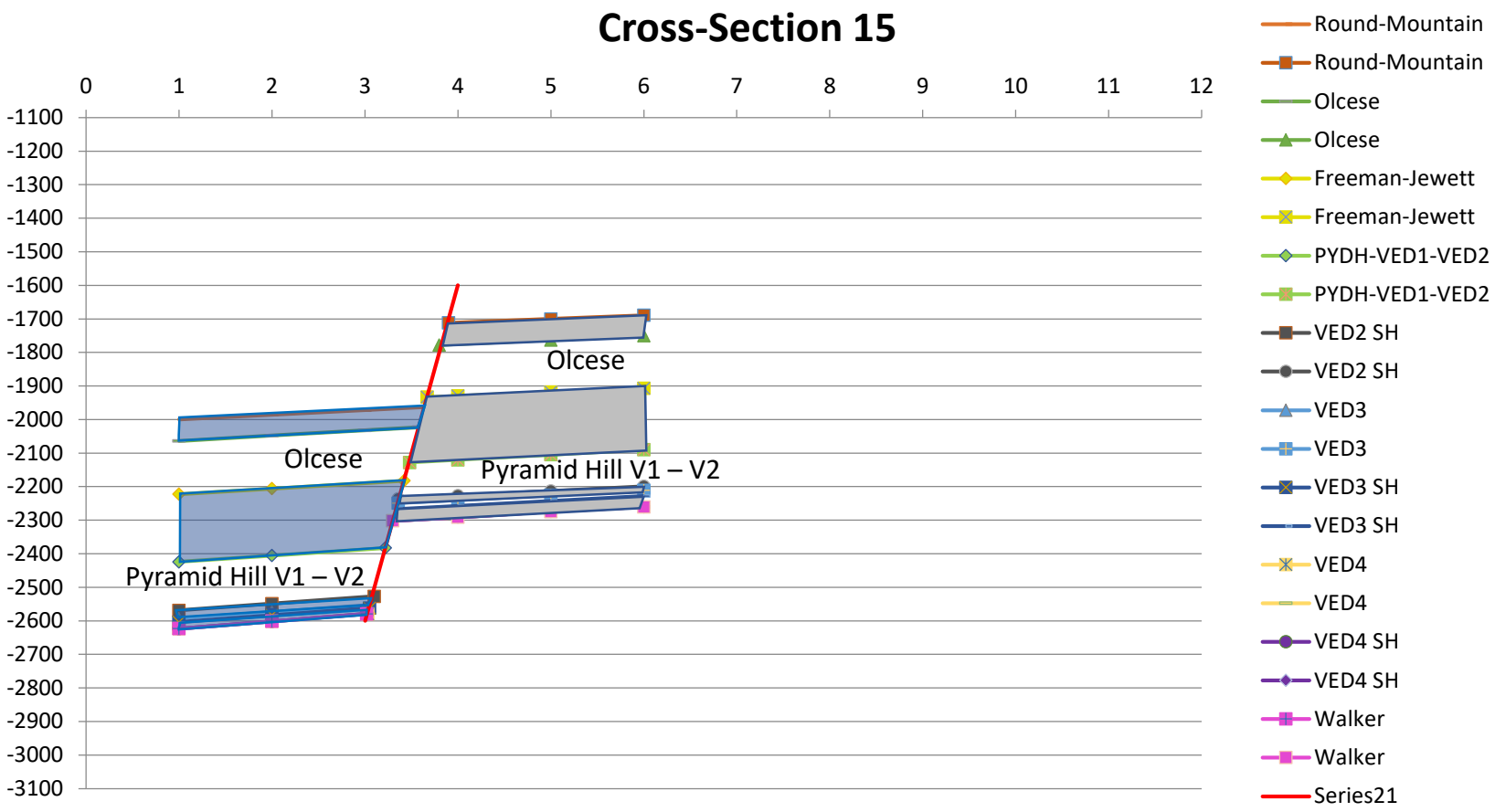

Cross Section 16:
south-central Pond-Poso Creek Fault trend

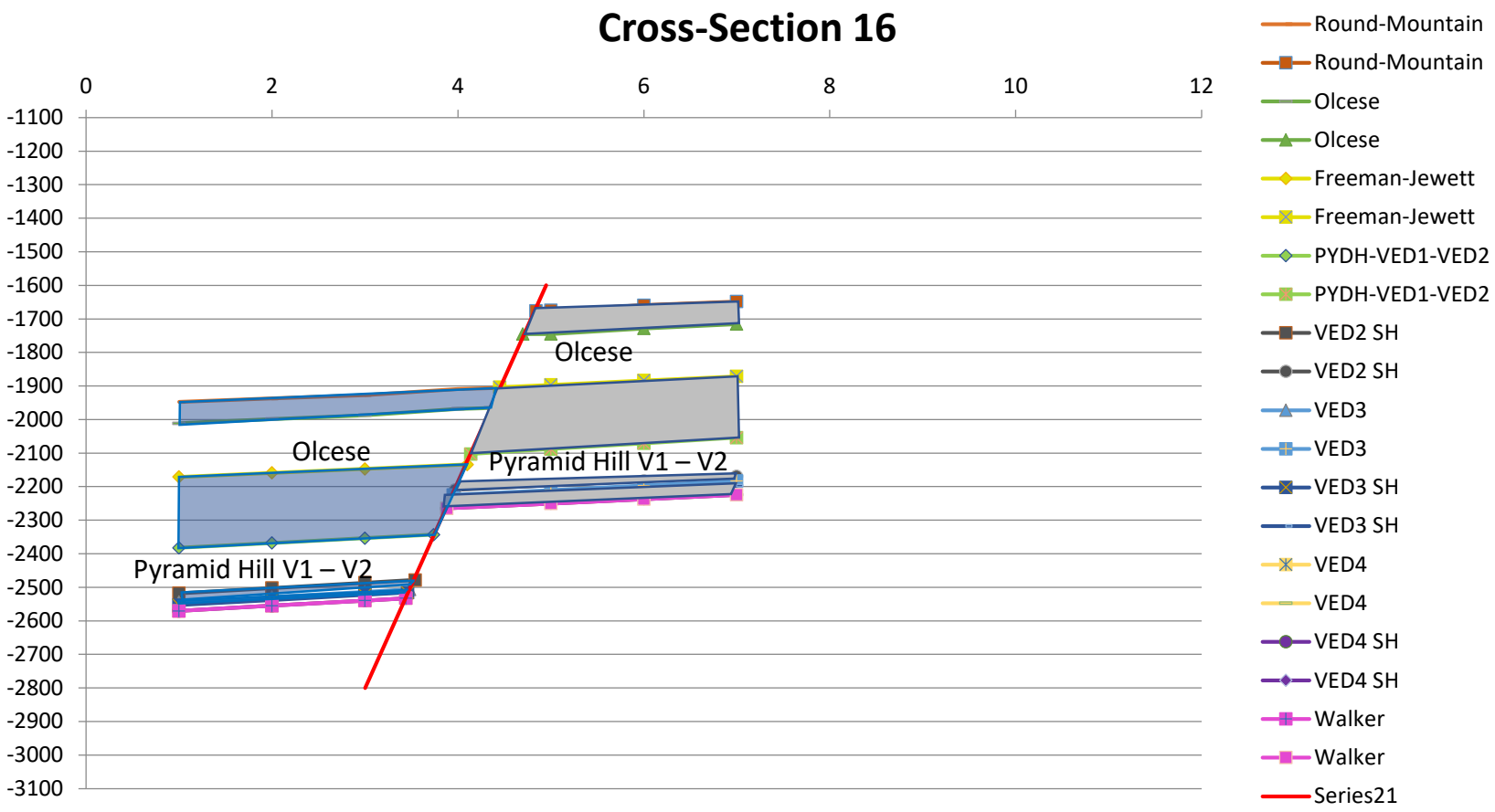

Cross Section 17:
south-central Pond-Poso Creek Fault trend

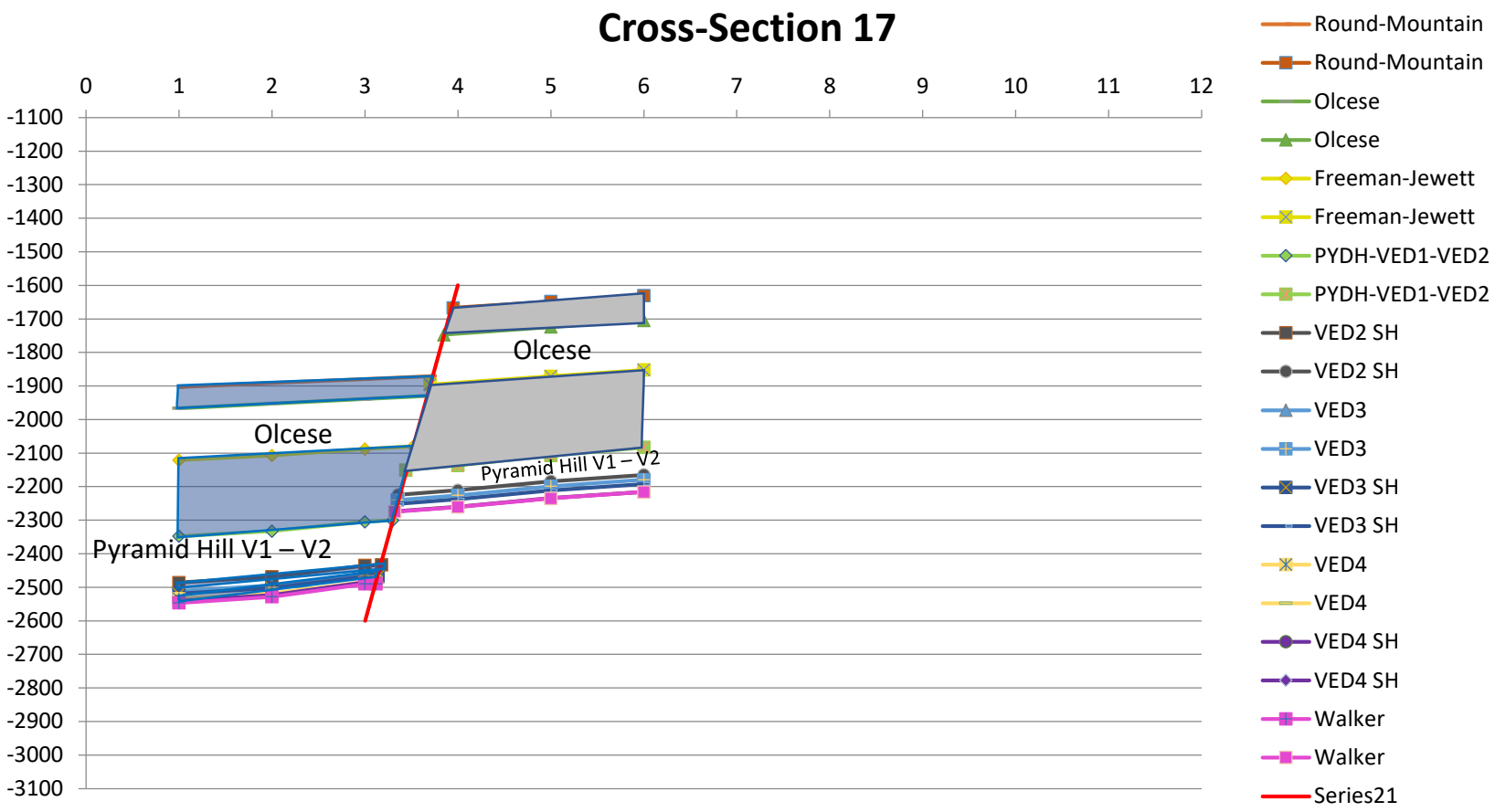

Cross Section 18:
south-central Pond-Poso Creek Fault trend

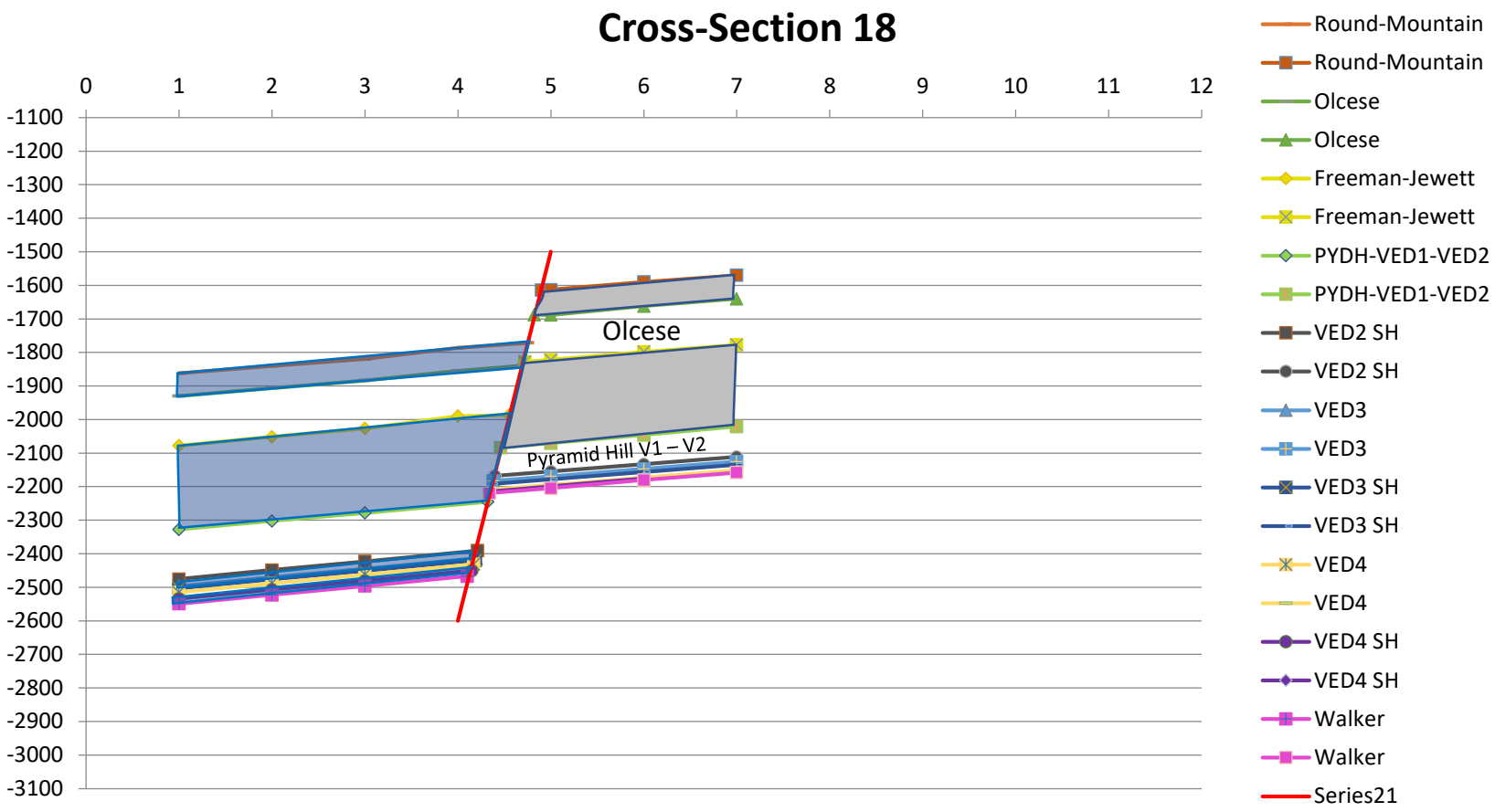

Cross Section 19:
south Pond-Poso Creek Fault trend

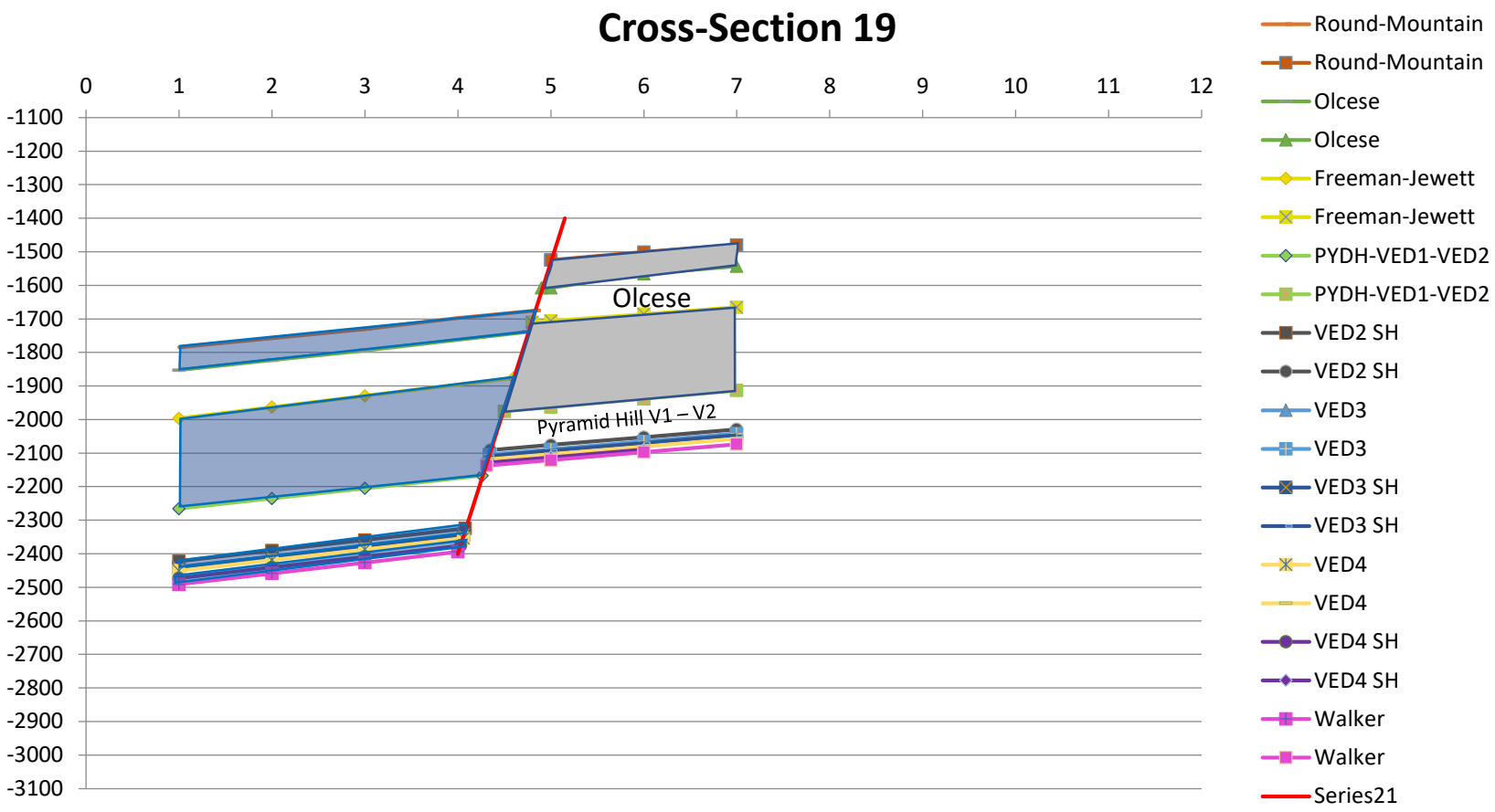

Cross Section 20:
south Pond-Poso Creek Fault trend

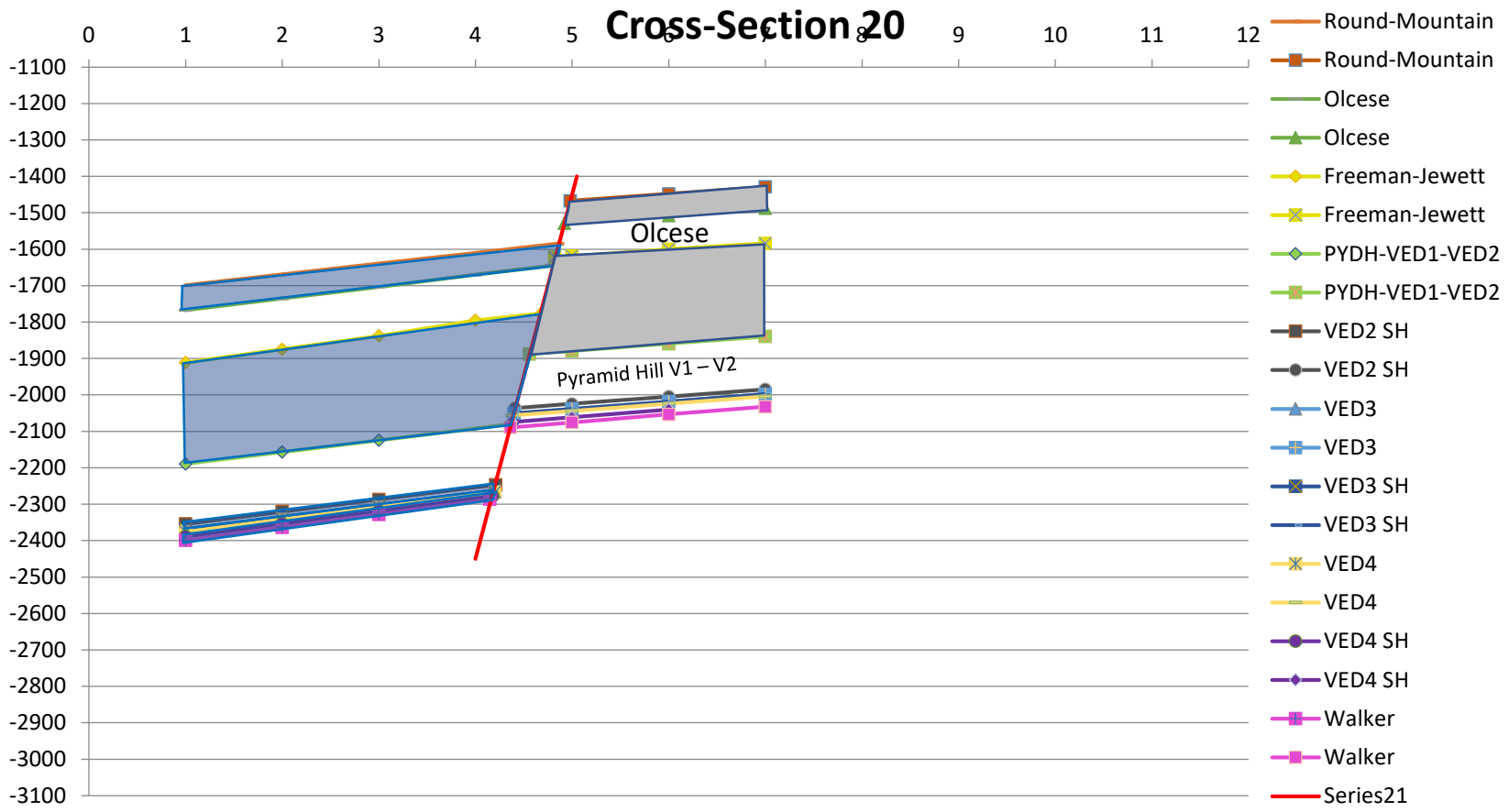

Cross Section 21:
south Pond-Poso Creek Fault trend

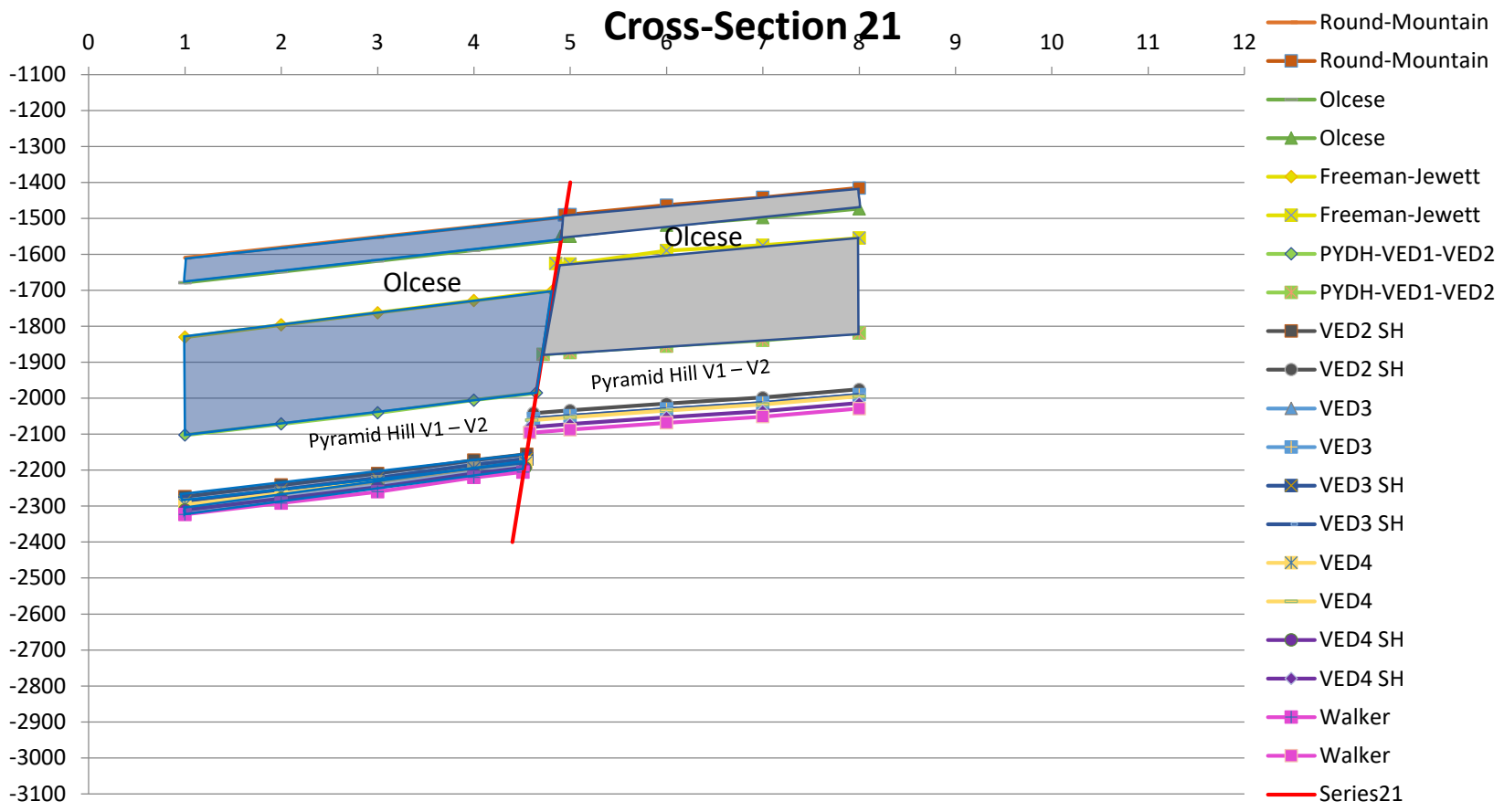

Cross Section 22:
south Pond-Poso Creek Fault trend

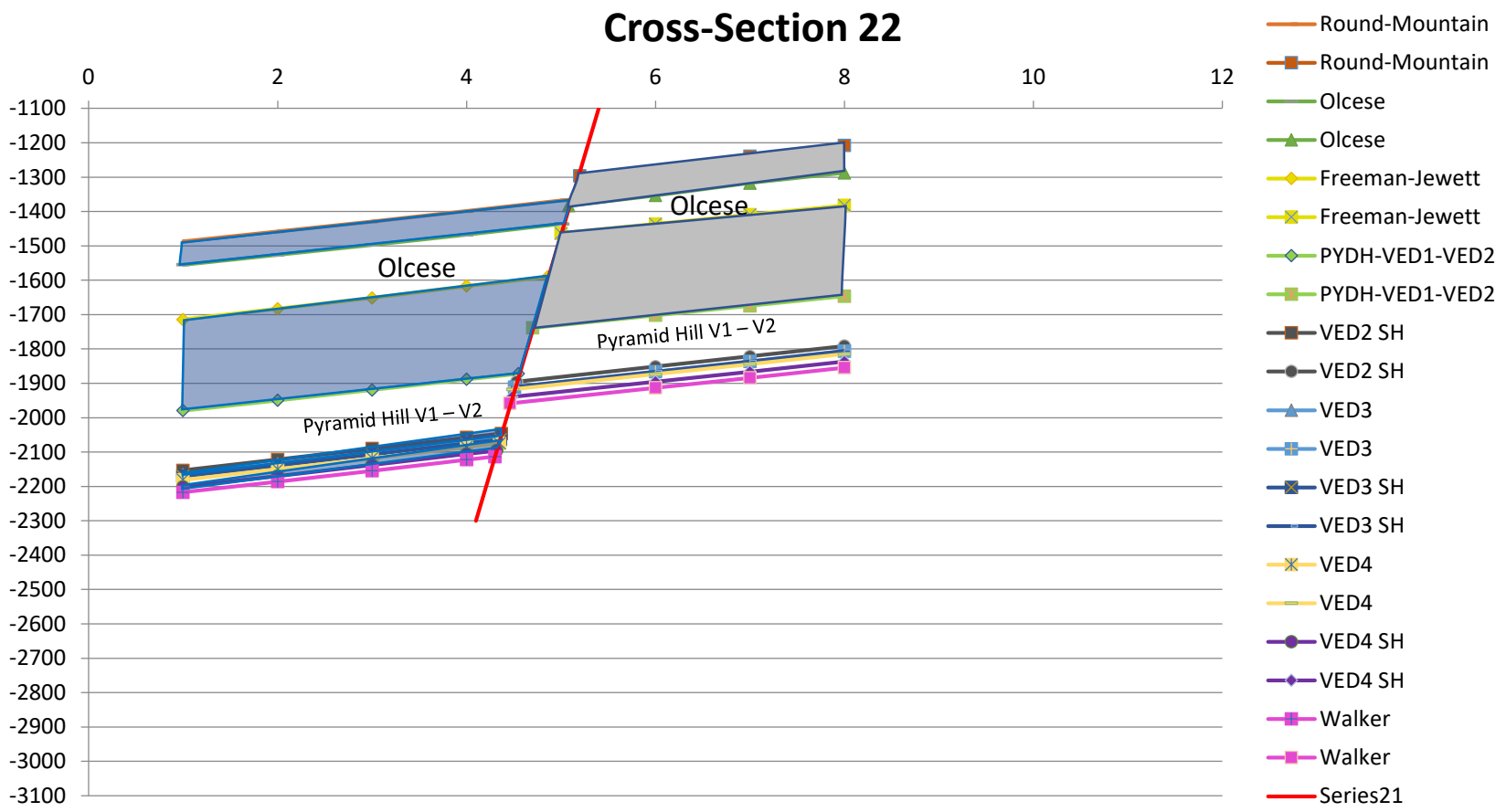

Cross Section 23:
south Pond-Poso Creek Fault trend

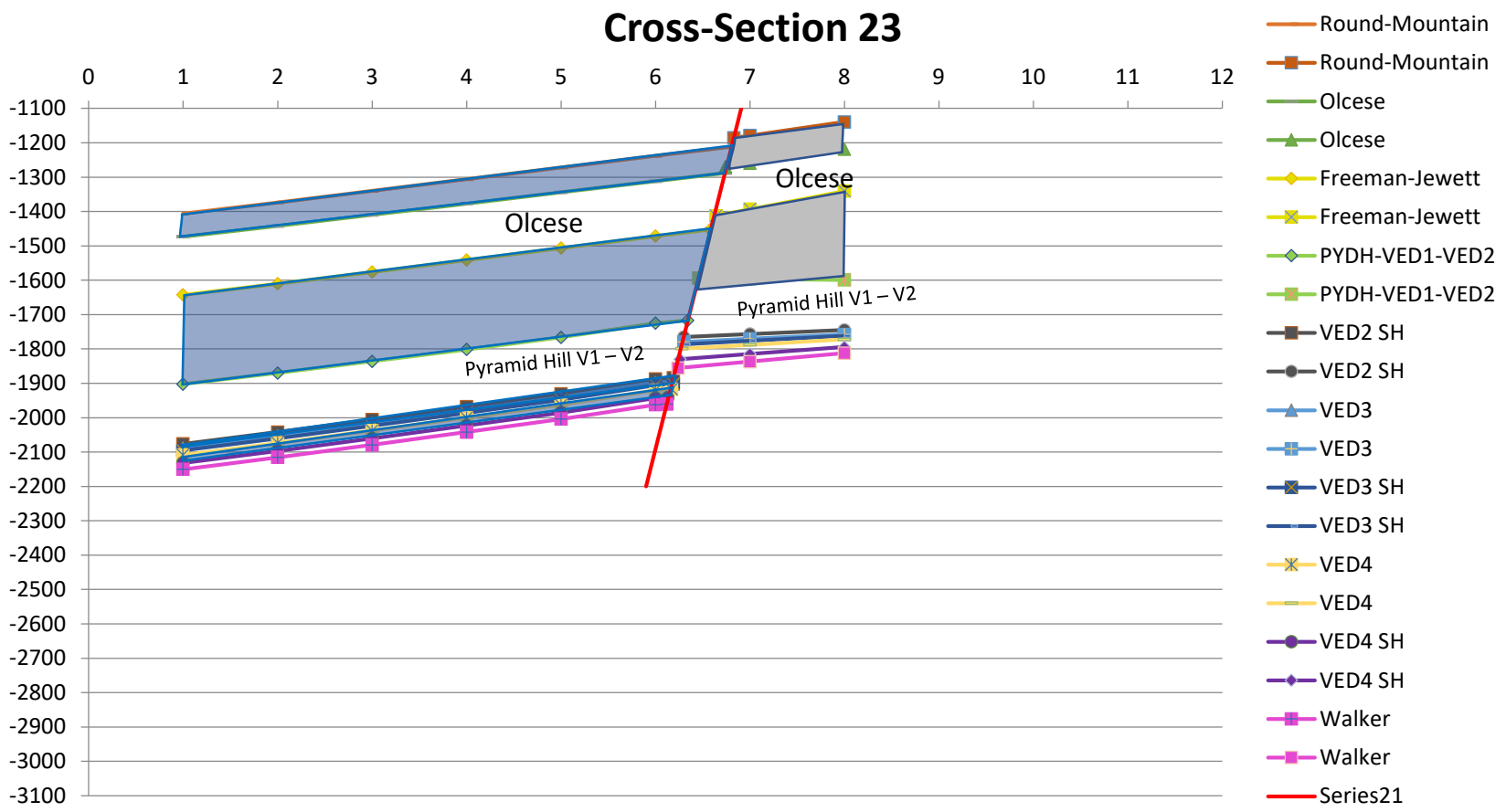

Appendix F: Best Core Services Laboratory Reports

MicroCT:
Sample Screening Images

Operator: Best Core Services

Project Name: J9

Premier Job No.: US-21-J9

Date: 02/24/2021

MicroCT Basic Information:

All sample data was collected on a Zeiss Xradia 510 Versa instrument. The images in this report are presented on a grey scale that ranges from the lowest measured attenuation to the highest. The attenuation of X-rays is a function of the density of electrons in a given material; this can be considered alternatively as a function of atomic number of elements present and the bulk density of the object. Darker regions in the images are low-attenuation materials like air and bright regions are highly electron-dense like lead or pyrite.

The intensity of the brightness of a sample is a function of many different factors such as the objective used, the age of the X-ray source, the distance from the sample to the source and/or the detector, the filter used, image reconstruction technique, etc. If the scan parameters for a batch of samples are consistent, a standard of pyrite/stainless steel can be placed atop the sample to provide a means for standardizing the intensity; other times, qualitative methods are implemented to normalize the grey scale.

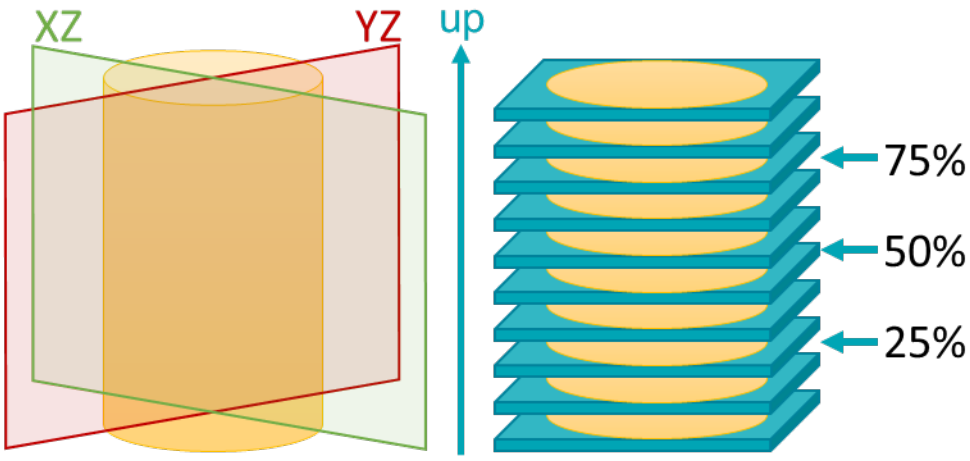

Analysis by: Andrea Di Girolamo

Report Prepared by: Andrea Di Girolamo

Micro CT Summary

Operator: Best Core Services
Well: RMA Jan-2021
County, State: Various

Premier Job No.: US-21-J9
Project Name: J9
Date: 2/24/2021

Sample ID	Depth	Longitudinal Image (YZ)	Cross-Section Image (50%)	Possible Fractures					Sample Comments
				YZ	XZ	25%	50%	75%	
6	4389	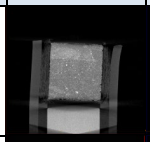	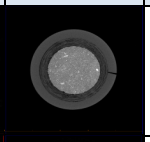	x	x			x	Diagonal fractures noted throughout sample.
6 Post-RMA	4389	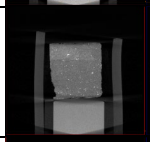	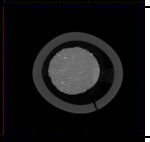	x	x			x	Diagonal and cross-sectional fractures noted throughout sample.
1	4801	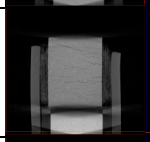	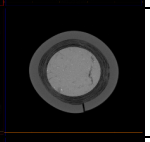	x	x	x	x	x	Multiple cross-sectional and diagonal fractures noted throughout entire sample.
1 Post-RMA	4801	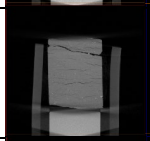	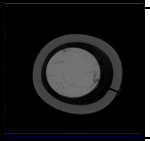	x	x	x	x	x	Diagonal and cross-sectional fractures noted throughout entire sample.
5	6194	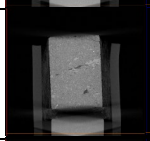	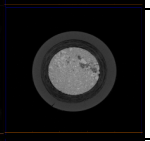	x	x		x		Diagonal fractures noted throughout sample.
5 Post-RMA	6194	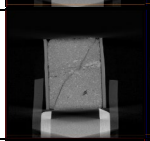	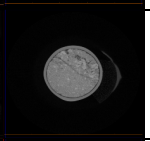	x	x	x	x	x	Diagonal fractures noted throughout sample.
3	8499	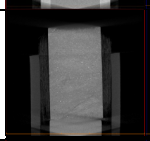	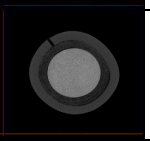	x	x	x			Cross-sectional and diagonal fractures noted throughout sample.
3 Post-RMA	8499	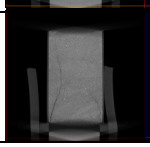	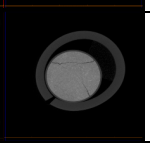	x	x	x	x	x	Diagonal and longitudinal fractures noted throughout sample.

Micro CT Images

Operator: Best Core Services
Premier Job No.: US-21-J9
Date: 2/23/2021

Sample ID: 6 **Depth:** 4389.00 ft

Comments:
Diagonal fractures noted throughout sample.

Cross-Sectional Images

25%	50%	75%
	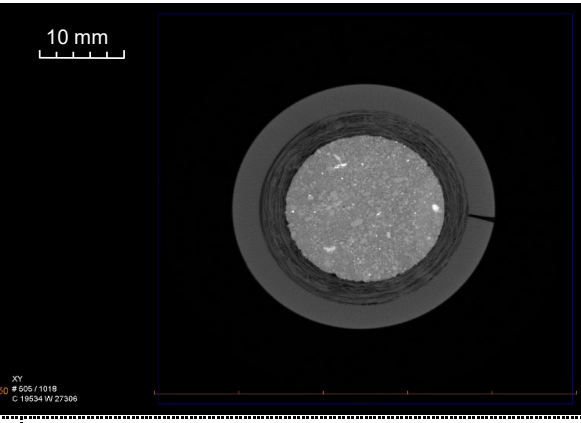	
Possible Fractures:		x

Longitudinal Images

YZ	XZ
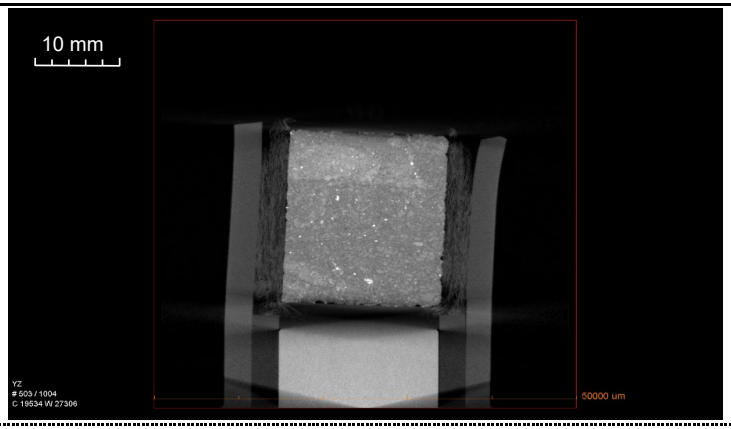	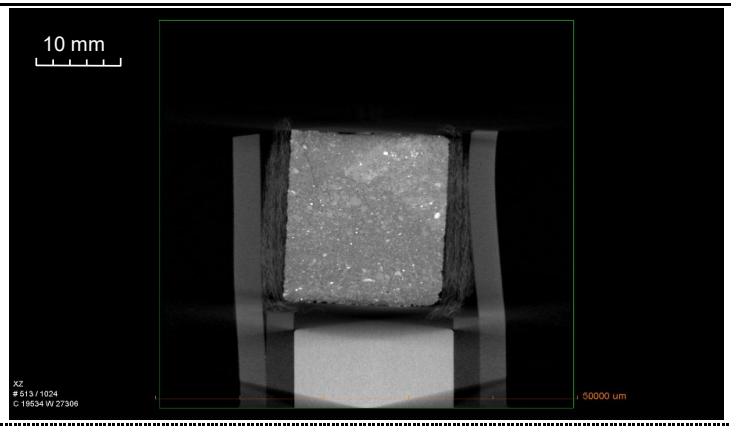
Possible Fractures: x	x

Back to Summary

Micro CT Images

Operator: Best Core Services
Premier Job No.: US-21-J9
Date: 2/24/2021

Sample ID: **6 Post-RMA** **Depth:** **4389.00 ft**

Comments:
Diagonal and cross-sectional fractures noted throughout sample.

Cross-Sectional Images

25%	50%	75%
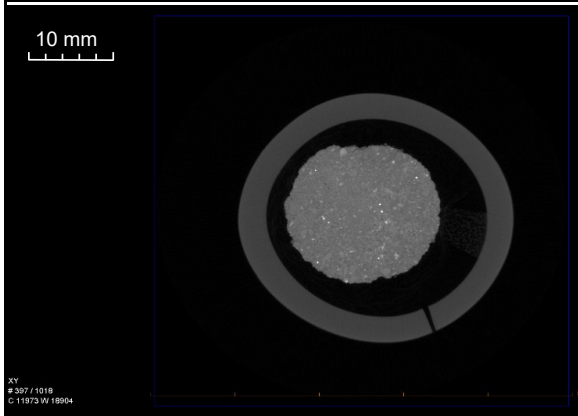	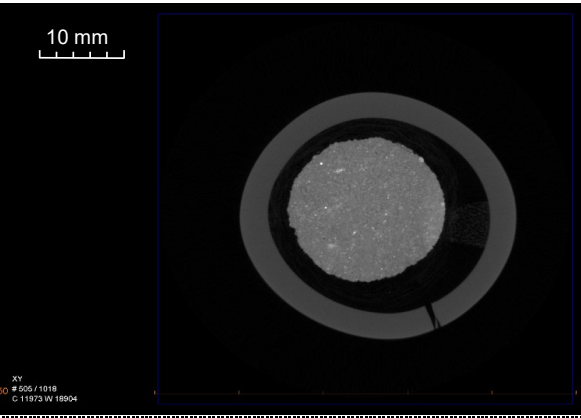	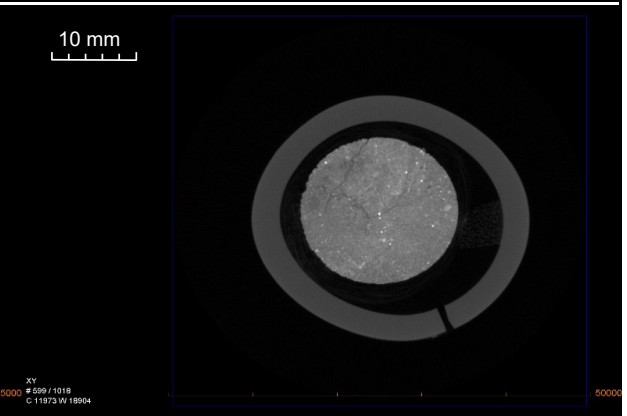
Possible Fractures:		x

Longitudinal Images

YZ	XZ
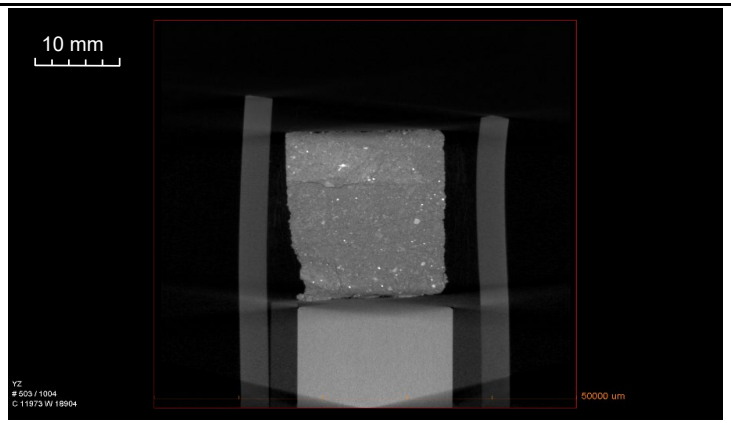	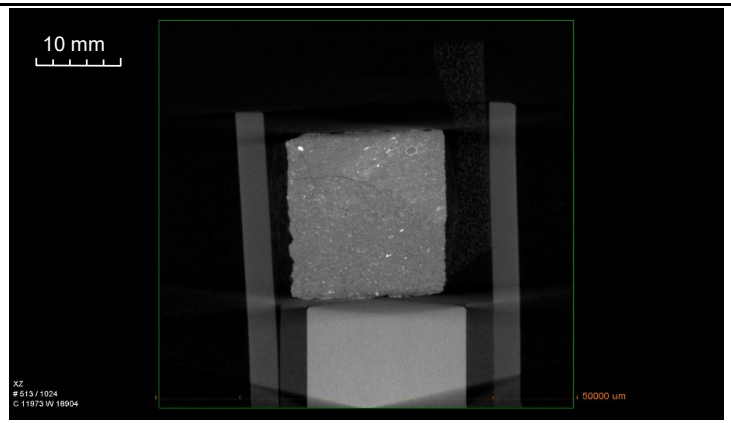
Possible Fractures: x	x

Back to Summary

Micro CT Images

Operator: Best Core Services
Premier Job No.: US-21-J9
Date: 2/23/2021

Sample ID: 1 **Depth:** 4801.00 ft

Comments:
Multiple cross-sectional and diagonal fractures noted throughout entire sample.

Cross-Sectional Images

25%	50%	75%
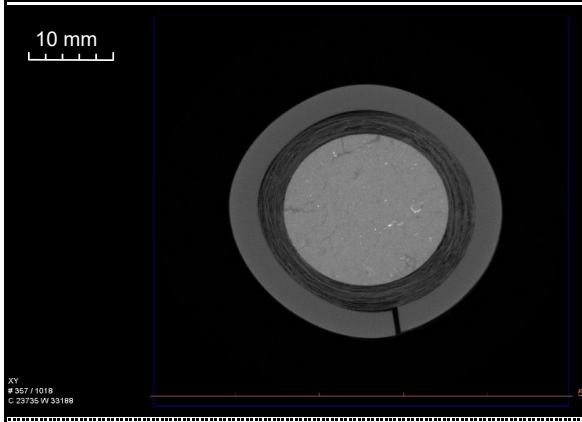	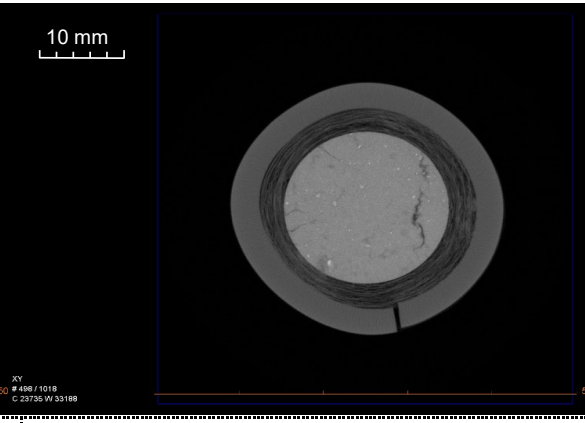	
Possible Fractures: x	x	x

Longitudinal Images

YZ	XZ
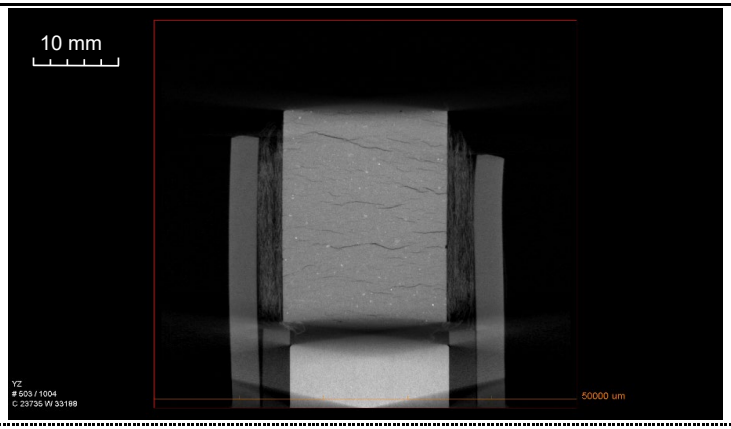	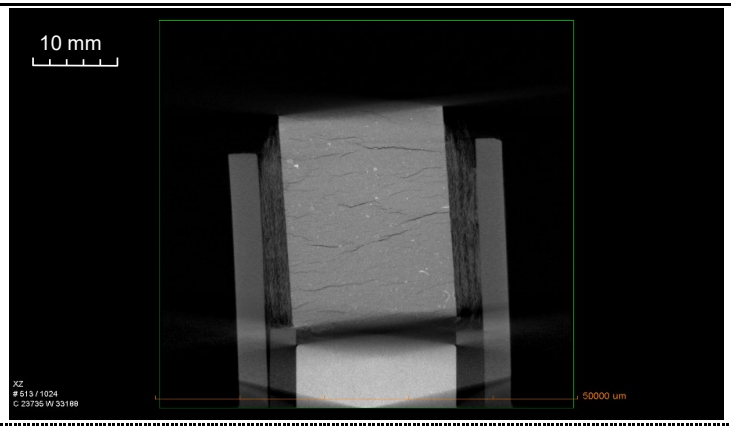
Possible Fractures: x	x

Back to Summary

Micro CT Images

Operator: Best Core Services
Premier Job No.: US-21-J9
Date: 2/24/2021

Sample ID: **1 Post-RMA** **Depth:** **4801.00 ft**

Comments:
Diagonal and cross-sectional fractures noted throughout entire sample.

Cross-Sectional Images

25%	50%	75%
	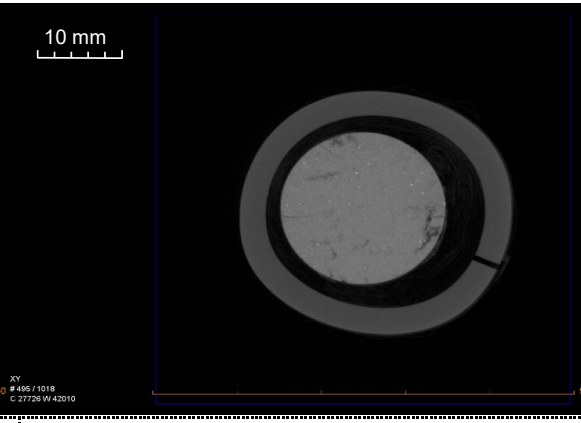	
Possible Fractures: x	x	x

Longitudinal Images

YZ	XZ
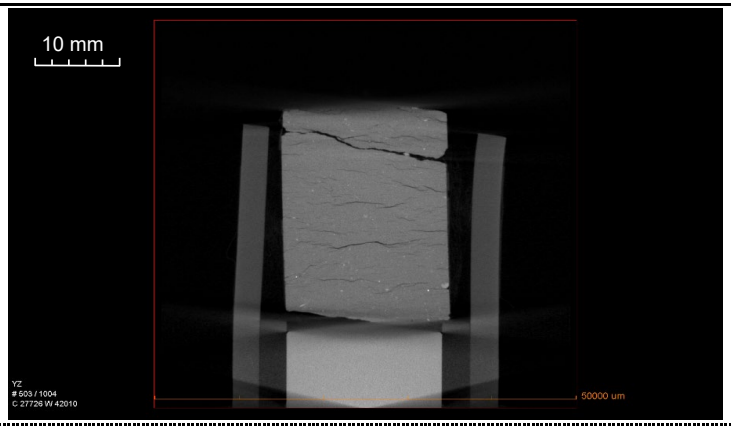	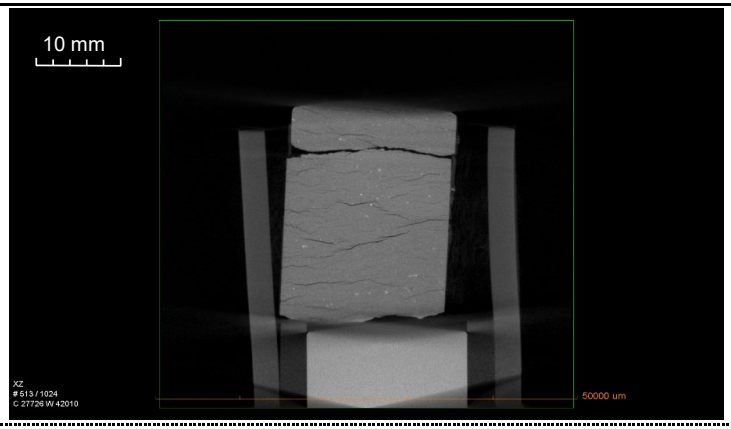
Possible Fractures: x	x

Back to Summary

Micro CT Images

Operator: Best Core Services
Premier Job No.: US-21-J9
Date: 2/23/2021

Sample ID: 5 **Depth:** 6194.00 ft

Comments:
Diagonal fractures noted throughout sample.

Cross-Sectional Images

25%	50%	75%
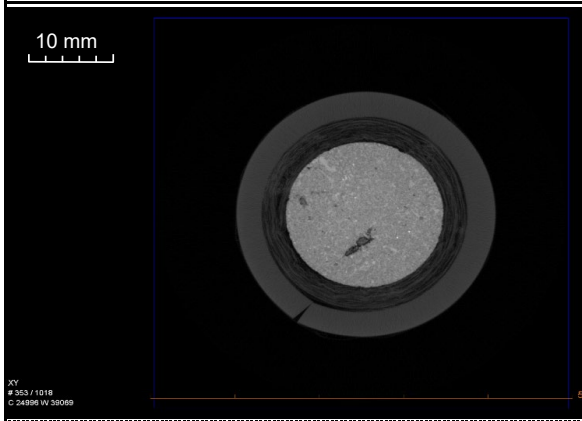	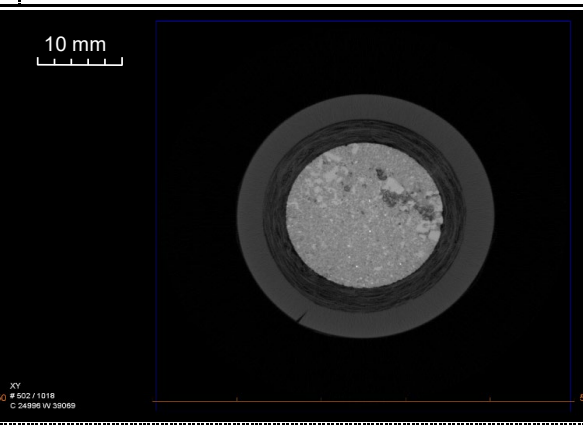	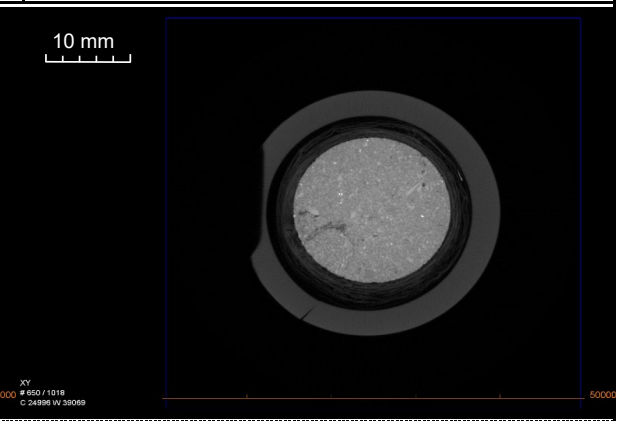
Possible Fractures:	x	

Longitudinal Images

YZ	XZ
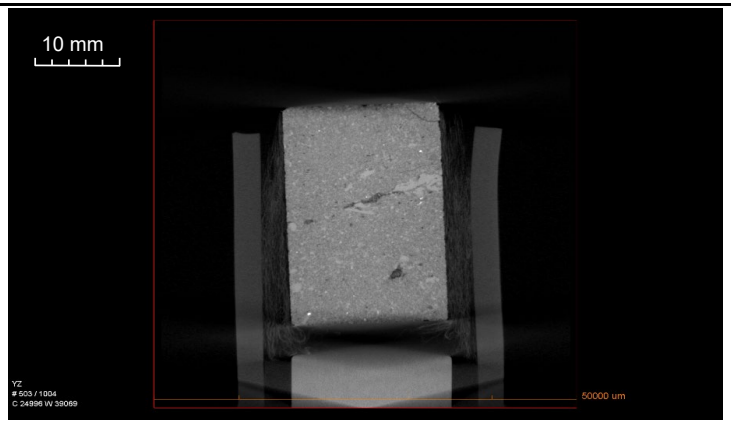	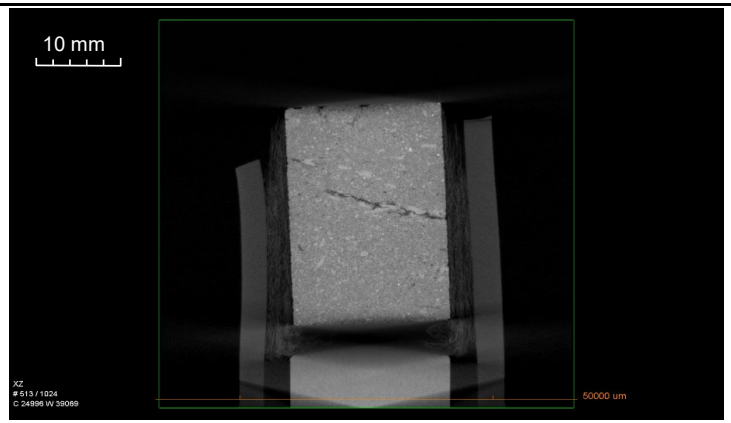
Possible Fractures: x	x

Back to Summary

Micro CT Images

Operator: Best Core Services
Premier Job No.: US-21-J9
Date: 2/24/2021

Sample ID: **5 Post-RMA** **Depth:** **6194.00 ft**

Comments:
Diagonal fractures noted throughout sample.

Cross-Sectional Images

25%	50%	75%
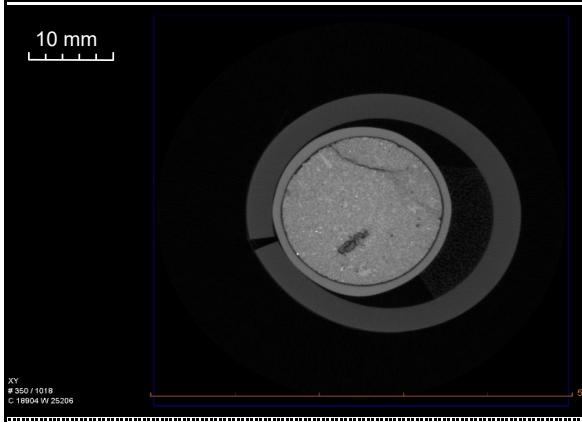	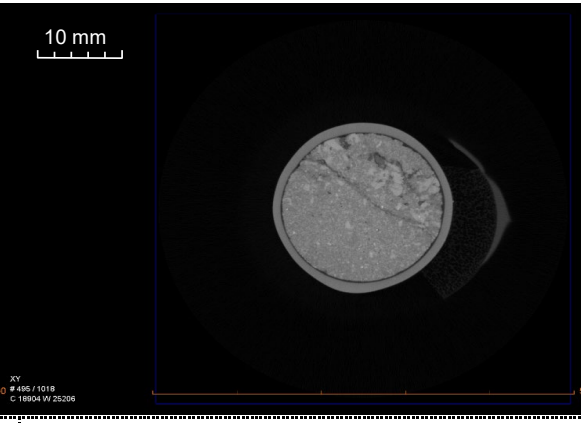	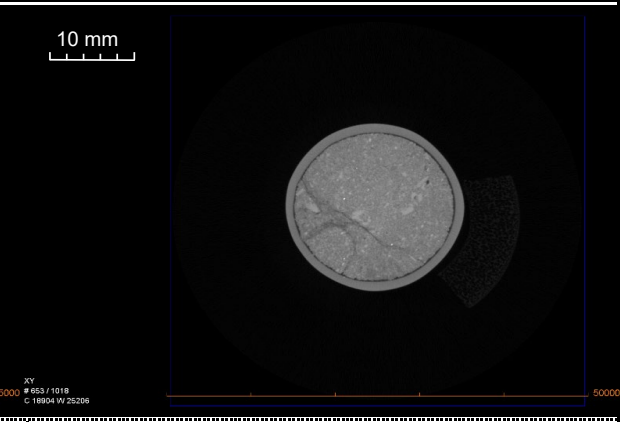
Possible Fractures: x	x	x

Longitudinal Images

YZ	XZ
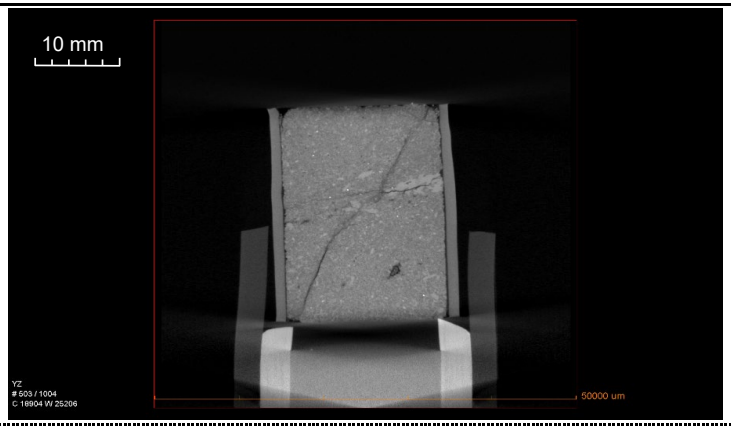	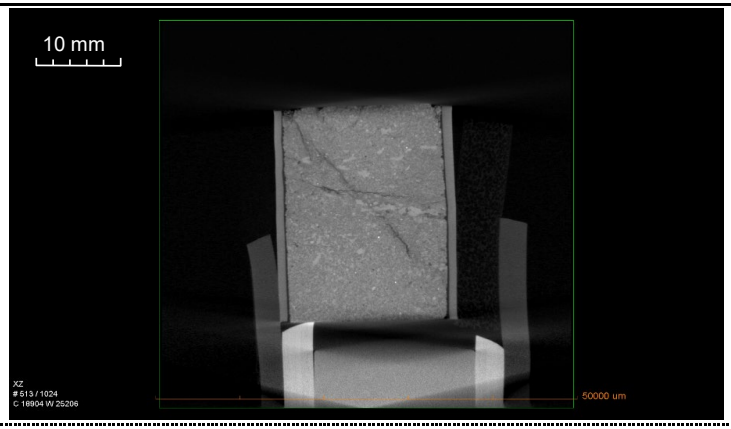
Possible Fractures: x	x

Back to Summary

Micro CT Images

Operator: Best Core Services
Premier Job No.: US-21-J9
Date: 2/23/2021

Sample ID: 3 **Depth:** 8499.00 ft

Comments:
Cross-sectional and diagonal fractures noted throughout sample.

Cross-Sectional Images

25%	50%	75%
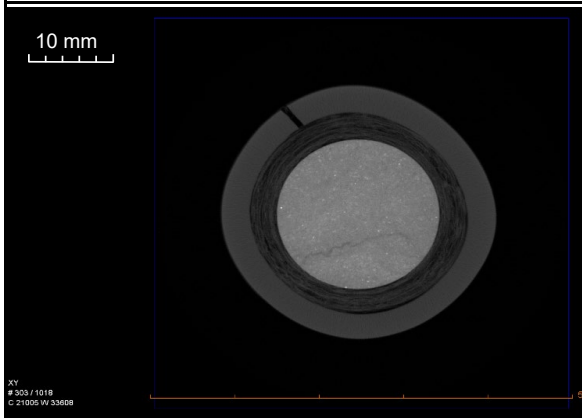	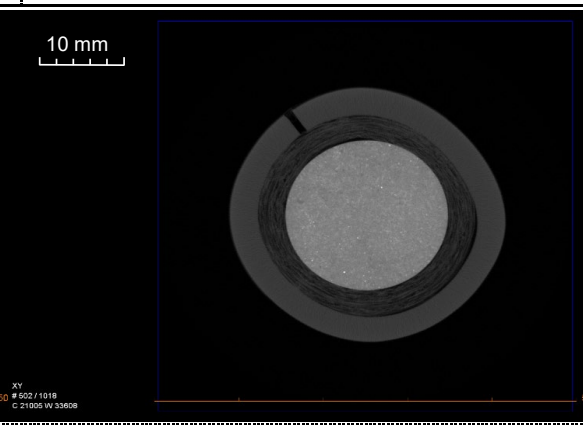	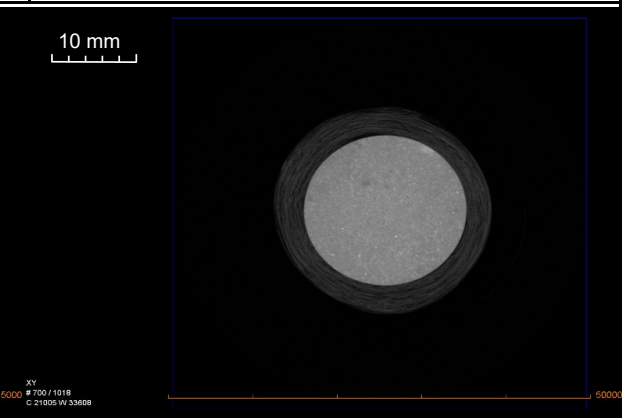
Possible Fractures: x		

Longitudinal Images

YZ	XZ
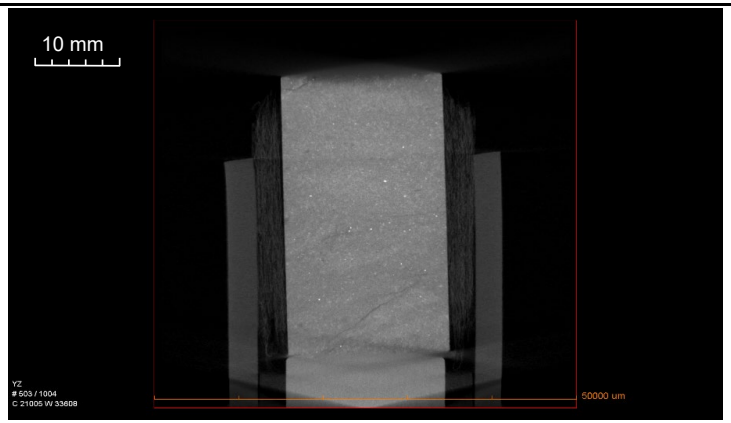	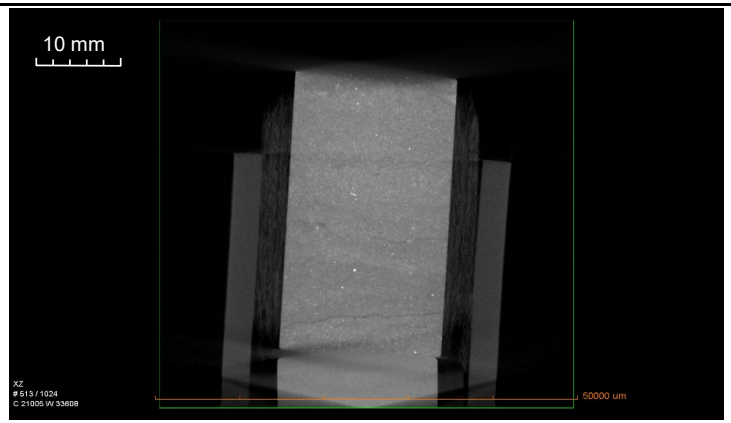
Possible Fractures: x	x

Back to Summary

Micro CT Images

Operator: Best Core Services
Premier Job No.: US-21-J9
Date: 2/24/2021

Sample ID: **3 Post-RMA** **Depth:** **8499.00 ft**

Comments:
Diagonal and longitudinal fractures noted throughout sample.

Cross-Sectional Images

25%	50%	75%
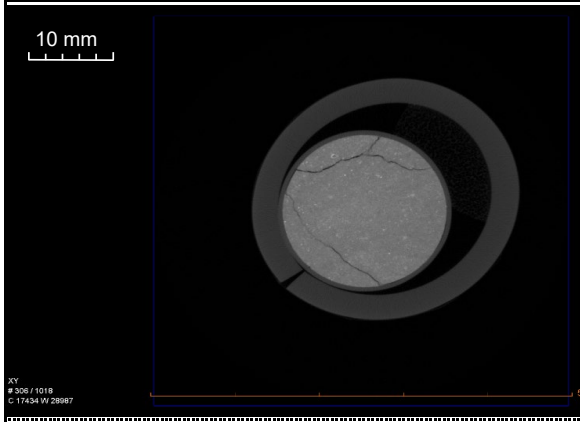	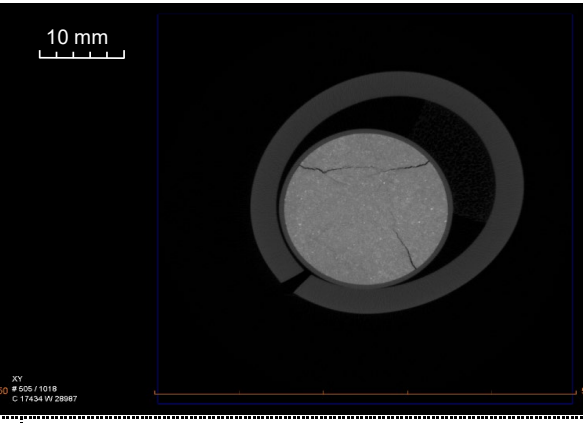	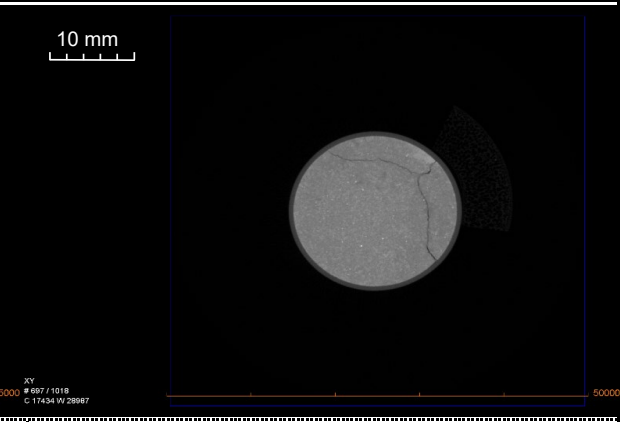
Possible Fractures: x	x	x

Longitudinal Images

YZ	XZ
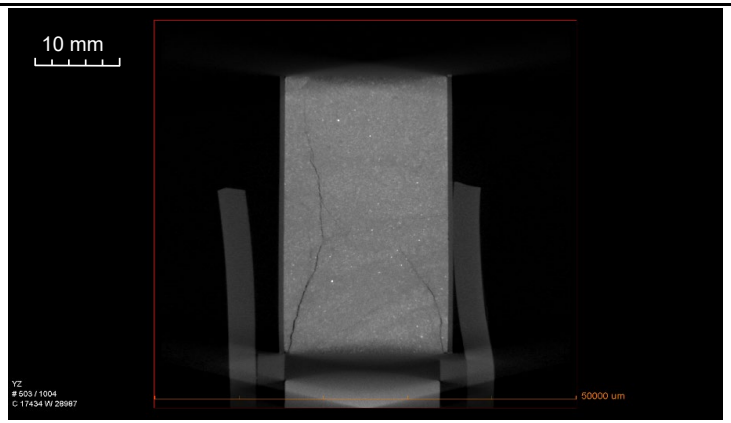	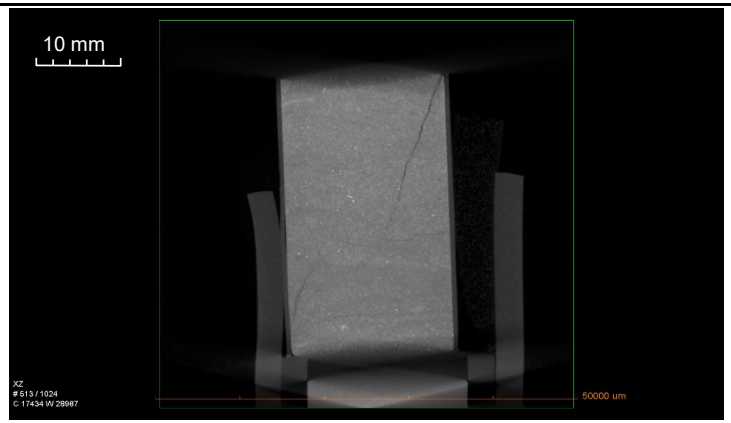
Possible Fractures: x	x

Back to Summary

Test Report

Client:	Best Core Services	MI#:	21013
Project:	Multiple Wells	Date:	03/01/21
Location:	N/A	Job #:	BCS#200083

Client	Best Core Services		
	Attn: Bryan Bell		
	111 Lake Street		
	Bakersfield, CA 93305		
Email	bryan.arval.bell@gmail.com	**Phone**	661-835-6001

Method(s)	Calibration Date	Timothy B. Murphy
X-ray Diffraction Thin Section Petrography Scanning Electron Microscopy	02/25/20	

- Conditions & Qualifications
  - 4308-4333; MI#21013-02
    - Thin Section • SEM
  - 4801-4805; MI#21013-04
    - Thin Section • SEM
  - 8161-8170; MI#21013-23
    - Thin Section • SEM
  - 8499-8510; MI#21013-27
    - Thin Section • SEM
  - 8633-8643; MI#21013-29
    - Thin Section • SEM
  - 6194; MI#21013-33
    - Thin Section • SEM

CONDITIONS AND QUALIFICATIONS

Mineralogy, Inc. will endeavor to provide accurate and reliable laboratory measurements of the samples provided by the client. The results of any x-ray diffraction, petrographic or core analysis test are necessarily influenced by the condition and selection of the samples to be analyzed. It should be recognized that geological samples are commonly heterogeneous and lack uniform properties. Mineralogical, geochemical and/or petrographic data obtained for a specific sample provides compositional data pertinent to that specific sampling location. Such "site-specific data" may fail to provide adequate characterization of the range of compositional variability possible within a given project area, thus the "projection" of these laboratory findings and values to adjoining, "untested" areas of the formation or project area is inherently risky, and exceeds the scope of the laboratory work request. Hence, Mineralogy, Inc. shall not assume any liability risk or responsibility for any loss or potential failure associated with the application of "site or sample-specific laboratory data" to "untested" areas of the formation or project area. Unless otherwise directed, the samples selected for analysis will be chosen to reflect a visually representative portion of the bulk sample submitted for analysis. Where provided, the interpretation of x-ray diffraction, petrographic or core analysis results constitutes the best geological judgment of Mineralogy, Inc., and is subject to the sampling limitations described above, and the detection limits inherent to semi-quantitative and/or qualitative mineralogical and microscopic analysis. Mineralogy, Inc. assumes no responsibility nor offers any guarantee of the productivity, suitability or performance of any oil or gas well, hydrocarbon recovery process, dimension stone, and/or ore material based upon the data or conclusions presented in this report.

This report is to only be replicated in its entirety.

Sample Retention: Samples will be stored for a period of 30 days and thereafter discarded. If additional sample storage time and/or return shipping is required, appropriate charges will be billed to the client.

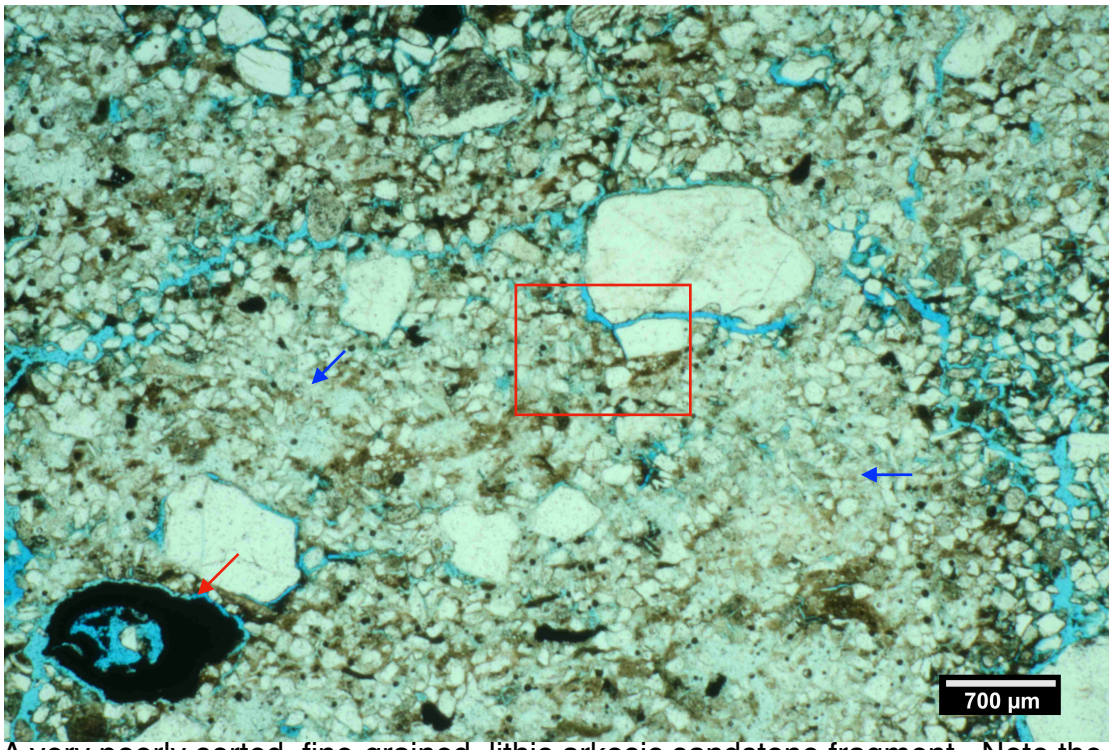

2A. A very poorly sorted, fine-grained, lithic arkosic sandstone fragment. Note the magnetite cement (black; red <) & the patches of pore-filling smectite matrix (white; blue <).

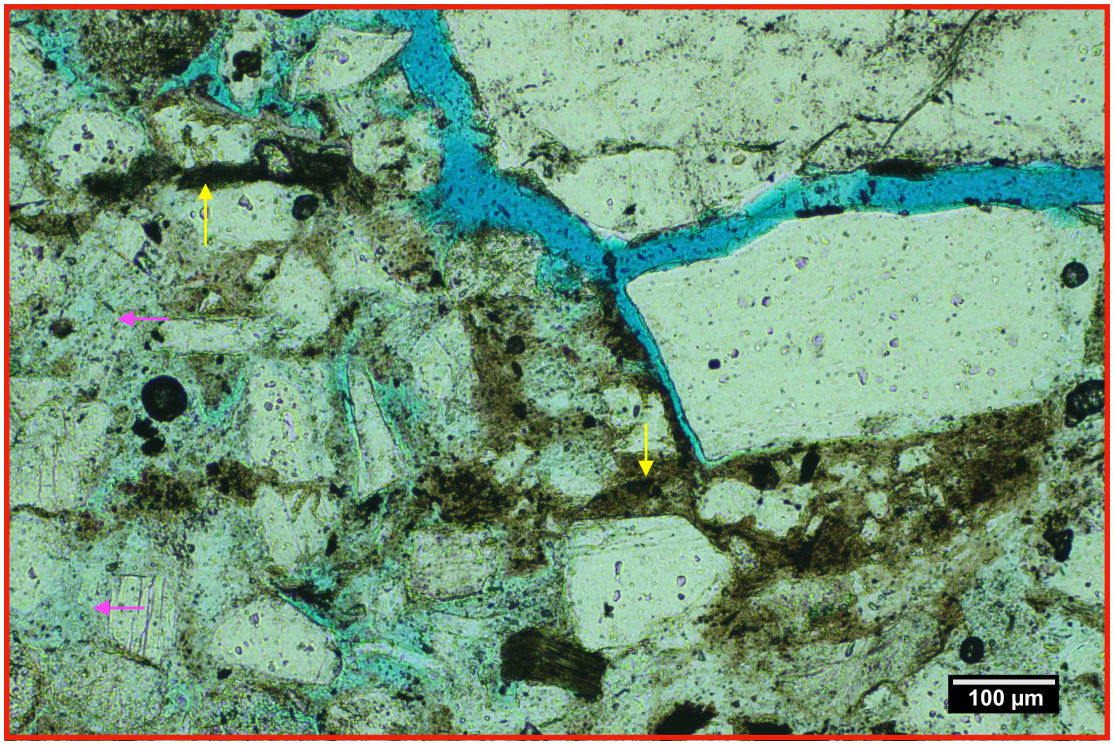

2B. Detailed view of the highlighted area from Figure 2A. Lenses of organic-rich detrital clay (brown; yellow <) are locally deformed due to compaction. Note the leached feldspar grains + (grain-replacement) microporous smectite (magenta <).

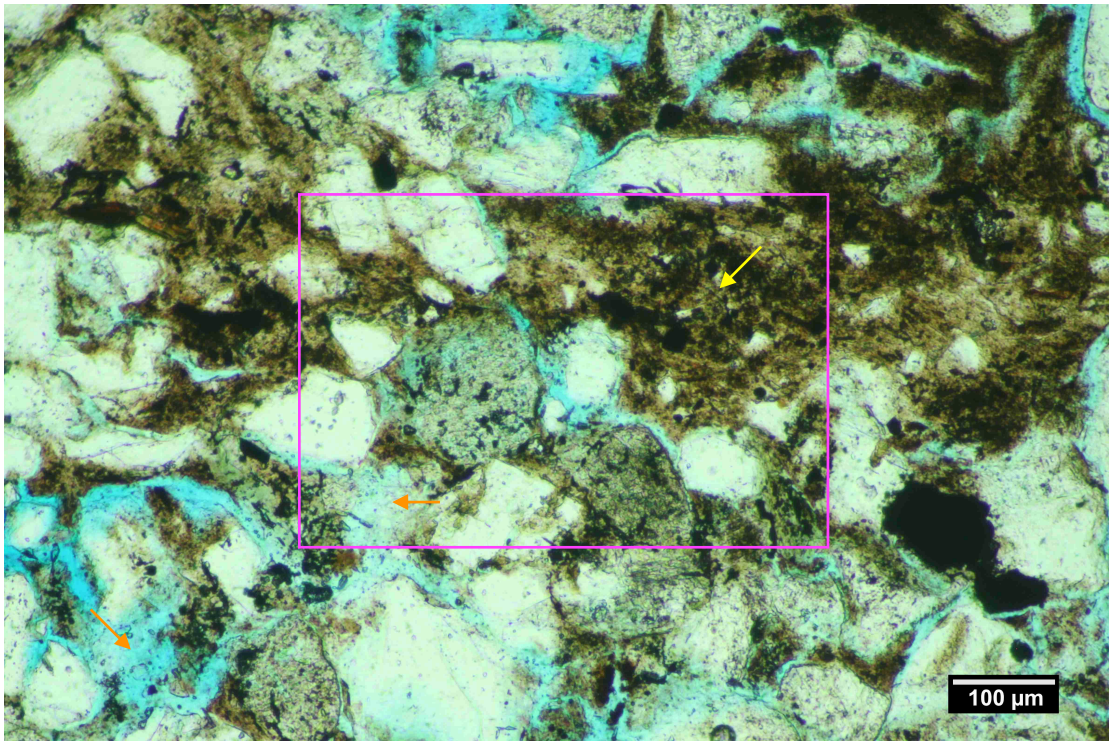

2C. A large concentration of silt-rich pore-filling detrital clay (yellow <). Note the secondary macro porosity (orange <). The highlighted area is detailed in Figure 2D.

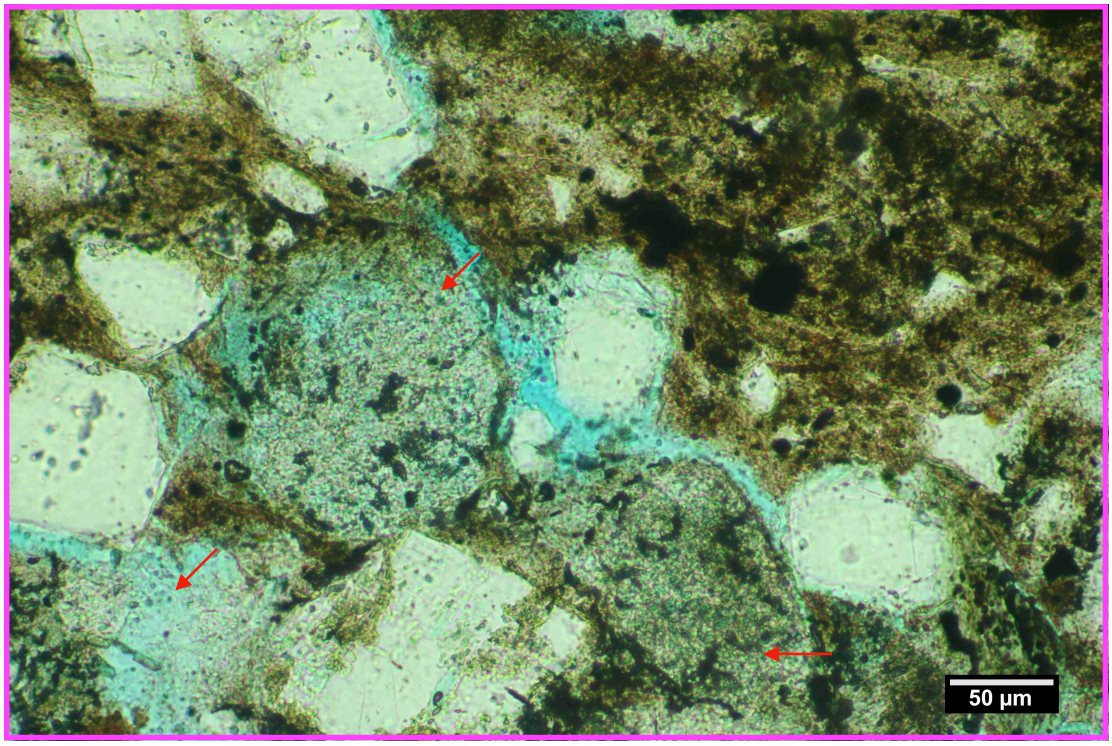

2D. Selected detrital sand grains (including feldspar & glass-rich volcanic RFs; red <) are extensively leached and replaced with authigenic smectite +/- kaolinite +/- magnetite).

Rocket Abrams 1

API_03-02930521

4308-4333 ft.

MI#21013-02 - SEM

Summary: This core fragment from the is characterized as a fine-grained, poorly sorted, matrix-rich, lithic arkosic sandstone. The sandstone framework is cross-bedded, burrow mottled, and comprised of feldspar + quartz + igneous rock fragments. Scattered concentrations of iron oxide (magnetite) and pyrite cements are present (likely as grain-replacements for particles of organic matter). The inter granular spaces are commonly filled with compact masses of infiltrated detrital clay matrix. XRD results estimate the concentration of amorphous material + total clay comprises ~ 35% of the sample mass, with smectite accounting for ~ 90% of the total clay fraction. The sequence of SEM images (21013-02A through 21013-02D) illustrate the massive and compact nature of the pore-filling, detrital smectite. Scattered concentrations of pyrite and magnetite are present as accessory authigenic cements (see 21013-02D). Residual inter-granular macro pores commonly occur as small localized voids protected by juxtaposed detrital grains. Dissolution macro porosity occurs as secondary grain-moldic and intra-granular dissolution voids - commonly associated with corroded feldspar grains and volcanic rock fragments. Figures 21013-02E through 21013—02G illustrate secondary dissolution void space attributed to feldspar corrosion. The skeletal remnants of the corroded feldspar grain frame the void & are encrusted with authigenic clay (smectite +/- kaolinite; e.g., 21013-02G).

20078-01 Photo Index: (bookmarks)

Sample ID	Magnification
21013-02A	260X
21013-02B	500X
21013-02C	2000X
21013-02D	8000X
21013-02E	500X
21013-02F	2000X
21013-02G	8000X

Detrital (smectite-rich) matrix	DM
Feldspar	F
Authigenic smectite	S
Pyrite cement	P

21013-02A 260X

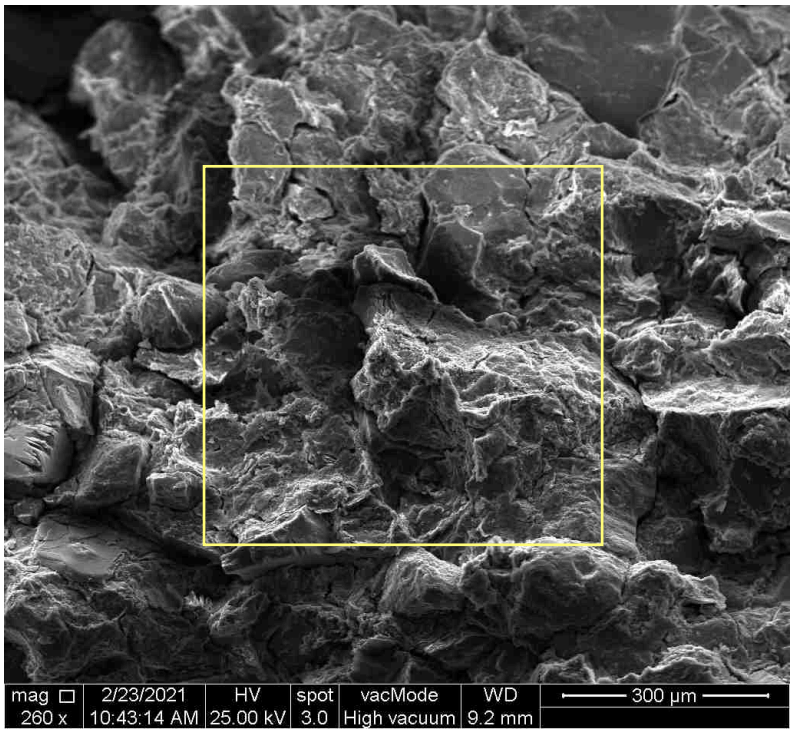

21013-02B 500X

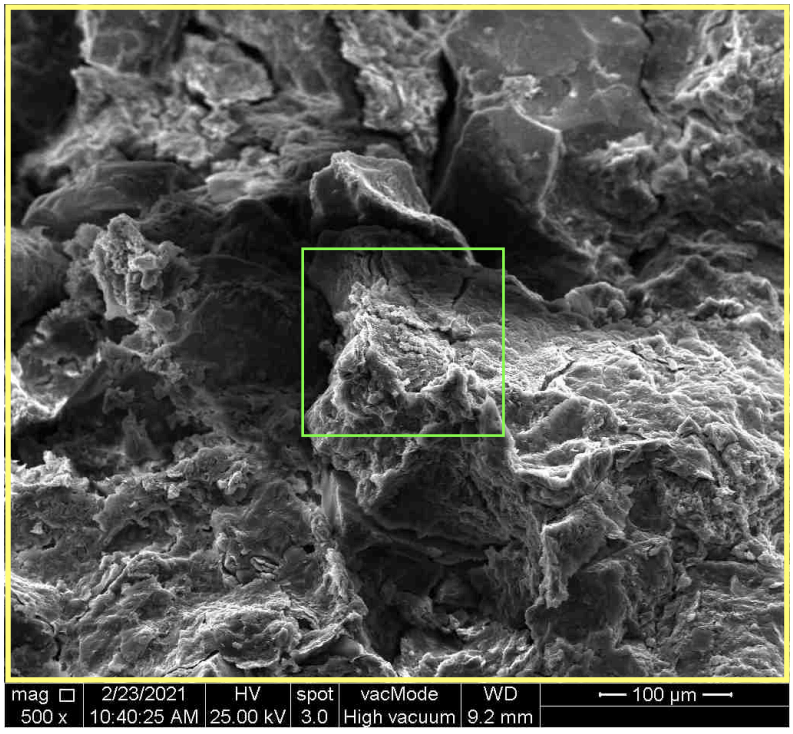

21013-02C 2000X

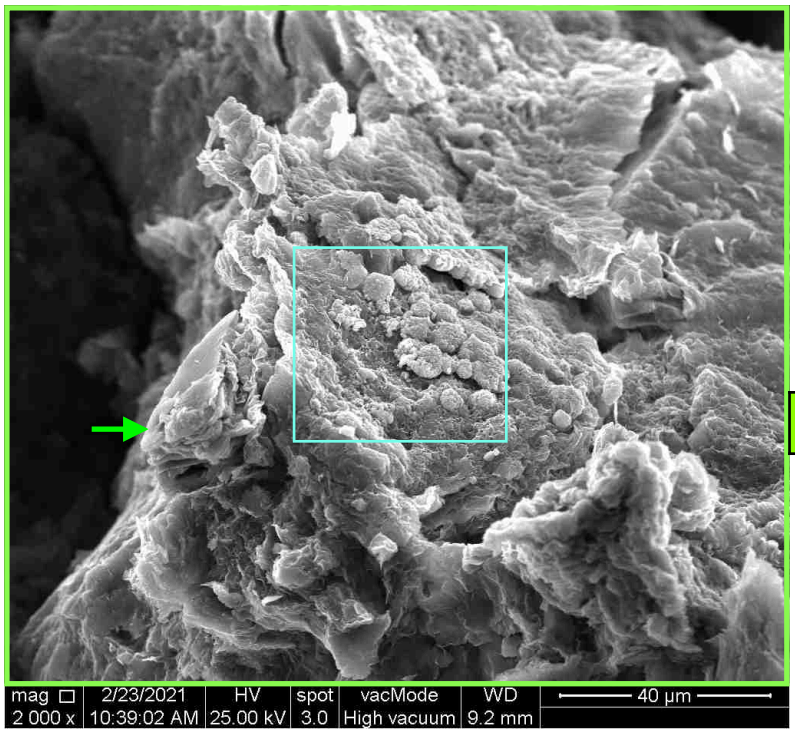

DM

21013-02D 8000X

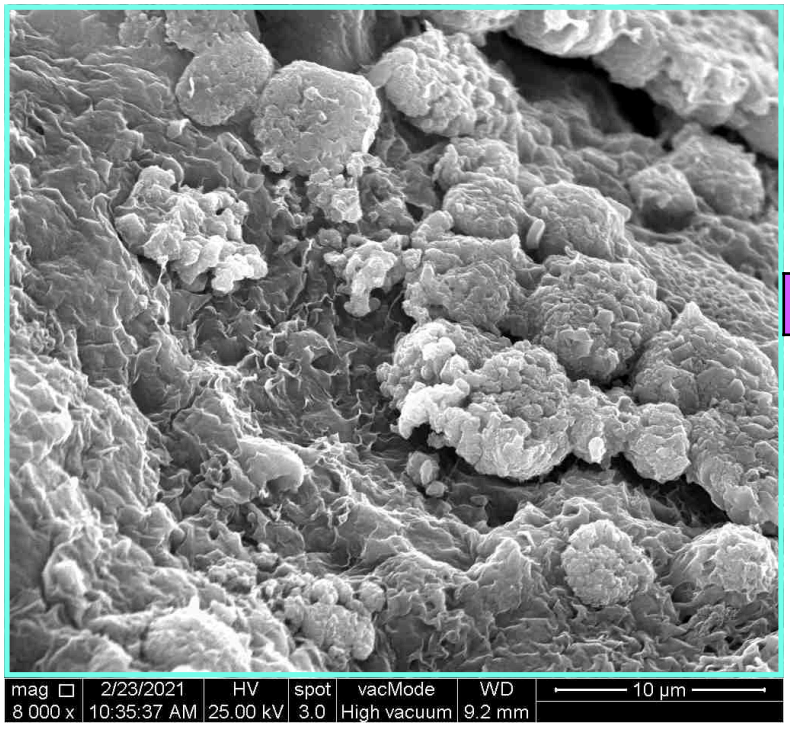

P

21013-02E 500X

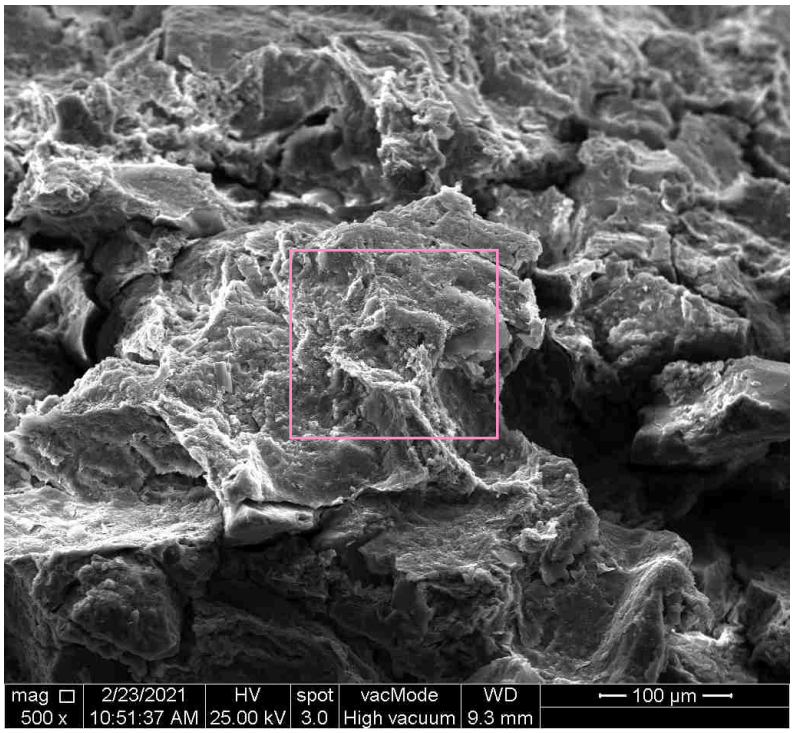

21013-02F 2000X

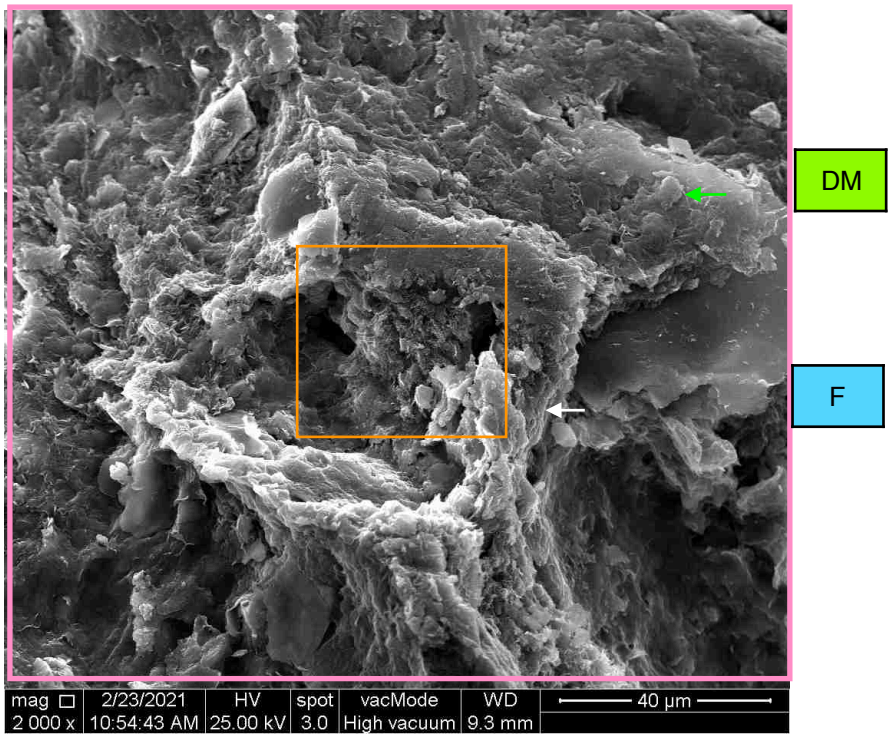

21013-02G 8000X

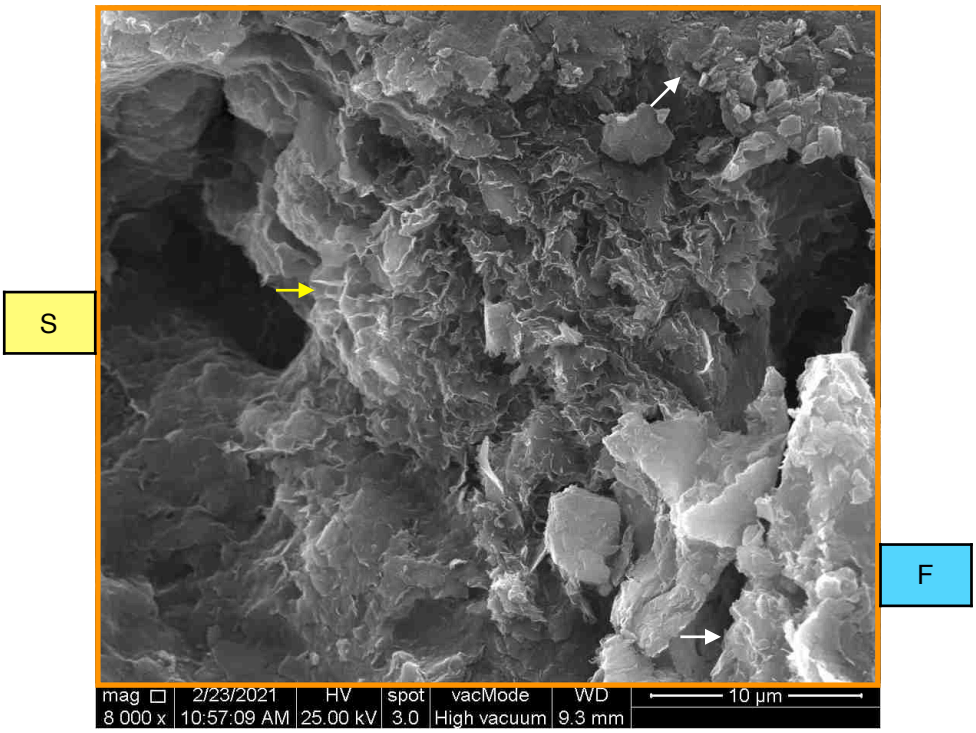

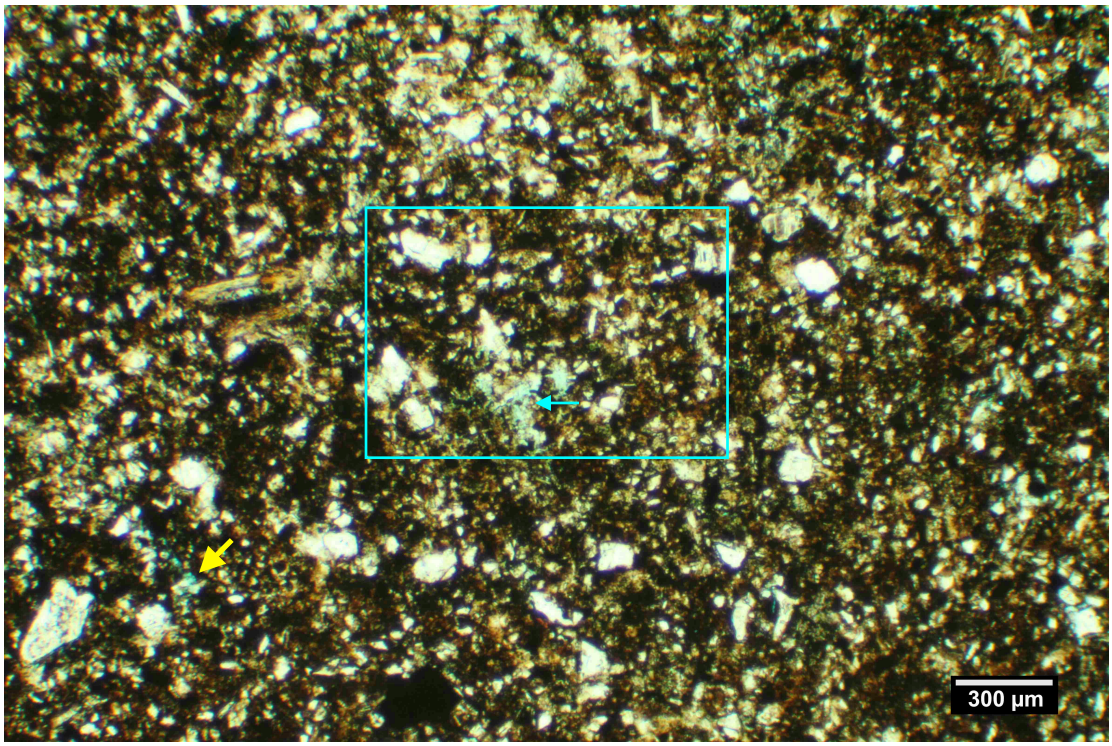

4A. An organic-rich, fossiliferous, silty mudstone. Note the scattered patches of macro porosity (blue <). The highlighted area is detailed in Figure 4B.

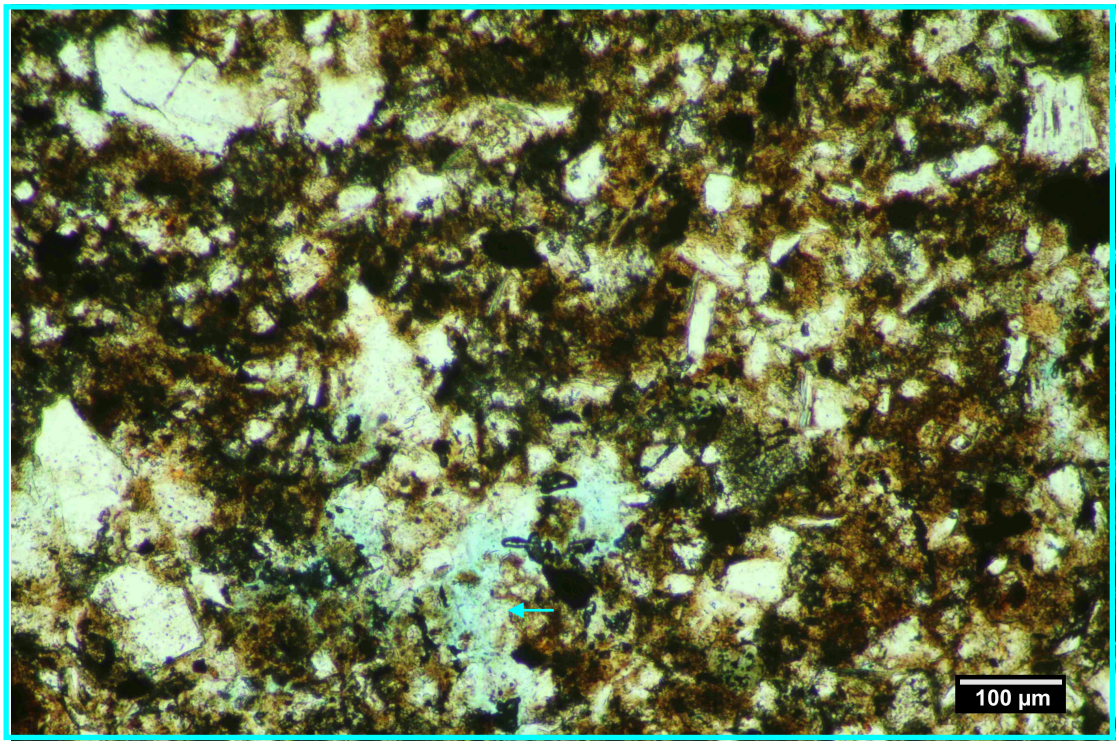

4B. A detailed view of the highlighted area from Figure 4A. This clay-rich sandstone contains an abundance of organic matter that has diminished the light transmission of the groundmass.

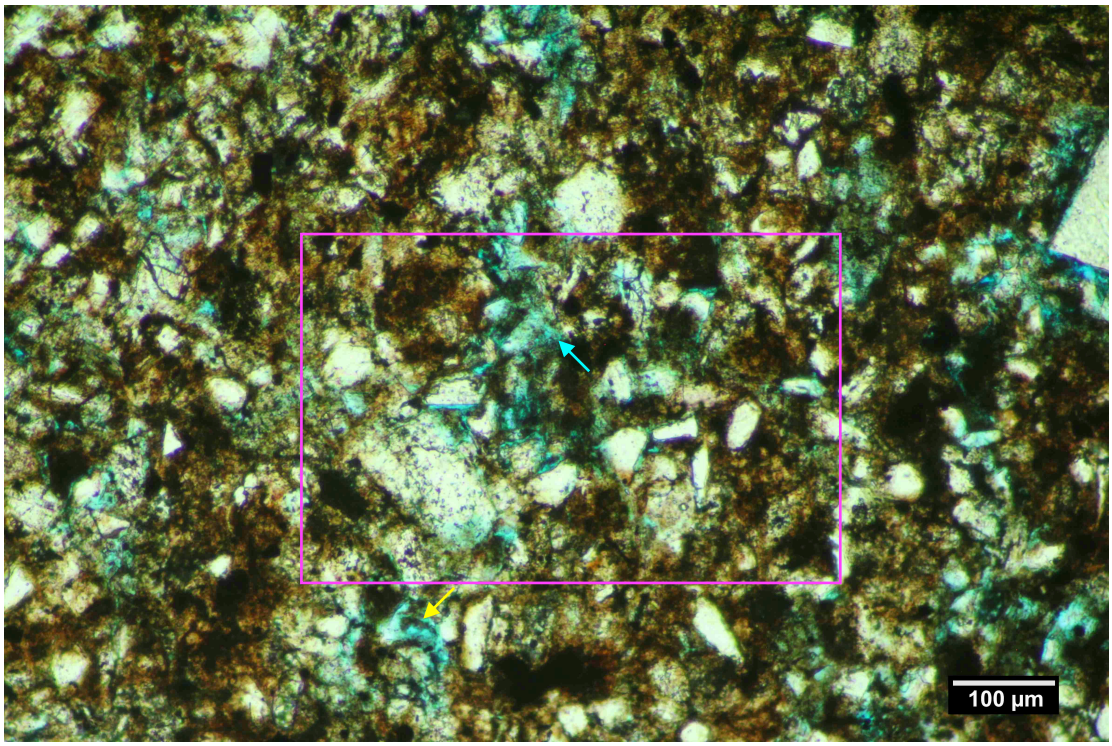

4C. Intergranular + secondary dissolution macro porosity (blue <). The highlighted area is detailed in Figure 4D.

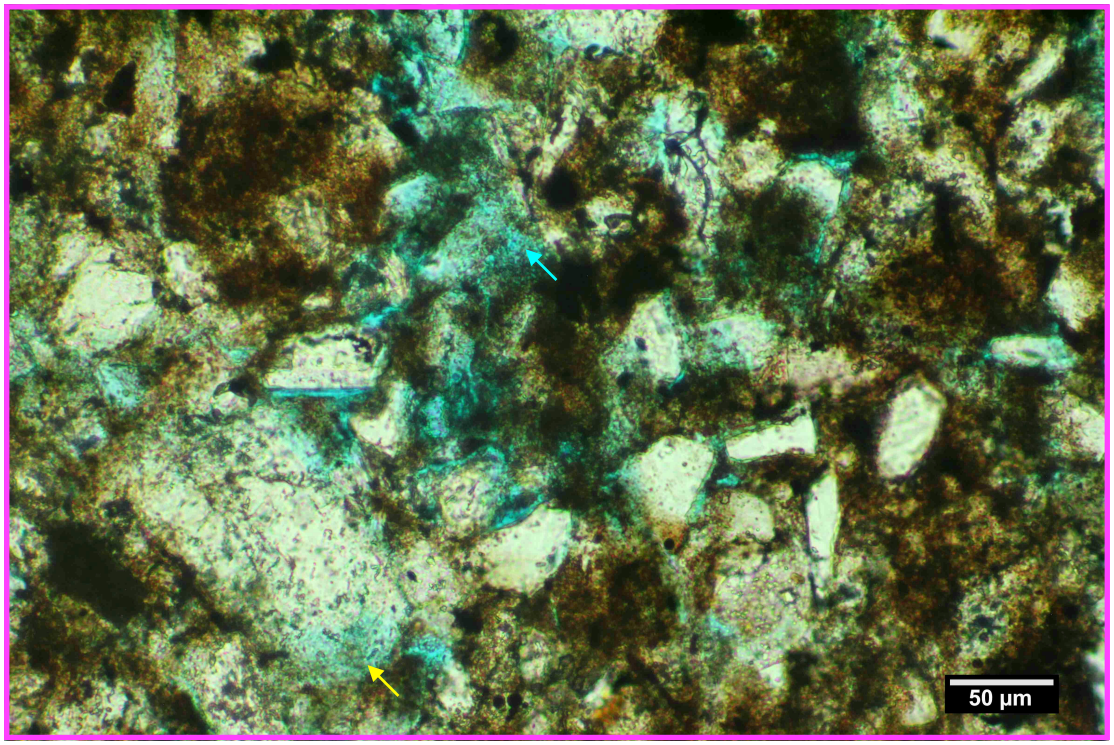

4D. Dissolution macro-porosity associated with leached feldspar grains (blue <) is a major contributor to the pore system. Intergranular pore throats are locally choked with smectite

Shell Bell 52-21
API_03-02930523

4801-4805 ft.
MI#21013-04 - SEM

Summary: This interval is comprised of organic matter-rich, fossiliferous, silty mudstone. Residues of organic matter pervade the micropores of the siltstone, and have contributed to the dense and locally opaque appearance of the matrix in transmitted light. Framework grains exhibit a lithic-arkosic composition that is dominated by feldspar + quartz + igneous rock fragments (RFs) + mudstone / shale RFs + opaline skeletal fragments. The XRD mineral composition for this silty mudstone indicates a clay-rich groundmass (~53%), comprised of smectite and minor amounts of illite + kaolinite. Opal A and C/T phases are present and comprise ~ 6% of the sample mass as per the XRD mineralogical assessment. Minor amounts of natrojarosite, pyrite, and gypsum are present as secondary, grain-replacement cements.

Sample ID	Magnification
21013-04A	200X
21013-04B	800X
21013-04C	3000X
21013-04D	12000X
21013-04E	800X
21013-04F	3000X

Detrital (smectite-rich) matrix	DM
Feldspar	F
Skeletal fragment	SF
Kaolinite	K

21013-04 Photo Index: (bookmarks)

21013-04A 200X

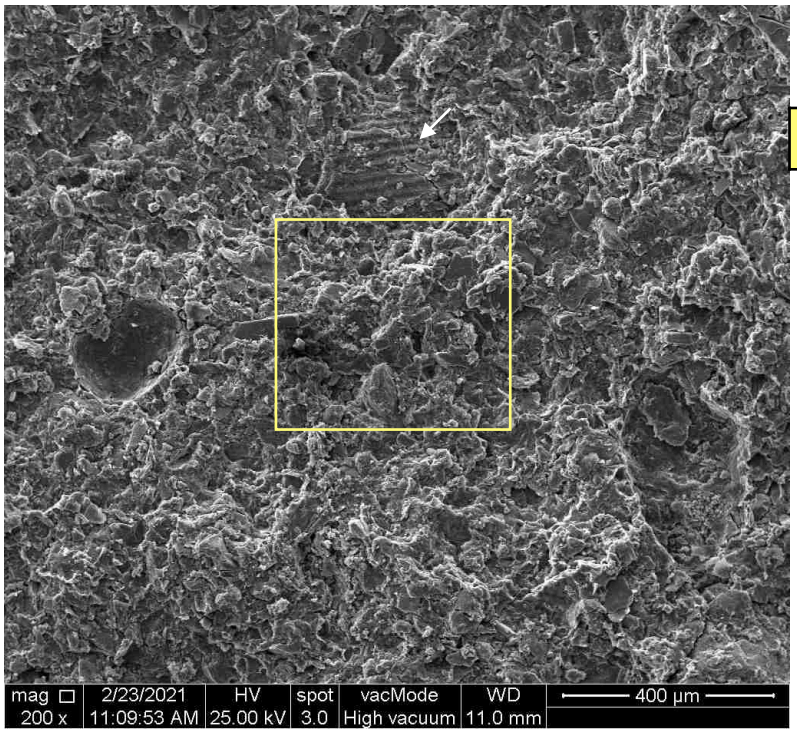

21013-04B 800X

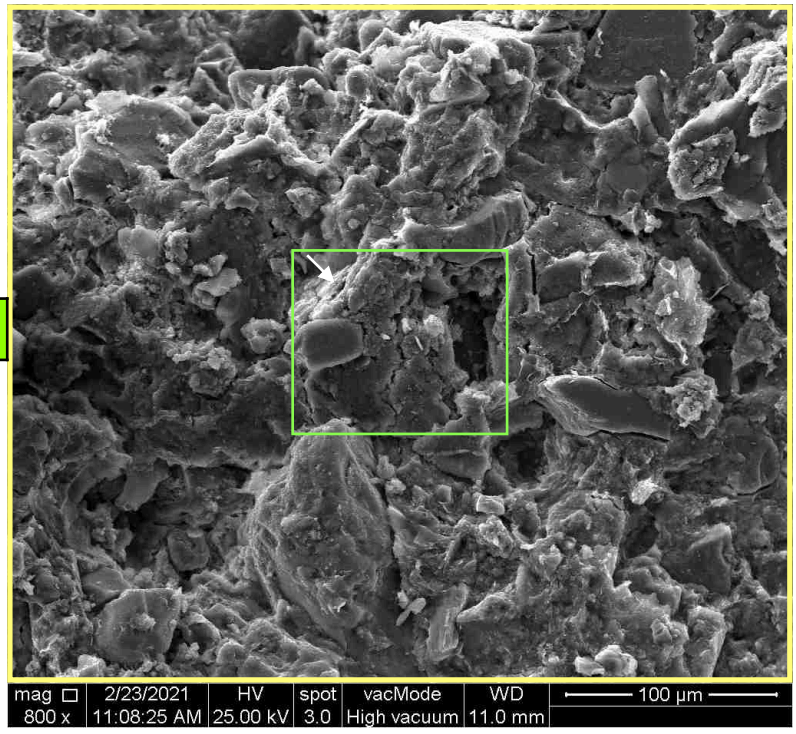

21013-04C 3000X

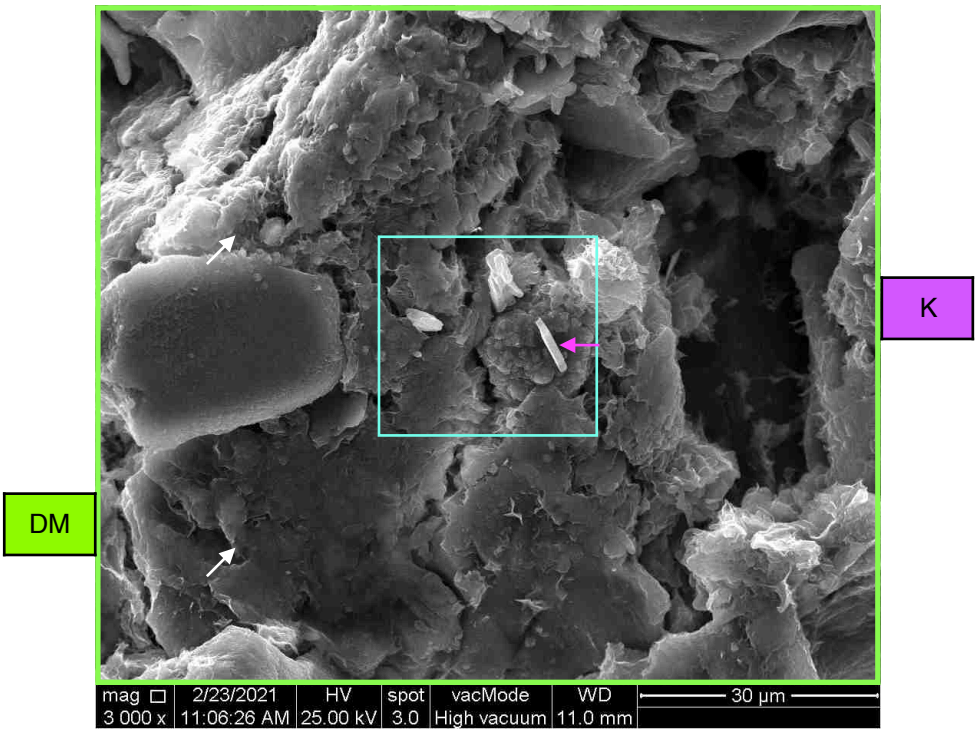

21013-04D 12000X

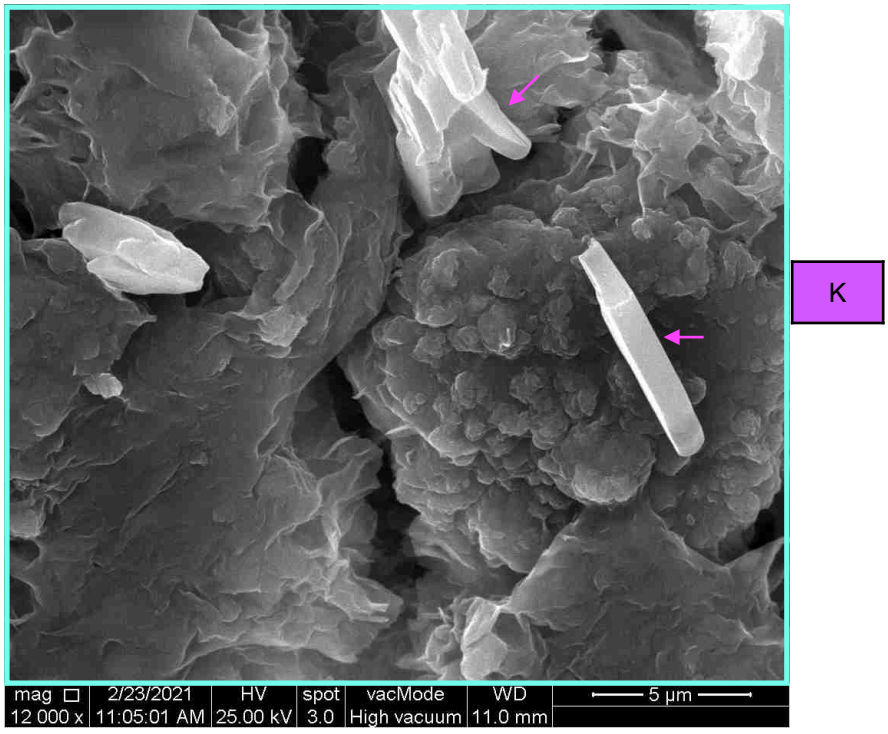

21013-04E 800X

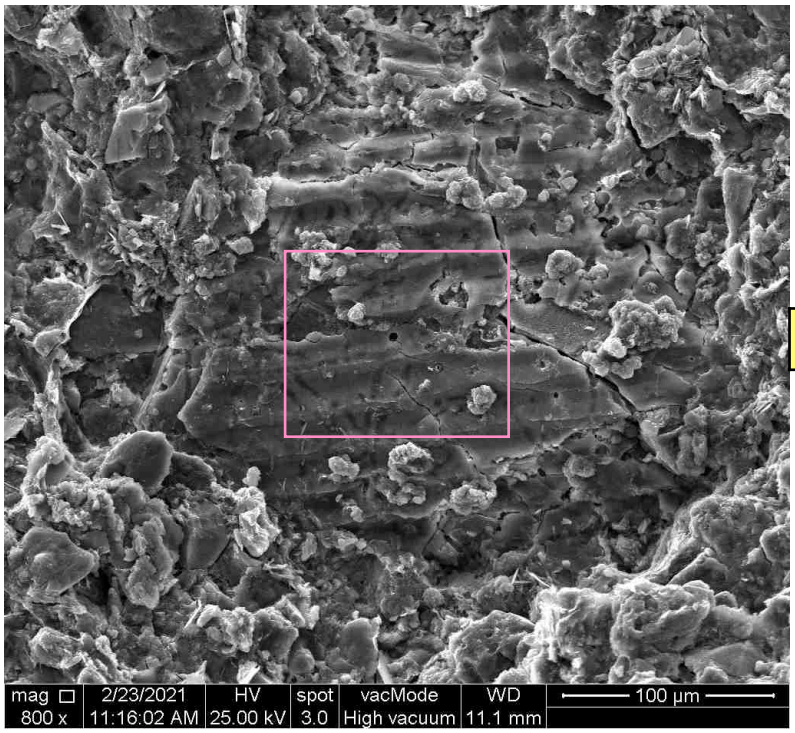

SF

21013-04F 3000X

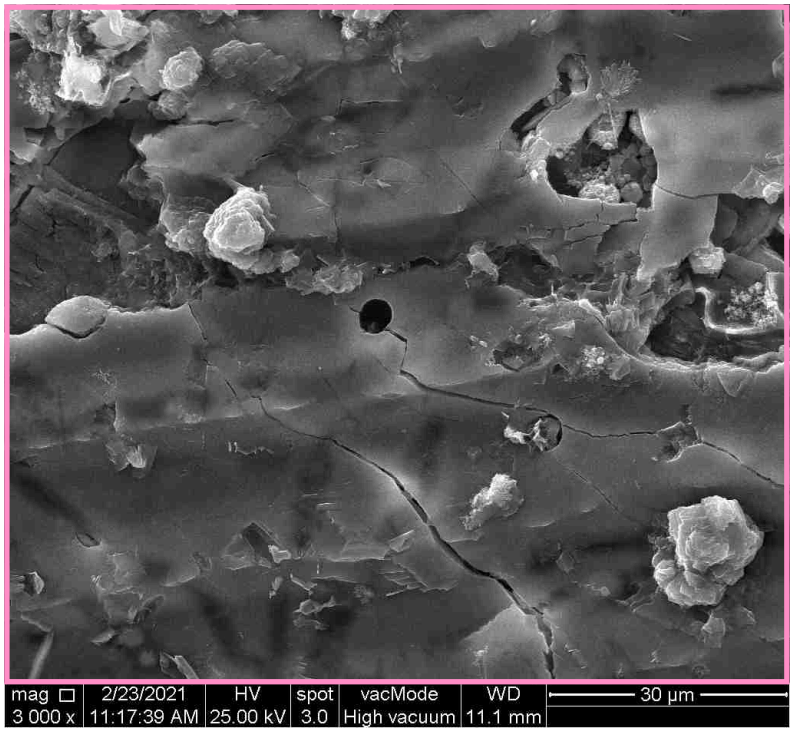

KCL A 83-35 (8161-8170 ft.); MI#21013-23

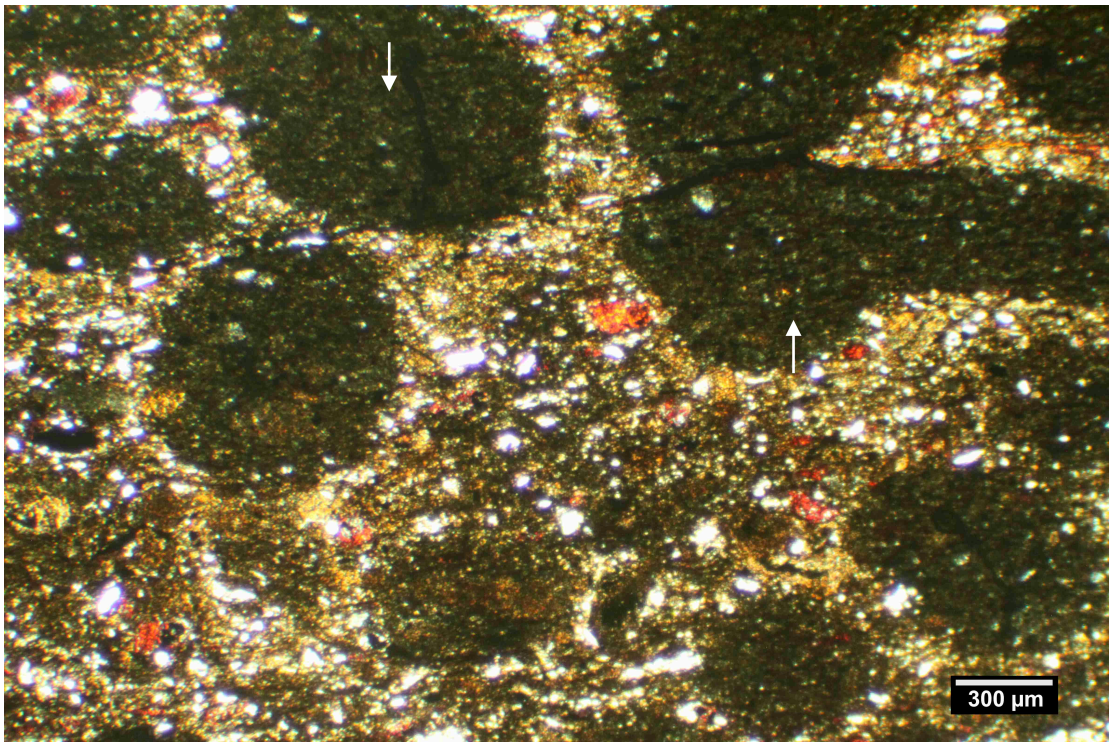

23A. A bio-siliceous, silty & sandy mudstone sample. The oval-shaped discolorations (white <) are fabric heterogeneities tentatively attributed to bioturbation.

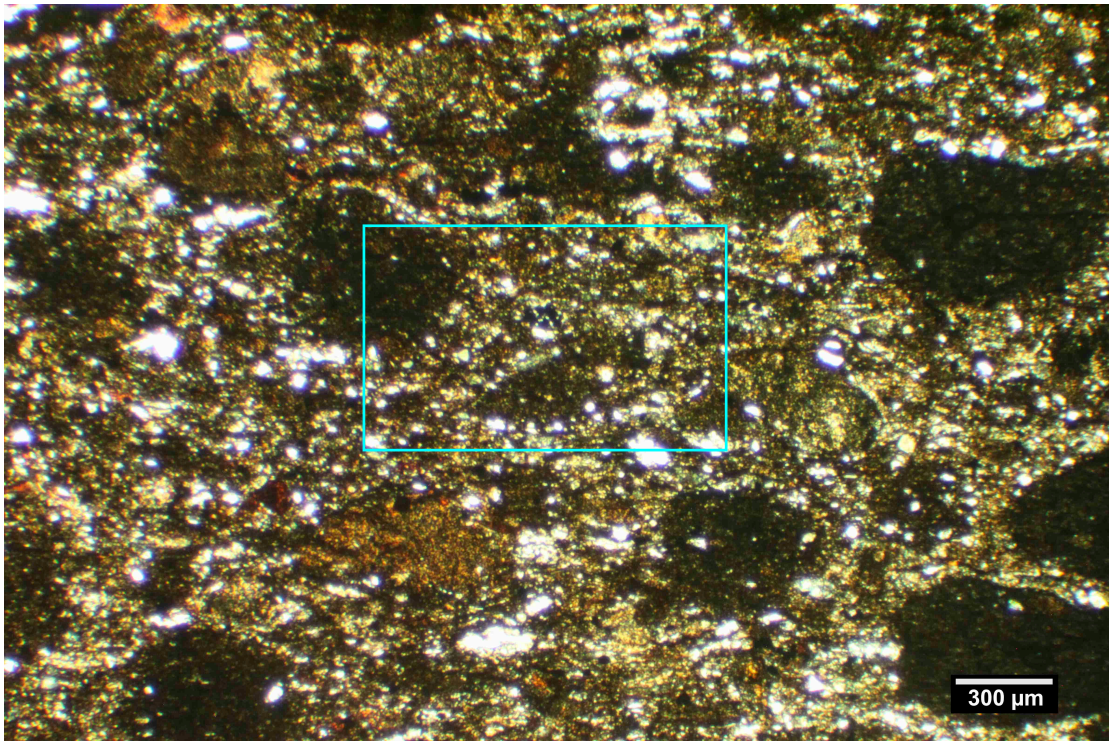

23B. The dense clay-rich groundmass incorporates lenses of opal C/T + microcrystalline pyrite & natrojarosite cements. The highlighted field is detailed in Figure 23C.

KCL A 83-35 (8161-8170 ft.); MI#21013-23

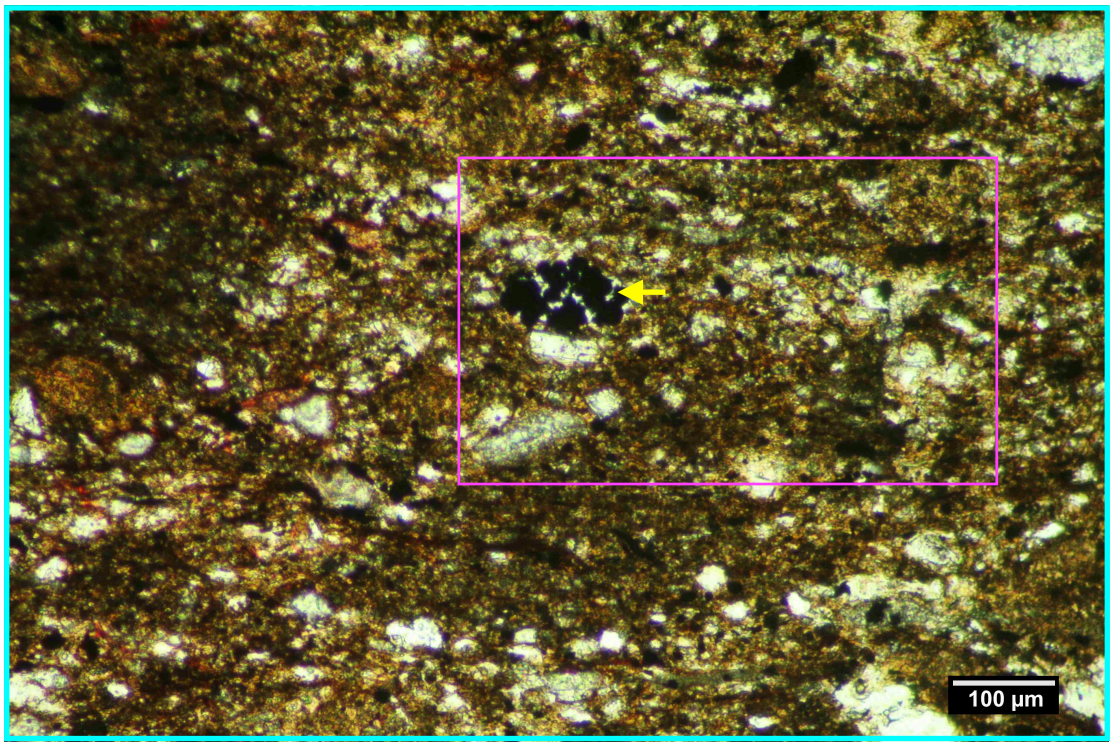

23C. Scattered rock fragments are replaced with pyrite cement (black; yellow <). The pore system appears limited to poorly interconnected micropores.

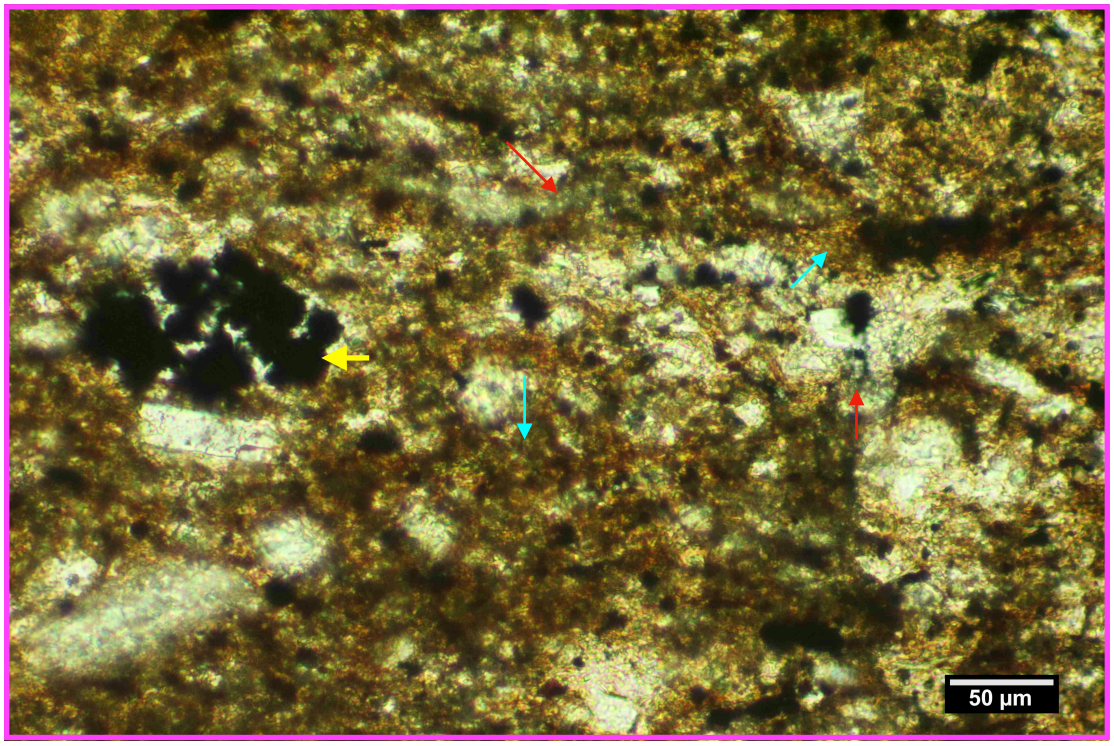

23D. Detailed view of the highlighted area from Figure 23C. Note the concentrations of microporous opaline cement (red <) inter-laminated with the lenses of silty & smectite-rich clay matrix (magenta <).

KCL A 83-35
API_03-02930606

8161-8170 ft.

Summary: This interval of the Freeman Siltstone FM is comprised of organic-rich bio-siliceous silty mudstone. The thin section contains scattered concentrations of opal-A (~15%) & opal-C/T (~9%) in a groundmass of silty, smectite-rich mudstone. The XRD mineralogical assessment for this rock indicates a clay suite dominated by smectite (~26%) + illite / mica (~19%) + kaolinite (~3%). Plagioclase feldspar (~15%), quartz (~8%) and k-feldspar (~3%) grains account for most of the silt & sand materials. Minor, grain-replacement cement materials include natrojarosite & pyrite. Inter-crystalline microporosity is is associated with the opal cement materials.

MI#21013-23 - SEM

21013-23 Photo Index: (bookmarks)

Sample ID	Magnification
21013-23A	400X
21013-23B	1500X
21013-23C	6000X
21013-23D	12000X
21013-23E	800X
21013-23F	3000X
21013-23G	6000X

Detrital (smectite-rich) matrix	DM
Feldspar	F
Skeletal fragment	SF
Kaolinite	K
Opal A	A

21013-23A 400X

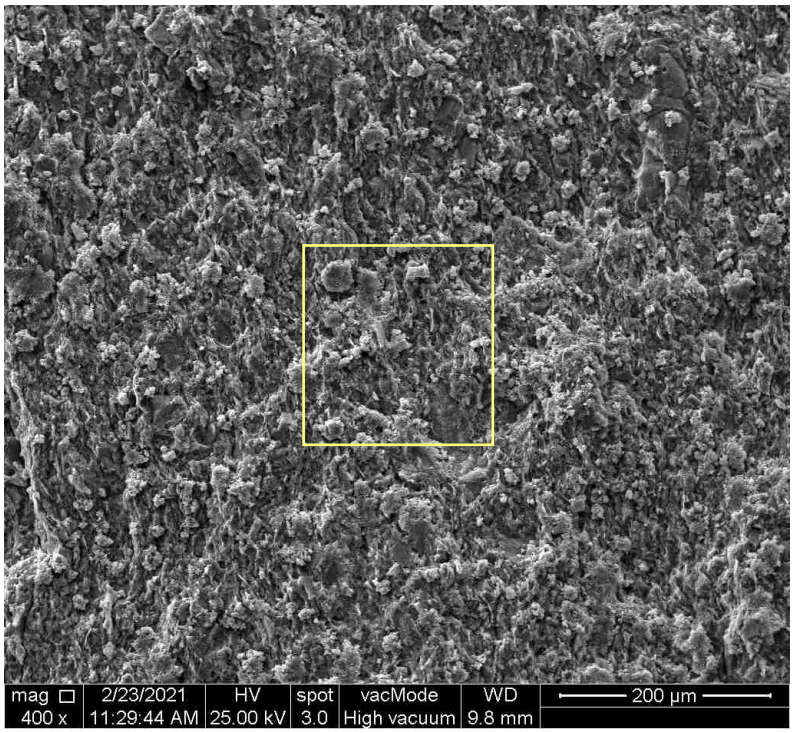

21013-23B 1500X

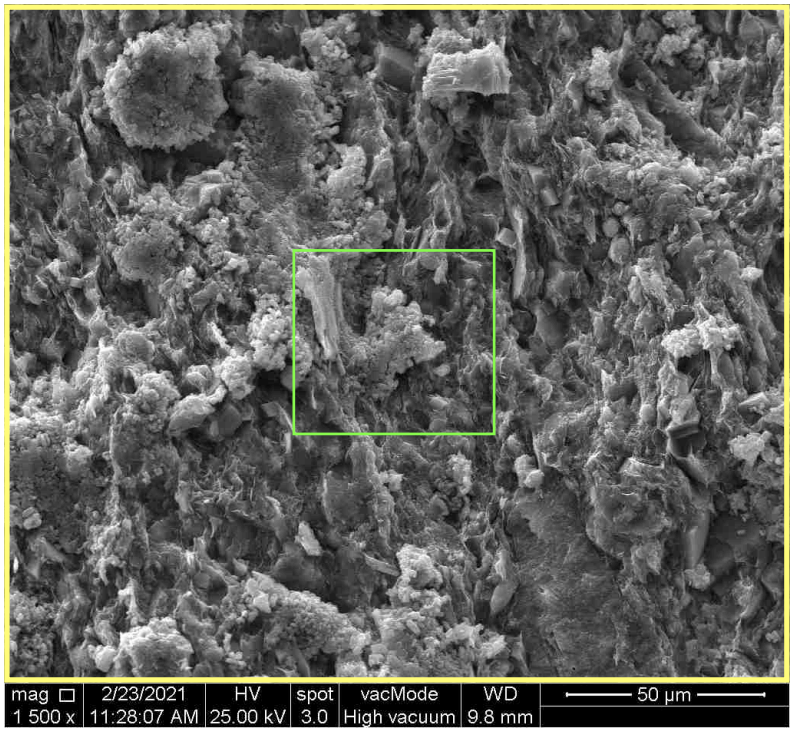

21013-23C 6000X

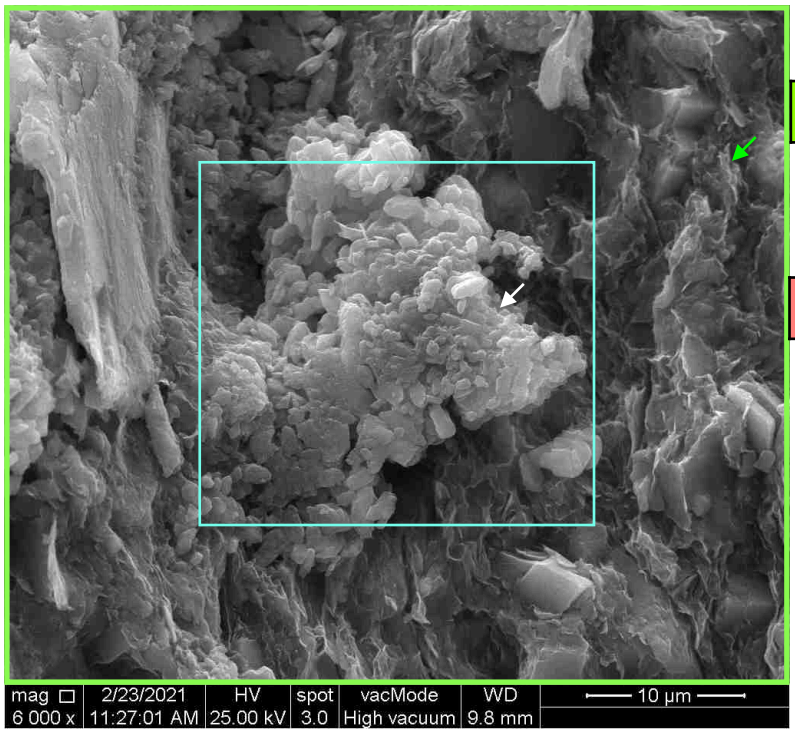

21013-23D 12000X

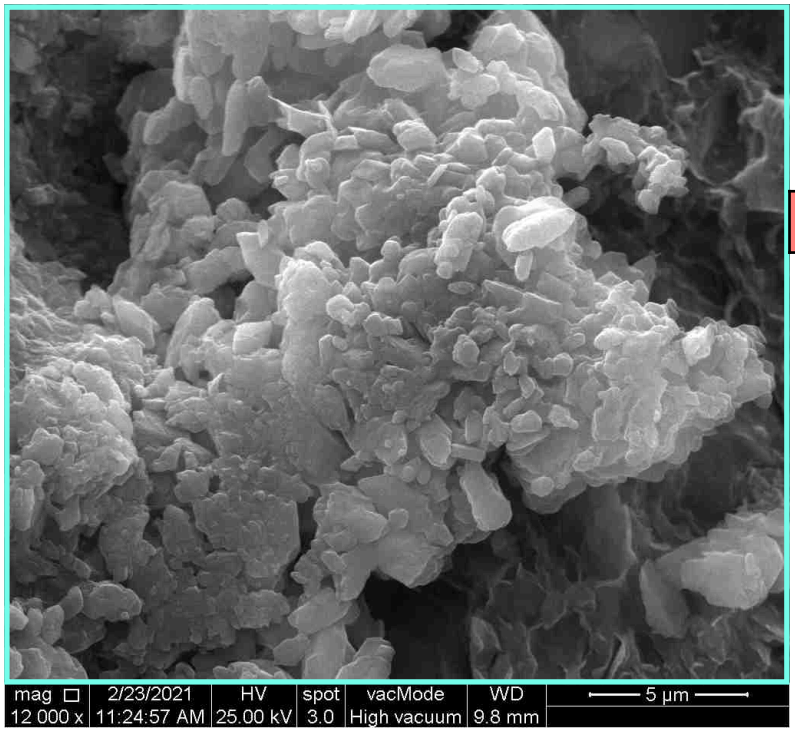

21013-23E 800X

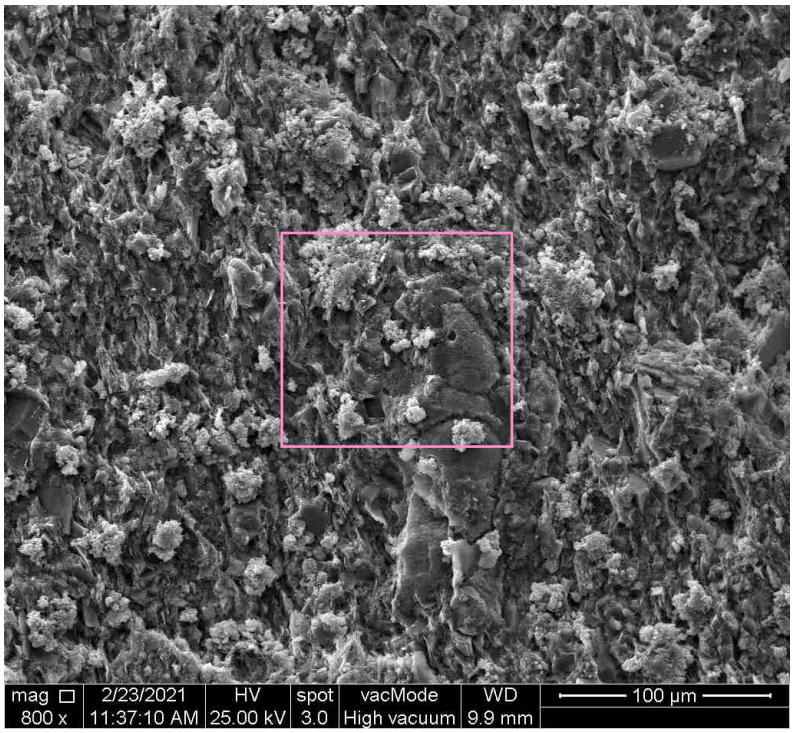

21013-23F 3000X

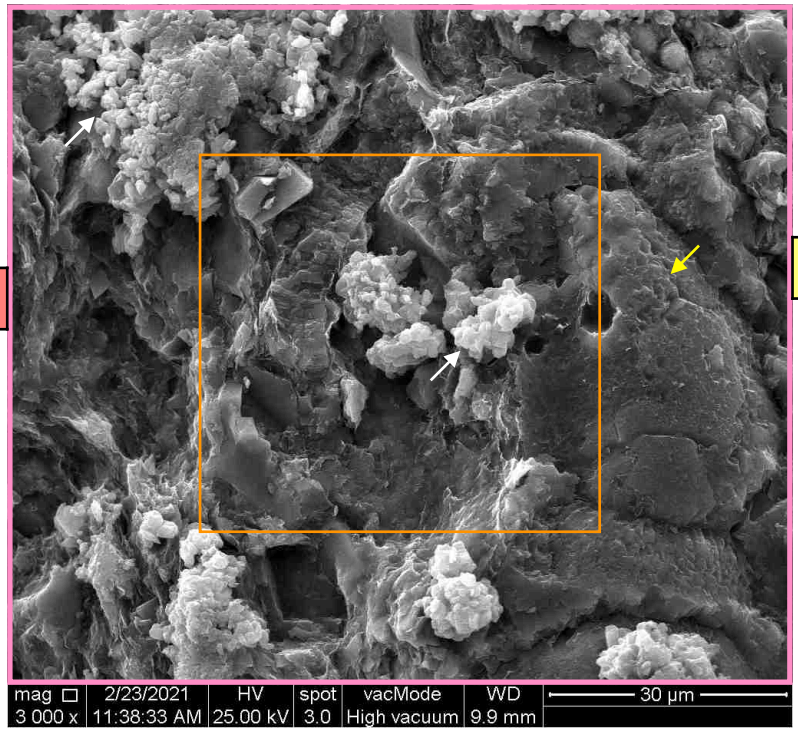

21013-23G 3000X

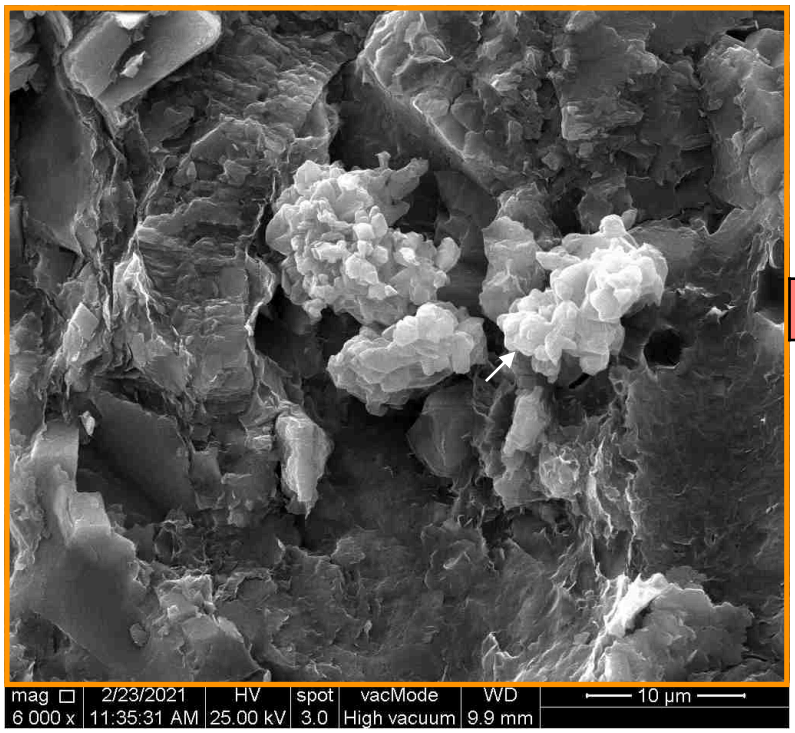

KCL A 83-35 (8499-8510 ft.); MI#21013-27

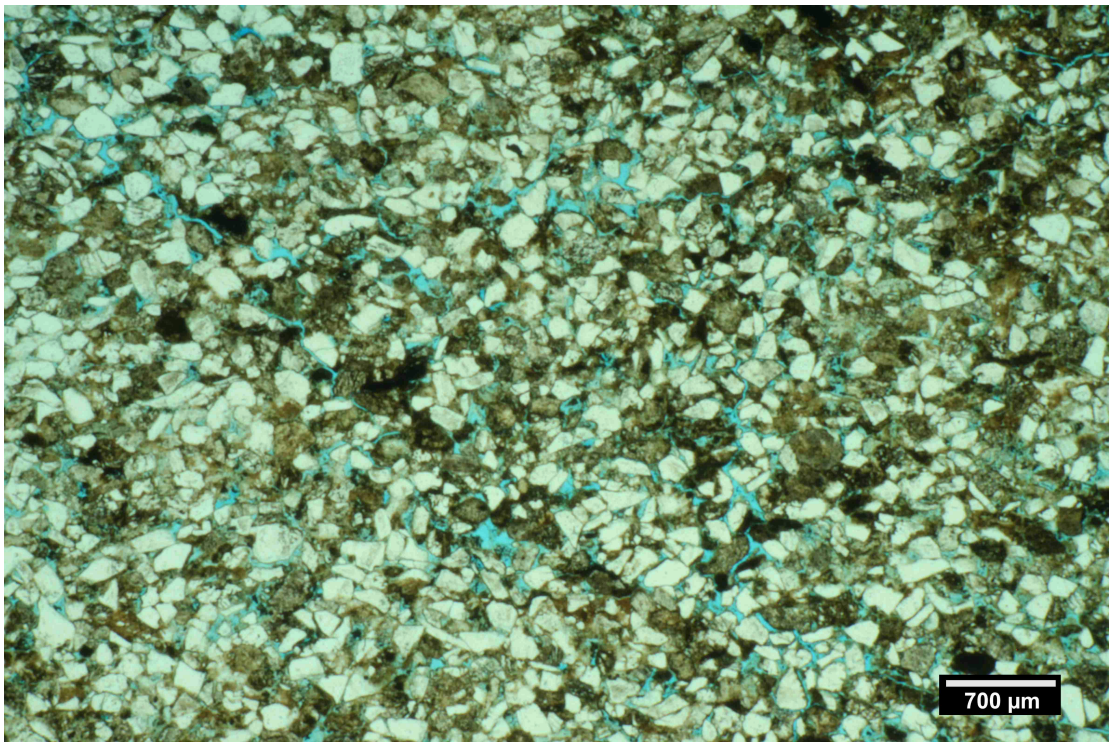

27A. A porous, smectite-rich, well-sorted, fine-grained, lithic arkosic sandstone. Macro pores (blue) include relatively well-preserved inter-granular & secondary dissolution voids.

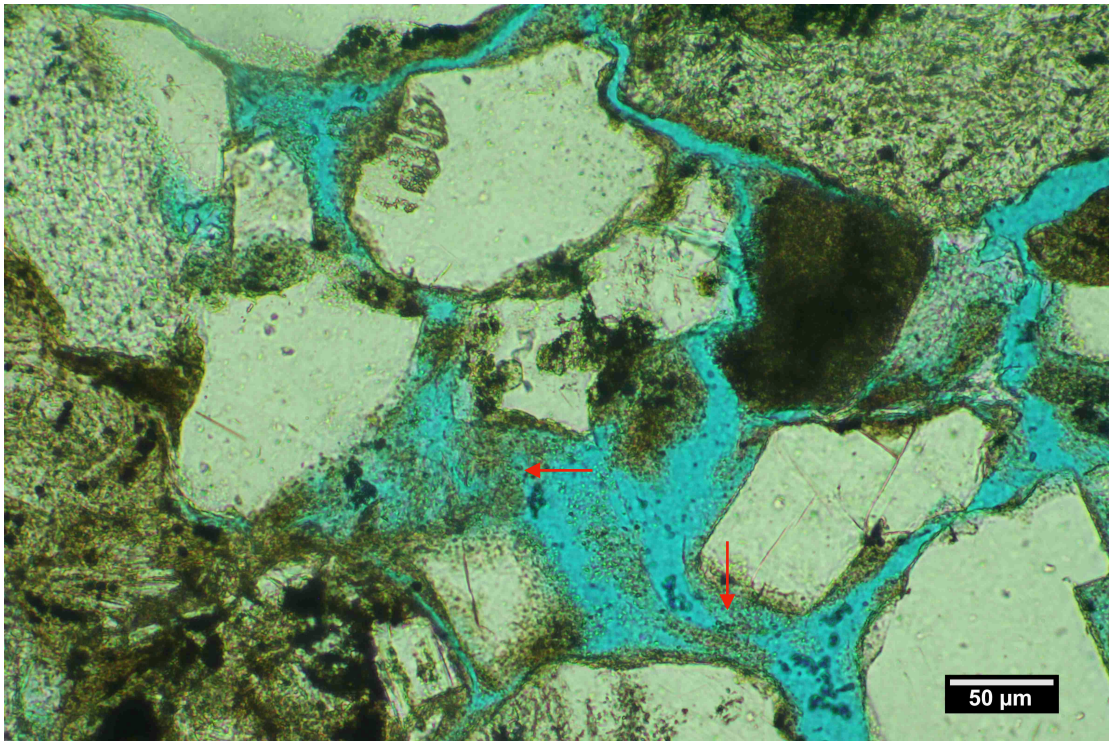

27B. Clusters of grain-replacement authigenic smectite (red <) are weakly attached to the grain surfaces & are susceptible to 'brush-piling' within the pore throats

KCL A 83-35 (8499-8510 ft.); MI#21013-27

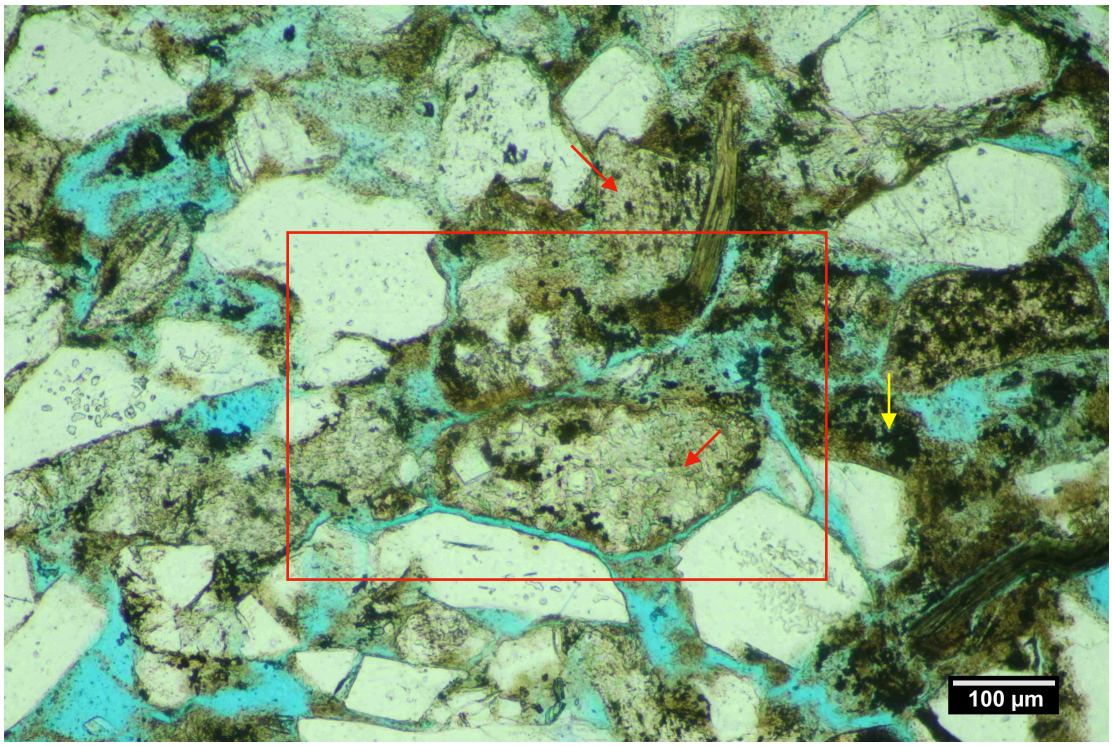

27C. Smectite-replaced detrital grains (mostly feldspar + igneous RFs; red <) + clusters of plastically deformed detrital clay & pseudo-matrix (yellow <).

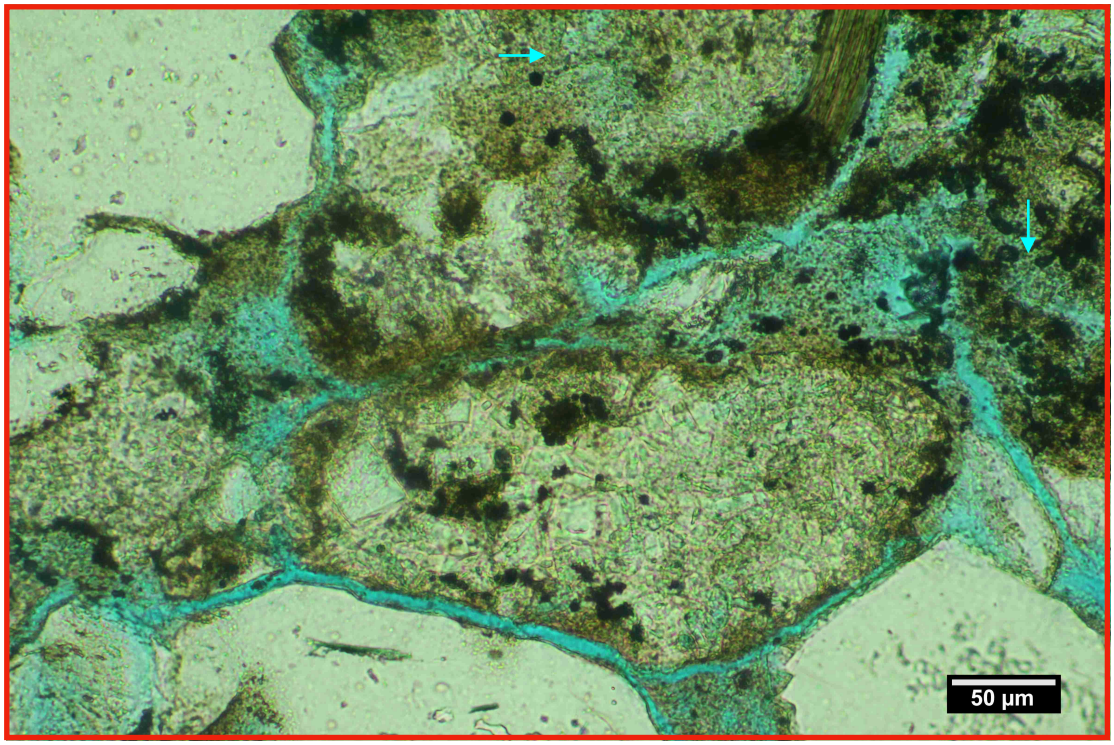

27D. Detailed view of the highlighted area from Figure 27C. Most of the *authigenic clay* in this sandstone has originated as grain-replacement smectite associated with corroded feldspar crystals & grains (blue <).

KCL A 83-35
API_03-02930606
8499-8510 ft.
MI#21013-27 - SEM

Summary: This core sample is comprised of moderately porous, cross-bedded, fine-grained, well-sorted, lithic arkosic sandstone. The sandstone is moderately packed and smectite-rich. The XRD mineralogical assessment indicates a sand-rich framework dominated by plagioclase feldspar (~40%), quartz (~29%), and k-feldspar (~7%). The clay fraction is dominated by smectite (~13%) + illite/mica (~2%). Magnetite (~2%), natrojarosite (~1%) and calcite (~1%) are present as minor authigenic cement materials. The clay population includes pockets of infiltrated, organic matter-rich detrital clay as well as authigenic grain-replacement clay. Detrital feldspar grains and volcanic RFs are locally corroded and replaced with authigenic smectite +/- kaolinite. Pore types include inter-granular macro porosity + secondary dissolution porosity (grain-moldic + intra-particle voids). Total porosity estimated for the thin section is ~ 11-14%.

21013-27 Photo Index: (bookmarks)

Sample ID	Magnification
21013-27A	100X
21013-27B	400X
21013-27C	1300X
21013-27D	5000X
21013-27E	3000X
21013-27F	6000X

Detrital (smectite-rich) matrix	DM
Feldspar	F
Authigenic smectite	S
Intra-particle porosity	wP
Opal A	A

21013-27A 100X

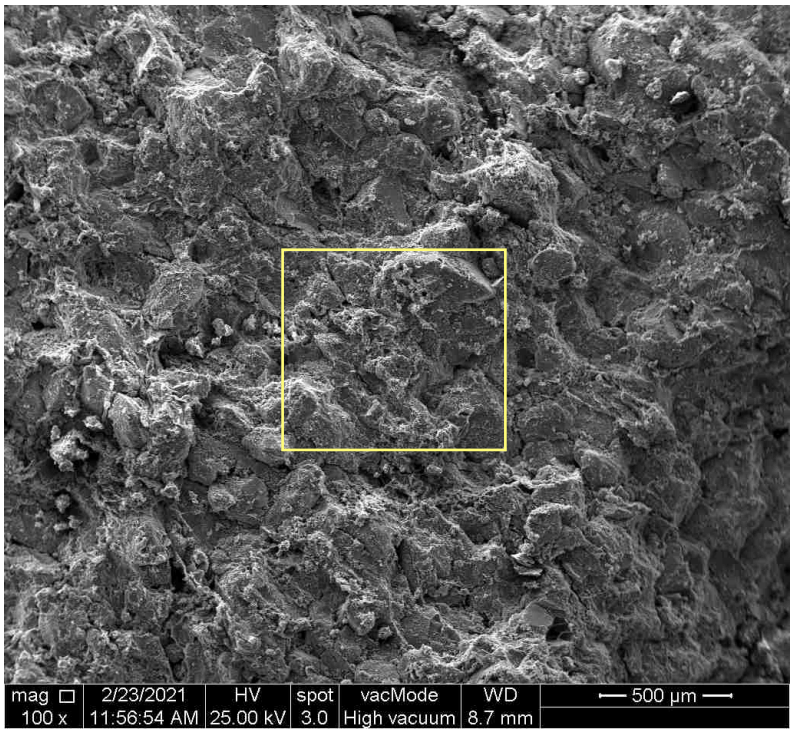

21013-27B 400X

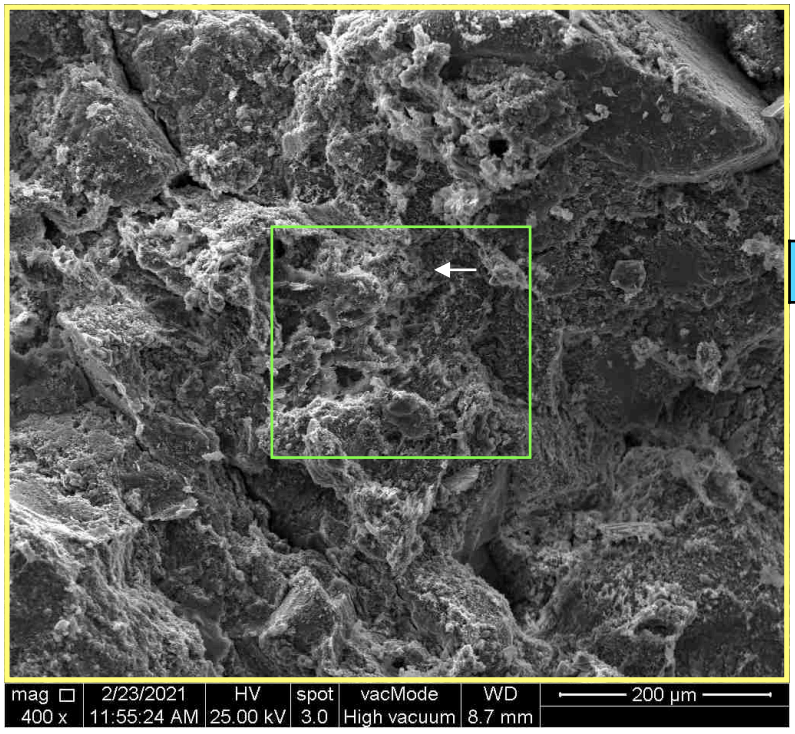

F

21013-27C 1300X

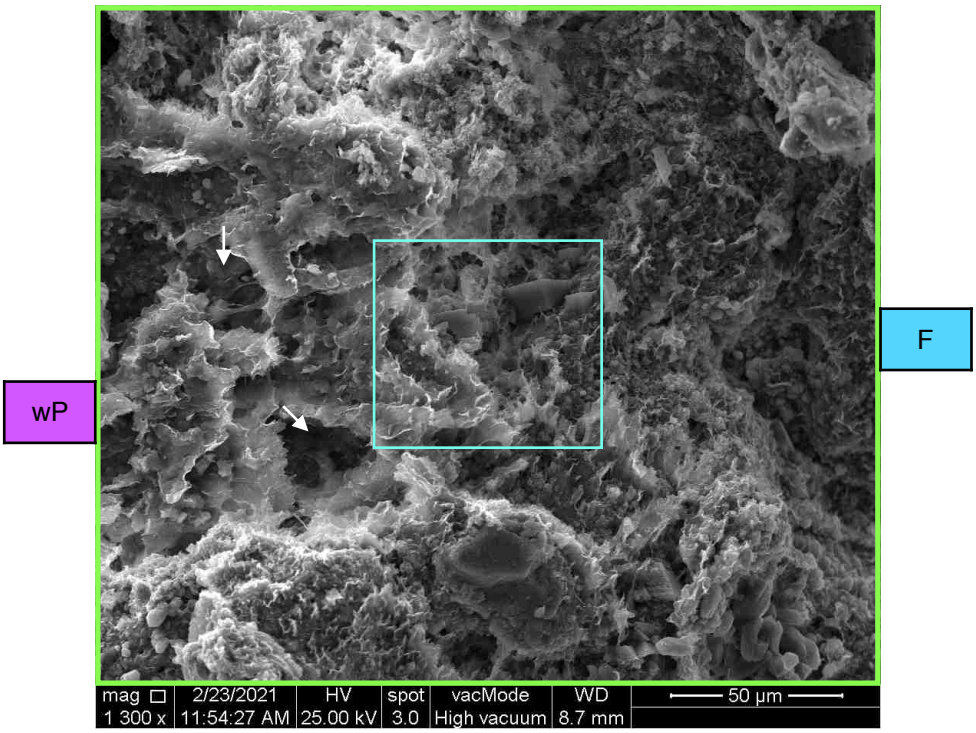

21013-27D 5000X

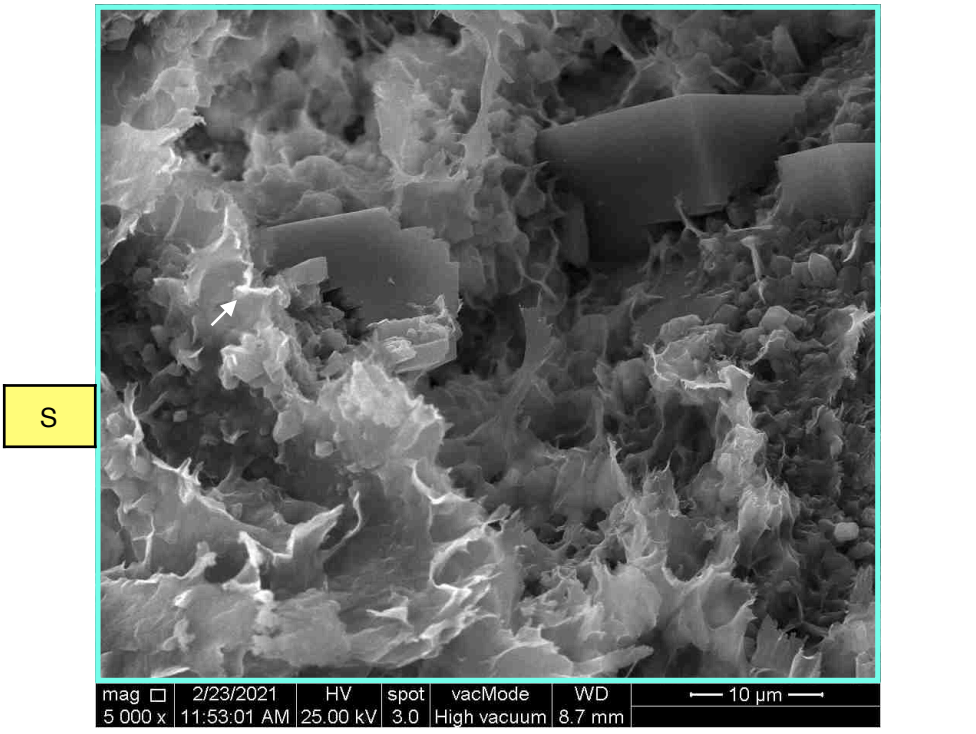

21013-27E 3000X

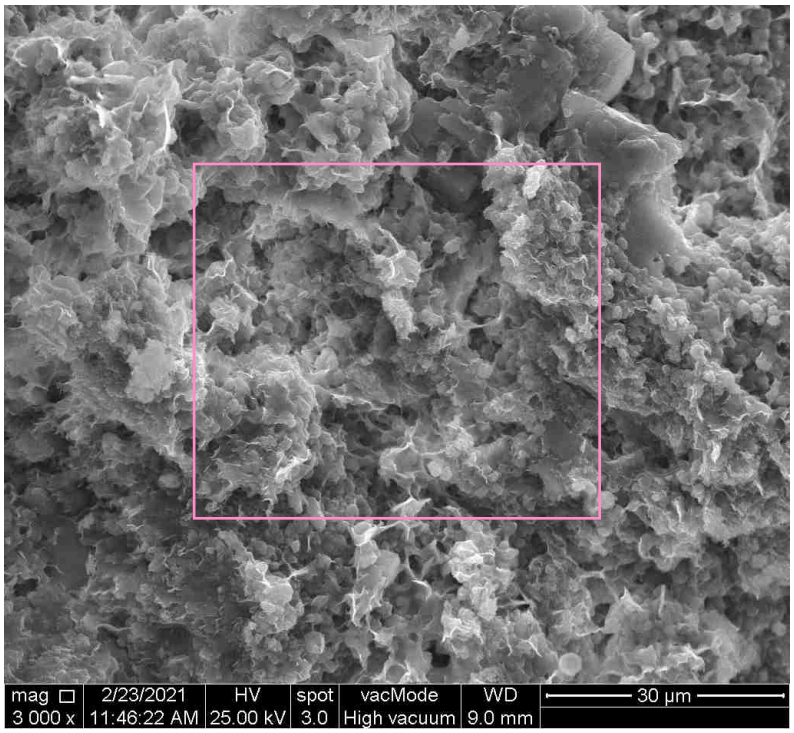

21013-27F 6000X

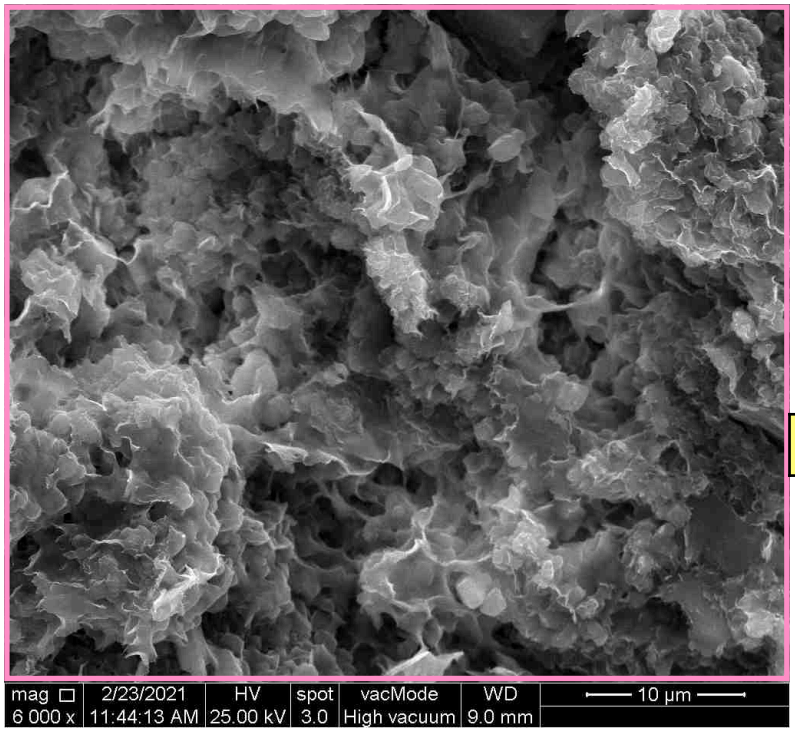

S

KCL A 83-35 (8633-8643 ft.); MI#21013-29

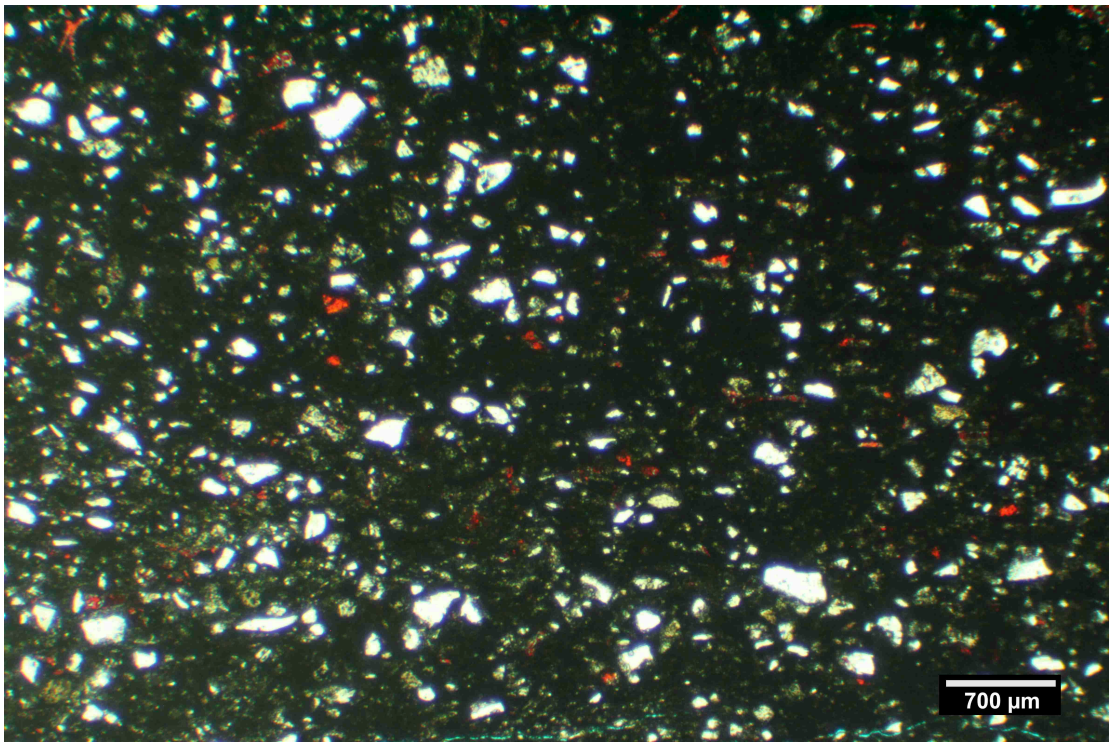

29A. A matrix-rich, lithic arkosic siltstone. Calcite-rich grains are stained red in this view. Dispersed organic matter accounts for the diminished light transmission of the matrix.

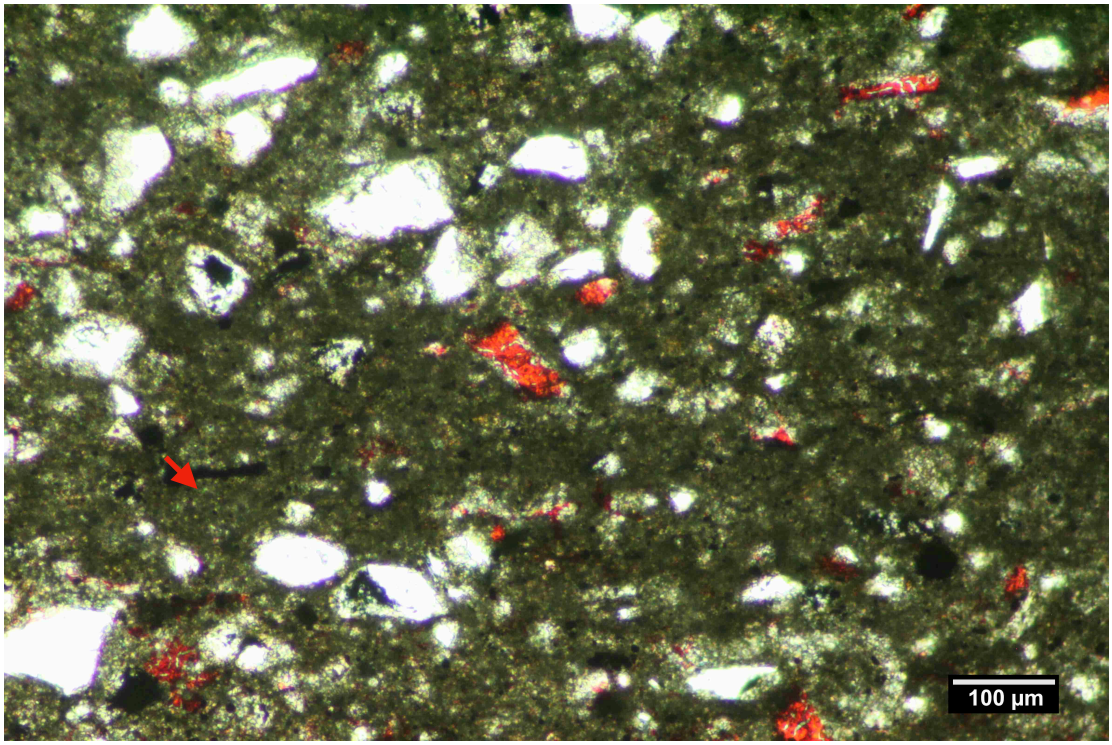

29B. Analcite (red <) is abundant throughout this siltstone as a microcrystalline cement that is admixed with the pore-filling smectite clay.

KCL A 83-35 (8633-8643 ft.); MI#21013-29

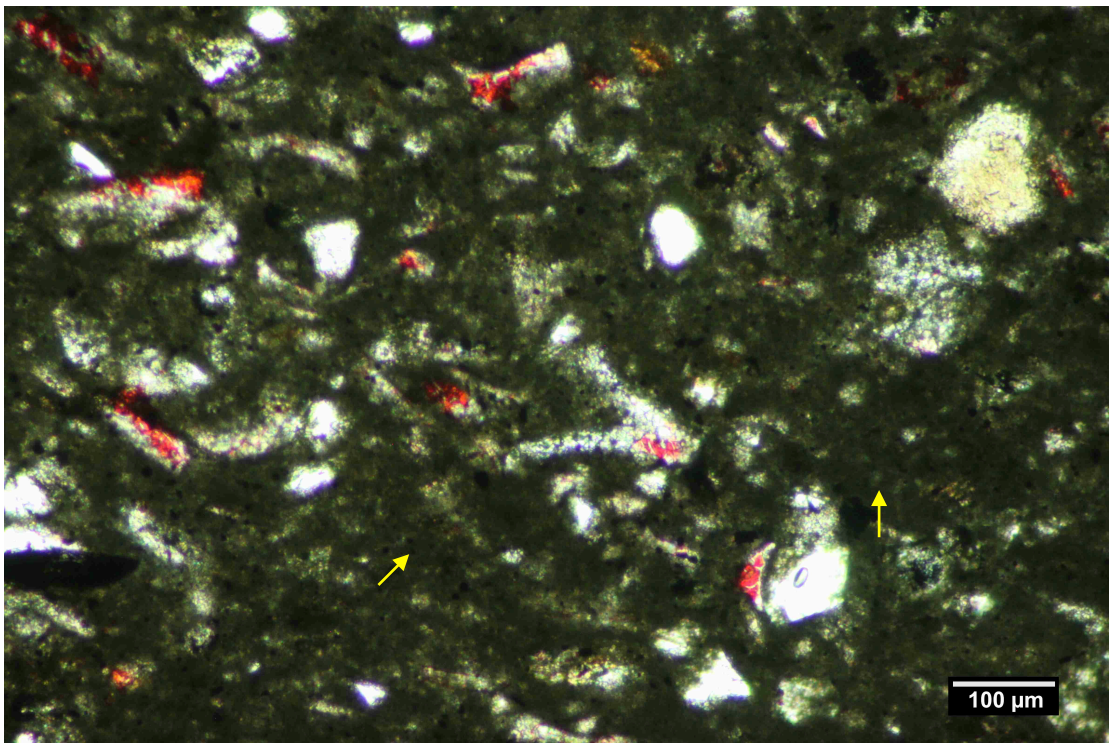

29C. Intercrystalline microporosity is locally preserved & sheltered within clusters of closely spaced silt grains (yellow <).

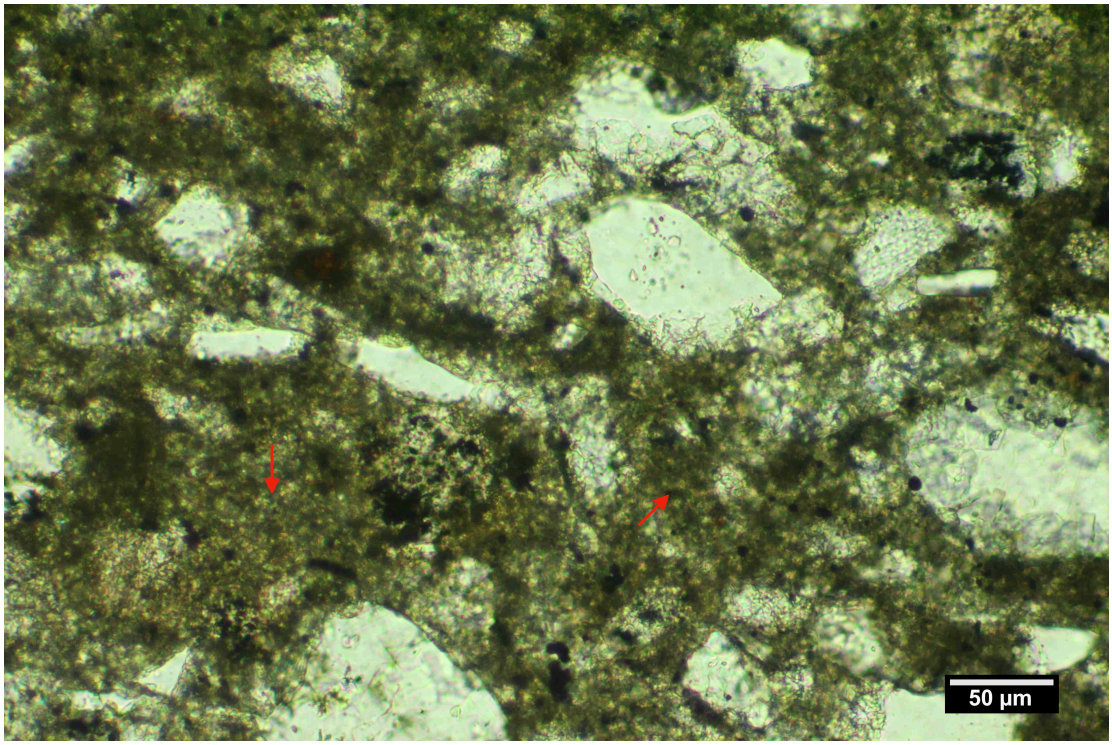

29D. The subtly mottled appearance of the groundmass (red <) is attributed to abundant analcite cement that is admixed with the smectite clay matrix.

8633-8643 ft.
KCL A 83-35
MI#21013-29 - SEM

Summary: This interval is comprised of non-porous, very poorly sorted, matrix & sand-rich, lithic arkosic siltstone. The detrital framework includes feldspar, quartz, igneous rock fragments (RFs), calcareous skeletal fragments, chert RFs, and particles of organic matter. The detrital fabric is densely packed, with intergranular spaces commonly filled with detrital clay (smectite + minor illite) + micro-crystalline analcite cement. Skeletal and dissolution grain-mold voids (commonly attributed to feldspar corrosion) are locally present & are commonly in-filled with clusters of microporous analcite +/- authigenic smectite +/- opal cement. The irregular patches of intercrystalline macro + microporosity are commonly surrounded by densely packed, relatively non-porous, clay-rich siltstone. The image sequence 21013-29A through 21013-29D highlights a secondary mold void (possibly from a leached feldspar sand grain), in-filled with analcite cement + traces of authigenic smectite. SEM images 21013-29E through 29G provide progressively more detailed views of a typical portion of the siltstone pore-filing matrix materials (mostly smectite clay + analcite).

21013-29 Photo Index: (bookmarks)

Sample ID	Magnification
21013-29A	400X
21013-29B	1500X
21013-29C	6000X
21013-29D	1000X
21013-29E	2000X
21013-29F	6000X

Detrital Matrix (smectite)	D
Analcite	An
Macro Pore	P

21013-29A 400X

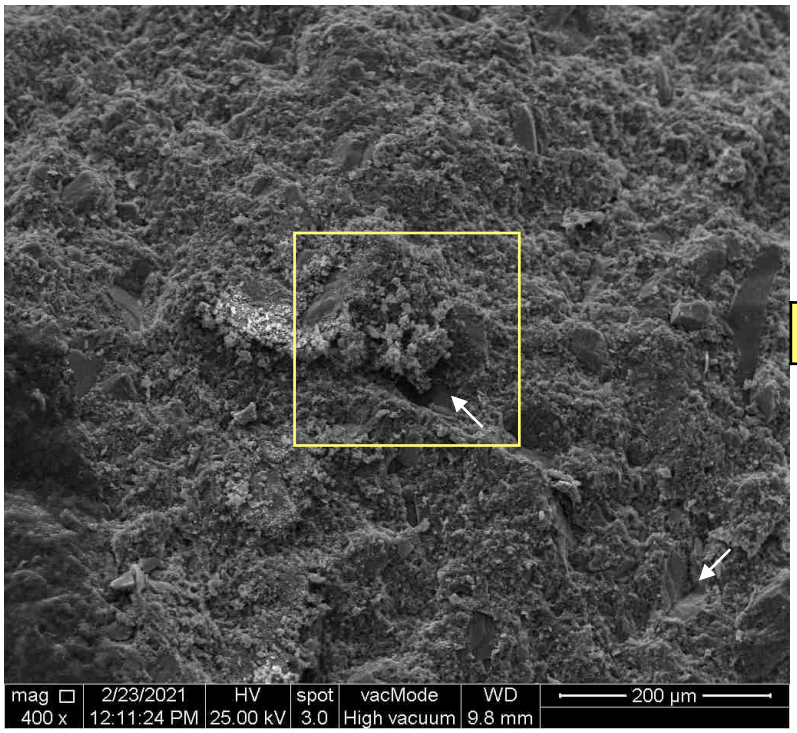

21013-29B 1500X

21013-29C 6000X

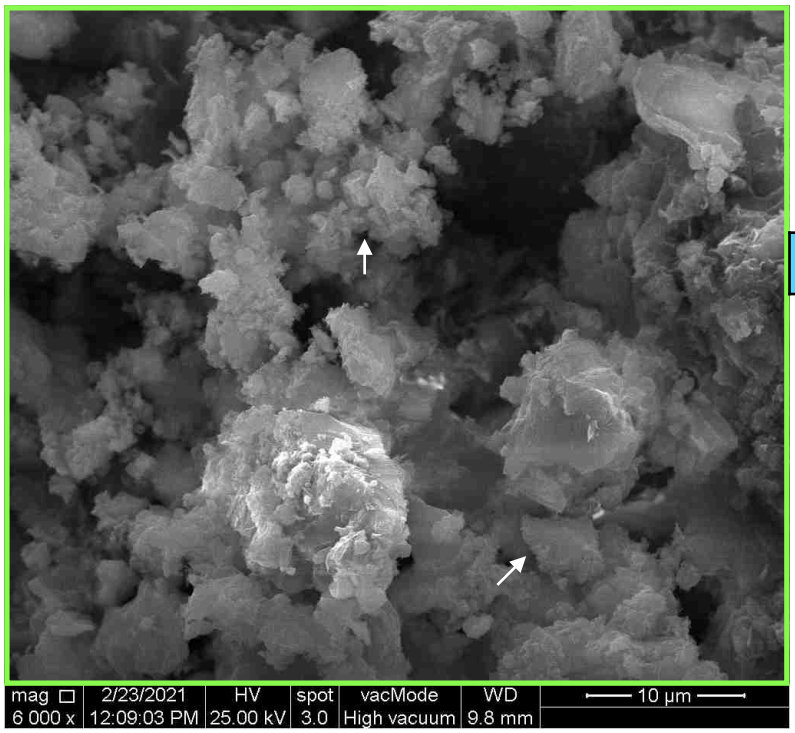

21013-29D 1000X

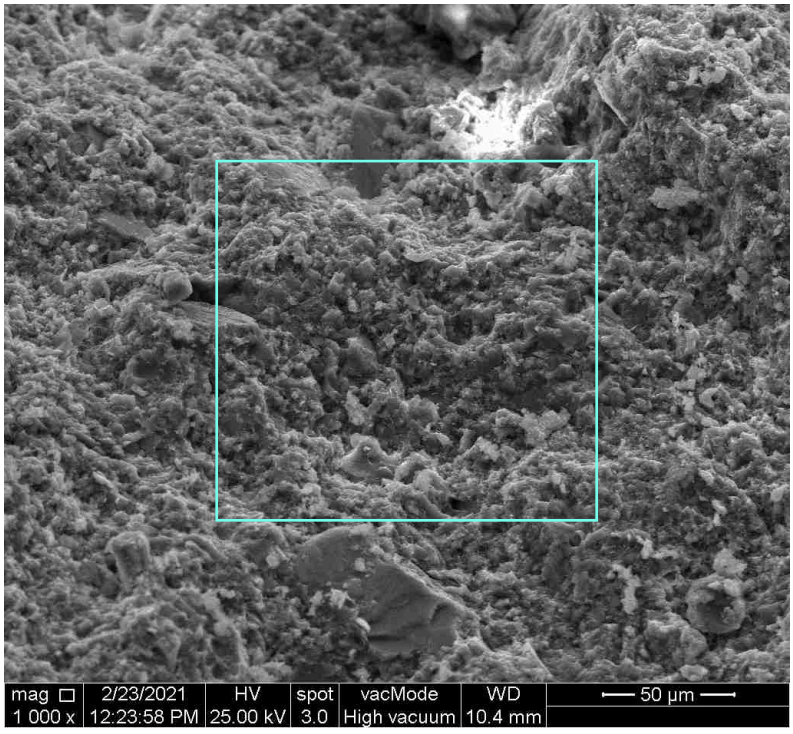

21013-29E 2000X

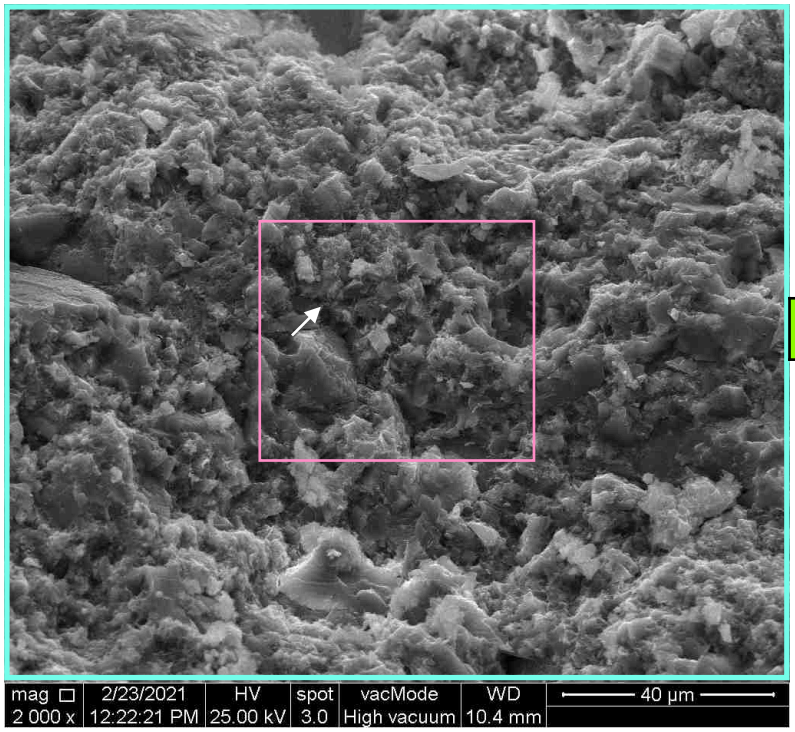

21013-29F 6000X

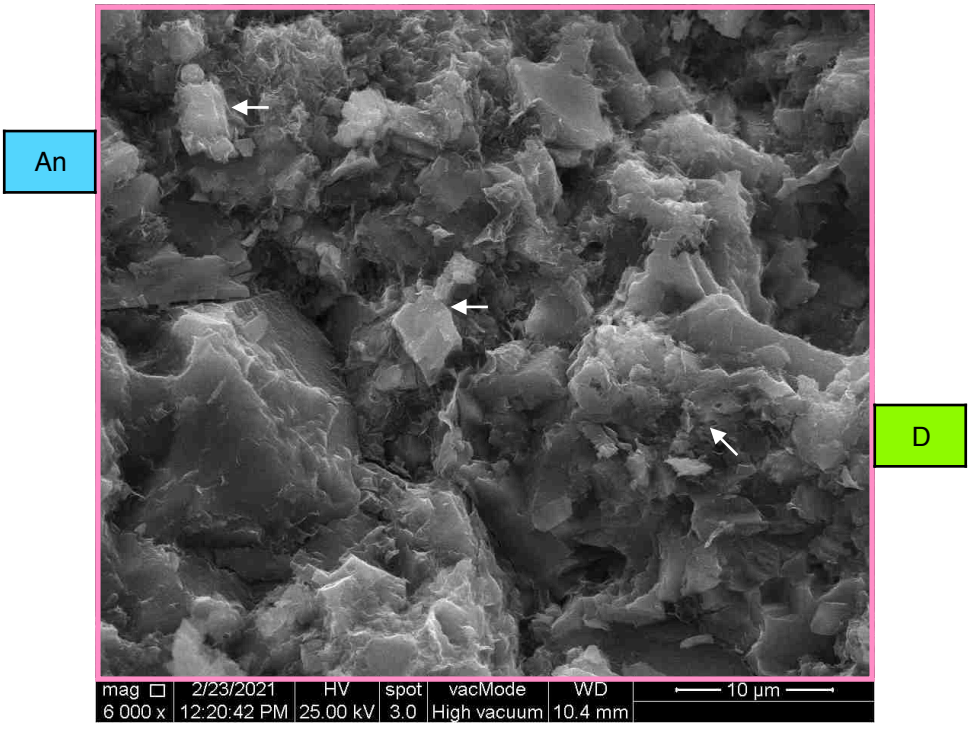

KCL25 #1 (6194 ft.); MI#21013-33

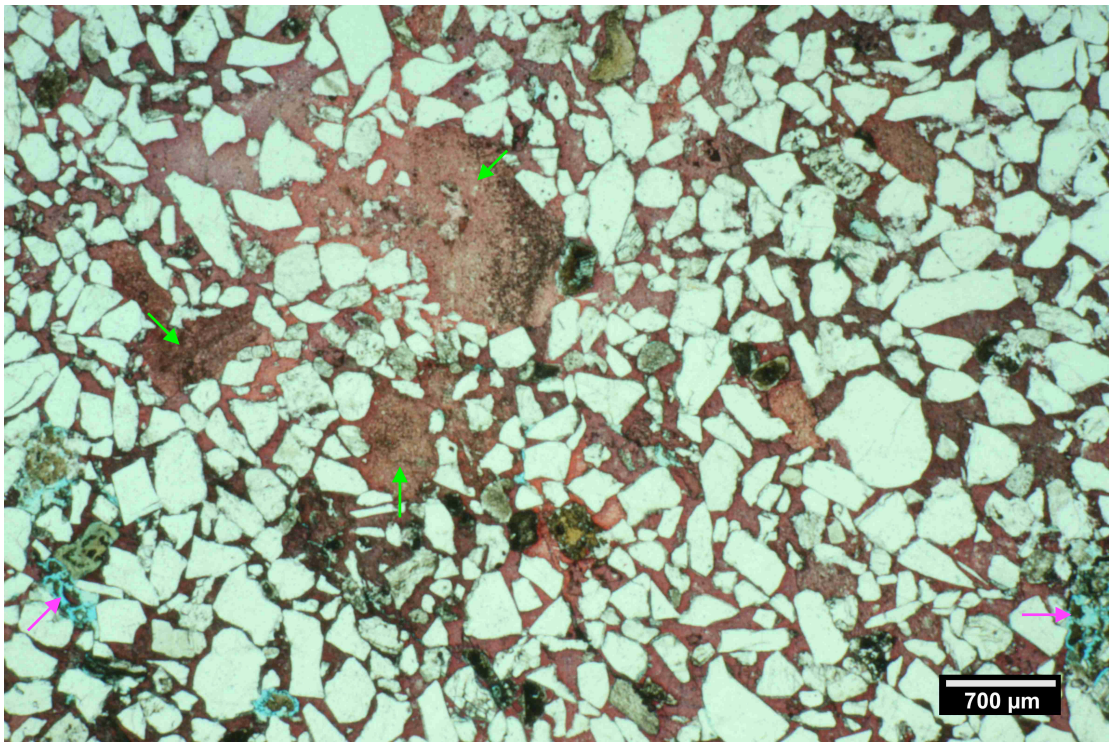

33A. Calcite-cemented sandstone with large echinoderm plates (green <) & abundant pore-filling calcite spar cement. Note the secondary macro pores (blue; magenta <).

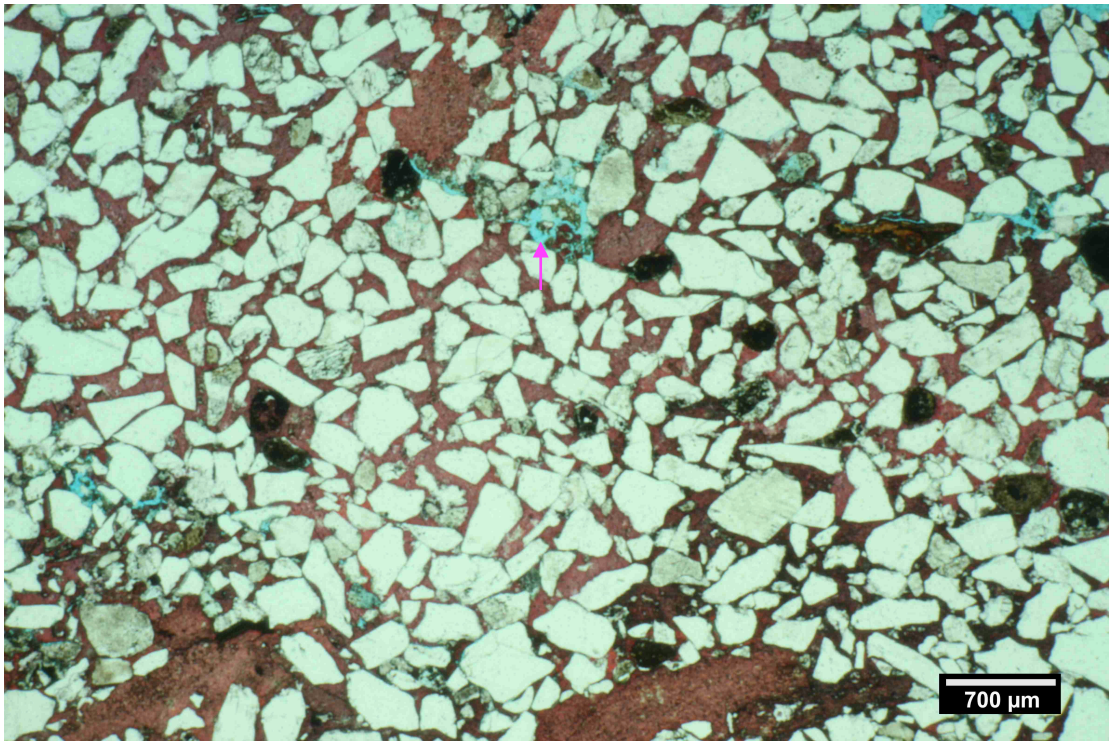

33B. The core sample is classified as a fossiliferous, lithic arkosic sandstone. Secondary intraparticle dissolution porosity (magenta <) is the most significant pore type in the sample.

KCL25 #1 (6194 ft.); MI#21013-33

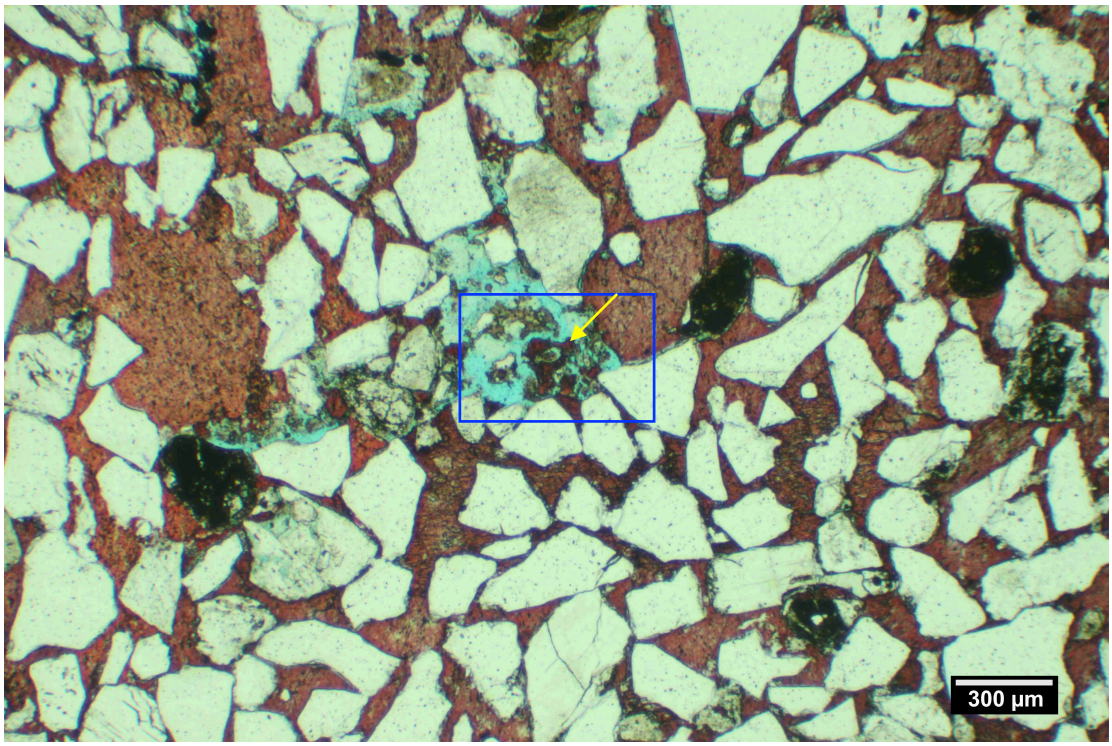

33C. Intraparticle dissolution porosity + grain-replacement smectite + calcite spar cement (yellow <). The highlighted area is detailed in Figure 33D.

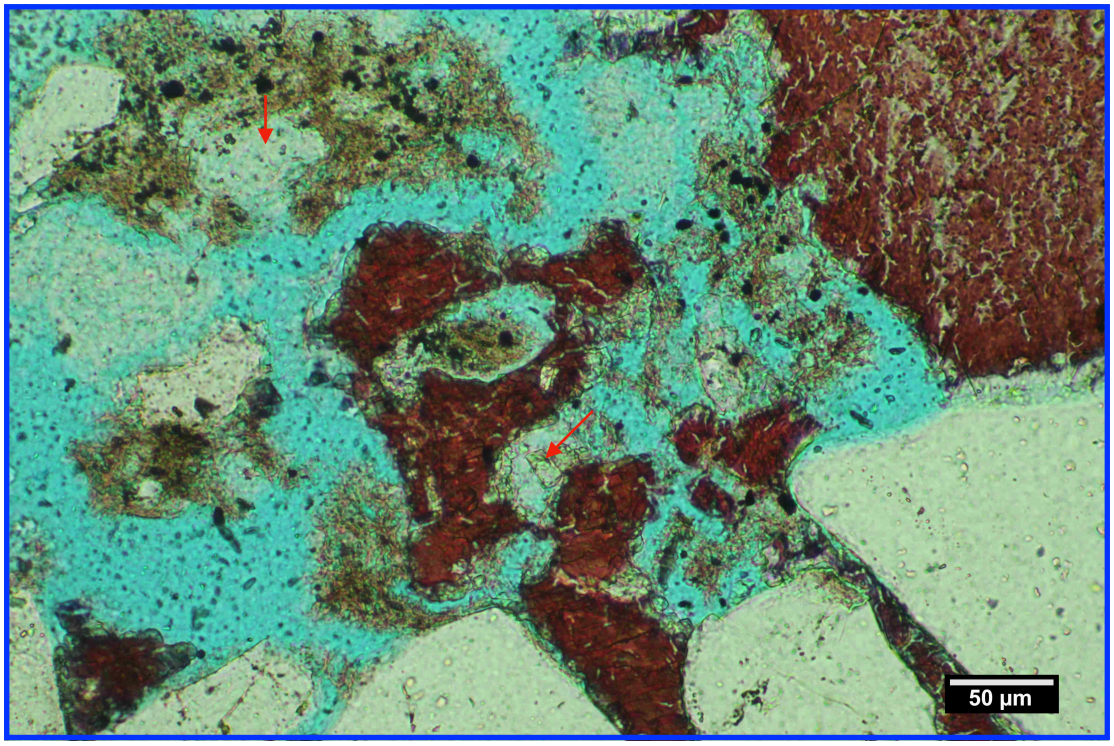

33D. The grain remnants (red <) are suggestive of corroded feldspar. Clusters of grain-replacement smectite are weakly attached & are susceptible to brush-piling.

6194 ft.
KCL 25 #1
MI#21013-33 - SEM

Summary: This core sample is comprised of medium-grained, moderately sorted, calcareous & fossiliferous lithic arkosic sandstone. The detrital framework includes feldspar, quartz, igneous rock fragments (RFs), calcareous skeletal fragments, chert RFs, phosphatic bone fragments (fluorapatite), and particles of organic matter. The calcareous skeletal fragments are commonly surrounded by rims of overgrowth calcite spar cement & include echinoderm plates + possible mollusk shell fragments. The detrital framework is well-cemented, with pore-filling calcite spar cement filling most of the available inter granular space. Secondary grain-moldic & intra-particle dissolution voids (commonly associated with feldspar corrosion) are locally present & locally contain corroded grain remnants + clusters of authigenic smectite +/- calcite spar cement. The secondary macro pores appear to be scattered and locally isolated in the SEM & thin section specimens prepared for this core sample. The image sequence 21013-33A through 21013-33C details the inter growth of calcite cement + authigenic smectite peripheral to a large secondary mold void (possibly from a leached feldspar sand grain). SEM images 21013-33D through 33F illustrate pore-filling calcite + authigenic smectite partially filling an inter granular pore space.

21013-33 Photo Index: (bookmarks)

Sample ID	Magnification
21013-33A	200X
21013-33B	800X
21013-33C	3000X
21013-33D	200X
21013-33E	800X
21013-33F	3000X

Calcite spar cement	C
Authigenic Smectite	S
Macro Pore	P

21013-33A 200X

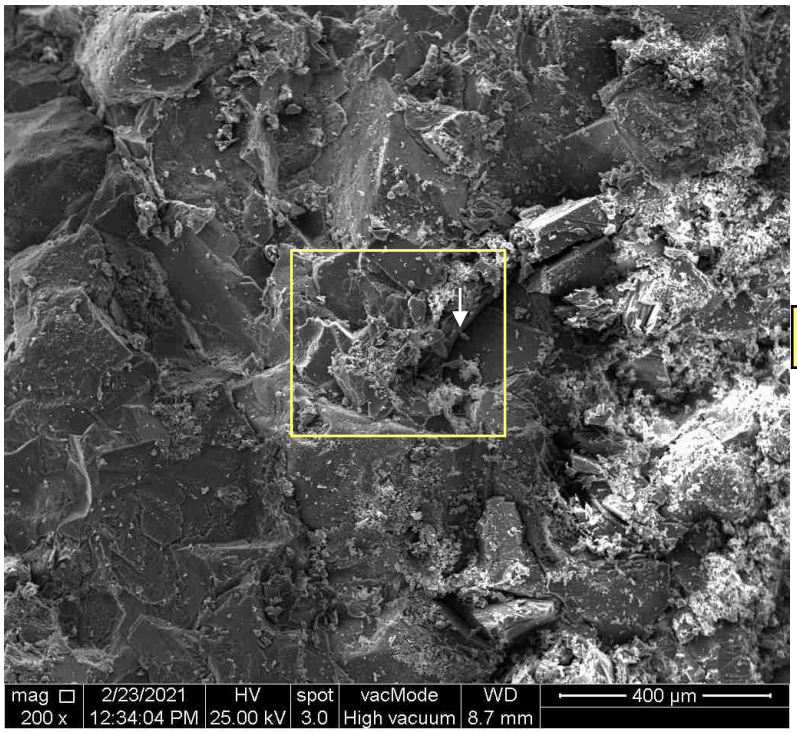

21013-33B 800X

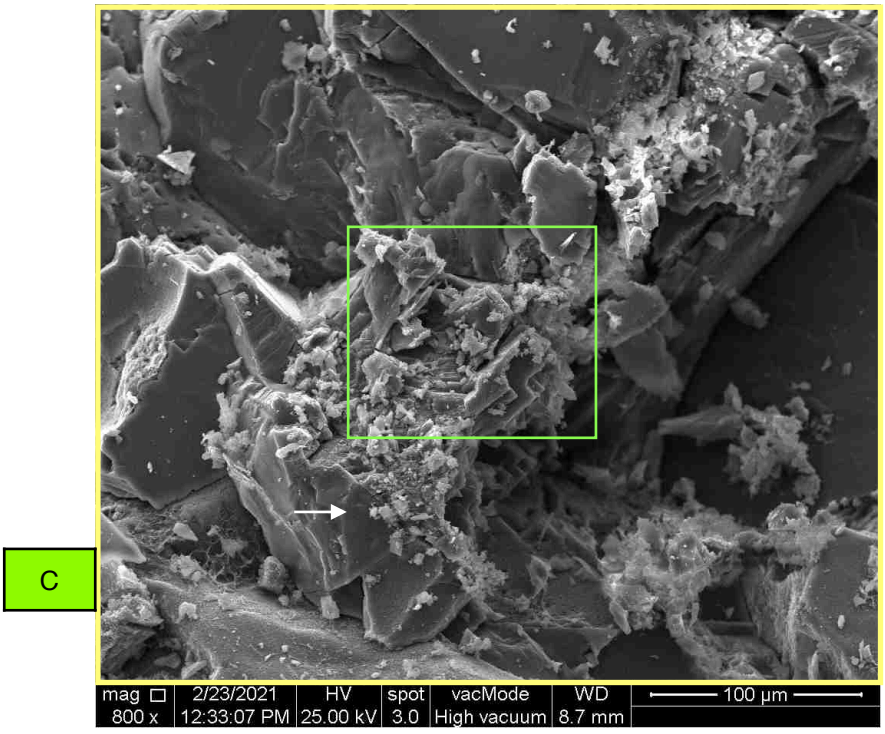

21013-33C 3000X

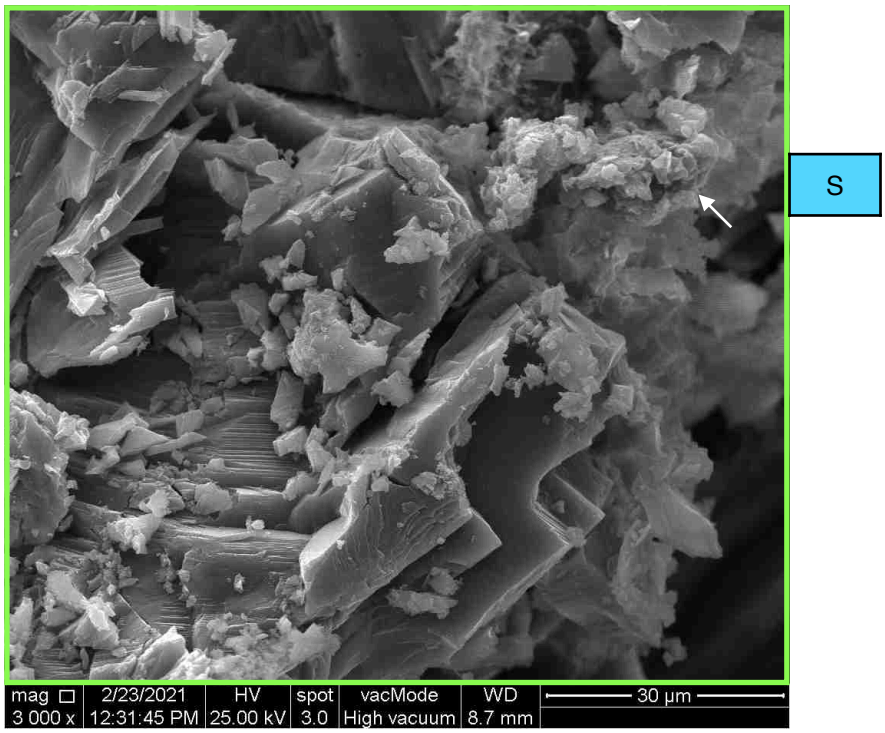

21013-33D 200X

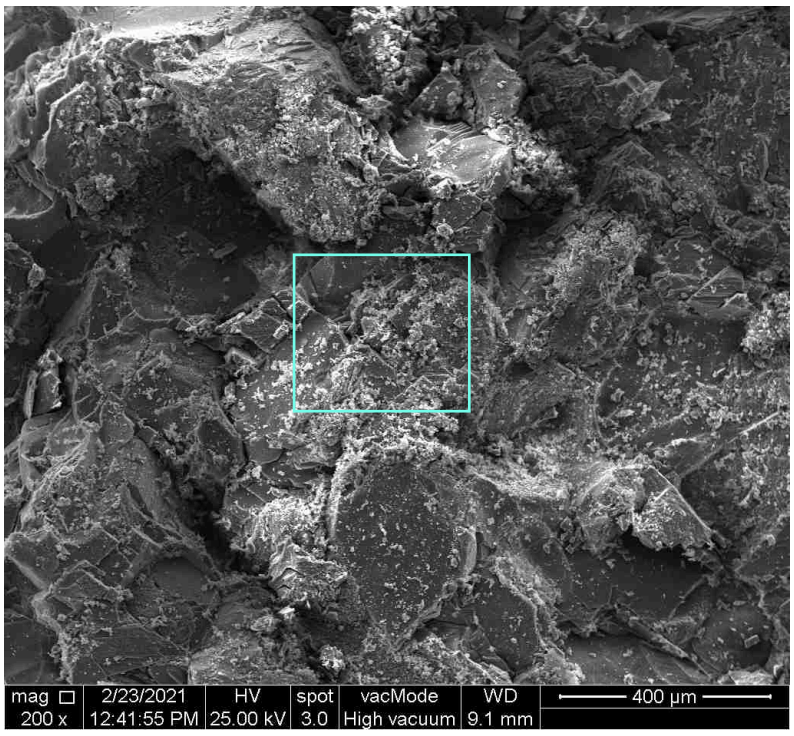

21013-33E 800X

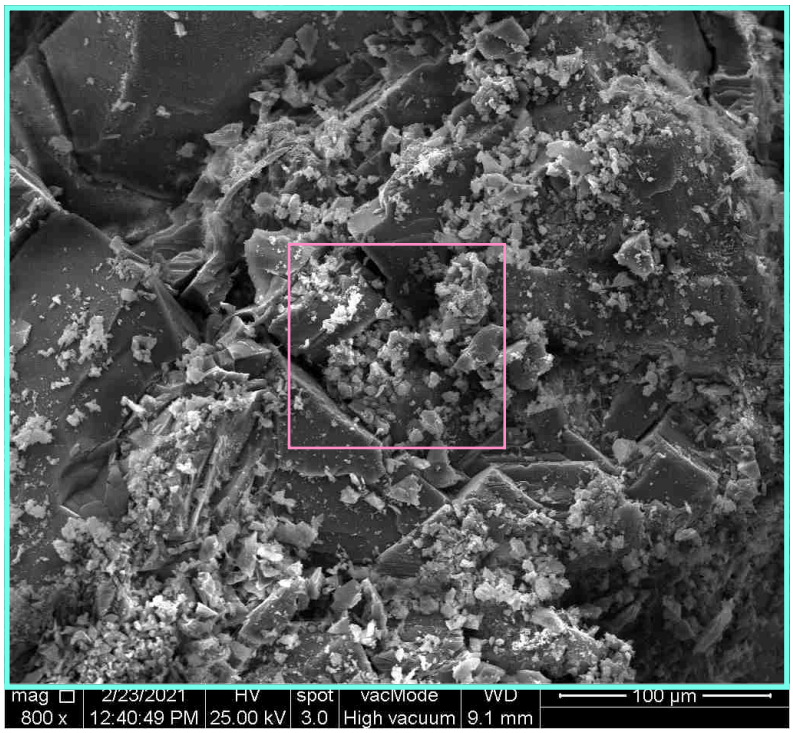

21013-33F 3000X

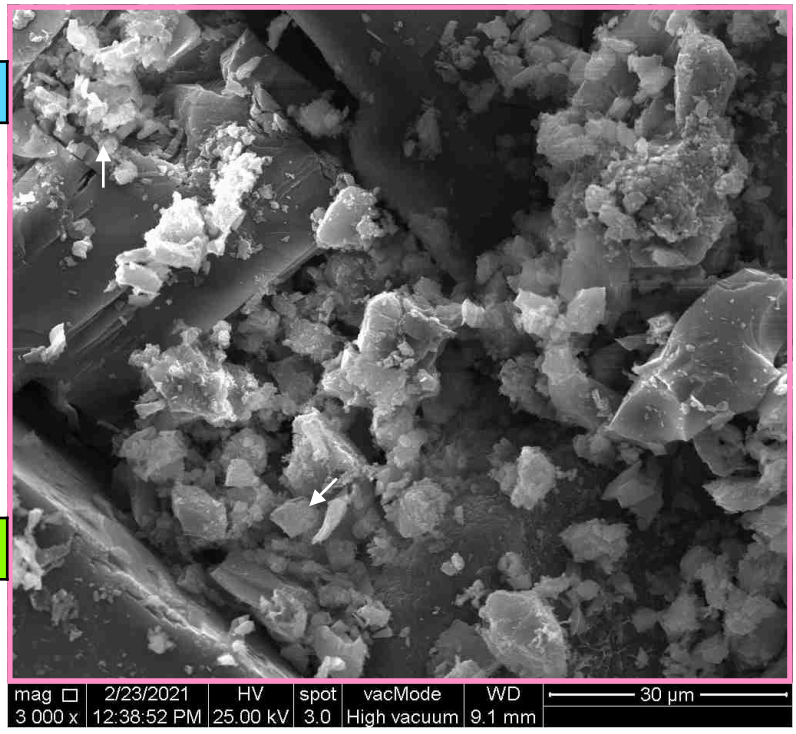

Chapter I

Mercury-Injection Capillary-Pressure Analysis

Introduction

Mercury-injection capillary-pressure (MICP) evaluation of reservoir lithologies, cap seals, intra-formational seals, and fault seals is conducted at the Australian School of Petroleum (ASP). MICP measurements may be integrated with seismic to microstructural data to provide a robust basis for interpretation of the reservoir potential, sealing capacity, and stability and strength of individual strata.

Mercury-Injection Capillary-Pressure Background

An understanding of capillary-pressure behavior is vital to accurately determine cap, intra-formational, and fault-sealing capacity. Investigation of the sealing capacity and pore-throat-aperture size distribution for seals and reservoir lithologies is conducted via mercury porosimetry using the latest Micromeritics Autopore-III porosimeter (Figure 1). This state-of-the-art equipment is capable of injecting non-wetting phase (mercury) in user-defined, step-like pressure increments up to 60,000 psi (~413MPa) into an evacuated, cleaned, and dried core plug or cut sample. Innovative laboratory processes are used to control injection direction. The volume of mercury injected at each pressure increment is automatically recorded until the maximum analytical pressure, or 100% pore-volume Hg saturation is achieved. Pressure is subsequently plotted against incremental Hg saturation readings to generate the drainage curve. Processes may be reversed to generate a non-wetting phase imbibition curve. Injection analysis can be conducted at reservoir conditions if pressure data are available; however, low reservoir pressures may inhibit total nonwetting phase saturation.

Figure 1. ASP's state-of-the-art high-pressure porosimeter. Analytical pressure tables are user-defined to ensure equilibrium at each stage of injection and withdrawal.

DOI: 10.1306/13241318St60227

Petrophysical Theory

Mercury porosimetry is based on the capillary law governing liquid penetration into small pores. Capillary forces in the reservoir and seal are functions of surface and interfacial liquid tensions, pore-throat size and shape, and the wetting properties of the rock. This law, in the case of a nonwetting liquid like mercury and assuming cylindrical pores is expressed by the Washburn (1921) equation:

$$Pc = - 2\gamma \cos\theta / rc \qquad (1)$$

Where, Pc = capillary pressure (dynes/cm^2), γ = surface tension of Hg, θ = the contact angle of mercury in air, and rc = the radius of the pore-throat aperture (μm) for a cylindrical pore.

The surface tension of mercury varies with purity. The interfacial tension for air-mercury is 485 dynes/cm^2. The contact angle (θ) between clean mercury and sample pores varies with specimen composition; however, 140° is generally accepted by industry.

Rearranging the Washburn equation in terms of rc, we get

$$rc = \left[\frac{107.6}{P_c}\right] \qquad (2)$$

This equation is used to calculate the critical pore-throat size, which is the pore-throat size that maximum intrusion of the nonwetting phase occurs for a relatively minor pressure increase (Figure 2). Critical pore-throat-size values are vital in reservoir characterization and threshold pressure and permeability identification and prediction.

Entry pressure and threshold pressure are terms referring to the critical points on the mercury-injection curve (Figure 2). The entry pressure on the mer-

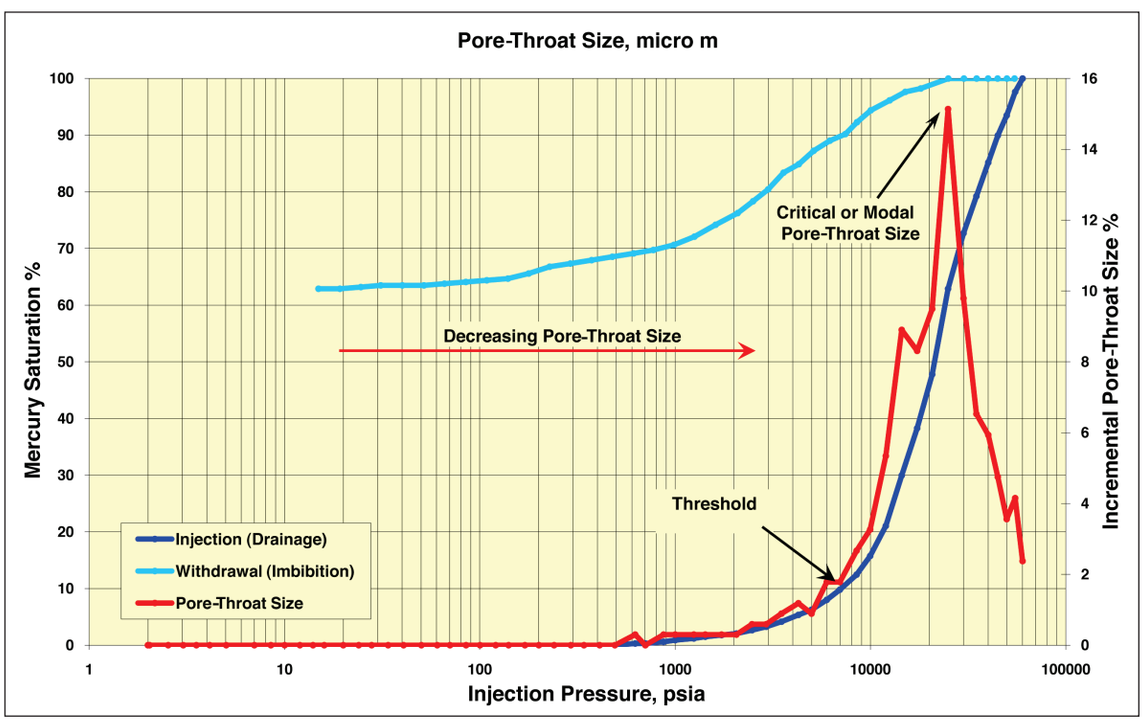

Figure 2. Pore-throat distribution, injection (drainage), and withdrawal (imbibition) MICP curves, highlighting threshold pressure, pore-throat size distribution and critical pore-throat size. Threshold pressure (P_{th}) is the pressure at which the mercury forms a continuous filament through the rock.

cury-injection curve is the point on the curve at which mercury initially enters the sample. This point is often indicative of the largest pore aperture size (Robinson, 1966). However, this parameter can be difficult to accurately determine as sample size and surface irregularities, relative to total pore-size distribution, create a boundary condition that affects the low-pressure portion of the curve. Surface irregularities also affect the low-mercury saturation portion of the MICP curve (Bliefnick and Kaldi, 1996). These irregularities do not follow the Washburn equation relationship and result in a conformance MICP injection error. This factor must be recognized when characterizing a reservoir or seal as conformance can lead to significant errors in calculating both entry and threshold pressures.

The most important factor when evaluating seal potential is determining the pressure required to form a connected filament of nonwetting fluid through the pore space of the sample. As mercury is a nonwetting fluid, pressure must be built up before it displaces the wetting phase. At a sample specific pressure, the percentage of mercury intruded increases rapidly, which is dependent on the pore-throat size. This point represents the threshold pressure and graphically corresponds to an upward convex inflection point on the mercury-injection curve and has been successfully utilized by Dewhurst et al., (2002a) for determining threshold pressures in seal rocks (Figure 2). The threshold pressure point has been experimentally proven by monitoring electrical resistance across a sample and noting the pressures at which continuity occurs (Katz and Thompson 1986, 1987).

Pittman (1992) and H. D. Winland (Amoco Production Company) have attempted to identify a mercury saturation percentile at which the reservoir threshold pressure can be predicted to occur. Three, five, and ten percent of the total mercury saturation are commonly used to predict this threshold pressure. Ten-percent mercury saturation is theoretically defined as the displacement pressure (Schowalter, 1979). Pittman (1992) also suggested that the apex of a peak obtained by plotting capillary pressure divided by the percentage of mercury intruded, against the percentage of mercury intrusion serves as an estimate of the threshold pressure. This suggestion is based on analysis of undeformed sandstones.

This method can be employed to vindicate the chosen threshold pressure apex when no clear threshold pressure indicator is present. Commonly, a sample with a large pore-throat distribution displays many minor MICP apexes. These additional apexes relate to distinct pore-throat aperture sizes within the sample created by the grain-size heterogeneity, authigenic cements, and poor sorting.

Table 1. Typical Workflow Spreadsheet for Determining Seal Capacity and Column Height, in this case for Supercritical CO_2*.

Depth of sample (TVDSS) m**	Pressure at sample depth (Mpa)	Temp at sample depth (°C)	Salinity at sample depth (ppm)	CO_2 density (g/cm^3)	Brine density (g/cm^3)	Interfacial tension (mN/m or dynes/cm)	Contact Angle (°)	Seal Threshold Pressure (air-Hg system) (psia)	Reservoir Threshold Pressure (air-Hg system) (psia)	Seal Threshold Pressure (brine-CO_2 system) (psia)	Reservoir Threshold Pressure (brine-CO_2 system) (psia)	Height of CO_2 Column (m)
1901.5	18.97697	77	25000	0.5878	1.0086	26.88	40	6972	10	390	0.6	652

* Subsurface pressure, temperature, and salinity are required to determine phase densities and interfacial tension.
** TVDSS = true vertical depth subsea.

Fault-Seal MICP Analysis

Ideally, separate samples from undeformed reservoirs and faults should be analyzed to accurately determine the height of the hydrocarbon column that the fault may support relative to the undeformed strata. For specimens where the fault zone is too narrow to cut, an additional sample can be cut with the fault zone, cutting horizontally across the center of the plug with regions of hanging wall and footwall flanking either side. To constrain the pore size of these thin fault rocks, the sample is sealed on all sides except the footwall base by coating in an epoxy resin. This procedure ensures directional injection across the fault and also minimizes closure effects during mercury-injection analysis on samples with large external surface areas to volume ratios.

The mercury-injection curves of sealed samples containing faults will display two threshold pressure indicators. The first inflection-point threshold is characteristically low and represents the initially intruded host lithology. The second threshold is dominantly at a greater injection pressure and represents the pressure at which the fault-seal zone is breached. This pressure value is employed to calculate the sealing capacity and height of the hydrocarbon column the faults may support.

Conversion of Air-Mercury Data to Oil-Water, Gas-Water, and Carbon Dioxide-Water Systems

Quantitative application of mercury capillary data to subsurface conditions requires the conversion of mercury capillary pressure values to subsurface hydrocarbon-water and/or gas-water and/or CO_2-water capillary pressure values (Vavra et al., 1992). The Hg/air-brine/hydrocarbon (CO_2) conversion factor can be expressed as:

$$Pc_{hw} = \frac{\gamma_{hw}}{\gamma_{ma}}\left[\frac{\cos\theta_{hw}}{\cos\theta_{ma}}\right] \text{x } Pc_{ma} \qquad (3)$$

where (Pc)hw = capillary pressure for the hydrocarbon/CO_2-water system, γhw = the interfacial tension of hydrocarbon and water in dynes/cm, θhw = the contact angle of hydrocarbon/CO_2 and water, γma =

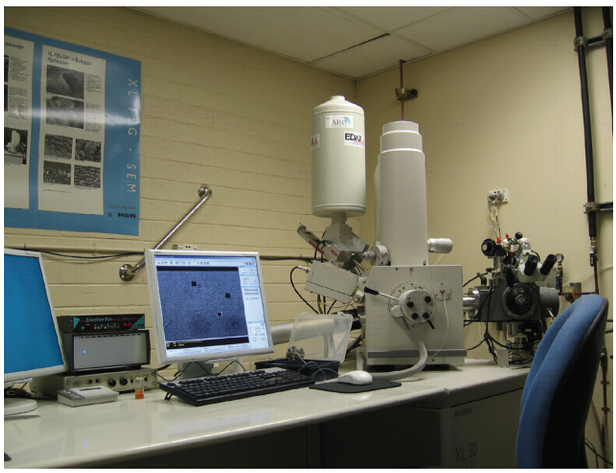

Figure 3. Scanning electron microscopy with energy dispersive x-ray analyzer. The instrument used is a Philips XL30 FEGSEM with Oxford CT1500HF Cryo stage and EDAX DX4 Integrated Energy Dispersive X-ray Analyzer. Microstructural and elemental constituents are imaged and analyzed with magnifications up to 50,000; i.e., image clarity at <200 nm (nanometer) scale (Figure 4). Imaging at this scale can be important when describing seals with calculated pore-throat sizes to 3 nm, which cannot be imaged with this instrument. Energy dispersive x-ray spectroscopy (EDS, EDX, or EDAX) is an analytical technique used for the elemental analysis of a sample. Its characterization capabilities are due in large part to the fundamental principle that each element has a unique atomic structure allowing x-rays that are chacteristic of an element's atomic structure to be identified uniquely from each other (Figure 5). Identification of the principal elements; C, O, Na, Mg, Al, Si, S, Cl, K, Ca, Ti, Mn, and Fe have been conducted on most samples using the EDS technique.

the interfacial tension of mercury plus air, and θma = the contact angle of mercury and air against the solid. The interfacial tension of mercury and air is ~480 dynes/cm at laboratory conditions. The contact angle between mercury and solid is 140° (Schowalter, 1979). Subsurface values for hydrocarbon or CO_2-water capillary pressures can be calculated by entering the subsurface hydrocarbon or CO_2-water interfacial tension value into the above conversion factor equation (Purcell, 1949). The laboratory-derived air-mercury threshold pressure values can be multiplied by this conversion factor to produce subsurface hydrocarbon/CO_2-water capillary pressure values. Subsurface hydrocarbon/CO_2-water interfacial tension values for all projects are calculated using specific reservoir temperature, and pressure (salinity) conditions. Note: gas-water interfacial tensions are generally greater than oil-water interfacial tensions for both surface and subsurface conditions with CO_2 having intermediate values. Gas-water threshold pressures are therefore greater than oil-water displacement pressures for the same rock. Carbon dioxide and water threshold pressures usually fall between hydrocarbon gas and hydrocarbon liquid as the CO_2-water contact angle can range between 0 and 130° depending on pressure, temperature, and substrate mineralogy (Daniel and Kaldi, 2008).

Methodologies Used in the Atlas

The seal capacity and characteristics of the regional, local, and intraformational seals for each area have been determined in large by mercury-injection capillary-pressure analysis (MICP), scanning electron microscopy (SEM) with an energy dispersive x-ray analyzer (EDS, EDX, or EDAX), x-ray diffraction analysis (XRD), and shale volume (V_{sh}). Techniques used to a lesser extent are thin-section petrography and grain- and pore-size distribution, coupled with lithofacies identification (see Tables 1 and 2 and Figures 3 to 7).

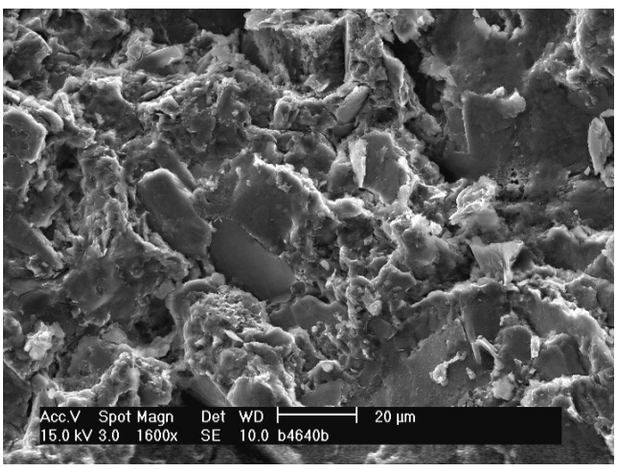

Figure 4. SEM example of a seal rock with clay platelets surrounding silt-sized quartz grains; perpendicular to bedding.

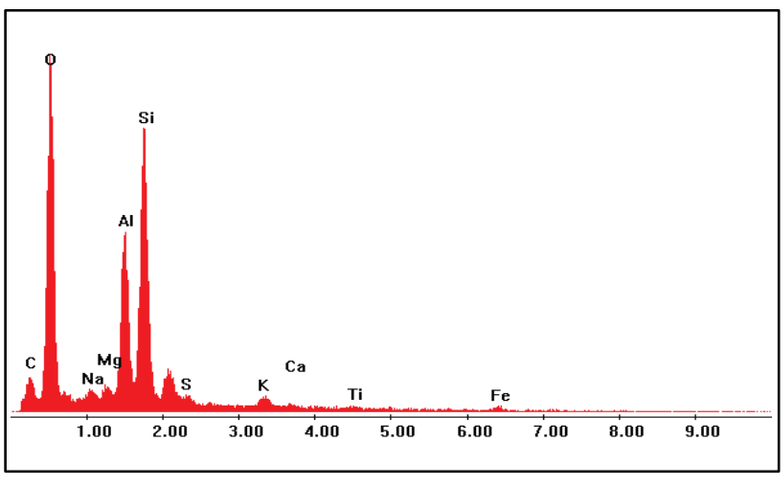

Figure 5. EDS spectrum indicates silica and kaolinite with minor calcite and muscovite; trace pyrite. The coating is platinum. Note: Au/C and Pt peaks are from the gold/carbon (limited) or platinum coating. Pt has mostly been used as the carbon then becomes relevant to the sample itself rather than the coating. Identifications from Weston (1984).

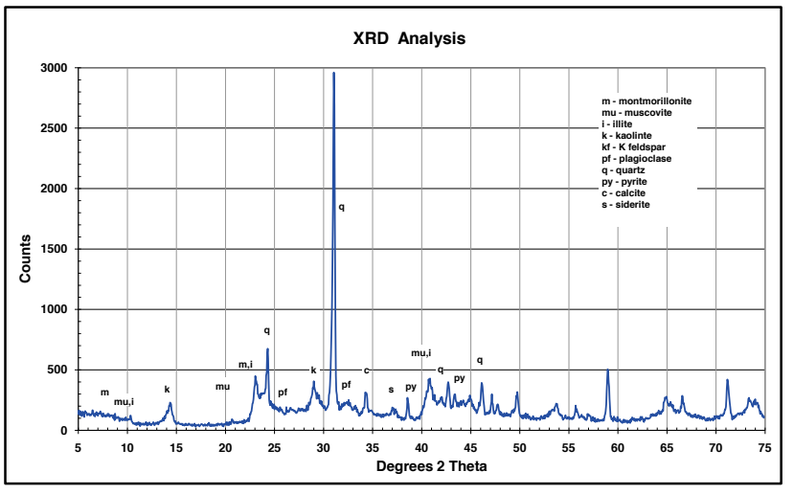

Figure 6. X-ray diffraction plot of a (powder) spectrum indicating the crystallographic peaks of minerals present; i.e., kaolinite and quartz with illite, smectite, and trace calcite and feldspar. Degrees 2-theta = angle of diffraction.

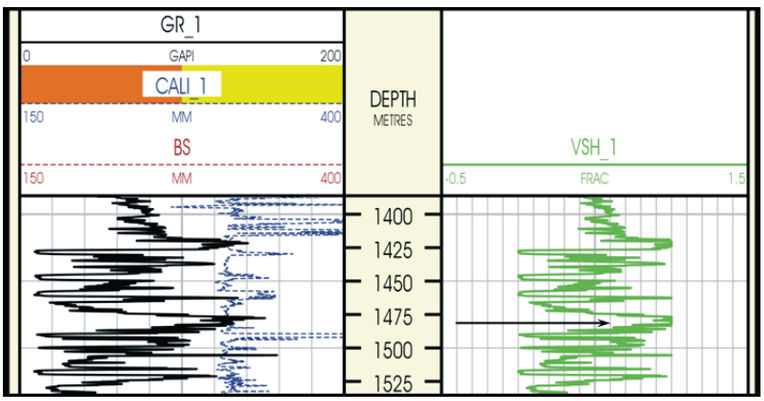

Figure 7. Part of a 400 m (1312 ft) section of a shale volume log (V_{sh}) centrally located on either side of the sample depth, highlighting mud-rich intervals. The curve is derived from the V_{sh} algorithm in the Geolog 6 desktop package. Gamma (GA) and calliper (CALI) curves are shown on the left. Bs = bitsize; GAPI = American Petroleum Institute gravity units; MM = millimeters.

Table 2. Possible Mineralogical Interpretations from EDS Element Combinations*

Elements Highlighted on EDS Spectra	Interpreted Mineralogy
Si with O	Silica
Si with O and significant Al with a combination of minor Na, Mg, K, Ca, or Fe	Clay; i.e., kaolinite, smectite, illite, montmorillonite
O with Ca/Mg and significant C	Calcite
O with Mg/Fe and significant C	Dolomite
O with Fe and significant C	Siderite
Fe and S	Pyrite
Si with O, Al, and K (sometimes K can relate to KCl drilling muds if cuttings are being analyzed)	K feldspar
Si with O, Al, and Na/Ca	Plagioclase
Ti (titanium) and O	Anatase/rutile
C (relatively high) usually with Fe and S (pyrite) and low Ca/Mg (i.e., not carbonate)	Carbonaceous material
Si with O and Al with Fe and K — no S (pyrite), nor C (carbonate)	Chlorite/berthierine

*Au/C and Pt peaks are from the gold/carbon (limited) or platinum coating. Pt has mostly been used as the carbon then becomes relevant to the sample itself rather than the coating.

Company: Geologic Asscoiates Inc.
Well: Various
Field: McFarland Area
County, State: Kern, CA

File No: 20083
API No:
Core Type: Various
Date: 2/23/2021

BEST CORE SERVICES

MICP ANALYSIS REPORT

						CO2/Brine	CO2/Brine QV	CO2/Brine QV	MICP								ROUTINE			
ID	WELL	DEPTH	Formation	Lithology	grain/clay	ENTRY	MAX HAFWL	SEAL CAP	Ka	Porosity	GD	BD	FE POR	SWIR	CEC	QV	Ka	Porosity	GD	BD
1	Rocket Abrams 1	4233-4258	Vedder	Sandstone	0.87	24.6	136.5	46.4	0.97	26.9	2.58	2.16	21.2	96.4	58.15	4.07	1.5	24.2	2.54	2.17
2	Rocket Abrams 1	4308-4333	Vedder	Sandstone	2.33	0.9	6.9	2.3	90.5	30.5	2.61	2.12	25.5	75.7	31.51	1.87	56.6	24.6	2.56	2.18
3	Gen Pet Stiles 1	2803-2806	San Joaquin	Sandstone	0.35	193.1	1639.1	557.1	0.039	26.5	2.60	2.18	20.2	100.0	82.49	5.95				
5	Gen Pet Stiles 1	4809-4812	Fruitvale	Sandstone	0.47	557.1	3951.5	1343.0	0.0023	18.1	2.52	2.25	1.8	100.0	77.28	8.81				
6	Armstrong 1	2105-2125	Etchegoin	Siltstone	0.96	37.0	700.4	238.0	0.17	46.5	2.51	1.81	40.3	97.9	55.66	1.61	0.8	45.8	2.56	1.84
13	Bailey Alta 1	1470	Etchegoin	Mudstone	0.46	55.5	476.2	161.9	0.13	35.4	2.55	2.00	23.2	99.9	76.05	3.54				
10	Bailey Alta 1	2028	Etchegoin	Mudstone	1.08	9.7	45.6	15.5	1.49	33.3	2.56	2.04	28.6	97.3	53.30	2.73				
11	Wright Bloemer 74-11	4369-4379	Pyramid Hills	Sandstone	1.63	7.4	50.1	17.0	2.12	21.9	2.63	2.28	18.2	95.3	38.00	3.58	3.4	26.2	2.60	2.18
12	Wright Bloemer 74-11	4389-4399	Pyramid Hills	Sandstone	2.33	1.0	13.8	4.7	23.3	30.0	2.63	2.14	28.8	67.2	27.57	1.70	12.2	18.8	2.63	2.32
36	Shell Bell 52-21	4801-4805	Freeman Jewett	Siltstone	0.80	7.4	41.5	14.1	2.33	18.9	2.45	2.18	17.5	93.8	58.15	6.11	2.0	24.1	2.53	2.16
14	Shell Bell 52-21	5057-5068	4th Vedder	Sandstone	5.25	0.5	2.8	0.9	395.8	34.3	2.65	2.08	32.3	38.1	17.45	0.89	121.8	27.7	2.60	2.15
7	KCL A 83-85	6400-6410	McClure	Mudstone	1.47	1466.7	11405.2	3876.2	0.0006	12.9	2.41	2.23	0.1	100.0	31.78	5.16				
9	KCL A 83-85	6410-6420	McClure	Mudstone	2.28	607.6	10440.0	3548.1	0.0010	14.3	2.26	2.08	0.8	100.0	19.88	2.69				
8	KCL A 83-85	6440-6450	McClure	Mudstone	1.04	328.0	3952.4	1343.3	0.0011	13.3	2.42	2.23	1.8	100.0	37.21	5.88				
15	KCL A 83-85	6720-6728	Fruitvale	Mudstone	1.38	391.4	3037.6	1032.4	0.0001	8.4	2.32	2.21	0.6	100.0	30.78	7.81				
16	KCL A 83-85	6971-6980	Olcese	Limestone	99.00	1.1	143.1	48.6	0.0093	1.9	2.69	2.66	1.3	50.6	0.00	0.00				
17	KCL A 83-85	7000-7010	Olcese	Sandstone	21.22	0.2	1.1	0.4	1800.8	32.5	2.61	2.08	32.2	7.4	2.52	0.14	1709.1	20.0	2.63	2.30
18	KCL A 83-85	7155-7177	Olcese	Sandstone	3.55	1.2	9.2	3.1	24.3	27.5	2.64	2.19	26.6	72.7	25.40	1.77				
19	KCL A 83-85	8161-8170	Freeman Silt	Siltstone	1.08	557.0	1500.4	509.9	0.0009	12.3	2.63	2.43	1.5	100.0	33.88	6.33	0.01	3.4	2.43	2.38
20	KCL A 83-85	8350-8360	RB Vedder	Sandstone	21.22	0.3	1.7	0.6	529.7	26.9	2.64	2.19	26.4	11.9	2.52	0.18				
21	KCL A 83-85	8360-8367	Vedder	Sandstone	24.00	0.4	2.0	0.7	227.1	25.6	2.66	2.24	24.9	17.2	3.58	0.28				
23	KCL A 83-85	8380-8390	Vedder	Sandstone	2.45	10.7	60.61	20.6	1.18	17.7	2.61	2.32	13.9	95.4	24.80	3.02				
24	KCL A 83-85	8499-8510	Vedder	Silty Sandstone	5.67	1.4	13.16	4.5	5.25	18.4	2.61	2.31	16.3	77.1	15.35	1.77	0.1	5.4	2.66	2.57
25	KCL A 83-85	8520-8530	Vedder	Sandstone	4.26	0.5	3.24	1.1	58.0	25.5	2.63	2.21	23.5	69.2	20.93	1.61				
26	KCL A 83-85	8633-8643	Vedder	Sandy Siltstone	6.14	103.7	1789.868	608.3	0.0026	9.8	2.61	2.46	4.6	100.0	14.20	3.41	0.2	10.3	2.62	2.45
27	KCL A 83-85	8833-8843	Vedder	Sandy Siltstone	2.33	11.7	124.78	42.4	0.105	14.8	2.64	2.40	9.7	98.3	32.63	4.96				
28	KCL A 83-85	8985-8991	Vedder	Mudstone	1.63	328.2	1374.178	467.0	0.0033	11.9	2.63	2.44	5.8	100.0	35.82	6.99				
29	KCL 25 1	6131	Gould Shale	Mudstone	5.25	358.3	1372.710	466.5	0.0003	9.6	2.20	2.09	1.1	100.0	17.45	3.64				
30	KCL 25 1	6194	Olcese	Limestone	99.00	3.9	15.25	5.2	0.46	6.2	2.67	2.57	5.9	29.4	1.18	0.48	1.2	4.1	2.67	2.60

*** QV calculated from XRD data**
SWIR=SW at reserovir Pc of 100PSI

GEOMECHANICAL ANALYSIS

TRIAXIAL COMPRESSIVE STRENGTH
STATIC & DYNAMIC PROPERTIES

FINAL REPORT - REVISED

Best Core Servcies

Multiple Wells
Sidewall Core Samples

Performed by
Igor Faoro, Senior Technical Advisor
Sean Arrington, Laboratory Supervisor

Report Issued
June 29,2021

Project No.
US-21-J9

GEOMECHANICAL REPORT - Summary Tables

Sidewall Core Plug Samples
Triaxial Compressive Strength (TXC) Testing

Client: Best Core Services
Well: Multiple (listed below)
Location: N/A

Revised Report Date: 6/29/2021
Premier Job Number: US-21-J9

TRIAXIAL COMPRESSIVE STRENGTH

Well Name	Sample ID	Core Depth (ft)	Sample Orientation	Orientation (degrees)	Diameter (in)	Length (in)	L:D ratio	Weight (g)	Bulk Density (g/cc)	Confining Stress (psi)	Peak Strength (psi)	Static PR µ1	Static YM (psi)	Dynamic YM (psi)
Shell Bell 52-21	1	4801.0	Horizontal	90										
Shell KCL A 83-85	3	8499.0	Horizontal	90	0.762	1.411	1.851	26.10	2.476	2850	11413	0.129	8.61E+05	1.78E+06
General Petroleum Co. KCL 25 #1	5	6194.0	Horizontal	90	0.738	1.109	1.504	19.02	2.450	2050	16061	0.338	1.85E+06	3.72E+06
Independent Exploration Co. Wright Bloemer 74-11	6	4389.0	Horizontal	90										

Notes & Observations:

Sample 1 (4801.0') and sample 6 (4389.0') failed during the initial loading into the test apparatus; no static or dynamic data was captured.
Dynamic Young's Modulus (YM) are always higher in magnitude than the Static YM in a given material tested at similar conditions.
This variation in Dynamic to Static YM values are generally inversely proportional to the modulus of elasticity (Young's Modulus) magnitude.
Low YM value material will generally have a higher spread in Dynamic:Static magnitudes with variation decreasing as YM magnitudes increase.

GEOMECHANICAL REPORT - Summary Tables

Sidewall Core Plug Samples

Triaxial Compressive Strength (TXC) Testing

Client: Best Core Services

Well: Multiple (listed below)

Location: N/A

Revised Report Date: 6/29/2021

Premier Job Number: US-21-J9

DYNAMIC PROPERTIES

Well Name	Sample ID	Core Depth (ft)	Sample Orientation	Confining Stress (psi)	Peak Strength (psi)	Comp. Wave Vp (ft/sec)	Shear Wave Vs (ft/sec)	Vp:Vs (ratio)	Dynamic Young's Modulus (psi)
Shell Bell 52-21	1	4801.0	Horizontal						
Shell KCL A 83-85	3	8499.0	Horizontal	2850	11413	13082	5667	2.31	1.78E+06
General Petroleum Co. KCL 25 #1	5	6194.0	Horizontal	2050	16061	14690	6319	2.32	3.72E+06
Independent Exploration Co. Wright Bloemer 74-11	6	4389.0	Horizontal						

Notes & Observations:

Sample 1 (4801.0') and sample 6 (4389.0') failed during the initial loading into the test apparatus; no static or dynamic data was captured.

Dynamic Young's Modulus (YM) are always higher in magnitude than the Static YM in a given material tested at similar conditions.

This variation in Dynamic to Static YM values are generally inversely proportional to the modulus of elasticity (Young's Modulus) magnitude.

Low YM value material will generally have a higher spread in Dynamic:Static magnitudes with variation decreasing as YM magnitudes increase.

GEOMECHANICAL REPORT

Sidewall Core Plug Samples
Triaxial Compressive Strength (TXC) Testing

Client: Best Core Services
Well: Multiple (listed Below)
Location: N/A

Report Date: 6/29/2021
Premier Job Number: US-21-J9

Well Name	Sample ID	Core Depth (ft)	Diameter (in)	Length (in)	Weight (g)	Bulk Density (g/cc)	Confining Stress (psi)	Peak Strength (psi)	Static PR µ1	Static YM (psi)	Dynamic YM (psi)
Shell KCL A 83-85	3	8499.0	0.762	1.411	26.10	2.476	2850	11413	0.129	8.61E+05	1.78E+06
General Petroleum Co. KCL 25 #1	5	6194.0	0.738	1.109	19.02	2.450	2050	16061	0.338	1.85E+06	3.72E+06

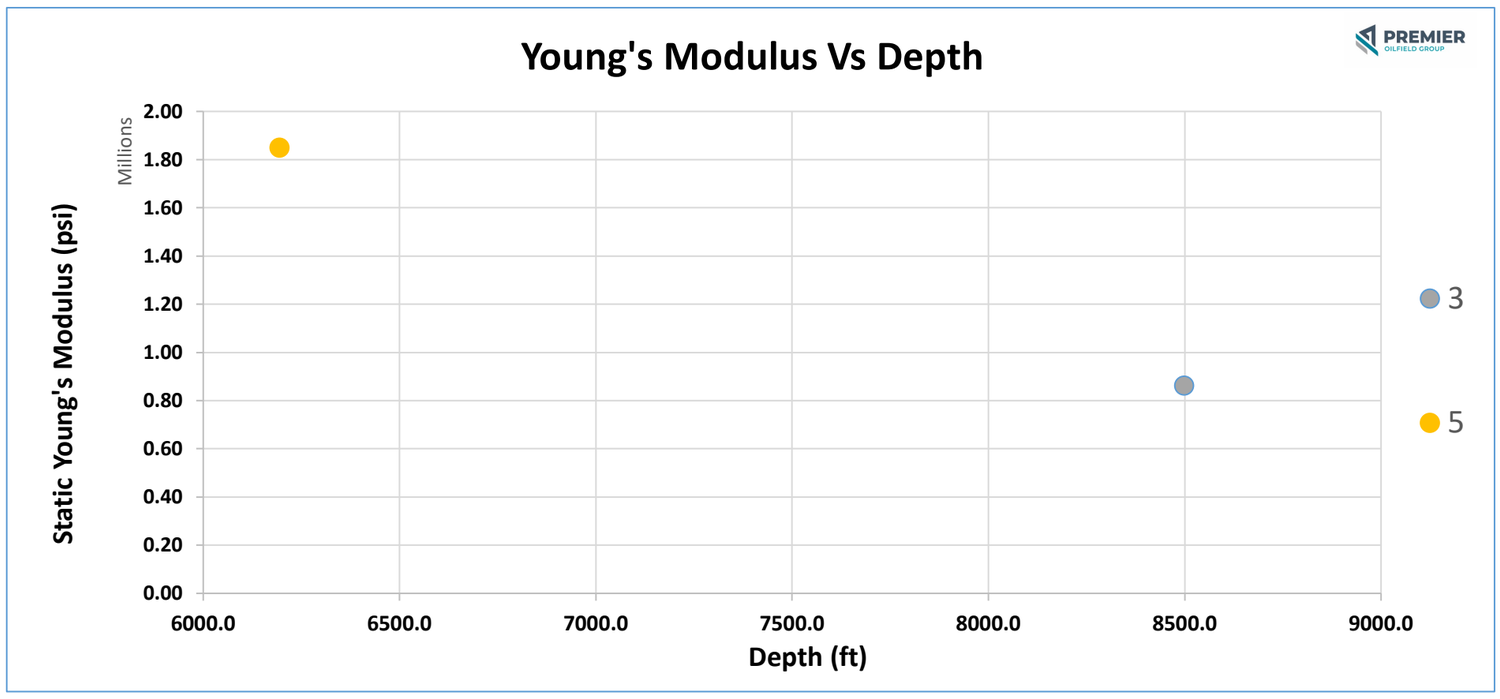

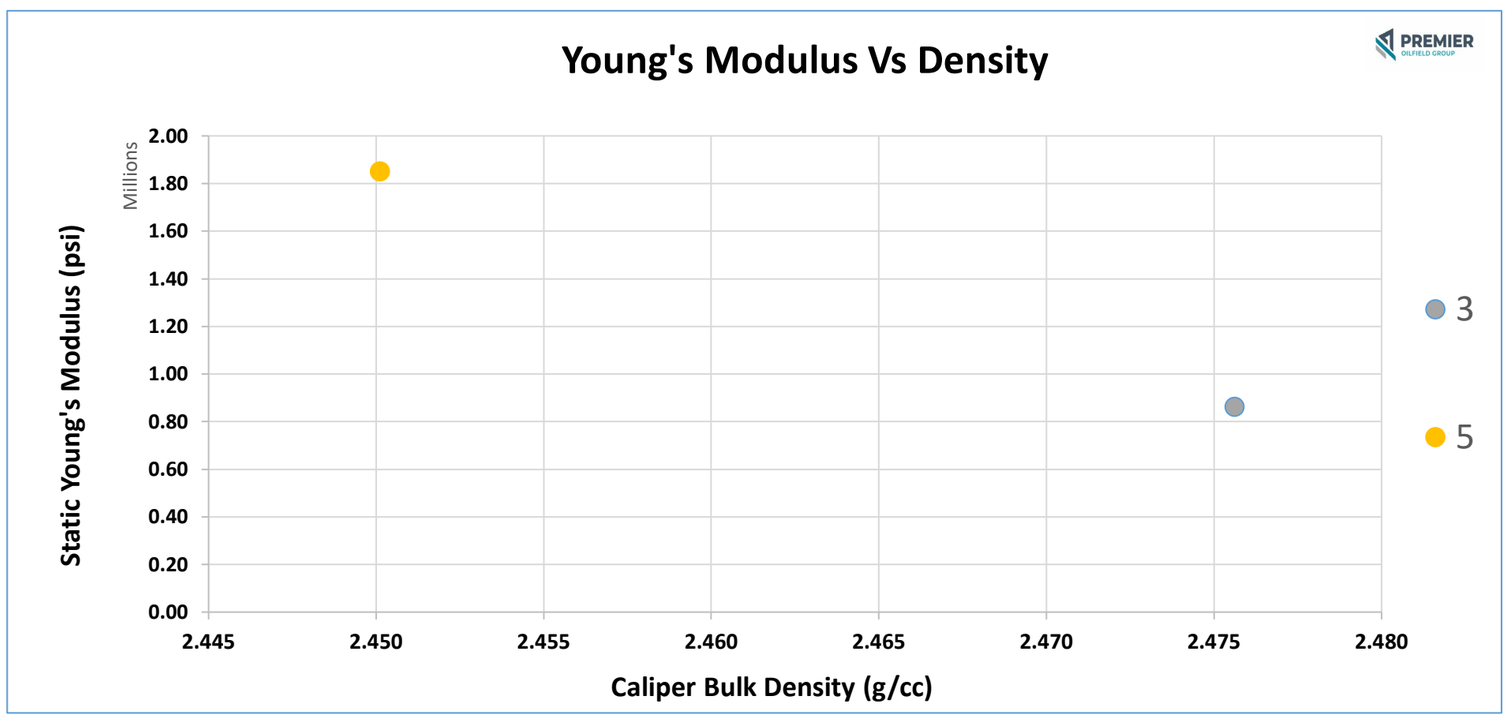

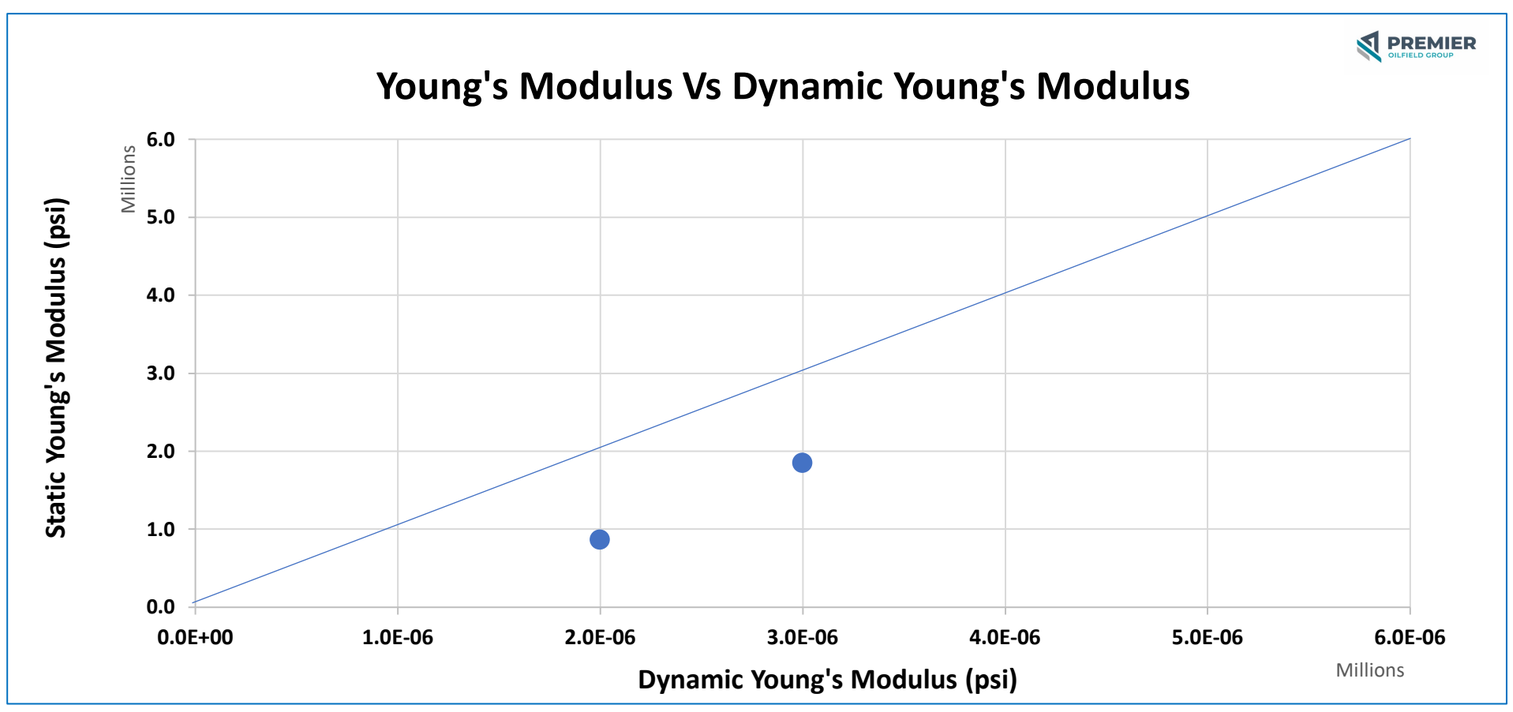

GEOMECHANICAL REPORT

Sidewall Core Plug Samples
Triaxial Compressive Strength (TXC) Testing

Client: Best Core Services
Well: Multiple (listed Below)
Location: N/A

Report Date: 6/29/2021
Premier Job Number: US-21-J9

Well Name	Sample ID	Core Depth (ft)	Diameter (in)	Length (in)	Weight (g)	Bulk Density (g/cc)	Confining Stress (psi)	Peak Strength (psi)	Static PR µ1	Static YM (psi)	Dynamic YM (psi)
Shell KCL A 83-85	3	8499.0	0.762	1.411	26.10	2.476	2850	11413	0.129	8.61E+05	1.78E+06
General Petroleum Co. KCL 25 #1	5	6194.0	0.738	1.109	19.02	2.450	2050	16061	0.338	1.85E+06	3.72E+06

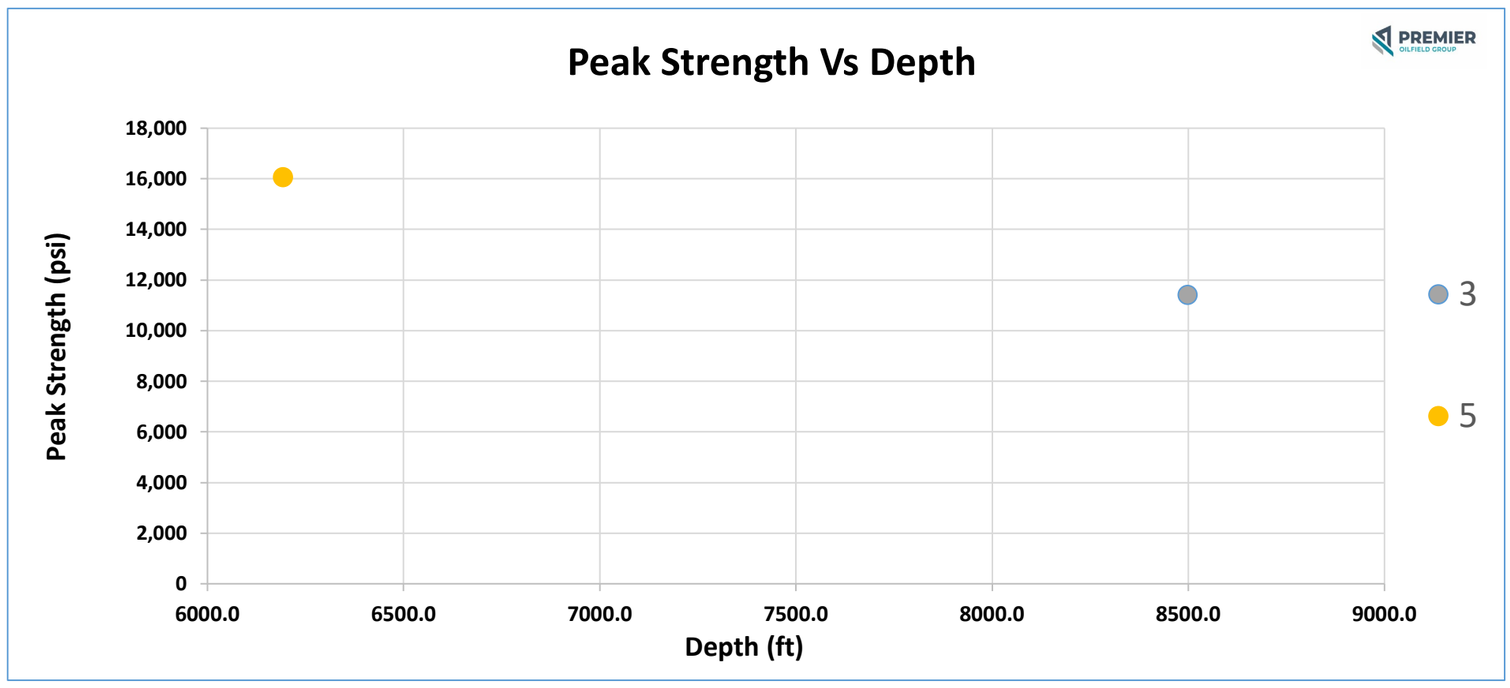

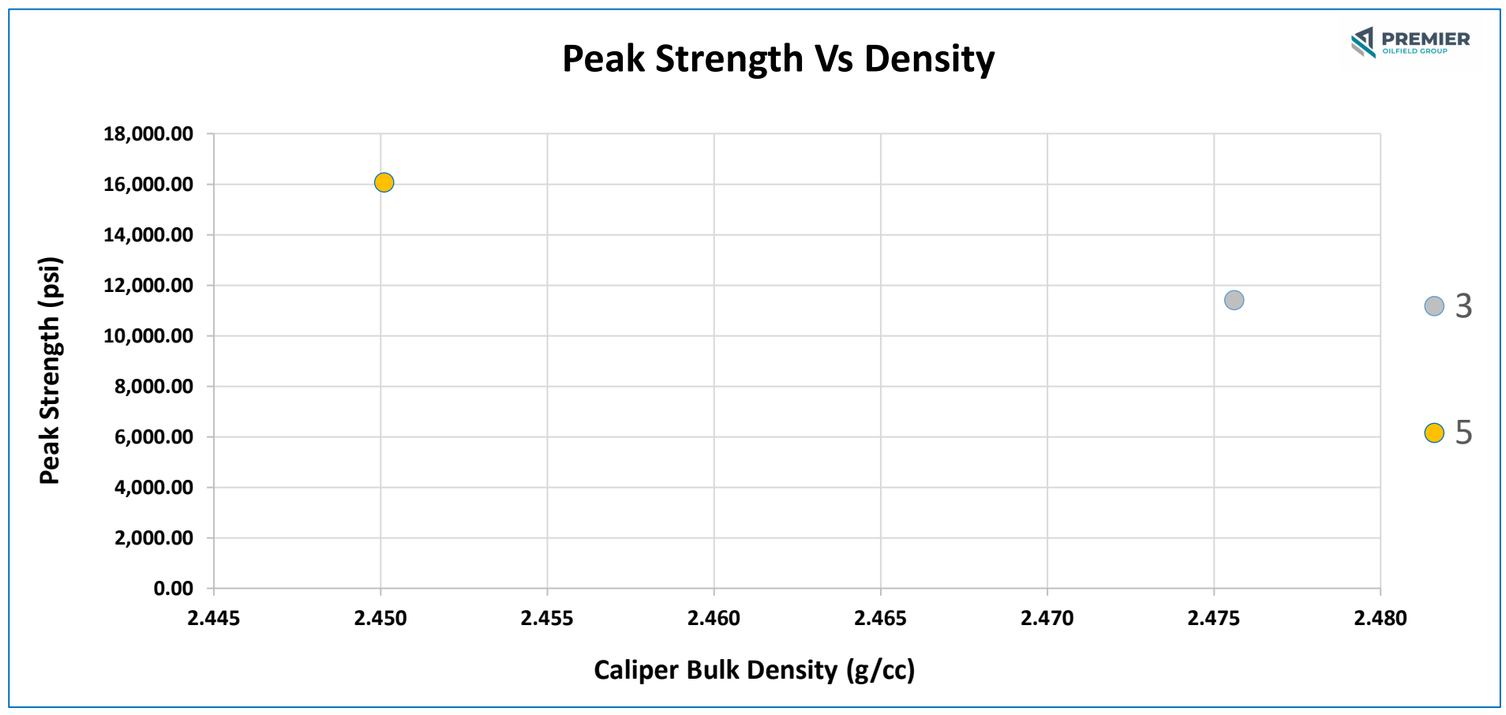

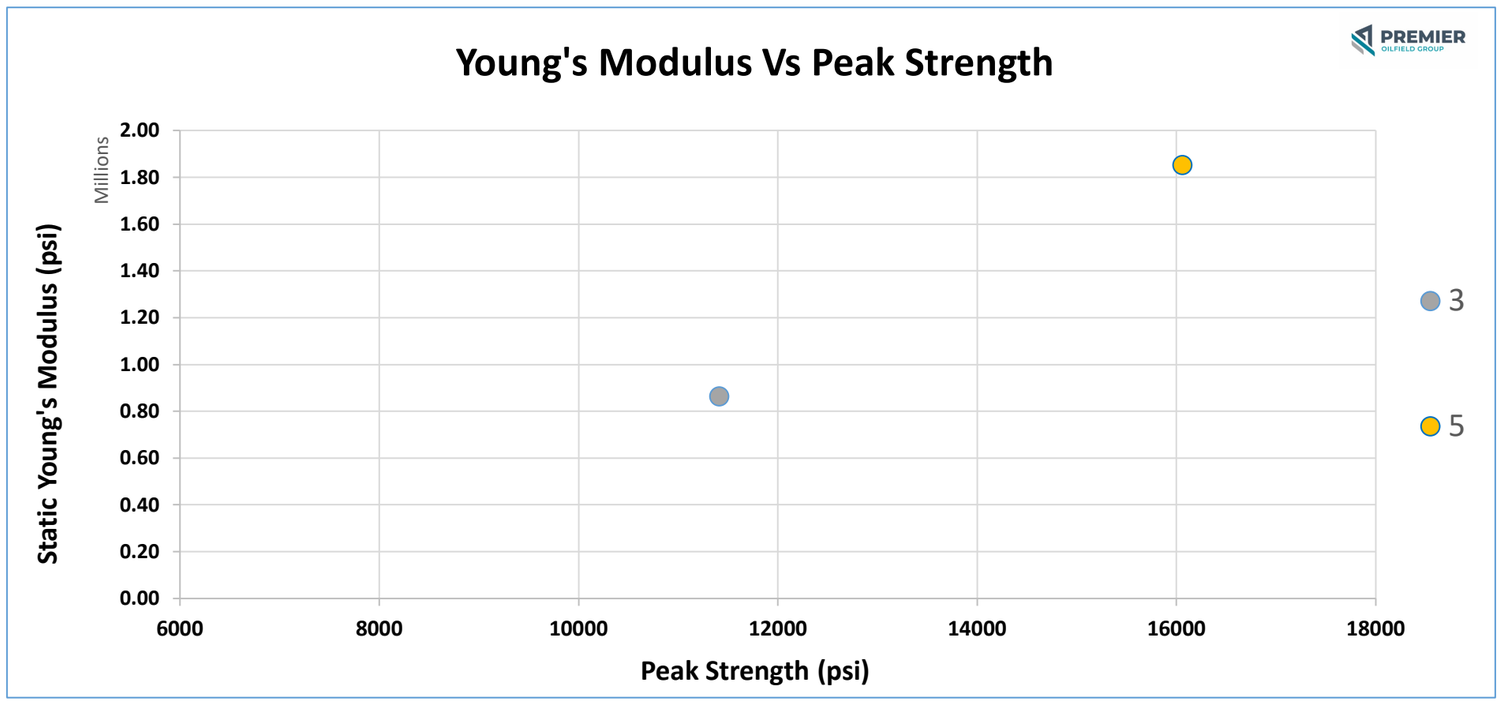

GEOMECHANICAL REPORT

Received Core Plug Samples

Triaxial Compressive Strength (TXC) Testing

Client: Best Core Services

Well: Multiple (listed Below)

Location: N/A

Report Date: 6/29/2021

Premier Job Number: US-21-J9

Well Name	Sample ID	Core Depth (ft)	Confining Stress (psi)	Peak Strength (psi)	Static PR µ1	Comp. Wave VP (ft/sec)	Shear Wave Vs (ft/sec)	Dynamic YM (Mpsi)
Shell KCL A 83-85	3	8499.0	2850	11413	0.129	13082	5667	1.78

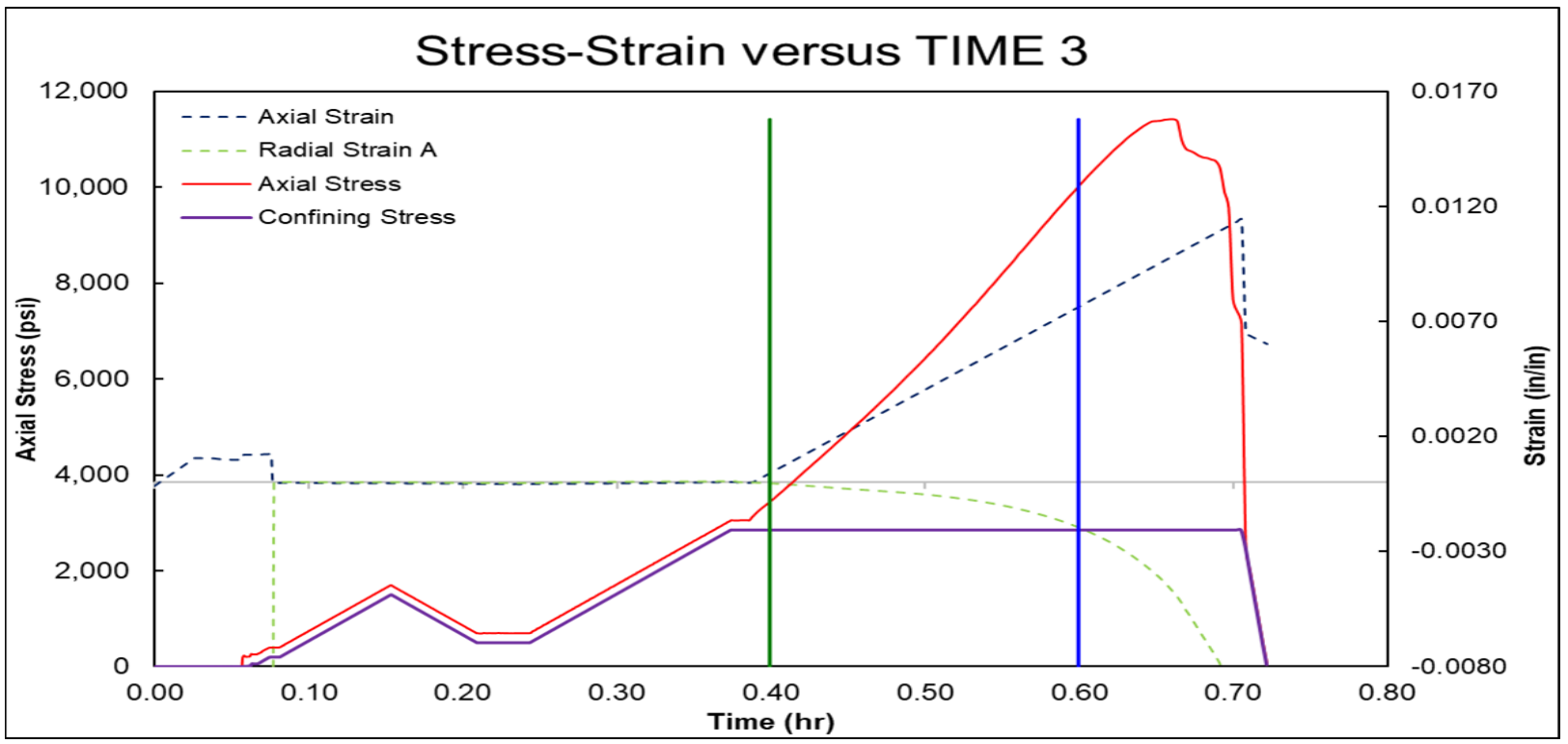

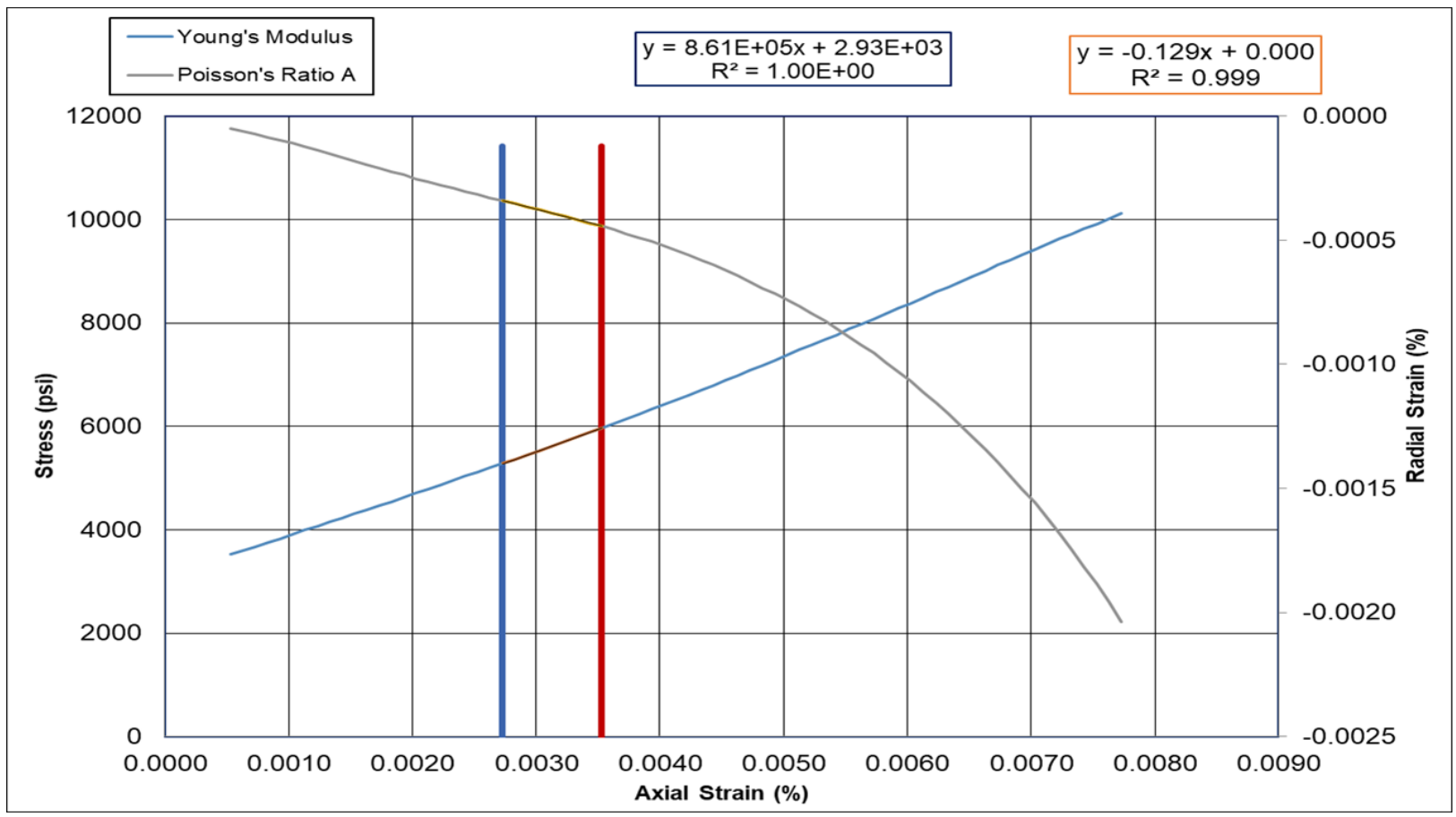

GEOMECHANICAL REPORT

Received Core Plug Samples

Triaxial Compressive Strength (TXC) Testing

Client: Best Core Services
Well: Multiple (listed Below)
Location: N/A

Report Date: 6/29/2021
Premier Job Number: US-21-J9

Well Name	Sample ID	Core Depth (ft)	Confining Stress (psi)	Peak Strength (psi)	Static PR μ1	Comp. Wave VP (ft/sec)	Shear Wave Vs (ft/sec)	Dynamic YM (Mpsi)
Shell KCL A 83-85	3	8499.0	2850	11413	0.129	13082	5667	1.78

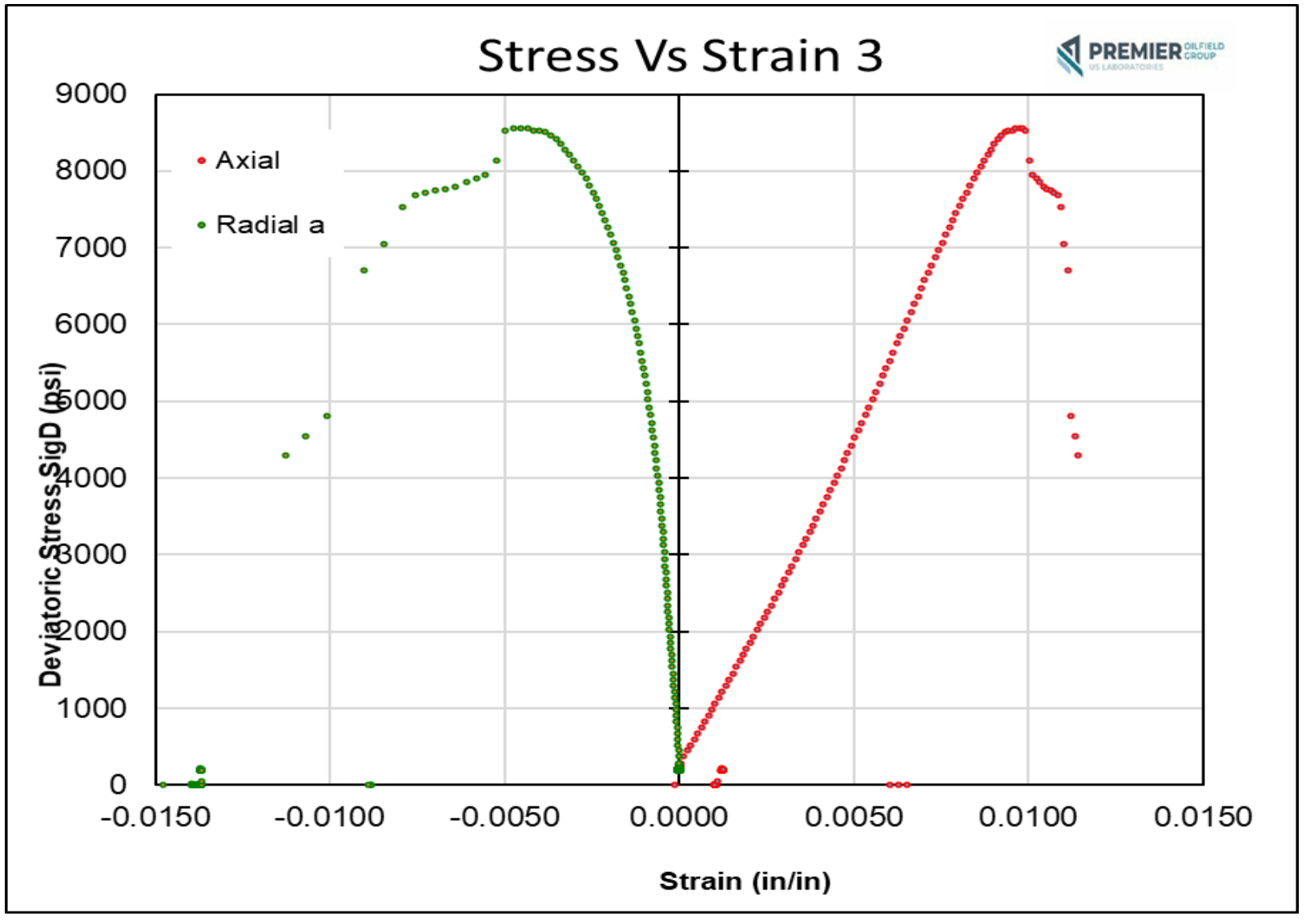

GEOMECHANICAL REPORT

Received Core Plug Samples
Triaxial Compressive Strength (TXC) Testing

Client: Best Core Services
Well: Multiple (listed Below)
Location: N/A

Report Date: 6/29/2021
Premier Job Number: US-21-J9

Well Name	Sample ID	Core Depth (ft)	Confining Stress (psi)	Peak Strength (psi)	Static PR μ1	Comp. Wave VP (ft/sec)	Shear Wave Vs (ft/sec)	Dynamic YM (Mpsi)
General Petroleum Co. KCL 25 #1	5	6194.0	1450	16061	0.338	14690	6319	3.72

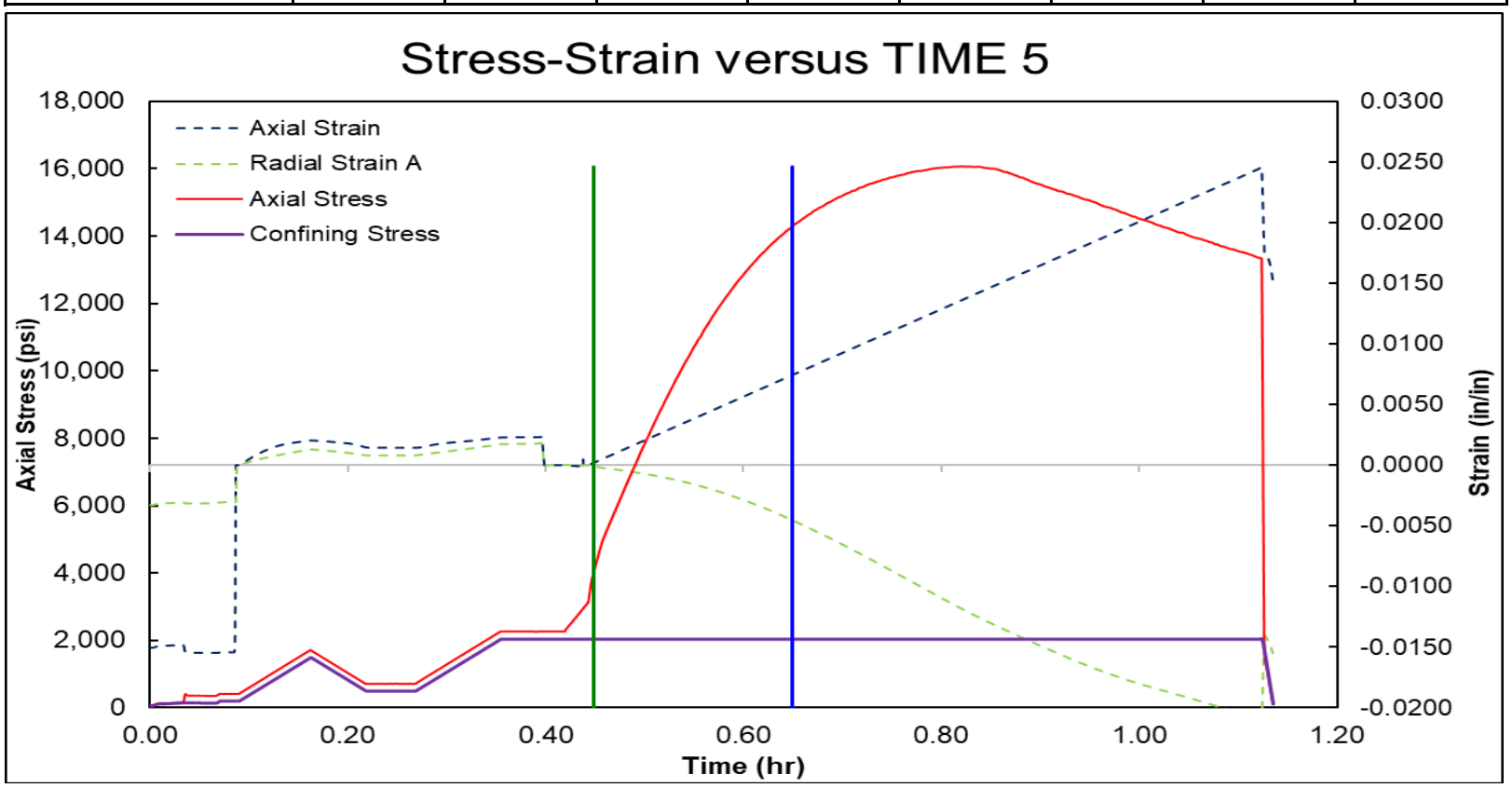

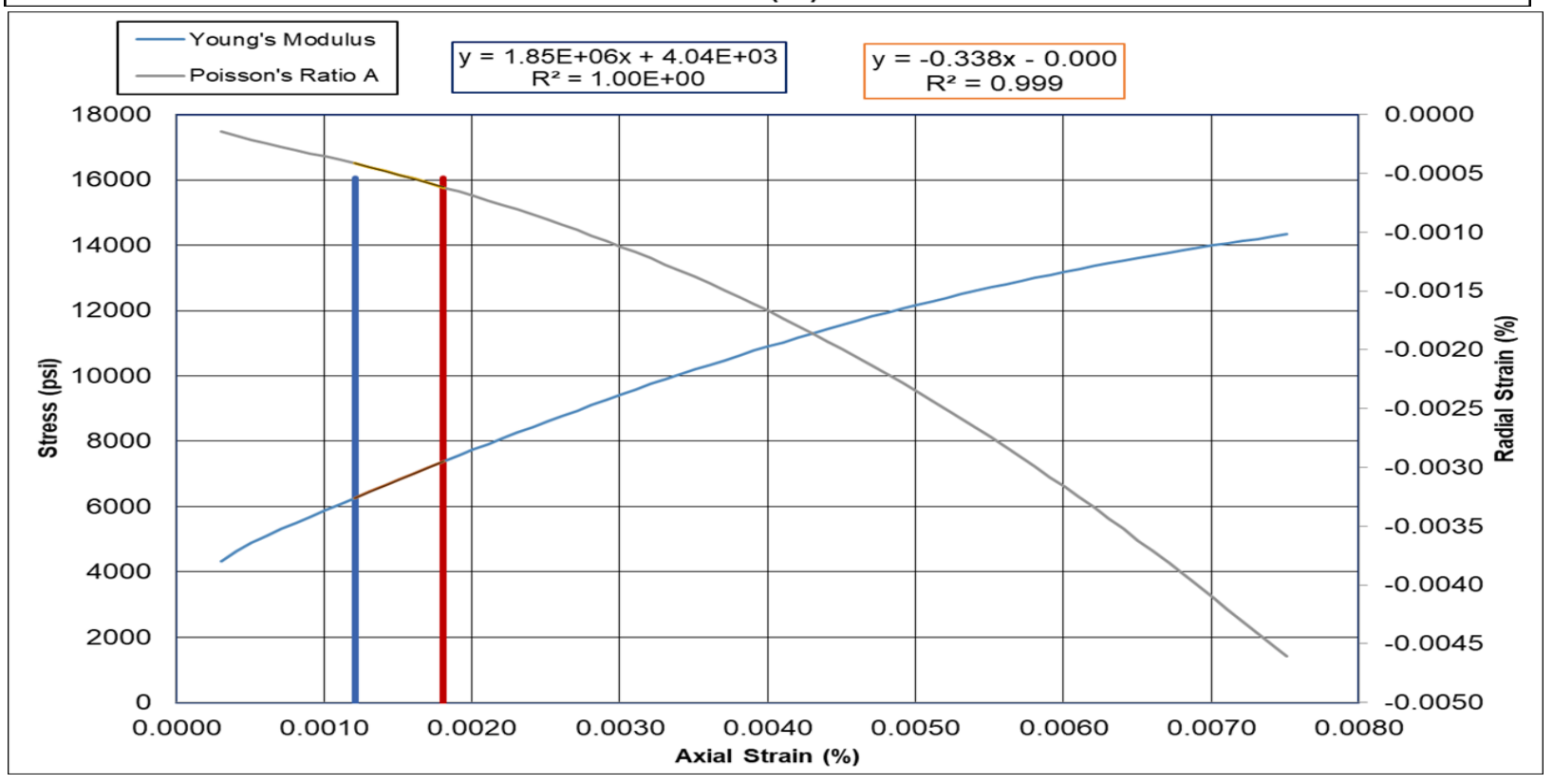

GEOMECHANICAL REPORT

Received Core Plug Samples

Triaxial Compressive Strength (TXC) Testing

Client: Best Core Services
Well: Multiple (listed Below)
Location: N/A

Report Date: 6/29/2021
Premier Job Number: US-21-J9

Well Name	Sample ID	Core Depth (ft)	Confining Stress (psi)	Peak Strength (psi)	Static PR μ1	Comp. Wave VP (ft/sec)	Shear Wave Vs (ft/sec)	Dynamic YM (Mpsi)
General Petroleum Co. KCL 25 #1	5	6194.0	1450	16061	0.338	14690	6319	3.72

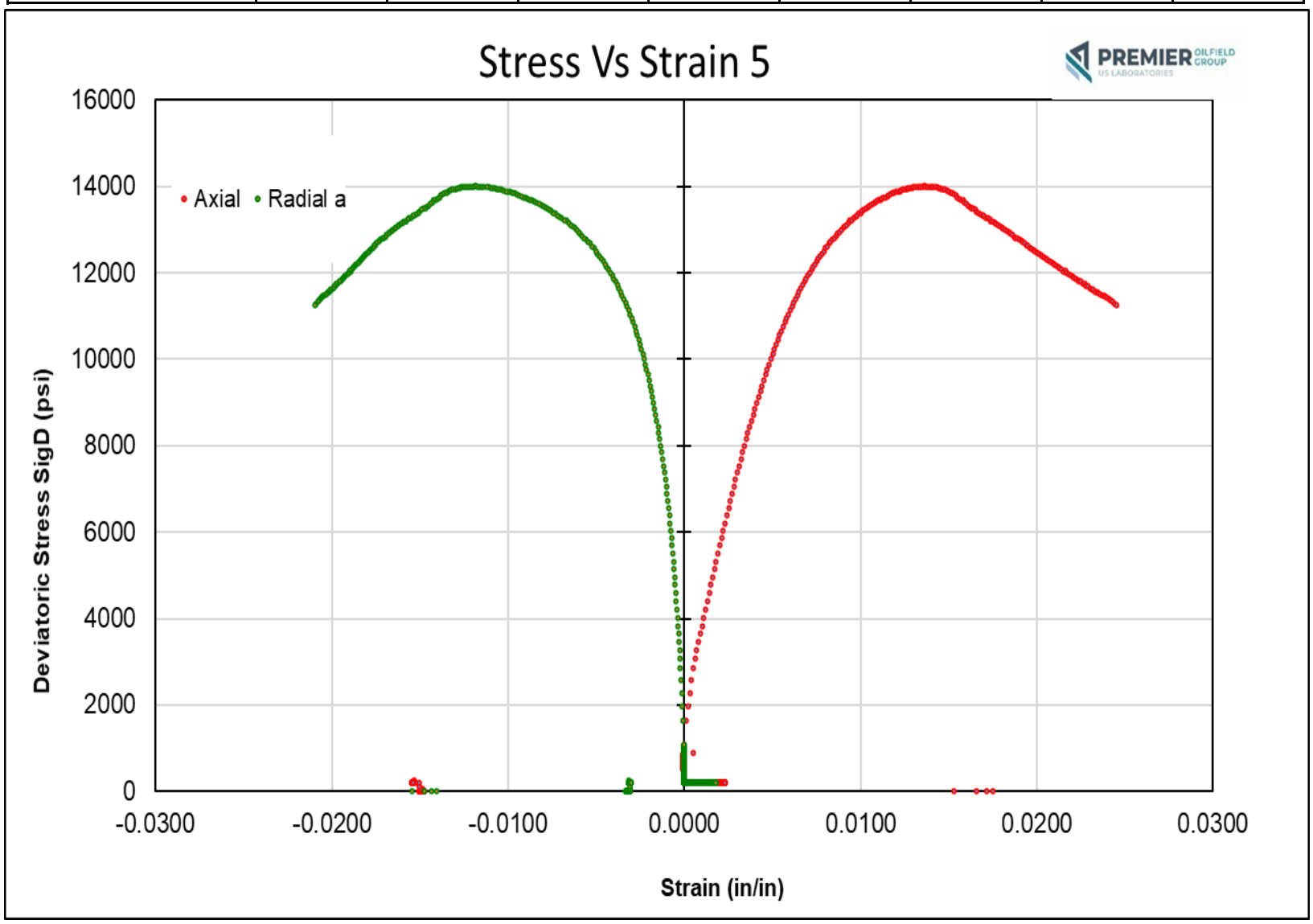

Testing Overview

Individual samples were tested triaxially for defined HRZ stress condition(s). Each sample was loaded via axial strain control at 1e-5 in/in/sec through catastrophic sample failure. All samples were vented to atmosphere. If applicable, samples were unloaded after reaching "residual" stress conditions or in the case of a jacket failure post test. UCS tests were unloaded immediately post failure. Testing was conducted in accordance to the following references:

-ASTM- D7012-14e1 Standard Test Methods for Compressive Strength and Elastic Moduli of Intact Rock Core Specimens under Varying States of Stress and Temperatures
-ISRM- Suggested Methods for Rock Characterization Testing and Monitoring.
-Developments in Petroleum Science, Vol 64 Chapter 12.4

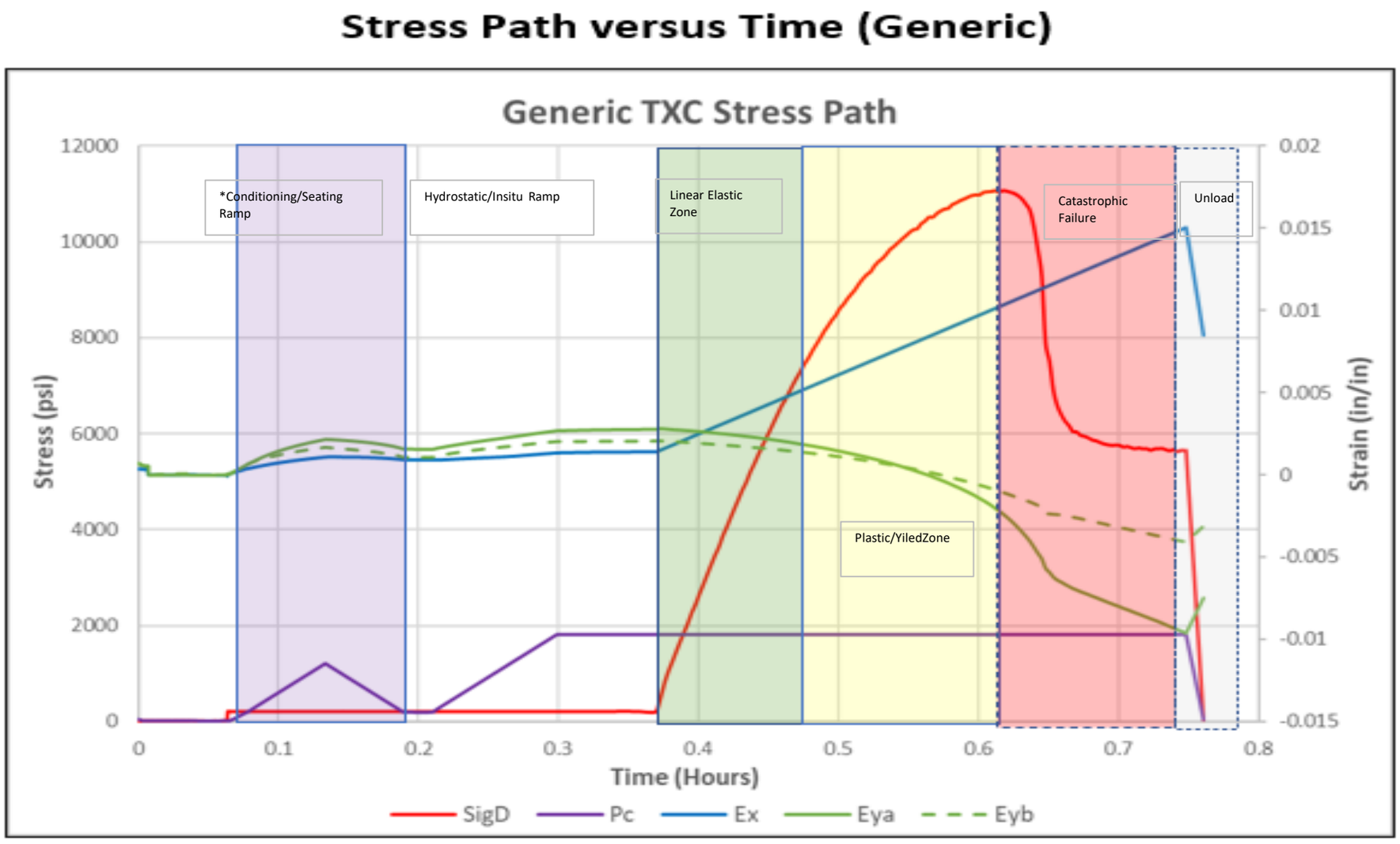

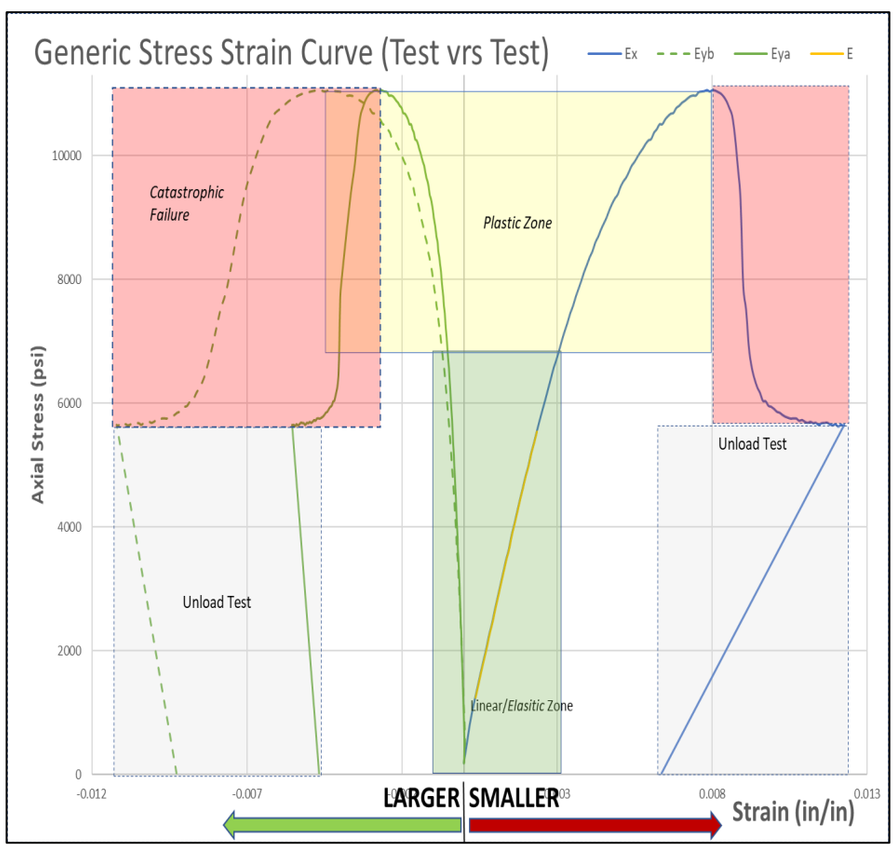

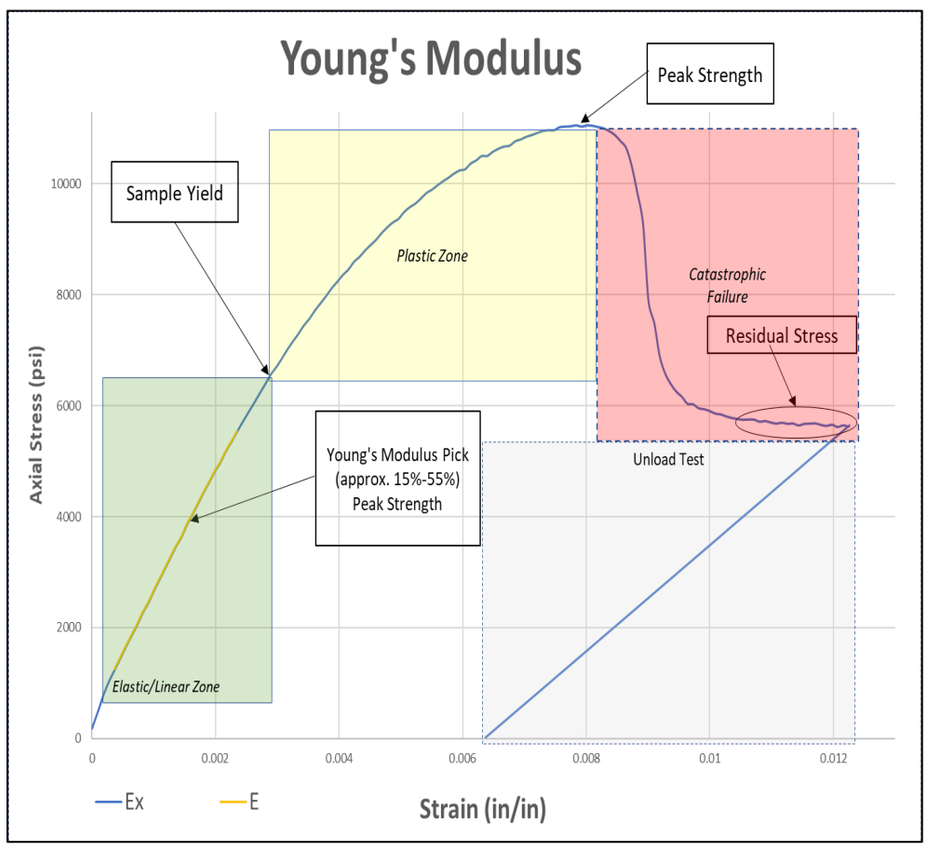

Testing Setup

***Sample size*:** All samples were strived to meet defined ASTM standards (2:1 length to diameter ratio, parallel within 0.001" 90-degree cylinder) in respect to Rock Mechanics testing. Sample size was 0.75" x 1.5" plugs. Parallelism was verified within 0.0005'. Sample length to diameter ratio was reported for each plug in the sample description overview. Generally, acceptable tolerance from 1.55 to 2.15.

1. ***Record Sample Information:*** The following information was recorded locally in a testing lab notebook and in DAQ software prior to testing: length, diameter, mass, density, orientation, depth and horizontal stress conditions.

2. ***Build Sample Stack*:** A "stack" is constructed consisting of a plug sandwiched between (2) Acoustic Endcaps (AEC). Axial and radial deformation sensors are attached and verified for alignment.

3. ***Load Stack in Testing Vessel:*** Sample record information is verified prior to a completed stack being inserted into the load-frame. All sensors are connected to the DAQ system and verified for functionality. Sensor alignment is verified one last time.

General Testing Procedures

1. ***Triaxial Compression Tests (all tests) (TXC)***: A segment test is defined/modified and initiated. The sample stack is then lifted into the pressure vessel and aligned on a reaction column. The pressure vessel is filled with oil. After stabilization is observed, horizontal In-situ stress is applied via confining pressure at a defined rate (3 psi/sec). After strain stabilization is observed, the load piston is applied in strain control at 1e-5 in/in/sec through sample failure. Tests are unloaded after reaching "residual" stress.

   Static and Dynamic data are monitored and collected throughout the entirety of the test.

1. ***Quality Control Initial Results***: All samples are visually inspected prior to testing. uCT is referenced for sample selection and QA purposes.

   In-test deformation and strain behavior are monitored continuously and evaluated for consistency. Any non-physical/suspect behavior observed results in the test being unloaded. An example of "non-physical" behavior is observing the sample diameter increasing (getting bigger) through a hydrostatic pressure increase. This is generally caused by a jacket leak where confining oil gains access to inside the sample stack.

   Test results are monitored real time and evaluated for viability, and against similar known materials and expected behaviors. Bulk densities are compared for a set of sister samples. Calculated values such as Young's Modulus and Poisson's ratio are monitored in-test and evaluated for feasibility. An example of a "red flag" would be observing a Poisson's ratio greater than 0.5 or less than 0.1. This could be caused by a poor-quality stack build, sensor alignment issues, or an already failed/poor quality sample.

1. ***Post-Test Processing***: The sample is removed from the load frame, stack and placed in its original sample bag. A post-test photograph is taken. Test data is reduced and transferred to the local POFG network. Data analysis and reporting is then completed.

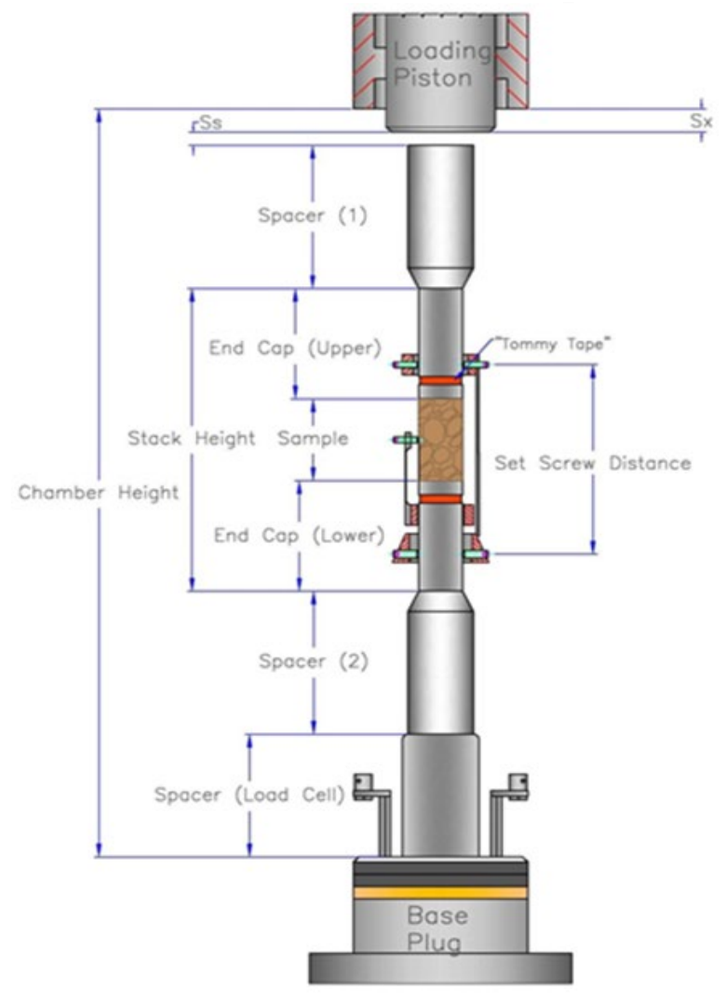

Calculations of Rock Mechanics

Below are the equations for the reported rock mechanical properties in both dynamic and static measurements:

	Dynamic*	Static
Young's Modulus	$E = \frac{\rho Vs^2(3Vp^2-4Vs^2)}{Vp^2-Vs^2}$	delta S_d /delta Ex
Poisson's Ratio	$V = \frac{Vp^2-2Vs^2}{2(Vp^2-Vs^2)}$	Ey/Ex
Bulk Modulus	$K = \rho\left(Vp^2 - \frac{4}{3Vs^2}\right)$	delta Sig3/delta Ev
Shear Modulus	ρVs^2	
Lame	$\rho(Vp^2 - 2Vs^2)$	
P-Wave Modulus	ρVp^2	
Constrained Modulus		Delta Sig1/Delta Ex (Uniax)

*Basic Isotropic Formula

General Nomenclatures

V or 0° and H or 90°: Vertically and horizontally oriented Plug/Property
S_d: Differential Stress (Axial Stress (S_1) – Confining Stress (S_3))
Vp(0): Compressional velocity through vertical plug (ft/sec)
Vp(90): Compressional velocity through horizontal plug(ft/sec)
V_{s1}: Velocity of shear wave polarized parallel to bedding (fast shear) (ft/sec)
V_{s2}: Velocity of shear wave polarized perpendicular to bedding (slow shear) (ft/sec)
Suffix s: Static Property
Suffix d: Dynamic Property
K: Bulk modulus (Mpsi)
E: Young's modulus (Mpsi)
PR: Poisson's ratio
G: Shear modulus (Mpsi)
Phi (ϕ): Porosity (%)
α_v: Vertical Biot's constant
α_h: Horizontal Biot's constant
S_v: Overburden stress (psi)
P_p: Pore Pressure
S_h: Total Minimum horizontal stress (psi)
$S_{h'}$: Effective Minimum horizontal stress (psi)
UCS: Unconfined Compressive Strength (psi)

Appendix G: Fracture Gradient Calculations

Determining reservoir pressures and overburden stress to estimate fracture initiation pressure is based on Pressure data from Jordan and Doughty (2009) indicates that reservoir pressure at 8000' should be 3400psi or 24 MPa and considering the assumption from Jordan and Doughty (2009) of a 50-50 sand/shale column, and from actual sample measurements from the whole stratigraphic column (Section 2.2.1) where bulk density of the measured data is 2.241 gm/cc. Average grain density is 2.572 gm/cc. and the average porosity is 21.04%. Porosity is brine filled (1.02 gm/cc)

From Petroleum and Gas Engineering.
http://2.bp.blogspot.com/RczfwoGtHNU/VqYT5mgngoI/AAAAAAAAFYw/ARmmnKxFcjo/s1600/gbgfgfb%2Bg.png

The equation for overburden gradient is used to determine stress at a given depth.

$$\sigma_{ovg} = 0.433[(1-\phi)\rho_{ma} + (\phi x \rho_f)]$$

where

σovg= overburden gradient, psi/ft

ϕ = porosity expressed as a fraction

ρ_f = formation fluid density, gm/cc

ρ_{ma} = matrix density, gm/cc

For overburden gradient the calculation would be = 0.433 ((1-.21.04)2.572 + (.21.04*1.02gm/cc))
.433 ((.7896)2.572 + .21.04*1.02))
.433((2.0308 + .2146))
.433 (2.24545)
Therefore, overburden gradient = 0.97228 psi/ft for the stratigraphic column.
Effective Stress at 8000' would therefore be 7,778.24 psi. The peak strength of the sample from the triaxial compressive strength test is 11,413psi.

Create the Fracture

- To cause the rock to break we supply pressure to the formation using a hydraulic fluid.
- The fluid is pumped to the formation at a rate that is faster than the pore space can accept.
- When we overload the matrix in this way, the applied pressure offsets the full pore pressure and effective horizontal stress.

- Expressed as a gradient this overload condition becomes -

$$\frac{\sigma_{Frac}}{D} = \frac{\nu}{1-\nu}\left(\frac{\sigma_V}{D} - \frac{p}{D}\right) + \frac{p}{D} \quad \text{psi/ft}$$

Where D = depth (feet)

Rock Mechanics – Absolute Vertical Stress

- Reservoirs exist at depth, buried by the overburden.
- The overburden exerts a pressure as a function of its density.
- The absolute vertical stress caused by the weight of the overburden is:

$$\sigma_v = \sigma_{SW} + \sigma_{ob}$$
$$\sigma_v = 0.433\gamma_{SW}D_{SW} + 0.433\gamma_{ob}D_s$$
$\sigma_v =$ absolute vertical stress (psi)
$\sigma_{SW} =$ sea water vertical stress (psi)
$\sigma_{ob} =$ sediment (overburden) vertical stress (psi)
$\gamma_{SW} =$ salt water specific gravity (1.02)
$D_{SW} =$ water depth (ft)
$\gamma_{ob} =$ average overburden specific gravity
$D_s =$ sediment depth (ft)

D	8000	depth (ft)		
v	0.129	poissons ratio(unitless)		
rhov	8000	vertical stress psi		
p	3400	pore pressure psi		
Calculated FG	0.5101607	psi/ft		
additional gradient	0.15	psi tectonic stress		
Frac Grad	0.6601607	total FG		

Based on the equations and utilizing the data from our samples, we calculate a fracture gradient of 0.5 psi/ft. Based on advice from engineers that have worked in the San Joaquin Basin of California, we have added a factor for tectonic stress of 0.15. This would indicate a total fracture gradient of 0.66 psi/ft.